

Научном већу Института за физику у Београду

Предлог за Студентску награду Института за физику у Београду

Поштовани,

Велико ми је задовољство да предложим др Душана Вудраговића за Студентску награду Института за физику у Београду за докторску дисертацију под називом "Faraday waves in ultracold dipolar Bose gases", коју је одбранио 24. децембра 2019. године на Физичком факултету Универзитета у Београду.

Др Душан Вудраговић се у свом научном раду бави проблемима ултрахладних бозонских гасова у присуству дипол-дипол интеракције, као и развојем паралелних нумеричких алгоритама и програма за нумеричке симулације ових физичких система.

У свом истраживању, које је детаљно описано у дисертацији, кандидат је проучавао феномене Фарадејевих и резонантних таласа густине, који настају као резултат хармонијске модулације система и представљају нелинеарне ексцитације система услед присуства интеракција, спрежањем колективних осцилација и параметарских резонанци. Мотивацију за ово представља добро познати класични феномен Фарадејевих таласа, који се појављују на површини плитког слоја течности уколико се посуда у којој се налази хармонијски осцилује у вертикалном смеру. У том случају појављују се површински таласи чије је патерне први посматрао и описао Мајкл Фарадеј почетком XIX века. Интерес за овакву врсту ексцитација појавио се поново осамдесетих година XX века у контексту нелинеарних течности, а у контексту ултрахладних гасова, Фарадејеви таласи су прво проучавани теоријски 2002. године. Иако су код течности у питању површински таласи, а у ултрахладним квантним гасовима се ради о таласима густине, користимо исти назив за те феномене. Након првих теоријских и нумеричких резултата за системе са контактном интеракцијом, у експериментима са Бозе-Ајнштајн кондензатом атома рубидијума су 2007. године Фарадејеви таласи измерени и карактерисани помоћу просторног периода, као и времена модулације које је потребно да се развију. У последњих неколико година феномен Фарадејевих таласа је поново добио на интересу због неколико важних експеримената који су објављени у водећим часописима (Nature, Physical Review Letters, Physical Review X).

С обзиром на све већи значај дугодометних интеракција и анизотропности система, што се посебно огледа у великом броју радова и експеримената који проучавају утицај дипол-дипол интеракције на особине ултрахладних бозонских система, кандидат се фокусирао на развој варијационог приступа за опис динамике Фарадејевих и резонантних таласа у диполним кондензатима, што раније није било урађено. Овај приступ је заснован на Гаусовом варијационом анзацу који за параметре има ширине кондензата, конјуговане фазе, а укључује и модулације густине како би описао динамику таласа густине.

Користећи развијени варијациони приступ, као и пун нумерички приступ, детаљно је проучавао особине таласа густине у диполним кондензатима на нултој температури, где дипол-дипол интеракција игра важну улогу због нарушења симетрије услед анизотропије система. Извео је једначине кретања које описују динамику модулисаних диполних бозонских система и идентификовао најнестабилније моде које одговарају Фарадејевим и резонантним таласима. Даље, на основу тога, извео је аналитичке изразе за просторне периоде оба типа таласа густине,

као и њихову зависност од јачине контактне и дипол-дипол интеракције. Добијене варијационе резултате упоредио је са резултатима детаљних нумеричких симулација које решавају диполну Грос-Питаевски једначину у три просторне димензије и добио веома добро слагање.

Кандидат је проучавао и утицај контактне и дипол-дипол интеракције на својства основног стања и колективних осцилација диполних кондензата. Док повећање јачине контактне интеракције увек доводи до ширења кондензата, ситуација је сложенија када се мења јачина дипол-дипол интеракције. За замку у облику цигаре у којој су диполи оријентисани у радијалном смеру, кандидат је показао да повећање јачине дипол-дипол интеракције доводи до ширења кондензата у лонгитудиналном правцу и у правцу поларизације, док се ширина у трећем правцу смањује. Поред тога, проучавао је и фреквенције колективних мода, где су ефекти интеракција мање изражени. Ово се посебно односи на монополну и квадруполну моду, чије вредности практично остају константне у целом распону експериментално релевантних вредности јачина интеракција. Са друге стране, фреквенција радијалне квадруполне моде је осетљивија на промену јачине интеракције, посебно јачине контактне интеракције, док при промени јачине дипол-дипол интеракције показује немонотон понашање.

Важан резултат докторске дисертације кандидата је и развој паралелних нумеричких метода за решавање тродимензионалне Грос-Питаевски једначине са контактним и диполним интеракционим чланом, помоћу које се описују проучавани ултрахладни бозонски системи. Временски зависна диполна Грос-Питаевски једначина је парцијална диференцијална једначина по просторним координатама и времену и има структуру нелинеарне Шредингерове једначине, тако да садржи први извод таласне функције по времену и друге изводе по просторним координатама. Диполни интеракциони члан је описан помоћу просторног интеграла, пошто је у питању дугодоментна интеракција. Развијени метод подељеног корака за решавање Грос-Питаевски једначине укључује дискретизацију по простору и времену, појединачну интеграцију по просторним координатама и временску пропагацију дискретизоване једначине. Уколико је познато решење у једном временском тренутку, ова метода омогућава налажење решења после малог временског корака пропагирањем дискретизоване једначине. У дисертацији кандидата кориштена је семи-имплицитна Кренк-Николсон дискретизациона шема која осигурава стабилност решења и чува норму таласне функције током пропагације у реалном времену. Нумерички алгоритми који су раније развијени за случај контактне интеракције су у оквиру доктората уопштени на Грос-Питаевски једначину са дипол-дипол интеракцијом. С обзиром на велику нумеричку захтевност тродимензионалних симулација за проучавање реалних физичких система, сви алгоритми су паралелизовани.

Кандидат је ове резултате приказао детаљно у оквиру докторске дисертације под називом "Faraday waves in ultracold dipolar Bose gases", која је написана на енглеском језику и има 7 поглавља. Најзначајнији радови у којима су објављени представљени резултати су:

1. **D. Vudragović**, I. Vidanović, A. Balaž, P. Muruganandam, and S. K. Adhikari, C Programs for Solving the Time-dependent Gross-Pitaevskii Equation in a Fully Anisotropic Trap, *Comput. Phys. Commun.* **183**, 2021 (2012). DOI: 10.1016/j.cpc.2012.03.022; ISSN: 0010-4655; **IF(2012) = 3.078**
2. R. Kishor Kumar, L. Young-S., **D. Vudragović**, A. Balaž, P. Muruganandam, and S. K. Adhikari, Fortran and C Programs for the Time-dependent Dipolar Gross-Pitaevskii Equation in an Anisotropic Trap, *Comput. Phys. Commun.* **195**, 117 (2015). DOI: 10.1016/j.cpc.2015.03.024; ISSN: 0010-4655; **IF(2015) = 3.635**

3. L. Young-S., **D. Vudragović**, P. Muruganandam, S. K. Adhikari, and A. Balaž,
OpenMP Fortran and C Programs for Solving the Time-dependent Gross-Pitaevskii Equation in an
Anisotropic Trap, *Comput. Phys. Commun.* **204**, 209 (2016).
DOI: 10.1016/j.cpc.2016.03.015; ISSN: 0010-4655; **IF(2016) = 3.936**
4. L. Young-S., P. Muruganandam, S. K. Adhikari, V. Loncar, **D. Vudragović**, and A. Balaž,
OpenMP GNU and Intel Fortran programs for solving the time-dependent Gross-Pitaevskii equation,
Comput. Phys. Commun. **220**, 503 (2017).
DOI: 10.1016/j.cpc.2017.07.013, ISSN: 0010-4655; **IF(2017) = 3.748**
5. **D. Vudragović** and A. Balaž,
Faraday and Resonant Waves in Dipolar Cigar-Shaped Bose-Einstein Condensates,
Symmetry **11**, 1090 (2019).
DOI: 10.3390/sym11091090; ISSN: 2073-8994; **IF(2018)=2.143**

У прилогу је дат релевантан списак публикација кандидата. Пошто је он у периоду од 2008. до 2012. године био члан АТЛАС колаборације, радови објављени у том контексту су наведени посебно, јер нису везани за докторску дисертацију која је овом приликом номинована за награду.

Др Душан Вудраговић је до сада објавио 22 рада у међународним часописима, 3 поглавља у монографијама, као и више саопштења са међународних скупова штампаних у целини и у изводу. Када се **изузму** публикације из периода ангажовања у АТЛАС колаборацији и друге публикације који нису везане за докторат, кандидат је објавио **8 радова** у међународним часописима, од чега **4 категорије M21a**, **2 категорије M21** и по један категорија M22 и M23, од чега је **на 3 рада водећи аутор**. Укупан **импакт фактор** ових радова је **21,102**. У ову групу релевантних публикација спадају и два поглавља категорије M13 и једно поглавље категорије M14, 2 саопштења категорије M33 и 6 саопштења категорије M34.

Према бази Web of Science, радови др Душана Вудраговића су цитирани укупно 1937 пута (без аутоцитата), уз $h=16$. Када се разматрају само публикације релевантне за докторат, онда је према истој бази **број цитата 293 (без аутоцитата)**, а $h=6$. Кандидат је био рецензент четири рада у часопису Data Technologies and Applications, два рада у часопису Physics Letters A и једног рада у часопису Simulation: Transactions of the Society for Modeling and Simulation International.

Имајући све наведено у виду, са задовољством предлажем др Душана Вудраговића за Студентску награду Института за физику у Београду за најбољу докторску тезу одбрањену током 2019. године.

У Београду, 29. 04. 2020. године



др Антун Балаж, научни саветник
руководилац Центра изузетних вредности
за изучавање комплексних система

Биографија др Душана Вудраговића

Душан Вудраговић је рођен 3. маја 1980. године у Сремској Митровици. Основну школу “Доситеј Обрадовић” завршио је у Путинцима, а Гимназију “Стеван Пузић” у Руми. Основне студије је похађао на Физичком факултету Универзитета у Београду на смеру Примењена физика и информатика у периоду од 1999. до 2005. године. Током студија добио је стипендије Министарства науке Републике Србије и Владе Републике Србије, као и награду 1000 најбољих студената у Србији Норвешке амбасаде у Београду. Дипломирао је 2005. године са просечном оценом 9.62. Дипломски рад под називом “Мерење ефективне трансверзалне емитансе јонског снопа” урадио је под руководством проф. др Ивана Аничина.

У периоду од 2006. до 2008. године боравио је у ЦЕРН-у (Женева) као сарадник на ФП6 пројектима SEE-GRID-2 (SEE-GRID eInfrastructure for regional eScience) и EGEE-II (Enabling Grids for E-sciencE). Свој истраживачки рад је започео на АТЛАС колаборацији 2008. године, који прекида 2012. године, након чега, под менторством др Антуна Балажа, прелази у Лабораторију за примену рачунара у науци Института за физику у Београду, у оквиру пројекта ОН171017.

Докторске студије на Физичком факултету Универзитета у Београду уписао је 2012. године. Докторску дисертацију под насловом “Faraday waves in ultracold dipolar Bose gases” (Фарадејеви таласи у ултрахладним диполним Бозе гасовима) урађену под менторством др Антуна Балажа, одбранио је 24. децембра 2019. године.

Душан Вудраговић је запослен у Институту за физику у Београду као истраживач сарадник у Лабораторији за примену рачунара у науци Националног центра изузетних вредности за изучавање комплексних система. У оквиру међународне сарадње, тренутно је ангажован на Хоризонт 2020 пројектима NI4OS-Europe (National Initiatives for Open Science in Europe) и SMARTCHAIN (Towards Innovation - driven and smart solutions in short food supply chains).

Др Душан Вудраговић је до сада објавио 22 рада у међународним часописима, 3 поглавља у монографијама, као и више саопштења са међународних скупова штампаних у целини и у изводу. Када се изузму публикације из периода ангажовања у АТЛАС колаборацији и друге публикације који нису везане за докторат, кандидат је објавио 8 радова у међународним часописима, од чега 4 категорије М21а, 2 категорије М21 и по један категорија М22 и М23. У ову групу релевантних публикација спадају и два поглавља категорије М13 и једно поглавље категорије М14, 2 саопштења категорије М33 и 6 саопштења категорије М34.

Према бази Web of Science, радови др Душана Вудраговића су цитирани укупно 1937 пута (без аутоцитата), уз $h=16$. Када се разматрају само публикације релевантне за докторат, онда је према истој бази број цитата 293 (без аутоцитата), а $h=6$.

Списак релевантних публикација др Душана Вудраговића

M13 – Монографска студија/поглавље у књизи M11 или рад у тематском зборнику водећег међународног значаја

1. **D. Vudragović**, and A. Balaž, *Science gateway for the Serbian condensed matter physics community*, [Science gateways for distributed computing infrastructures](#), Ed. Peter Kacsuk, p. 209-220, Springer (2014), DOI: 10.1007/978-3-319-11268-8.
2. O. Prnjat, A. Balaž, **D. Vudragović**, I. Liabotis, C. Sener, B. Marović, M. Kozlovsky, and G. Neagu, *SEE-GRID eInfrastructure for regional eScience*, [Data driven e-Science](#), Eds. S. C. Lin and E. Yen, p. 91, Springer (2011), DOI: 10.1007/978-1-4419-8014-4_7.

M14 – Монографска студија/поглавље у књизи M12 или рад у тематском зборнику водећег међународног значаја

1. D. Stanković, P. Jovanović, A. Jović, V. Slavnić, **D. Vudragović**, and A. Balaž, *Implementation and Benchmarking of New FFT Libraries in Quantum ESPRESSO*, [High-performance computing infrastructure for South East Europe's research communities](#), p. 155-162, Springer (2014), DOI: 10.1007/978-3-319-01520-0_19.

M21a – Радови у међународним часописима изузетних вредности

1. Luis E. Young-S., P. Muruganandam, S. K. Adhikari, V. Lončar, **D. Vudragović**, and A. Balaž, *OpenMP GNU and Intel Fortran programs for solving the time-dependent Gross-Pitaevskii equation*, [Comput. Phys. Commun.](#) **220**, 503 (2017), DOI: 10.1016/j.cpc.2017.07.013; IF(2017) = 3.748.
2. Luis E. Young-S., **D. Vudragović**, P. Muruganandam, S. K. Adhikari, and A. Balaž, *OpenMP Fortran and C programs for solving the time-dependent Gross-Pitaevskii equation in an anisotropic trap*, [Comput. Phys. Commun.](#) **204**, 209 (2016), DOI: 10.1016/j.cpc.2016.03.015; IF(2016) = 3.936.
3. R. K. Kumar, Luis E. Young-S., **D. Vudragović**, A. Balaž, P. Muruganandam, and S. K. Adhikari, *Fortran and C programs for the time-dependent dipolar Gross-Pitaevskii equation in an anisotropic trap*, [Comput. Phys. Commun.](#) **195**, 117 (2015), DOI: 10.1016/j.cpc.2015.03.024; IF(2015) = 3.635.
4. **D. Vudragović**, I. Vidanović, A. Balaž, P. Muruganandam, and S. K. Adhikari, *C Programs for solving the time-dependent Gross-Pitaevskii equation in a fully anisotropic trap*, [Comput. Phys. Commun.](#) **183**, 2021 (2012), DOI: 10.1016/j.cpc.2009.04.015; IF(2012) = 3.078.

M21 – Радови у врхунским међународним часописима

1. A. Balaž, I. Vidanović, D. Stojiljković, **D. Vudragović**, A. Belić, and A. Bogojević, *SPEEDUP code for calculation of transition amplitudes via the effective action approach*, [Commun. Comput. Phys.](#) **11**, 739 (2012), DOI: 10.4208/cicp.131210.180411a, IF(2012) = 1.863.

2. A. Balaž, O. Prnjat, **D. Vudragović**, V. Slavnić, I. Liabotis, E. Atanasov, B. Jakimovski, and M. Savić, *Development of Grid e-Infrastructure in South-Eastern Europe*, *J. Grid Comput.* **9**, 135 (2011), DOI: 10.1007/s10723-011-9185-0, IF(2011) = 1.310.

M22 – Радови у истакнутим међународним часописима

1. **D. Vudragović**, and A. Balaž, *Faraday and Resonant Waves in Dipolar Cigar-Shaped Bose-Einstein Condensates*, *Symmetry* **11**, 1090 (2019), DOI: 10.3390/sym11091090; IF(2018) = 2.143.

M23 – Радови у међународним часописима

1. **D. Vudragović**, L. Ilić, P. Jovanović, S. Ničković, A. Bogojević, and A. Balaž, *VI-SEEM DREAMCLIMATE Service*, *Scal. Comput. Pract. Exp.* **19**, 215 (2018), DOI: 10.12694/scpe.v19i2.1396.

M33 – Саопштења са међународних скупова штампана у целини

1. **D. Vudragović**, P. Jovanović, and A. Balaž, *VI-SEEM virtual research environment*, *The 10th RO-LCG Conference*, Sinaia, Romania, 26-28 October 2017.
2. J. Lappalainen, **D. Vudragović**, A. Balaž, F. Ruggieri, R. Barbera, R. Lovas, G. Stoitsis, and K. Kastrantas, *Federating computation and storage resources to support agricultural science communities*, *EFITA-WCCA-CIGR conference*, Turin, Italy, 24-27 June 2013.

M34 – Саопштења са међународних скупова штампана у изводу

1. **D. Vudragović**, V. Veljić, I. Vasić, and A. Balaž, *Ground state and collective modes of dipolar BECs*, *The 7th International School and Conference on Photonics*, Belgrade, Serbia, 26-30 August 2019.
2. V. Lončar, **D. Vudragović**, S. K. Adhikari, and A. Balaž, *Parallel solvers for dipolar Gross-Pitaevskii equation*, *The 6th International School and Conference on Photonics*, Belgrade, Serbia, 28 August - 1 September 2017.
3. V. Lončar, **D. Vudragović**, A. Balaž, and A. Pelster, *Rosensweig instability due to three-body interaction or quantum fluctuations?*, *DPG Spring Meeting 2016*, Hannover, Germany, 29 February - 4 March 2016.
4. **D. Vudragović**, and A. Balaž, *Faraday waves in dipolar Bose-Einstein condensates*, *The 19th Symposium on Condensed Matter Physics - SFKM 2015*, Belgrade, Serbia, 7-11 September 2015.
5. **D. Vudragović**, and A. Balaž, *Faraday waves in dipolar Bose-Einstein condensates*, *The 5th International School and Conference on Photonics*, Belgrade, Serbia, 24-28 August 2015.
6. V. Lončar, **D. Vudragović**, A. Balaž, and A. Pelster, *Faraday waves in dipolar Bose-Einstein condensates*, *DPG Spring Meeting 2015*, Heidelberg, Germany, 23-27 March 2015.

Списак осталих публикација др Душана Вудраговића, које ни- су везане за рад на докторату (АТЛАС колаборација и друго)

Радови у међународним часописима изузетних вредности (M21a)

1. G. Aad, B. Abbott, J. Abdallah, ... **D. Vudragović**, and et al., *Charged-particle multiplicities in pp interactions at $\sqrt{s}=900$ GeV measured with the ATLAS detector at the LHC*, *Phys. Lett. B* **688**, 21 (2010).
2. G. Aad, B. Abbott, J. Abdallah, ... **D. Vudragović**, and et al., *Search for new particles in two-jet final states in 7 TeV proton-proton collisions with the ATLAS detector at the LHC*, *Phys. Rev. Lett.* **105**, 161801 (2010).

Радови у врхунским међународним часописима (M21)

1. B. P. Marinković, V. Vujčić, G. Sushko, **D. Vudragović**, S. Đorđević, S. Ivanović, M. Nešić, D. Jevremović, A. V. Solov'yov, and N. J. Mason, *Development of collisional data base for elementary processes of electron scattering by atoms and molecules*, *Nucl. Instrum. Meth. B* **354**, 90 (2015).
2. G. Aad, B. Abbott, J. Abdallah, ... **D. Vudragović**, and et al., *Search for quark contact interactions in dijet angular distributions in pp collisions at $\sqrt{s}=7$ TeV measured with the ATLAS detector*, *Phys. Lett. B* **694**, 327 (2011).
3. G. Aad, B. Abbott, J. Abdallah, ... **D. Vudragović**, and et al., *Performance of the ATLAS detector using first collision data*, *J. High Energy Phys.* **9**, 056 (2010).

Радови у истакнутим међународним часописима (M22)

1. G. Aad, B. Abbott, J. Abdallah, ... **D. Vudragović**, and et al., *Studies of the performance of the ATLAS detector using cosmic-ray muons*, *Eur. Phys. J. C* **71**, 1593 (2011).
2. G. Aad, B. Abbott, J. Abdallah, ... **D. Vudragović**, and et al., *Measurement of inclusive jet and dijet cross sections in proton-proton collisions at 7 TeV centre-of-mass energy with the ATLAS detector*, *Eur. Phys. J. C* **71**, 1512 (2011).
3. G. Aad, B. Abbott, J. Abdallah, ... **D. Vudragović**, and et al., *Readiness of the ATLAS liquid argon calorimeter for LHC collisions*, *Eur. Phys. J. C* **70**, 723 (2010).
4. G. Aad, B. Abbott, J. Abdallah, ... **D. Vudragović**, and et al., *Drift time measurement in the ATLAS liquid argon electromagnetic calorimeter using cosmic muons*, *Eur. Phys. J. C* **70**, 755 (2010).
5. G. Aad, B. Abbott, J. Abdallah, ... **D. Vudragović**, and et al., *The ATLAS inner detector commissioning and calibration*, *Eur. Phys. J. C* **70**, 787 (2010).
6. G. Aad, B. Abbott, J. Abdallah, ... **D. Vudragović**, and et al., *The ATLAS simulation infrastructure*, *Eur. Phys. J. C* **70**, 823 (2010).
7. G. Aad, B. Abbott, J. Abdallah, ... **D. Vudragović**, and et al., *Commissioning of the ATLAS muon spectrometer with cosmic rays*, *Eur. Phys. J. C* **70**, 875 (2010).

8. G. Aad, B. Abbott, J. Abdallah, ... **D. Vudragović**, and et al., *Readiness of the ATLAS tile calorimeter for LHC collisions*, [Eur. Phys. J. C 70, 1193 \(2010\)](#).

Радови у међународним часописима (M23)

1. G. Aad, B. Abbott, J. Abdallah, ... **D. Vudragović**, and et al., *The ATLAS experiment at the CERN large hadron collider*, [J. Instrum. 3, S08003 \(2008\)](#).
2. Lj. Simić, N. Vranješ, D. Reljić, **D. Vudragović**, and D. S. Popović, *WW production and triple gauge boson couplings at ATLAS*, [Acta Phys. Pol. B 38, 525 \(2007\)](#).

Саопштења са међународних скупова штампана у целини (M33)

1. V. Slavnić, B. Acković, **D. Vudragović**, A. Balaž, A. Belić, and M. Savić, *Grid site monitoring tools developed and used at SCL*, [SEE-GRID-SCI User Forum 2009](#), Istanbul, Turkey, 9-10 December 2009.
2. V. Slavnić, B. Acković, **D. Vudragović**, A. Balaž, and A. Belić, *Operational Grid tools developed at SCL*, [SEE-GRID-SCI User Forum 2009](#), Istanbul, Turkey, 9-10 December 2009.
3. **D. Vudragović**, A. Balaž, V. Slavnić, and A. Belić, *Serbian participation in Grid computing projects*, [NEC 2009](#), Varna, Bulgaria, 7-14 September 2009.
4. O. Prnjat, A. Balaž, T. Gurov, M. Kon-Popovska, I. Liabotis, G. Neagu, B. Ortakaya, C. Sener, and **D. Vudragović**, *National Grid initiatives set-up and monitoring guidelines*, [The first EELA-2 conference](#), Bogota, Colombia, 25-27 February 2009.
5. N. Vranješ, Lj. Simić, D. Reljić, **D. Vudragović**, and D. S. Popović, *WW Production at the LHC in NLO Simulations*, [6th international conference of the Balkan physical union](#), Istanbul, Turkey, 22-26 August 2006.

Саопштења са међународних скупова штампана у изводу (M34)

1. **D. Vudragović**, V. Slavnić, I. Spasojević, V. Nedović, and A. Balaž, *AgINFRA - a data infrastructure to support agricultural scientific communities: promoting data sharing and development of trust in agricultural sciences*, [12th Congress of Nutrition](#), Belgrade, Serbia, 31 October 2012.
2. N. Manouselis, C. Thanopoulos, A. Balaž, **D. Vudragović**, V. Nedović, and I. Spasojević, *AgINFRA - a data infrastructure to support agricultural scientific communities: promoting data sharing and development of trust in agricultural sciences*, [6th Central European Congress on Food](#), Novi Sad, Serbia, 23-26 May 2012.

Саопштења са скупова националног значаја штампана у целини (M63)

1. **D. Vudragović**, A. Balaž, A. Belić, C. Kourkoumelis, D. Fassouliotis, and S. Vourakis, *Hybrid Pupil's Analysis Tool for Interactions in ATLAS*, [MIPRO 2010](#), Opatia, Croatia, 24-28 May 2010.
2. **D. Vudragović**, A. Balaž, A. Belić, and A. Bogojević, *QSPEEDUP: Quasi-MC Implementation of the SPEEDUP Path Integral Code*, [INFOTEH 2010](#), Jahorina, Bosnia and Herzegovina, 17-19 March 2010.

3. **D. Vudragović**, V. Slavnić, A. Balaž, and A. Belić, *WMSMON - GLite WMS Monitoring Tool*, [MIPRO 2009](#), Opatia, Croatia, 25-29 May 2009.
4. **D. Vudragović**, A. Balaž, V. Slavnić, and A. Belić, *Dwarf - the Framework for Authorized YUM/APT Repositories Management*, [INFOTEH 2009](#), Jahorina, Bosnia and Herzegovina, 18-20 March 2009.

Web of Science



Search Tools Searches and alerts Search History Marked List

Results: 26
(from All Databases)

Sort by: Date Times Cited Usage Count Relevance More

1 of 1

You searched for: AUTHOR:
(vudragovic, d*)
Timespan: All years. **Databases:**
WOS, KJD, RSCI, SCIELO.
Search language=Auto
...Less

Create an alert

Select Page Export... Add to Marked List

Analyze Results
Create Citation Report

Refine Results

Search within results for...

Filter results by:

Open Access (18)

Refine

Publication Years

- 2019 (1)
- 2018 (1)
- 2017 (1)
- 2016 (1)
- 2015 (2)

more options / values...

Refine

Research Domains

SCIENCE TECHNOLOGY (26)

Refine

Databases

Web of Science Core Collection (26)

Refine

Document Types

Funding Agencies

Authors

Authors - Korean

1. **Faraday and Resonant Waves in Dipolar Cigar-Shaped Bose-Einstein Condensates**



By: **Vudragovic, Dusan**; Balaz, Antun
SYMMETRY-BASEL Volume: 11 Issue: 9 Article Number: 1090 Published: SEP 2019

Free Full Text from Publisher View Abstract

Times Cited: 0
(from All Databases)

Usage Count

2. **VI-SEEM DREAMCLIMATE SERVICE**



By: **Vudragovic, Dusan**; Ilic, Luka; Jovanovic, Petar; et al.
SCALABLE COMPUTING-PRACTICE AND EXPERIENCE Volume: 19 Issue: 2
Special Issue: SI Pages: 215-221 Published: JUN 2018

Free Full Text from Publisher View Abstract

Times Cited: 0
(from All Databases)

Usage Count

3. **OpenMP GNU and Intel Fortran programs for solving the time-dependent Gross-Pitaevskii equation**



By: Young-S, Luis E.; Muruganandam, Paulsamy; Adhikari, Sadhan K.; et al.
COMPUTER PHYSICS COMMUNICATIONS Volume: 220 Pages: 503-506
Published: NOV 2017

Full Text from Publisher Free Published Article From Repository
View Abstract

Times Cited: 18
(from All Databases)

Usage Count

4. **OpenMP Fortran and C programs for solving the time-dependent Gross-Pitaevskii equation in an anisotropic trap**



By: Young-S, Luis E.; **Vudragovic, Dusan**; Muruganandam, Paulsamy; et al.
COMPUTER PHYSICS COMMUNICATIONS Volume: 204 Pages: 209-213
Published: JUL 2016

Full Text from Publisher Free Published Article From Repository
View Abstract

Times Cited: 42
(from All Databases)

Usage Count

5. **Fortran and C programs for the time-dependent dipolar Gross-Pitaevskii equation in an anisotropic trap**



By: Kumar, R. Kishor; Young-S, Luis E.; **Vudragovic, Dusan**; et al.
COMPUTER PHYSICS COMMUNICATIONS Volume: 195 Pages: 117-128
Published: OCT 2015

Full Text from Publisher Free Published Article From Repository
View Abstract

Times Cited: 69
(from All Databases)

Usage Count

6. **Development of collisional data base for elementary processes of electron scattering by atoms and molecules**

By: Marinkovic, Bratislav P.; Vujcic, Veljko; Sushko, Gennady; et al.
NUCLEAR INSTRUMENTS & METHODS IN PHYSICS RESEARCH SECTION B-BEAM INTERACTIONS WITH MATERIALS AND ATOMS Volume: 354 Pages: 90-95
Published: JUL 1 2015

Full Text from Publisher View Abstract




















Times Cited: 8
(from All Databases)

Usage Count

View all options

For advanced refine options, use

Analyze Results

7. **Implementation and Benchmarking of New FFT Libraries in Quantum ESPRESSO**  **Times Cited: 0**
(from All Databases) **Usage Count** 
- By: Stankovic, Dusan; Jovanovic, Petar; Jovic, Aleksandar; et al.
Conference: HP-SEE User Forum Location: Natl Lib Serbia, Belgrade, SERBIA Date: OCT 17-19, 2012
Sponsor(s): Inst Phys Belgrade
HIGH-PERFORMANCE COMPUTING INFRASTRUCTURE FOR SOUTH EAST EUROPE'S RESEARCH COMMUNITIES: RESULTS OF THE HP-SEE USER FORUM 2012 Book Series: Modeling and Optimization in Science and Technologies Volume: 2 Pages: 155-162 Published: 2014
[View Abstract](#) 
8. **C programs for solving the time-dependent Gross-Pitaevskii equation in a fully anisotropic trap**  **Times Cited: 144**
(from All Databases) **Usage Count** 
- By: Vudragovic, Dusan; Vidanovic, Ivana; Balaz, Antun; et al.
COMPUTER PHYSICS COMMUNICATIONS Volume: 183 Issue: 9 Pages: 2021-2025 Published: SEP 2012
[Full Text from Publisher](#) [View Abstract](#) 
9. **SPEEDUP Code for Calculation of Transition Amplitudes via the Effective Action Approach**  **Times Cited: 6**
(from All Databases) **Usage Count** 
- By: Balaz, Antun; Vidanovic, Ivana; Stojiljkovic, Danica; et al.
COMMUNICATIONS IN COMPUTATIONAL PHYSICS Volume: 11 Issue: 3 Pages: 739-755 Published: MAR 2012
[Full Text from Publisher](#) [View Abstract](#) 
10. **Development of Grid e-Infrastructure in South-Eastern Europe**  **Times Cited: 23**
(from All Databases) **Usage Count** 
- By: Balaz, Antun; Prnjat, Ognjen; Vudragovic, Dusan; et al.
JOURNAL OF GRID COMPUTING Volume: 9 Issue: 2 Special Issue: SI Pages: 135-154 Published: JUN 2011
[Full Text from Publisher](#) [View Abstract](#) 
11. **Studies of the performance of the ATLAS detector using cosmic-ray muons** **Times Cited: 19**
(from All Databases) **Usage Count** 
- By: Aad, G.; Abbott, B.; Abdallah, J.; et al.
Group Author(s): ATLAS Collaboration
EUROPEAN PHYSICAL JOURNAL C Volume: 71 Issue: 3 Article Number: 1593 Published: MAR 2011
[Free Full Text from Publisher](#) [View Abstract](#) 
12. **Measurement of inclusive jet and dijet cross sections in proton-proton collisions at 7 TeV centre-of-mass energy with the ATLAS detector** **Times Cited: 123**
(from All Databases) **Usage Count** 
- By: Aad, G.; Abbott, B.; Abdallah, J.; et al.
Group Author(s): ATLAS Collaboration
EUROPEAN PHYSICAL JOURNAL C Volume: 71 Issue: 2 Article Number: 1512 Published: FEB 2011
[Free Full Text from Publisher](#) [View Abstract](#) 
13. **Search for quark contact interactions in dijet angular distributions in pp collisions at root s=7 TeV measured with the ATLAS detector** **Times Cited: 61**
(from All Databases) **Usage Count** 
- By: Aad, G.; Abbott, B.; Abdallah, J.; et al.
Group Author(s): ATLAS Collaboration
PHYSICS LETTERS B Volume: 694 Issue: 4-5 Pages: 327-345 Published: JAN 3 2011
[Free Full Text from Publisher](#) [View Abstract](#) 
14. **SEE-GRID Infrastructure for Regional eScience** **Times Cited: 1**
(from All Databases) 
- By: Prnjat, Ognjen; Balaz, Antun; Vudragovic, Dusan; et al.
Conference: International Symposium on Grid Computing Location:

	Academia Sinica, Taipei, TAIWAN Date: MAR 09-12, 2010 DATA DRIVEN E-SCIENCE, ISGC 2010: USE CASES AND SUCCESSFUL APPLICATIONS OF DISTRIBUTED COMPUTING INFRASTRUCTURES Pages: 91-103 Published: 2011 View Abstract ▼	Usage Count ▼
<input type="checkbox"/>	15. Readiness of the ATLAS Tile Calorimeter for LHC collisions By: Aad, G.; Abbott, B.; Abdallah, J.; et al. Group Author(s): ATLAS Collaboration EUROPEAN PHYSICAL JOURNAL C Volume: 70 Issue: 4 Published: DEC 8 2010 Free Full Text from Publisher View Abstract ▼	Times Cited: 84 <i>(from All Databases)</i> Usage Count ▼
<input type="checkbox"/>	16. Readiness of the ATLAS liquid argon calorimeter for LHC collisions By: Aad, G.; Abbott, B.; Abdallah, J.; et al. Group Author(s): ATLAS Collaboration EUROPEAN PHYSICAL JOURNAL C Volume: 70 Issue: 3 Pages: 723-753 Published: DEC 2010 Free Full Text from Publisher View Abstract ▼	Times Cited: 42 <i>(from All Databases)</i> Usage Count ▼
<input type="checkbox"/>	17. Drift Time Measurement in the ATLAS Liquid Argon Electromagnetic Calorimeter using Cosmic Muons By: Aad, G.; Abbott, B.; Abdallah, J.; et al. Group Author(s): ATLAS Collaboration EUROPEAN PHYSICAL JOURNAL C Volume: 70 Issue: 3 Pages: 755-785 Published: DEC 2010 Free Full Text from Publisher View Abstract ▼	Times Cited: 10 <i>(from All Databases)</i> Usage Count ▼
<input type="checkbox"/>	18. The ATLAS Simulation Infrastructure By: Aad, G.; Abbott, B.; Abdallah, J.; et al. Group Author(s): ATLAS Collaboration EUROPEAN PHYSICAL JOURNAL C Volume: 70 Issue: 3 Pages: 823-874 Published: DEC 2010 Free Full Text from Publisher View Abstract ▼	Times Cited: 904 <i>(from All Databases)</i> Usage Count ▼
<input type="checkbox"/>	19. Commissioning of the ATLAS Muon Spectrometer with cosmic rays By: Aad, G.; Abbott, B.; Abdallah, J.; et al. Group Author(s): ATLAS Collaboration EUROPEAN PHYSICAL JOURNAL C Volume: 70 Issue: 3 Pages: 875-916 Published: DEC 2010 Free Full Text from Publisher View Abstract ▼	Times Cited: 15 <i>(from All Databases)</i> Usage Count ▼
<input type="checkbox"/>	20. Measurement of the $W \rightarrow l\nu$ and $Z/\gamma^* \rightarrow ll$ production cross sections in proton-proton collisions at $\sqrt{s}=7$ TeV with the ATLAS detector By: Aad, G.; Abbott, B.; Abdallah, J.; et al. Group Author(s): ATLAS Collaboration JOURNAL OF HIGH ENERGY PHYSICS Issue: 12 Article Number: 060 Published: DEC 2010 Free Full Text from Publisher View Abstract ▼	Times Cited: 56 <i>(from All Databases)</i> Usage Count ▼
<input type="checkbox"/>	21. Search for New Particles in Two-Jet Final States in 7 TeV Proton-Proton Collisions with the ATLAS Detector at the LHC By: Aad, G.; Abbott, B.; Abdallah, J.; et al. Group Author(s): ATLAS Collaboration PHYSICAL REVIEW LETTERS Volume: 105 Issue: 16 Article Number: 161801 Published: OCT 11 2010 Free Full Text from Publisher View Abstract ▼	Times Cited: 120 <i>(from All Databases)</i> Usage Count ▼
<input type="checkbox"/>	22. Performance of the ATLAS detector using first collision data	Times Cited: 22

By: [Aad, G.](#); [Abat, E.](#); [Abbott, B.](#); et al. (from All Databases)
 Group Author(s): ATLAS Collaboration
 JOURNAL OF HIGH ENERGY PHYSICS Issue: 9 Article Number: 056
 Published: SEP 2010
[Free Full Text from Publisher](#) [View Abstract](#) Usage Count

23. **The ATLAS Inner Detector commissioning and calibration** Times Cited: 74
(from All Databases)
 By: [Aad, G.](#); [Abbott, B.](#); [Abdallah, J.](#); et al.
 Group Author(s): ATLAS Collaboration
 EUROPEAN PHYSICAL JOURNAL C Volume: 70 Issue: 3 Published: AUG 20 2010
[Free Full Text from Publisher](#) [View Abstract](#) Usage Count

24. **Charged-particle multiplicities in pp interactions at root s=900 GeV measured with the ATLAS detector at the LHC ATLAS Collaboration** Times Cited: 149
(from All Databases)
 By: [Aad, G.](#); [Abat, E.](#); [Abbott, B.](#); et al.
 Group Author(s): ATLAS Collaboration
 PHYSICS LETTERS B Volume: 688 Issue: 1 Pages: 21-42 Published: APR 26 2010
[Free Full Text from Publisher](#) [View Abstract](#) Usage Count

25. **WW production and triple gauge boson couplings at ATLAS** Times Cited: 0
(from All Databases)
 By: [Simic, L. J.](#); [Vranjes, N.](#); [Reljic, D.](#); et al.
 Conference: 3rd Physics at LHC Conference Location: Cracow, POLAND
 Date: JUL 03-08, 2006
 Sponsor(s): Inst Nucl Phys Polish Acad Sci; AGH Univ Sci & Technol; Polish Acad Arts Sci; Univ Florida; CERN; DAPHNIA CEA; Polish Minist Educ & Sci; Charles Univ; Czech Tech Univ
 ACTA PHYSICA POLONICA B Volume: 38 Issue: 2 Pages: 525-530
 Published: FEB 2007
[View Abstract](#) Usage Count

26. **WW production at the LHC in NLO simulations** Times Cited: 0
(from All Databases)
 By: [Vranjes, N.](#); [Simic, Lj.](#); [Reljic, D.](#); et al.
 Conference: 6th International Conference of the Balkan-Physical-Union
 Location: Istanbul, TURKEY Date: AUG 22-26, 2006
 Sponsor(s): Balkan Phys Union; Turkish Phys Soc; Istanbul Univ; Yildiz Tech Univ; Bogaz Univ; Dogus Univ; European Phys Soc; Govt Istanbul; Istanbul Metropolitan Municipal; Turkish Atomic Energy Author; Sci & Technol Res Council Turkey; United Natl Educ Sci & Cultural Org; NEL Electronik
 SIX INTERNATIONAL CONFERENCE OF THE BALKAN PHYSICAL UNION Book Series: AIP Conference Proceedings Volume: 899 Pages: 225-+
 Published: 2007
[View Abstract](#) Usage Count

Select Page [Export...](#) [Add to Marked List](#)

Sort by: Date Times Cited Usage Count Relevance More ◀ 1 of 1 ▶
 Show: 50 per page

26 records matched your query of the 49,522,491 in the data limits you selected.

Web of Science



Search Search Results Tools Searches and alerts Search History Marked List

Citation report for 26 results from All Databases between 1980 and 2020 Go

You searched for: AUTHOR: (vudragovic, d*)
 Timespan: All years. Databases: WOS, KJD, RSCI, SCIELO.
[...Less](#)

This report reflects citations to source items indexed within All Databases.

Export Data: Save to Excel File

Total Publications Analyze

26

h-index i

16

Average citations per item

75.35

Sum of Times Cited i

1,959

Without self citations

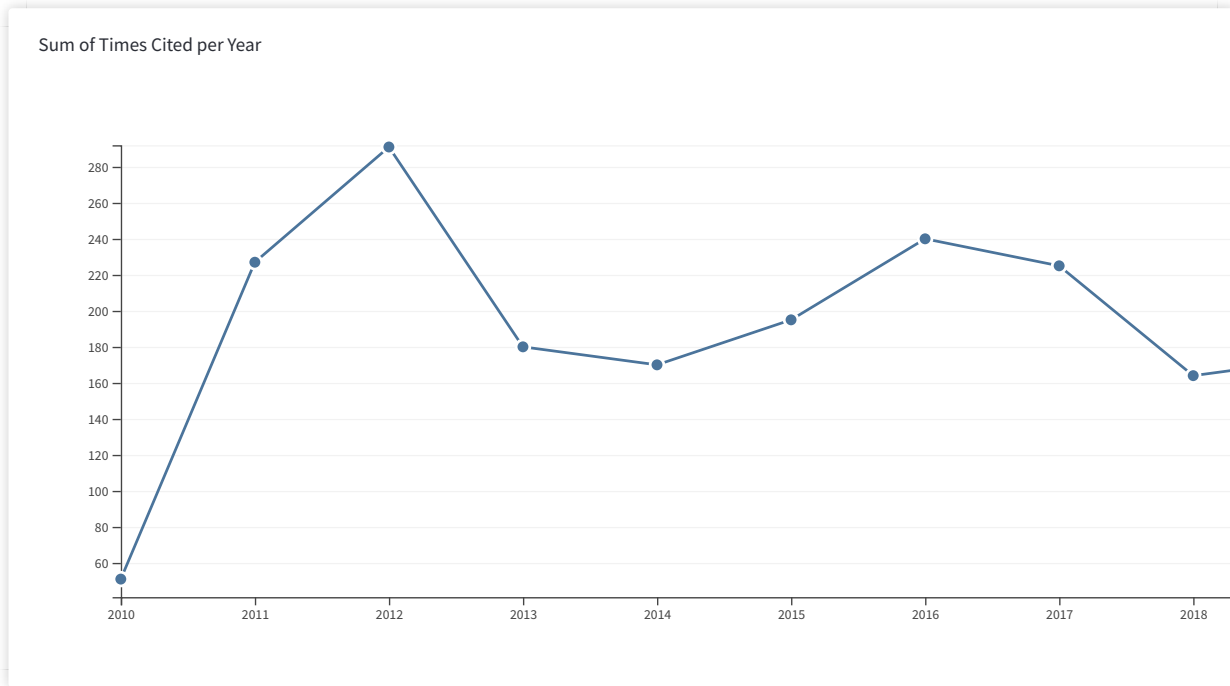
1,937

Citing articles i

1,566 Analyze

Without self citations

1,558 Analyze



Sort by: **Times Cited** Date More



1 of 3

i How are these totals calculated?

2016	2017	2018	2019	2020	Total	Average Citations per Year
240	225	164	174	42	1959	178.09

Use the checkboxes to remove individual items from this Citation Report

or restrict to items published between 1980 and 2020 Go

<input type="checkbox"/>	1.	The ATLAS Simulation Infrastructure	By: Aad, G.; Abbott, B.; Abdallah, J.; et al. Group Author(s): ATLAS Collaboration EUROPEAN PHYSICAL JOURNAL C Volume: 70 Issue: 3 Pages: 823-874 Published: DEC 2010	127	99	91	88	25	904	82.18
<input type="checkbox"/>	2.	Charged-particle multiplicities in pp interactions at root s=900 GeV measured with the ATLAS detector at the LHC	By: Aad, G.; Abat, E.; Abbott, B.; et al. Group Author(s): ATLAS Collaboration PHYSICS LETTERS B Volume: 688 Issue: 1 Pages: 21-42 Published: APR 26 2010	8	6	1	4	1	149	13.55
<input type="checkbox"/>	3.	 C programs for solving the time-dependent Gross-Pitaevskii equation in a fully anisotropic trap	By: Vudragovic, Dusan; Vidanovic, Ivana; Balaz, Antun; et al. COMPUTER PHYSICS COMMUNICATIONS Volume: 183 Issue: 9 Pages: 2021-2025 Published: SEP 2012	28	23	14	18	4	144	16.00
<input type="checkbox"/>	4.	Measurement of inclusive jet and dijet cross sections in proton-proton collisions at 7 TeV centre-of-mass energy with the ATLAS detector	By: Aad, G.; Abbott, B.; Abdallah, J.; et al. Group Author(s): ATLAS Collaboration EUROPEAN PHYSICAL JOURNAL C Volume: 71 Issue: 2 Article Number: 1512 Published: FEB 2011	5	8	6	3	0	123	12.30
<input type="checkbox"/>	5.	Search for New Particles in Two-Jet Final States in 7 TeV Proton-Proton Collisions with the ATLAS Detector at the LHC	By: Aad, G.; Abbott, B.; Abdallah, J.; et al. Group Author(s): ATLAS Collaboration PHYSICAL REVIEW LETTERS Volume: 105 Issue: 16 Article Number: 161801 Published: OCT 11 2010	9	12	7	7	0	120	10.91
<input type="checkbox"/>	6.	Readiness of the ATLAS Tile Calorimeter for LHC collisions	By: Aad, G.; Abbott, B.; Abdallah, J.; et al. Group Author(s): ATLAS Collaboration EUROPEAN PHYSICAL JOURNAL C Volume: 70 Issue: 4 Published: DEC 8 2010	9	10	6	10	1	84	7.64
<input type="checkbox"/>	7.	The ATLAS Inner Detector commissioning and calibration	By: Aad, G.; Abbott, B.; Abdallah, J.; et al. Group Author(s): ATLAS Collaboration EUROPEAN PHYSICAL JOURNAL C Volume: 70 Issue: 3 Published: AUG 20 2010	6	12	7	2	1	74	6.73
<input type="checkbox"/>	8.	 Fortran and C programs for the time-dependent dipolar Gross-Pitaevskii equation in an anisotropic trap	By: Kumar, R. Kishor; Young-S, Luis E.; Vudragovic, Dusan; et al. COMPUTER PHYSICS COMMUNICATIONS Volume: 195 Pages: 117-128 Published: OCT 2015	21	18	12	12	2	69	11.50
<input type="checkbox"/>	9.	Search for quark contact interactions in dijet angular distributions in pp collisions at root s=7 TeV measured with the ATLAS detector	By: Aad, G.; Abbott, B.; Abdallah, J.; et al. Group Author(s): ATLAS Collaboration PHYSICS LETTERS B Volume: 694 Issue: 4-5 Pages: 327-345 Published: JAN 3 2011	2	8	3	1	0	61	6.10
<input type="checkbox"/>	10.	Measurement of the W -> lv and Z/gamma* -> ll production cross sections in proton-proton collisions at root s=7 TeV with the ATLAS detector	By: Aad, G.; Abbott, B.; Abdallah, J.; et al. Group Author(s): ATLAS Collaboration JOURNAL OF HIGH ENERGY PHYSICS Issue: 12 Article Number: 060 Published: DEC 2010	4	0	0	0	0	56	5.09

Select Page



Save to Excel File

Web of Science



Search Search Results Tools Searches and alerts Search History Marked List

Citation report for 10 results from All Databases between 2010 and 2020 Go

You searched for: AUTHOR: (vudragovic, d*) ...More

This report reflects citations to source items indexed within All Databases.

Export Data: Save to Excel File

Total Publications Analyze

10

2000 2019

h-index i

6

Average citations per item

30.3

Sum of Times Cited i

303

Without self citations

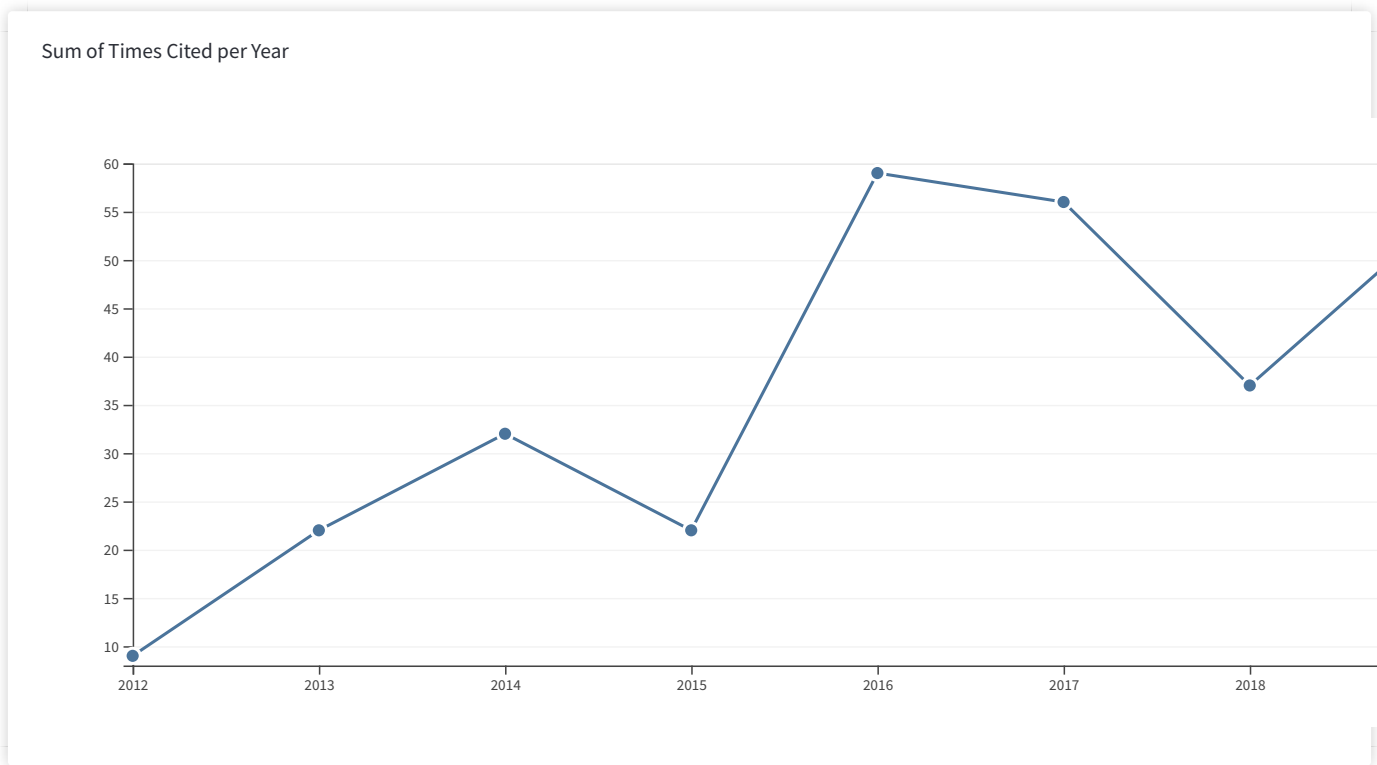
293

Citing articles i

197 Analyze

Without self citations

193 Analyze



Sort by: Times Cited Date More


1 of 1

How are these totals calculated?

2016	2017	2018	2019	2020	Total	Average Citations
◀				▶		

Use the checkboxes to remove individual items from this Citation Report

or restrict to items published between and

							per Year
	59	56	37	54	12	303	33.67
<input type="checkbox"/> 1. C programs for solving the time-dependent Gross-Pitaevskii equation in a fully anisotropic trap  By: Vudragovic, Dusan; Vidanovic, Ivana; Balaz, Antun; et al. COMPUTER PHYSICS COMMUNICATIONS Volume: 183 Issue: 9 Pages: 2021-2025 Published: SEP 2012	28	23	14	18	4	144	16.00
<input type="checkbox"/> 2. Fortran and C programs for the time-dependent dipolar Gross-Pitaevskii equation in an anisotropic trap  By: Kumar, R. Kishor; Young-S, Luis E.; Vudragovic, Dusan; et al. COMPUTER PHYSICS COMMUNICATIONS Volume: 195 Pages: 117-128 Published: OCT 2015	21	18	12	12	2	69	11.50
<input type="checkbox"/> 3. OpenMP Fortran and C programs for solving the time-dependent Gross-Pitaevskii equation in an anisotropic trap  By: Young-S, Luis E.; Vudragovic, Dusan; Muruganandam, Paulsamy; et al. COMPUTER PHYSICS COMMUNICATIONS Volume: 204 Pages: 209-213 Published: JUL 2016	7	11	9	12	3	42	8.40
<input type="checkbox"/> 4. Development of Grid e-Infrastructure in South-Eastern Europe  By: Balaz, Antun; Prnjat, Ognjen; Vudragovic, Dusan; et al. JOURNAL OF GRID COMPUTING Volume: 9 Issue: 2 Special Issue: SI Pages: 135-154 Published: JUN 2011	2	2	0	1	0	23	2.30
<input type="checkbox"/> 5. OpenMP GNU and Intel Fortran programs for solving the time-dependent Gross-Pitaevskii equation  By: Young-S, Luis E.; Muruganandam, Paulsamy; Adhikari, Sadhan K.; et al. COMPUTER PHYSICS COMMUNICATIONS Volume: 220 Pages: 503-506 Published: NOV 2017	0	2	2	11	3	18	4.50
<input type="checkbox"/> 6. SPEEDUP Code for Calculation of Transition Amplitudes via the Effective Action Approach  By: Balaz, Antun; Vidanovic, Ivana; Stojiljkovic, Danica; et al. COMMUNICATIONS IN COMPUTATIONAL PHYSICS Volume: 11 Issue: 3 Pages: 739-755 Published: MAR 2012	1	0	0	0	0	6	0.67
<input type="checkbox"/> 7. SEE-GRID eInfrastructure for Regional eScience  By: Prnjat, Ognjen; Balaz, Antun; Vudragovic, Dusan; et al. Conference: International Symposium on Grid Computing Location: Academia Sinica, Taipei, TAIWAN Date: MAR 09-12, 2010 DATA DRIVEN E-SCIENCE, ISGC 2010: USE CASES AND SUCCESSFUL APPLICATIONS OF DISTRIBUTED COMPUTING INFRASTRUCTURES Pages: 91-103 Published: 2011	0	0	0	0	0	1	0.10
<input type="checkbox"/> 8. Faraday and Resonant Waves in Dipolar Cigar-Shaped Bose-Einstein Condensates  By: Vudragovic, Dusan; Balaz, Antun SYMMETRY-BASEL Volume: 11 Issue: 9 Article Number: 1090 Published: SEP 2019	0	0	0	0	0	0	0.00
<input type="checkbox"/> 9. VI-SEEM DREAMCLIMATE SERVICE  By: Vudragovic, Dusan; Ilic, Luka; Jovanovic, Petar; et al. SCALABLE COMPUTING-PRACTICE AND EXPERIENCE Volume: 19 Issue: 2 Special Issue: SI Pages: 215-221 Published: JUN 2018	0	0	0	0	0	0	0.00

10. **Implementation and Benchmarking of New FFT Libraries in Quantum**



ESPRESSO

By: [Stankovic, Dusan](#); [Jovanovic, Petar](#); [Jovic, Aleksandar](#); et al.
Conference: HP-SEE User Forum Location: Natl Lib Serbia, Belgrade, SERBIA Date: OCT 17-19, 2012
Sponsor(s): Inst Phys Belgrade
HIGH-PERFORMANCE COMPUTING INFRASTRUCTURE FOR SOUTH EAST EUROPE'S RESEARCH COMMUNITIES: RESULTS OF THE HP-SEE USER FORUM 2012 Book
Series: Modeling and Optimization in Science and Technologies Volume: 2 Pages: 155-162 Published: 2014

0	0	0	0	0	0	0.00
---	---	---	---	---	---	------

Select Page



Save to Excel File

Sort by: Times Cited Date More

◀ 1 of 1 ▶

10 records matched your query of the 28,368,280 in the data limits you selected.

Clarivate
Accelerating innovation

© 2020 Clarivate [Copyright notice](#) [Terms of use](#) [Privacy statement](#) [Cookie policy](#)

Sign up for the Web of Science newsletter Follow us



OpenMP GNU and Intel Fortran programs for solving the time-dependent Gross–Pitaevskii equation



Luis E. Young-S.^a, Paulsamy Muruganandam^b, Sadhan K. Adhikari^c, Vladimir Lončar^d, Dušan Vudragović^d, Antun Balaž^{d,*}

^a Departamento de Ciencias Básicas, Universidad Santo Tomás, 150001 Tunja, Boyacá, Colombia

^b Department of Physics, Bharathidasan University, Palkalaiperur Campus, Tiruchirappalli–620024, Tamil Nadu, India

^c Instituto de Física Teórica, UNESP - Universidade Estadual Paulista, 01.140-70 São Paulo, São Paulo, Brazil

^d Scientific Computing Laboratory, Center for the Study of Complex Systems, Institute of Physics Belgrade, University of Belgrade, Serbia

ARTICLE INFO

Article history:

Received 11 July 2017

Accepted 14 July 2017

Available online 10 August 2017

Keywords:

Bose–Einstein condensate

Gross–Pitaevskii equation

Split-step Crank–Nicolson scheme

Intel and GNU Fortran programs

Open Multi-Processing

OpenMP

Partial differential equation

ABSTRACT

We present Open Multi-Processing (OpenMP) version of Fortran 90 programs for solving the Gross–Pitaevskii (GP) equation for a Bose–Einstein condensate in one, two, and three spatial dimensions, optimized for use with GNU and Intel compilers. We use the split-step Crank–Nicolson algorithm for imaginary- and real-time propagation, which enables efficient calculation of stationary and non-stationary solutions, respectively. The present OpenMP programs are designed for computers with multi-core processors and optimized for compiling with both commercially-licensed Intel Fortran and popular free open-source GNU Fortran compiler. The programs are easy to use and are elaborated with helpful comments for the users. All input parameters are listed at the beginning of each program. Different output files provide physical quantities such as energy, chemical potential, root-mean-square sizes, densities, etc. We also present speedup test results for new versions of the programs.

New version program summary

Program title: BEC-GP-OMP-FOR software package, consisting of: (i) imag1d-th, (ii) imag2d-th, (iii) imag3d-th, (iv) imagaxi-th, (v) imagcir-th, (vi) imagsph-th, (vii) real1d-th, (viii) real2d-th, (ix) real3d-th, (x) realaxi-th, (xi) realcir-th, (xii) realsph-th.

Program files doi: <http://dx.doi.org/10.17632/y8zk3jgn84.2>

Licensing provisions: Apache License 2.0

Programming language: OpenMP GNU and Intel Fortran 90.

Computer: Any multi-core personal computer or workstation with the appropriate OpenMP-capable Fortran compiler installed.

Number of processors used: All available CPU cores on the executing computer.

Journal reference of previous version: Comput. Phys. Commun. **180** (2009) 1888; *ibid.* **204** (2016) 209.

Does the new version supersede the previous version?: Not completely. It does supersede previous Fortran programs from both references above, but not OpenMP C programs from Comput. Phys. Commun. **204** (2016) 209.

Nature of problem: The present Open Multi-Processing (OpenMP) Fortran programs, optimized for use with commercially-licensed Intel Fortran and free open-source GNU Fortran compilers, solve the time-dependent nonlinear partial differential (GP) equation for a trapped Bose–Einstein condensate in one (1d), two (2d), and three (3d) spatial dimensions for six different trap symmetries: axially and radially symmetric traps in 3d, circularly symmetric traps in 2d, fully isotropic (spherically symmetric) and fully anisotropic traps in 2d and 3d, as well as 1d traps, where no spatial symmetry is considered.

Solution method: We employ the split-step Crank–Nicolson algorithm to discretize the time-dependent GP equation in space and time. The discretized equation is then solved by imaginary- or real-time propagation, employing adequately small space and time steps, to yield the solution of stationary and non-stationary problems, respectively.

* Corresponding author.

E-mail addresses: luis.young@usantoto.edu.co (L.E. Young-S), anand@cncld.bdu.ac.in (P. Muruganandam), adhikari@ift.unesp.br (S.K. Adhikari), vladimir.loncar@ipb.ac.rs (V. Lončar), dusan.vudragovic@ipb.ac.rs (D. Vudragović), antun.balaz@ipb.ac.rs (A. Balaž).

Reasons for the new version: Previously published Fortran programs [1,2] have now become popular tools [3] for solving the GP equation. These programs have been translated to the C programming language [4] and later extended to the more complex scenario of dipolar atoms [5]. Now virtually all computers have multi-core processors and some have motherboards with more than one physical computer processing unit (CPU), which may increase the number of available CPU cores on a single computer to several tens. The C programs have been adopted to be very fast on such multi-core modern computers using general-purpose graphic processing units (GPGPU) with Nvidia CUDA and computer clusters using Message Passing Interface (MPI) [6]. Nevertheless, previously developed Fortran programs are also commonly used for scientific computation and most of them use a single CPU core at a time in modern multi-core laptops, desktops, and workstations. Unless the Fortran programs are made aware and capable of making efficient use of the available CPU cores, the solution of even a realistic dynamical 1d problem, not to mention the more complicated 2d and 3d problems, could be time consuming using the Fortran programs. Previously, we published auto-parallel Fortran programs [2] suitable for Intel (but not GNU) compiler for solving the GP equation. Hence, a need for the full OpenMP version of the Fortran programs to reduce the execution time cannot be overemphasized. To address this issue, we provide here such OpenMP Fortran programs, optimized for both Intel and GNU Fortran compilers and capable of using all available CPU cores, which can significantly reduce the execution time.

Summary of revisions: Previous Fortran programs [1] for solving the time-dependent GP equation in 1d, 2d, and 3d with different trap symmetries have been parallelized using the OpenMP interface to reduce the execution time on multi-core processors. There are six different trap symmetries considered, resulting in six programs for imaginary-time propagation and six for real-time propagation, totaling to 12 programs included in BEC-GP-OMP-FOR software package.

All input data (number of atoms, scattering length, harmonic oscillator trap length, trap anisotropy, etc.) are conveniently placed at the beginning of each program, as before [2]. Present programs introduce a new input parameter, which is designated by `Number_of_Threads` and defines the number of CPU cores of the processor to be used in the calculation. If one sets the value 0 for this parameter, all available CPU cores will be used. For the most efficient calculation it is advisable to leave one CPU core unused for the background system's jobs. For example, on a machine with 20 CPU cores such that we used for testing, it is advisable to use up to 19 CPU cores. However, the total number of used CPU cores can be divided into more than one job. For instance, one can run three simulations simultaneously using 10, 4, and 5 CPU cores, respectively, thus totaling to 19 used CPU cores on a 20-core computer.

The Fortran source programs are located in the directory `src`, and can be compiled by the `make` command using the `makefile` in the root directory `BEC-GP-OMP-FOR` of the software package. The examples of produced output files can be found in the directory `output`, although some large density files are omitted, to save space. The programs calculate the values of actually used dimensionless nonlinearities from the physical input parameters, where the input parameters correspond to the identical nonlinearity values as in the previously published programs [1], so that the output files of the old and new programs can be directly compared. The output files are conveniently named such that their contents can be easily identified, following the naming convention introduced in Ref. [2]. For example, a file named `<code>-out.txt`, where `<code>` is a name of the individual program, represents the general output file containing input data, time and space steps, nonlinearity, energy and chemical potential, and was named `fort.7` in the old Fortran version of programs [1]. A file named `<code>-den.txt` is the output file with the condensate density, which had the names `fort.3` and `fort.4` in the old Fortran version [1] for imaginary- and real-time propagation programs, respectively. Other possible density outputs, such as the initial density, are commented out in the programs to have a simpler set of output files, but users can uncomment and re-enable them, if needed. In addition, there are output files for reduced (integrated) 1d and 2d densities for different programs. In the real-time programs there is also an output file reporting the dynamics of evolution of root-mean-square sizes after a perturbation is introduced. The supplied real-time programs solve the stationary GP equation, and then calculate the dynamics. As the imaginary-time programs are more accurate than the real-time programs for the solution of a stationary problem, one can first solve the stationary problem using the imaginary-time programs, adapt the real-time programs to read the pre-calculated wave function and then study the dynamics. In that case the parameter `NSTP` in the real-time programs should be set to zero and the space mesh and nonlinearity parameters should be identical in both programs. The reader is advised to consult our previous publication where a complete description of the output files is given [2]. A `readme.txt` file, included in the root directory, explains the procedure to compile and run the programs.

We tested our programs on a workstation with two 10-core Intel Xeon E5-2650 v3 CPUs. The parameters used for testing are given in sample input files, provided in the corresponding directory together with the programs. In Table 1 we present wall-clock execution times for runs on 1, 6, and 19 CPU cores for programs compiled using Intel and GNU Fortran compilers. The corresponding columns "Intel speedup" and "GNU speedup" give the ratio of wall-clock execution times of runs on 1 and 19 CPU cores, and denote the actual measured speedup for 19 CPU cores. In all cases and for all numbers of CPU cores, although the GNU Fortran compiler gives excellent results, the Intel Fortran compiler turns out to be slightly faster. Note that during these tests we always ran only a single simulation on a workstation at a time, to avoid any possible interference issues. Therefore, the obtained wall-clock times are more reliable than the ones that could be measured with two or more jobs running simultaneously. We also studied the speedup of the programs as a function of the number of CPU cores used. The performance of the Intel and GNU Fortran compilers is illustrated in Fig. 1, where we plot the speedup and actual wall-clock times as functions of the number of CPU cores for 2d and 3d programs. We see that the speedup increases monotonically with the number of CPU cores in all cases and has large values (between 10 and 14 for 3d

programs) for the maximal number of cores. This fully justifies the development of OpenMP programs, which enable much faster and more efficient solving of the GP equation. However, a slow saturation in the speedup with the further increase in the number of CPU cores is observed in all cases, as expected.

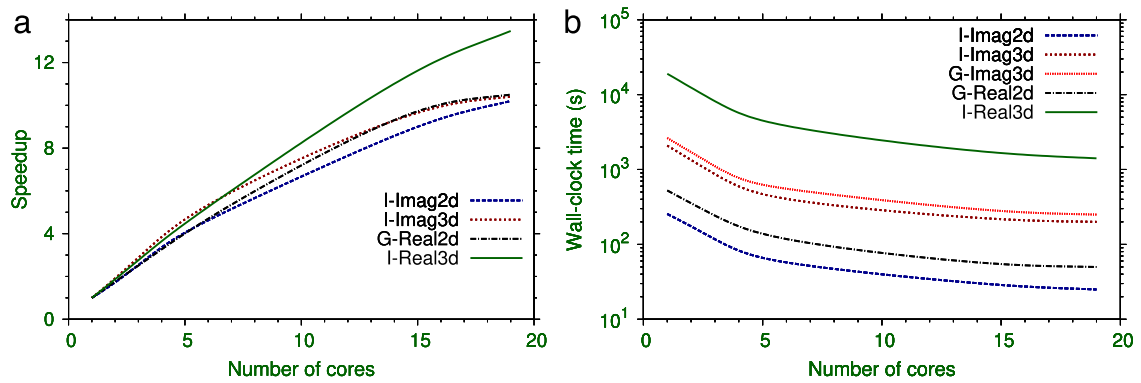


Fig. 1. (a) Speedup for 2d and 3d programs compiled with the Intel (I) and GNU (G) Fortran compilers as a function of the number of CPU cores, measured on a workstation with two Intel Xeon E5-2650 v3 CPUs. (b) Wall-clock execution time (in seconds) of 2d and 3d programs compiled with the Intel (I) and GNU (G) Fortran compilers as a function of the number of CPU cores.

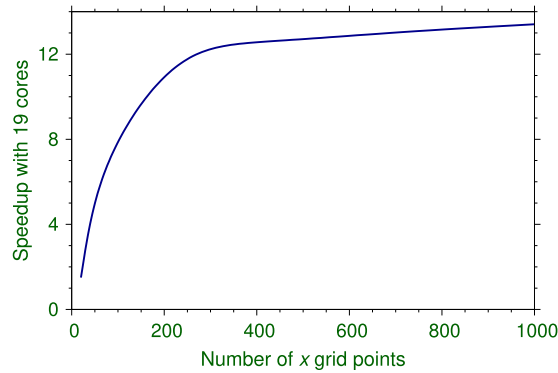


Fig. 2. Speedup of real2d-th program, compiled with the Intel Fortran 90 compiler and executed on 19 CPU cores on a workstation with two Intel Xeon E5-2650 v3 CPUs, as a function of the number of spatial discretization points $NX=NY$.

Table 1

Wall-clock execution times (in seconds) for runs with 1, 6, and 19 CPU cores of different programs using the Intel Fortran (`ifort`) and GNU Fortran (`gfortran`) compilers on a workstation with two Intel Xeon E5-2650 v3 CPUs, with a total of 20 CPU cores, and the obtained speedups for 19 CPU cores.

# of cores	1	1	6	6	19	19	19	19
Fortran	Intel time	GNU time	Intel time	GNU time	Intel time	GNU time	Intel speedup	GNU speedup
imag1d	52	60	22	22	20	22	2.6	2.7
imagcir	22	30	14	15	14	15	1.6	2.0
imagsph	24	30	12	15	12	14	2.4	2.1
real1d	205	345	76	108	62	86	3.3	4.0
realcir	145	220	55	73	48	59	3.0	3.7
realsph	155	250	57	76	46	61	3.4	2.7
imag2d	255	415	52	84	27	40	9.4	10.4
imagaxi	260	435	62	105	30	55	8.7	7.9
real2d	325	525	74	107	32	50	10.1	10.5
realaxi	160	265	35	49	16	24	10.0	11.0
imag3d	2080	2630	370	550	200	250	10.4	10.5
real3d	19500	26000	3650	5600	1410	2250	13.8	11.6

The speedup tends to increase for programs in higher dimensions, as they become more complex and have to process more data. This is why the speedups of the supplied 2d and 3d programs are larger than those of 1d programs. Also, for a single program the speedup increases with the size of the spatial grid, i.e., with the number of spatial discretization points, since this increases the amount of calculations performed by the program. To demonstrate this, we tested the supplied real2d-th program and varied the number of spatial discretization points $NX=NY$ from 20 to 1000. The measured speedup obtained when running this program on 19 CPU cores as a function of the number of discretization points is shown in Fig. 2. The speedup first increases rapidly with the number of discretization points and eventually saturates.

Additional comments: Example inputs provided with the programs take less than 30 minutes to run on a workstation with two Intel Xeon E5-2650 v3 processors (2 QPI links, 10 CPU cores, 25 MB cache, 2.3 GHz).
© 2017 Elsevier B.V. All rights reserved.

Acknowledgments

V.L., D.V., and A.B. acknowledge support by the Ministry of Education, Science, and Technological Development of the Republic of Serbia under projects ON171017 and III43007. P.M. acknowledges support by the Science and Engineering Research Board, Department of Science and Technology, Government of India under project no. EMR/2014/000644. S.K.A. acknowledges support by the CNPq of Brazil under project 303280/2014-0, and by the FAPESP of Brazil under project 2012/00451-0. Numerical tests were partially carried out on the PARADOX supercomputing facility at the Scientific Computing Laboratory of the Institute of Physics Belgrade.

References

- [1] P. Muruganandam, S.K. Adhikari, *Comput. Phys. Comm.* 180 (2009) 1888.
- [2] L.E. Young-S., D. Vudragović, P. Muruganandam, S.K. Adhikari, A. Balaž, *Comput. Phys. Comm.* 204 (2016) 209.
- [3] H. Fabrelli, et al., *J. Opt.* 19 (2017) 075501;
S.K. Adhikari, *Laser Phys. Lett.* 14 (2017) 065402;
A.N. Malmi-Kakkada, O.T. Valls, C. Dasgupta, *Phys. Rev. B* 95 (2017) 134512;
P.S. Vinayagam, R. Radha, S. Bhuvaneshwari, R. Ravisankar, P. Muruganandam, *Commun. Nonlinear Sci. Numer. Simul.* 50 (2017) 68;
O. Voronich, et al., *Comput. Phys. Comm.* 215 (2017) 246;
V. Veljić, A. Balaž, A. Pelster, *Phys. Rev. A* 95 (2017) 053635;
A.M. Martin, et al., *J. Phys.: Condens. Matter.* 29 (2017) 103004;
R.R. Sakhel, A.R. Sakhel, *J. Phys. B: At. Mol. Opt. Phys.* 50 (2017) 105301;
E. Chiquillo, *J. Phys. A* 50 (2017) 105001;
G.A. Sekh, *Phys. Lett. A* 381 (2017) 852;
W. Wen, B. Chen, X. Zhang, *J. Phys. B: At. Mol. Opt. Phys.* 50 (2017) 035301;
S.K. Adhikari, *Phys. Rev. A* 95 (2017) 023606;
S. Gautam, S.K. Adhikari, *Phys. Rev. A* 95 (2017) 013608;
S.K. Adhikari, *Laser Phys. Lett.* 14 (2017) 025501;
D. Mihalache, *Rom. Rep. Phys.* 69 (2017) 403;
X.-F. Zhang, et al., *Ann. Phys.* 375 (2016) 368;
G. Vergez, et al., *Comput. Phys. Comm.* 209 (2016) 144;
S. Bhuvaneshwari, et al., *J. Phys. B: At. Mol. Opt. Phys.* 49 (2016) 245301;
C.-Y. Lai, C.-C. Chien, *Sci. Rep.* 6 (2016) 37256;
C.-Y. Lai, C.-C. Chien, *Phys. Rev. Appl.* 5 (2016) 034001;
H. Gargoubi, et al., *Phys. Rev. E* 94 (2016) 043310;
S.K. Adhikari, *Phys. Rev. E* 94 (2016) 032217;
I. Vasić, A. Balaž, *Phys. Rev. A* 94 (2016) 033627;
R.R. Sakhel, A.R. Sakhel, *J. Low Temp. Phys.* 184 (2016) 1092;
J.B. Sudharsan, et al., *J. Phys. B: At. Mol. Opt. Phys.* 49 (2016) 165303;
A. Li, et al., *Phys. Rev. A* 94 (2016) 023626;
R.K. Kumar, et al., *J. Phys. B: At. Mol. Opt. Phys.* 49 (2016) 155301;
K. Nakamura, et al., *J. Phys. A* 49 (2016) 315102;
S.K. Adhikari, *Laser Phys. Lett.* 13 (2016) 085501;
A. Paredes, H. Michinel, *Phys. Dark Universe* 12 (2016) 50;
W. Bao, Q. Tang, Y. Zhang, *Commun. Comput. Phys.* 19 (2016) 1141;
A.R. Sakhel, *Physica B* 493 (2016) 72;
J. Akram, B. Girodias, A. Pelster, *J. Phys. B: At. Mol. Opt. Phys.* 49 (2016) 075302;
J. Akram, A. Pelster, *Phys. Rev. A* 93 (2016) 033610;
T. Khellil, A. Balaž, A. Pelster, *New J. Phys.* 18 (2016) 063003;
D. Hocker, J. Yan, H. Rabitz, *Phys. Rev. A* 93 (2016) 053612;
J. Akram, A. Pelster, *Phys. Rev. A* 93 (2016) 023606;
S. Subramanian, *Eur. Phys. J. D* 70 (2016) 109;
Z. Marojević, E. Goeklue, C. Laemmerzahl, *Comput. Phys. Comm.* 202 (2016) 216;
R.R. Sakhel, et al., *Eur. Phys. J. D* 70 (2016) 66;
K. Manikandan, et al., *Phys. Rev. E* 93 (2016) 032212;
S.K. Adhikari, *Laser Phys. Lett.* 13 (2016) 035502;
S. Gautam, S.K. Adhikari, *Phys. Rev. A* 93 (2016) 013630;
T. Mithun, K. Porsezian, B. Dey, *Phys. Rev. A* 93 (2016) 013620;
D.-S. Wang, Y. Xue, Z. Zhang, *Romanian J. Phys.* 61 (2016) 827;
S. Sabari, K. Porsezian, P. Muruganandam, *Romanian Rep. Phys.* 68 (2016) 990;
J. Akram, A. Pelster, *Laser Phys.* 26 (2016) 065501;
R.R. Sakhel, A.R. Sakhel, H.B. Ghassib, *Physica B* 478 (2015) 68;
J.B. Sudharsan, et al., *Phys. Rev. A* 92 (2015) 053601.
- [4] D. Vudragović, I. Vidanović, A. Balaž, P. Muruganandam, S.K. Adhikari, *Comput. Phys. Comm.* 183 (2012) 2021.
- [5] R. Kishor Kumar, L.E. Young-S., A. Vudragović, P. Balaž, D. Muruganandam, S.K. Adhikari, *Comput. Phys. Comm.* 195 (2015) 117.
- [6] V. Lončar, A. Balaž, A. Bogojević, S. Škrbić, P. Muruganandam, S.K. Adhikari, *Comput. Phys. Comm.* 200 (2016) 406;
V. Lončar, L.E. Young-S., S. Škrbić, P. Muruganandam, S.K. Adhikari, A. Balaž, *Comput. Phys. Comm.* 209 (2016) 190;
B. Satarić, V. Slavnić, A. Belić, A. Balaž, P. Muruganandam, S.K. Adhikari, *Comput. Phys. Comm.* 200 (2016) 411.



Contents lists available at ScienceDirect

Computer Physics Communications

journal homepage: www.elsevier.com/locate/cpc

OpenMP Fortran and C programs for solving the time-dependent Gross–Pitaevskii equation in an anisotropic trap



Luis E. Young-S.^{a,*}, Dušan Vudragović^b, Paulsamy Muruganandam^c,
Sadhan K. Adhikari^a, Antun Balaž^b

^a Instituto de Física Teórica, UNESP – Universidade Estadual Paulista, 01.140-70 São Paulo, São Paulo, Brazil

^b Scientific Computing Laboratory, Institute of Physics Belgrade, University of Belgrade, Pregrevica 118, 11080 Belgrade, Serbia

^c School of Physics, Bharathidasan University, Palkalaiperur Campus, Tiruchirappalli 620024, Tamil Nadu, India

ARTICLE INFO

Article history:

Received 22 February 2016

Received in revised form

9 March 2016

Accepted 22 March 2016

Available online 6 April 2016

Keywords:

Bose–Einstein condensate

Gross–Pitaevskii equation

Split-step Crank–Nicolson scheme

Real- and imaginary-time propagation

C program

Fortran program

OpenMP

Partial differential equation

ABSTRACT

We present new version of previously published Fortran and C programs for solving the Gross–Pitaevskii equation for a Bose–Einstein condensate with contact interaction in one, two and three spatial dimensions in imaginary and real time, yielding both stationary and non-stationary solutions. To reduce the execution time on multicore processors, new versions of parallelized programs are developed using Open Multi-Processing (OpenMP) interface. The input in the previous versions of programs was the mathematical quantity nonlinearity for dimensionless form of Gross–Pitaevskii equation, whereas in the present programs the inputs are quantities of experimental interest, such as, number of atoms, scattering length, oscillator length for the trap, etc. New output files for some integrated one- and two-dimensional densities of experimental interest are given. We also present speedup test results for the new programs.

New version program summary

Program title: BEC-GP-OMP package, consisting of: (i) imag1d, (ii) imag2d, (iii) imag3d, (iv) imagaxi, (v) imagcir, (vi) imagsph, (vii) real1d, (viii) real2d, (ix) real3d, (x) realaxi, (xi) realcir, (xii) realsph.

Catalogue identifier: AEDU_v4_0.

Program Summary URL: http://cpc.cs.qub.ac.uk/summaries/AEDU_v4_0.html

Program obtainable from: CPC Program Library, Queen's University of Belfast, N. Ireland.

Licensing provisions: Apache License 2.0

No. of lines in distributed program, including test data, etc.: 130308.

No. of bytes in distributed program, including test data, etc.: 929062.

Distribution format: tar.gz.

Programming language: OpenMP C; OpenMP Fortran.

Computer: Any multi-core personal computer or workstation.

Operating system: Linux and Windows.

RAM: 1 GB.

Number of processors used: All available CPU cores on the executing computer.

Classification: 2.9, 4.3, 4.12.

Catalogue identifier of previous version: AEDU_v1_0, AEDU_v2_0.

Journal reference of previous version: Comput. Phys. Commun. 180 (2009) 1888; *ibid.* 183 (2012) 2021.

Does the new version supersede the previous version?: No. It does supersede versions AEDU_v1_0 and AEDU_v2_0, but not AEDU_v3_0, which is MPI-parallelized version.

* Corresponding author.

E-mail addresses: luisevery@gmail.com (L.E. Young-S.), dusan.vudragovic@ipb.ac.rs (D. Vudragović), anand@cniid.bdu.ac.in (P. Muruganandam), adhikari@ift.unesp.br (S.K. Adhikari), antun.balaz@ipb.ac.rs (A. Balaž).

<http://dx.doi.org/10.1016/j.cpc.2016.03.015>

0010-4655/© 2016 Elsevier B.V. All rights reserved.

Nature of problem: The present OpenMP Fortran and C programs solve the time-dependent nonlinear partial differential Gross–Pitaevskii (GP) equation for a Bose–Einstein condensate in one (1D), two (2D), and three (3D) spatial dimensions in a harmonic trap with six different symmetries: axial- and radial-symmetry in 3D, circular-symmetry in 2D, and fully anisotropic in 2D and 3D.

Solution method: The time-dependent GP equation is solved by the split-step Crank–Nicolson method by discretizing in space and time. The discretized equation is then solved by propagation, in either imaginary or real time, over small time steps. The method yields the solution of stationary and/or non-stationary problems.

Reasons for the new version: Previously published Fortran and C programs [1,2] for solving the GP equation are recently enjoying frequent usage [3] and application to a more complex scenario of dipolar atoms [4]. They are also further extended to make use of general purpose graphics processing units (GPGPU) with Nvidia CUDA [5], as well as computer clusters using Message Passing Interface (MPI) [6]. However, a vast majority of users use single-computer programs, with which the solution of a realistic dynamical 1D problem, not to mention the more complicated 2D and 3D problems, could be time consuming. Now practically all computers have multicore processors, ranging from 2 up to 18 and more CPU cores. Some computers include motherboards with more than one physical CPU, further increasing the possible number of available CPU cores on a single computer to several tens. The present programs are parallelized using OpenMP over all the CPU cores and can significantly reduce the execution time. Furthermore, in the old version of the programs [1,2] the inputs were based on the mathematical quantity nonlinearity for the dimensionless form of the GP equation. The inputs for the present versions of programs are given in terms of phenomenological variables of experimental interest, as in Refs. [4,5], i.e., number of atoms, scattering length, harmonic oscillator length of the confining trap, etc. Also, the output files are given names which make identification of their contents easier, as in Refs. [4,5]. In addition, new output files for integrated densities of experimental interest are provided, and all programs were thoroughly revised to eliminate redundancies.

Summary of revisions: Previous Fortran [1] and C [2] programs for the solution of time-dependent GP equation in 1D, 2D, and 3D with different trap symmetries have been modified to achieve two goals. First, they are parallelized using OpenMP interface to reduce the execution time in multicore processors. Previous C programs [2] had OpenMP-parallelized versions of 2D and 3D programs, together with the serial versions, while here all programs are OpenMP-parallelized. Secondly, the programs now have input and output files with quantities of phenomenological interest. There are six trap symmetries and both in C and in Fortran there are twelve programs, six for imaginary-time propagation and six for real-time propagation, totaling to 24 programs. In 3D, we consider full radial symmetry, axial symmetry and full anisotropy. In 2D, we consider circular symmetry and full anisotropy. The structure of all programs is similar.

For the Fortran programs the input data (number of atoms, scattering length, harmonic oscillator trap length, trap anisotropy, etc.) are conveniently placed at the beginning of each program. For the C programs the input data are placed in separate input files, examples of which can be found in a directory named input. The examples of output files for both Fortran and C programs are placed in the corresponding directories called output. The programs then calculate the dimensionless nonlinearities actually used in the calculation. The provided programs use physical input parameters that give identical nonlinearity values as the previously published programs [1,2], so that the output files of the old and new programs can be directly compared. The output files are conveniently named so that their contents can be easily identified, following Refs. [4,5]. For example, file named <code>-out.txt, where <code> is a name of the individual program, is the general output file containing input data, time and space steps, nonlinearity, energy and chemical potential, and was named fort.7 in the old Fortran version. The file <code>-den.txt is the output file with the condensate density, which had the names fort.3 and fort.4 in the old Fortran version for imaginary- and real-time propagation, respectively. Other density outputs, such as the initial density, are commented out to have a simpler set of output files. The users can re-introduce those by taking out the comment symbols, if needed.

Table 1

Wall-clock execution times (in seconds) for runs with 1, 6 and 20 CPU cores with different programs using the Intel Fortran ifort (F-1, F-6 and F-20, respectively) and Intel C icc (C-1, C-6 and C-20, respectively) compilers using a workstation with two Intel Xeon E5-2650 v3 CPUs, with a total of 20 CPU cores, and obtained speedups (speedup-F = F-1/F-20, -speedup-C = C-1/C-20) for 20 CPU cores.

	F-1	F-6	F-20	speedup-F	C-1	C-6	C-20	speedup-C
imag1d	32	26	26	1.2	45	28	27	1.7
imagcir	15	15	15	1.0	21	15	15	1.4
imagsph	12	12	12	1.0	19	12	10	1.9
real1d	194	84	72	2.7	304	110	98	3.1
realcir	132	62	57	2.3	182	78	64	2.8
realsph	119	68	67	1.8	191	76	61	3.1
imag2d	190	66	52	3.7	394	77	33	11.9
imagaxi	240	74	56	4.3	499	113	55	9.1
real2d	269	70	47	5.7	483	96	35	13.8
realaxi	132	37	25	5.3	237	51	22	10.8
imag3d	1682	472	366	4.6	2490	545	202	12.3
real3d	15,479	3494	2082	7.4	22,228	4558	1438	15.5

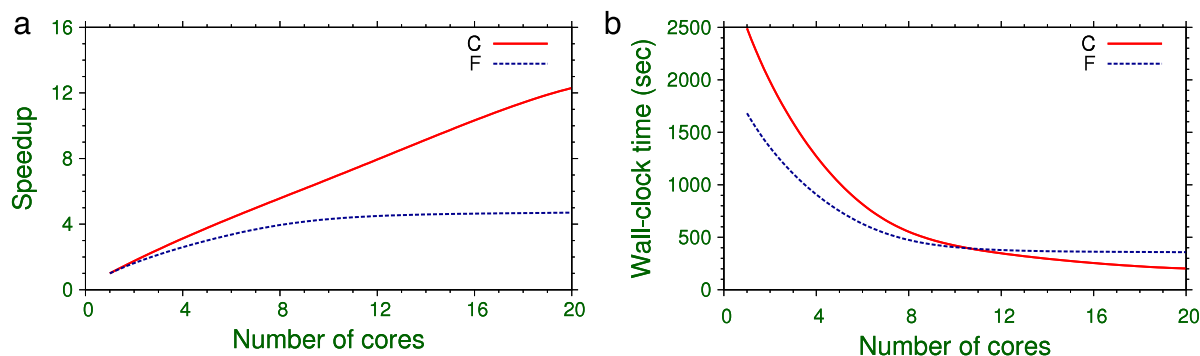


Fig. 1. (a) Speedup of the C and Fortran (F) imag3d programs as a function of the number of CPU cores, measured in a workstation with two Intel Xeon E5-2650 v3 CPUs. The speedup for the run with N CPU cores was calculated as the ratio between wall-clock execution times with one and N CPU cores. (b) Wall-clock time of the same runs as a function of the number of CPU cores.

Also, some new output files are introduced in this version of programs. The files `<code>-rms.txt` are the output files with values of root-mean-square (rms) sizes in the multi-variable cases. There are new files with integrated densities, such as `imag2d-den1d_x.txt`, where the first part (`imag2d`) denotes that the density was calculated with the 2D program `imag2d`, and the second part (`den1d_x`) stands for the 1D density in the x -direction, obtained after integrating out the 2D density $|\phi(x, y)|^2$ in the x - y plane over y -coordinate,

$$n_{1D}(x) = \int_{-\infty}^{\infty} dy |\phi(x, y)|^2. \quad (1)$$

Similarly, `imag3d-den1d_x.txt` and `real3d-den1d_x.txt` represent 1D densities from a 3D calculation obtained after integrating out the 3D density $|\phi(x, y, z)|^2$ over y - and z -coordinate. The files `imag3d-den2d_xy.txt` and `real3d-den2d_xy.txt` are the integrated 2D densities in the x - y plane from a 3D calculation obtained after integrating out the 3D density over the z -coordinate, and similarly for other output files. Again, calculation and saving of these integrated densities is commented out in the programs, and can be activated by the user, if needed.

In real-time propagation programs there are additional results for the dynamics saved in files, such as `real2d-dyna.txt`, where the first column denotes time, the second, third and fourth columns display rms sizes for the x -, y -, and r -coordinate, respectively. The dynamics is generated by multiplying the nonlinearity with a pre-defined factor during the NRUN iterations, and starting with the wave function calculated during the NPAS iterations. Such files were named `fort.8` in the old Fortran versions of programs. There are similar files in the 3D real-time programs as well.

Often it is needed to get a precise stationary state solution by imaginary-time propagation and then use it in the study of dynamics using real-time propagation. For that purpose, if the integer number NSTP is set to zero in real-time propagation, the density obtained in the imaginary-time simulation is used as initial wave function for real-time propagation, as in Refs. [4,5]. In addition, at the end of output files `<code>-out.txt`, we have introduced two new outputs, wall-clock execution time and CPU time for each run.

We tested our programs on a workstation with two 10-core Intel Xeon E5-2650 v3 CPUs, and present results for all programs compiled with the Intel compiler. In Table 1 we show different wall-clock execution times for runs on 1, 6 and 20 CPU cores for Fortran and C. The corresponding columns “speedup-F” and “speedup-C” give the ratio of wall-clock execution times of runs on 1 and 20 CPU cores, and denote the actual measured speedup for 20 CPU cores. For the programs with effectively one spatial variable, the Fortran programs turn out to be quicker for small number of cores, whereas for larger number of CPU cores and for the programs with three spatial variables the C programs are faster. We also studied the speedup of the programs as a function of the number of available CPU cores. The performance for the imag3d Fortran and C programs is illustrated in Fig. 1(a) and (b), where we plot the speedup and actual wall-clock time of the imag3d C and Fortran programs as a function of number of CPU cores in a workstation with two Intel Xeon E5-2650 v3 CPUs, with a total of 20 CPU cores. The plot in Fig. 1(a) shows that the C program parallelizes more efficiently than the Fortran program. However, as the wall-clock time in Fortran for a single CPU core is less than that in C, the wall-clock times in both cases are comparable, viz. Fig. 1(b). A saturation of the speedup with the increase of the number of CPU cores is expected in all cases. However, the saturation is attained quicker in Fortran than in C programs, and therefore the use of C programs could be recommended for larger number of CPU cores. For a small number of CPU cores the Fortran programs should be preferable. For example, from Table 1 we see that for 6 CPU cores the Fortran programs are faster than the C programs. In Fig. 1(a) the saturation of the speedup of the Fortran program is achieved for approximately 10 CPU cores, when the wall-clock time of the C program crosses that of the Fortran program.

Additional comments:

This package consists of 24 programs, see Program title above. For the particular purpose of each program, please see descriptions below.

Running time:

Example inputs provided with the programs take less than 30 min in a workstation with two Intel Xeon Processors E5-2650 v3, 2 QPI links, 10 CPU cores (25 MB cache, 2.3 GHz).

Program summary (i), (v), (vi), (vii), (xi), (xii)

Program title: imag1d, imagcir, imagsph, real1d, realcir, realsph.

Title of electronic files in C: (imag1d.c and imag1d.h), (imagcir.c and imagcir.h), (imagsph.c and imagsph.h), (real1d.c and real1d.h), (realcir.c and realcir.h), (realsph.c and realsph.h).

Title of electronic files in Fortran 90: imag1d.f90, imagcir.f90, imagsph.f90, real1d.f90, realcir.f90, realsph.f90.

Maximum RAM memory: 1 GB for the supplied programs.

Programming language used: OpenMP C and Fortran 90.

Typical running time: Minutes on a modern four-core PC.

Nature of physical problem: These programs are designed to solve the time-dependent nonlinear partial differential GP equation in one spatial variable.

Method of solution: The time-dependent GP equation is solved by the split-step Crank–Nicolson method by discretizing in space and time. The discretized equation is then solved by propagation in imaginary time over small time steps. The method yields the solution of stationary problems.

Program summary (ii), (iv), (viii), (x)

Program title: imag2d, imagaxi, real2d, realaxi.

Title of electronic files in C: (imag2d.c and imag2d.h), (imagaxi.c and imagaxi.h), (real2d.c and real2d.h), (realaxi.c and realaxi.h).

Title of electronic files in Fortran 90: imag2d.f90, imagaxi.f90, real2d.f90, realaxi.f90.

Maximum RAM memory: 1 GB for the supplied programs.

Programming language used: OpenMP C and Fortran 90.

Typical running time: Hour on a modern four-core PC.

Nature of physical problem: These programs are designed to solve the time-dependent nonlinear partial differential GP equation in two spatial variables.

Method of solution: The time-dependent GP equation is solved by the split-step Crank–Nicolson method by discretizing in space and time. The discretized equation is then solved by propagation in imaginary time over small time steps. The method yields the solution of stationary problems.

Program summary (iii), (ix)

Program title: imag3d, real3d.

Title of electronic files in C: (imag3d.c and imag3d.h), (real3d.c and real3d.h).

Title of electronic files in Fortran 90: imag3d.f90, real3d.f90.

Maximum RAM memory: 1 GB for the supplied programs.

Programming language used: OpenMP C and Fortran 90.

Typical running time: Few hours on a modern four-core PC.

Nature of physical problem: These programs are designed to solve the time-dependent nonlinear partial differential GP equation in three spatial variables.

Method of solution: The time-dependent GP equation is solved by the split-step Crank–Nicolson method by discretizing in space and time. The discretized equation is then solved by propagation in imaginary time over small time steps. The method yields the solution of stationary problems.

© 2016 Elsevier B.V. All rights reserved.

Acknowledgments

L.E. Y.-S. acknowledges support by the FAPESP of Brazil under project 2012/21871-7 and 2014/16363-8. D.V. and A.B. acknowledge support by the Ministry of Education, Science, and Technological Development of the Republic of Serbia under projects OI1611005, ON171017 and III43007. P.M. acknowledges support by the Science and Engineering Research Board, Department of Science and Technology, Government of India under project No. EMR/2014/000644. S.K.A. acknowledges support by the CNPq of Brazil under project 303280/2014-0, and by the FAPESP of Brazil under project 2012/00451-0.

References

- [1] P. Muruganandam, S.K. Adhikari, *Comput. Phys. Commun.* **180** (2009) 1888.
- [2] D. Vudragović, I. Vidanović, A. Balaž, P. Muruganandam, S.K. Adhikari, *Comput. Phys. Commun.* **183** (2012) 2021.
- [3] S. Gautam, (2016) e-print [arXiv:1601.06020](https://arxiv.org/abs/1601.06020);
I. Vasić, A. Balaž, (2016) e-print [arXiv:1602.03538](https://arxiv.org/abs/1602.03538);
T. Khellil, A. Balaž, A. Pelster, *New J. Phys.* (2016) e-print [arXiv:1510.04985](https://arxiv.org/abs/1510.04985);
T. Khellil, A. Pelster, *J. Stat. Mech.-Theory Exp.* (2016) e-print [arXiv:1511.08882](https://arxiv.org/abs/1511.08882);
J. Akram, A. Pelster, *Phys. Rev. A* **93** (2016) 023606;
J. Akram, A. Pelster, *Phys. Rev. A* **93** (2016) 033610;
T. Mithun, K. Porsezian, B. Dey, *Phys. Rev. A* **93** (2016) 013620;
L. Salasnich, S.K. Adhikari, *Acta Phys. Pol. A* **128** (2015) 979;
Y.H. Wang, A. Kumar, F. Jendrzejewski, R.M. Wilson, M. Edwards, S. Eckel, G.K. Campbell, C.W. Clark, *New J. Phys.* **17** (2015) 125012;
J.B. Sudharsan, R. Radha, H. Fabrelli, A. Gammal, B.A. Malomed, *Phys. Rev. A* **92** (2015) 053601;
V.S. Bagnato, D.J. Frantzeskakis, P.G. Kevrekidis, B.A. Malomed, D. Mihalache, *Rom. Rep. Phys.* **67** (2015) 5;
K.-T. Xi, J. Li, D.-N. Shi, *Phys. B* **459** (2015) 6;
H.L.C. Couto, W.B. Cardoso, *J. Phys. B: At. Mol. Opt. Phys.* **48** (2015) 025301;
E. Chiquillo, *J. Phys. A: Math. Theor.* **48** (2015) 475001;
S. Sabari, C.P. Jisha, K. Porsezian, V.A. Brazhnyi, *Phys. Rev. E* **92** (2015) 032905;
W. Wen, T.K. Shui, Y.F. Shan, C.P. Zhu, *J. Phys. B: At. Mol. Opt. Phys.* **48** (2015) 175301;
P. Das, P.K. Panigrahi, *Laser Phys.* **25** (2015) 125501;

- Y.S. Wang, S.T. Ji, Y.E. Luo, Z.Y. Li, J. Korean. Phys. Soc. 67 (2015) L1504;
 S.K. Adhikari, J. Phys. B: At. Mol. Opt. Phys. 48 (2015) 165303;
 F.I. Moxley III, T. Byrnes, B. Ma, Y. Yan, W. Dai, J. Comput. Phys. 282 (2015) 303;
 S.K. Adhikari, Phys. Rev. E 92 (2015) 042926;
 R.R. Sakhel, A.R. Sakhel, H.B. Ghassib, Physica B 478 (2015) 68;
 S. Gautam, S.K. Adhikari, Phys. Rev. A 92 (2015) 023616;
 D. Novoa, D. Tommasini, J.A. Nóvoa-López, Phys. Rev. E 91 (2015) 012904;
 S. Gautam, S.K. Adhikari, Laser Phys. Lett. 12 (2015) 045501;
 K.-T. Xi, J. Li, D.-N. Shi, Physica B 459 (2015) 6;
 S. Gautam, S.K. Adhikari, Phys. Rev. A 91 (2015) 013624;
 A.I. Nicolin, M.C. Raportaru, A. Balaž, Rom. Rep. Phys. 67 (2015) 143;
 S. Gautam, S.K. Adhikari, Phys. Rev. A 91 (2015) 063617;
 E.J.M. Madarassy, V.T. Toth, Phys. Rev. D 91 (2015) 044041;
 X. Antoine, R. Duboscq, Comput. Phys. Commun. 185 (2014) 2969;
 S.K. Adhikari, L.E. Young-S, J. Phys. B: At. Mol. Opt. Phys. 47 (2014) 015302;
 K. Manikandan, P. Muruganandam, M. Senthilvelan, M. Lakshmanan, Phys. Rev. E 90 (2014) 062905;
 S.K. Adhikari, Phys. Rev. A 90 (2014) 055601;
 A. Balaž, R. Paun, A.I. Nicolin, S. Balasubramanian, R. Ramaswamy, Phys. Rev. A 89 (2014) 023609;
 S.K. Adhikari, Phys. Rev. A 89 (2014) 013630;
 J. Luo, Commun. Nonlinear Sci. Numer. Simul. 19 (2014) 3591;
 S.K. Adhikari, Phys. Rev. A 89 (2014) 043609;
 K.-T. Xi, J. Li, D.-N. Shi, Physica B 436 (2014) 149;
 M.C. Raportaru, J. Jovanovski, B. Jakimovski, D. Jakimovski, A. Mishev, Rom. J. Phys. 59 (2014) 677;
 S. Gautam, S.K. Adhikari, Phys. Rev. A 90 (2014) 043619;
 A.I. Nicolin, A. Balaž, J.B. Sudharsan, R. Radha, Rom. J. Phys. 59 (2014) 204;
 K. Sakkaravarthi, T. Kanna, M. Vijayajayanthi, M. Lakshmanan, Phys. Rev. E 90 (2014) 052912;
 S.K. Adhikari, J. Phys. B: At. Mol. Opt. Phys. 47 (2014) 225304;
 R.K. Kumar, P. Muruganandam, Numerical studies on vortices in rotating dipolar Bose-Einstein condensates, in: Proceedings of the 22nd International Laser Physics Workshop, J. Phys. Conf. Ser. 497 (2014) 012036;
 A.I. Nicolin, I. Rata, Density waves in dipolar Bose-Einstein condensates by means of symbolic computations, in: High-Performance Computing Infrastructure for South East Europe's Research Communities: Results of the HP-SEE User Forum 2012, in: Springer Series: Modeling and Optimization in Science and Technologies, vol. 2, 2014, p. 15;
 S.K. Adhikari, Phys. Rev. A 89 (2014) 043615;
 R.K. Kumar, P. Muruganandam, Eur. Phys. J. D 68 (2014) 289;
 I. Vidanović, N.J. van Druten, M. Haque, New J. Phys. 15 (2013) 035008;
 S. Balasubramanian, R. Ramaswamy, A.I. Nicolin, Rom. Rep. Phys. 65 (2013) 820;
 L.E. Young-S, S.K. Adhikari, Phys. Rev. A 87 (2013) 013618;
 H. Al-Jibbouri, I. Vidanović, A. Balaž, A. Pelster, J. Phys. B: At. Mol. Opt. Phys. 46 (2013) 065303;
 X. Antoine, W. Bao, C. Besse, Comput. Phys. Commun. 184 (2013) 2621;
 B. Nikolić, A. Balaž, A. Pelster, Phys. Rev. A 88 (2013) 013624;
 H. Al-Jibbouri, A. Pelster, Phys. Rev. A 88 (2013) 033621;
 S.K. Adhikari, Phys. Rev. A 88 (2013) 043603;
 J.B. Sudharsan, R. Radha, P. Muruganandam, J. Phys. B: At. Mol. Opt. Phys. 46 (2013) 155302;
 R.R. Sakhel, A.R. Sakhel, H.B. Ghassib, J. Low Temp. Phys. 173 (2013) 177;
 E.J.M. Madarassy, V.T. Toth, Comput. Phys. Commun. 184 (2013) 1339;
 R.K. Kumar, P. Muruganandam, B.A. Malomed, J. Phys. B: At. Mol. Opt. Phys. 46 (2013) 175302;
 W. Bao, Q. Tang, Z. Xu, J. Comput. Phys. 235 (2013) 423;
 A.I. Nicolin, Proc. Rom. Acad. Ser. A-Math. Phys. 14 (2013) 35;
 R.M. Caplan, Comput. Phys. Commun. 184 (2013) 1250;
 S.K. Adhikari, J. Phys. B: At. Mol. Opt. Phys. 46 (2013) 115301;
 Ž. Marojević, E. Göklü, C. Lämmerzahl, Comput. Phys. Commun. 184 (2013) 1920;
 L.E. Young-S, S.K. Adhikari, Phys. Rev. A 86 (2012) 063611;
 S.K. Adhikari, J. Phys. B: At. Mol. Opt. Phys. 45 (2012) 235303.
 [4] R. Kishor Kumar, L.E. Young-S, D. Vudragović, A. Balaž, P. Muruganandam, S.K. Adhikari, Comput. Phys. Commun. 195 (2015) 117.
 [5] V. Lončar, A. Balaž, A. Bogojević, S. Skrbčić, P. Muruganandam, S.K. Adhikari, Comput. Phys. Commun. 200 (2016) 406.
 [6] B. Satarić, V. Slavnić, A. Belić, A. Balaž, P. Muruganandam, S.K. Adhikari, Comput. Phys. Commun. 200 (2016) 411.



Fortran and C programs for the time-dependent dipolar Gross–Pitaevskii equation in an anisotropic trap[☆]



R. Kishor Kumar^a, Luis E. Young-S.^b, Dušan Vudragović^c, Antun Balaž^c, Paulsamy Muruganandam^d, S.K. Adhikari^{b,*}

^a Instituto de Física, Universidade de São Paulo, 05508-090 São Paulo, SP, Brazil

^b Instituto de Física Teórica, UNESP – Universidade Estadual Paulista, 01.140-070 São Paulo, São Paulo, Brazil

^c Scientific Computing Laboratory, Institute of Physics Belgrade, University of Belgrade, Pregrevica 118, 11080 Belgrade, Serbia

^d School of Physics, Bharathidasan University, Palkalaiperur Campus, Tiruchirappalli – 620024, Tamil Nadu, India

ARTICLE INFO

Article history:

Received 27 May 2014

Received in revised form

4 March 2015

Accepted 30 March 2015

Available online 25 April 2015

Keywords:

Bose–Einstein condensate

Gross–Pitaevskii equation

Split-step Crank–Nicolson scheme

Real- and imaginary-time propagation

Fortran and C programs

Dipolar atoms

ABSTRACT

Many of the static and dynamic properties of an atomic Bose–Einstein condensate (BEC) are usually studied by solving the mean-field Gross–Pitaevskii (GP) equation, which is a nonlinear partial differential equation for short-range atomic interaction. More recently, BEC of atoms with long-range dipolar atomic interaction are used in theoretical and experimental studies. For dipolar atomic interaction, the GP equation is a partial integro-differential equation, requiring complex algorithm for its numerical solution. Here we present numerical algorithms for both stationary and non-stationary solutions of the full three-dimensional (3D) GP equation for a dipolar BEC, including the contact interaction. We also consider the simplified one- (1D) and two-dimensional (2D) GP equations satisfied by cigar- and disk-shaped dipolar BECs. We employ the split-step Crank–Nicolson method with real- and imaginary-time propagations, respectively, for the numerical solution of the GP equation for dynamic and static properties of a dipolar BEC. The atoms are considered to be polarized along the z axis and we consider ten different cases, e.g., stationary and non-stationary solutions of the GP equation for a dipolar BEC in 1D (along x and z axes), 2D (in x – y and x – z planes), and 3D, and we provide working codes in Fortran 90/95 and C for these ten cases (twenty programs in all). We present numerical results for energy, chemical potential, root-mean-square sizes and density of the dipolar BECs and, where available, compare them with results of other authors and of variational and Thomas–Fermi approximations.

Program summary

Program title: (i) imag1dZ, (ii) imag1dX, (iii) imag2dXY, (iv) imag2dXZ, (v) imag3d, (vi) real1dZ, (vii) real1dX, (viii) real2dXY, (ix) real2dXZ, (x) real3d

Catalogue identifier: AEWL_v1_0

Program summary URL: http://cpc.cs.qub.ac.uk/summaries/AEWL_v1_0.html

Program obtainable from: CPC Program Library, Queens University, Belfast, N. Ireland

Licensing provisions: Standard CPC licence, <http://cpc.cs.qub.ac.uk/licence/licence.html>

No. of lines in distributed program, including test data, etc.: 111384

No. of bytes in distributed program, including test data, etc.: 604013

Distribution format: tar.gz

© 2015 Elsevier B.V. All rights reserved.

[☆] This paper and its associated computer program are available via the Computer Physics Communication homepage on ScienceDirect (<http://www.sciencedirect.com/science/journal/00104655>).

* Corresponding author.

E-mail addresses: kishor@if.usp.br (R. Kishor Kumar), luis@ift.unesp.br (L.E. Young-S.), dusan@ipb.ac.rs (D. Vudragović), antun@ipb.ac.rs (A. Balaž), anand@cnld.bdu.ac.in (P. Muruganandam), adhikari@ift.unesp.br (S.K. Adhikari).

<http://dx.doi.org/10.1016/j.cpc.2015.03.024>

0010-4655/© 2015 Elsevier B.V. All rights reserved.

1. Introduction

After the experimental realization of atomic Bose–Einstein condensate (BEC) of alkali-metal and some other atoms, there has been a great deal of theoretical activity in studying the statics and dynamics of the condensate using the mean-field time-dependent Gross–Pitaevskii (GP) equation under different trap symmetries [1]. The GP equation in three dimensions (3D) is a

nonlinear partial differential equation in three space variables and a time variable and its numerical solution is indeed a difficult task specially for large nonlinearities encountered in realistic experimental situations [2]. Very special numerical algorithms are necessary for its precise numerical solution. In the case of alkali-metal atoms the atomic interaction in dilute BEC is essentially of short-range in nature and is approximated by a contact interaction and at zero temperature is parametrized by a single parameter in a dilute BEC – the s -wave atomic scattering length. Under this approximation the atomic interaction is represented by a cubic nonlinearity in the GP equation. Recently, we published the Fortran [3] and C [4] versions of useful programs for the numerical solution of the time-dependent GP equation with cubic nonlinearity under different trap symmetries using split-step Crank–Nicolson scheme and real- and imaginary-time propagations. Since then, these programs enjoyed widespread use [5].

More recently, there has been experimental observation of BEC of ^{52}Cr [6], ^{164}Dy [7] and ^{168}Er [8] atoms with large magnetic dipole moments. In this paper, for all trap symmetries the dipolar atoms are considered to be polarized along the z axis. In these cases the atomic interaction has a long-range dipolar counterpart in addition to the usual contact interaction. The s -wave contact interaction is local and spherically symmetric, whereas the dipolar interaction acting in all partial waves is nonlocal and asymmetric. The resulting GP equation in this case is a partial integro-differential equation and special algorithms are required for its numerical solution. Different approaches to the numerical solution of the dipolar GP equation have been suggested [9–14]. Yi and You [10] solve the dipolar GP equation for axially-symmetric trap while they perform the angular integral of the dipolar term, thus reducing it to one in axial (z, z') and radial (ρ, ρ') variables involving standard Elliptical integrals. The dipolar term is regularized by a cut-off at small distances and then evaluated numerically. The dipolar GP equation is then solved by imaginary-time propagation. Goral and Santos [11] treat the dipolar term by a convolution theorem without approximation, thus transforming it to an inverse Fourier transformation (FT) of a product of the FT of the dipolar potential and the condensate density. The FT and inverse FT are then numerically evaluated by standard fast Fourier transformation (FFT) routines in Cartesian coordinates. The ground state of the system is obtained by employing a standard split-operator technique in imaginary time. This approach is used by some others [15]. Ronen et al. perform the angular integral in the dipolar term using axial symmetry. To evaluate it, in stead of FT in x, y , and z [11], they use Hankel transformation in the radial ρ variable and FT in the axial z variable. The ground state wave function is then obtained by imaginary-time propagation and dynamics by real-time propagation. This approach is also used by some others [16]. Bao et al. use Euler sine pseudospectral method for computing the ground states and a time-splitting sine pseudospectral method for computing the dynamics of dipolar BECs [9]. Blakie et al. solve the projected dipolar GP equation using a Hermite polynomial-based spectral representation [13]. Lahaye et al. use FT in x, y , and z to evaluate the dipolar term and employ imaginary- and real-time propagation after Crank–Nicolson discretization for stationary and nonstationary solution of the dipolar GP equation [14].

Here we provide Fortran and C versions of programs for the solution of the dipolar GP equation in a fully anisotropic 3D trap by real- and imaginary-time propagation. We use split-step Crank–Nicolson scheme for the nondipolar part as in Refs. [3,4] and the dipolar term is treated by FT in x, y, z variables. We also present the Fortran and C programs for reduced dipolar GP equation in one (1D) and two dimensions (2D) appropriate for a cigar- and disk-shaped BEC under tight radial (ρ) and axial (z) trapping, respectively [17]. In the 1D case, we consider two possibilities: the 1D BEC could be aligned along the polarization direction z or be aligned

perpendicular to the polarization direction along x axis. Similarly, in the 2D case, two possibilities are considered taking the 2D plane as x – y , perpendicular to polarization direction z or as x – z containing the polarization direction. This amounts to five different trapping possibilities – two in 1D and 2D each and one in 3D – and two solution schemes involving real- and imaginary-time propagation resulting in ten programs each in Fortran and C.

In Section 2 we present the 3D dipolar GP equation in an anisotropic trap. In addition to presenting the mean-field model and a general scheme for its numerical solution in Sections 2.1 and 2.2, we also present two approximate solution schemes in Sections 2.3 and 2.4 – Gaussian variational approximation and Thomas–Fermi (TF) approximation – in this case. The reduced 1D and 2D GP equations appropriate for a cigar- and a disk-shaped dipolar BEC are next presented in Sections 2.5 and 2.6, respectively. The details about the computer programs, and their input/output files, etc. are given in Section 3. The numerical method and results are given in Section 4. Finally, a brief summary is given in Section 5.

2. Gross–Pitaevskii (GP) equation for dipolar condensates in three dimensions

2.1. The mean-field Gross–Pitaevskii equation

At ultra-low temperatures the properties of a dipolar condensate of N_{at} atoms, each of mass m , can be described by the mean-field GP equation with nonlocal nonlinearity of the form: [10,18]

$$i\hbar \frac{\partial \phi(\mathbf{r}, t)}{\partial t} = \left[-\frac{\hbar^2}{2m} \nabla^2 + V_{\text{trap}}(\mathbf{r}) + \frac{4\pi \hbar^2 a N_{\text{at}}}{m} |\phi(\mathbf{r}, t)|^2 + N_{\text{at}} \int U_{\text{dd}}(\mathbf{r} - \mathbf{r}') |\phi(\mathbf{r}', t)|^2 d\mathbf{r}' \right] \phi(\mathbf{r}, t), \quad (1)$$

where $\int d\mathbf{r} |\phi(\mathbf{r}, t)|^2 = 1$. The trapping potential, V_{trap} is assumed to be fully asymmetric of the form

$$V_{\text{trap}}(\mathbf{r}) = \frac{1}{2} m (\omega_x^2 x^2 + \omega_y^2 y^2 + \omega_z^2 z^2)$$

where ω_x, ω_y and ω_z are the trap frequencies, a the atomic scattering length. The dipolar interaction, for magnetic dipoles, is given by [11,16]

$$U_{\text{dd}}(\mathbf{R}) = \frac{\mu_0 \bar{\mu}^2}{4\pi} \frac{1 - 3 \cos^2 \theta}{|\mathbf{R}|^3}, \quad (2)$$

where $\mathbf{R} = \mathbf{r} - \mathbf{r}'$ determines the relative position of dipoles and θ is the angle between \mathbf{R} and the direction of polarization z , μ_0 is the permeability of free space and $\bar{\mu}$ is the dipole moment of the condensate atom. To compare the contact and dipolar interactions, often it is useful to introduce the length scale $a_{\text{dd}} \equiv \mu_0 \bar{\mu}^2 m / (12\pi \hbar^2)$ [6].

Convenient dimensionless parameters can be defined in terms of a reference frequency $\bar{\omega}$ and the corresponding oscillator length $l = \sqrt{\hbar / (m\bar{\omega})}$. Using dimensionless variables $\bar{\mathbf{r}} = \mathbf{r}/l, \bar{\mathbf{R}} = \mathbf{R}/l, \bar{a} = a/l, \bar{a}_{\text{dd}} = a_{\text{dd}}/l, \bar{t} = t\bar{\omega}, \bar{x} = x/l, \bar{y} = y/l, \bar{z} = z/l, \bar{\phi} = l^{3/2} \phi$, Eq. (1) can be rewritten (after removing the overhead bar from all the variables) as

$$i \frac{\partial \phi(\mathbf{r}, t)}{\partial t} = \left[-\frac{1}{2} \nabla^2 + \frac{1}{2} (\gamma^2 x^2 + \nu^2 y^2 + \lambda^2 z^2) + 4\pi a N_{\text{at}} |\phi|^2 + 3N_{\text{at}} a_{\text{dd}} \int V_{\text{dd}}^{3D}(\mathbf{R}) |\phi(\mathbf{r}', t)|^2 d\mathbf{r}' \right] \phi(\mathbf{r}, t), \quad (3)$$

with

$$V_{\text{dd}}^{3D}(\mathbf{R}) = \frac{1 - 3 \cos^2 \theta}{|\mathbf{R}|^3}, \quad (4)$$

where $\gamma = \omega_x/\bar{\omega}$, $\nu = \omega_y/\bar{\omega}$, $\lambda = \omega_z/\bar{\omega}$. The reference frequency $\bar{\omega}$ can be taken as one of the frequencies ω_x , ω_y or ω_z or their geometric mean $(\omega_x\omega_y\omega_z)^{1/3}$. In the following we shall use Eq. (3) where we have removed the ‘bar’ from all variables.

Although we are mostly interested in the numerical solution of Eq. (3), in the following we describe two *analytical* approximation methods for its solution in the axially-symmetric case. These approximation methods – the Gaussian variational and TF approximations – provide reasonably accurate results under some limiting conditions and will be used for comparison with the numerical results. Also, we present reduced 1D and 2D mean-field GP equations appropriate for the description of a cigar and disk-shaped dipolar BEC under appropriate trapping condition. The numerical solution and variational approximation of these reduced equations will be discussed in this paper. A brief algebraic description of these topics are presented for the sake of completeness as appropriate for this study. For a full description of the same the reader is referred to the original publications.

2.2. Methodology

We perform numerical simulation of the 3D GP equation (3) using the split-step Crank–Nicolson method described in detail in Ref. [3]. Here we present the procedure to include the dipolar term in that algorithm. The inclusion of the dipolar integral term in the GP equation in coordinate space is not straightforward due to the singular behavior of the dipolar potential at short distances. It is interesting to note that this integral is well defined and finite. This problem has been tackled by evaluating the dipolar term in the momentum (k) space, where we do not face a singular behavior. The integral can be simplified in Fourier space by means of convolution as

$$\int d\mathbf{r}' V_{\text{dd}}^{3D}(\mathbf{r} - \mathbf{r}') n(\mathbf{r}', t) = \int \frac{d\mathbf{k}}{(2\pi)^3} e^{-i\mathbf{k}\cdot\mathbf{r}} \tilde{V}_{\text{dd}}^{3D}(\mathbf{k}) \tilde{n}(\mathbf{k}, t), \quad (5)$$

where $n(\mathbf{r}, t) = |\phi(\mathbf{r}, t)|^2$. The Fourier transformation (FT) and inverse FT, respectively, are defined by

$$\tilde{A}(\mathbf{k}) = \int d\mathbf{r} A(\mathbf{r}) e^{i\mathbf{k}\cdot\mathbf{r}}, \quad A(\mathbf{r}) = \frac{1}{(2\pi)^3} \int d\mathbf{k} \tilde{A}(\mathbf{k}) e^{-i\mathbf{k}\cdot\mathbf{r}}. \quad (6)$$

The FT of the dipole potential can be obtained analytically [19]

$$\tilde{V}_{\text{dd}}^{3D}(\mathbf{k}) \equiv \frac{4\pi}{3} h_{3D}(\mathbf{k}) = \frac{4\pi}{3} \left(\frac{3k_z^2}{k^2} - 1 \right), \quad (7)$$

so that

$$\int d\mathbf{r}' V_{\text{dd}}^{3D}(\mathbf{r} - \mathbf{r}') n(\mathbf{r}', t) = \frac{4\pi}{3} \int \frac{d\mathbf{k}}{(2\pi)^3} e^{-i\mathbf{k}\cdot\mathbf{r}} h_{3D}(\mathbf{k}) \tilde{n}(\mathbf{k}, t). \quad (8)$$

To obtain Eq. (7), first the angular integration is performed. Then a cut-off at small r is introduced to perform the radial integration and eventually the zero cut-off limit is taken in the final result as shown in Appendix A of Ref. [19]. The FT of density $n(\mathbf{r})$ is evaluated numerically by means of a standard FFT algorithm. The dipolar integral in Eq. (3) involving the FT of density multiplied by FT of dipolar interaction is evaluated by the convolution theorem (5). The inverse FT is taken by means of the standard FFT algorithm. The FFT algorithm is carried out in Cartesian coordinates and the GP equation is solved in 3D irrespective of the symmetry of the trapping potential. The dipolar interaction integrals in 1D and 2D GP equations are also evaluated in momentum spaces. The solution algorithm of the GP equation by the split-step Crank–Nicolson method is adopted from Refs. [3,4].

The 3D GP equation (3) is numerically the most difficult to solve involving large RAM and CPU time. A requirement for the success

of the split-step Crank–Nicolson method using a FT continuous at the origin is that on the boundary of the space discretization region the wave function and the interaction term should vanish. For the long-range dipolar potential this is not true and the FT (7) is discontinuous at the origin. The space domain (from $-\infty$ to $+\infty$) cannot be restricted to a small region in space just covering the spatial extension of the BEC as the same domain is also used to calculate the FT and inverse FT used in treating the long-range dipolar potential. The use and success of FFT implies a set of noninteracting 3D periodic lattice of BECs in different unit cells. This is not true for long-range dipolar interaction which will lead to an interaction between BECs in different cells. Thus, boundary effects can play a role when finding the FT. Hence a sufficiently large space domain is to be used to have accurate values of the FT involving the long-range dipolar potential. It was suggested [12] that this could be avoided by truncating the dipolar interaction conveniently at large distances $r = R$ so that it does not affect the boundary, provided R is taken to be larger than the size of the condensate. Then the truncated dipolar potential will cover the whole condensate wave function and will have a continuous FT at the origin. This will improve the accuracy of a calculation using a small space domain. The FT of the dipolar potential truncated at $r = R$, as suggested in Ref. [12], is used in the numerical routines

$$\tilde{V}_{\text{dd}}^{3D}(\mathbf{k}) = \frac{4\pi}{3} \left(\frac{3k_z^2}{k^2} - 1 \right) \left[1 + 3 \frac{\cos(kR)}{k^2 R^2} - 3 \frac{\sin(kR)}{k^3 R^3} \right], \quad (9)$$

$$k = |\mathbf{k}|.$$

Needless to say, the difficulty in using a large space domain is the most severe in 3D. In 3D programs the cut-off R of Eq. (9) improves the accuracy of calculation and a smaller space region can be used in numerical treatment. In 1D and 2D, a larger space domain can be used relatively easily and no cut-off has been used. Also, no convenient and efficient analytic cut-off is known in 1D and 2D [12]. The truncated dipolar potential (9) has only been used in the numerical programs in 3D, e.g., *imag3d** and *real3d**. In all other numerical programs in 1D and 2D, and in all analytic results reported in the following the untruncated potential (7) has been used.

2.3. Gaussian variational approximation

In the axially-symmetric case ($\gamma = \nu$), convenient analytic Lagrangian variational approximation of Eq. (3) can be obtained with the following Gaussian ansatz for the wave function [20]

$$\phi(\mathbf{r}, t) = \frac{\pi^{-3/4}}{w_\rho(t)\sqrt{w_z(t)}} \times \exp \left[-\frac{\rho^2}{2w_\rho^2(t)} - \frac{z^2}{2w_z^2(t)} + i\alpha(t)\rho^2 + i\beta(t)z^2 \right] \quad (10)$$

where $\mathbf{r} = \{\rho, z\}$, $\rho = \{x, y\}$, $w_\rho(t)$ and $w_z(t)$ are widths and $\alpha(t)$ and $\beta(t)$ are chirps. The time dependence of the variational parameters $w_\rho(t)$, $w_z(t)$, $\alpha(t)$ and $\beta(t)$ will not be explicitly shown in the following.

The Lagrangian density corresponding to Eq. (3) is given by

$$\begin{aligned} \mathcal{L}(\mathbf{r}) = & \frac{i}{2} \left[\phi(\mathbf{r}) \frac{\phi^*(\mathbf{r})}{\partial t} - \phi^*(\mathbf{r}) \frac{\partial \phi(\mathbf{r})}{\partial t} \right] + \frac{|\nabla \phi(\mathbf{r})|^2}{2} \\ & + \frac{1}{2} (\gamma^2 \rho^2 + \lambda^2 z^2) |\phi(\mathbf{r})|^2 + 2\pi a N_{\text{at}} |\phi(\mathbf{r})|^4 \\ & + \frac{3a_{\text{dd}} N_{\text{at}}}{2} |\phi(\mathbf{r})|^2 \int V_{\text{dd}}(\mathbf{R}) |\phi(\mathbf{r}')|^2 d\mathbf{r}'. \end{aligned} \quad (11)$$

Consequently, the effective Lagrangian $L \equiv \int \mathcal{L}(\mathbf{r}) d\mathbf{r}$ (per particle) becomes [6,21]

$$L = \omega_\rho^2 \dot{\alpha} + \frac{\omega_z^2 \dot{\beta}}{2} + \frac{\gamma^2 \omega_\rho^2}{2} + \frac{\lambda^2 \omega_z^2}{4} + \frac{1}{2\omega_\rho^2} + \frac{1}{4\omega_z^2} + 2\omega_\rho^2 \alpha^2 + \omega_z^2 \beta^2 + \frac{N_{\text{at}}[a - a_{\text{ddf}}(\kappa)]}{\sqrt{2\pi} \omega_\rho^2 \omega_z}. \quad (12)$$

The Euler–Lagrangian equations with this Lagrangian leads to the following set of coupled ordinary differential equations (ODE) for the widths w_ρ and w_z [22]:

$$\ddot{w}_\rho + \gamma^2 w_\rho = \frac{1}{w_\rho^3} + \frac{N_{\text{at}}}{\sqrt{2\pi}} \frac{[2a - a_{\text{ddf}}(\kappa)]}{w_\rho^3 w_z}, \quad (13)$$

$$\ddot{w}_z + \lambda^2 w_z = \frac{1}{w_z^3} + \frac{2N_{\text{at}}}{\sqrt{2\pi}} \frac{[a - a_{\text{ddc}}(\kappa)]}{w_\rho^2 w_z^2}, \quad (14)$$

with $\kappa = w_\rho/w_z$ and

$$g(\kappa) = \frac{2 - 7\kappa^2 - 4\kappa^4 + 9\kappa^4 d(\kappa)}{(1 - \kappa^2)^2}, \quad (15)$$

$$c(\kappa) = \frac{1 + 10\kappa^2 - 2\kappa^4 - 9\kappa^2 d(\kappa)}{(1 - \kappa^2)^2}, \quad (16)$$

$$f(\kappa) = \frac{1 + 2\kappa^2 - 3\kappa^2 d(\kappa)}{1 - \kappa^2}, \quad d(\kappa) = \frac{\text{atanh}\sqrt{1 - \kappa^2}}{\sqrt{1 - \kappa^2}}. \quad (17)$$

The widths of a (time-independent) stationary state are obtained from Eqs. (13) and (14) by setting $\ddot{w}_\rho = \ddot{w}_z = 0$. The energy (per particle) of the stationary state is the Lagrangian (12) with $\alpha = \beta = 0$, e.g.,

$$\frac{E}{N_{\text{at}}} = \frac{1}{2w_\rho^2} + \frac{1}{4w_z^2} + \frac{N_{\text{at}}[a - a_{\text{ddf}}(\kappa)]}{\sqrt{2\pi} w_\rho w_z} + \frac{\gamma^2 w_\rho^2}{2} + \frac{\lambda^2 w_z^2}{4}. \quad (18)$$

The chemical potential $\mu = \partial E/\partial N_{\text{at}}$ of the stationary state is given by [22]

$$\mu = \frac{1}{2w_\rho^2} + \frac{1}{4w_z^2} + \frac{2N_{\text{at}}[a - a_{\text{ddf}}(\kappa)]}{\sqrt{2\pi} w_\rho w_z} + \frac{\gamma^2 w_\rho^2}{2} + \frac{\lambda^2 w_z^2}{4}. \quad (19)$$

2.4. Thomas–Fermi (TF) approximation

In the time-dependent axially-symmetric GP equation (3), when the atomic interaction term is large compared to the kinetic energy gradient term, the kinetic energy can be neglected and the useful TF approximation emerges. We assume the normalized density of the dipolar BEC of the form [1,23–25]

$$n(\mathbf{r}, t) \equiv |\phi(\mathbf{r}, t)|^2 = \frac{15}{8\pi R_\rho^2(t) R_z(t)} \left[1 - \frac{\rho^2}{R_\rho^2(t)} - \frac{z^2}{R_z^2(t)} \right], \quad (20)$$

where $R_\rho(t)$ and $R_z(t)$ are the radial and axial sizes. The time dependence of these sizes will not be explicitly shown in the following. Using the parabolic density (20), the energy functional E_{TF} may be written as [24]

$$E_{\text{TF}} \equiv E_{\text{trap}} + E_{\text{int}} = \left[\frac{N(2\gamma^2 R_\rho^2 + \lambda^2 R_z^2)}{14} \right] + \left[\frac{15}{28\pi} \frac{4\pi a N_{\text{at}}^2}{R_\rho^2 R_z} \left\{ 1 - \frac{a_{\text{ddf}}}{a} f(\bar{\kappa}) \right\} \right], \quad (21)$$

where $\bar{\kappa} = R_\rho/R_z$ is the ratio of the condensate sizes and $f(\bar{\kappa})$ is given by Eq. (17). In Eq. (21), E_{trap} is the energy in the trap and E_{int} is the interaction or release energy in the TF approximation. In the TF

regime one has the following set of coupled ODEs for the evolution of the condensate sizes [23]:

$$\ddot{R}_\rho = -R_\rho \gamma^2 + \frac{15aN_{\text{at}}}{R_\rho R_z} \left[\frac{1}{R_\rho^2} - \frac{a_{\text{dd}}}{a} \left(\frac{1}{R_\rho^2} + \frac{3}{2} \frac{f(\bar{\kappa})}{R_\rho^2 - R_z^2} \right) \right], \quad (22)$$

$$\ddot{R}_z = -\lambda^2 R_z + \frac{15aN_{\text{at}}}{R_\rho^2} \left[\frac{1}{R_z^2} + \frac{2a_{\text{dd}}}{a} \left(\frac{1}{R_z^2} + \frac{3}{2} \frac{f(\bar{\kappa})}{R_\rho^2 - R_z^2} \right) \right]. \quad (23)$$

The sizes of a stationary state can be calculated from Eqs. (22) and (23) by setting the time derivatives \ddot{R}_ρ and \ddot{R}_z to zero leading to the transcendental equation for $\bar{\kappa}$ [23]:

$$3\bar{\kappa}^2 \frac{a_{\text{dd}}}{a} \left[\left(1 + \frac{\lambda^2}{2\gamma^2} \right) \frac{f(\bar{\kappa})}{1 - \bar{\kappa}^2} - 1 \right] + \left(\frac{a_{\text{dd}}}{a} - 1 \right) \left(\bar{\kappa}^2 - \frac{\lambda^2}{\gamma^2} \right) = 0, \quad (24)$$

and

$$R_\rho = \left[\frac{15aN_{\text{at}}\bar{\kappa}}{\gamma^2} \left\{ 1 + \frac{a_{\text{dd}}}{a} \left(\frac{3}{2} \frac{\bar{\kappa}^2 f(\bar{\kappa})}{1 - \bar{\kappa}^2} - 1 \right) \right\} \right]^{1/5}, \quad (25)$$

with $R_z = R_\rho/\bar{\kappa}$. The chemical potential is given by [24]

$$\mu_{\text{TF}} \equiv E_{\text{trap}} + 2E_{\text{int}} = \frac{15}{8\pi} \frac{4\pi a N_{\text{at}}}{R_\rho^2 R_z} \left[1 - \frac{a_{\text{dd}}}{a} f(\bar{\kappa}) \right]. \quad (26)$$

We have the identities $E_{\text{TF}}/N_{\text{at}} = 5\mu_{\text{TF}}/7$, $E_{\text{int}}/N_{\text{at}} = 2\mu_{\text{TF}}/7$, $E_{\text{trap}}/N_{\text{at}} = 3\mu_{\text{TF}}/7$.

2.5. One-dimensional GP equation for a cigar-shaped dipolar BEC

2.5.1. z direction

For a cigar-shaped dipolar BEC with a strong axially-symmetric ($v = \gamma$) radial trap ($\lambda < v, \gamma$), we assume that the dynamics of the BEC in the radial direction is confined in the radial ground state [22,26,27]

$$\phi(\boldsymbol{\rho}) = \exp(-\rho^2/2d_\rho^2)/(d_\rho\sqrt{\pi}), \quad \gamma d_\rho^2 = 1, \quad \boldsymbol{\rho} \equiv (x, y), \quad (27)$$

of the transverse trap and the wave function $\phi(\mathbf{r})$ can be written as

$$\phi(\mathbf{r}, t) \equiv \phi_{1D}(z, t) \times \phi(\boldsymbol{\rho}) = \frac{1}{\sqrt{\pi} d_\rho^2} \exp \left[-\frac{\rho^2}{2d_\rho^2} \right] \phi_{1D}(z, t), \quad (28)$$

where $\phi_{1D}(z, t)$ is the effective 1D wave function for the axial dynamics and d_ρ is the radial harmonic oscillator length.

To derive the effective 1D equation for the cigar-shaped dipolar BEC, we substitute the ansatz (28) in Eq. (3), multiply by the ground-state wave function $\phi(\boldsymbol{\rho})$ and integrate over $\boldsymbol{\rho}$ to get the 1D equation [22,26]

$$i \frac{\partial \phi_{1D}(z, t)}{\partial t} = \left[-\frac{\partial_z^2}{2} + \frac{\lambda^2 z^2}{2} + \frac{2aN_{\text{at}}|\phi_{1D}|^2}{d_\rho^2} + 3a_{\text{dd}}N_{\text{at}} \int_{-\infty}^{\infty} V_{\text{dd}}^{1D}(|z - z'|) |\phi_{1D}(z', t)|^2 dz' \right] \phi_{1D}(z, t), \quad (29)$$

$$V_{\text{dd}}^{1D}(Z) = \frac{2\pi}{\sqrt{2}d_\rho} \left[\frac{4}{3} \delta(\sqrt{w}) + 2\sqrt{w} - \sqrt{\pi}(1 + 2w)e^w \{1 - \text{erf}(\sqrt{w})\} \right], \quad (30)$$

where $w = [Z/(\sqrt{2}d_\rho)]^2$, $Z = |z - z'|$. Here and in all reductions in Sections 2.5 and 2.6 we use the untruncated dipolar potential

(7) and not the truncated potential (9). The integral term in the 1D GP equation (29) is conveniently evaluated in momentum space using the following convolution identity [22]

$$\int_{-\infty}^{\infty} V_{\text{dd}}^{1D}(|z-z'|)|\phi_{1D}(z',t)|^2 dz' = \frac{4\pi}{3} \int_{-\infty}^{\infty} \frac{dk_z}{2\pi} e^{-ik_z z} \tilde{n}(k_z, t) h_{1D}\left(\frac{k_z d_\rho}{\sqrt{2}}\right), \quad (31)$$

where

$$\tilde{n}(k_z, t) = \int_{-\infty}^{\infty} e^{ik_z z} |\phi_{1D}(z, t)|^2 dz, \quad (32)$$

$$\tilde{n}(\mathbf{k}_\rho) = \int e^{i\mathbf{k}_\rho \cdot \boldsymbol{\rho}} |\phi_{2D}(\boldsymbol{\rho})|^2 d\rho = e^{-k_\rho^2 d_\rho^2/4}, \quad k_\rho = \sqrt{k_x^2 + k_y^2} \quad (33)$$

$$h_{1D}(\zeta) \equiv \frac{1}{(2\pi)^2} \int d\mathbf{k}_\rho \left[\frac{3k_z^2}{\mathbf{k}^2} - 1 \right] |\tilde{n}(\mathbf{k}_\rho)|^2 = \frac{1}{2\pi d_\rho^2} \int_0^\infty du \left[\frac{3\zeta^2}{u + \zeta^2} - 1 \right] e^{-u}, \quad \zeta = \frac{k_z d_\rho}{\sqrt{2}}. \quad (34)$$

The 1D GP equation (29) can be solved analytically using the Lagrangian variational formalism with the following Gaussian ansatz for the wave function [22]:

$$\phi_{1D}(z, t) = \frac{\pi^{-1/4}}{\sqrt{w_z(t)}} \exp\left[-\frac{z^2}{2w_z^2(t)} + i\beta(t)z^2\right], \quad (35)$$

where $w_z(t)$ is the width and $\beta(t)$ is the chirp. The Lagrangian variational formalism leads to the following equation for the width $w_z(t)$ [22]:

$$\ddot{w}_z(t) + \lambda^2 w_z(t) = \frac{1}{w_z^3(t)} + \frac{2N_{\text{at}}}{\sqrt{2\pi}} \frac{[a - a_{\text{dd}}c(\hat{\kappa})]}{d_\rho^2 w_z^2(t)},$$

$$\hat{\kappa} = \frac{d_\rho}{w_z(t)}. \quad (36)$$

The time-independent width of a stationary state can be obtained from Eq. (36) by setting $\ddot{w}_z(t) = 0$. The variational chemical potential for the stationary state is given by [22]

$$\mu = \frac{1}{4w_z^2} + \frac{2N_{\text{at}}[a - a_{\text{dd}}f(\hat{\kappa})]}{\sqrt{2\pi} w_z d_\rho^2} + \frac{\lambda^2 w_z^2}{4}. \quad (37)$$

The energy per particle is given by

$$\frac{E}{N_{\text{at}}} = \frac{1}{4w_z^2} + \frac{N_{\text{at}}[a - a_{\text{dd}}f(\hat{\kappa})]}{\sqrt{2\pi} w_z d_\rho^2} + \frac{\lambda^2 w_z^2}{4}. \quad (38)$$

2.5.2. x direction

For a cigar-shaped dipolar BEC with a strong axially-symmetric ($\nu = \lambda$) radial trap ($\gamma < \nu, \lambda$), we assume that the dynamics of the BEC in the radial direction is confined in the radial ground state [22,26,27]

$$\phi(\boldsymbol{\rho}) = \exp(-\rho^2/2d_\rho^2)/(d_\rho\sqrt{\pi}), \quad \nu d_\rho^2 = 1, \quad \boldsymbol{\rho} \equiv (y, z), \quad (39)$$

of the transverse trap and the wave function $\phi(\mathbf{r})$ can be written as

$$\phi(\mathbf{r}, t) \equiv \phi_{1D}(x, t) \times \phi(\boldsymbol{\rho}) = \frac{1}{\sqrt{\pi d_\rho^2}} \exp\left[-\frac{\rho^2}{2d_\rho^2}\right] \phi_{1D}(x, t), \quad (40)$$

where $\phi_{1D}(x, t)$ is the effective 1D wave function for the dynamics along x axis and d_ρ is the radial harmonic oscillator length.

To derive the effective 1D equation for the cigar-shaped dipolar BEC, we substitute the ansatz (40) in Eq. (3), multiply by the

ground-state wave function $\phi(\boldsymbol{\rho})$ and integrate over $\boldsymbol{\rho}$ to get the 1D equation

$$i \frac{\partial \phi_{1D}(x, t)}{\partial t} = \left[-\frac{\partial_x^2}{2} + \frac{\gamma^2 x^2}{2} + \frac{2aN_{\text{at}}|\phi_{1D}|^2}{d_\rho^2} + 4\pi a_{\text{dd}}N_{\text{at}} \int_{-\infty}^{\infty} \frac{dk_x}{2\pi} e^{-ik_x x} \tilde{n}(k_x, t) j_{1D}(\tau_x) \right] \phi_{1D}(x, t), \quad (41)$$

where $\tau_x = d_\rho k_x/\sqrt{2}$ and

$$j_{1D}(\tau_x) \equiv \frac{1}{(2\pi)^2} \int d\mathbf{k}_\rho \left[\frac{3k_z^2}{\mathbf{k}^2} - 1 \right] |\tilde{n}(\mathbf{k}_\rho)|^2 = \frac{\sqrt{2}}{2\pi d_\rho} \int_{-\infty}^{\infty} d\tau_y e^{-\tau_y^2} h_{2D}(\tau), \quad \tau_y = \frac{d_\rho k_y}{\sqrt{2}}, \quad \tau = \sqrt{\tau_x^2 + \tau_y^2}, \quad (42)$$

$$h_{2D}(\tau) = \frac{1}{\sqrt{2\pi}d_\rho} [2 - 3\sqrt{\pi}e^{\tau^2}\tau\{1 - \text{erf}(\tau)\}]. \quad (43)$$

To derive Eq. (41), the dipolar term in Eq. (3) is first written in momentum space using Eq. (8) and the integrations over k_y and k_z are performed in the dipolar term.

2.6. Two-dimensional GP equation for a disk-shaped dipolar BEC

2.6.1. x - y plane

For an axially-symmetric ($\nu = \gamma$) disk-shaped dipolar BEC with a strong axial trap ($\lambda > \nu, \gamma$), we assume that the dynamics of the BEC in the axial direction is confined in the axial ground state

$$\phi(z) = \exp(-z^2/2d_z^2)/(\pi d_z^2)^{1/4}, \quad d_z = \sqrt{1/(\lambda)}, \quad (44)$$

and we have for the wave function

$$\phi(\mathbf{r}) \equiv \phi(z) \times \phi_{2D}(\boldsymbol{\rho}, t) = \frac{1}{(\pi d_z^2)^{1/4}} \exp\left[-\frac{z^2}{2d_z^2}\right] \phi_{2D}(\boldsymbol{\rho}, t), \quad (45)$$

where $\boldsymbol{\rho} \equiv (x, y)$, $\phi_{2D}(\boldsymbol{\rho}, t)$ is the effective 2D wave function for the radial dynamics and d_z is the axial harmonic oscillator length. To derive the effective 2D equation for the disk-shaped dipolar BEC, we use ansatz (45) in Eq. (3), multiply by the ground-state wave function $\phi(z)$ and integrate over z to get the 2D equation [22,28]

$$i \frac{\partial \phi_{2D}(\boldsymbol{\rho}, t)}{\partial t} = \left[-\frac{\nabla_\rho^2}{2} + \frac{\gamma^2 x^2 + \nu^2 y^2}{2} + \frac{4\pi aN_{\text{at}}|\phi_{2D}|^2}{\sqrt{2\pi}d_z} + 4\pi a_{\text{dd}}N_{\text{at}} \int \frac{d\mathbf{k}_\rho}{(2\pi)^2} e^{-i\mathbf{k}_\rho \cdot \boldsymbol{\rho}} \tilde{n}(\mathbf{k}_\rho, t) h_{2D}\left(\frac{k_\rho d_z}{\sqrt{2}}\right) \right] \phi_{2D}(\boldsymbol{\rho}, t), \quad (46)$$

where $k_\rho = \sqrt{k_x^2 + k_y^2}$, and

$$\tilde{n}(\mathbf{k}_\rho, t) = \int d\boldsymbol{\rho} e^{i\mathbf{k}_\rho \cdot \boldsymbol{\rho}} |\phi_{2D}(\boldsymbol{\rho}, t)|^2, \quad (47)$$

$$\tilde{n}(k_z) = \int dz e^{ik_z z} |\phi(z)|^2 = e^{-k_z^2 d_z^2/4},$$

$$h_{2D}(\xi) \equiv \frac{1}{2\pi} \int_{-\infty}^{\infty} dk_z \left[\frac{3k_z^2}{\mathbf{k}^2} - 1 \right] |\tilde{n}(k_z)|^2 = \frac{1}{\sqrt{2\pi}d_z} [2 - 3\sqrt{\pi}\xi \exp(\xi^2)\{1 - \text{erf}(\xi)\}], \quad \xi = \frac{k_\rho d_z}{\sqrt{2}}. \quad (48)$$

To derive Eq. (46), the dipolar term in Eq. (3) is first written in momentum space using Eq. (8) and the integration over k_z is performed in the dipolar term.

The 2D GP equation (46) can be solved analytically using the Lagrangian variational formalism with the following Gaussian ansatz for the wave function [22]:

$$\phi_{2D}(\boldsymbol{\rho}, t) = \frac{\pi^{-1/2}}{w_\rho(t)} \exp \left[-\frac{\rho^2}{2w_\rho^2(t)} + i\alpha(t)\rho^2 \right], \quad (49)$$

where $w_\rho(t)$ is the width and $\alpha(t)$ is the chirp. The Lagrangian variational formalism leads to the following equation for the width w_ρ [22]:

$$\ddot{w}_\rho(t) + \gamma^2 w_\rho(t) = \frac{1}{w_\rho^3(t)} + \frac{N_{\text{at}}}{\sqrt{2\pi}} \frac{[2a - a_{\text{dd}}g(\bar{k})]}{w_\rho^3(t)d_z},$$

$$\bar{k} = \frac{w_\rho(t)}{d_z}. \quad (50)$$

The time-independent width of a stationary state can be obtained from Eq. (50) by setting $\ddot{w}_\rho(t) = 0$. The variational chemical potential for the stationary state is given by [22]

$$\mu = \frac{1}{2w_\rho^2} + \frac{2N_{\text{at}}[a - a_{\text{dd}}f(\bar{k})]}{\sqrt{2\pi}d_z w_\rho^2} + \frac{\gamma^2 w_\rho^2}{2}. \quad (51)$$

The energy per particle is given by

$$\frac{E}{N_{\text{at}}} = \frac{1}{2w_\rho^2} + \frac{N_{\text{at}}[a - a_{\text{dd}}f(\bar{k})]}{\sqrt{2\pi}d_z w_\rho^2} + \frac{\gamma^2 w_\rho^2}{2}. \quad (52)$$

2.6.2. x - z plane

For a disk-shaped dipolar BEC with a strong axial trap along y direction ($\nu > \lambda, \gamma$), we assume that the dynamics of the BEC in the y direction is confined in the ground state

$$\phi(y) = \exp(-y^2/2d_y^2)/(\pi d_y^2)^{1/4}, \quad d_y = \sqrt{1/\nu}, \quad (53)$$

and we have for the wave function

$$\phi(\mathbf{r}) \equiv \phi(y) \times \phi_{2D}(\boldsymbol{\rho}, t) = \frac{1}{(\pi d_y^2)^{1/4}} \exp \left[-\frac{y^2}{2d_y^2} \right] \phi_{2D}(\boldsymbol{\rho}, t), \quad (54)$$

where now $\boldsymbol{\rho} \equiv (x, z)$, and $\phi_{2D}(\boldsymbol{\rho}, t)$ is the circularly-asymmetric effective 2D wave function for the 2D dynamics and d_y is the harmonic oscillator length along y direction. To derive the effective 2D equation for the disk-shaped dipolar BEC, we use ansatz (54) in Eq. (3), multiply by the ground-state wave function $\phi(y)$ and integrate over y to get the 2D equation

$$i \frac{\partial \phi_{2D}(\boldsymbol{\rho}, t)}{\partial t} = \left[-\frac{\nabla_\rho^2}{2} + \frac{\gamma^2 x^2 + \lambda^2 z^2}{2} + \frac{4\pi a N_{\text{at}} |\phi_{2D}|^2}{\sqrt{2\pi} d_y} \right. \\ \left. + 4\pi a_{\text{dd}} N_{\text{at}} \int \frac{d\mathbf{k}_\rho}{(2\pi)^2} e^{-i\mathbf{k}_\rho \cdot \boldsymbol{\rho}} \tilde{n}(\mathbf{k}_\rho, t) j_{2D} \left(\frac{k_\rho d_y}{\sqrt{2}} \right) \right] \phi_{2D}(\boldsymbol{\rho}, t), \quad (55)$$

where $k_\rho = \sqrt{k_x^2 + k_z^2}$, and

$$j_{2D}(\xi) \equiv \frac{1}{2\pi} \int_{-\infty}^{\infty} dk_y \left[\frac{3k_z^2}{k^2} - 1 \right] |\tilde{n}(k_y)|^2 \\ = \frac{1}{\sqrt{2\pi} d_y} \left[-1 + 3\sqrt{\pi} \frac{\xi_z^2}{\xi} \exp(\xi^2) \{1 - \text{erf}(\xi)\} \right], \\ \xi = \frac{k_\rho d_y}{\sqrt{2}}, \quad \xi_z = \frac{k_z d_y}{\sqrt{2}}. \quad (56)$$

To derive Eq. (55), the dipolar term in Eq. (3) is first written in momentum space using Eq. (8) and the integration over k_y is performed in the dipolar term.

3. Details about the programs

3.1. Description of the programs

In this subsection we describe the numerical codes for solving the dipolar GP equations (29) and (41) in 1D, Eqs. (46) and (55) in 2D, and Eq. (3) in 3D using real- and imaginary-time propagations. The real-time propagation yields the time-dependent dynamical results and the imaginary-time propagation yields the time-independent stationary solution for the lowest-energy state for a specific symmetry. We use the split-step Crank–Nicolson method for the solution of the equations described in Ref. [3]. The present programs have the same structure as in Ref. [3] with added subroutines to calculate the dipolar integrals. In the absence of dipolar interaction the present programs will be identical with the previously published ones [3]. A general instruction to use these programs in the nondipolar case can be found in Ref. [3] and we refer the interested reader to this article for the same.

The present Fortran programs named ('imag1dX.f90', 'imag1dZ.f90'), ('imag2dXY.f90', 'imag2dXZ.f90'), 'imag3d.f90', ('real1dX.f90', 'real1dZ.f90'), ('real2dXY.f90', 'real2dXZ.f90'), 'real3d.f90', deal with imaginary- and real-time propagations in 1D, 2D, and 3D and are to be contrasted with previously published programs [3] 'imagtime1d.F', 'imagtime2d.f90', 'imagtime3d.f90', 'realtime1d.F', 'realtime2d.f90', and 'realtime3d.f90', for the nondipolar case. The input parameters in Fortran programs are introduced in the beginning of each program. The corresponding C codes are called (imag1dX.c, imag1dX.h, imag1dZ.c, imag1dZ.h), (imag2dXY.c, imag2dXY.h, imag2dXZ.c, imag2dXZ.h), (imag3d.c, imag3d.h), (real1dX.c, real1dX.h, real1dZ.c, real1dZ.h), (real2dXY.c, real2dXY.h, real2dXZ.c, real2dXZ.h), (real3d.c, real3d.h), with respective input files ('imag1dX-input', 'imag1dZ-input'), ('imag2dXY-input', 'imag2dXZ-input'), 'imag3d-input', ('real1dX-input', 'real1dZ-input'), ('real2dXY-input', 'real1dXZ-input'), 'real3d-input', which perform identical executions as in the Fortran programs.

We present in the following a description of input parameters. The parameters NX, NY, and NZ in 3D (NX and NY in 2DXY, NX and NZ in 2DXZ), and N in 1D stand for total number of space points in x , y and z directions, where the respective space steps DX, DY, and DZ can be made equal or different; DT is the time step. The parameters NSTP, NPAS, and NRUN denote number of time iterations. The parameters GAMMA (γ), NU (ν), and LAMBDA (λ) denote the anisotropy of the trap. The number of atoms is denoted NATOMS (N_{at}), the scattering length is denoted AS (a) and dipolar length ADD (a_{dd}). The parameters G0 ($4\pi N_{\text{at}} a$) and GDD0 ($3a_{\text{dd}} N_{\text{at}}$) are the contact and dipolar nonlinearities. The parameter OPTION = 2 (default) defines the equations of the present paper with a factor of half before the kinetic energy and trap; OPTION = 1 defines a different set of GP equations without these factors, viz Ref. [3]. The parameter AHO is the unit of length and Bohr_a0 is the Bohr radius. In 1D the parameter DRHO is the radial harmonic oscillator d_ρ and in 2D the parameter D_Z or D_Y is the axial harmonic oscillator length d_z or d_y . The parameter CUTOFF is the cut-off R of Eq. (9) in the 3D programs. The parameters GPAR and GPAR are constants which multiply the nonlinearities G0 and GDD0 in realtime routines before NRUN time iterations to study the dynamics.

The programs, as supplied, solve the GP equations for specific values of dipolar and contact nonlinearities and write the wave function, chemical potential, energy, and root-mean-square (rms) size(s), etc. For solving a stationary problem, the imaginary-time programs are far more accurate and should be used. The real-time programs should be used for studying non-equilibrium problems reading an initial wave function calculated by the imaginary-time program with identical set of parameters (set NSTP = 0, for this

purpose, in the real-time programs). The real-time programs can also calculate stationary solutions in NSTP time steps (set NSTP \neq 0 in real-time programs), however, with less accuracy compared to the imaginary-time programs. The larger the value of NSTP in real-time programs, more accurate will be the result [3]. The nonzero integer parameter NSTP refers to the number of time iterations during which the nonlinear terms are slowly introduced during the time propagation for calculating the wave function. After introducing the nonlinearities in NSTP iterations the imaginary-time programs calculate the final result in NPAS plus NRUN time steps and write some of the results after NPAS steps to check convergence. The real-time programs run the dynamics during NPAS steps with unchanged initial parameters so as to check the stability and accuracy of the results. Some of the nonlinearities are then slightly modified after NPAS iterations and the small oscillation of the system is studied during NRUN iterations.

Each program is preset at fixed values of contact and dipolar nonlinearities as calculated from input scattering length(s), dipolar strength(s), and number of atom(s), correlated DX–DT values and NSTP, NPAS, and NRUN, etc. A study of the correlated DX and DT values in the nondipolar case can be found in Ref. [3]. Smaller the steps DX, DY, DZ and DT, more accurate will be the result, provided we integrate over a reasonably large space region by increasing NX, NY, and NZ, etc. Each supplied program produces result up to a desired precision consistent with the parameters employed – G0, GDD0, DX, DY, DZ, DT, NX, NY, NZ, NSTP, NPAS, and NRUN, etc.

3.2. Description of Output files

Programs ‘imagnd*’ ($n = 1, 2, 3, C$ and Fortran): They write final density in files ‘imagnd-den.txt’ after NRUN iterations. In addition, in 2D and 3D, integrated 1D densities ‘imagnd*-den1d_x.txt’, ‘imagnd*-den1d_y.txt’, ‘imagnd*-den1d_z.txt’, along $x, y,$ and $z,$ etc., are given. These densities are obtained by integrating the densities over eliminated space variables. In addition, in 3D integrated 2D densities ‘imag3d-den2d_xy.txt’, ‘imag3d-den2d_yz.txt’, ‘imag3d-den2d_zx.txt’, in $xy, yz,$ and zx planes can be written (commented out by default). The files ‘imagnd*-out.txt’ provide different initial input data, as well as chemical potential, energy, size, etc. at different stages (initial, after NSTP, NPAS, and after NRUN iterations), from which a convergence of the result can be inferred. The files ‘imagnd*-rms.txt’ provide the different rms sizes at different stages (initial, after NSTP, NPAS, and after NRUN iterations).

Programs ‘realnd*’ ($n = 1, 2, 3, C$ and Fortran): The same output files as in the imaginary-time programs are available in the real-time programs. The real-time densities are reported after NPAS iterations. In addition in the ‘realnd*-dyna.txt’ file the temporal evolution of the widths are given during NPAS and NRUN iterations. Before NRUN iterations the nonlinearities G0 and GDD0 are multiplied by parameters GPAR and GDPAR to start an oscillation dynamics.

3.3. Running the programs

In addition to installing the respective Fortran and C compilers one needs also to install the FFT routine FFTW in the computer. To run the Fortran programs the supplied routine fftw3.f03 should be included in compilation. The commands for running the Fortran programs using INTEL, GFortran, and Oracle Sun compilers are given inside the Fortran programs. The programs are submitted in directories with option to compile using the command ‘make’. There are two files with general information about the programs and FT for user named ‘readme.txt’ and ‘readme-fftw.txt’. The Fortran and C programs are in directories ./f_program and ./c_program. Inside these directories there are subdirectories such as ./input, ./output, ./src. The subdirectory ./output contains

output files the programs generate, ./input contains input files for C programs, and ./src contains the different programs. The command ‘make’ in the directory ./f_program or ./c_program compiles all the programs and generates the corresponding executable files to run. The command ‘make’ for INTEL, GFortran and OracleSun Fortran are given.

4. Numerical results

In this section we present results for energy, chemical potential and root-mean-square (rms) sizes for different stationary BECs in 1D, 2D, and 3D, and compare with those obtained by using Gaussian variational and TF approximations, wherever possible. We also compare with available results by other authors. For a fixed space and time step, sufficient number of space discretizing points and time iterations are to be allowed to get convergence.

First we present in Table 1 numerical results for the energy E , chemical potential μ , and rms size $\langle z \rangle$ calculated using the imaginary-time program for the 1D dipolar GP Eq. (29) for ^{52}Cr atoms with $a = 6 \text{ nm}$ ($\approx 113a_0$ with a_0 the Bohr radius), and $a_{dd} = 16a_0$ for $\lambda = 1, d_\rho = 1, l = 1 \mu\text{m}$ and for different number of atoms N_{at} and different space and time steps dz and dt . The Gaussian variational approximations obtained from Eqs. (36)–(38) are also given for comparison. The variational results provide better approximation to the numerical solution for a smaller number of atoms.

In Table 2 we present results for the energy E , chemical potential μ , and rms size $\langle \rho \rangle$ of the 2D GP Eq. (46) for $\gamma = \nu = 1, d_z = 1, l = 1 \mu\text{m}$. The numerical results are calculated using different space and time steps dx, dy and dt and different number N_{at} of ^{52}Cr atoms with $a_{dd} = 16a_0$ and $a = 6 \text{ nm}$. Axially-symmetric Gaussian variational approximations obtained from Eqs. (50)–(52) are also presented for comparison.

Now we present results of the solution of the 3D GP Eq. (3) with some axially-symmetric traps. In this case we take advantage of the cut-off introduced in Eq. (9) to improve the accuracy of the numerical calculation. The cut-off parameter R was taken larger than the condensate size and smaller than the discretization box. First we consider the model 3D GP equation with $a = 0$ and different $g_{dd} = 3a_{dd}N_{\text{at}} = 1, 2, 3, 4$ in an axially-symmetric trap with $\lambda = 1/2$ and $\nu = \gamma = 1$. The numerical results for different number of space and time steps together with Gaussian variational results obtained from Eqs. (18) and (19) are shown in Table 3. These results for energy E and chemical potential μ are compared with those calculated by Asad-uz-Zaman et al. [16,29]. The present calculation is performed in the Cartesian x, y, z coordinates and the dipolar term is evaluated by FT to momentum space. Asad-uz-Zaman et al. take advantage of the axial symmetry and perform the calculation in the axial ρ, z ($\rho \equiv x, y$) variables and evaluate the dipolar term by a combined Hankel–Fourier transformation to momentum space for ρ and z , respectively. The calculations of Asad-uz-Zaman et al. for stationary states involving two variables (ρ and z) thus could be more economic and accurate than the present calculation involving three Cartesian variables for the axially-symmetric configuration considered in Table 3. However, the present method, unlike that of Ref. [16], is readily applicable to the fully asymmetric configurations. Moreover, the present calculation for dynamics (non-stationary states) in 3D are more realistic than the calculations of Asad-uz-Zaman et al., where one degree of freedom is frozen. For example, a vortex could be unstable [30] in a full 3D calculation, whereas a 2D calculation could make the same vortex stable.

Next we consider the solution of the 3D GP Eq. (3) for a model condensate of ^{52}Cr atoms in a cigar-shaped axially-symmetric trap with $\gamma = \nu = 1, \lambda = 1/2$, first considered by Bao et al. [9]. The nonlinearities considered there ($4\pi a = 0.20716, 4\pi a_{dd} = 0.033146$) correspond to the following approximate values of

Table 1

The energy per particle E/N_{at} , chemical potential μ , and rms size $\langle z \rangle$ of the 1D GP Eq. (29) for $\lambda = 1$, $d_\rho = 1 \mu\text{m}$ for the ^{52}Cr BEC with $a = 6 \text{ nm}$, $a_{\text{dd}} = 16a_0$ and different number of atoms N_{at} . In Eqs. (3) and (29) the lengths are expressed in oscillator unit: $l = 1 \mu\text{m}$. Numerical results are calculated for parameters (A) $dx = dy = 0.1$, $dt = 0.0005$, $N = 2048$ (B) $dz = 0.1$, $dt = 0.001$, $N = 1024$ and compared with variational results obtained from Eqs. (36)–(38).

N_{at}	$\langle z \rangle$ var	$\langle z \rangle$ (B)	$\langle z \rangle$ (A)	E/N_{at} var	E/N_{at} (B)	E/N_{at} (A)	μ var	μ (B)	μ (A)
100	0.7939	0.7937	0.7937	0.7239	0.7222	0.7222	0.9344	0.9297	0.9297
500	1.0425	1.0381	1.0381	1.4371	1.4166	1.4166	2.2157	2.1691	2.1691
1000	1.2477	1.2375	1.2375	2.1376	2.0920	2.0920	3.4165	3.3234	3.3234
5000	2.0249	1.9939	1.9939	5.8739	5.6910	5.6910	9.6671	9.3488	9.3488
10,000	2.5233	2.4815	2.4815	9.2129	8.913	8.913	15.223	14.715	14.715
50,000	4.2451	4.1719	4.1719	26.505	25.622	25.622	43.993	42.527	42.527

Table 2

The energy per particle E/N_{at} , chemical potential μ , and rms size $\langle \rho \rangle$ of the 2D GP Eq. (46) for $\gamma = \nu = 1$, $d_z = 1 \mu\text{m}$ for the ^{52}Cr BEC with $a = 6 \text{ nm}$, $a_{\text{dd}} = 16a_0$ and different number of atoms N_{at} . In Eqs. (3) and (46) the lengths are expressed in oscillator unit: $l = 1 \mu\text{m}$. Numerical results are calculated for space and time steps (A) $dx = dy = 0.1$, $dt = 0.0005$, $NX = NY \equiv \mathcal{N} = 768$, (B) $dx = dy = 0.2$, $dt = 0.002$, $\mathcal{N} = 384$, and compared with variational results obtained from Eqs. (50), (51) and (52).

N_{at}	$\langle \rho \rangle$ var	$\langle \rho \rangle$ (B)	$\langle \rho \rangle$ (A)	E/N_{at} var	E/N_{at} (B)	E/N_{at} (A)	μ var	μ (B)	μ (A)
100	1.0985	1.097	1.097	1.2182	1.2156	1.2157	1.4187	1.4120	1.4119
500	1.3514	1.342	1.342	1.8653	1.8383	1.8383	2.5437	2.4840	2.4840
1000	1.5482	1.530	1.531	2.4571	2.3988	2.3988	3.5070	3.3901	3.3901
5000	2.2549	2.208	2.208	5.2206	4.9989	4.9989	7.8005	7.4249	7.4249
10,000	2.6824	2.619	2.619	7.3787	7.029	7.029	11.090	10.522	10.522
50,000	4.0420	3.934	3.934	16.680	15.793	15.793	25.161	23.789	23.789

Table 3

Energy per particle E/N_{at} and chemical potential μ from a solution of Eq. (3) for $\gamma = \nu = 1$, $\lambda^2 = 0.25$, $a = 0$ and different nonlinearity $g_{\text{dd}} \equiv 3a_{\text{dd}}N_{\text{at}}$. The present numerical results are compared with Gaussian variational results obtained from Eqs. (18) and (19) as well as numerical results of Asad-uz-Zaman et al. [16,29]. Numerical results are calculated for the following space and time steps and the following space discretizing points in the Crank–Nicolson discretization: (A) $dx = dy = dz = 0.05$, $dt = 0.0004$, ($NX = NY = NZ \equiv \mathcal{N} = 384$); (B) 0.1 , $dt = 0.002$, ($\mathcal{N} = 128$, $R = 6$); and (C) 0.2 , $dt = 0.007$, ($\mathcal{N} = 64$, $R = 6$).

g_{dd}	E/N_{at} var	E/N_{at} (C)	E/N_{at} (B)	E/N_{at} (A)	E/N_{at} [29]	μ var	μ (C)	μ (B)	μ (A)	μ [29]
0	1.2500	1.2498	1.2500	1.2500	1.2500	1.2500	1.2498	1.2500	1.2500	1.2500
1	1.2230	1.2220	1.2222	1.2222	1.2222	1.1934	1.1910	1.1912	1.1911	1.1911
2	1.1907	1.1872	1.1875	1.1874	1.1874	1.1203	1.1100	1.1100	1.1100	1.1100
3	1.1521	1.143	1.1439	1.1438	1.1437	1.0253	0.995	0.996	0.996	0.9955
4	1.1051	1.085	1.0857	1.0857	1.0856	0.8950	0.805	0.803	0.806	0.8062

Table 4

Energy per particle E/N_{at} , and chemical potential μ from a solution of Eq. (3) for $\gamma = \nu = 1$, $\lambda^2 = 0.25$, $4\pi a = 0.20716$, $4\pi a_{\text{dd}} = 0.033146$ and different number N_{at} of atoms. These nonlinearity parameters taken from Ref. [9] correspond to a ^{52}Cr dipolar BEC with $a \approx 100a_0$ and $a_{\text{dd}} \approx 16a_0$ and oscillator length $l \approx 0.321 \mu\text{m}$. Variational and TF results as well as numerical results of Bao et al. [9] are also shown. Numerical results are calculated using the following space and time steps and the following space discretizing points in the Crank–Nicolson discretization: (A) $dx = dy = dz = 0.15$, $dt = 0.002$; (B) $dx = dy = dz = 0.3$, $dt = 0.005$. In (A) we take $NX = NY = NZ \equiv \mathcal{N} = 128$, $R = 9$ for $N_{\text{at}} = 100, 500, 1000$ and $\mathcal{N} = 192$, $R = 14$, for $N_{\text{at}} = 5000, 10,000, 50,000$; and in (B) we take $\mathcal{N} = 64$, $R = 9$, for $N_{\text{at}} = 100, 500, 1000$ and $\mathcal{N} = 96$, $R = 14$, for $N_{\text{at}} = 5000, 10,000, 50,000$.

N_{at}	E/N_{at} var	E/N_{at} TF	E/N_{at} (B)	E/N_{at} (A)	E/N_{at} [9]	μ var	μ TF	μ (B)	μ (A)	μ [9]
100	1.579	0.945	1.567	1.567	1.567	1.840	1.322	1.813	1.813	1.813
500	2.287	1.798	2.224	2.224	2.225	2.951	2.518	2.835	2.835	2.837
1000	2.836	2.373	2.728	2.728	2.728	3.767	3.322	3.583	3.582	3.583
5000	5.036	4.517	4.744	4.744	4.745	6.935	6.324	6.485	6.486	6.488
10,000	6.563	5.960	6.146	6.146	6.147	9.100	8.344	8.475	8.475	8.479
50,000	12.34	11.35	11.46	11.46	11.47	17.23	15.89	15.96	15.97	15.98

Table 5

The rms sizes $\langle x \rangle$ and $\langle z \rangle$ for the same systems illustrated in Table 4 using the same cut-off parameter R .

N	$\langle z \rangle$ TF	$\langle z \rangle$ var	$\langle z \rangle$ (B)	$\langle z \rangle$ (A)	$\langle z \rangle$ [9]	$\langle x \rangle$ TF	$\langle x \rangle$ var	$\langle x \rangle$ (B)	$\langle x \rangle$ (A)	$\langle x \rangle$ [9]
100	1.285	1.316	1.305	1.303	1.299	0.600	0.799	0.794	0.795	0.796
500	1.773	1.797	1.752	1.752	1.745	0.828	0.952	0.938	0.939	0.940
1000	2.037	2.079	2.014	2.014	2.009	0.951	1.054	1.035	1.035	1.035
5000	2.810	2.904	2.795	2.795	2.790	1.313	1.392	1.353	1.353	1.354
10,000	3.228	3.345	3.217	3.216	3.212	1.508	1.586	1.537	1.537	1.538
50,000	4.454	4.629	4.450	4.450	4.441	2.080	2.171	2.093	2.093	2.095

a , a_{dd} and l : $a \approx 100a_0$, $a_{\text{dd}} \approx 16a_0$, and $l = 0.321 \mu\text{m}$. We present results for energy E and chemical potential μ in Table 4 and rms sizes $\langle z \rangle$ and $\langle x \rangle$ in Table 5. We also present

variational and Thomas–Fermi (TF) results in this case together with results of numerical calculation of Bao et al. [9]. The TF energy and chemical potential in Table 4 are calculated using Eqs. (21)

Table 6

Energy per particle E/N_{at} , chemical potential μ , and rms sizes from a solution of Eq. (3) for ^{52}Cr atoms with $\gamma = 1$, $\nu^2 = 1/2$, $\lambda^2 = 1/4$, $a = 110a_0$, $a_{\text{dd}} = 16a_0$, and harmonic oscillator length $l = 1 \mu\text{m}$ for different N_{at} . Numerical results are calculated using the following space and time steps and the following space discretizing points in the Crank–Nicolson discretization: (A) $dx = dy = dz = 0.1$, $dt = 0.001$; and (B) 0.2 , $dt = 0.003$. In (A) we take $NX = NY = NZ \equiv \mathcal{N} = 128$, $R = 6$ for $N_{\text{at}} = 100, 500, 1000$ and $\mathcal{N} = 256$, $R = 10.5$, for $N_{\text{at}} = 5000, 10,000, 50,000$; and in (B) we take $\mathcal{N} = 64$, $R = 6$, for $N_{\text{at}} = 100, 500, 1000$ and $\mathcal{N} = 128$, $R = 12$, for $N_{\text{at}} = 5000, 10,000, 50,000$.

N	E/N_{at} (B)	E/N_{at} (A)	μ (B)	μ (A)	$\langle x \rangle$ (B)	$\langle y \rangle$ (B)	$\langle z \rangle$ (B)	$\langle x \rangle$ (A)	$\langle y \rangle$ (A)	$\langle z \rangle$ (A)
100	1.219	1.219	1.321	1.321	0.742	0.901	1.120	0.742	0.901	1.119
500	1.525	1.525	1.830	1.830	0.818	1.032	1.379	0.818	1.032	1.379
1000	1.784	1.784	2.232	2.232	0.874	1.128	1.559	0.874	1.129	1.558
5000	2.885	2.885	3.857	3.858	1.079	1.463	2.132	1.079	1.463	2.132
10,000	3.673	3.673	4.992	4.992	1.206	1.660	2.450	1.206	1.660	2.449
50,000	6.713	6.713	9.306	9.306	1.609	2.260	3.383	1.609	2.260	3.383

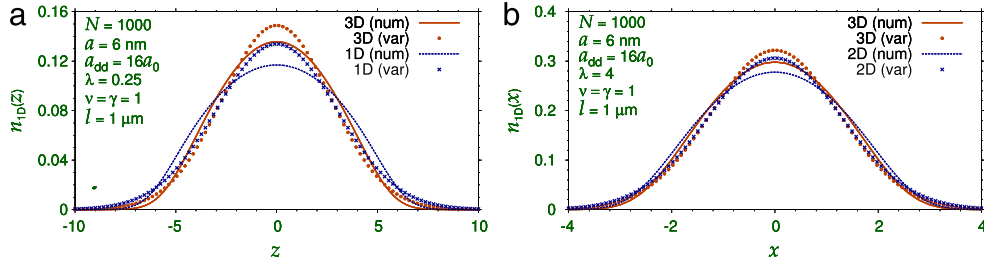


Fig. 1. (a) Numerical (num) and variational (var) results for the one-dimensional axial density $n_{1D}(z) = |\phi_{1D}(z)|^2$ along z axis for $\nu = \gamma = 1$, $\lambda = 0.25$ of a cigar-shaped BEC of $N_{\text{at}} = 1000$ atoms obtained using the 1D Eq. (29) and that obtained after integrating the 3D density from Eq. (3) over x and y : $n_{1D}(z) = \int |\phi(\mathbf{r})|^2 dx dy$. (b) Numerical (num) and variational (var) results for the 1D radial density $n_{1D}(x) = \int |\phi(\mathbf{r})|^2 dy dz$ along x axis for $\nu = \gamma = 1$, $\lambda = 4$ of a disk-shaped BEC of $N_{\text{at}} = 1000$ atoms obtained after integrating the 3D density from Eq. (3) over y and z and after integrating the 2D density from Eq. (46) over y as follows: $n_{1D}(x) = \int dy dz |\phi_{2D}(x, y, z)|^2$ and $n_{1D}(x) = \int dy dz |\phi_{3D}(x, y, z)|^2$. In all cases $a = 6 \text{ nm}$ and $a_{\text{dd}} = 16a_0$.

and (26), respectively. The TF sizes $\langle x \rangle$ and $\langle z \rangle$ in Table 5 are obtained from Eqs. (24) and (25) using the TF density (20). For small nonlinearities or small number of atoms, the Gaussian variational results obtained from Eqs. (13), (14), (18), and (19) are in good agreement with the numerical calculations as the wave function for small nonlinearities has a quasi-Gaussian shape. However, for large nonlinearities or large number of atoms, the wave function has an approximate TF shape (20), and the TF results provide better approximation to the numerical results, as can be seen from Tables 4 and 5.

After the consideration of 3D axially-symmetric trap now we consider a fully anisotropic trap in 3D. In Table 6 we present the results for energy E/N_{at} , chemical potential μ and rms sizes $\langle x \rangle$, $\langle y \rangle$, $\langle z \rangle$ of a ^{52}Cr BEC in a fully anisotropic trap with $\gamma = 1$, $\nu = 1/\sqrt{2}$, $\lambda = 1/2$ for different number of atoms. In this case we take $a = 110a_0$, $a_{\text{dd}} = 16a_0$ and $l = 1 \mu\text{m}$. The convergence of the calculation is studied by taking reduced space and time steps dx and dt and different number of space discretization points. Sufficient number of time iterations are to be allowed in each case to obtain convergence. In 3D the estimated numerical error in the calculation is less than 0.05%. The error is associated with the intrinsic accuracy of the FFT routine for long-range dipolar interaction.

The 1D and 2D GP Eqs. (29) and (46) are valid for cigar- and disk-shaped BECs, respectively. In case of cigar shape the 1D GP equation yields results for axial density and in this case it is appropriate to compare this density with the reduced axial density obtained by integrating the 3D density over radial coordinates: $n(z) \equiv |\varphi(z)|^2 = \int |\phi(x, y, z)|^2 dx dy$. In Fig. 1(a) we compare two axial densities obtained from the 1D and 3D GP equations. We also show the densities calculated from the Gaussian variational approximation in both cases. In the cigar case the trap parameters are $\nu = \gamma = 1$, $\lambda = 1/4$. Similarly, for the disk shape it is interesting to compare the density along the radial direction in the plane of the disk as obtained from the 3D Eq. (3) and the 2D Eq. (46). In this case it is appropriate to calculate the 1D radial density along, say, x direction by integrating 2D and 3D densities as follows: $n_{1D}(x) = \int dy |\phi_{2D}(x, y)|^2$ and $n_{1D}(x) = \int dy dz |\phi_{3D}(x, y, z)|^2$.

In Fig. 1(b) we compare two radial densities obtained from the 2D and 3D GP equations. We also show the densities calculated from the Gaussian variational approximation in both cases. For this illustration, we consider the trap parameters $\nu = \gamma = 1$, $\lambda = 4$. In both Figs. 1(a) and (b), the densities obtained from the solution of the 3D GP equation are in satisfactory agreement with those obtained from a solution of the reduced 1D and 2D equations. In Fig. 1, the numerical and variational densities are pretty close to each other, so are the results obtained from the 3D Eq. (3), on the one hand, and the ones obtained from the 1D and 2D Eqs. (29) and (46), on the other.

A dipolar BEC is stable for the number of atoms N_{at} below a critical value [31]. Independent of trap parameters, such a BEC collapses as N_{at} crosses the critical value. This can be studied by solving the 3D GP equation using imaginary-time propagation with a nonzero value of NSTP while the nonlinearities are slowly increased. In Fig. 2(a) we present the $N_{\text{at}} - a$ stability phase plot for a ^{164}Dy BEC with $a_{\text{dd}} = 130a_0$ in the disk-shaped trap with $\nu = \gamma = 1$, $\lambda = 5$ and 7. The oscillator length is taken to be $l = 1 \mu\text{m}$. The shaded area in these plots shows a metastable region where biconcave structure in 3D density appears. The metastable region corresponds to a local minimum in energy in contrast to a global minimum for a stable state. It has been established that this metastability is a manifestation of roton instability encountered by the system in the shaded region [31]. The biconcave structure in 3D density in a disk-shaped dipolar BEC is a direct consequence of dipolar interaction: the dipolar repulsion in the plane of the disk removes the atoms from the center to the peripheral region thus creating a biconcave shape in density. In Fig. 2(b) and (c) we plot the 3D isodensity contour of the condensate for $\lambda = 5$ with parameters in the shaded region corresponding to metastability. In Fig. 2(b) the density on the contour is 0.001 whereas in Fig. 2(c), it is 0.027. Only for a larger density on the contour the biconcave shape is visible. The biconcave shape predominates near the central region of the metastable dipolar BEC.

In Fig. 1 we critically tested the reduced 1D and 2D Eqs. (29) and (46) along the z axis and in the x - y plane, respectively, by

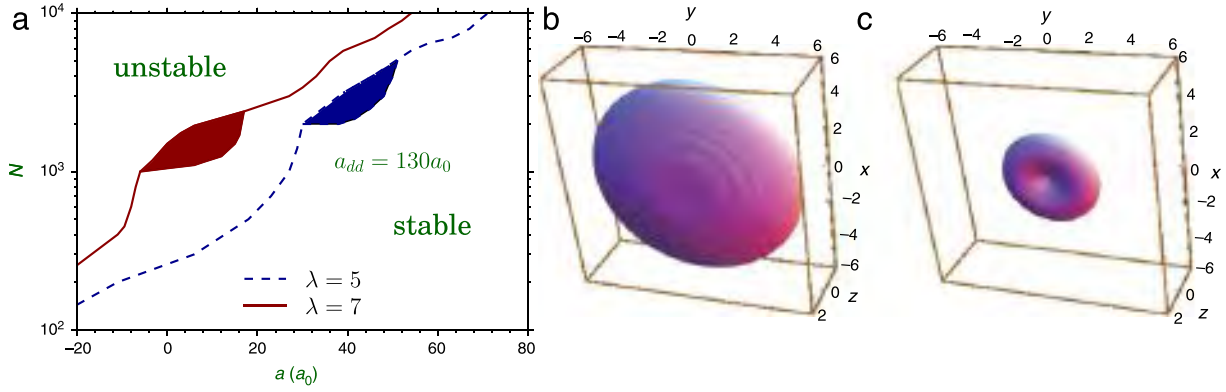


Fig. 2. (a) The $N_{\text{at}} - a$ stability phase plot for a ^{164}Dy BEC with $a_{\text{dd}} = 130a_0$ in a disk-shaped trap with $\nu = \gamma = 1$, $\lambda = 5$ and 7 and harmonic oscillator length $l = 1 \mu\text{m}$. The 3D isodensity contour plot of density of a disk-shaped ^{164}Dy BEC with $a_{\text{dd}} = 130a_0$ for $\nu = \gamma = 1$, $\lambda = 5$, $l = 1 \mu\text{m}$, $N_{\text{at}} = 3000$ and $a = 40a_0$ for densities $|\phi(x, y, z)|^2 =$ (b) 0.001 and (c) 0.027 on the contour.

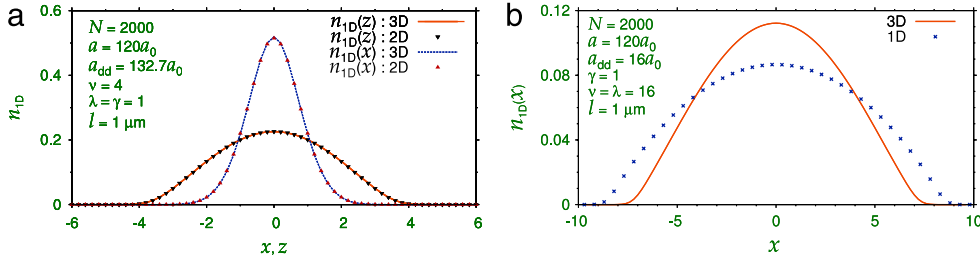


Fig. 3. (a) Numerical results for the 1D radial density $n_{1D}(x) = \int |\phi(\mathbf{r})|^2 dy dz$ along x axis and $n_{1D}(z) = \int |\phi(\mathbf{r})|^2 dx dy$ along z axis for $\lambda = \gamma = 1$, $\nu = 4$ of a disk-shaped BEC of $N_{\text{at}} = 2000$ ^{164}Dy atoms obtained after integrating the 3D density from Eq. (3) and the 2D density from Eq. (55) over the eliminated variables. (b) Numerical results for the 1D axial density $n_{1D}(x) = \int |\phi(\mathbf{r})|^2 dz dy$ along x axis for $\nu = \lambda = 16$, $\gamma = 1$ of a cigar-shaped BEC of $N_{\text{at}} = 2000$ ^{52}Cr atoms obtained using the 1D Eq. (41) and that obtained after integrating the 3D density from Eq. (3) over z and y : $n_{1D}(x) = \int |\phi(\mathbf{r})|^2 dz dy$. In all cases $a = 120a_0$ and (a) $a_{\text{dd}} = 132.7a_0$ (b) $a_{\text{dd}} = 16a_0$.

comparing the different 1D densities from these equations with those obtained from a solution of the 3D Eq. (3) as well as with the variational densities. Now we perform a similar test with the reduced 1D and 2D Eqs. (41) and (55) along the x axis and in the x - z plane, respectively. We consider a BEC of 2000 atoms in a disk-shaped trap in the x - z plane with $\lambda = \gamma = 1$ and $\nu = 4$. Because of the strong trap in the y direction, the resultant BEC is of quasi-2D shape in the x - z plane without circular symmetry in that plane because of the anisotropic dipolar interaction. The integrated linear density along the x and z axes as calculated from the 2D GP Eq. (55) and the 3D GP Eq. (3) are illustrated in Fig. 3(a). Next we consider the BEC of 2000 atoms in a cigar-shaped trap along the x axis with $\nu = \lambda = 16$ and $\gamma = 1$. The integrated linear density along the x axis in this case calculated from the 3D Eq. (3) is compared with the same as calculate using the reduced 1D Eq. (41) in Fig. 3(b). In both cases the densities calculated from the 3D GP equation are in reasonable agreement with those calculated using the reduced Eqs. (55) and (41). Another interesting feature emerges from Figs. 1 and 3: the reduced 2D GP Eqs. (46) and (55) with appropriate disk-shaped traps yield results for densities in better agreement with the 3D GP Eq. (3) as compared to the 1D GP Eqs. (29) and (41) with appropriate cigar-shaped traps. This feature, also observed in non-dipolar BECs [17], is expected as the derivation of the reduced 1D equations involving two spatial integrations represent more drastic approximation compared to the same of the reduced 2D equations involving one spatial integration.

Now we report the dynamics of the dipolar BEC by real-time propagation using the stationary state calculated by imaginary-time propagation. In Fig. 4(a) we show the oscillation of the rms sizes (z) and (ρ) from the reduced 1D and 2D GP Eqs. (29) and (46), respectively. In Fig. 4(a) we consider $N_{\text{at}} = 10,000$, $a_{\text{dd}} = 16a_0$ (appropriate for ^{52}Cr), $a = 6 \text{ nm}$ ($\approx 113a_0$) and oscillator length $l = 1 \mu\text{m}$. In 1D, we take $dx = 0.025$, $dt = 0.0001$, $\lambda = 1$, $d_\rho = 1$,

number of space points $N = 2048$, and in 2D, we take $dx = dy = 0.2$, $dt = 0.001$, $\gamma = \nu = 1$, $d_z = 1$, $N_x = N_y = 512$. in real-time simulation the oscillation is started by multiplying the nonlinearities with the factor 1.05. To implement this, in real-time routine we take $\text{GPAR} = \text{GDPAR} = 1.1$ and also take $\text{NSTP} = 0$ to read the initial wave function. In 1D and 2D we also present results of the Gaussian variational approximations after a numerical solution of Eqs. (36) and (50), respectively. The frequency of the resultant oscillations agree well with the numerical 1D and 2D calculations. However, slight adjustment of the initial conditions, or initial values of width and its derivative, were necessary to get an agreement of the amplitude of oscillation obtained from variational approximation and numerical simulation. The initial values of width and its derivative are necessary to solve the variational equations (36) and (50). In Fig. 4(b) we illustrate the oscillation of the rms sizes (x), (y), and (z) in 3D using Eq. (3), where we perform real-time simulation using the bound state obtained by imaginary-time simulation as the initial state. The parameters used are $N_{\text{at}} = 1000$, $a = 110a_0$, $a_{\text{dd}} = 16a_0$, $\gamma = 1$, $\nu = 1/\sqrt{2}$, $\lambda = 1/2$, $l = 1 \mu\text{m}$, $N_x = N_y = N_z = 128$, $dx = dy = dz = 0.2$, $dt = 0.002$ in both real- and imaginary-time simulations. In addition, in real-time simulation the oscillation is started by multiplying the nonlinearities with the factor 1.1. To implement this, in real-time routine we take $\text{GPAR} = \text{GDPAR} = 1.1$ and also take $\text{NSTP} = 0$ to read the initial wave function.

5. Summary

We have presented useful numerical programs in Fortran and C for solving the dipolar GP equation including the contact interaction in 1D, 2D, 3D. Two sets of programs are provided. The imaginary-time programs are appropriate for solving the stationary problems, while the real-time codes can be used for

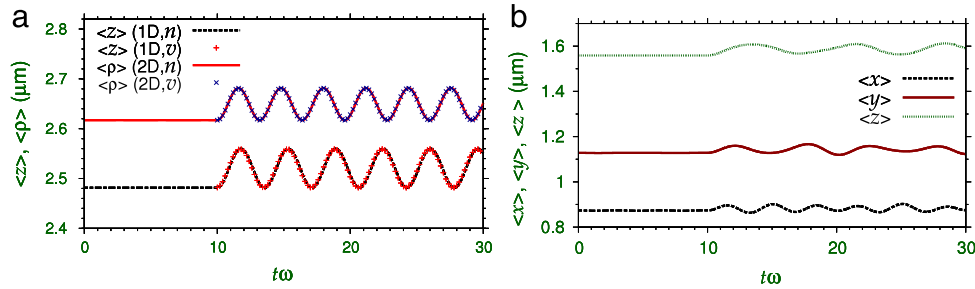


Fig. 4. (a) Numerical (n) and variational (v) results for oscillation of rms sizes (z) and (ρ) from the real-time simulation using Eq. (29) in 1D and Eq. (46) in 2D, respectively, for $N_{\text{at}} = 10,000$, $a = 6$ nm, $a_{\text{dd}} = 16a_0$, $l = 1$ μm , while a and a_{dd} were both multiplied by 1.05 after NPAS iterations at $t = 10$. The wave function was first calculated by imaginary-time routine with parameters $dx = 0.025$, $dt = 0.0001$, $\lambda = 1$, $d_\rho = 1$, NPAS = 10^5 , $N = 2048$ in 1D, and $dx = dy = 0.2$, $dt = 0.001$, $\gamma = 1$, $d_z = 1$ NPAS = 10^4 , $NX = NY = 512$ in 2D. The results of the variational approximations in 1D and 2D as obtained from a numerical solution of Eqs. (36) and (50) are also shown. (b) Numerical results for oscillation of rms sizes (x), (y) and (z) from the real-time simulation in 3D using Eq. (3), for $N_{\text{at}} = 1000$, $a = 110a_0$, $a_{\text{dd}} = 16a_0$, $l = 1$ μm , $\gamma = 1$, $v = 1/\sqrt{2}$, $\lambda = 1/2$, $NX = NY = NZ = 128$, $dx = dy = dz = 0.2$, and $dt = 0.002$ while a and a_{dd} were both multiplied by 1.1 after NPAS iterations. In all cases the real-time calculation was performed with NSTP = 0 reading the 3D density from the numerical solution of the imaginary-time program using the same parameters.

studying non-stationary dynamics. The programs are developed in Cartesian coordinates. We have compared the results of numerical calculations for statics and dynamics of dipolar BECs with those of Gaussian variational approximation, Thomas–Fermi approximation, and numerical calculations of other authors, where possible.

Acknowledgments

The authors thank Drs. Weizhu Bao, Doerte Blume, Hiroki Saito, and Luis Santos for helpful comments on numerical calculations. RKK acknowledges support from the TWAS (Third World Academy of Science, Trieste, Italy) - CNPq (Brazil) project Fr 3240256079, DST (India) - DAAD (Germany) project SR/S2/HEP-03/2009, PM from CSIR Project 03(1186)/10/EMR-II, (India), DST-DAAD (Indo-German, project INT/FRG/DAAD/P-220/2012), SKA from the CNPq project 303280/2014-0 (Brazil) and FAPESP project 2012/00451-0 (Brazil), LEYS from the FAPESP project 2012/21871-7 (Brazil). DV and AB acknowledge support by the Ministry of Education, Science and Technological Development of the Republic of Serbia under project ON171017 and by DAAD (Germany) under project NAI-DBEC, and by the European Commission under EU FP7 projects PRACE-3IP and EGI-INSPIRE.

References

- [1] F. Dalfovo, S. Giorgini, L.P. Pitaevskii, S. Stringari, Theory of Bose–Einstein condensation in trapped gases, *Rev. Modern Phys.* 71 (1999) 463–512; A.J. Leggett, Bose–Einstein condensation in the alkali gases: Some fundamental concepts, *Rev. Modern Phys.* 73 (2001) 307–356; L. Pitaevskii, S. Stringari, *Bose–Einstein Condensation*, Clarendon Press, Oxford, New York, 2003; C.J. Pethick, H. Smith, *Bose–Einstein Condensation in Dilute Gases*, Cambridge University Press, Cambridge, 2002.
- [2] S.K. Adhikari, P. Muruganandam, Bose–Einstein condensation dynamics from the numerical solution of the Gross–Pitaevskii equation, *J. Phys. B* 35 (2002) 2831–2843; P. Muruganandam, S.K. Adhikari, Bose–Einstein condensation dynamics in three dimensions by the pseudospectral and finite-difference methods, *J. Phys. B* 36 (2003) 2501–2513; S.K. Adhikari, Numerical study of the spherically symmetric Gross–Pitaevskii equation in two space dimensions, *Phys. Rev. E* 62 (2000) 2937–2944; S.K. Adhikari, Numerical solution of the two-dimensional Gross–Pitaevskii equation for trapped interacting atoms, *Phys. Lett. A* 265 (2000) 91–96.
- [3] P. Muruganandam, S.K. Adhikari, Fortran programs for the time-dependent Gross–Pitaevskii equation in a fully anisotropic trap, *Comput. Phys. Commun.* 180 (2009) 1888–1912.
- [4] D. Vudragović, I. Vidanović, A. Balaž, P. Muruganandam, S.K. Adhikari, C programs for solving the time-dependent Gross–Pitaevskii equation in a fully anisotropic trap, *Comput. Phys. Commun.* 183 (2012) 2021–2025.
- [5] W. Wen, C. Zhao, X. Ma, Dark-soliton dynamics and snake instability in superfluid Fermi gases trapped by an anisotropic harmonic potential, *Phys. Rev. A* 88 (2013) 063621; K.-T. Xi, J. Li, D.-N. Shi, Localization of a two-component Bose–Einstein condensate in a two-dimensional bichromatic optical lattice, *Physica B* 436 (2014) 149–156; Y.-S. Wang, Z.-Y. Li, Z.-W. Zhou, X.-F. Diao, Symmetry breaking and a dynamical property of a dipolar Bose–Einstein condensate in a double-well potential, *Phys. Lett. A* 378 (2014) 48–52; E.J.M. Madarassy, V.T. Toth, Numerical simulation code for self-gravitating Bose–Einstein condensates, *Comput. Phys. Commun.* 184 (2013) 1339–1343; R.M. Caplan, NLSEmagic: Nonlinear Schrödinger equation multi-dimensional Matlab-based GPU-accelerated integrators using compact high-order schemes, *Comput. Phys. Commun.* 184 (2013) 1250–1271; I. Vidanovic, A. Balaž, H. Al-Jibbouri, A. Pelster, Nonlinear Bose–Einstein condensate dynamics induced by a harmonic modulation of the s-wave scattering length, *Phys. Rev. A* 84 (2011) 013618; Y. Cai, H. Wang, Analysis and computation for ground state solutions of Bose–Fermi mixtures at zero temperature, *SIAM J. Appl. Math.* 73 (2013) 757–779; A. Balaž, R. Paun, A.I. Nicolin, S. Balasubramanian, R. Ramaswamy, Faraday waves in collisionally inhomogeneous Bose–Einstein condensates, *Phys. Rev. A* 89 (2014) 023609; H. Al-Jibbouri, A. Pelster, Breakdown of the Kohn theorem near a Feshbach resonance in a magnetic trap, *Phys. Rev. A* 88 (2013) 033621; E. Yomba, G.-A. Zakeri, Solitons in a generalized space- and time-variable coefficients nonlinear Schrödinger equation with higher-order terms, *Phys. Lett. A* 377 (2013) 2995–3004; X. Antoine, W. Bao, C. Besse, Computational methods for the dynamics of the nonlinear Schrödinger/Gross–Pitaevskii equations, *Comput. Phys. Commun.* 184 (2013) 2621–2633; N. Murray, et al., Probing the circulation of ring-shaped Bose–Einstein condensates, *Phys. Rev. A* 88 (2013) 053615; A. Khan, P.K. Panigrahi, Bell solitons in ultra-cold atomic Fermi gas, *J. Phys. B* 46 (2013) 115302; E. Yomba, G.-A. Zakeri, Exact solutions in nonlinearly coupled cubic-quintic complex Ginzburg–Landau equations, *Phys. Lett. A* 377 (2013) 148–157; W. Bao, Q. Tang, Z. Xu, Numerical methods and comparison for computing dark and bright solitons in the nonlinear Schrödinger equation, *J. Comput. Phys.* 235 (2013) 423–445; W. Wen, H.-J. Li, Interference between two superfluid Fermi gases, *J. Phys. B* 46 (2013) 035302; H. Zheng, Y. Hao, Q. Gu, Dynamics of double-well Bose–Einstein condensates subject to external Gaussian white noise, *J. Phys. B* 46 (2013) 065301; Y. Wang, F.-D. Zong, F.-B. Li, Three-dimensional Bose–Einstein condensate vortex solitons under optical lattice and harmonic confinements, *Chinese Phys. B* 22 (2013) 030315; P.-G. Yan, S.-T. Ji, X.-S. Liu, Symmetry breaking and tunneling dynamics of $F = 1$ spinor Bose–Einstein condensates in a triple-well potential, *Phys. Lett. A* 377 (2013) 878–884; R.R. Sakhel, A.R. Sakhel, H.B. Ghassib, Nonequilibrium dynamics of a Bose–Einstein condensate excited by a red laser inside a power-law trap with hard walls, *J. Low Temp. Phys.* 173 (2013) 177–206; A. Trichet, E. Durupt, F. Médard, S. Datta, A. Minguzzi, M. Richard, Long-range correlations in a 97% excitonic one-dimensional polariton condensate, *Phys. Rev. B* 88 (2013) 121407; X. Yue, et al., Observation of diffraction phases in matter-wave scattering, *Phys. Rev. A* 88 (2013) 013603; S. Prabhakar, et al., Annihilation of vortex dipoles in an oblate Bose–Einstein condensate, *J. Phys. B* 46 (2013) 125302; Z. Marojevic, E. Goeklu, C. Laemmerzahl, Energy eigenfunctions of the 1D Gross–Pitaevskii equation, *Comput. Phys. Commun.* 184 (2013) 1920–1930; T. Mithun, K. Porsezian, B. Dey, Vortex dynamics in cubic-quintic Bose–Einstein condensates, *Phys. Rev. E* 88 (2013) 012904; M. Edwards, M. Krygier, H. Seddiqi, B. Benton, C.W. Clark, Approximate mean-field equations of motion for quasi-two-dimensional Bose–Einstein condensate systems, *Phys. Rev. E* 86 (2012) 056710; J. Li, F.-D. Zong, C.-S. Song, Y. Wang, F.-B. Li, Dynamics of analytical three-dimensional solutions in Bose–Einstein condensates with time-dependent gain and potential, *Phys. Rev. E* 85 (2012) 036607;

- P. Verma, A.B. Bhattacharjee, M. Mohan, Oscillations in a parametrically excited Bose–Einstein condensate in combined harmonic and optical lattice trap, *Central Eur. J. Phys.* 10 (2012) 335–341;
- E.R.F. Ramos, F.E.A. dos Santos, M.A. Caracanhas, V.S. Bagnato, Coupling collective modes in a trapped superfluid, *Phys. Rev. A* 85 (2012) 033608;
- W.B. Cardoso, A.T. Avelar, D. Bazeia, Modulation of localized solutions in a system of two coupled nonlinear Schrödinger equations, *Phys. Rev. E* 86 (2012) 027601;
- P.-G. Yan, Y.-S. Wang, S.-T. Ji, X.-S. Liu, Symmetry breaking of a Bose–Fermi mixture in a triple-well potential, *Phys. Lett. A* 376 (2012) 3141–3145;
- H.L. Zheng, Y.J. Hao, Q. Gu, Dissipation effect in the double-well Bose–Einstein condensate, *Eur. Phys. J. D* 66 (2012) 320;
- P. Verma, A.B. Bhattacharjee, M. Mohan, Oscillations in a parametrically excited Bose–Einstein condensate in combined harmonic and optical lattice trap, *Central Eur. J. Phys.* 10 (2012) 335–341;
- W.B. Cardoso, A.T. Avelar, D. Bazeia, One-dimensional reduction of the three-dimensional Gross–Pitaevskii equation with two- and three-body interactions, *Phys. Rev. E* 83 (2011) 036604;
- R.R. Sakhel, A.R. Sakhel, H.B. Ghassib, Self-interfering matter-wave patterns generated by a moving laser obstacle in a two-dimensional Bose–Einstein condensate inside a power trap cut-off by box potential boundaries, *Phys. Rev. A* 84 (2011) 033634;
- A. Balaž, A.I. Nicolin, Faraday waves in binary nonmiscible Bose–Einstein condensates, *Phys. Rev. A* 85 (2012) 023613;
- S. Yang, M. Al-Amri, J. Evers, M.S. Zubairy, Controllable optical switch using a Bose–Einstein condensate in an optical cavity, *Phys. Rev. A* 83 (2011) 053821;
- Z. Sun, W. Yang, An exact short-time solver for the time-dependent Schrödinger equation, *J. Chem. Phys.* 134 (2011) 041101;
- G.K. Chaudhary, R. Ramakumar, Collapse dynamics of a $(176)\text{Yb}-(174)\text{Yb}$ Bose–Einstein condensate, *Phys. Rev. A* 81 (2010) 063603;
- S. Gautam, D. Angom, Rayleigh–Taylor instability in binary condensates, *Phys. Rev. A* 81 (2010) 053616;
- S. Gautam, D. Angom, Ground state geometry of binary condensates in axisymmetric traps, *J. Phys. B* 43 (2010) 095302;
- G. Mazzarella, L. Salasnich, Collapse of triaxial bright solitons in atomic Bose–Einstein condensates, *Phys. Lett. A* 373 (2009) 4434–4437.
- [6] T. Koch, T. Lahaye, Fröhlich, A. Griesmaier, T. Pfau, Stabilization of a purely dipolar quantum gas against collapse, *Nat. Phys.* 4 (2008) 218–222.
- [7] M. Lu, N.Q. Burdick, Seo Ho Youn, B.L. Lev, Strongly dipolar Bose–Einstein condensate of dysprosium, *Phys. Rev. Lett.* 107 (2011) 190401.
- [8] K. Aikawa, et al., Bose–Einstein condensation of Erbium, *Phys. Rev. Lett.* 108 (2012) 210401.
- [9] W. Bao, Y. Cai, H. Wang, Efficient numerical methods for computing ground states and dynamics of dipolar Bose–Einstein condensates, *J. Comput. Phys.* 229 (2010) 7874–7892.
- [10] S. Yi, L. You, Trapped condensates of atoms with dipole interactions, *Phys. Rev. A* 63 (2001) 053607;
- S. Yi, L. You, H. Pu, Quantum phases of dipolar spinor condensates, *Phys. Rev. Lett.* 93 (2004) 040403.
- [11] K. Góral, L. Santos, Ground state and elementary excitations of single and binary Bose–Einstein condensates of trapped dipolar gases, *Phys. Rev. A* 66 (2002) 023613.
- [12] S. Ronen, D.C.E. Bortolotti, J.L. Bohn, Bogoliubov modes of a dipolar condensate in a cylindrical trap, *Phys. Rev. A* 74 (2006) 013623.
- [13] P.B. Blakie, C. Ticknor, A.S. Bradley, A.M. Martin, M.J. Davis, Y. Kawaguchi, Numerical method for evolving the dipolar projected Gross–Pitaevskii equation, *Phys. Rev. E* 80 (2009) 016703.
- [14] T. Lahaye, J. Metz, B. Fröhlich, T. Koch, M. Meister, A. Griesmaier, T. Pfau, H. Saito, Y. Kawaguchi, M. Ueda, d -Wave collapse and explosion of a dipolar Bose–Einstein condensate, *Phys. Rev. Lett.* 101 (2008) 080401.
- [15] N.G. Parker, C. Ticknor, A.M. Martin, D.H.J. O’Dell, Structure formation during the collapse of a dipolar atomic Bose–Einstein condensate, *Phys. Rev. A* 79 (2009) 013617;
- C. Ticknor, N.G. Parker, A. Melatos, S.L. Cornish, D.H.J. O’Dell, A.M. Martin, Collapse times of dipolar Bose–Einstein condensate, *Phys. Rev. A* 78 (2008) 061607.
- [16] M. Asad-uz-Zaman, D. Blume, Aligned dipolar Bose–Einstein condensate in a double-well potential: From cigar shaped to pancake shaped, *Phys. Rev. A* 80 (2009) 053622.
- [17] L. Salasnich, A. Parola, L. Reatto, Effective wave equations for the dynamics of cigar-shaped and disk-shaped Bose condensates, *Phys. Rev. A* 65 (2002) 043614.
- [18] L. Santos, V. Shlyapnikov, G. P. Zoller, M. Lewenstein, Bose–Einstein condensation in trapped dipolar gases, *Phys. Rev. Lett.* 85 (2000) 1791–1794.
- [19] T. Lahaye, C. Menotti, L. Santos, M. Lewenstein, T. Pfau, The physics of dipolar bosonic quantum gases, *Rep. Progr. Phys.* 72 (2009) 126401.
- [20] V.M. Pérez-García, H. Michinel, J.I. Cirac, M. Lewenstein, P. Zoller, *Phys. Rev. A* 56 (1997) 1424–1432.
- [21] S. Giovanazzi, A. Görlitz, T. Pfau, Ballistic expansion of a dipolar condensate, *J. Opt. B* 5 (2003) S208–S211.
- [22] P. Muruganandam, S.K. Adhikari, Numerical and variational solutions of the dipolar Gross–Pitaevskii equation in reduced dimensions, *Laser Phys.* 22 (2012) 813–820.
- [23] D. O’Dell, S. Giovanazzi, C. Eberlein, Exact Hydrodynamics of a dipolar Bose–Einstein condensate, *Phys. Rev. Lett.* 92 (2004) 250401.
- [24] C. Eberlein, S. Giovanazzi, D.H.J. O’Dell, Exact solution of the Thomas–Fermi equation for a trapped Bose–Einstein condensate with dipole–dipole interactions, *Phys. Rev. A* 71 (2005) 033618.
- [25] N.G. Parker, D.H.J. O’Dell, Thomas–Fermi versus one- and two-dimensional regimes of a trapped dipolar Bose–Einstein condensate, *Phys. Rev. A* 78 (2008) 41601(R).
- [26] S. Sinha, L. Santos, Cold dipolar gases in quasi-one-dimensional geometries, *Phys. Rev. Lett.* 99 (2007) 140406;
- F. Deuretzbacher, J.C. Cremon, S.M. Reimann, Ground-state properties of few dipolar bosons in a quasi-one-dimensional harmonic trap, *Phys. Rev. A* 81 (2010) 063616.
- [27] S. Giovanazzi, D.H.J. O’Dell, *Eur. Phys. J. D* 31 (2004) 439–445.
- [28] U.R. Fischer, Stability of quasi-two-dimensional Bose–Einstein condensates with dominant dipole–dipole interactions, *Phys. Rev. A* 73 (2006) 031602;
- P. Pedri, L. Santos, Two-dimensional bright solitons in dipolar Bose–Einstein condensates, *Phys. Rev. Lett.* 95 (2005) 200404.
- [29] M. Asad-uz-Zaman, D. Blume, private Communication, 2010.
- [30] A. Aftalion, Q. Du, Vortices in a rotating Bose–Einstein condensate: Critical angular velocities and energy diagrams in the Thomas–Fermi regime, *Phys. Rev. A* 64 (2001) 063603.
- [31] S. Ronen, D.C.E. Bortolotti, J.L. Bohn, Radial and angular Rotons in trapped dipolar gases, *Phys. Rev. Lett.* 98 (2007) 030406;
- R.M. Wilson, S. Ronen, J.L. Bohn, H. Pu, Manifestations of the Roton mode in dipolar Bose–Einstein condensates, *Phys. Rev. Lett.* 100 (2008) 245302;
- L. Santos, G.V. Shlyapnikov, M. Lewenstein, Roton–Maxon spectrum and stability of trapped dipolar Bose–Einstein condensates, *Phys. Rev. Lett.* 90 (2003) 250403;
- M. Asad-uz-Zaman, D. Blume, Modification of roton instability due to the presence of a second dipolar Bose–Einstein condensate, *Phys. Rev. A* 83 (2011) 033616.



C programs for solving the time-dependent Gross–Pitaevskii equation in a fully anisotropic trap[☆]

Dušan Vudragović^a, Ivana Vidanović^a, Antun Balaž^{a,*}, Paulsamy Muruganandam^b, Sadhan K. Adhikari^c

^a Scientific Computing Laboratory, Institute of Physics Belgrade, University of Belgrade, Pregrevica 118, 11080 Belgrade, Serbia

^b School of Physics, Bharathidasan University, Palkalaiperur Campus, Tiruchirappalli – 620024, Tamil Nadu, India

^c Instituto de Física Teórica, UNESP – Universidade Estadual Paulista, 01.140-70 São Paulo, São Paulo, Brazil

ARTICLE INFO

Article history:

Received 2 March 2012

Accepted 21 March 2012

Available online 21 April 2012

Keywords:

Bose–Einstein condensate

Gross–Pitaevskii equation

Split-step Crank–Nicolson scheme

Real- and imaginary-time propagation

C program

OpenMP

Partial differential equation

ABSTRACT

We present C programming language versions of earlier published Fortran programs (Muruganandam and Adhikari (2009) [1]) for calculating both stationary and non-stationary solutions of the time-dependent Gross–Pitaevskii (GP) equation. The GP equation describes the properties of dilute Bose–Einstein condensates at ultra-cold temperatures. C versions of programs use the same algorithms as the Fortran ones, involving real- and imaginary-time propagation based on a split-step Crank–Nicolson method. In a one-space-variable form of the GP equation, we consider the one-dimensional, two-dimensional, circularly-symmetric, and the three-dimensional spherically-symmetric harmonic-oscillator traps. In the two-space-variable form, we consider the GP equation in two-dimensional anisotropic and three-dimensional axially-symmetric traps. The fully-anisotropic three-dimensional GP equation is also considered. In addition to these twelve programs, for six algorithms that involve two and three space variables, we have also developed threaded (OpenMP parallelized) programs, which allow numerical simulations to use all available CPU cores on a computer. All 18 programs are optimized and accompanied by makefiles for several popular C compilers. We present typical results for scalability of threaded codes and demonstrate almost linear speedup obtained with the new programs, allowing a decrease in execution times by an order of magnitude on modern multi-core computers.

New version program summary

Program title: GP-SCL package, consisting of: (i) imagtime1d, (ii) imagtime2d, (iii) imagtime2d-th, (iv) imagtimecir, (v) imagtime3d, (vi) imagtime3d-th, (vii) imagtimeaxial, (viii) imagtimeaxial-th, (ix) imagtimesph, (x) realtime1d, (xi) realtime2d, (xii) realtime2d-th, (xiii) realtimecir, (xiv) realtime3d, (xv) realtime3d-th, (xvi) realtimeaxial, (xvii) realtimeaxial-th, (xviii) realltimesph.

Catalogue identifier: AEDU_v2_0.

Program Summary URL: http://cpc.cs.qub.ac.uk/summaries/AEDU_v2_0.html.

Program obtainable from: CPC Program Library, Queen's University of Belfast, N. Ireland.

Licensing provisions: Standard CPC licence, <http://cpc.cs.qub.ac.uk/licence/licence.html>.

No. of lines in distributed program, including test data, etc.: 180 583.

No. of bytes in distributed program, including test data, etc.: 1 188 688.

Distribution format: tar.gz.

Programming language: C and C/OpenMP.

Computer: Any modern computer with C language compiler installed.

Operating system: Linux, Unix, Mac OS, Windows.

RAM: Memory used with the supplied input files: 2–4 MB (i, iv, ix, x, xiii, xvi, xvii, xviii), 8 MB (xi, xii), 32 MB (vii, viii), 80 MB (ii, iii), 700 MB (xiv, xv), 1.2 GB (v, vi).

Number of processors used: For threaded (OpenMP parallelized) programs, all available CPU cores on the computer.

Classification: 2.9, 4.3, 4.12.

[☆] D.V., I.V., and A.B. acknowledge support by the Ministry of Education and Science of the Republic of Serbia under projects No. ON171017 and NAD-BEC, by DAAD - German Academic and Exchange Service under project NAD-BEC, and by the European Commission under EU FP7 projects PRACE-1IP, PRACE-2IP, HP-SEE, and EGI-InSPIRE. P.M. acknowledges support by DST and CSIR of India. S.K.A. acknowledges support by FAPESP and CNPq of Brazil.

* Corresponding author.

E-mail address: antun@ipb.ac.rs (A. Balaž).

Catalogue identifier of previous version: AEDU_v1_0.

Journal reference of previous version: Comput. Phys. Commun. 180 (2009) 1888.

Does the new version supersede the previous version?: No.

Nature of problem: These programs are designed to solve the time-dependent Gross–Pitaevskii (GP) nonlinear partial differential equation in one-, two- or three-space dimensions with a harmonic, circularly-symmetric, spherically-symmetric, axially-symmetric or fully anisotropic trap. The GP equation describes the properties of a dilute trapped Bose–Einstein condensate.

Solution method: The time-dependent GP equation is solved by the split-step Crank–Nicolson method by discretizing in space and time. The discretized equation is then solved by propagation, in either imaginary or real time, over small time steps. The method yields solutions of stationary and/or non-stationary problems.

Reasons for the new version: Previous Fortran programs [1] are used within the ultra-cold atoms [2–11] and nonlinear optics [12,13] communities, as well as in various other fields [14–16]. This new version represents translation of all programs to the C programming language, which will make it accessible to the wider parts of the corresponding communities. It is well known that numerical simulations of the GP equation in highly experimentally relevant geometries with two or three space variables are computationally very demanding, which presents an obstacle in detailed numerical studies of such systems. For this reason, we have developed threaded (OpenMP parallelized) versions of programs *imagtime2d*, *imagtime3d*, *imagtimeaxial*, *realtime2d*, *realtime3d*, *realtimeaxial*, which are named *imagtime2d-th*, *imagtime3d-th*, *imagtimeaxial-th*, *realtime2d-th*, *realtime3d-th*, *realtimeaxial-th*, respectively. Fig. 1 shows the scalability results obtained for OpenMP versions of programs *realtime2d* and *realtime3d*. As we can see, the speedup is almost linear, and on a computer with the total of 8 CPU cores we observe in Fig. 1(a) a maximal speedup of around 7, or roughly 90% of the ideal speedup, while on a computer with 12 CPU cores we find in Fig. 1(b) that the maximal speedup is around 9.6, or 80% of the ideal speedup. Such a speedup represents significant improvement in the performance.

Summary of revisions: All Fortran programs from the previous version [1] are translated to C and named in the same way. The structure of all programs is identical. We have introduced the use of comprehensive input files, where all parameters are explained in detail and can be set by a user. We have also included makefiles with tested and verified settings for GNU's gcc compiler, Intel's icc compiler, IBM's xlc compiler, PGI's pgcc compiler, and Oracle's suncc (former Sun's) compiler. In addition to this, 6 new threaded (OpenMP parallelized) programs are supplied (*imagtime2d-th*, *imagtime3d-th*, *imagtimeaxial-th*, *realtime2d-th*, *realtime3d-th*, *realtimeaxial-th*) for algorithms involving two or three space variables. They are written by OpenMP-parallelizing the most computationally demanding loops in functions performing time evolution (*calcnu*, *calclux*, *calcluy*, *calcluz*), normalization (*calcnorm*), and calculation of physical quantities (*calcmuen*, *calcrms*). Since some of the dynamically allocated array variables are used within such loops, they had to be made private for each thread. This was done by allocating matrices instead of arrays, with the first index in all such matrices corresponding to a thread number.

Additional comments: This package consists of 18 programs, see Program title above, out of which 12 programs (i, ii, iv, v, vii, ix, x, xi, xiii, xiv, xvi, xviii) are serial, while 6 programs (iii, vi, viii, xii, xv, xvii) are threaded (OpenMP parallelized). For the particular purpose of each program, please see descriptions below.

Running time: All running times given in descriptions below refer to programs compiled with gcc on quad-core Intel Xeon X5460 at 3.16 GHz (CPU1), and programs compiled with icc on quad-core Intel Nehalem E5540 at 2.53 GHz (CPU2). With the supplied input files, running times on CPU1 are: 5 min (i, iv, ix, xii, xiii, xvii, xviii), 10 min (viii, xvi), 15 min (iii, x, xi), 30 min (ii, vi, vii), 2 h (v), 4 h (xv), 15 h (xiv). On CPU2, running times are: 5 min (i, iii, iv, viii, ix, xii, xiii, xvi, xvii, xviii), 10 min (vi, x, xi), 20 min (ii, vii), 1 h (v), 2 h (xv), 12 h (xiv).

© 2012 Elsevier B.V. All rights reserved.

New version program summary (i)

Program title: *imagtime1d*.

Title of electronic files: *imagtime1d.c*, *imagtime1d.h*.

Computer: Any modern computer with C language compiler installed.

Maximum RAM memory: 4 MB.

Programming language used: C.

Typical running time: 2 min (CPU1), 1 min (CPU2).

Nature of physical problem: This program is designed to solve the time-dependent GP nonlinear partial differential equation in one space dimension with a harmonic trap. The GP equation describes the properties of a dilute trapped Bose–Einstein condensate.

Method of solution: The time-dependent GP equation is solved by the split-step Crank–Nicolson method by discretizing in space and time. The discretized equation is then solved by propagation in imaginary time over small time steps. The method yields solutions of stationary problems.

New version program summary (ii)

Program title: *imagtime2d*.

Title of electronic files: *imagtime2d.c*, *imagtime2d.h*.

Computer: Any modern computer with C language compiler installed.

Maximum RAM memory: 80 MB.

Programming language used: C.

Typical running time: 30 min (CPU1), 20 min (CPU2).

Nature of physical problem: This program is designed to solve the time-dependent GP nonlinear partial differential equation in two space dimensions with an anisotropic trap. The GP equation describes the properties of a dilute trapped Bose–Einstein condensate.

Method of solution: The time-dependent GP equation is solved by the split-step Crank–Nicolson method by discretizing in space and time. The discretized equation is then solved by propagation in imaginary time over small time steps. The method yields solutions of stationary problems.

New version program summary (iii)

Program title: imagtime2d-th.

Title of electronic files: imagtime2d-th.c, imagtime2d-th.h.

Computer: Any modern computer with C language compiler installed.

Maximum RAM memory: 80 MB.

Programming language used: C/OpenMP.

Typical running time: 15 min (CPU1), 5 min (CPU2).

Nature of physical problem: This program is designed to solve the time-dependent GP nonlinear partial differential equation in two space dimensions with an anisotropic trap. The GP equation describes the properties of a dilute trapped Bose–Einstein condensate.

Method of solution: The time-dependent GP equation is solved by the split-step Crank–Nicolson method by discretizing in space and time. The discretized equation is then solved by propagation in imaginary time over small time steps. The method yields solutions of stationary problems.

New version program summary (iv)

Program title: imagtimecir.

Title of electronic files: imagtimecir.c, imagtimecir.h.

Computer: Any modern computer with C language compiler installed.

Maximum RAM memory: 2 MB.

Programming language used: C.

Typical running time: 2 min (CPU1), 1 min (CPU2).

Nature of physical problem: This program is designed to solve the time-dependent GP nonlinear partial differential equation in two space dimensions with a circularly-symmetric trap. The GP equation describes the properties of a dilute trapped Bose–Einstein condensate.

Method of solution: The time-dependent GP equation is solved by the split-step Crank–Nicolson method by discretizing in space and time. The discretized equation is then solved by propagation in imaginary time over small time steps. The method yields solutions of stationary problems.

New version program summary (v)

Program title: imagtime3d.

Title of electronic files: imagtime3d.c, imagtime3d.h.

Computer: Any modern computer with C language compiler installed.

Maximum RAM memory: 1.2 GB.

Programming language used: C.

Typical running time: 1.5 h (CPU1), 1 h (CPU2).

Nature of physical problem: This program is designed to solve the time-dependent GP nonlinear partial differential equation in three space dimensions with an anisotropic trap. The GP equation describes the properties of a dilute trapped Bose–Einstein condensate.

Method of solution: The time-dependent GP equation is solved by the split-step Crank–Nicolson method by discretizing in space and time. The discretized equation is then solved by propagation in imaginary time over small time steps. The method yields solutions of stationary problems.

New version program summary (vi)

Program title: imagtime3d-th.

Title of electronic files: imagtime3d-th.c, imagtime3d-th.h.

Computer: Any modern computer with C language compiler installed.

Maximum RAM memory: 1.2 GB.

Programming language used: C/OpenMP.

Typical running time: 25 min (CPU1), 10 min (CPU2).

Nature of physical problem: This program is designed to solve the time-dependent GP nonlinear partial differential equation

in three space dimensions with an anisotropic trap. The GP equation describes the properties of a dilute trapped Bose–Einstein condensate.

Method of solution: The time-dependent GP equation is solved by the split-step Crank–Nicolson method by discretizing in space and time. The discretized equation is then solved by propagation in imaginary time over small time steps. The method yields solutions of stationary problems.

New version program summary (vii)

Program title: imagtimeaxial.

Title of electronic files: imagtimeaxial.c, imagtimeaxial.h.

Computer: Any modern computer with C language compiler installed.

Maximum RAM memory: 32 MB.

Programming language used: C.

Typical running time: 30 min (CPU1), 20 min (CPU2).

Nature of physical problem: This program is designed to solve the time-dependent GP nonlinear partial differential equation in three space dimensions with an axially-symmetric trap. The GP equation describes the properties of a dilute trapped Bose–Einstein condensate.

Method of solution: The time-dependent GP equation is solved by the split-step Crank–Nicolson method by discretizing in space and time. The discretized equation is then solved by propagation in imaginary time over small time steps. The method yields solutions of stationary problems.

New version program summary (viii)

Program title: imagtimeaxial-th.

Title of electronic files: imagtimeaxial-th.c, imagtimeaxial-th.h.

Computer: Any modern computer with C language compiler installed.

Maximum RAM memory: 32 MB.

Programming language used: C/OpenMP.

Typical running time: 10 min (CPU1), 5 min (CPU2).

Nature of physical problem: This program is designed to solve the time-dependent GP nonlinear partial differential equation in three space dimensions with an axially-symmetric trap. The GP equation describes the properties of a dilute trapped Bose–Einstein condensate.

Method of solution: The time-dependent GP equation is solved by the split-step Crank–Nicolson method by discretizing in space and time. The discretized equation is then solved by propagation in imaginary time over small time steps. The method yields solutions of stationary problems.

New version program summary (ix)

Program title: imagtimesph.

Title of electronic files: imagtimesph.c, imagtimesph.h.

Computer: Any modern computer with C language compiler installed.

Maximum RAM memory: 2.5 MB.

Programming language used: C.

Typical running time: 2 min (CPU1), 1 min (CPU2).

Nature of physical problem: This program is designed to solve the time-dependent GP nonlinear partial differential equation in three space dimensions with a spherically-symmetric trap. The GP equation describes the properties of a dilute trapped Bose–Einstein condensate.

Method of solution: The time-dependent GP equation is solved by the split-step Crank–Nicolson method by discretizing in space and time. The discretized equation is then solved by propagation in imaginary time over small time steps. The method yields solutions of stationary problems.

New version program summary (x)

Program title: realtime1d.

Title of electronic files: realtime1d.c, realtime1d.h.

Computer: Any modern computer with C language compiler installed.

Maximum RAM memory: 4 MB.

Programming language used: C.

Typical running time: 15 min (CPU1), 10 min (CPU2).

Nature of physical problem: This program is designed to solve the time-dependent GP nonlinear partial differential equation in one space dimension with a harmonic trap. The GP equation describes the properties of a dilute trapped Bose–Einstein condensate.

Method of solution: The time-dependent GP equation is solved by the split-step Crank–Nicolson method by discretizing in space and time. The discretized equation is then solved by propagation in real time over small time steps. The method yields solutions of stationary and non-stationary problems.

New version program summary (xi)

Program title: realtime2d.

Title of electronic files: realtime2d.c, realtime2d.h.

Computer: Any modern computer with C language compiler installed.

Maximum RAM memory: 8 MB.

Programming language used: C.

Typical running time: 15 min (CPU1), 10 min (CPU2).

Nature of physical problem: This program is designed to solve the time-dependent GP nonlinear partial differential equation in two space dimensions with an anisotropic trap. The GP equation describes the properties of a dilute trapped Bose–Einstein condensate.

Method of solution: The time-dependent GP equation is solved by the split-step Crank–Nicolson method by discretizing in space and time. The discretized equation is then solved by propagation in real time over small time steps. The method yields solutions of stationary and non-stationary problems.

New version program summary (xii)

Program title: realtime2d-th.

Title of electronic files: realtime2d-th.c, realtime2d-th.h.

Computer: Any modern computer with C language compiler installed.

Maximum RAM memory: 8 MB.

Programming language used: C/OpenMP.

Typical running time: 5 min (CPU1), 2 min (CPU2).

Nature of physical problem: This program is designed to solve the time-dependent GP nonlinear partial differential equation in two space dimensions with an anisotropic trap. The GP equation describes the properties of a dilute trapped Bose–Einstein condensate.

Method of solution: The time-dependent GP equation is solved by the split-step Crank–Nicolson method by discretizing in space and time. The discretized equation is then solved by propagation in real time over small time steps. The method yields solutions of stationary and non-stationary problems.

New version program summary (xiii)

Program title: realtimecir.

Title of electronic files: realtimecir.c, realtimecir.h.

Computer: Any modern computer with C language compiler installed.

Maximum RAM memory: 3 MB.

Programming language used: C.

Typical running time: 5 min (CPU1), 5 min (CPU2).

Nature of physical problem: This program is designed to solve the time-dependent GP nonlinear partial differential equation in two space dimensions with a circularly-symmetric trap. The GP equation describes the properties of a dilute trapped Bose–Einstein condensate.

Method of solution: The time-dependent GP equation is solved by the split-step Crank–Nicolson method by discretizing in space and time. The discretized equation is then solved by propagation in real time over small time steps. The method yields solutions of stationary and non-stationary problems.

New version program summary (xiv)

Program title: realtime3d.

Title of electronic files: realtime3d.c, realtime3d.h.

Computer: Any modern computer with C language compiler installed.

Maximum RAM memory: 700 MB.

Programming language used: C.

Typical running time: 15 h (CPU1), 12 h (CPU2).

Nature of physical problem: This program is designed to solve the time-dependent GP nonlinear partial differential equation in three space dimensions with an anisotropic trap. The GP equation describes the properties of a dilute trapped Bose–Einstein condensate.

Method of solution: The time-dependent GP equation is solved by the split-step Crank–Nicolson method by discretizing in space and time. The discretized equation is then solved by propagation in real time over small time steps. The method yields solutions of stationary and non-stationary problems.

New version program summary (xv)

Program title: realtime3d-th.

Title of electronic files: realtime3d-th.c, realtime3d-th.h.

Computer: Any modern computer with C language compiler installed.

Maximum RAM memory: 700 MB.

Programming language used: C/OpenMP.

Typical running time: 4 h (CPU1), 1.8 h (CPU2).

Nature of physical problem: This program is designed to solve the time-dependent GP nonlinear partial differential equation in three space dimensions with an anisotropic trap. The GP equation describes the properties of a dilute trapped Bose–Einstein condensate.

Method of solution: The time-dependent GP equation is solved by the split-step Crank–Nicolson method by discretizing in space and time. The discretized equation is then solved by propagation in real time over small time steps. The method yields solutions of stationary and non-stationary problems.

New version program summary (xvi)

Program title: realtimeaxial.

Title of electronic files: realtimeaxial.c, realtimeaxial.h.

Computer: Any modern computer with C language compiler installed.

Maximum RAM memory: 4 MB.

Programming language used: C.

Typical running time: 10 min (CPU1), 5 min (CPU2).

Nature of physical problem: This program is designed to solve the time-dependent GP nonlinear partial differential equation in three space dimensions with an axially-symmetric trap. The GP equation describes the properties of a dilute trapped Bose–Einstein condensate.

Method of solution: The time-dependent GP equation is solved by the split-step Crank–Nicolson method by discretizing in space and time. The discretized equation is then solved by propagation in real time over small time steps. The method yields solutions of stationary and non-stationary problems.

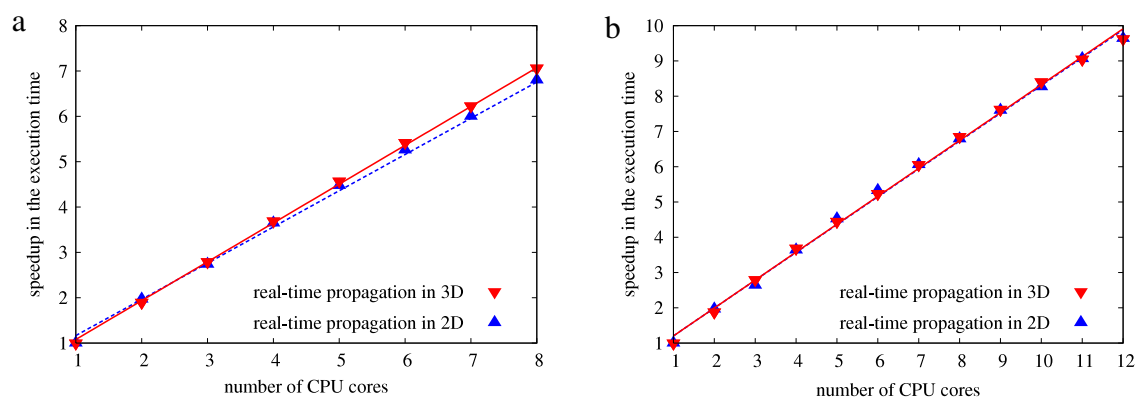


Fig. 1. (Colour online) Speedup in the execution time of realtime2d-th and realtime3d-th threaded (OpenMP parallelized) programs as a function of the number of CPU cores used. The results are obtained: (a) on an 8-core machine with $2 \times$ quad-core Intel Nehalem E5540 CPU at 2.53 GHz, using the icc compiler, (b) on a 12-core machine with $2 \times$ six-core Intel Nehalem X5650 CPU at 2.66 GHz, using the pgcc compiler. The spatial grid sizes used are 2000×2000 (realtime2d-th) and $1000 \times 1000 \times 300$ (realtime3d-th).

New version program summary (xvii)

Program title: realtimeaxial-th.

Title of electronic files: realtimeaxial-th.c, realtimeaxial-th.h.

Computer: Any modern computer with C language compiler installed.

Maximum RAM memory: 4 MB.

Programming language used: C/OpenMP.

Typical running time: 5 min (CPU1), 1 min (CPU2).

Nature of physical problem: This program is designed to solve the time-dependent GP nonlinear partial differential equation in three space dimensions with an axially-symmetric trap. The GP equation describes the properties of a dilute trapped Bose–Einstein condensate.

Method of solution: The time-dependent GP equation is solved by the split-step Crank–Nicolson method by discretizing in space and time. The discretized equation is then solved by propagation in real time over small time steps. The method yields solutions of stationary and non-stationary problems.

New version program summary (xviii)

Program title: reallimesph.

Title of electronic files: reallimesph.c, reallimesph.h.

Computer: Any modern computer with C language compiler installed.

Maximum RAM memory: 2.5 MB.

Programming language used: C.

Typical running time: 5 min (CPU1), 5 min (CPU2).

Nature of physical problem: This program is designed to solve the time-dependent GP nonlinear partial differential equation in three space dimensions with a spherically-symmetric trap. The GP equation describes the properties of a dilute trapped Bose–Einstein condensate.

Method of solution: The time-dependent GP equation is solved by the split-step Crank–Nicolson method by discretizing in space and time. The discretized equation is then solved by propagation in real time over small time steps. The method yields solutions of stationary and non-stationary problems.

References

- [1] P. Muruganandam, S.K. Adhikari, Fortran programs for the time-dependent Gross–Pitaevskii equation in a fully anisotropic trap, *Comput. Phys. Commun.* 180 (2009) 1888.
- [2] G. Mazzarella, L. Salasnich, Collapse of triaxial bright solitons in atomic Bose–Einstein condensates, *Phys. Lett. A* 373 (2009) 4434.
- [3] Y. Cheng, S.K. Adhikari, Symmetry breaking in a localized interacting binary Bose–Einstein condensate in a bichromatic optical lattice, *Phys. Rev. A* 81 (2010) 023620; S.K. Adhikari, H. Lu, H. Pu, Self-trapping of a Fermi superfluid in a double-well potential in the Bose–Einstein-condensate-unity crossover, *Phys. Rev. A* 80 (2009) 063607.
- [4] S. Gautam, D. Angom, Rayleigh–Taylor instability in binary condensates, *Phys. Rev. A* 81 (2010) 053616; S. Gautam, D. Angom, Ground state geometry of binary condensates in axisymmetric traps, *J. Phys. B* 43 (2010) 095302; S. Gautam, P. Muruganandam, D. Angom, Position swapping and pinching in Bose–Fermi mixtures with two-color optical Feshbach resonances, *Phys. Rev. A* 83 (2011) 023605.
- [5] S.K. Adhikari, B.A. Malomed, L. Salasnich, F. Toigo, Spontaneous symmetry breaking of Bose–Fermi mixtures in double-well potentials, *Phys. Rev. A* 81 (2010) 053630.
- [6] G.K. Chaudhary, R. Ramakumar, Collapse dynamics of a $(176)\text{Yb}-(174)\text{Yb}$ Bose–Einstein condensate, *Phys. Rev. A* 81 (2010) 063603.
- [7] S. Sabari, R.V.J. Raja, K. Porsezian, P. Muruganandam, Stability of trapless Bose–Einstein condensates with two- and three-body interactions, *J. Phys. B* 43 (2010) 125302.
- [8] L.E. Young-S, L. Salasnich, S.K. Adhikari, Dimensional reduction of a binary Bose–Einstein condensate in mixed dimensions, *Phys. Rev. A* 82 (2010) 053601.
- [9] I. Vidanović, A. Balaž, H. Al-Jibbouri, A. Pelster, Nonlinear Bose–Einstein-condensate dynamics induced by a harmonic modulation of the s -wave scattering length, *Phys. Rev. A* 84 (2011) 013618.
- [10] R.R. Sakhel, A.R. Sakhel, H.B. Ghassib, Self-interfering matter-wave patterns generated by a moving laser obstacle in a two-dimensional Bose–Einstein condensate inside a power trap cut off by box potential boundaries, *Phys. Rev. A* 84 (2011) 033634.
- [11] A. Balaž, A.I. Nicolin, Faraday waves in binary nonmiscible Bose–Einstein condensates, *Phys. Rev. A* 85 (2012) 023613; A.I. Nicolin, Variational treatment of Faraday waves in inhomogeneous Bose–Einstein condensates, *Physica A* 391 (2012) 1062; A.I. Nicolin, Resonant wave formation in Bose–Einstein condensates, *Phys. Rev. E* 84 (2011) 056202; A.I. Nicolin, Faraday waves in Bose–Einstein condensates subject to anisotropic transverse confinement, *Rom. Rep. Phys.* 63 (2011) 1329; A.I. Nicolin, M.C. Raportaru, Faraday waves in high-density cigar-shaped Bose–Einstein condensates, *Physica A* 389 (2010) 4663.
- [12] S. Yang, M. Al-Amri, J. Evers, M.S. Zubairy, Controllable optical switch using a Bose–Einstein condensate in an optical cavity, *Phys. Rev. A* 83 (2011) 053821.
- [13] W. Hua, X.-S. Liu, Dynamics of cubic and quintic nonlinear Schrödinger equations, *Acta Phys. Sinica* 60 (2011) 110210.
- [14] Z. Sun, W. Yang, An exact short-time solver for the time-dependent Schrödinger equation, *J. Chem. Phys.* 134 (2011) 041101.
- [15] A. Balaž, I. Vidanović, A. Bogojević, A. Belić, A. Pelster, Fast converging path integrals for time-dependent potentials: I. Recursive calculation of short-time expansion of the propagator, *J. Stat. Mech. Theory Exp.* (2011) P03004.
- [16] W.B. Cardoso, A.T. Avelar, D. Bazeia, One-dimensional reduction of the three-dimensional Gross–Pitaevskii equation with two- and three-body interactions, *Phys. Rev. E* 83 (2011) 036604.

SPEEDUP Code for Calculation of Transition Amplitudes via the Effective Action Approach

Antun Balaž*, Ivana Vidanović, Danica Stojiljković,
Dušan Vudragović, Aleksandar Belić and Aleksandar Bogojević

*Scientific Computing Laboratory, Institute of Physics Belgrade,
University of Belgrade, Pregrevica 118, 11080 Belgrade, Serbia.*

Received 13 December 2010; Accepted 18 April 2011

Communicated by Leonardo Golubovic

Available online 28 October 2011

Abstract. We present Path Integral Monte Carlo C code for calculation of quantum mechanical transition amplitudes for 1D models. The SPEEDUP C code is based on the use of higher-order short-time effective actions and implemented to the maximal order $p=18$ in the time of propagation (Monte Carlo time step), which substantially improves the convergence of discretized amplitudes to their exact continuum values. Symbolic derivation of higher-order effective actions is implemented in SPEEDUP Mathematica codes, using the recursive Schrödinger equation approach. In addition to the general 1D quantum theory, developed Mathematica codes are capable of calculating effective actions for specific models, for general 2D and 3D potentials, as well as for a general many-body theory in arbitrary number of spatial dimensions.

AMS subject classifications: 81Q05, 81Q15, 65Y04, 65B99

Key words: Transition amplitude, effective action, path integrals, Monte Carlo.

1 Introduction

Exact solution of a given many-body model in quantum mechanics is usually expressed in terms of eigenvalues and eigenfunction of its Hamiltonian

$$\hat{H} = \sum_{i=1}^M \frac{\hat{\mathbf{p}}_i^2}{2m_i} + \hat{V}(\hat{\mathbf{q}}_1, \dots, \hat{\mathbf{q}}_M), \quad (1.1)$$

but it can be also expressed through analytic solution for general transition amplitude $A(\mathbf{a}, \mathbf{b}; T) = \langle \mathbf{b} | e^{-iT\hat{H}/\hbar} | \mathbf{a} \rangle$ from the initial state $|\mathbf{a}\rangle$ to the final state $|\mathbf{b}\rangle$ during the time of

*Corresponding author. *Email addresses:* antun@ipb.ac.rs (A. Balaž), ivanavi@ipb.ac.rs (I. Vidanović), danica@ipb.ac.rs (D. Stojiljković), dusan@ipb.ac.rs (D. Vudragović), abelic@ipb.ac.rs (A. Belić), alex@ipb.ac.rs (A. Bogojević)

propagation T . Calculation of transition amplitudes is more suitable if one uses path integral formalism [1–3], but in principle, if eigenproblem of the Hamiltonian can be solved, one should be able to calculate general transition amplitudes, and vice versa. However, mathematical difficulties may prevent this, and even more importantly, exact solutions can be found only in a very limited number of cases. Therefore, use of various analytic approximation techniques or numerical treatment is necessary for detailed understanding of the behavior of almost all models of interest.

In numerical approaches it could be demanding and involved to translate numerical knowledge of transition amplitudes to (or from) eigenstates, but practically can be always achieved. It has been implemented in various setups, e.g. through extraction of the energy spectra from the partition function [2–5], and using the diagonalization of space-discretized matrix of the evolution operator, i.e. matrix of transition amplitudes [6–10]. All these applications use the imaginary-time formalism [11, 12], typical for numerical simulations of such systems.

Recently introduced effective action approach [13–17] provides an ideal framework for exact numerical calculation of quantum mechanical amplitudes. It gives systematic short-time expansion of amplitudes for a general potential, thus allowing accurate calculation of short-time properties of quantum systems directly, as has been demonstrated in [8–10]. For numerical calculations that require long times of propagation to be considered using e.g. Monte Carlo method, effective action approach provides improved discretized actions leading to the speedup in the convergence of numerically calculated discretized quantities to their exact continuum values. This has been also demonstrated in Monte Carlo calculations of energy expectation values using the improved energy estimators [5, 18].

In this paper we present SPEEDUP codes [19] which implement the effective action approach, and which were used for numerical simulations in [4, 5, 8–10, 13–17]. The paper is organized as follows. In Section 2 we briefly review the recursive approach for analytic derivation of higher-order effective actions. SPEEDUP Mathematica codes capable of symbolic derivation of effective actions for a general one- and many-body theory as well as for specific models is described in detail in Section 3, while in Section 4 we describe SPEEDUP Path Integral Monte Carlo C code, developed for numerical calculation of transition amplitudes for 1D models. Section 5 summarizes presented results and gives outlook for further development of the code.

2 Theoretical background

From inception of the path integral formalism, expansion of short-time amplitudes in the time of propagation was used for the definition of path integrals through the time-discretization procedure [2, 3]. This is also straightforwardly implemented in the Path Integral Monte Carlo approaches [20], where one usually relies on the naive discretization of the action. Several improved discretized actions, mainly based on the Trotter formula

and its generalizations, were developed and used in the past [21–23]. A recent analysis of this method can be found in Jang et al [24]. Several related investigations dealing with the speed of convergence have focused on improvements in short-time propagation [25, 26] or the action [27]. More recently, split-operator method has also been developed [28–32], later extended to include higher-order terms [33–36], and systematically improved using the multi-product expansion [37–39].

The effective action approach is based on the ideal discretization concept [16]. It was introduced first for single-particle 1D models [13–15] and later extended to general many-body systems in arbitrary number of spatial dimensions [5, 17]. This approach allows systematic derivation of higher-order terms to a chosen order p in the short time of propagation.

Recursive method for deriving discretized effective actions, established in [17], is based on solving the underlying Schrödinger equation for the amplitude. It has proven to be the most efficient tool for treatment of higher-order expansion. In this section we give brief overview of the recursive method, which will be implemented in Mathematica in the next section. We start with the case of single particle in 1D, used in the SPEEDUP C code. Throughout the paper we will use natural system of units, in which \hbar and all masses are set to unity.

2.1 One particle in one dimension

In the effective action approach, transition amplitudes are expressed in terms of the ideal discretized action S^* in the form

$$A(a, b; T) = \frac{1}{\sqrt{2\pi T}} e^{-S^*(a, b; T)}, \quad (2.1)$$

which can be also seen as a definition of the ideal action [16]. Therefore, by definition, the above expression is correct not only for short times of propagation, but for arbitrary large times T . We also introduce the ideal effective potential W ,

$$S^*(a, b; T) = T \left[\frac{1}{2} \left(\frac{b-a}{T} \right)^2 + W \right], \quad (2.2)$$

reminiscent of the naive discretized action, with the arguments of the effective potential (a, b, T) usually written as $W\left(\frac{a+b}{2}, \frac{b-a}{2}; T\right)$, to emphasize that we will be using mid-point prescription.

However, ideal effective action and effective potential can be calculated analytically only for exactly solvable models, while in all other cases we have to use some approximative method. We use expansion in the time of propagation, assuming that the time T is small. If this is not the case, we can always divide the propagation into N time steps, so that $\varepsilon = T/N$ is small. Long-time amplitude is then obtained by integrating over all short-time ones,

$$A(a, b; T) = \int dq_1 \cdots dq_{N-1} A(a, q_1; \varepsilon) A(q_1, q_2; \varepsilon) \cdots A(q_{N-1}, b; \varepsilon), \quad (2.3)$$

paving the way towards Path Integral Monte Carlo calculation, which is actually implemented in the SPEEDUP C code.

If we consider general amplitude $A(q, q'; \varepsilon)$, introduce the mid-point coordinate $x = (q + q')/2$ and deviation $\bar{x} = (q' - q)/2$, and express A using the effective potential,

$$A(q, q'; \varepsilon) = \frac{1}{\sqrt{2\pi\varepsilon}} e^{-\frac{2}{\varepsilon}\bar{x}^2 - \varepsilon W(x, \bar{x}; \varepsilon)}, \quad (2.4)$$

the time-dependent Schrödinger equation for the amplitude leads to the following equation for W

$$W + \bar{x}\bar{\partial}W + \varepsilon\partial_\varepsilon W - \frac{1}{8}\varepsilon\partial^2W - \frac{1}{8}\varepsilon\bar{\partial}^2W + \frac{1}{8}\varepsilon^2(\partial W)^2 + \frac{1}{8}\varepsilon^2(\bar{\partial}W)^2 = \frac{1}{2}(V_+ + V_-), \quad (2.5)$$

where $V_\pm = V(x \pm \bar{x})$, i.e. $V_- = V(q)$, $V_+ = V(q')$. The short-time expansion assumes that we expand W to power series in ε to a given order, and calculate the appropriate coefficients using Eq. (2.5). We could further expect that this results in coefficients depending on the potential $V(x)$ and its higher derivatives. However, this scheme is not complete, since the effective potential depends not only on the mid-point x , but also on the deviation \bar{x} , and the obtained equations for the coefficients cannot be solved in a closed form. In order to resolve this in a systematic way, we make use of the fact that, for short time of propagation, deviation \bar{x} is on the average given by the diffusion relation $\bar{x}^2 \propto \varepsilon$, allowing double expansion of W in the form

$$W(x, \bar{x}; \varepsilon) = \sum_{m=0}^{\infty} \sum_{k=0}^m c_{m,k}(x) \varepsilon^{m-k} \bar{x}^{2k}. \quad (2.6)$$

Restricting the above sum over m to $p-1$ leads to level p effective potential $W_p(x, \bar{x}; \varepsilon)$ which gives expansion of the effective action S_p^* to order ε^p , and hence the level designation p for both the effective action and the corresponding potential W_p . Thus, if the diffusion relation is applicable (which is always the case in Monte Carlo calculations), instead of the general double expansion in \bar{x} and ε , we are able to obtain simpler, systematic expansion in ε only.

As shown previously [13–15], when used in Path Integral Monte Carlo simulations for calculation of long time amplitudes according to Eq. (2.3), use of level p effective action leads to the convergence of discretized amplitudes proportional to ε^p , i.e. as $1/N^p$, where N is the number of time steps used in the discretization.

If we insert the above level p expansion of the effective potential to Eq. (2.5), we obtain the recursion relation derived in [17],

$$\begin{aligned} 8(m+k+1)c_{m,k} &= (2k+2)(2k+1)c_{m,k+1} + c''_{m-1,k} - \sum_{l=0}^{m-2} \sum_r c'_{l,r} c'_{m-l-2,k-r} \\ &\quad - \sum_{l=1}^{m-2} \sum_r 2r(2k-2r+2)c_{l,r} c_{m-l-1,k-r+1}, \end{aligned} \quad (2.7)$$

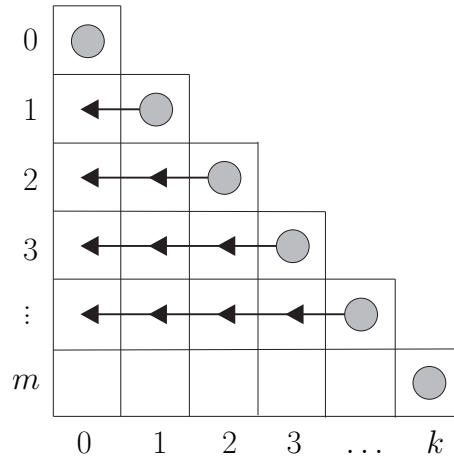


Figure 1: Order in which the coefficients $c_{m,k}$ are calculated: diagonal ones from Eq. (2.8), off-diagonal from recursion (2.7).

where the sum over r goes from $\max\{0, k-m+l+2\}$ to $\min\{k, l\}$. This recursion can be used to calculate all coefficients $c_{m,k}$ to a given level p , starting from the known initial condition, $c_{0,0} = V$. The diagonal coefficients can be calculated immediately,

$$c_{m,m} = \frac{V^{(2m)}}{(2m+1)!} \tag{2.8}$$

and for a given value of $m=0, \dots, p-1$, the coefficients $c_{m,k}$ follow recursively from evaluating (2.7) for $k=m-1, \dots, 1, 0$, as illustrated in Fig. 1.

2.2 Extension to many-body systems

The above outlined approach can be straightforwardly applied to many-body systems. Again the amplitude is expressed through the effective action and the corresponding effective potential, which now depends on mid-point positions and deviations of all particles. For simplicity, these vectors are usually combined into $D \times M$ dimensional vectors \mathbf{x} and $\bar{\mathbf{x}}$, where D is spatial dimensionality, and M is the number of particles. In this notation,

$$A(\mathbf{q}, \mathbf{q}'; \epsilon) = \frac{1}{(2\pi\epsilon)^{DM/2}} e^{-\frac{2}{\epsilon}\bar{\mathbf{x}}^2 - \epsilon W(\mathbf{x}, \bar{\mathbf{x}}; \epsilon)}, \tag{2.9}$$

where initial and final position $\mathbf{q} = (\mathbf{q}_1, \dots, \mathbf{q}_M)$ and $\mathbf{q}' = (\mathbf{q}'_1, \dots, \mathbf{q}'_M)$ are analogously defined $D \times M$ dimensional vectors. Here we will not consider quantum statistics of particles. The required symmetrization or antisymmetrization must be applied after transition amplitudes are calculated using the effective potential.

Many-body transition amplitudes satisfy $D \times M$ -dimensional generalization of the time-dependent Schrödinger equation, which leads to the equation for the effective po-

tential similar to Eq. (2.5), with vectors replacing previously scalar quantities,

$$W + \bar{\mathbf{x}} \cdot \bar{\partial} W + \varepsilon \partial_\varepsilon W - \frac{1}{8} \varepsilon \partial^2 W - \frac{1}{8} \varepsilon \bar{\partial}^2 W + \frac{1}{8} \varepsilon^2 (\partial W)^2 + \frac{1}{8} \varepsilon^2 (\bar{\partial} W)^2 = \frac{1}{2} (V_+ + V_-). \quad (2.10)$$

The effective potential for short-time amplitudes again can be written in the form of the double expansion in ε and $\bar{\mathbf{x}}$. However, it turns out to be advantageous to use the expansion

$$W(\mathbf{x}, \bar{\mathbf{x}}; \varepsilon) = \sum_{m=0}^{\infty} \sum_{k=0}^m \varepsilon^{m-k} W_{m,k}(\mathbf{x}, \bar{\mathbf{x}}), \quad (2.11)$$

and work with fully contracted quantities $W_{m,k}$

$$W_{m,k}(\mathbf{x}, \bar{\mathbf{x}}) = \bar{x}_{i_1} \bar{x}_{i_2} \cdots \bar{x}_{i_{2k}} c_{m,k}^{i_1, \dots, i_{2k}}(\mathbf{x}), \quad (2.12)$$

rather than with the respective coefficients $c_{m,k}^{i_1, \dots, i_{2k}}$. In this way we avoid the computationally expensive symmetrization over all indices i_1, \dots, i_{2k} . After inserting the above expansion into the equation for the effective potential, we obtain the recursion relation which represents a generalization of previously derived Eq. (2.7) for 1D case, and has the form

$$\begin{aligned} 8(m+k+1)W_{m,k} &= \partial^2 W_{m-1,k} + \bar{\partial}^2 W_{m,k+1} - \sum_{l=0}^{m-2} \sum_r (\partial W_{l,r}) \cdot (\partial W_{m-l-2,k-r}) \\ &\quad - \sum_{l=1}^{m-2} \sum_r (\bar{\partial} W_{l,r}) \cdot (\bar{\partial} W_{m-l-1,k-r+1}). \end{aligned} \quad (2.13)$$

The sum over r runs from $\max\{0, k-m+l+2\}$ to $\min\{k, l\}$, while diagonal quantities $W_{m,m}$ can be calculated directly,

$$W_{m,m} = \frac{1}{(2m+1)!} (\bar{\mathbf{x}} \cdot \partial)^{2m} V. \quad (2.14)$$

The above recursion disentangles, in complete analogy with the previously outlined case of one particle in 1D, and is solved in the order shown in Fig. 1.

3 SPEEDUP Mathematica codes for deriving the higher-order effective actions

The effective action approach can be used for numerically exact calculation of short-time amplitudes if the effective potential W_p can be analytically derived to sufficiently high values of p such that the associated error is smaller than the required numerical precision. The error ε^p for the effective action, obtained when level p effective potential is used, translates into $\varepsilon^{p-DM/2}$ for a general many-body short-time amplitude. However, when amplitudes are calculated using the Path Integral Monte Carlo SPEEDUP C

code [19], which will be presented in the next section, the errors of numerically calculated amplitudes are always proportional to $\varepsilon^p \sim 1/N^p$, where N is number of time-steps in the discretization of the propagation time T .

Therefore, accessibility of higher-order effective actions is central to the application of this approach if it is used for direct calculation of short-time amplitudes [8–10], as well as in the case when PIMC code is used [4, 5, 18]. However, increase in the level p leads to the increase in complexity of analytic expressions for the effective potential. On one hand, this limits the maximal accessible level p by the amount of memory required for symbolic derivation of the effective potential. On the other hand, practical use of large expressions for W_p may slow down numerical calculations, and one can opt to use lower than the maximal available level p when optimizing total CPU time required for numerical simulation. The suggested approach is to study time-complexity of the algorithm in practical applications, and to choose optimal level p by minimizing the execution time required to achieve fixed numerical precision.

We have implemented efficient symbolic derivation of higher-order effective actions in Mathematica using the recursive approach. All source files described in this section are located in the Mathematica directory of the SPEEDUP code distribution.

3.1 General 1D Mathematica code

SPEEDUP code [19] for symbolic derivation of the effective potential to specified level p is implemented in Mathematica [40], and is available in the `EffectiveAction-1D.nb` notebook. It implements the algorithm depicted in Fig. 1 and calculates the coefficients $c_{m,k}$ for $m = 0, \dots, p-1$ and $k = m, \dots, 0$, starting from the initial condition $c_{0,0} = V$. For a given value of m , the diagonal coefficient $c_{m,m}$ is first calculated from Eq. (2.8), and then all off-diagonal coefficients are calculated from the recursion (2.7).

In this code the potential $V(x)$ is not specified, and the effective potential is derived for a general one-particle 1D theory. The resulting coefficients $c_{m,k}$ and the effective potential are expressed in terms of the potential V and its higher derivatives. Level p effective potential, constructed as

$$W_p(x, \bar{x}; \varepsilon) = \sum_{m=0}^{p-1} \sum_{k=0}^m c_{m,k}(x) \varepsilon^{m-k} \bar{x}^{2k}, \quad (3.1)$$

contains derivatives of V to order $2p-2$.

The only input parameter of this Mathematica code is the level p to which the effective potential should be calculated. As the code runs, it prints used amount of memory (in MB) and CPU time. This information can be used to estimate the required computing resources for higher values of p . The calculated coefficients can be exported to a file, and later imported for further numerical calculations. As an illustration, the file `EffectiveAction-1D-export-p5.m` contains exported definition of all the coefficients $c_{m,k}$ calculated at level $p=5$, while the notebook `EffectiveAction-1D-matching-p5.nb`

contains matching output from the interactive session used to produce the above $p = 5$ result.

The execution of this code on a typical 2 GHz CPU for level $p = 10$ requires 10-15 MB of RAM and several seconds of CPU time. We have successfully run this code for levels as high as $p = 35$ [19]. SPEEDUP C code implements effective actions to the maximal level $p = 18$, with the size of the corresponding C function around 2 MB. If needed, higher levels p can be easily implemented in C and added to the existing SPEEDUP code.

3.2 General 2D and 3D Mathematica code

Although we have developed Mathematica code capable of deriving effective actions for a general many-body theory in arbitrary number of spatial dimensions, in practical applications in 2D and 3D it can be very advantageous to use simpler codes, able to produce results to higher levels p than the general code [9, 10].

This is done in files `EffectiveAction-2D.nb` and `EffectiveAction-3D.nb`, where the recursive approach is implemented directly in 2D and 3D. Execution of these codes requires more memory: for $p = 10$ effective action one needs 60 MB in 2D case, while in 3D case the needed amount of memory increases to 860 MB. On the other hand, the execution time is several minutes for 2D code and around 30 minutes for 3D code.

The distribution of the SPEEDUP code contains exported $p = 5$ definitions of contractions $W_{m,k}$ for both 2D and 3D general potential, as well as matching outputs from interactive sessions used to generate these results.

3.3 Model-specific Mathematica codes

When general expressions for the effective actions, obtained using the above described SPEEDUP Mathematica codes, are used in numerical simulations, one has to specify the potential V and its higher derivatives to order $2p - 2$ in order to be able to calculate transition amplitudes. Such approach is justified for systems where the complexity of higher derivatives increases. However, for systems where this is not the case, or where only a limited number of derivatives is non-trivial (e.g. polynomial interactions), it might be substantially beneficial to specify the potential at the beginning of the Mathematica code and calculate the derivatives explicitly when iterating the recursion.

Using this approach, one is able to obtain coefficients $c_{m,k}$ and the effective potential W directly as functions of the mid-point x . This is implemented in the notebooks `EffectiveAction-1D-AHO.nb` and `EffectiveAction-2D-AHO.nb` for the case of anharmonic oscillators in 1D and 2D,

$$V_{1D-AHO}(x) = \frac{A}{2}x^2 + \frac{g}{24}x^4, \quad (3.2)$$

$$V_{2D-AHO}(x) = \frac{A}{2}(x^2 + y^2) + \frac{g}{24}(x^2 + y^2)^2. \quad (3.3)$$

These codes can be easily executed within few seconds and with the minimal amounts of memory even for $p = 20$. For 1D anharmonic oscillator we have successfully calculated effective actions to excessively large value $p = 144$, and in 2D to $p = 67$ [19], to illustrate the advantage of this model-specific method.

Similar approach can be also used in another extreme case, when the complexity of higher derivatives of the potential V increases very fast, so that entering the corresponding expressions to the code becomes impractical. Even in this situation expressions for effective actions can be usually simplified using some appropriate model-specific ansatz. The form of such ansatz can be deduced from the form of model-specific effective potentials, and then used to simplify their derivation. Such use-case is illustrated in the SPEEDUP Mathematica code for the modified Pöschl-Teller potential,

$$V_{1D-MPT}(x) = -\frac{\lambda}{(\cosh \alpha x)^2}. \quad (3.4)$$

For this potential, the coefficients $c_{m,k}$ of the effective potential can be expressed in the form

$$c_{m,k}(x) = \sum_{l=0}^m d_{m,k,l} \frac{(\tanh \alpha x)^{2l}}{(\cosh \alpha x)^{2m-2l+2}}, \quad (3.5)$$

and newly introduced constant coefficients $d_{m,k,l}$ can be calculated using the model-specific recursion in `EffectiveAction-1D-MPT.nb`. The form of the ansatz (3.5) is deduced from the results of executing general 1D Mathematica code, with the model-specific potential (3.4) defined before the recursion calculation of the coefficients is performed. Using this approach, we were able to obtain maximal level $p = 41$ effective action [19].

3.4 General many-body Mathematica code

SPEEDUP Mathematica code for calculation of effective action for a general many-body theory is implemented using the `MathTensor` [41] package for tensorial calculations in Mathematica. This general implementation required some new functions related to the tensor calculus to be defined in the source notebook `EffectiveAction-ManyBody.nb` provided with the SPEEDUP code.

The function `GenNewInd[n]` generates the required number n of upper and lower indices using the `MathTensor` function `UpLo`, with the assigned names `up1, lo1, ...`, as well as lists `upi` and `loi`, each containing n strings corresponding to the names of generated indices. These new indices are used in the implementation of the recursion for calculation of derivatives of $W_{m,k}$, contractions of the effective potential, and for this reason had to be explicitly named and properly introduced.

The expressions obtained by iterating the recursion contain large numbers of contractions, and function `NewDefUnique[contr]` replaces all contracted indices with the newly-introduced dummy ones in the contraction `contr`, so that they do not interfere with the calculation of derivatives in the recursion. This is necessary since the derivatives in recursion do not distinguish contracted indices from non-contracted ones if their names

happen to be generated by the function `GenNewInd`. Note that the expression `contr` does not have to be full contraction, i.e. function `NewDefUnique` will successfully act on tensors of any kind if they have contracted indices, while it will leave them unchanged if no contractions are present.

The function `NewDerivativeVec[contr, vec, ind]` implements calculation of the first derivative of the tensor `contr` (which may or may not contain contracted indices, but if it does, they are supposed to be uniquely defined dummy ones, which is achieved using the function `NewDefUnique`). The derivative is calculated with respect to vector `vec` with the vectorial index `ind`. The index `ind` can be either lower or upper one, and has to be generated previously by the function `GenNewInd`.

Finally, the function `NewLaplacianVec[contr, vec]` implements the Laplacian of the tensor `contr` with respect to the vector `vec`, i.e. it performs the calculation of contractions of the type

$$\frac{\partial}{\partial \text{vec}_i} \frac{\partial}{\partial \text{vec}^i} \text{contr}. \quad (3.6)$$

After all described functions are defined, the execution of the code proceeds by setting the desired level of the effective action p , generating the needed number of named indices using the function call `GenNewInd[2 p + 2]`, and then by performing the recursion according to the scheme illustrated in Fig. 1. The use of `MathTensor` function `CanAll` in the recursion ensures that the obtained expressions for $W[m, k]$ will be simplified if possible. This is achieved in `MathTensor` by sorting and renaming all dummy indices using the same algorithm and trying to simplify the expression obtained in such way. By default, `Mathematica` will distinguish contracted indices in two expressions if they are named differently, and `MathTensor` works around it using the renaming scheme implemented in `CanAll`.

The computing resources required for the execution of the many-body SPEEDUP `Mathematica` code depend strongly on the level of the effective action. For example, for level $p = 5$ the code can be run within few seconds with the minimal memory requirements. The notebook with the matching output of this calculation is available as `EffectiveAction-ManyBody-matching-p5.nb`, and the exported results for $W[m, k]$ are available in `EffectiveAction-ManyBody-export-p5.m`. We were able to achieve maximal level $p = 10$ [19], with the CPU time of around 2 days on a recent 2 GHz processor. The memory used by `Mathematica` was approximately 1.6 GB.

Note that exporting the definition of the effective potential from `Mathematica` to a file will yield lower and upper indices named `ll1`, `uu1`, etc. In order to import previous results and use them for further calculations with the provided `Mathematica` code, it is necessary to replace indices in the exported file to the proper index names used by the function `GenNewInd`. This is easily done using `find/replace` feature of any text editor. Prior to importing definition of the effective potential, it is necessary to initialize `MathTensor` and all additional functions defined in the notebook `EffectiveAction-ManyBody.nb`, and to generate the needed number of named indices using the function call `GenNewInd[2p+2]`.

4 SPEEDUP C codes for Monte Carlo calculation of 1D transition amplitudes

For short times of propagation, the effective actions derived using the above described Mathematica codes can be directly used. This has been extensively used in [8, 9], where SPEEDUP codes were applied for numerical studies of several lower-dimensional models and calculation of large number of energy eigenvalues and eigenfunctions. The similar approach is used in [10], where SPEEDUP code was used to study properties of fast-rotating Bose-Einstein condensates in anharmonic trapping potentials. The availability of a large number of eigenstates allowed not only precise calculation of global properties of the condensate (such as condensation temperature and ground state occupancy), but also study of density profiles and construction of time-of-flight absorption graphs, with the exact quantum treatment of all available eigenfunctions.

However, in majority of applications the time of propagation cannot be assumed to be small. The effective actions are found to have finite radius of convergence [8], and if the typical propagation times in the considered case exceed this critical value, Path Integral Monte Carlo approach must be used in order to accurately calculate the transition amplitudes and the corresponding expectation values [4, 18]. As outlined earlier, in this case the time of propagation T is divided into N time steps, such that $\varepsilon = T/N$ is sufficiently small and that the effective action approach can be used. The discretization of the propagation time leads to the following expression for the discretized amplitude

$$A_N^{(p)}(a, b; T) = \int \frac{dq_1 \cdots dq_{N-1}}{(2\pi\varepsilon)^{N/2}} e^{-S_N^{(p)}}, \quad (4.1)$$

where $S_N^{(p)}$ stands for the discretized level p effective action,

$$S_N^{(p)} = \sum_{k=0}^{N-1} \left[\frac{(q_{k+1} - q_k)^2}{2\varepsilon} + \varepsilon W_p(x_k, \bar{x}_k; \varepsilon) \right], \quad (4.2)$$

and $q_0 = a$, $q_N = b$, $x_k = (q_{k+1} + q_k)/2$, $\bar{x}_k = (q_{k+1} - q_k)/2$.

Level p discretized effective action is constructed from the corresponding effective potential W_p , calculated as power series expansion to order ε^{p-1} . Since it enters the action multiplied by ε , this leads to discretized actions correct to order ε^p , i.e. with the errors of the order ε^{p+1} . The long-time transition amplitude $A_N^{(p)}(a, b; T)$ is a product of N short-time amplitudes, and its errors are expected to scale as $N \cdot \varepsilon^{p+1} \sim 1/N^p$, as has been shown in [5, 13–15] for transition amplitudes, and in [5, 18] for expectation values, calculated using the corresponding consistently improved estimators.

4.1 Algorithm and structure of the code

SPEEDUP C source is located in the `src` directory of the code distribution [19]. It uses the standard Path Integral Monte Carlo algorithm for calculation of transition amplitudes.

The trajectories are generated by the bisection algorithm [20], hence the number of time-steps N is always given as a power of two, $N = 2^s$. When the amplitude is calculated with 2^s time steps, we can also easily calculate all discretized amplitudes in the hierarchy $2^{s-1}, \dots, 2^0$ at no extra cost. This requires only minor additional CPU time and memory, since the needed trajectories are already generated as subsets of maximal trajectories with 2^s time-steps.

The trajectory is constructed starting from bisection level $n = 0$, where we only have initial and final position of the particle. At bisection level $n = 1$ the propagation is divided into two time-steps, and we have to generate coordinate q of the particle at the moment $T/2$, thus constructing the piecewise trajectory connecting points a at the time $t = 0$, q at $t = T/2$, and b at $t = T$. The coordinate q is generated from the Gaussian probability density function centered at $(a+b)/2$ and with the width $\sigma_1 = \sqrt{T/2}$. The procedure continues iteratively, and each time a set of points is added to the piecewise trajectory. At each bisection level n the coordinates are generated from the Gaussian centered at midpoint of coordinates generated at level $n - 1$, with the width $\sigma_n = \sqrt{T/2^n}$. To generate numbers η from the Gaussian centered at zero we use Box-Müller method,

$$\eta = \sqrt{-2\sigma_n^2 \ln \zeta_1} \cos 2\pi \zeta_2, \quad (4.3)$$

where numbers ζ_1 and ζ_2 are generated from the uniform distribution on the interval $[0,1]$, using the SPRNG library [42]. If the target bisection level is s , then at bisection level $n \leq s$ we generate 2^{n-1} numbers using the above formula, and construct the new trajectory by adding to already existing points the new ones, according to

$$q[(1+2i) \cdot 2^{s-n}] = \eta_i + \frac{q[i \cdot 2^{s-n+1}] + q[(i+1) \cdot 2^{s-n+1}]}{2}, \quad (4.4)$$

where i runs from 0 to $2^{n-1} - 1$. This ensures that at bisection level s we get trajectory with $N = 2^s$ time-steps, consisting of $N + 1$ points, with boundary conditions $q[0] = a$ and $q[N] = b$. At each lower bisection level n , the trajectory consists of $2^n + 1$ points obtained from the maximal one (level s trajectory) as a subset of points $q[i \cdot 2^{s-n}]$ for $i = 0, 1, \dots, 2^n$.

The use of trajectories generated by the bisection algorithm requires normalization factors from all Gaussian probability density functions with different widths to be taken into account. This normalization is different for each bisection level, but can be calculated easily during the initialization phase.

The basic C code is organized in three source files, `main.c`, `p.c` and `potential.c`, with the accompanying header files. The file `potential.c` (its name can be changed, and specified at compile time) must contain a user-supplied function `V0()`, defining the potential V . For a given input value of the coordinate, `V0()` should initialize appropriate variables to the value of the potential V and its higher derivatives to the required order $2p - 2$. When this file is prepared, SPEEDUP code can be compiled and used. The distributed source contains definition of 1D-AHO potential in the file `potential.c`, the same as in the file `1D-AHO.c`.

The execution of the SPEEDUP code starts with the initialization and allocation of memory in the `main()` function, and then the array of amplitudes and associated MC error estimates for each bisection level $n = 0, \dots, s$ is calculated by calling the function `mc()`. After printing the output, `main()` deallocates used memory and exits. Function `mc()` which implements the described MC algorithm is also located in the file `main.c`, as well as the function `distr()`, which generates maximal (level s) trajectories.

The function `mc()` contains main MC sampling loop. In each step new level s trajectory is generated by calling the function `distr()`. Afterwards, for each bisection level n , function `func()` is invoked. This function is located in the file `p.c`, and returns the value of the function e^{-S} , properly normalized, as described earlier. This value (and its square) is accumulated in the MC loop for each bisection level n and later averaged to obtain the estimate of the corresponding discretized amplitude and the associated MC error.

The function `func()` makes use of C implementation of earlier derived effective actions for a general 1D potential. For a given trajectory at the bisection level n , `func()` will first initialize appropriate variables with the values of the potential and its higher derivatives (to the required level $2p-2$) by calling the user-supplied function `V0()`, located in the file `potential.c`. Afterwards the effective action is calculated according to Eq. (4.2), where the effective potential is calculated by the function `Wp()`, located in the file `p.c`. The desired level p of the effective action is selected by defining the appropriate pre-processor variable when the code is compiled.

In addition to this basic mode, when SPEEDUP code uses general expression for level p effective action, we have also implemented model-specific mode, described earlier. If effective actions are derived for a specific model, then user can specify an alternative `p.c` file to be used within the directory `src/models/<model>`, where `<model>` corresponds to the name of the model. If this mode is selected at compile time, the compiler will ignore `p.c` from the top `src` directory, and use the model-specific one, defined by the user. The distributed source contains model definitions for 1D-AHO and 1D-MPT potentials in directories `src/models/1D-AHO` and `src/models/1D-MPT`. Note that in this mode the potential is specified directly in the definition of the effective potential, and therefore the function `V0()` is not used (nor the `potential.c` file).

4.2 Compiling and using SPEEDUP C code

SPEEDUP C source can be easily compiled using the `Makefile` provided in the top directory of the distribution. The compilation has been thoroughly tested with GNU, Intel and IBM XLC compilers. In order to compile the code one has to specify the compiler which will be used in the `Makefile` by setting appropriately the variable `COMPILER`, and then to proceed with the standard command of the type `make <target>`, where `<target>` could be one of `all`, `speedup`, `sprng`, `clean-all`, `clean-speedup`, `clean-sprng`.

The SPRNG library [42] is an external dependency, and for this reason it is located in the directory `src/deps/sprng4.0`. In principle, it has to be compiled only once, after the compiler has been set. This is achieved by executing the command `make sprng`. After-

wards the SPEEDUP code can be compiled and easily linked with the already compiled SPRNG library. Note that if the compiler is changed, SPRNG library has to be recompiled with the same compiler in order to be successfully linked with the SPEEDUP code.

To compile the code with level $p=10$ effective action and user-supplied function $V0()$ located in the file `src/1D-AH0.c`, the following command can be used:

```
make speedup P=10 POTENTIAL=1D-AH0.c
```

If not specified, `POTENTIAL=potential.c` is used, while the default level of the effective action is $P=1$. To compile the code using a model-specific definition of the effective potential, instead of the `POTENTIAL` variable, we have to appropriately set the `MODEL` variable on the command line. For example, to compile the supplied `p.c` file for 1D-MPT model located in the directory `src/models/1D-MPT` using the level $p=5$ effective action, the following command can be used:

```
make speedup P=5 MODEL=1D-MPT
```

All binaries compiled using the `POTENTIAL` mode are stored in the `bin` directory, while the binaries for the `MODEL` mode are stored in the appropriate `bin/models/<model>` directory. This information is provided by the `make` command after each successful compilation is done.

The compilation is documented in more details in the supplied `README.txt` files. The distribution of the SPEEDUP code also contains examples of compilation with the GNU, Intel and IBM XLC compilers, as well as matching outputs and results of the execution for each tested compiler, each model, and for a range of levels of the effective action p .

Once compiled, the SPEEDUP code can be used to calculate long-time amplitudes of a system in the specified potential V . If executed without any command-line arguments, the binary will print help message, with details of the usage. The obligatory arguments are time of propagation T , initial and final position a and b , maximal bisection level s , number of MC samples N_{mc} and `seed` for initialization of the SPRNG random number generator. All further arguments are converted to numbers of the `double` type and made available in the array `par` to the function $V0()$, or to the model-specific functions in the file `src/models/<model>/p.c`. The output of the execution contains calculated value of the amplitude for each bisection level $n=0, \dots, s$ and the corresponding MC estimate of its error (standard deviation). At bisection level $n=0$, where no integrals are actually calculated and the discretized $N=1$ amplitude is simply given by an analytic expression, zero is printed as the error estimate.

Fig. 2 illustrates the typical results obtained from the SPEEDUP code on the example of 1D-MPT theory. In this figure we can see the convergence of numerically calculated amplitudes with the number of time-steps N to the exact continuum value, obtained in the limit $N \rightarrow \infty$. Such convergence is obtained for each level p of the effective action used. However, the convergence is much faster when higher-order effective action is used. Note that all results corresponding to the one value of level p on the graph are obtained from a single run of the SPEEDUP code with the maximal bisection level $s=10$. The simplest way to estimate the continuum value of the amplitude is to fit numerical

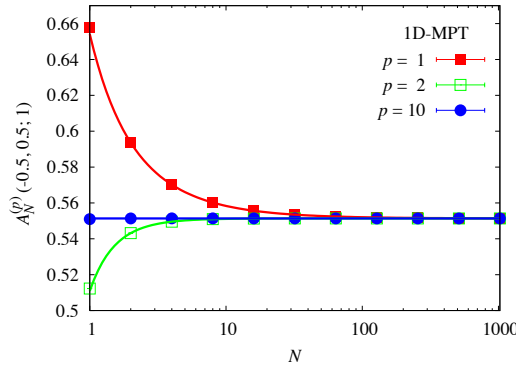


Figure 2: Convergence of SPEEDUP Monte-Carlo results for the transition amplitude $A_N^{(p)}(-0.5,0.5;1)$ of 1D-MPT potential as a function of the number of time steps N , calculated with level $p=1,2,10$ effective actions, with the parameters of the potential $\lambda=\alpha=1$. The full lines give the fitted functions (4.5), where the constant term A_p corresponds to the continuum-theory amplitude $A(-0.5,0.5;1)$. The number of Monte-Carlo samples was $N_{MC}=10^6$.

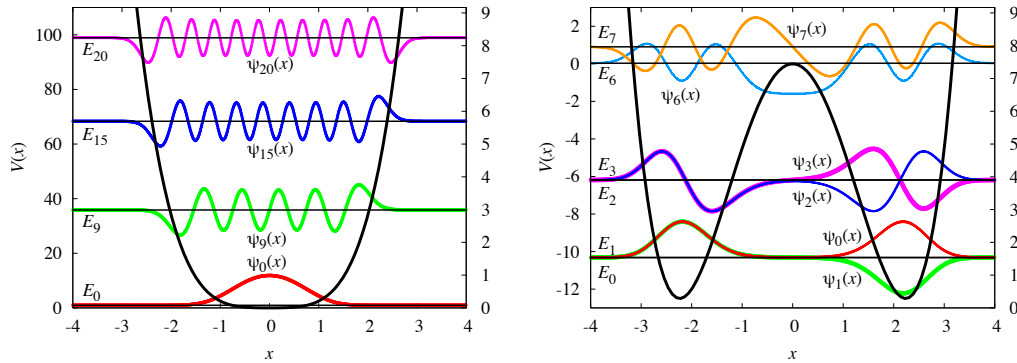


Figure 3: (left) The anharmonic potential 1D-AHO, its energy eigenvalues (horizontal lines) and eigenfunctions, obtained by direct diagonalization of the space-discretized matrix of the evolution operator with level $p=21$ effective action and parameters $A=1, g=48$. The discretization cutoff was $L=8$, spacing $\Delta=9.76 \cdot 10^{-4}$, and time of propagation $t=0.02$. (right) Results for the double-well potential, $A=-10, g=12, L=10, \Delta=1.22 \cdot 10^{-3}, t=0.1$. On both graphs, left y -axis corresponds to $V(x)$ and energy eigenvalues, while scale on the right y -axis corresponds to values of eigenfunctions, each vertically shifted to level with the appropriate eigenvalue.

results from single run of the code to the appropriate level p fitting function [13–15],

$$A_N^{(p)} = A^{(p)} + \frac{B^{(p)}}{N^p} + \frac{C^{(p+1)}}{N^{p+1}} + \dots \tag{4.5}$$

The constant term obtained by fitting corresponds to the best estimate of the exact amplitude which can be found from the available numerical results.

As mentioned earlier, the effective action approach can be used for accurate calculation of a large number of energy eigenstates and eigenvalues by diagonalization of the space-discretized matrix of transition amplitudes [6–10]. Fig. 3 illustrates this for the case

of an anharmonic and double-well potential. The graph on the left gives several eigenvalues and eigenstates for 1D-AHO potential with $A = 1$ and quartic anharmonicity $g = 48$, while the graph on the right gives low-lying spectrum and eigenfunctions of the double-well potential, obtained for $A = -10$, with the moderate anharmonicity $g = 12$. More details on this approach, including study of all errors associated with the discretization process, can be found in [8,9].

5 Conclusions

In this paper we have presented SPEEDUP Mathematica and C codes, which implement the effective action approach for calculation of quantum mechanical transition amplitudes. The developed Mathematica codes provide an efficient tool for symbolic derivation of effective actions to high orders for specific models, for a general 1D, 2D and 3D single-particle theory, as well as for a general many-body systems in arbitrary number of spatial dimensions. The recursive implementation of the code allows symbolic calculation of extremely high levels of effective actions, required for high-precision calculation of transition amplitudes.

For calculation of long-time amplitudes we have developed SPEEDUP C Path Integral Monte Carlo code. The C implementation of a general 1D effective action to maximal level $p = 18$ and model-specific effective actions provide fast $1/N^p$ convergence to the exact continuum amplitudes.

Further development of the SPEEDUP C codes will include parallelization using MPI, OPENMP and hybrid programming model, C implementation of the effective potential to higher levels p , as well as providing model-specific effective actions for relevant potentials, including many-body systems.

Acknowledgments

The authors gratefully acknowledge useful discussions with Axel Pelster and Vladimir Slavnić. This work was supported in part by the Ministry of Education and Science of the Republic of Serbia, under project No. ON171017, and bilateral project NAD-BEC funded jointly with the German Academic Exchange Service (DAAD), and by the European Commission under EU FP7 projects PRACE-1IP, HP-SEE and EGI-InSPIRE.

References

- [1] R. P. Feynman, *Rev. Mod. Phys.* 20, 367 (1948).
- [2] R. P. Feynman and A. R. Hibbs, *Quantum Mechanics and Path Integrals* (McGraw-Hill, New York, 1965).
- [3] H. Kleinert, *Path Integrals in Quantum Mechanics, Statistics, Polymer Physics, and Financial Markets*, 5th ed. (World Scientific, Singapore, 2009).

- [4] D. Stojiljković, A. Bogojević, and A. Balaž, Phys. Lett. A 360, 205 (2006).
- [5] A. Bogojević, I. Vidanović, A. Balaž, and A. Belić, Phys. Lett. A 372, 3341 (2008).
- [6] A. Sethia, S. Sanyal, and Y. Singh, J. Chem. Phys. 93, 7268 (1990).
- [7] A. Sethia, S. Sanyal, and F. Hirata, Chem. Phys. Lett. 315, 299 (1999).
- [8] I. Vidanović, A. Bogojević, and A. Belić, Phys. Rev. E 80, 066705 (2009).
- [9] I. Vidanović, A. Bogojević, A. Balaž, and A. Belić, Phys. Rev. E 80, 066706 (2009).
- [10] A. Balaž, I. Vidanović, A. Bogojević, and A. Pelster, Phys. Lett. A 374, 1539 (2010).
- [11] R. P. Feynman, Statistical Mechanics (W. A. Benjamin, New York, 1972).
- [12] G. Parisi, Statistical Field Theory (Addison Wesley, New York, 1988).
- [13] A. Bogojević, A. Balaž, and A. Belić, Phys. Rev. Lett. 94, 180403 (2005).
- [14] A. Bogojević, A. Balaž, and A. Belić, Phys. Rev. B 72, 064302 (2005).
- [15] A. Bogojević, A. Balaž, and A. Belić, Phys. Lett. A 344, 84 (2005).
- [16] A. Bogojević, A. Balaž, and A. Belić, Phys. Rev. E 72, 036128 (2005).
- [17] A. Balaž, A. Bogojević, I. Vidanović, and A. Pelster, Phys. Rev. E 79, 036701 (2009).
- [18] J. Grujić, A. Bogojević, and A. Balaž, Phys. Lett. A 360, 217 (2006).
- [19] SPEEDUP code distribution, <http://www.scl.rs/speedup/>
- [20] D. M. Ceperley, Rev. Mod. Phys. 67, 279 (1995).
- [21] M. Takahashi and M. Imada, J. Phys. Soc. Jpn. 53, 3765 (1984).
- [22] X. P. Li and J. Q. Broughton, J. Chem. Phys. 86, 5094 (1987).
- [23] H. De Raedt and B. De Raedt, Phys. Rev. A 28, 3575 (1983).
- [24] S. Jang, S. Jang, and G. Voth, J. Chem. Phys. 115, 7832 (2001).
- [25] N. Makri and W. H. Miller, Chem. Phys. Lett. 151, 1 (1988); N. Makri and W. H. Miller, J. Chem. Phys. 90, 904 (1989).
- [26] N. Makri, Chem. Phys. Lett. 193, 435 (1992).
- [27] M. Alford, T. R. Klassen, and G. P. Lepage, Phys. Rev. D 58, 034503 (1998).
- [28] S. A. Chin and E. Krotscheck, Phys. Rev. E 72, 036705 (2005).
- [29] E. R. Hernández, S. Janecek, M. Kaczmariski, E. Krotscheck, Phys. Rev. B 75, 075108 (2007).
- [30] O. Ciftja and S. A. Chin, Phys. Rev. B 68, 134510 (2003).
- [31] K. Sakkos, J. Casulleras, and J. Boronat, J. Chem. Phys. 130, 204109 (2009).
- [32] S. Janecek and E. Krotscheck, Comput. Phys. Comm. 178, 835 (2008).
- [33] A. D. Bandrauk and H. Shen, J. Chem. Phys. 99, 1185 (1993).
- [34] S. A. Chin and C. R. Chen, J. Chem. Phys. 117, 1409 (2002).
- [35] I. P. Omelyan, I. M. Mryglod, and R. Folk, Comput. Phys. Commun. 151, 272 (2003).
- [36] G. Goldstein and D. Baye, Phys. Rev. E 70, 056703 (2004).
- [37] S. A. Chin, arXiv:0809.0914.
- [38] S. A. Chin, S. Janecek, and E. Krotscheck, Comput. Phys. Comm. 180, 1700 (2009).
- [39] S. A. Chin, S. Janecek, and E. Krotscheck, Chem. Phys. Lett. 470, 342 (2009).
- [40] Mathematica software package, <http://www.wolfram.com/mathematica/>
- [41] MathTensor package, <http://smc.vnet.net/mathtensor.html>
- [42] Scalable Parallel Random Number Generator library, <http://sprng.fsu.edu/>

Development of Grid e-Infrastructure in South-Eastern Europe

Antun Balaž · Ognjen Prnjat · Dušan Vudragović · Vladimir Slavnić ·
Ioannis Liabotis · Emanouil Atanassov · Boro Jakimovski · Mihajlo Savić

Received: 5 July 2010 / Accepted: 17 February 2011 / Published online: 23 March 2011
© Springer Science+Business Media B.V. 2011

Abstract Over the period of six years and three phases, the SEE-GRID programme has established a strong regional human network in the area of distributed scientific computing and has set up a powerful regional Grid infrastructure. It attracted a number of user communities and applications from diverse fields from countries throughout the South-Eastern Europe. From the infrastructure point view, the first project phase has established a pilot Grid infrastructure with more than 20 resource centers in 11 countries. During the subsequent two phases of the project,

the infrastructure has grown to currently 55 resource centers with more than 6,600 CPUs and 750 TBs of disk storage, distributed in 16 participating countries. Inclusion of new resource centers to the existing infrastructure, as well as a support to new user communities, has demanded setup of regionally distributed core services, development of new monitoring and operational tools, and close collaboration of all partner institution in managing such a complex infrastructure. In this paper we give an overview of the development and current status of SEE-GRID regional infrastructure and describe its transition to the NGI-based Grid model in EGI, with the strong SEE regional collaboration.

A. Balaž (✉) · D. Vudragović · V. Slavnić
SCL, Institute of Physics Belgrade,
University of Belgrade, Belgrade, Serbia
e-mail: antun@ipb.ac.rs

O. Prnjat · I. Liabotis
Greek Research and Technology Network—GRNET,
Athens, Greece

E. Atanassov
Institute for Parallel Processing,
Bulgarian Academy of Sciences,
Sofia, Bulgaria

B. Jakimovski
SS. Cyril and Methodius University, Skopje,
FYR of Macedonia

M. Savić
University of Banja Luka, Banja Luka,
Bosnia and Herzegovina

Keywords Grid · e-Infrastructure ·
Distributed computing

1 Introduction

The transition of the traditional science to e-Science is fueled by the ever increasing need for processing of exceedingly large amounts of data and exponentially increasing computational requirements: in order to realistically describe and solve real-world problems, numerical simulations are becoming more detailed, experimental sciences use more sophisticated sensors to make precise measurements; and shift from the

individuals-based science work towards collaborative research model now starts to dominate.

Computing resources and services able to support needs of such a new model of scientific work are available at different layers: local computing centers, national and regional computing centers, and supercomputing centers. The gap between the needs of various user communities and dispersed computing resources able to satisfy their requirements is effectively bridged by introduction of Grid technology on the top of the networking layer and local resource management layers.

Computing Grids are conceptually not unlike electrical Grids. In an electrical Grid, the wall outlets allow us to link to and use an infrastructure of resources, which generate, distribute, and bill for electrical power. When we connect to the electrical Grid, we do not need to know details on the power plant currently generating the electricity we use. In the same way Grid technology uses middleware layer to coordinate and organize into one logical resource a set of available distributed computing and storage resources across a network, allowing users to access them in a unified fashion. The computing Grids, like electrical Grids, aim to provide users with easy access to all the resources they need, whenever they need them, regardless of the underlying physical topology and management model of individual clusters.

Grids address two distinct but related goals: providing remote access to information technology (IT) assets, and aggregating processing and storage power. The most obvious resources included in Grids are processors (CPUs) and data storage systems, but Grids also can encompass various sensors, applications, and other advanced types of resources. One of the first commonly known Grid initiatives was the SETI@HOME project, which solicited several millions of volunteers to download a screensaver, which was able to use idle processor time to analyze the astronomical data in the search for extraterrestrial life.

In the past six years the European Commission has funded, through a number of targeted initiatives, activation of new user communities and enabling collaborative research across a number of fields in order to close existing technological and scientific gaps. In addition, this helps in bridging the digital divide, stimulating research

and consequently alleviating the brain drain in the less-developed regions of Europe. This was especially successful in the South-Eastern Europe (SEE), where a number of such initiatives show excellent results. In the Grid arena, the South-East European GRid e-Infrastructure Development (SEE-GRID) series of projects [1, 2], through its first two 2-year phases, has established a strong human network in the area of scientific computing and has set up a powerful regional Grid infrastructure, attracting large number of applications from diverse fields from countries throughout the South-Eastern Europe. The third 2-year phase of the SEE-GRID programme, SEE-GRID-SCI [3] project, has aimed and succeeded in having a catalytic effect on a number of SEE user groups, with a strong focus on the key seismological, meteorological, and environmental communities.

One of the main successes of the SEE-GRID programme is cumulative structuring effort on the establishment of National Grid Initiatives (NGIs) in SEE countries and collaborative work on achieving sustainable model of operation, supported strongly from national funding sources. The regional SEE-GRID initiative has also supported and coordinated a successful transition of all SEE countries from the centralized operations model to the NGI-based EGI infrastructure, which is clearly visible from the participation of all partner countries in the 4-year EGI-InSPIRE project [4].

2 Resource Centers

The regional Grid infrastructure operated by SEE-GRID-SCI project was built on top of the pilot infrastructure established by the first SEE-GRID project (2004–2006), which was since then substantially extended and enlarged in terms of resources and number of Grid sites, and upgraded in terms of the deployed middleware and core services provided to existing and new user communities during the SEE-GRID-2 project (2006–2008).

The operations activity adopted the pragmatic model of the 2-layered infrastructures in which mature sites were migrated to the EGEE [5]

production infrastructure, while the start-up sites from new institutes and user communities were incubated within the SEE-GRID infrastructure until they were ready to follow the requirements of the full-scale production infrastructure. In this way, both SEE-wide and national-level applications were able to benefit from the computing resources of both infrastructures, by mainly using the pilot infrastructure in the incubation phase and production infrastructure later, when they reach the production phase. Moreover, this approach ensured that smaller sites, typical for the region, have a chance to be a part of the regional SEE-GRID infrastructure acting as an incubator for their maturing into EGEE production.

As applications developed in the region have matured, new Virtual Organizations (VOs) have spun off with the relevant core services supported by the SEE-GRID-SCI operations activity SA1. Discipline-specific services were deployed in multiple instances (for failover and for achieving load-balancing through a wide geographic distribution) over the e-Infrastructure and operationally maintained and supported by SA1. Sophisticated operational tools, some of them being developed within the joint research activity JRA1 of the

SEE-GRID-SCI project, were used to enhance infrastructure performance.

SEE-GRID-SCI project has continued to operate and further extend, develop and improve this infrastructure, with the aim to cater for the needs of all activated user communities in the region, with special emphasis on the three identified target areas: meteorology, seismology, and environmental sciences. Apart from computing and storage resources made available to these user communities, SA1 activity provided and maintained a set of existing and new operational and monitoring tools so as to ensure proper operation of the infrastructure, and a set of primary and secondary core services for all deployed VOs in order to ensure optimal geographical distribution according to the underlying network structure, load sharing, and quality of the service to end users.

Currently SEE-GRID-SCI infrastructure encompasses approximately 55 Grid sites, more than 6600 CPUs, and around 750 TBs of available data storage capacity, which is illustrated in Fig. 1, with further details given in Table 1. Overall number of CPUs has grown from 2400 at the beginning of the SEE-GRID-SCI project in May 2008 to cur-



Fig. 1 Overview of the SEE-GRID-SCI infrastructure

Table 1 SEE-GRID-SCI computing and storage resources

Country	Total number of CPUs	Total storage [TB]
Greece	1,200	66.8
Bulgaria	1,210	42.3
Romania	120	4.0
Turkey	2,380	528.0
Hungary	8	2.0
Albania	34	1.3
Bosnia-Herzegovina	80	1.1
FYR of Macedonia	80	4.1
Serbia	974	97.0
Montenegro	40	0.6
Moldova	24	6.5
Croatia	44	0.2
Armenia	424	0.2
Georgia	16	0.1
Total	6,634	754.2

rently more than 6600, while the number of dedicated CPUs for SEE-GRID-SCI VOs is currently around 1500. Grid operations activity successfully maintains such a large, geographically disperse and ever-growing infrastructure, harmonizing its operation with the pan-European EGEE/EGI infrastructure. In addition to this, one of the most important achievements of SA1 activity is transfer of knowledge and Grid know-how to all participating countries, and support to their NGI operation teams to reach the level of expertise needed for sustainable NGI-based operational model in EGI.

After the completion of the SEE-GRID-SCI project in April 2010, the regional Grid infrastructure was seamlessly integrated to the EGI infrastructure, and continues to support all deployed Virtual Organizations (VOs) and applications developed during the 6-year SEE-GRID programme. The strong human network remains in place and still supports on-going transition of all countries to independent NGI operations through the SEE Regional Operations Centre. The catch-all SEE-GRID Certification Authority will continue its operation until all the countries from the region deploy their own national certification authorities. In terms of Grid operations, currently almost all (with only a few exceptions) NGI operations teams and infrastructures are fully validated by EGI teams, while validation for the remaining

SEE countries is expected to finish within a few months, i.e. by mid-2011.

3 User Communities

The core objective of the SEE-GRID-SCI project was to engage user communities from different regional countries in close collaboration. This strategy had a structuring effect for crucial regional communities. The target applications were selected from core earth science disciplines in the region, namely, seismology, meteorology and environmental protection. Thus, the focus of the project was to engage these three core cross-border communities in the research fields crucial for the region, structured in the form of Virtual Organizations (VO):

- Seismology VO had six applications ranging from Seismic Data Service to Earthquake Location Finding, from Numerical Modelling of Mantle Convection to Seismic Risk Assessment [6–12].
- Meteorology VO, with two large-scale applications, follows an innovative approach to weather forecasting that uses a multitude of weather models and bases the final forecast on an ensemble of weather model outputs. The other problem tackled within this VO is the reproduction/forecasting of the airflow over complex terrain [13–21].
- Environmental Protection VO supports eight applications focusing on environmental protection/response and environment-oriented satellite image processing [22–32].

In the Seismology VO, the work was organized around the development of Seismic Data Server (SDS) application services, providing distributed storage and serving of seismic data from different partner countries, logical organization and indexing of distributed seismic data, and programming tools (called iterators) that provide easy access to seismic data. In terms of applications, the focus was on gridification of five seismology applications from different South-eastern European countries: Seismic Risk Assessment (SRA), Numerical Modeling of Mantle Convection (NMMC3D), Fault Plane Solution (FPS),

Earthquake Location Finding (ELF) and Massive Digital Seismological Signal Processing with the Wavelet Analysis (MDSSP-WA).

In the Meteorology VO, with the aim to contribute to the improvement of the forecasts in the Mediterranean, among other techniques, the regional ensemble forecasting technique has been explored in the frame of the SEE-GRID-SCI. Indeed the regional ensemble forecasting system built over the Mediterranean, involves the need of large infrastructure that was not easily available at medium-scale research centres and institutions. For that reason, the Grid infrastructure was explored for its ability to support the high CPU and storage needs of such a regional ensemble forecasting system. This application allowed the meteorological entities participating in the project to assess the probability of a particular weather event to occur. This information is being made freely available (to the participants and to the general public, etc) through the project web page, helping thus when needed, to make the necessary decisions based on this probabilistic information. In addition, another set of applications permitted the entities participating in the project to improve the quality of the understanding and forecasting of the airflow over regions characterized by the complex terrain. Further an important benefit of this application is the possibility offered to use this model for operational weather forecasting. Operational weather forecasting model chains based on this model have been developed in the frame of this project over Bosnia and Herzegovina, Armenia and Georgia. This is considered as an important benefit for the meteorological services of the aforementioned countries that did not have up to now the infrastructure support to run op-

erationally weather forecasting models for their region.

The Environmental VO has dealt with several important problem areas in the domain of environmental modeling and environmental protection and the applications developed within the VO advanced the scientific knowledge and affected the policy and decision-making process, responding to the EU directives and national priorities. New modeling techniques and algorithms were employed in several of the applications, using the power of the Grid in order to increase the spatial and temporal resolution and obtain more adequate representation of the natural processes under investigation. In other applications, established techniques were used, combined with filters and scripts developed by the project partners in order to accommodate these systems to the specifics of the Balkan region. The beneficiaries of the systems developed during the projects lifetime include not only environmental scientists, but also the relevant governmental and international organizations, for example the international air quality monitoring bodies. By employing the Grid to increase the resolution these applications are now starting to target new beneficiaries like municipal authorities, small and medium enterprises and media. For many of the applications the validation of the models and standardizing the computational processes has been an important achievement, since the methodological aspect of these studies was a challenging one, especially in the Balkan region.

Figure 2 gives some details on the size of activated user communities, and the distribution of computing resources they have utilized during the project lifetime. Overall, during the period 2008–

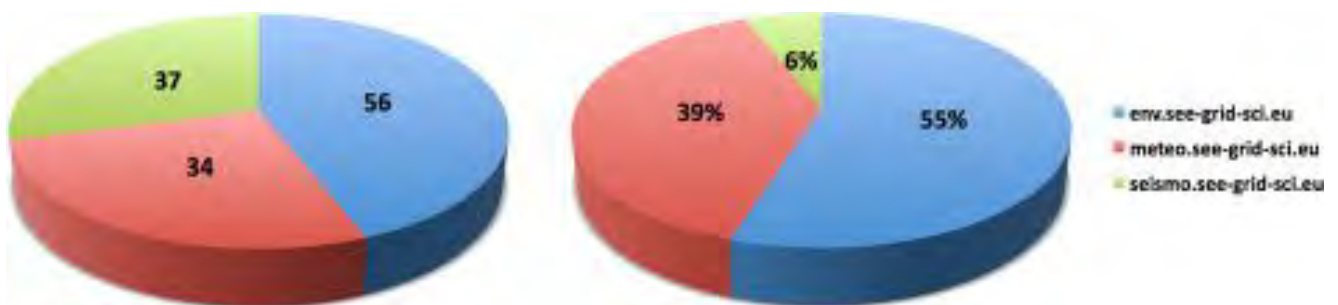


Fig. 2 The distribution of the size of three target user communities (*left*, number of end users per VO), and the distribution of the computing resources used by VOs (*right*)

2010, SEE-GRID-SCI project has provided more than 22.5 million elapsed CPU hours or 2,566 CPU years, and more than 4.5 million jobs were executed on the regional infrastructure. Out of this, SEE-GRID-SCI and national VOs amounted to 16.4 million CPU hours or 1,872 CPU years (73%). The total utilization of dedicated resources (based on the average number of 1050 available CPUs) was quite high, around 89%, and this has attracted the growth of supported user communities, and enabled them to achieve the enormous amount of new scientific results, as can be seen by the large number of scientific papers published in peer-reviewed research journals [33–38] and presented at numerous scientific conferences [6–32]. The project itself has organized SEE-GRID-SCI User Forum in December 2009, where the most significant results were presented.

4 Core Services

To operationally provide computational and storage resource to the three target scientific commu-

nities supported by the SEE-GRID-SCI project, three different VOs have been created: METEO, SEISMO, and ENV VO. The support for these VOs, as well as to the catch-all SEEGRID VO, has been configured on all Resource Centres participating in the regional infrastructure, and a set of core services was installed and deployed by SA1 activity, as illustrated in Fig. 3.

For each VO a primary and secondary VO Management Service (VOMS) has been deployed and maintained by institutes involved in the corresponding VO application development. Additionally, a set of core Grid services was deployed in order to support job management operations (Workload Management System—WMS, Logging and Bookkeeping—LB), Grid information system (Berkeley Database Information Index—BDII), data storage and transfer operations (Logical File Catalog—LFC, File Transfer Service—FTS, ARDA Metadata Grid Application—AMGA), and management of digital credentials (MyProxy—PX). Deployment details of primary core Grid services are given in Table 2.



Fig. 3 Geographical distribution of core services

Table 2 List of primary core services deployed per VO

Service	METEO VO	ENV VO	SEISMO VO
VOMS	voms.grid.auth.gr	voms.ipp.acad.bg	voms.ulakbim.gov.tr
WMS & LB	wms.ipb.ac.rs	wms.ipp.acad.bg	wms.ulakbim.gov.tr
BDII	bdii.ipb.ac.rs	bdii.ipp.acad.bg	bdii.ulakbim.gov.tr
LFC	grid02.rcub.bg.ac.rs	lfc01.mosigrid.utcluj.ro	lfc.ulakbim.gov.tr
FTS	grid16.rcub.bg.ac.rs		fts.ulakbim.gov.tr
AMGA	grid16.rcub.bg.ac.rs		amga.ulakbim.gov.tr
PX	myproxy.ipb.ac.rs	myproxy.ipp.acad.bg	myproxy.ulakbim.gov.tr

5 Grid Operations

This section gives brief description of operational procedures and key tools developed during the course of the SEE-GRID programme. In addition, a number of operational tools have been developed, improved and deployed by the SEE-GRID-SCI SA1 activity and used in day-to-day infrastructure management, as illustrated in Fig. 4. Table 3 lists all currently deployed tools including those used for monitoring of the infrastructure, some of which are described in more detail in the next section, while Fig. 4 gives their geographical distribution, as well as distribution of respon-

sibilities for their deployment and maintaining. The interactions and collaboration on the development and usage of described tools with other Grid initiatives/projects are emphasized wherever applicable.

Recognizing that improvements in the quality and shaping-up of the SEE-GRID infrastructure are an important and continuous effort, necessary for the successful work of SEE-GRID application developers, as well as for the usage of our infrastructure by the existing user communities, the pro-active monitoring of Grid sites in the region was organized through rotating shifts by SA1 country representatives (Grid Infrastructure



Fig. 4 Geographical distribution of SEE-GRID operational and monitoring tools

Table 3 Deployment of operational and monitoring tools in the SEE-GRID infrastructure

Service	Service URL
HGSM	https://hgsm.grid.org.tr/
BBmSAM	https://c01.grid.etfbl.net/bbmsam/
BBmobileSAM	https://c01.grid.etfbl.net/bbmsam/mobile.php
Gstat	http://gstat.gridops.org/gstat/seegrid/
Accounting Portal	http://gserv4.ipp.acad.bg:8080/AccountingPortal/
Nagios	https://portal.ipp.acad.bg:7443/seegridnagios/
Googlemap	http://www.grid.org.tr/eng/
MonALISA	http://monitor.seegrid.grid.pub.ro:8080/
Real Time Monitor	http://gridportal.hep.ph.ic.ac.uk/rtm/applet.html
WatG Browser	http://watgbrowser.scl.rs:8080/
WMS Monitoring Tool	http://wmsmon.scl.rs/
Repository Service	http://rpm.egee-see.org/yum/SEE-GRID/
Dwarf	https://dwarf.scl.rs/
Grid-Operator-On-Duty	http://wiki.egee-see.org/index.php/SG_GOOD
Helpdesk	http://helpdesk.see-grid.eu/
SEE-GRID Wiki	http://wiki.egee-see.org/index.php/SEE-GRID_Wiki
P-Grade Portal	http://portal.p-grade.hu/multi-grid

Managers—GIMs). During each shift, the corresponding GIM is designated as Grid-Operator-On-Duty, or GOOD [39].

Basically, the idea is that each GIM (i.e. GIM team from one country) is on duty during one week overseeing the infrastructure and opening trouble tickets in the SEE-GRID Helpdesk to sites from all countries where operational problems are identified using the available monitoring tools. Of course, all GIMs are expected to continually monitor and provide support to sites from their countries—this is their day-to-day duty, in addition to regular regional GOOD shifts. Details of the organization of GOOD shifts are given at the SEE-GRID Wiki [39, 40]. For problems identified by GOODs, trouble tickets were created in the SEE-GRID Helpdesk [42], and site managers were expected to deal with such operational problems and provide feedback on the steps taken. Typically, simple problems were resolved within one working day, while for more complex issues typical resolution time was up to three working days.

On the request of applications which need MPI support on sites, GOODs are expected to test MPI setup on all SEE-GRID sites which support MPI. The MPI setup tests are performed at least once a week, and GOODs ensure that the test parallel jobs run at the same time on at least two WNs (to test ssh setup as well). More details

can be found on the Wiki page on Testing MPI support [40].

In this section we describe two selected tools used for Grid operations: HGSM database (used for maintaining the database of Grid resources and personnel), Dwarf portal related to software development and repositories (especially important in maintaining updated of Grid middleware and application software).

5.1 HGSM

Hierarchical Grid Site Management—HGSM [43] is a web based management application primarily geared towards Grid site administrators. At the beginning it was designed to store static information about Grid sites and personnel responsible for the sites, but later it evolved to the central information hub, also used for other Grid monitoring and checking services.

The idea behind the HGSM is to reflect the natural hierarchy present in the infrastructure. For each supported infrastructure, HGSM has a ROC (Regional Operational Centers) associated with it at the top. These ROCs contain the countries that participate in a particular infrastructure. Grid sites of each country are listed under the respective country tree, and all details related to a specific Grid site can be viewed under the respective site entry in the web front end of HGSM (Fig. 5). The

HGSM (Hierarchical Grid Site Management) English 12

SEEGRID >

ID	Country Id	Name	email	Phone	Comments
1	AL	Albania	neki.trashon@gmail.com	+355 66 22 59 497	Admin List
2	BA	Bosnia and Herzegovina	badaboom@ybb.net	+387 51 221660	Admin List
3	BG	Bulgaria	emanouil@parallel.bae.bg	+359 2 9796783	Admin List
4	RS	Serbia	grid-admin@ipb.ac.rs	+381 11 3713152	Admin List
5	GR	Greece	labos@gnet.gr	+302107474248	Admin List
6	HR	Croatia	kg-admin@ip.hr	+385 1 4561188	Admin List
7	HU	Hungary	kg@ipds.szaki.hu	+361 2 796066	Admin List
8	MK	FYR of Macedonia	boroj@i.edu.mk	+389 70 326718	Admin List
9	RO	Romania	stancu@grid.icp.ro	+40 21 2241265	Admin List
10	TR	Turkey	grid@uakbim.gov.tr	+90 312 2880853	Admin List
11	ME	Montenegro	luka@hcg.ac.yu	+381 81 242077	Admin List
12	MD	Moldavia	svv@invm.md		Admin List
13	CH	Switzerland	dusan.vudragovic@cern.ch		Admin List
14	AM	Armenia	grid-admin@sci.am	+374 94 361138	Admin List
15	GE	Georgia	grid-admin@grns.ge	+995 32 250591	Admin List
16	AZ	Azerbaijan	ai.emajilov@eeo.org		Admin List

Important: This site works best with Firefox

© 2006 TUBITAK - ULAKBIM

/C=RS/O=AEGIS/OU=Institute of Physics Belgrade/CN=Dusan Vudragovic

Fig. 5 Overview of HGSM portal

management personnel information is also stored for each organizational level (ROC, country, site), containing contacts with both administrative and management privileges.

While HGSM holds vast information about Grid sites and core services, it also contains personal information for named contacts (names, e-mail addresses and phone numbers). To properly protect this information, HGSM uses a digital certificate-based authentication system. HGSM server only authorizes people with a valid Grid certificate to view the information in HGSM web front-end. Editing information is only allowed to authorized personnel with administrative privileges. The authorization is organized in a hierarchical manner, so that an administrator at the higher level can manage every aspect (including the administrators) at lower organizational levels.

HGSM has already been used by communities and projects other than SEE-GRID, e.g., by the Deployment of Remote Instrumentation Infrastructure—DORII project [44], as well as by the Spanish and Portuguese NGIs [45].

5.2 Dwarf

Web-based Dwarf tool is composed of the Dwarf web portal [46], Dwarf modules and Dwarf data-

base. Using the Public Key Infrastructure (PKI), Dwarf framework provides digital certificate-based management of RPM uploading and creation of APT and YUM repositories. The Dwarf web portal home page, shown in Fig. 6, gives an overview of repository structure together with information on the context of each repository, and latest build's timestamp.

From the Dwarf web portal, properly authenticated and authorized user can perform the following operations on the repository:

- Create and change repository structure: Users can create paths to new distributions and components, by specifying their names. In the current implementation of the Dwarf framework, the users are able to create APT and YUM repositories, as well as to create a MIRROR to an existing remote repository.
- Package uploading: Users can upload different software packages, but only to sections of the repository for which they are authorized as contributors.
- Build repository: After each RPM upload, a user should re-build the repository structure. If not, Dwarf system will do it automatically, through a cron job.



Fig. 6 Overview of the SEE-GRID Dwarf web portal

Dwarf modules are implemented as bash scripts which handle appropriate build actions on various repositories.

After a new APT repository structure is created from the Dwarf web portal, the RPMs must be indexed to create the APT database. This is done by the APT Dwarf module, which uses the `genbasedir` tool for this purpose. It analyzes RPM packages in a directory tree and builds information files so that that directory tree can be used as a proper APT repository.

The Dwarf database contains information on security (authentication and authorization), repositories types and metadata, mirror repositories, and logging information. Dwarf database contains metadata repository information on build's timestamps, contexts, and descriptions of the repositories, as well as repository types. The rules for creation of mirror repositories are also kept in the Dwarf database. In addition, for security and auditing reasons, the database contains a log of all user-initiated actions. The Dwarf database is realized using the MySQL database technology.

Once the repository is constructed, it is made available by HTTP and FTP servers configured and working on the Dwarf web portal. The DWARF framework provides configurations that should be included in the local HTTP and FTP servers configuration files in order to provide the context of repositories.

6 Monitoring of SEE-GRID Infrastructure

The monitoring of the heterogeneous and widely geographically dispersed Grid infrastructure is an essential task for achieving the required quality of service to supported user communities. This has been defined through the SEE-GRID Service Level Agreement (SLA), which has served as a prototype for the later adopted EGEE SLA. The monitoring of the performance of sites is not only used for formal assessment of the conformance to SLA, but also for day-to-day Grid operations, since various monitoring tools provide the main channel for identification and diagnostics of operational problems by Grid Operators on Duty and

GIMs. The most important such tools are listed in Table 3, and we briefly describe them in this section. To illustrate how the conformance of availabilities of Grid services to the adopted SLA was monitored and assessed, Fig. 7 gives overview of the availability monitoring results for the second year of the SEE-GRID-SCI project (May 2009 to April 2010). Using the BBmSAM tool (described below), precise measurement of the availability of all services was systematically done, and detailed results were provided at different levels or granularity: per service, per site, per country, and per SEE-GRID infrastructure. For example, the overall availability of resources (weighted by the CPU number of individual clusters) for the last four quarters increased from around 78% in Q5 (May–July 2009) to around 89% in Q8 (February–April 2010). Strict enforcement of SLA lead to a steady increase in the availability and reliability of Grid services offered to our target user communities.

6.1 BBmSAM

Availability monitoring of the infrastructure is carried out using the Service Availability Monitoring—SAM [47] framework developed in EGEE project [5], which is further developed and extended by SEE-GRID series of projects and deployed by its SA1 activity. The original SAM system consists of server and client components which communicate using web services. The client

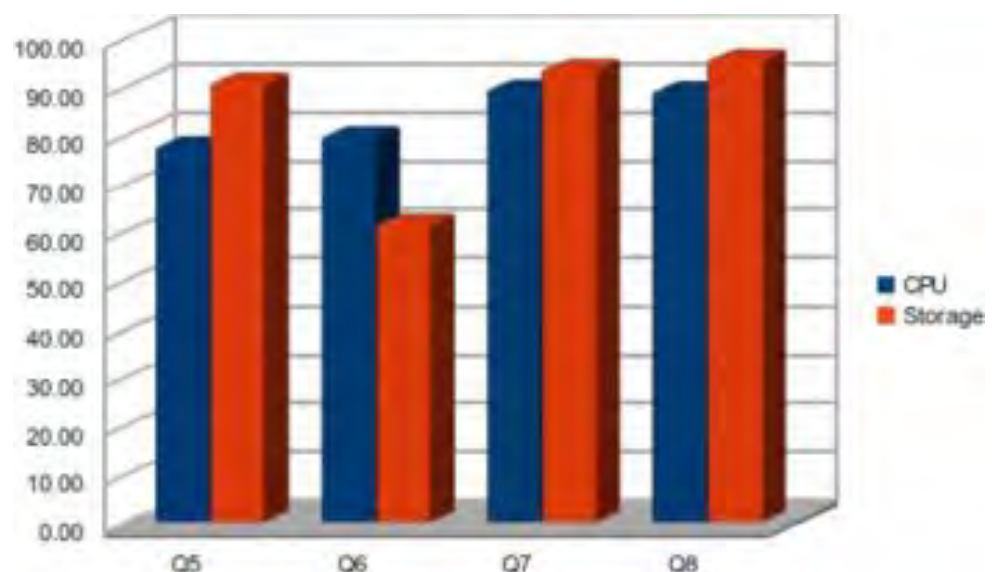
initiates periodical tests of the infrastructure and publishes data to the server which stores them in the Oracle database. Main change in the SAM framework in its adaptation for the SEE-GRID community was its porting to MySQL, suitable for the deployment in the region and in line with the SEE-GRID open source philosophy.

BBmSAM [48–50] Platform is a web application coded in PHP and using the MySQL Database as data storage back-end (although any standard-compliant SQL database server could be used, since it does not rely on any of MySQL-specific features). It has been tested under Apache HTTPD and Microsoft IIS web servers, and should work with any web server supporting PHP (at least through CGI). Main features of BBmSAM system are:

- Use of unaltered client and sensor components of EGEE SAM system.
- Synchronization with central HGSM service.
- Use of free and open source technologies.

BBmSAM client and sensors are the same as ones used in the standard EGEE SAM distribution, and they operate in identical way. In designing BBmSAM portal and dependent web services, special care was taken so that the solution would be compatible with EGEE/EGI tools and practices. This was achieved by implementing the same web services in PHP/MySQL implementation as

Fig. 7 Overview of availability of Grid services within the SEE-GRID-SCI infrastructure per quarter in the second (final) year of the project (May 2009 to April 2010)



the ones used in the original Java/Oracle-based SAM.

Main part of the BBmSAM web front-end, shown in Fig. 8, is a summary of current results for all tested Grid sites, containing site names, countries and other relevant details for each service.

6.2 SEE-GRID Accounting Portal

Accounting Portal [51] is a web-service based utility to collect and statistically present information

on the CPU accounting data for the SEE-GRID computing resources. Its main purpose is to collect and manage accounting data for the sites in SEE-GRID infrastructure. Recently a new publisher was released, capable of collecting and processing data for parallel MPI jobs, which are not properly accounted for when using the standard publisher provided by gLite. The accounting processing structure is based on two services: MPI log parser and accounting publisher. The MPI log parser tool processes PBS Server logs and inserts the data on MPI jobs in the MPI accounting database on the

SITE	COUNTRY	TIER	STATUS	TYPE	SERVICE STATUS
AEGIS01-IPB-SCL	Serbia	1	Certified	Production	CE: ce64 - ok 2.0 d SE: se - ok 15.2 d SRM: se - ok 1.0 d LFC: lfc - ok 3.1 d SRMv2: se - ok 3.0 d LFC_C: lfc - ok 3.0 d LFC_L: lfc - ok 3.0 d MPI: ce64 - ok 31+
AEGIS02-RCUB	Serbia	2	Certified	Production	CE: grid01 - ok 1.3 d SE: grid15 - ok 6.6 d SRM: grid15 - ok 12.3 h LFC: grid02 - ok 3.1 d LFC_C: grid02 - ok 3.0 d MPI: grid01 - ok 30.5 d
AEGIS03-ELEF-LEDA	Serbia	1	Certified	Production	CE: grid01 - ok 2.0 d SE: grid02 - ok 15.2 d SRM: grid02 - ok 1.0 d SRMv2: grid02 - ok 3.0 d MPI: grid01 - ok 31+
AEGIS04-KG	Serbia	1	Certified	Production	CE: cluster1 - ok 2.0 d SE: se - ok 2.3 d SRM: se - ok 2.3 d MPI: cluster1 - ok 31+
AEGIS05-ETFBBG	Serbia	2	Certified	Production	CE: grid-ce - ok 2.0 d SE: grid-ce - ok 3.0 d
AEGIS06-AOB	Serbia	2	Uncertified	Production	
AEGIS08-IPB-DEMO	Serbia	2	Uncertified	Candidate	CE: ce-demo - ok 2.0 d SE: se-demo - ok 5.2 d SRM: se-demo - ok 5.2 d SRMv2: se-demo - ok 3.0 d MPI: ce-demo - ok 31+
AEGIS09-FTN-KM	Serbia	2	Uncertified	Production	
AEGIS11-MISANU	Serbia	2	Uncertified	Candidate	CE: ce - ok 2.0 d MPI: ce - ok 31+

Fig. 8 Overview of the SEE-GRID BBmSAM web portal

MON node. Afterwards, the accounting publisher aggregates the data from the standard accounting database and MPI database and sends it to the central accounting portal database. The publisher is based on an independent module architecture which allow the two modules (MPI and standard serial) to work independently, so that sites that do not support MPI can use the same publisher.

New web front-end interface of the accounting portal (Fig. 9) is created to dynamically generates account statistics and charts. It is written in Adobe Flex and Java and implements the MVC design pattern. The View module of the portal is written in Flex, offering an interactive environment with dynamic visualization of the accounting data managed in tables, bar and pie charts. The Interface module is a Java web service which accepts input parameters such as data type, job type, period, rows and columns for the tables. In addition, it is capable of filtering the data by VO, country and site, offering more flexible data organization. It can also generate SQL queries based on the pro-

vided parameters and extract required data from the accounting database. The data are returned in XML form, suitable for import to a variety of other applications. The web portal is hosted on a web server running under Apache Tomcat with installed Apache Axis web-service framework.

6.3 WatG Browser

The What is at the Grid—WatG Browser [52] is a web-based Grid Information System (GIS) visualization application providing detailed overview of the status and availability of various Grid resources in a given gLite-based e-Infrastructure. It is able to query and present data obtained from Grid information systems at different layers: from local resource information system for a particular Grid service (GRIS), to the Grid site information system (site BDII), and to the top-level information system for the whole Grid infrastructure (top-level BDII).

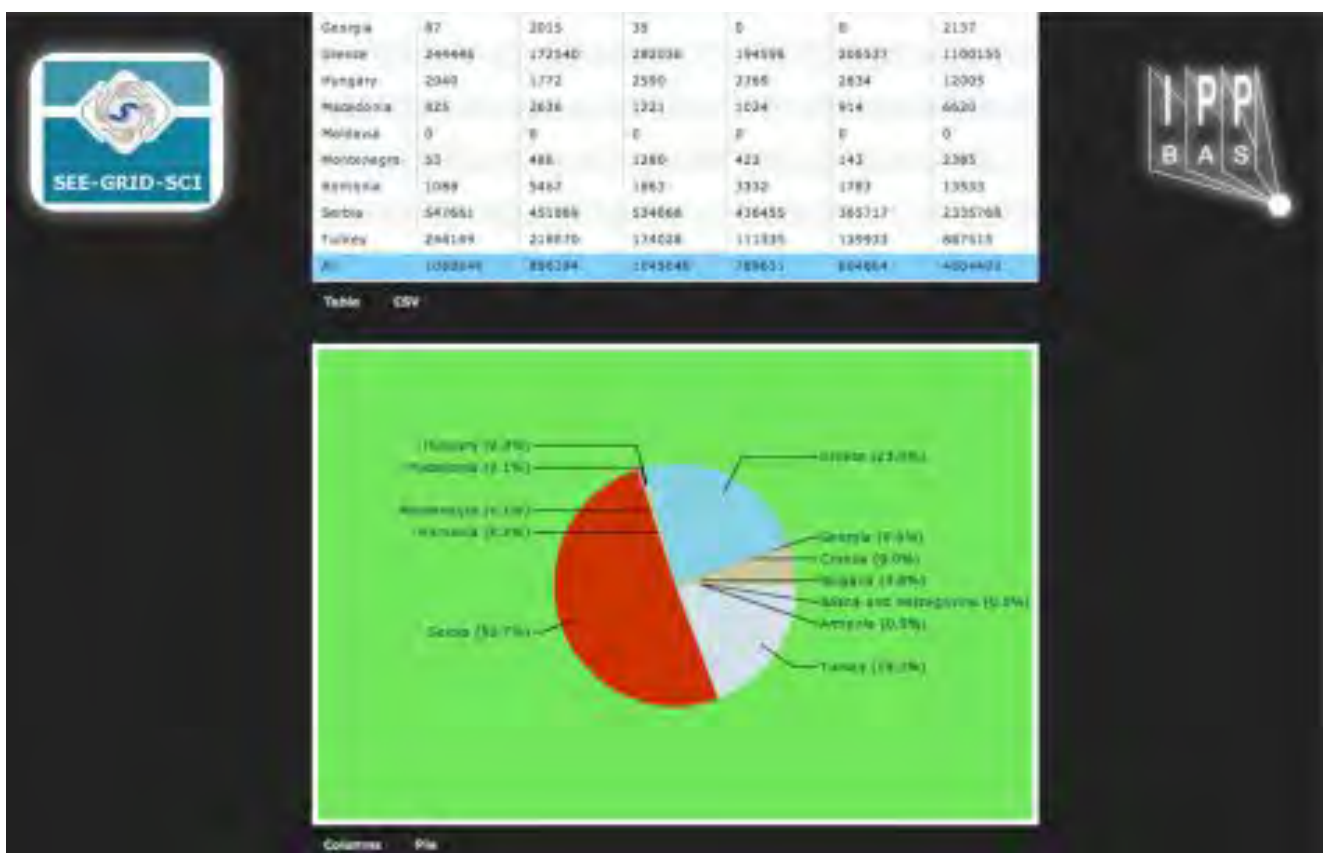


Fig. 9 Overview of the SEE-GRID accounting portal

The efficient implementation of WatG Browser allows quick and easy navigation through entries and objects of the LDAP tree retrieved by the specified query, even if the size of the output is huge and hierarchically very complex. Highly responsibility is achieved with implementation of partial refreshes and asynchronization of a web page. A partial refresh of WatG application can be observed when an interaction event is triggered, for example click on the plus icon of the LDAP tree. The server processes the information and returns a limited response specific to the data it receives, for example LDAP's subtree that requires given condition. One may notice that WatG server does not send back an entire page, like the conventional “click, wait and refresh” web applications. Instead, WatG client updates the page based on the response. This means that only part of the page is updated. In other words, WatG's initial page (Fig. 10) is treated like a template: WatG server and client exchange the data and the client updates parts of the template based on the data it receives from the server. Another way to

think about it is to consider WatG application as driven by events and data, whereas conventional web applications are driven by pages. Asynchronization of the WatG application is reflected in the fact that after sending data to the server, the client can continue processing while the server does its processing in the background. During all this, a user can continue interacting with the client without noticing interruption or a lag in the response. For example, a user can click on any plus or minus icon even during the loading, and in that way a new request will be created and executed afterwards. The client does not have to wait for a response from the server before continuing, as is the case in the traditional, synchronous approach. The WatG Browser is deployed by SCL [53] and publicly available at the address given in [52].

6.4 WMS Monitoring Tool

The complex task of computing resources discovery and management on behalf of user applications in the gLite Grid environment is done by the



Fig. 10 Overview of WatG Browser

Workload Management System (WMS) service. WMS monitoring tool WMSMon [54] provides reliable, site-independent, centralized, and uniform monitoring of gLite WMS services.

WMSMon tool, developed and deployed by SCL [53], is based on the collector-agent architecture that ensures monitoring of all properties relevant for successful operation of gLite WMS service and triggering of the alarms if certain monitored parameter values exceed predefined limits. In addition, the tool provides links to the appropriate troubleshooting guides when problems are identified.

WMSMon tool consists of two parts of software. The first one, WMSMon Agent, should be installed on all monitored WMS services, and locally aggregates the values of all relevant parameters described in the previous section. The second component of WMSMon software is WMSMon Collector, installed on a specific ma-

chine equipped with the web server and gridFTP client, with the aim to collect the data from all WMSMon Agents and to provide web interface to the graphical presentation of the collected data.

WMSMon web portal presents information from diverse WMS sources in a unified way, as can be seen in Fig. 11. The main page provides the aggregated status view of all monitored WMS services from the target Grid infrastructure. This part of the portal presents the data in a simplified way, with the emphasis on WMS services identified not to work properly. The portal also provides links to pages with detailed information and graphs for each monitored WMS service. These pages contain the latest data, as well as historical data presented in the graphical form.

In addition to the main WMSMon instance deployed by SCL [53], other instances of WMSMon are installed and used at Grid Operations Centre at CERN [55] and at NIKHEF [56].



Fig. 11 Overview of WMSMon Portal

7 SEE Involvement in High Performance Computing

The Grid developments in the region, described in this paper, are currently being complemented with supercomputing/High-Performance Computing (HPC) actions. The HP-SEE project [57] (High-Performance Computing Infrastructure for South East Europe's Research Communities) is currently work across several strategic lines of action. First, it is linking the existing HPC facilities in the region into a common infrastructure, and providing operational and management solutions for it. Second, it is striving to open this infrastructure to a wide range of new user communities, including those of non-resourced countries, fostering collaboration and providing advanced capabilities to more researchers, with an emphasis on strategic groups in computational physics, computational chemistry and life sciences. Finally, it acts as a catalyst for establishment of national HPC initiatives, and will act as a SEE bridge for DEISA [58], also presented in this edition, as well as PRACE [59] infrastructure.

Figure 12 depicts the multi-dimensional regional e-Infrastructure in South-East Europe, where HP-SEE effectively adds the new Research Infrastructure: HPC infrastructure and knowledge/user layer, on top of the existing network plane, and parallel to the existing Grid plane, thus

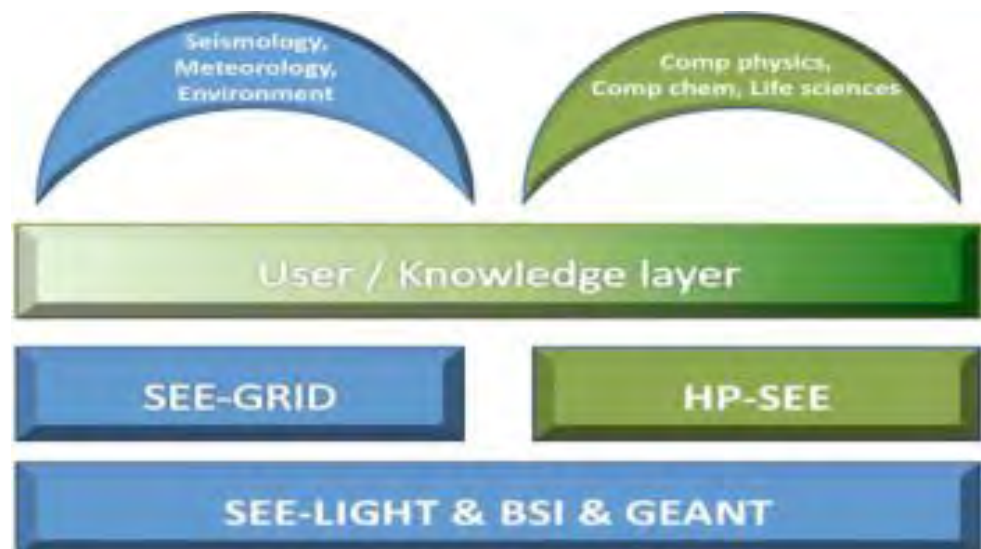
Table 4 Current and planned computing power (TFlops) by HP-SEE countries (double precision for CPU and single precision for GPU)

Country	2010	2011	2012
Greece	0	40	80
Serbia	0	20	40
Bulgaria	25	30+8 GPU	40+20 GPU
Romania	10	20+100 GPU	30+100 GPU
Hungary	1	30	60
Overall	36	140+108 GPU	250+120 GPU

optimising all layers and further enabling a wide range of new cross-border e-Science applications to be deployed over the regional e-Infrastructure. This approach effectively creates an integrated e-Infrastructure for new virtual research communities, and provides a platform for collaboration between ICT engineers and computational scientists dealing with the infrastructure on one hand, and on the other the scientists from diverse scientific communities in the region.

It should be noted that this vision will provide an integrated infrastructure, where Grid and HPC layers and not mutually exclusive but rather complementary, and tailored for the type of applications supported. Table 4 gives the overview of the current and planned HPC resources that will be available to the HP-SEE Virtual Research Communities within the project.

Fig. 12 SEE e-Infrastructure with HPC, and new user communities



The available resources will be integrated into a common infrastructure available for the regional Virtual Research Communities. The current and planned HPC infrastructure is heterogeneous, comprising of BlueGene supercomputers, Intel/AMD clusters and enhanced with GPU computing accelerators. Concerning the middleware deployments, we believe the upcoming Unified Middleware Distribution, which will combine Unicore, gLite and ARC will be well suited for the regional HPC infrastructure, taking into account the current situation, where various combinations of these middleware stacks with batch systems and workflow management systems exist. The regional HP-SEE infrastructure will be operated through the operations centre that will be established within the project, which will carry out analysis, requirements capture and evaluation, and deployment of the existing solutions for system management of the regional infrastructure; will identify missing components, and provide optimal solutions. Solutions by system vendors and successful developments from European projects, especially DEISA, and PRACE, will be taken into account. Wherever possible the existing solutions will be adapted and enhanced for deployment in the regional infrastructure. A set of operational tools will be deployed, including user administration, accounting, distributed data management, security, authentication and authorization, monitoring of distributed resources, resource management and allocation, and helpdesk for user support.

The identified target user communities include computational physics, computational chemistry and life sciences. Computational physics is represented by 8 applications from 6 countries and covers the fields of many-body condensed matter physics, including modeling of electron transport, modeling of complex gas dynamics and convection, plasma physics and image processing. Computational chemistry community includes 7 applications from 6 countries, covering the fields of molecular dynamics and simulations, and materials science. Life sciences community has 7 applications from 5 countries, covering the fields of computational biology, computational genomics, computational biophysics and DNA sequencing.

8 Transition to EGI and Conclusions

Over the period of six years and three phases, the SEE-GRID programme aimed at creating independent and sustainable NGIs in each country of the South-Eastern Europe. That has allowed all the countries to participate as full-fledged members of the wider European Grid infrastructure realized through the series of EGEE projects and currently by the European Grid Initiative, EGI [4]. EGI is established as a coordinating organization for the European Grid Infrastructure, based on the federation of individual NGIs, aiming to support a wide variety of multi-disciplinary user communities. To facilitate the above aim, the SEE-GRID programme has focused both at stimulating the support to policy makers as well as for creating sustainable operational structures in each of the countries in the region.

In particular, on the policy level, the last two years of the SEE-GRID programme have focused on monitoring and improving the status of NGIs in partner countries, and providing support for their evolution and integration into the environment standardized by EGI, aiming to achieve sustainability as active partners in this new pan-European collaboration model. This effort resulted in one of main successes of the project, with all countries of the region currently members or associate members of EGI and participating as partners in the EGI-InSPIRE project.

On the operational level, the focus of SEE-GRID was to create and increase the capacity of Grid resources in the region, create independent and stable operational structures, increase the availability of Grid resources, deploy core services in all countries of the region, as well as to develop geographically distributed network of Grid experts able to provide operational and application level support to end users. At the end of the 6th year of the SEE-GRID programme, all SEE countries are providing such an operational infrastructure for the local and international user communities from the pan-European EGI infrastructure, either as independent NGIs or as a part of the South-Eastern Europe Regional Operations Centre.

We describe below the procedure taken by most of the countries in the region in order to

become fully independent operational NGIs from the technical point of view. The new NGIs use EGIs Grid Operations Database, GOCDB [60] to register their NGI management structure, sites and operational personnel. Most of the SEE NGIs base their operational portal on the central portal that is provided by EGI, performing operations via the NGI view that it offers. In cases like the Greek NGI, a standalone operational portal has been setup. During the course of the SEE-GRID projects the regional Helpdesk was based on OneOrZero as it has also been discussed in Section 4. The SEE-GRID Helpdesk by the end of the SEE-GRID projects was fully integrated with GGUS and therefore it is a candidate system for NGIs, to use as their national Helpdesk solution integrated with the Global Grid User Support, GGUS [61]. Further to that Request Tracker, RT [62] has been integrated with GGUS and can offer the same functionality. Based on the above the NGIs of the regional can select which helpdesk solution to use (either directly GGUS, OneOrZero, or RT). Since infrastructure monitoring in EGI has moved from SAM to Nagios, all new NGIs install and operate their own instance of Nagios that integrates with the rest of EGIs monitoring systems. Finally, SEE NGIs use the Unified Middleware Distribution (UMD) as a central repository for installing basic middleware components while still use the regional repository or even some national repositories, for software packages that are tailored to specific needs of their countries and are not available in UMD.

Towards the end of the SEE-GRID-SCI project (May 2010) all NGIs of the project where migrated to EGEE/EGI via the SEE-ROC, utilizing the existing ROC infrastructure and services. Since May 2010 and up to now (January 2011) almost all the NGIs have migrated to the EGI operational model. The average time for an NGI to migrate its operational structure from SEE-ROC to EGI is between 1 and 3 months.

The SEE-GRID programme had pivotal role in bridging the digital divide in the SEE region, in spearheading regional research collaborations, and in creating a strong human network in ICT field paving the way towards full integration of the region into the European Research Area (ERA). This work continues with the HP-SEE project

[57], that aims at bringing together the national HPC infrastructures in the region of South Eastern Europe and the regional Virtual Research Communities of Computational Physics, Computational Chemistry and Life Sciences. Enabling of those user communities to get access to HPC resources for their scientific work is the prime goal of this new project, and demonstrates the success of SEE-GRID series of projects in involving scientists from the region in the development and production use of distributed research infrastructures.

Acknowledgements This work was supported by the European Commission under FP7 project SEE-GRID-SCI (INFRA-2007-1.2.2. Grant No. 211338), and by the Ministry of Science and Technological Development of the Republic of Serbia (project No. ON141035 and ON171017).

References

1. SEE-GRID Project. <http://www.see-grid.org/>. Accessed 28 Feb 2011
2. SEE-GRID-2 Project. <http://www.see-grid.eu/>. Accessed 28 Feb 2011
3. SEE-GRID-SCI Project. <http://www.see-grid-sci.eu/>. Accessed 28 Feb 2011
4. EGI: European Grid Initiative. <http://www.egi.eu/>. Accessed 28 Feb 2011
5. EGEE Portal: Enabling Grids for e-Science. <http://www.eu-egee.org/>. Accessed 28 Feb 2011
6. Ulgen, E.B., Akkaya, A., Kocair Ç., Şener, C.: Seismic Risk Assessment: A Grid-based approach for the South-East European Region. In: Proceedings of the SEE-GRID-SCI User Forum 2009, pp. 29–34, 9–10 December 2009, Istanbul (2009)
7. Ozturan, C., Bektas, B., Yilmazer, M.: Seismic data server application service and web interface. In: Proceedings of the SEE-GRID-SCI User Forum 2009, pp. 187–192, 9–10 December 2009, Istanbul (2009)
8. Yilmazer, M., Bektas, B., Ozturan, C., Arikian, R.: Parallelization of Earthquake Location Finding (ELF) Application. In: Proceedings of the SEE-GRID-SCI User Forum 2009, pp. 177–180, 9–10 December 2009, Istanbul (2009)
9. Jordanovski, Lj., Jakimovski, B., Mišev, A.: Massively parallel seismic data wavelet processing using advanced grid workflows. In: ICT Innovations Conference 2009, Ohrid, 28–29 September 2009
10. Kozlovsky, M., Balaskó, Á., Süle, B.: Enabling numerical modeling of mantle convection on the grid. In: Proceedings of the EGEE User Forum 2009, Catania (2009)
11. Balaskó, Á., Kozlovsky, M., Süle B.: Numerical modeling of mantle convection on the SEE-GRID-SCI Infrastructure. In: Proceedings of the SEE-GRID-SCI

- User Forum 2009, pp. 51–55, 9–10 December 2009, Istanbul (2009)
12. Ozturan, C., Bektas, B., Yilmazer, M., Şener, C.: Challenges faced in building a virtual organization for seismology in south Eastern Europe, e-Challenges-2009, Istanbul (2009)
 13. Kotroni, V., Floros, E., Lagouvardos, K., Pejanović, G., Ilić, L., Živković, M.: Regional scale multi-model and multi-analysis ensemble weather forecasting on the Grid. In: Proceedings of the SEE-GRID-SCI User Forum 2009, pp. 35–42, 9–10 December 2009, Istanbul (2009)
 14. Lagouvardos, K., Floros, E., Kotroni, V.: A Grid-enabled regional-scale ensemble forecasting system in the Mediterranean. *J. Grid. Computing* **8**, 181–197 (2010)
 15. Kotroni, V., Floros, E., Lagouvardos, K., Pejanović, G., Ilić, L., Živković, M.: Multi-model multi-analysis ensemble weather forecasting on the Grid for the South Eastern Mediterranean Region. *Earth Sci. Inform.* **3**, 209–218 (2010)
 16. Davidović, D., Belušić, D., Telisman-Prtenjak, M.: Grid implementation of the Weather Research and Forecasting model. In: Proceedings of the SEE-GRID-SCI User Forum 2009, pp. 43–50, 9–10 December 2009, Istanbul (2009)
 17. Davidović, D., Skala, K., Belušić, D., Telisman-Prtenjak, M.: Grid implementation of the Weather Research and Forecasting model. *Earth Sci. Inform.* **3**, 199–208 (2010)
 18. Davitashvili, T., Kobiashvili, G., Kvatadze, R., Kutaladze, N., Mikuchadze, G.: WRF-ARW Application for Georgia. In: Proceedings of the SEE-GRID-SCI User Forum 2009, pp. 7–10, 9–10 December 2009, Istanbul (2009)
 19. Davidović, D., Skala, K.: Grid implementation and application of the WRF-ARW prognostic model. In: Proceedings of the EGEE User Forum 2010, Uppsala (2010)
 20. Hadžismailović, I., Pajović, A., Davidović, D.: WRF-ARW model and its implementation in weather forecast, research and usage on the GRID. In: Proceedings of the SEE-GRID-SCI User Forum 2009, pp. 105–111, 9–10 December 2009, Istanbul (2009)
 21. Ozturan, C., Kotroni, V., Atanassov, E.: Development of virtual organizations, applications and services for earth science on grid e-Infrastructures. *Earth Sci. Inform.* **3**, 197–198 (2010)
 22. Petcu, D., Zaharie, D., Neagul, M., Panica, S., Frincu, M., Gorgan, D., Stefanut, T., Bacu, V.: Remote sensed image processing on Grids for training in earth observation. In: Y.-S. Chen (ed.) *Image Processing*. ISBN: 978-953-307-026-1, pp. 115–140 (2009)
 23. Gorgan, D., Bacu, V., Stefanut, T., Rodila, D.: Grid based Satellite Image Processing Platform for Earth Observation Applications Development. In: IDAACS'2009 - IEEE Fifth International Workshop on Intelligent Data Acquisition and Advanced Computing Systems: Technology and Applications. 21–23 September 2009, Rende, Cosenza, Italy (2009)
 24. Mihon, D., Bacu, V., Mészáros, R., Gelybó, G., Gorgan, D.: Satellite Image Interpolation and Analysis through GreenView Application. In: Proceedings of the ADiS-2010. First International Workshop on Autonomic Distributed Systems, Krakow, Poland (2010)
 25. Gorgan, D., Bacu, V., Rodila, D., Pop, F., Petcu, D.: Experiments on ESIP - Environment oriented Satellite Data Processing Platform. In: Proceedings of the SEE-GRID-SCI User Forum 2009, pp. 157–166, 9–10 December 2009, Istanbul (2009)
 26. Ganev, K., Syrakov, D., Prodanova, M., Hristov, Hr., Atanasov, E., Gurov, T., Karaivanova, A., Miloshev, N.: Grid Computing for Air Quality and Environmental Studies in Bulgaria. In: Proceedings of 23rd EnviroInfo 2009 Conference - Environmental Informatics and Industrial Environmental Protection: Concepts, Methods and Tools, Berlin, 9–11 September 2009
 27. Karaivanova, A., Atanassov, E., Ivanovska, S., Gurov, T., Durchova, M.: Parallel Quasi-Monte Carlo Integration with Application in Environmental Studies. Proceedings of the SEE-GRID-SCI User Forum 2009, pp. 67–71, 9–10 December 2009, Istanbul (2009)
 28. Syrakov, D., Prodanova, M., Ganev, K., Miloshev, N., Atanassov, E., Gurov, T., Karaivanova, A.: Grid computing for multi-scale atmospheric composition modeling for the Balkan region. *Journal of International Scientific Publication: Ecology & Safety* **3**, 4–21 (2009)
 29. Ganev, K., Syrakov, D., Prodanova, M., Miloshev, N., Jordanov, G., Gadjev, G., Todorova, A.: Atmospheric composition modeling for the Balkan region. In: Proceedings of the SEE-GRID-SCI User Forum 2009, pp. 77–85, 9–10 December 2009, Istanbul (2009)
 30. Syrakov, D., Ganev, K., Prodanova, M., Miloshev, N., Jordanov, G., Gadjev, G., Todorova, A.: Climate change impact assessment of air quality over Bulgaria. In: Proceedings of the SEE-GRID-SCI User Forum 2009, pp. 95–103, 9–10 December 2009, Istanbul (2009)
 31. Mihon, D., Bacu, V., Stefanut, T., Gorgan, D.: Grid-based Environment Application Development - GreenView Applciation, ICCP2009 Conference, 27 August 2009, Cluj-Napoca, Romania (2009)
 32. Mihon, D., Bacu, V., Gorgan, D., Mészáros, R., Gelybó, G.: Practical considerations on the green-view application development and execution over SEE-GRID. In: Proceedings of the SEE-GRID-SCI User Forum 2009, pp. 167–175, 9–10 December 2009, Istanbul (2009)
 33. Balaž, A., Bogojević, A., Vidanović, I., Pelster, A.: Recursive Schrödinger equation approach to faster converging path integrals. *Phys. Rev. E* **79**, 036701 (2009)
 34. Novaković, B., Balaž, A., Knežević Z., Potočnik M.: Computation of asteroid proper elements on the Grid. *Serb. Astron. J.* **179**, 75 (2009)
 35. Vidanović, I., Bogojević, A., Belić, A.: Properties of quantum systems via diagonalization of transition amplitudes. I. Discretization effects. *Phys. Rev. E* **80**, 066705 (2009)
 36. Vidanović, I., Bogojević, A., Balaž, A., Belić, A.: Properties of Quantum Systems Via Diagonalization of Transition Amplitudes. II. Systematic Improvements

- of Short-time Propagation. *Phys. Rev. E* **80**, 066706 (2009)
37. Milovanović, M.V., Jolicoeur, T., Vidanović, I.: Modified Coulomb Gas Construction of Quantum Hall States from Nonunitary Conformal Field Theories. *Phys. Rev. B* **80**, 155324 (2009)
 38. Stanković, I.E.: Towards Understanding of Influence of Restricted Geometry on Self-Diffusion in Porous Media. *Acta Phys. Pol.* **116**, 701 (2009)
 39. Grid Operator on Duty web page. http://wiki.egee-see.org/index.php/SG_GOOD. Accessed 28 Feb 2011
 40. Testing MPI support. http://wiki.egee-see.org/index.php/Testing_MPI_support. Accessed 28 Feb 2011
 41. SEE-GRID Wiki. http://wiki.egee-see.org/index.php/SEE-GRID_Wiki. Accessed 28 Feb 2011
 42. SEE-GRID Helpdesk. <https://helpdesk.see-grid.eu/>. Accessed 28 Feb 2011
 43. Hierarchical Grid Site Management (HGSM). <https://hgsm.grid.org.tr/>. Accessed 28 Feb 2011
 44. Deployment of Remote Instrumentation Infrastructure (DORII). <http://www.dorii.eu/>. Accessed 28 Feb 2011
 45. Ibergrid Operation Center Database. <https://rnagios.ngi.cesga.es/hgsm/>. Accessed 28 Feb 2011
 46. Dwarf Portal. <https://dwarf.scl.rs/>. Accessed 28 Feb 2011
 47. Service Availability Monitoring (SAM). <https://lcg-sam.cern.ch:8443/sam/sam.py>. Accessed 28 Feb 2011
 48. BBmSAM Web Portal. <https://c01.grid.etfbl.net/bbmsam/>. Accessed 28 Feb 2011
 49. BBmobileSAM Portal. <https://c01.grid.etfbl.net/mobile.php>. Accessed 28 Feb 2011
 50. Standalone SAM package. <http://www.irb.hr/users/vvidic/seegrid/ssam.tar.gz>. Accessed 28 Feb 2011
 51. SEE-GRID Accounting Portal. <http://gserv4.ipp.acad.bg:8080/AccountingPortal/>. Accessed 28 Feb 2011
 52. WatG Browser. <http://watgbrowser.scl.rs:8080/>. Accessed 28 Feb 2011
 53. Scientific Computing Laboratory, Institute of Physics Belgrade. <http://www.scl.rs/>. Accessed 28 Feb 2011
 54. WMSMon Portal. <http://wmsmon.scl.rs/>. Accessed 28 Feb 2011
 55. European Organization for Nuclear Research (CERN). <http://www.cern.ch/>. Accessed 28 Feb 2011
 56. National Institute for Subatomic Physics, The Netherlands. <http://www.nikhef.nl/>. Accessed 28 Feb 2011
 57. HP-SEE Project. <http://www.hp-see.eu/>. Accessed 28 Feb 2011
 58. DEISA Infrastructure. <http://www.deisa.eu/>. Accessed 28 Feb 2011
 59. PRACE Infrastructure. <http://www.prace-project.eu/>. Accessed 28 Feb 2011
 60. Grid Operations Database (GOCDB). <http://goc.gridops.org/>. Accessed 28 Feb 2011
 61. Global Grid User Support (GGUS). <http://www.ggus.org/>. Accessed 28 Feb 2011
 62. Request Tracker (RT). <http://bestpractical.com/rt/>. Accessed 28 Feb 2011

Article

Faraday and Resonant Waves in Dipolar Cigar-Shaped Bose-Einstein Condensates

Dušan Vudragović  and Antun Balaž * 

Scientific Computing Laboratory, Center for the Study of Complex Systems, Institute of Physics Belgrade, University of Belgrade, Pregrevica 118, 11080 Belgrade, Serbia

* Correspondence: antun.balaz@ipb.ac.rs

Received: 7 August 2019; Accepted: 21 August 2019; Published: 1 September 2019



Abstract: Faraday and resonant density waves emerge in Bose-Einstein condensates as a result of harmonic driving of the system. They represent nonlinear excitations and are generated due to the interaction-induced coupling of collective oscillation modes and the existence of parametric resonances. Using a mean-field variational and a full numerical approach, we studied density waves in dipolar condensates at zero temperature, where breaking of the symmetry due to anisotropy of the dipole-dipole interaction (DDI) plays an important role. We derived variational equations of motion for the dynamics of a driven dipolar system and identify the most unstable modes that correspond to the Faraday and resonant waves. Based on this, we derived the analytical expressions for spatial periods of both types of density waves as functions of the contact and the DDI strength. We compared the obtained variational results with the results of extensive numerical simulations that solve the dipolar Gross-Pitaevskii equation in 3D, and found a very good agreement.

Keywords: Bose-Einstein condensate; pattern formation; dipole-dipole interaction; parametric resonance; interaction effects

1. Introduction

After pioneering experiments that realized Bose-Einstein condensates (BEC) in systems with weak contact interactions, it took a decade of work on improvements of experimental techniques to enable measurement of effects of the dipole-dipole interaction (DDI) that exist between atoms or molecules with a permanent or induced electrical or magnetic dipole moment. The very first such experiment was realized in 2005 with chromium atoms ^{52}Cr [1], followed by the experiments with atoms with much larger magnetic moments, such as dysprosium ^{164}Dy [2] and erbium ^{168}Er [3]. Furthermore, the dipolar BECs comprised of polar molecules with much stronger electrical [4] and magnetic [5] dipole moments were also realized. While the contact interaction is symmetric and has a short-range, the DDI between atoms or molecules is anisotropic and long-range. These features are responsible for a whole series of new phenomena that appear in ultracold dipolar gases [6]. If we take into account that the strength of the contact interactions can be varied over many orders of magnitude using the Feshbach resonance [7] technique, and that the DDI strength can be also tuned using a fast rotating magnetic or electric field [8,9], it is easy to see that such a versatility of dipolar quantum gases is unparalleled and makes them an obligatory element in a toolbox for engineering quantum devices and sensors.

Bose-Einstein condensates are usually termed quantum fluids, which encompasses a broader range of physical systems where quantum effects are either dominant or very much pronounced. Despite their name, some of quantum fluids do not share the trademark property of classical fluids, incompressibility. In fact, the BECs are made of rarefied gases, but their fluid-like behavior stems from the quantum coherence of such systems. Therefore, while in classical fluids density modulations can

be excited only under extreme conditions, in quantum fluids the density waves represent one of the natural collective excitations. They appear due to nonlinearity in ultracold quantum gases, and can be induced by a harmonic modulation of the trap frequencies or interaction strengths. However, the motivation for study of such excitations comes from the classical phenomenon of Faraday waves, which may appear on the surface of the shallow layer of liquid under certain conditions. Namely, if the container with the liquid is harmonically oscillated in a vertical direction, the wave patterns may emerge, depending on the ratio of the liquid depth and the container size, as well as depending on the modulation frequency. This phenomenon was first studied and described by Michael Faraday at the beginning of 19th century [10]. The interest for this type of excitations arose again during the 1980s, as a consequence of the study of nonlinear liquids. In the context of ultracold gases, Faraday waves were first investigated theoretically in 2002 by Staliunas [11]. After these theoretical and numerical results for the systems with contact interaction, where it was assumed that the interaction strength is harmonically modulated, the Faraday waves were first measured in BEC experiments with ^{87}Rb in 2007 by Engels [12], and more recently with ^7Li by Hulet and Bagnato [13,14]. In the first experiment, the radial part of the harmonic trap was modulated, while the other two experiments have modulated the contact interaction strength. However, qualitatively, this leads to the same type of density waves.

Parametric driving of system parameters can lead to pattern formation not only in BECs, where Faraday waves are experimentally observed in cigar-shaped condensates [12–14], but also in helium cells [15]. The actual experimental observation of this phenomenon in 2007 was preceded by numerical studies starting in 2002 [11,16–20], all focusing on systems with short-range, contact interactions. More recently, Faraday waves have been studied in dipolar [21–23] and two-component condensates, including the systems with spatially-dependent contact interaction [24,25]. Numerical studies of Faraday waves have also been extended to mixtures of Bose and Fermi gases [26], as well as Fermi gases exhibiting superfluid behavior [27,28].

Faraday waves in ultracold gases are a consequence of the existence of parametric resonances in the system. While the spatial period of these waves depends on the geometry of the system and other parameters, the frequency of their oscillations is constant and is two times smaller than the modulation frequency. This is a characteristic of all parametric resonant phenomena, and in the variational approach leads to the Mathieu's differential equation [29], which gives the observed ratio of the frequency of Faraday waves and the modulation. The Faraday density waves with half of the modulation frequency are not the only nonlinear excitation of the system. In a driven system, there are always excitations with the same frequency as the modulation. However, they become resonant when the modulation frequency corresponds to one of the collective modes or the trap frequencies, or their linear combination. The resonant waves develop in the system and grow exponentially [30], faster than the Faraday waves. Therefore, these two phenomena can be easily distinguished, not only by comparing their frequencies, but also the corresponding onset times. We note that resonant behavior can appear not only due to the modulation of the interaction strength or the trapping potential, but also due to its spatial modulation [31–40].

In the context of dipolar BECs, the study of Faraday waves was limited mostly to their excitation spectrum in one-dimensional and two-dimensional systems [21], while the properties of resonant waves, to the best of our knowledge, have not been studied yet. In Section 2, we develop a mean-field variational approach for the dynamics of a driven dipolar BEC at zero temperature and identify the instability of the system leading to the emergence of Faraday and resonant waves. Using this approach, we derive analytic expressions for the dependence of density wave properties on the strength of the contact and the dipole-dipole interaction. In Section 3, we numerically study how such waves develop and can be characterized in ultracold systems of three experimentally relevant magnetic dipolar species: chromium ^{52}Cr , erbium ^{168}Er , and dysprosium ^{164}Dy . In Section 4, the analytically obtained expressions for the spatial period of Faraday are compared to results of the extensive numerical simulations, which solve the full three-dimensional mean-field equations for a dipolar BEC. The emergence of resonant

waves and comparison of the corresponding analytical and numerical results is given in Section 5. Finally, Section 6 summarizes our conclusions and presents outlook for future research.

2. Variational Approach

We consider the system in an experimentally-inspired setup, where the condensate is confined into a cigar-shaped harmonic trap, with the equilibrium frequencies $\omega_x = 2\pi \times 7$ Hz, $\omega_y = \omega_z = \Omega_0 = 2\pi \times 160.5$ Hz. These are typical values taken from Reference [12]. The dipole moments of the atoms are assumed to be oriented along z direction, i.e., orthogonal to the weak-confinement axis x (which we refer to as the longitudinal axis), since this maximizes the stability of the system. To ensure stability of the system, we consider the condensate to have $N = 10^4$ atoms for all three species. The driving of the system is achieved by harmonic modulation of the radial ($y - z$) part of the trap,

$$\omega_y(t) = \omega_z(t) = \Omega_0 (1 + \epsilon \sin \omega_m t), \quad (1)$$

where $\epsilon = 0.1 - 0.2$ is the modulation amplitude and ω_m is the modulation frequency.

For a variational study of Faraday and resonant waves in dipolar condensates, we use a modification of the Gaussian ansatz [16–20,23–25,30,41,42] to capture the induced density waves in the longitudinal, weak-confinement direction x ,

$$\psi(x, y, z, t) = A e^{-\frac{x^2}{2u_x^2} - \frac{y^2}{2u_y^2} - \frac{z^2}{2u_z^2} + ix^2\phi_x + iy^2\phi_y + iz^2\phi_z} [1 + (\alpha + i\beta) \cos kx], \quad (2)$$

where the normalization of the wave function to unity is ensured by the prefactor

$$A \equiv A(u_x, u_y, u_z, \alpha, \beta, k) = \frac{1}{\pi^{3/4} \sqrt{u_x u_y u_z}} \frac{\sqrt{2}}{\sqrt{2 + \alpha^2 + \beta^2 + 4\alpha e^{-k^2 u_x^2/4} + (\alpha^2 + \beta^2) e^{-k^2 u_x^2}}}. \quad (3)$$

The above variational ansatz involves eight variational parameters $\{u_i, \phi_i, \alpha, \beta\}$, which are functions of time. The parameters u_i represent the condensate widths, while ϕ_i are the conjugated phases, which are necessary to properly describe the system's dynamics. Note that these phases can be omitted when we are interested only in the ground state. The multiplicative factor $1 + (\alpha + i\beta) \cos kx$ describes the density modulation along x direction, and the variational parameters α and β represent the real and the imaginary part of the amplitude of the wave. The wave vector k , which is related to the spatial period ℓ of the density waves by $\ell = 2\pi/k$, is not treated here as a variational parameter. We determine its value from the condition for the instability emergence, which leads to Faraday or resonant waves.

The use of the Gaussian variational ansatz corresponds to the weak interaction regime with low density of atoms, while the Thomas-Fermi profile is more appropriate for systems with high particle density. Although the emergence of Faraday and resonant waves leads to higher particle densities, we still use the Gaussian ansatz in all regimes. This is done since we are mostly interested just in the onset of longitudinal density modulations, but also for mathematical convenience. Let us note that tunability of all variational parameters may improve the accuracy of the applied approximation. Nevertheless, the use of this ansatz can be fully justified only a posteriori, by comparison with numerical results [16].

Note that we use the dimensionless units, where a chosen referent frequency ω_r defines the length scale through the harmonic oscillator length $\sqrt{\hbar/(m\omega_r)}$, where m is the mass of the corresponding atomic species, the time scale as $1/\omega_r$, and the energy scale as $\hbar\omega_r$. The trapping frequencies are also expressed in units of ω_r through the trap aspect ratios $\gamma = \omega_x/\omega_r$, $\nu = \omega_y/\omega_r$, and $\lambda = \omega_z/\omega_r$, as well as the modulation frequency $\eta_m = \omega_m/\omega_r$. We choose below the value $\omega_r = \Omega_0$, corresponding to $\nu = \lambda = 1$, but for now we keep all three aspect ratios as free parameters, for generality.

If we insert the modified Gaussian ansatz (Equation (2)) into the Lagrangian density that yields the dipolar Gross-Pitaevskii equation, we can express the Lagrangian of the system as a sum of five terms. The first term reads

$$L_1(t) = \frac{i}{2} \int d\mathbf{r} (\psi^* \dot{\psi} - \psi \dot{\psi}^*) = -\frac{1}{2} \left(u_x^2 \dot{\phi}_x + u_y^2 \dot{\phi}_y + u_z^2 \dot{\phi}_z \right) - \frac{\alpha \dot{\beta} - \beta \dot{\alpha}}{2 + \alpha^2 + \beta^2}, \quad (4)$$

while the kinetic and the potential energy terms yield, respectively,

$$L_2(t) = \frac{1}{2} \int d\mathbf{r} \psi^* \Delta \psi = -\frac{1}{4} \left(\frac{1}{u_x^2} + \frac{1}{u_y^2} + \frac{1}{u_z^2} + 4u_x^2 \phi_x^2 + 4u_y^2 \phi_y^2 + 4u_z^2 \phi_z^2 \right) - \frac{(\alpha^2 + \beta^2) k^2}{2(2 + \alpha^2 + \beta^2)}, \quad (5)$$

$$L_3(t) = - \int d\mathbf{r} \left(\frac{1}{2} \gamma^2 x^2 + \frac{1}{2} v^2 y^2 + \frac{1}{2} \lambda^2 z^2 \right) |\psi|^2 = -\frac{1}{4} \left(\gamma^2 u_x^2 + v^2 u_y^2 + \lambda^2 u_z^2 \right). \quad (6)$$

The contact interaction term corresponds to

$$L_4(t) = -2\pi N a_s \int d\mathbf{r} |\psi|^4 = -\frac{N a_s}{\sqrt{2\pi} u_x u_y u_z} \left(1 + \frac{\alpha^4 + 16\alpha^2 + 2\alpha^2 \beta^2 + \beta^4}{2(2 + \alpha^2 + \beta^2)^2} \right), \quad (7)$$

where a_s is the s -wave scattering length of atoms, expressed in units of the harmonic oscillator length. The Lagrangian term that corresponds to the DDI energy is given by

$$L_5(t) = -\frac{3N a_{\text{dd}}}{2} \int d\mathbf{r} d\mathbf{r}' \psi^*(\mathbf{r}) \psi^*(\mathbf{r}') U_{\text{dd}}(\mathbf{r} - \mathbf{r}') \psi(\mathbf{r}') \psi(\mathbf{r}), \quad (8)$$

where the dipolar potential reads $U_{\text{dd}}(\mathbf{r}) = (1 - 3 \cos^2 \theta)/r^3$, θ is the angle between the dipoles' orientation (z axis) and vector \mathbf{r} , and a_{dd} is the DDI interaction strength, that depends on the dipole moment of atoms d and their mass m as $a_{\text{dd}} = \mu_0 m d^2 / (12\pi \hbar^2)$. Note that it is conveniently expressed in units of length and cast into a dimensionless quantity as outlined above. However, due to the spatial modulation term in the modified Gaussian ansatz, it is not possible to perform exact integration and obtain $L_5(t)$. Using the convolution theorem, the DDI term can be written as

$$L_5(t) = -\frac{3N a_{\text{dd}}}{2(2\pi)^3} \int d\mathbf{k} \mathcal{F}[U_{\text{dd}}](\mathbf{k}) \mathcal{F}[|\psi|^2]^2(\mathbf{k}), \quad (9)$$

where \mathcal{F} stands for the Fourier transform, and

$$\mathcal{F}[|\psi|^2](\mathbf{k}) = B(k_x, u_x, \alpha, \beta, k) e^{-\frac{1}{4}(k_x^2 u_x^2 + k_y^2 u_y^2 + k_z^2 u_z^2)}. \quad (10)$$

The coefficient B can be explicitly calculated and reads

$$B(k_x, u_x, \alpha, \beta, k) = \frac{4 + 4(e^{-\frac{k}{4}(k-2k_x)u_x^2} + e^{-\frac{k}{4}(k+2k_x)u_x^2}) \alpha + (2 + e^{-k(k-k_x)u_x^2} + e^{-k(k+k_x)u_x^2})(\alpha^2 + \beta^2)}{2 \left[2 + 4e^{-\frac{1}{4}k^2 u_x^2} \alpha + (1 + e^{-k^2 u_x^2})(\alpha^2 + \beta^2) \right]}. \quad (11)$$

To proceed further, we take into account that the condensate width in the weak confinement direction is large compared to the other widths, as well as compared to the spatial period of the density waves, such that $ku_x \gg 1$. We also take into account that the wave amplitude is small immediately after the waves emerge, such that $\alpha, \beta \ll 1$. Since the integral over \mathbf{k} in Equation (9) cannot be analytically performed even using these approximations, we replace B^2 , stemming from the square of the Fourier transform $\mathcal{F}[|\psi|^2]$, by its average over k_x , and neglect all terms proportional to $e^{-k^2 u_x^2/8}$ and its powers, as already argued that ku_x is a large quantity. The integration over \mathbf{k} can now proceed smoothly, yielding

$$L_5(t) = \frac{Na_{\text{dd}}}{\sqrt{2\pi} u_x u_y u_z} f\left(\frac{u_x}{u_z}, \frac{u_y}{u_z}\right) \left(1 - \frac{8\alpha^2}{(2 + \alpha^2 + \beta^2)^2}\right), \quad (12)$$

where f is the standard dipolar anisotropy function [43].

Now that we have the explicit expression for the Lagrangian of the system $L(t) = \sum_{i=1}^5 L_i(t)$, we can derive the corresponding Euler-Lagrange equations. We assume that the wave amplitudes α and β are small, such that their quadratic and higher order terms can be neglected in the equations of motion. The three equations for the phases yield $\phi_i = \dot{u}_i / (2u_i)$ and can be used to eliminate the phases ϕ_i from the corresponding set of equations for the condensate widths u_i , which have the form of the second order differential equations,

$$\ddot{u}_x + \gamma^2 u_x - \frac{1}{u_x^3} - \sqrt{\frac{2}{\pi}} \frac{N}{u_x^2 u_y u_z} \left[a_s - a_{\text{dd}} f\left(\frac{u_x}{u_z}, \frac{u_y}{u_z}\right) + a_{\text{dd}} \frac{u_x}{u_z} f_1\left(\frac{u_x}{u_z}, \frac{u_y}{u_z}\right) \right] = 0, \quad (13)$$

$$\ddot{u}_y + \nu^2 u_y - \frac{1}{u_y^3} - \sqrt{\frac{2}{\pi}} \frac{N}{u_x u_y^2 u_z} \left[a_s - a_{\text{dd}} f\left(\frac{u_x}{u_z}, \frac{u_y}{u_z}\right) + a_{\text{dd}} \frac{u_y}{u_z} f_2\left(\frac{u_x}{u_z}, \frac{u_y}{u_z}\right) \right] = 0, \quad (14)$$

$$\ddot{u}_z + \lambda^2 u_z - \frac{1}{u_z^3} - \sqrt{\frac{2}{\pi}} \frac{N}{u_x u_y u_z^2} \left[a_s - a_{\text{dd}} f\left(\frac{u_x}{u_z}, \frac{u_y}{u_z}\right) - a_{\text{dd}} \frac{u_x}{u_z} f_1\left(\frac{u_x}{u_z}, \frac{u_y}{u_z}\right) - a_{\text{dd}} \frac{u_y}{u_z} f_2\left(\frac{u_x}{u_z}, \frac{u_y}{u_z}\right) \right] = 0, \quad (15)$$

where f_1 and f_2 are partial derivatives of the anisotropy function with respect to the first and the second argument. The Euler-Lagrange equation for the variational parameter β yields $\beta = 2\alpha/k^2$, which we use to eliminate β from the corresponding equation for the parameter α , as was done with the phases. With this, the equation for α turns out to be the second order differential equation,

$$\ddot{\alpha} + \left[\frac{k^4}{4} + \sqrt{\frac{2}{\pi}} \frac{N}{u_x u_y u_z} \left(a_s + a_{\text{dd}} f\left(\frac{u_x}{u_z}, \frac{u_y}{u_z}\right) \right) k^2 \right] \alpha = 0. \quad (16)$$

In the context of variational analysis of Faraday and resonant waves, the above equation of motion for the wave amplitude α is usually cast into the form of the Mathieu-like equation [29]

$$\ddot{\alpha} + [a(k) + \epsilon b(k) \sin 2\tau] \alpha = 0. \quad (17)$$

This equation can be solved perturbatively in the small modulation amplitude ϵ . Assuming a solution in the form of a harmonic oscillator

$$\alpha(\tau, \epsilon) = P(\epsilon\tau) \cos\left(\tau\sqrt{a(k)}\right) + Q(\epsilon\tau) \sin\left(\tau\sqrt{a(k)}\right), \quad (18)$$

we obtain that functions P and Q are exponentials of the form $e^{\pm i\zeta\epsilon\tau}$, where ζ is a complex number. The existence of the imaginary part of ζ leads to the instability, i.e., to the exponential growth of the wave amplitude, which yields Faraday or resonant waves. It was shown in Reference [29] that the nonvanishing imaginary part of ζ appears for $a(k) = n^2$, where $n \in \mathbb{N}$, and this represents the mathematical form of the instability condition.

To cast Equation (16) into the Mathieu-like form (Equation (17)), we need to take into account that the radial trap frequencies are modulated, such that the corresponding trap aspect ratio is given by $\nu(t) = \lambda(t) = \lambda_0(1 + \epsilon \sin \eta_m t)$, where $\lambda_0 = \Omega_0/\omega_r$. This generates the dynamics of the system and we need to obtain approximate expressions for the condensate widths in order to get explicit form of the quantities $a(k)$ and $b(k)$. We assume that the condensate width u_x slowly varies, and can be taken to be constant at the onset of instability. We also assume that second derivatives of the radial widths

u_y and u_z , with respect to time, can be neglected, since they are proportional to the small modulation amplitude ϵ . Furthermore, for simplicity, we assume $u_y \approx u_z \equiv u_\rho$, which now satisfies the modified Equation (14) or (15) in the form

$$\lambda^2(t)u_\rho^4 = 1 + \sqrt{\frac{2}{\pi}} \frac{N}{u_x} \left[a_s + \frac{a_{\text{dd}}}{2} f_s \left(\frac{u_\rho}{u_x} \right) - a_{\text{dd}} f'_s \left(\frac{u_\rho}{u_x} \right) \right], \quad (19)$$

where $f_s(x) = f(x, x)$. On the right-hand side of the above equation, we assume that the ratio u_ρ/u_x is constant and equal to the corresponding ratio for the ground state, which can be calculated from Equations (13)–(15). If we express u_ρ^2 from Equation (19), and use it to estimate the quantity $u_y u_z \approx u_\rho^2$ in Equation (16), we obtain the equation for the variational parameter α in the form

$$\ddot{\alpha} + \left[\frac{k^4}{4} + \frac{\Lambda k^2}{4} \lambda(t) \right] \alpha = 0, \quad (20)$$

where Λ is given by

$$\Lambda = \frac{4\sqrt{\frac{2}{\pi}} N \left[a_s - \frac{a_{\text{dd}}}{2} f_s \left(\frac{u_\rho}{u_x} \right) \right]}{u_x \left\{ 1 + \sqrt{\frac{2}{\pi}} \frac{N}{u_x} \left[a_s + \frac{a_{\text{dd}}}{2} f_s \left(\frac{u_\rho}{u_x} \right) - a_{\text{dd}} f'_s \left(\frac{u_\rho}{u_x} \right) \right] \right\}^{1/2}}. \quad (21)$$

After inserting the explicit form for $\lambda(t)$ into Equation (20), we still need to make a variable change $\eta_m t \rightarrow 2\tau$ in order to transform it into the Mathieu-like Equation (17). This finally yields the expressions for the coefficients $a(k)$ and $b(k)$,

$$a(k) = \frac{k^4}{\eta_m^2} + \frac{\lambda_0 \Lambda k^2}{\eta_m^2}, \quad b(k) = \frac{\lambda_0 \Lambda k^2}{\eta_m^2}. \quad (22)$$

As previously discussed, the instability condition for the Faraday waves reads $a(k) = 1$, which can be used to calculate the wave vector of density waves shortly after their emergence,

$$k_F = \sqrt{-\frac{\lambda_0 \Lambda}{2} + \sqrt{\frac{\lambda_0^2 \Lambda^2}{4} + \eta_m^2}}. \quad (23)$$

This represents our analytical result for the wave vector k_F and the spatial period $\ell_F = 2\pi/k_F$ of the Faraday waves, which can be directly compared with numerical or experimental results. Let us also stress that the above analysis is consistent with the main characteristic of the Faraday waves, namely, that their oscillation frequency is half that of the driving frequency. This can be concluded according to $\tau = \eta_m t/2$ and Equation (18), where we see that indeed the solution of the derived Mathieu-like equation oscillates with the frequency whose aspect ratio is $\eta_m/2$, i.e., with the frequency $\omega_m/2$.

If the modulation frequency is close to one of the characteristic oscillation modes of the system, it will exhibit resonant behavior, which is suppressed for an arbitrary value of the modulation frequency. While the system's dynamics will certainly include the Faraday mode at the frequency $\omega_m/2$ even close to a resonance, the resonant mode with the frequency ω_m will have a larger amplitude and will develop much faster. Although it is clear that the above analysis would break down, the condition for the emergence of resonant waves still corresponds to $a(k) = 2^2$, i.e., the wave vector of the resonant wave is given by

$$k_R = \sqrt{-\frac{\lambda_0 \Lambda}{2} + \sqrt{\frac{\lambda_0^2 \Lambda^2}{4} + 4\eta_m^2}}. \quad (24)$$

In that case, according to $\tau = \eta_m t / 2$ and Equation (18), the resonant density wave will oscillate with the frequency whose aspect ratio is $(\eta_m / 2) \sqrt{2} = \eta_m$, i.e., with the frequency ω_m . Depending on the system's parameters, higher resonant modes can also appear corresponding to the conditions $a(k) = n^2$, where n is an integer, corresponding to the oscillation frequencies $n\omega_m / 2$.

3. Faraday Waves in Chromium, Erbium, and Dysprosium Condensates

To study Faraday waves in dipolar condensates, we performed extensive numerical simulations of the real-time dynamics and solved the dipolar Gross-Pitaevskii equation using the programs described in References [44–52]. The parameters of these simulations match the physical parameters of BECs of chromium ^{52}Cr , erbium ^{168}Er , and dysprosium ^{164}Dy , which, respectively, have the dipole moments $d = 6\mu_B$, $d = 7\mu_B$, and $d = 10\mu_B$, where B is the Bohr magneton. The corresponding background s -wave scattering lengths are $a_s = 105a_0$, $a_s = 100a_0$, and $a_s = 100a_0$, where a_0 is the Bohr radius. We used these interaction strengths, unless otherwise specified.

As discussed previously, Faraday waves are expected as a main excitation mode of the system when the modulation frequency ω_m does not match any of the characteristic frequencies of the system. For this reason, we used the value $\omega_m = 200 \times 2\pi$ Hz, for which we verified that these conditions are satisfied. To characterize the density waves, we typically analyze their FFT spectra in the time-frequency and spatial-frequency domains. However, instead of directly analyzing their density profiles, for FFT, it is advantageous to have a clearer signal, which can be obtained by considering only the density variations compared to the initial state, i.e., the ground state of the system, before the modulation is switched on. Therefore, Figure 1 shows time dependence of the integrated density profile variations in the weak confinement direction $\delta n(x, t) = n(x, t) - n(x, t = 0)$. Here, $n(x, t)$ is the column density profile calculated by integrating the 3D condensate density $|\psi|^2$ over the radial coordinates y and z .

The emergence of spatial patterns is clearly visible for all three atomic species after around 150 ms. This is consistent with earlier experimental observations [12–14] and theoretical results [16,24,25]. The density waves in x direction from Figure 1 take time to develop and are a result of the transfer of energy from the modes that are directly excited in the radial directions, where the trap is modulated. On the other hand, the density waves in the radial directions (which are not shown here) emerge immediately after the modulation is switched on at $t = 0$, and their frequency is equal to the modulation frequency. By looking at Figure 1, we can even estimate the main oscillation frequency, e.g., counting the number of maxima or minima in a given time interval. For instance, in the last 50 ms in each of the panels in Figure 1, we count five periods, which corresponds to the frequency $100 \times 2\pi$ Hz = $\omega_m / 2$. This is a distinguishing characteristic of Faraday waves, and therefore we can directly determine that in this case the system develops this type of collective oscillations.

However, this way we can determine only the main excitation modes. The dynamics of the system contains other modes as well, and over the time they can develop and even start to dominate the behavior of the system. Therefore, it is important to analyze the spectra in more detail. This is done in Figure 2 for all integrated density profile variations, separately for each spatial direction. For simplicity, the FFT analysis is performed for the profiles at the trap center. As expected, in the weak confinement direction (left column of Figure 2), the main excitation mode has a frequency $\omega_m / 2$. In addition to this, we observe two other modes, at ω_m and $3\omega_m / 2$. This is expected from the theoretical analysis in Section 2, but could not be discerned directly from the density profiles or their variations.

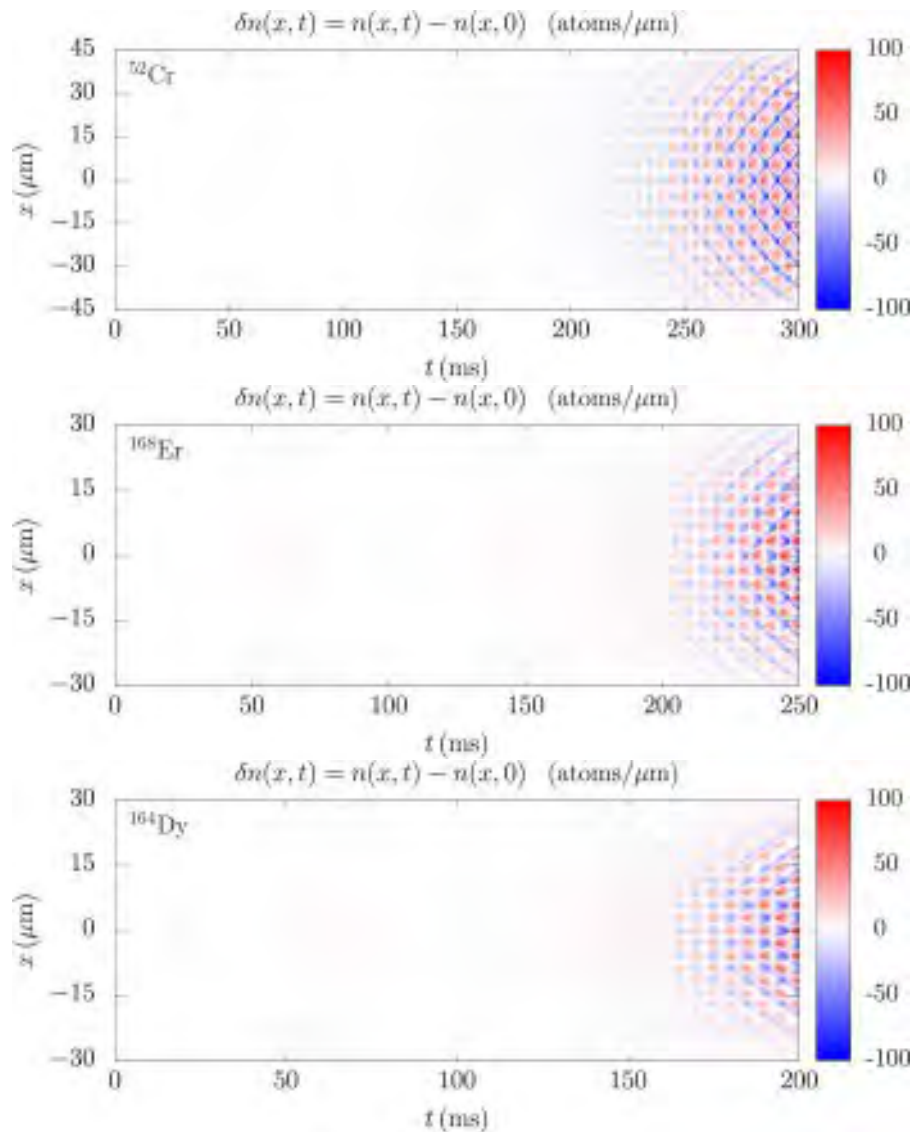


Figure 1. Time evolution of the integrated density profile variation $\delta n(x, t)$ in the weak-confinement direction for a BEC of chromium ^{52}Cr (top), erbium ^{168}Er (middle), and dysprosium ^{164}Dy (bottom), for the modulation frequency $\omega_m = 200 \times 2\pi$ Hz and amplitude $\epsilon = 0.2$, and the system parameters given in Section 2.

In the Fourier spectra of the integrated density profile variations in the radial directions (middle and right columns of Figure 2), we see a somewhat richer set of excitation modes. In addition to the main mode corresponding to the trap modulation at ω_m , we see that also the breathing mode is excited at the frequency $\omega_B \approx 321 \times 2\pi$ Hz. This value can be calculated by linearizing the equations of motion from Section 2. The spectra prominently contain the second modulation harmonic at $2\omega_m$ as well. We also see some other peaks, for instance the small peak at around $120 \times 2\pi$ Hz, which can be due to the linear combination of the modes $\omega_B - \omega_m$. However, such an identification would require further theoretical and numerical analysis, which is out of the scope of the present paper.

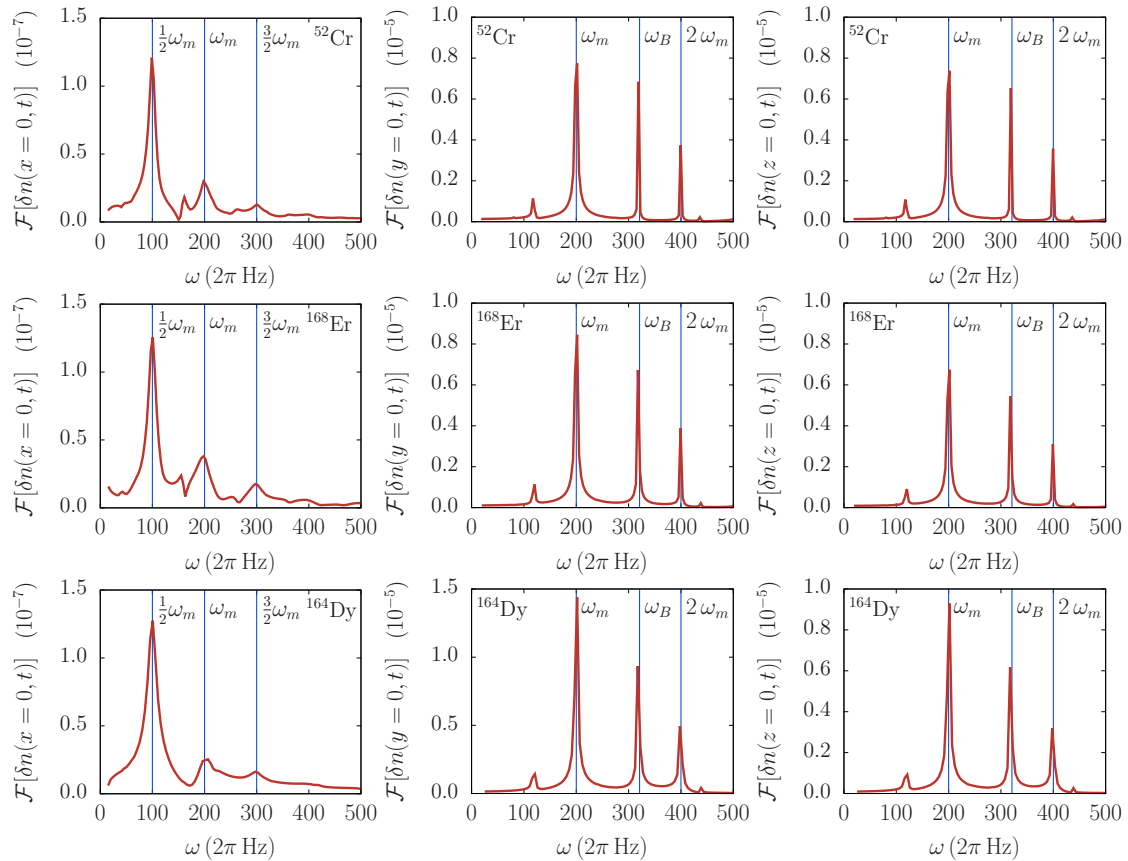


Figure 2. The Fourier spectrum in the time-frequency domain of the integrated 1D density profile variations of Faraday waves at the trap center $\delta n(x = 0, t)$ in x direction (**left column**), $\delta n(y = 0, t)$ in y direction (**middle column**), and $\delta n(z = 0, t)$ in z direction (**right column**) for a BEC of chromium ^{52}Cr (**top row**), erbium ^{168}Er (**middle row**), and dysprosium ^{164}Dy (**bottom row**). Vertical blue lines represent theoretical predictions, where $\omega_m/2$ corresponds to Faraday waves, ω_m , $3\omega_m/2$, and $2\omega_m$ to resonant waves, and ω_B is the variational result for the breathing mode frequency, which is obtained by linearization of the equations of motion from Section 2.

While the Fourier analysis in the time-frequency domain can be used to determine the character of the induced density waves (Faraday, collective, and resonant), the analysis in the spatial-frequency domain enables us to characterize the density patterns and calculate their spatial period. This is illustrated in Figure 3 for Faraday waves for all three considered atomic species. The integrated density profile variations are analyzed at appropriate times, which are determined to correspond to the evolution stage when Faraday waves have fully emerged, but the system is still far from the violent dynamics that inevitably follows after the long driving period.

In all three panels of Figure 3, the main peak corresponds to the wave vector k_F of the Faraday waves, and we see significant differences: for ^{52}Cr , we obtained $k_F = 0.57 \mu\text{m}^{-1}$, yielding the spatial period $\ell_F = 2\pi/k_F = 11.02 \mu\text{m}$; for ^{168}Er , we obtained $k_F = 0.98 \mu\text{m}^{-1}$ and $\ell_F = 6.41 \mu\text{m}$; and, for ^{164}Dy , we obtained $k_F = 1.10 \mu\text{m}^{-1}$ and $\ell_F = 5.71 \mu\text{m}$. The variational analysis presented in Section 2 yields results which are in good agreement with the numerical ones, namely $k_F = 0.51 \mu\text{m}^{-1}$ for ^{52}Cr , $k_F = 0.91 \mu\text{m}^{-1}$ for ^{168}Er , and $k_F = 1.06 \mu\text{m}^{-1}$ for ^{164}Dy . These variational results are shown in Figure 3 by vertical blue lines, which illustrate their agreement with the Fourier analysis. The presented spectra also contain some additional peaks that correspond to other geometrical features of the analyzed density profile variations, such as the condensate widths and their higher harmonics, as well as the higher harmonics of the Faraday waves periods, and linear combinations of all of these. However, they are not of interest for our analysis and we did not study them further.

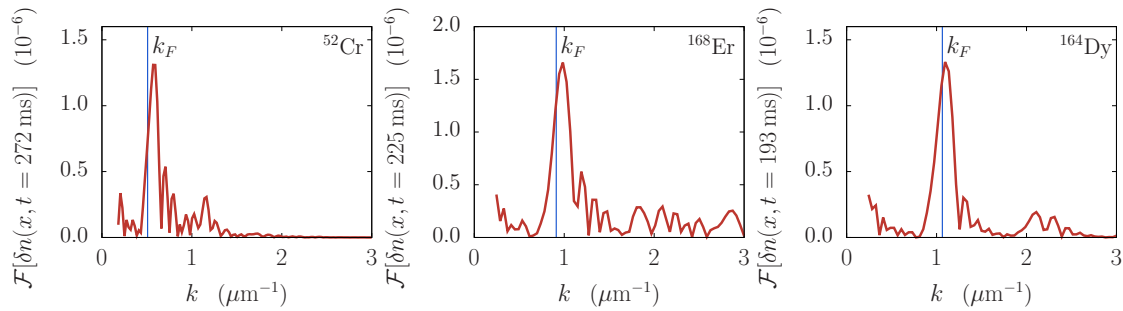


Figure 3. The Fourier spectrum in the spatial-frequency domain of the integrated 1D density profile variations of Faraday waves in x direction $\delta n(x, t = 272 \text{ ms})$ for ^{52}Cr (**left**), $\delta n(x, t = 225 \text{ ms})$ for ^{168}Er (**middle**), and $\delta n(x, t = 193 \text{ ms})$ for ^{164}Dy (**right**) BECs with $N = 10^4$ atoms. The corresponding density profile variations are shown in Figure 1. Vertical blue lines represent theoretical predictions for the wave vector k_F of the Faraday waves, Equation (23).

Note that the spatial period of Faraday waves can also be determined by directly looking at the density profile variations in Figure 1, and estimating the spacing between the consecutive minima or maxima at the appropriate evolution time. For instance, for chromium, we count three minima over the spatial extent of $30 \mu\text{m}$, yielding an estimate $\ell_F \approx 10 \mu\text{m}$, and similarly for other species. Obviously, such estimates are not as precise as the Fourier analysis results, and therefore we rely on FFT spectra to systematically determine the spatial periods of Faraday waves and their functional dependencies on the contact and the DDI strength.

4. Interaction Effects and Properties of Faraday Waves

In the previous section, we show how the Fourier analysis can be used to calculate the spatial period of Faraday waves. Next, we systematically studied the interaction effects, namely how the contact and the DDI strength affect the properties of generated density waves. First, we explored the influence of the contact interaction on the emergence time and the spatial period of Faraday waves for a fixed value of the DDI strength. In experiments, this can be achieved by employing the Feshbach resonance technique, which allows tuning a_s by changing the external magnetic field, thus changing the electronic structure of atoms and their scattering properties.

The existence of Faraday waves is a consequence of nonlinearity of the system, i.e., the presence of the contact and the DDI terms in the Hamiltonian. In a linear system, described by the pure Schrödinger equation, the harmonic modulation of the trap in the radial direction would not be transferred into the longitudinal direction. Therefore, the emergence time of Faraday waves (and other types of density waves in the longitudinal direction) critically depends on the strength of interatomic interactions. However, if interaction strengths become sufficiently large, the emergence time is less sensitive to their changes. Since the DDI is strong in erbium and dysprosium, we can expect that the emergence time of Faraday waves significantly depends on the contact interaction strength only in chromium, where a_{dd} is small.

This is illustrated in Figure 4, where we see the density profile variations for chromium for three different values of a_s . Let us first note that the amplitude of density variations is much smaller in the top panel for $a_s = 60 a_0$ than in the middle panel for $a_s = 80 a_0$, and significantly smaller than in the bottom panel for $a_s = 150 a_0$. This is also evident from the fact that in the top and middle panel we can clearly see the quadrupole collective oscillation mode, which has a frequency of around $\omega_Q = 12 \times 2\pi \text{ Hz}$. This can be estimated from the figure and compared to the variational value of ω_Q , which can be obtained by linearizing the equations of motion in Section 2. When the interaction is sufficiently large, the amplitude of Faraday waves is much larger than those of the collective modes, and they cannot be even discerned in the bottom panel in Figure 4. Only for a weak interaction the amplitude of the Faraday waves is comparable to the amplitude of the collective modes, and this is why we can see them all for small values of a_s .

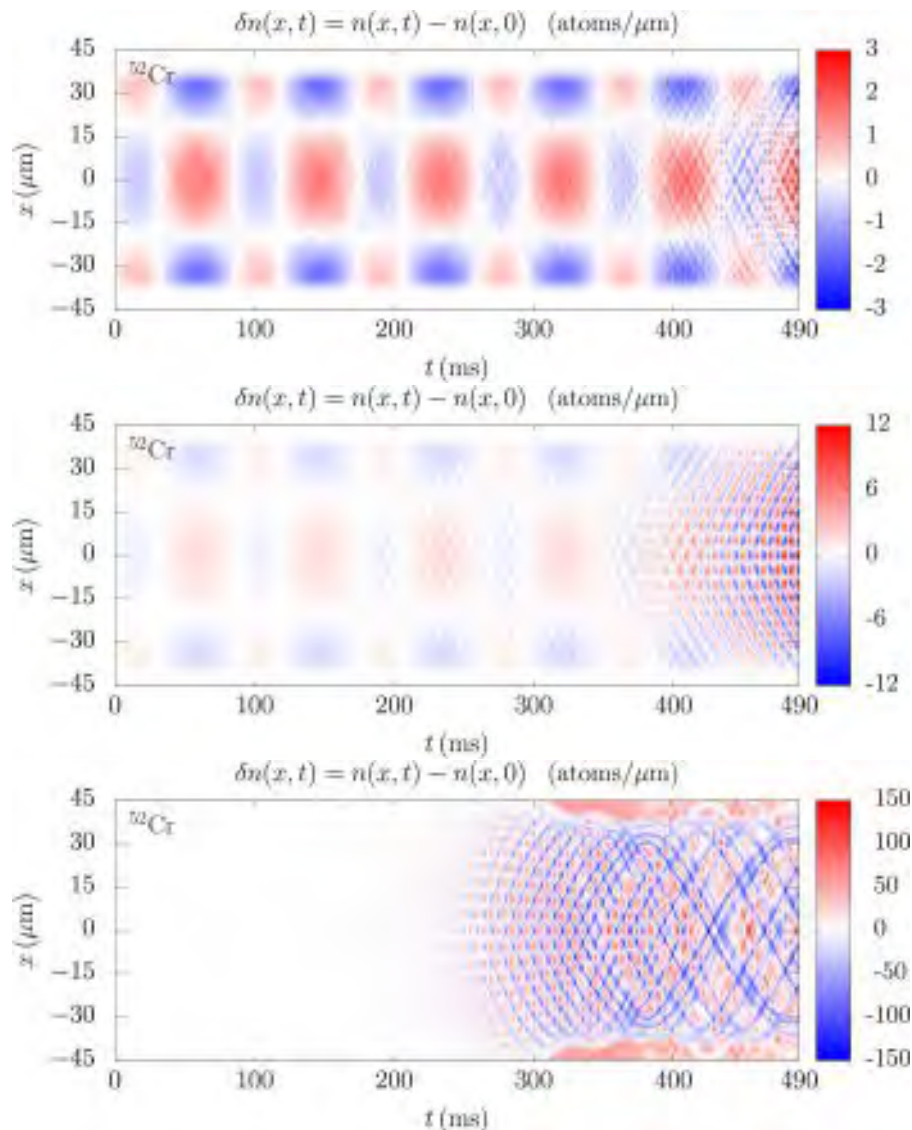


Figure 4. Emergence of Faraday waves for different strengths of the contact interaction: $a_s = 60 a_0$ (top), $a_s = 80 a_0$ (middle), and $a_s = 150 a_0$ (bottom) for a BEC of ^{52}Cr . We observe that Faraday waves emerge faster as the contact interaction strength increases.

As with all other excitations, Faraday waves start to develop immediately after the modulation is switched on. The question on their emergence time is related to their amplitude, which is time-dependent and grows exponentially, as can be seen from the solution (Equation (18)) of the Mathieu-like equation that describes the dynamics of the Faraday density oscillations. The imaginary part of the parameter ζ in Equation (18) is responsible for the exponential growth of the Faraday waves' amplitude, which is not the case for collective modes. Therefore, in practical terms, the definition of the emergence time of Faraday waves is always arbitrary and can be expressed as a time needed for the density variations to reach a certain absolute or relative (compared to the total density) value. One can even relate this to the experimental point of view, where there is a threshold for the density variations that can be observed, due to measurement errors. However, in numerical simulations, there are no such limitations and one can easily use an arbitrary definition to estimate the emergence time of density waves. The more relevant quantity to study would be the exponent that governs the growth of the wave amplitude, which depends on the interaction strength.

Now, we turn our attention to spatial features of the Faraday waves. Figure 5 presents the dependence of the wave vector k_F on the s -wave scattering length a_s for all three considered species.

We also show the variational results for the dependence $k_F(a_s)$ derived in Section 2. The agreement is very good, with errors of the order of 10–15%. We stress that the derived variational expression closely follows the numerical results not only by their values, but, more importantly, also their functional dependence properly.

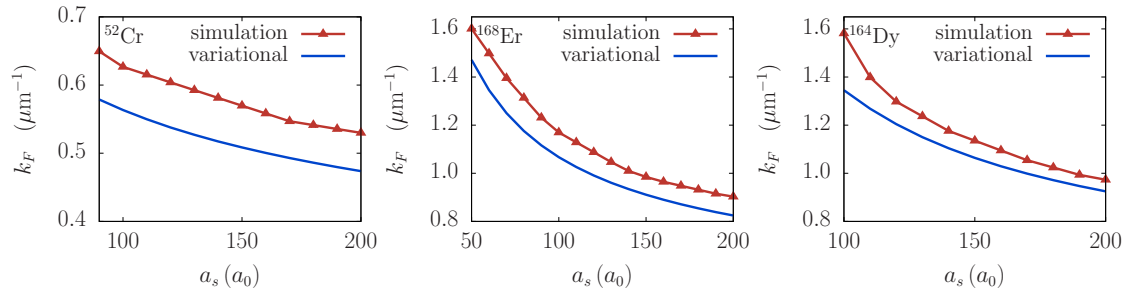


Figure 5. Wave vector of the Faraday waves k_F as a function of the contact interaction strength for a BEC of ^{52}Cr (left), ^{168}Er (middle), and ^{164}Dy (right), for a fixed DDI strength. Red upper triangles were numerically obtained values using the FFT analysis as in Figure 3, and blue lines are the variational results according to Equation (23).

Next, we studied the effects of the DDI strength for a fixed value of the contact interaction. Figure 6 shows the corresponding dependence of k_F on a_{dd} . In contrast to the contact interaction dependence, where k_F is a decreasing function of a_s , here we see that k_F increases as the DDI strength is increased. Figure 6 also shows the variational results, where the level of agreement with the numerically obtained results is different, with errors as small as 7% for chromium and up to around 25% for erbium and dysprosium for largest values of a_{dd} . Due to complex approximations made in the derivation of variational results, in particular those related to the DDI term, the obtained functional dependence is not as good as in the case of contact interaction, but still provides reasonable estimates of the wave vector values for the Faraday waves.

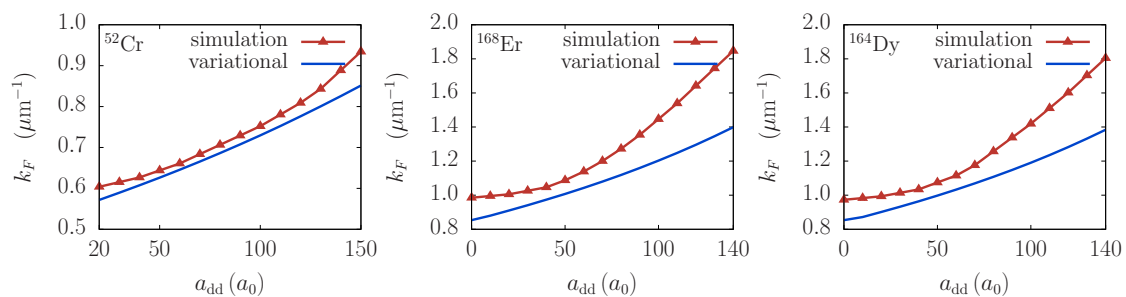


Figure 6. Wave vector of the Faraday waves k_F as a function of the DDI strength for a BEC of ^{52}Cr (left), ^{168}Er (middle), and ^{164}Dy (right), for a fixed contact interaction strength. Red upper triangles represent numerically obtained values using the FFT analysis as in Figure 3, and blue lines are the variational results according to Equation (23).

5. Resonant Waves

In the presence of interactions, various excitation modes in dipolar BECs are coupled and the energy pumped into the system by periodic driving can be transferred from the driving direction to other, orthogonal directions. In the previous section, we show this for non-resonant driving, when the harmonic modulation in the radial direction was transferred to the longitudinal direction in the form of Faraday waves, which were the main excitation mode generated. The main distinguishing property of these excitations is halving of the oscillation frequency, i.e., the induced density waves have the frequency $\omega_m/2$. Next, we studied the other important case, when the modulation frequency is resonant, such that the induced density waves have the same frequency. This happens when ω_m is close to one of the characteristic frequencies of the system, e.g., one of the frequencies of the collective

oscillation modes or one of the trap frequencies. Although Faraday waves and all other collective oscillation modes are also excited in this case, the largest amplitude corresponds to resonant waves with the frequency ω_m . When generated, these resonant waves dominate the behavior of the system and make all other excitations negligible for the dynamics.

Figure 7 shows the integrated density profile variation of ^{168}Er for a resonant wave induced by a harmonic modulation of the radial part of the trapping potential at $\omega_m = \Omega_0$, i.e., when the modulation frequency coincides with the radial trapping frequency. The density waves in this case develop much more quickly than for the non-resonant modulation and are clearly visible already after 55 ms. Due to a violent dynamics that emerges in the system very quickly, it is not easy to estimate the frequency of the waves directly from Figure 7, as was possible before. Therefore, we relied on the Fourier analysis in the time-frequency domain, as presented in the left panel of Figure 8. The obtained FFT spectrum clearly shows that the main excitation mode has the frequency equal to ω_m . We also see that the spectrum is continuous, practically without distinct individual peaks, and only the second harmonic at $2\omega_m = 321 \times 2\pi$ Hz yields a small local maximum. This demonstrates that the system is far from the regime of small perturbations, where individual excitation modes can be observed.

In the right panel of Figure 8, we see the Fourier spectrum in the spatial-frequency domain, which yields the wave factor k_R of resonant waves. The FFT results give the value $k_R = 1.59 \mu\text{m}^{-1}$ and the corresponding spatial period $\ell_R = 2\pi/k_R = 3.95 \mu\text{m}$ for ^{168}Er . In the figure we also present the variational result $k_R = 1.40 \mu\text{m}^{-1}$, calculated using Equation (24). The agreement is again quite good, which indicates that the variational approach developed in this paper can be reliably used not only for the Faraday waves, but also for the resonant waves.

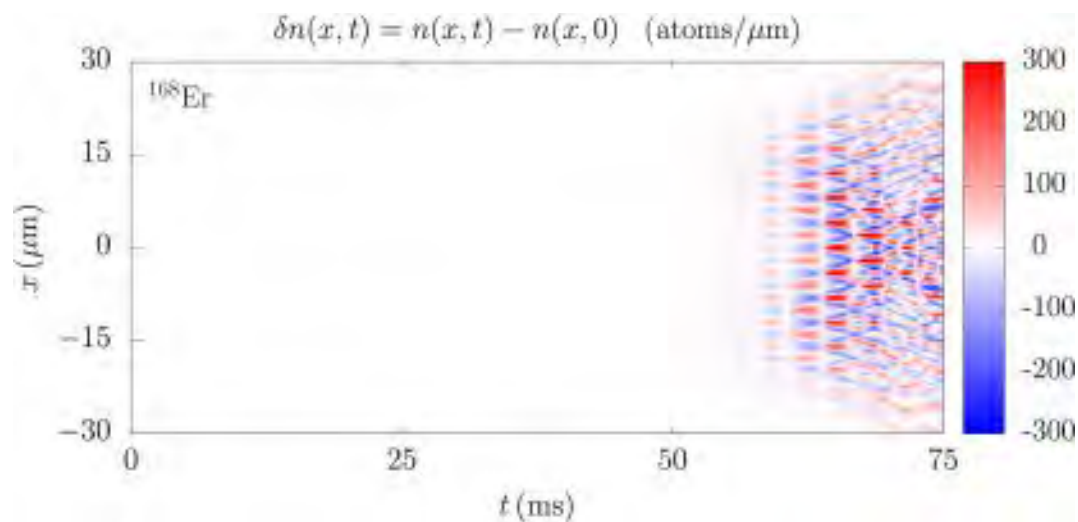


Figure 7. Time evolution of the integrated density profile variation in the weak confinement direction for a BEC of ^{168}Er , with the modulation frequency equal to the weak confinement frequency, $\omega_m = \Omega_0$. We observe resonant behavior corresponding to the first harmonic of the resonant frequency Ω_0 , which sets in after around 55 ms.

This can also be concluded from Figure 9, which presents the results for the dependence of the resonant wave vector k_R on the contact and the DDI strength. The agreement between the numerical and variational results is of the order of 10% over the whole experimentally relevant domain. We see similar behavior for the resonant waves as for the Faraday ones, namely the wave vector decreases as the contact interaction strength increases, while the opposite is true for the DDI. Again, the functional dependence obtained from the variational approach properly describes the numerical results, thus confirming that Equation (24) can be used to calculate spatial period of resonant waves.

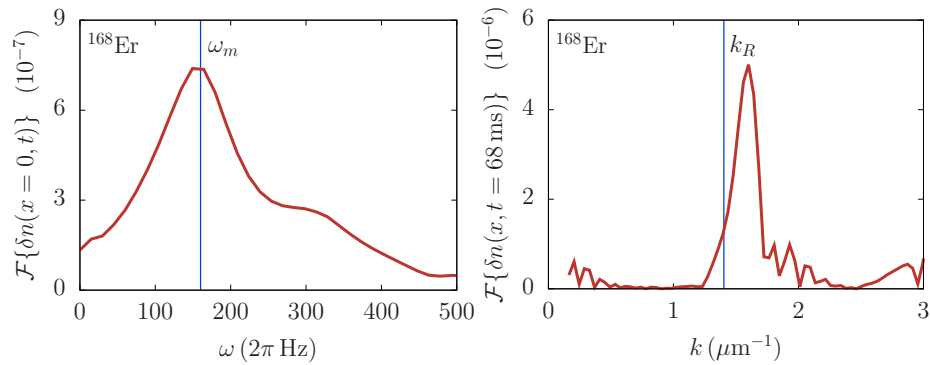


Figure 8. The Fourier spectrum of the integrated 1D density profile variations $\delta n(x, t)$ at the trap center in the time-frequency domain (**left**), and of the density profile variations in x direction $\delta n(x, t = 68 \text{ ms})$ in the spatial-frequency domain (**right**) of resonant waves for a BEC of ^{168}Er . Vertical blue line in the left panel represents the modulation frequency ω_m , while in the right panel it corresponds to the theoretical prediction for the wave vector k_R of the resonant waves, Equation (24).

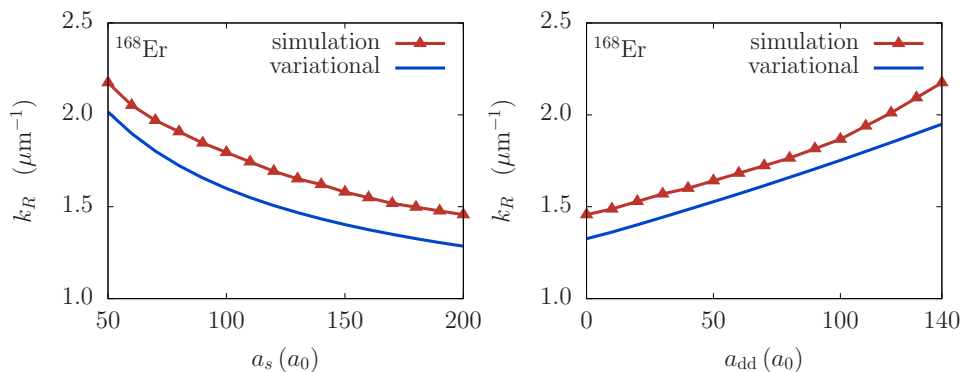


Figure 9. Wave vector of the resonant waves k_R as a function of the contact (**left**) and the DDI (**right**) strength for a BEC of ^{168}Er . The results in the left panel are obtained for a fixed DDI strength, and similarly in the right panel a fixed contact interaction strength is used. In both panels, red upper triangles represent numerically obtained values using the FFT analysis as in the right panel of Figure 8, and blue lines are the variational results according to Equation (24).

It is interesting to note that resonant behavior appears not only under conditions mentioned above, when ω_m is equal to one of the characteristic frequencies, but also when it matches their higher harmonics. Figure 10 illustrates this for ^{168}Er , which is harmonically modulated at twice the radial trapping frequency, $\omega_m = 2\Omega_0 = 321 \times 2\pi \text{ Hz}$. In this case, the amplitude of the resonant mode grows even more quickly and significant density variations can be observed already after 30 ms. Therefore, we see that the modulation at the second harmonic yields even more violent dynamics than the first harmonic. The Fourier analysis in the time-frequency domain reveals that the main excitation mode again has a frequency of Ω_0 , but the mode at $\omega_m = 2\Omega_0$ is also present. From the experimental point of view, resonant driving is very dangerous and leads to the destruction of the system in a matter of tens of milliseconds. While numerical simulations can be performed for longer time periods, the atoms leave the condensate due to a large, resonant transfer of energy to the system. As the condensate is depleted, the mean-field description of the system breaks down and it can no longer be simulated by the dipolar Gross-Pitaevskii equation.

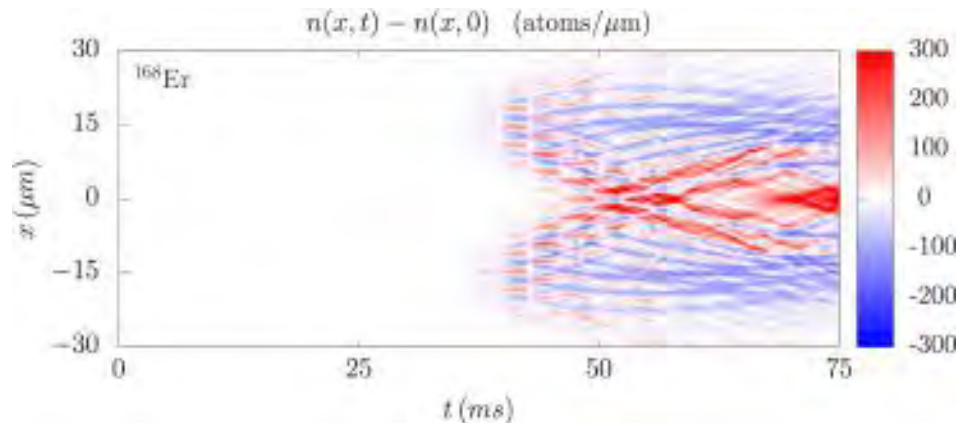


Figure 10. Time evolution of the integrated density profile variation in the weak confinement direction for a BEC of ^{168}Er . The modulation frequency is equal to twice the weak confinement frequency, $\omega_m = 2\Omega_0$. We observe resonant behavior corresponding to the second harmonic of the resonant frequency Ω_0 , which sets in more quickly than the first harmonic, already after around 30 ms.

6. Conclusions

We investigated here the Faraday and resonant density waves in ultracold dipolar Bose-Einstein condensates for experimentally relevant atomic species with the permanent magnetic dipole moment: chromium ^{52}Cr , erbium ^{168}Er , and dysprosium ^{164}Dy . The interplay of the contact and the dipole-dipole interaction in such systems is a hot research topic today, but detailed understanding of their dynamics and even their stability is still lacking. Our results contribute to variational and numerical description of driven dipolar systems and their properties, which are important for ongoing experiments, and will be of particular interest as the strongly dipolar regime becomes experimentally available.

To describe the dynamics of the Faraday and resonant waves in dipolar BECs, we relied here on the variational approach introduced in Ref. [16] (and references therein), which was already used in various setups [17–20,23–25,30,41,42]. This approach is based on the Gaussian variational ansatz and includes the condensate widths and the conjugated dynamical phases as parameters. The ansatz also includes the density modulations in order to capture the dynamics of density waves. Using our variational approach, the obtained equations for the dynamical evolution of the system are cast into the form of the Mathieu-like differential equation. This allowed us to identify the most unstable solutions of the Mathieu's equation with the Faraday and the resonant waves, which we observed numerically. Based on this idea, we derived analytical expressions for the periods of these two types of density waves. Performing the FFT analysis of the results of extensive numerical simulations, we were able to calculate the corresponding periods numerically, as functions of the contact and the dipole-dipole interaction strength. The comparison of variational and numerical results shows very good agreement and demonstrates that the derived analytical expressions provide full understanding of the properties of density waves in dipolar condensates.

In the future, we plan to study onset times for the emergence of Faraday and resonant waves, and in particular the corresponding exponents and their dependence on the contact and the DDI. It is well known that the periodic driving of a dipolar system may lead to its collapse, and we plan to investigate if recently observed quantum droplets, that appear as a result of stabilization due to quantum fluctuations, may also appear in a scenario which leads to Faraday waves.

Author Contributions: Conceptualization, methodology, software, validation, formal analysis, writing—original draft preparation, and writing—review and editing, both authors; investigation, data curation, and visualization, D.V.; and resources, supervision, project administration, and funding acquisition, A.B.

Funding: This research was funded by the Ministry of Education, Science, and Technological Development of the Republic of Serbia under project ON171017.

Acknowledgments: We would like to acknowledge inspiring discussions with Vladimir Veljić and Ivana Vasić. Numerical simulations were run on the PARADOX-IV supercomputing facility at the Scientific Computing Laboratory, National Center of Excellence for the Study of Complex Systems, Institute of Physics Belgrade.

Conflicts of Interest: The authors declare no conflict of interest.

References

1. Lahaye, T.; Koch, T.; Fröhlich, B.; Fattori, M.; Metz, J.; Griesmaier, A.; Giovanazzi, S.; Pfau, T. Strong dipolar effects in a quantum ferrofluid. *Nature* **2007**, *448*, 672. [[CrossRef](#)] [[PubMed](#)]
2. Lu, M.; Burdick, N.Q.; Youn, S.H.; Lev, B.L. Strongly dipolar Bose-Einstein condensate of dysprosium. *Phys. Rev. Lett.* **2011**, *107*, 190401. [[CrossRef](#)] [[PubMed](#)]
3. Aikawa, K.; Frisch, A.; Mark, M.; Baier, S.; Rietzler, A.; Grimm, R.; Ferlaino, F. Bose-Einstein condensation of erbium. *Phys. Rev. Lett.* **2012**, *108*, 210401. [[CrossRef](#)] [[PubMed](#)]
4. De Miranda, M.H.G.; Chotia, A.; Neyenhuis, B.; Wang, D.; Quemener, G.; Ospelkaus, S.; Bohn, J.L.; Ye, J.; Jin, D.S. Controlling the quantum stereodynamics of ultracold bimolecular reactions. *Nat. Phys.* **2011**, *7*, 502. [[CrossRef](#)]
5. Frisch, A.; Mark, M.; Aikawa, K.; Baier, S.; Grimm, R.; Petrov, A.; Kotochigova, S.; Quemener, G.; Lepers, M.; Dulieu, O.; Ferlaino, F. Ultracold dipolar molecules composed of strongly magnetic atoms. *Phys. Rev. Lett.* **2015**, *115*, 203201. [[CrossRef](#)] [[PubMed](#)]
6. Baranov, M.A. Theoretical progress in many-body physics with ultracold dipolar gases. *Phys. Rep.* **2008**, *464*, 71. [[CrossRef](#)]
7. Inouye, S.; Andrews, M.R.; Stenger, J.; Miesner, H.J.; Stamper-Kurn, D.M.; Ketterle, W. Observation of Feshbach resonances in a Bose-Einstein condensate. *Nature* **1998**, *392*, 32354. [[CrossRef](#)]
8. Giovanazzi, S.; Görlitz, A.; Pfau, T. Tuning the Dipolar Interaction in Quantum Gases. *Phys. Rev. Lett.* **2002**, *89*, 130401. [[CrossRef](#)]
9. Tang, Y.; Kao, W.; Li, K.Y.; Lev, B.L. Tuning the Dipole-Dipole Interaction in a Quantum Gas with a Rotating Magnetic Field. *Phys. Rev. Lett.* **2018**, *120*, 230401. [[CrossRef](#)]
10. Faraday, M. On a peculiar class of acoustical figures; and on certain forms assumed by groups of particles upon vibrating elastic surfaces. *Phil. Trans. R. Soc. Lond.* **1831**, *121*, 299. [[CrossRef](#)]
11. Staliunas, K.; Longhi, S.; de Valcárcel, G.J. Faraday patterns in Bose-Einstein condensates. *Phys. Rev. Lett.* **2002**, *89*, 210406. [[CrossRef](#)] [[PubMed](#)]
12. Engels, P.; Atherton, C.; Hofer, M.A. Observation of Faraday waves in a Bose-Einstein condensate. *Phys. Rev. Lett.* **2007**, *98*, 095301. [[CrossRef](#)] [[PubMed](#)]
13. Pollack, S.E.; Dries, D.; Hulet, R.G.; Magalhães, K.M.F.; Henn, E.A.L.; Ramos, E.R.F.; Caracanhas, M.A.; Bagnato, V.S. Collective excitation of a Bose-Einstein condensate by modulation of the atomic scattering length. *Phys. Rev. A* **2010**, *81*, 053627. [[CrossRef](#)]
14. Nguyen, J.H.V.; Tsatsos, M.C.; Luo, D.; Lode, A.U.J.; Telles, G.D.; Bagnato, V.S.; Hulet, R.G. Parametric Excitation of a Bose-Einstein Condensate: From Faraday Waves to Granulation. *Phys. Rev. X* **2019**, *9*, 011052. [[CrossRef](#)]
15. Abe, H.; Ueda, T.; Morikawa, M.; Saitoh, Y.; Nomura, R.; Okuda, Y. Faraday instability of superfluid surface. *Phys. Rev. E* **2007**, *76*, 046305. [[CrossRef](#)] [[PubMed](#)]
16. Nicolin, A.I.; Carretero-González, R.; Kevrekidis, P.G. Faraday waves in Bose-Einstein condensates. *Phys. Rev. A* **2007**, *76*, 063609. [[CrossRef](#)]
17. Nicolin, A.I.; Raportaru, M.C. Faraday waves in high-density cigar-shaped Bose-Einstein condensates. *Phys. A* **2010**, *389*, 1062. [[CrossRef](#)]
18. Nicolin, A.I.; Raportaru, M.C. Faraday waves in one-dimensional Bose-Einstein condensates. *Proc. Rom. Acad.* **2011**, *12*, 209.
19. Nicolin, A.I. Faraday waves in Bose-Einstein condensates subject to anisotropic transverse confinement. *Rom. Rep. Phys.* **2011**, *63*, 1329.
20. Balasubramanian, S.; Ramaswamy, R.; Nicolin, A.I. Faraday waves in cigar-shaped Bose-Einstein condensates with radially inhomogeneous scattering lengths. *Rom. Rep. Phys.* **2013**, *65*, 820.
21. Nath, R.; Santos, L. Faraday patterns in two-dimensional dipolar Bose-Einstein condensates. *Phys. Rev. A* **2010**, *81*, 033626. [[CrossRef](#)]

22. Łakomy, K.; Nath, R.; Santos, L. Faraday patterns in coupled one-dimensional dipolar condensates. *Phys. Rev. A* **2012**, *86*, 023620. [[CrossRef](#)]
23. Nicolin, A.I. Density waves in dipolar Bose-Einstein condensates. *Proc. Rom. Acad.* **2013**, *14*, 35.
24. Balaž, A.; Nicolin, I. Faraday waves in binary nonmiscible Bose-Einstein condensates. *Phys. Rev. A* **2012**, *85*, 023613. [[CrossRef](#)]
25. Balaž, A.; Paun, R.; Nicolin, A.I.; Balasubramanian, S.; Ramaswamy, R. Faraday waves in collisionally inhomogeneous Bose-Einstein condensates. *Phys. Rev. A* **2014**, *89*, 023609. [[CrossRef](#)]
26. Abdullaev, F.K.; Ögren, M.; Sørensen, M.P. Faraday waves in quasi-one-dimensional superfluid Fermi-Bose mixtures. *Phys. Rev. A* **2013**, *87*, 023616. [[CrossRef](#)]
27. Capuzzi, P.; Vignolo, P. Faraday waves in elongated superfluid fermionic clouds. *Phys. Rev. A* **2008**, *78*, 043613. [[CrossRef](#)]
28. Tang, R.A.; Li, H.C.; Xue, J.K. Faraday instability and Faraday patterns in a superfluid Fermi gas. *J. Phys. B* **2011**, *44*, 115303. [[CrossRef](#)]
29. McLachlan, N.W. *Theory and Application of Mathieu Functions*; Oxford University Press: New York, NY, USA, 1951.
30. Nicolin, A.I. Resonant wave formation in Bose-Einstein condensates. *Phys. Rev. E* **2011**, *84*, 056202. [[CrossRef](#)]
31. Capuzzi, P.; Gattobigio, M.; Vignolo, P. Suppression of Faraday waves in a Bose-Einstein condensate in the presence of an optical lattice. *Phys. Rev. A* **2011**, *83*, 013603. [[CrossRef](#)]
32. Staliunas, K. Removal of excitations of Bose-Einstein condensates by space- and time-modulated potentials. *Phys. Rev. A* **2011**, *84*, 013626. [[CrossRef](#)]
33. Gaul, C.; Díaz, E.; Lima, R.P.A.; Domínguez-Adame, F.; Müller, C.A. Stability and decay of Bloch oscillations in the presence of time-dependent nonlinearity. *Phys. Rev. A* **2011**, *84*, 053627. [[CrossRef](#)]
34. Díaz, E.; Mena, A.G.; Asakura, K.; Gaul, C. Super-Bloch oscillations with modulated interaction. *Phys. Rev. A* **2013**, *87*, 015601. [[CrossRef](#)]
35. Brouzos, I.; Schmelcher, P. Controlled excitation and resonant acceleration of ultracold few-boson systems by driven interactions in a harmonic trap. *Phys. Rev. A* **2012**, *85*, 033635. [[CrossRef](#)]
36. Diakonov, F.K.; Kalozoumis, P.A.; Karanikas, A.I.; Manifavas, N.; Schmelcher, P. Geometric-phase-propagator approach to time-dependent quantum systems. *Phys. Rev. A* **2012**, *85*, 062110. [[CrossRef](#)]
37. Al-Jibbouri, H.; Pelster, A. Breakdown of the Kohn theorem near a Feshbach resonance in a magnetic trap. *Phys. Rev. A* **2013**, *88*, 033621. [[CrossRef](#)]
38. Kobayakov, D.; Bezett, A.; Lundh, E.; Marklund, M.; Bychkov, V. Quantum swapping of immiscible Bose-Einstein condensates as an alternative to the Rayleigh-Taylor instability. *Phys. Rev. A* **2012**, *85*, 013630. [[CrossRef](#)]
39. Hu, W.H.; Jin, L.; Song, Z. Dynamics of one-dimensional tight-binding models with arbitrary time-dependent external homogeneous fields. *Quantum Inf. Process.* **2013**, *12*, 3569. [[CrossRef](#)]
40. Sakhel, R.R.; Sakhel, A.R.; Ghassib, H.B. Nonequilibrium Dynamics of a Bose-Einstein Condensate Excited by a Red Laser Inside a Power-Law Trap with Hard Walls. *J. Low Temp. Phys.* **2013**, *173*, 177. [[CrossRef](#)]
41. Sudharsan, J.B.; Radha, R.; Raportaru, M.C.; Nicolin, A.I.; Balaz, A. Faraday and resonant waves in binary collisionally-inhomogeneous Bose-Einstein condensates. *J. Phys. B* **2016**, *49*, 165303. [[CrossRef](#)]
42. Nicolin, A.I. Variational treatment of Faraday waves in inhomogeneous Bose-Einstein condensates. *Phys. A* **2012**, *391*, 1062. [[CrossRef](#)]
43. Giovanazzi, S.; Pedri, P.; Santos, L.; Griesmaier, A.; Fattori, M.; Koch, T.; Stuhler, J.; Pfau, T. Expansion dynamics of a dipolar Bose-Einstein condensate. *Phys. Rev. A* **2006**, *74*, 013621. [[CrossRef](#)]
44. Muruganandam, P.; Adhikari, S.K. Fortran programs for the time-dependent Gross-Pitaevskii equation in a fully anisotropic trap. *Comput. Phys. Commun.* **2009**, *180*, 1888. [[CrossRef](#)]
45. Vudragović, D.; Vidanović, I.; Balaž, A.; Muruganandam, P.; Adhikari, S.K. C Programs for solving the time-dependent Gross-Pitaevskii equation in a fully anisotropic trap. *Comput. Phys. Commun.* **2012**, *183*, 2021. [[CrossRef](#)]
46. Kumar, R.K.; Young-S., L.E.; Vudragović, D.; Balaž, A.; Muruganandam, P.; Adhikari, S.K. Fortran and C programs for the time-dependent dipolar Gross-Pitaevskii equation in an anisotropic trap. *Comput. Phys. Commun.* **2015**, *195*, 117. [[CrossRef](#)]

47. Lončar, V.; Balaž, A.; Bogojević, A.; Škrbić, S.; Muruganandam, P.; Adhikari, S.K. CUDA programs for solving the time-dependent dipolar Gross-Pitaevskii equation in an anisotropic trap. *Comput. Phys. Commun.* **2016**, *200*, 406. [[CrossRef](#)]
48. Satarić, B.; Slavnić, V.; Belić, A.; Balaž, A.; Muruganandam, P.; Adhikari, S.K. Hybrid OpenMP/MPI programs for solving the time-dependent Gross-Pitaevskii equation in a fully anisotropic trap. *Comput. Phys. Commun.* **2016**, *200*, 411. [[CrossRef](#)]
49. Young-S., L.E.; Vudragović, D.; Muruganandam, P.; Adhikari, S.K.; Balaž, A. OpenMP Fortran and C programs for solving the time-dependent Gross-Pitaevskii equation in an anisotropic trap. *Comput. Phys. Commun.* **2016**, *204*, 209. [[CrossRef](#)]
50. Young-S., L.E.; Muruganandam, P.; Adhikari, S.K.; Lončar, V.; Vudragović, D.; Balaž, A. OpenMP GNU and Intel Fortran programs for solving the time-dependent Gross-Pitaevskii equation. *Comput. Phys. Commun.* **2017**, *220*, 503. [[CrossRef](#)]
51. Lončar, V.; Young-S., L.E.; Škrbić, S.; Muruganandam, P.; Adhikari, S.K.; Balaž, A. OpenMP, OpenMP/MPI, and CUDA/MPI C programs for solving the time-dependent dipolar Gross-Pitaevskii equation. *Comput. Phys. Commun.* **2016**, *209*, 190. [[CrossRef](#)]
52. Kumar, R.K.; Lončar, V.; Muruganandam, P.; Adhikari, S.K.; Balaž, A. C and Fortran OpenMP programs for rotating Bose-Einstein condensates. *Comput. Phys. Commun.* **2019**, *240*, 74. [[CrossRef](#)]



© 2019 by the authors. Licensee MDPI, Basel, Switzerland. This article is an open access article distributed under the terms and conditions of the Creative Commons Attribution (CC BY) license (<http://creativecommons.org/licenses/by/4.0/>).



VI-SEEM DREAMCLIMATE SERVICE

DUŠAN VUDRAGOVIĆ*, LUKA ILIĆ†, PETAR JOVANOVIĆ‡, SLOBODAN NIČKOVIĆ§, ALEKSANDAR BOGOJEVIĆ¶
AND ANTUN BALAZŽ||

Abstract. Premature human mortality due to cardiopulmonary disease and lung cancer is found in epidemiological studies to be correlated to increased levels of atmospheric particulate matter. Such negative dust effects on the human mortality in the North Africa – Europe – Middle East region can be successfully studied by the DREAM dust model. However, to assess health effects of dust and its other impacts on the environment, a detailed modelling of the climate for a period of one year in a high-resolution mode is required. We describe here a parallel implementation of the DREAM dust model, the DREAMCLIMATE service, which is optimised for use on the high-performance regional infrastructure provided by the VI-SEEM project. In addition to development and integration of this service, we also present a use-case study of premature mortality due to desert dust in the North Africa – Europe – Middle East region for the year 2005, to demonstrate how the newly deployed service can be used.

Key words: DREAM model, dust effects, human mortality, VI-SEEM project, application service

AMS subject classifications. 68W10, 68M14, 68N30

1. Introduction. Exposure to airborne mineral dust particles can significantly influence human health. Atmospheric dust particles are primarily driven by mesoscale and synoptic processes, and may be present in high concentrations near the sources and carried over long distances while having adverse health effects. Drought and desertification, as climate-related changes and human activities such as changes in land use, affect potential dust sources of fine particulate matter in arid areas. Therefore, numerical modelling with sufficiently high resolution of the processes of the atmospheric dust cycle that drive dust emissions and transport is a useful approach to assessment of the potential health effects of exposure to dust.

The previously developed Dust REgional Atmospheric Modeling (DREAM) system [1] is a component of a comprehensive atmospheric model designed to simulate and predict the atmospheric cycle of mineral dust aerosols. The DREAM provides a climatology of dust based on long-term re-analysis of the model. It is widely used by the research and operational dust forecasting communities in more than 20 countries, including its recent use in a series of NASA-funded projects [2, 3, 4, 5] dealing with health aspects of dust suspended in the air. The Institute of Physics Belgrade group, which is a partner in the Sand and Dust Storm Warning Advisory and Assessment System (SDS-WAS) project of the World Meteorological Organization, uses DREAM to provide daily dust forecasts to the SDS-WAS model inter-comparisons and validation activities. Also, it is used for investigation on how fine particulate matter contributes to air pollution in North Africa – Europe – Middle East region.

To assess health effects of dust in the region and other dust impacts on the environment, it is usual to consider at least a one-year modelling climatology for the given region. In this case this was achieved by solving the DREAM model in a high-resolution mode with the horizontal grid resolution of 15 km. Such a high resolution model is capable to accurately describe the behaviour of small-scale dust sources in the desert areas (Sahara, Middle East), as well as the mesoscale atmospheric conditions. However, due to numerical complexity it requires a parallelised version of the DREAM code, which we created and optimised for usage on high-performance computing infrastructures available today.

*Scientific Computing Laboratory, Center for the Study of Complex Systems, Institute of Physics Belgrade, University of Belgrade, Serbia (dusan.vudragovic@ipb.ac.rs).

†Environmental Physics Laboratory, Institute of Physics Belgrade, University of Belgrade, Serbia (luka.ilic@ipb.ac.rs).

‡Scientific Computing Laboratory, Center for the Study of Complex Systems, Institute of Physics Belgrade, University of Belgrade, Serbia (petar.jovanovic@ipb.ac.rs).

§Environmental Physics Laboratory, Institute of Physics Belgrade, University of Belgrade, Serbia (slobodan.nickovic@ipb.ac.rs).

¶Scientific Computing Laboratory, Center for the Study of Complex Systems, Institute of Physics Belgrade, University of Belgrade, Serbia (aleksandar.bogojevic@ipb.ac.rs).

||Scientific Computing Laboratory, Center for the Study of Complex Systems, Institute of Physics Belgrade, University of Belgrade, Serbia (antun.balaz@ipb.ac.rs).

In parallel to development of the DREAM model, a number of initiatives were crucial for enabling high-quality climate research in the region. This was achieved by providing e-Infrastructure resources, application support and training through the VI-SEEM project [6], funded by the EU H2020 programme. The project brings together regional e-Infrastructures in order to build capacity and better utilise synergies, as well as to provide improved service within a unified virtual research environment for several inter-disciplinary scientific user communities. The overall aim is to offer a user-friendly integrated e-Infrastructure platform for regional cross-border scientific communities in climatology, life sciences, and cultural heritage. This includes integration of computing, data, and visualisation resources, as well as services, models, software solutions and tools. The VI-SEEM virtual research environment provides the support to scientists in a full lifecycle of collaborative research.

By efforts of the DREAM code developers and the VI-SEEM support team, the DREAM model was successfully refactored and tuned for usage on high-performance computing infrastructures in a form of the DREAMCLIMATE service, presented here. Section 2 briefly describes the DREAM model, which is capable of producing results in the required high-resolution mode for a one year period. The DREAMCLIMATE service is presented in detail in Section 3, while Section 4 describes produced datasets and main results. By using an order of magnitude finer DREAM model grid than available before, we perform a detailed analysis of dust impacts to public health.

2. DREAM model. Premature human mortality due to cardiopulmonary disease and lung cancer is found in epidemiological studies to be correlated to increased levels of atmospheric particulate matter, in particular to long-term exposure to particulate matter with an aerodynamic diameter smaller than $2.5 \mu\text{m}$. In order to estimate the premature mortality caused by the long-term exposure to airborne desert dust, we use results of the DREAM gridded model dust climatology of fine particulate matter and dust concentrations. This analysis follows the previous study [7] that indicates that there is a large number of premature deaths by cardiopulmonary disease and a significant number of deaths by lung cancer, mostly in the dust belt region neighbouring Sahara and Middle East deserts.

The DREAM model is developed as an add-on component of a comprehensive atmospheric model and is designed to simulate and/or predict the atmospheric cycle of mineral dust aerosols. It solves a coupled system of the Euler-type partial differential nonlinear equations for dust mass continuity, one equation for each particle size class, which is one of the governing prognostic equations in an atmospheric numerical prediction model [8, 9, 10]. The DREAM model takes into account all major processes of the atmospheric dust cycle. During the model simulation, calculation of the surface dust emission fluxes is made over the model cells declared as deserts. A viscous sub-layer parameterisation regulates the amount of dust mass emission for a range of near-surface turbulent regimes. Once injected into the air, dust aerosols are driven by the atmospheric dynamics and corresponding physical quantities: by turbulence in the early stage of the process, when dust is lifted from the ground to the upper levels; by winds in later phases of the process, when dust travels away from the sources; and finally, by thermodynamic processes, rainfall and land cover features that provide wet and dry deposition of dust over the Earth surface.

The model is implemented as a bundle of Fortran programs and libraries. These components are divided into three groups: the preprocessing system, the model operational system, and post-processing and visualisation tools. The preprocessing consists of two phases. The first is the setup in which the simulation domain, model configuration and interpolation of terrestrial data are defined. These parameters are mostly hard-coded and any change to parameters in this phase requires recompilation. The second stage of preprocessing is interpolation of the meteorological input data from the global meteorological model to the current simulation domain, as well as a setup of initial boundary conditions for the dust model. The model operational system is the main component, and it runs the numerical integration program. Post-processing and visualisation tools include GrADS [11] with conversion from Arakawa E-grid to geo-referenced grid and plots.

The code is predominantly written in the style of the Fortran 77 standard. Some of the more pressing constraints of the standard were the lack of support for dynamic memory allocation and command line arguments. These two constraints required for a number of parameters to be hard-coded. As a consequence, this limited the number of users who could use the application independently, and the number of parallel tests that could be ran at once. Recompilation also requires a deep technical knowledge of the implementation itself, which reduces

usability and dissemination of the model.

3. DREAMCLIMATE service. Within the framework of the VI-SEEM project, the DREAM model was successfully re-factored and tuned for usage on high-performance computing infrastructures. The DREAMCLIMATE service was developed and deployed using the VI-SEEM infrastructure modules. Configuration of the considered physical system is separated from the source code of the application, and all relevant parameters are grouped into a single configuration file. Such an improved configuration approach enabled more user-friendly way to configure various model setups, without the need for each user to dive into the code and technical details of the implementation. This also enables multiple users to run their model instances independently. Important additional improvements include significant reduction of the disk-space consumption, as well as standardisation of its usage through an environment-module approach.

Configuration files follow the format of the Python configuration parser, which is a convenient, flexible, and powerful way for parsing configuration files. It uses simple INI style configuration syntax, i.e., a text file with a basic structure composed of sections, properties, and values. Parameters are divided into sections which are designated by square brackets. Within one section, each parameter is specified in a separate line and its name and value are delimited by the equals sign. In-line comments are also permissible and corresponding lines begin with a semicolon. In addition to this, a support for variable interpolation is included as well.

The DREAM processing stages remain similar to the original version of the code, and consist of the pre-processing, the model operational processing, and the post-processing phase. Majority of changes are related to reducing the complexity of configuration in the setup stage of preprocessing. In a typical use-case, a user begins the simulation project by loading the environment module for the DREAMCLIMATE service, which sets the environment paths for the commands used to initialise and prepare the DREAM model simulation. Afterwards, by invoking the `dreamclimate_init` script the default configuration file is created in the working directory and files needed for a configuration of the local simulation instance are created in the `.dreamclimate` subdirectory. After the parameters are set in the configuration file, the `dreamclimate_reconfig` script is called to execute the setup stage, which encapsulates recompilation of the components, depending on the parameters changed. The resulting binaries, which are used to run simulation, are placed in the `.dreamclimate/bin` directory. This step isolates each user's simulation instance from others and enables multiple instances to work without interference. The next step in this stage generates and interpolates vegetation and soil texture for the forecast domain, by calling the `gt30mounth`, `gt30source`, `gt30vegetadirect`, `text4eta`, and `texteta` components.

After the setup, preprocessing continues by invoking the `dreamclimate_preproc` script whose role is to prepare input data for the Eta model grid. This script invokes the following components:

- `climsst` – horizontal grid (IMT, JMT) Eta model indexing from the SST as a function of the month,
- `anecw` – horizontal grid (IMT, JMT) Eta model indexing from global initial data,
- `pusiWRF` – set of the vertical variables and vertical interpolation of the pressure to sigma surfaces,
- `const` – conversion of the initial fields in Eta model coordinates from 2D horizontal (IMT, JMT) indexing to 1D (IMJM), definition of dummy initial boundary soil moisture and temperature values, and calculation of the constants needed for the 1D version of the soil model,
- `dboco` – creation of the boundary condition files,
- `gfdlco2` – interpolation of the transmission functions grid, for which the transmission functions have been pre-calculated, to the grid structure.

This preprocessing step produces binary files interpolated to the model grid (i.e., Arakawa E-grid) in the output directory specified in the configuration file. All the routines of the model itself, which describe atmospheric processes including the dust cycle, are built into the main executable file. This is a parallel MPI program that runs the simulation and is submitted to the job scheduling system using the job description script, which is automatically generated earlier in the setup stage. The post-processing includes the conversion of the main GrADS output file from the Arakawa E-grid to the GrADS grid. These steps are handled by the `dreamclimate_post-process` script.

Many of the configuration parameters in the generated configuration file have sensible default values, to minimise the need for users to search through lengthy lists of output file locations. The domain parameters of interest for configuring the model itself, inside the ALLINC section, are:

- `TLM0D` – longitude of the centre point of the domain,

- TPH0D – latitude of the centre point of the domain,
- WBD – western boundary of the domain with respect to the centre point (always less than 0),
- SBD – southern boundary of the domain with respect to the centre point (always less than 0),
- DLMD – longitudinal model grid resolution,
- DPHD – latitudinal model grid resolution,
- DTB – time step of the model, which depends on DLMD and DPHD values by means of the Courant-Friedrichs-Lewy (CFL) criteria,
- LM – the number of vertical levels.

Another set of commonly changed model parameters are dimensions of the model grid. These are grouped in the PARMETA section of the configuration file:

- IM – the number of mass grid points along the first row, essentially half of the total number of grid points in the west-east direction, due to the horizontal staggering of mass and wind points,
- JM – the number of rows in the north-south direction.

These parameters also influence the number of processes and the topology of the MPI parallel execution.

The rest of the parameters in the configuration file specify paths for input, output and intermediate files. With these paths defined during configuration, a significant reduction in disk space usage was achieved, as the data files no longer need to be copied together with the code, and no longer have to be in fixed relative locations.

The DREAMCLIMATE service is deployed during the first VI-SEEM development access call at the PARADOX high-performance computing cluster [12], hosted by the Scientific Computing Laboratory, Center for the Study of Complex Systems of the Institute of Physics Belgrade. This cluster is part of the VI-SEEM infrastructure, and consists of 106 working nodes. Working nodes (HP ProLiant SL250s Gen8) are configured with two Intel Xeon E5-2670 8-core Sandy Bridge processors, at a frequency of 2.6 GHz and 32 GB of RAM. The total number of CPU-cores available in the cluster is 1696, and each working node contains an additional GP-GPU card (NVIDIA Tesla M2090) with 6 GB of RAM. The peak computing power is 105 TFlops. The PARADOX provides a data storage system, which consists of two service nodes (HP DL380p Gen8) and 5 additional disk enclosures. One disk enclosure is configured with 12 SAS drives of 300 GB each (3.6 TB in total), while the other four disk enclosures are configured each with 12 SATA drives of 2 TB (96 TB in total), so that the cluster provides around 100 TB of storage space. Storage space is distributed via a Lustre high-performance parallel file system that uses Infiniband QDR interconnect technology, and is available on both working and service nodes.

Although the DREAMCLIMATE code is a copyright-protected software, it can be obtained for research purposes with the permission of the principal investigator (S. Ničković). Therefore, the DREAMCLIMATE service source code is only internally available at the VI-SEEM code repository [13], as well as a module at the PARADOX cluster software repository. Transfer of the software to third parties or its use for commercial purposes is not permitted, unless a written permission from the author is received.

4. Produced datasets and results. Using the DREAMCLIMATE service at PARADOX during the first VI-SEEM call for production use of resources and services, we produced a dataset with the aerosol optical thickness and surface dust concentration for the one-year period. We selected the year 2005 for this analysis, which serves as an example and demonstrates usability of DREAMCLIMATE service. The dataset covers wide region of North Africa, Southern Europe and Middle East in 30 km horizontal resolution with 28 vertical levels, and is made publicly available via the VI-SEEM data repository [14].

In addition to this initial dataset, we also produced a dataset with a higher resolution of 15 km for the same region and period of time. The global mean DREAMCLIMATE-modelled dust concentration for year 2005 is presented in Fig. 4.1.

Using the human health impact function introduced in Refs. [15, 16], we can relate the changes in pollutant concentrations to the changes in human mortality, and estimate the global annual premature mortality due to airborne desert dust. For this, we use as a baseline the mortality rate estimated by the World Health Organization (WHO) Statistical Information System on the country-level based on the International Classification of Diseases 10th Revision (ICD-10) classification, and regional data from the WHO Global burden of disease for countries with no data. Population statistics we used for the year 2005 is based on the United Nations Department of Economic and Social Affairs (UNDES 2011) database, while gridded global population numbers

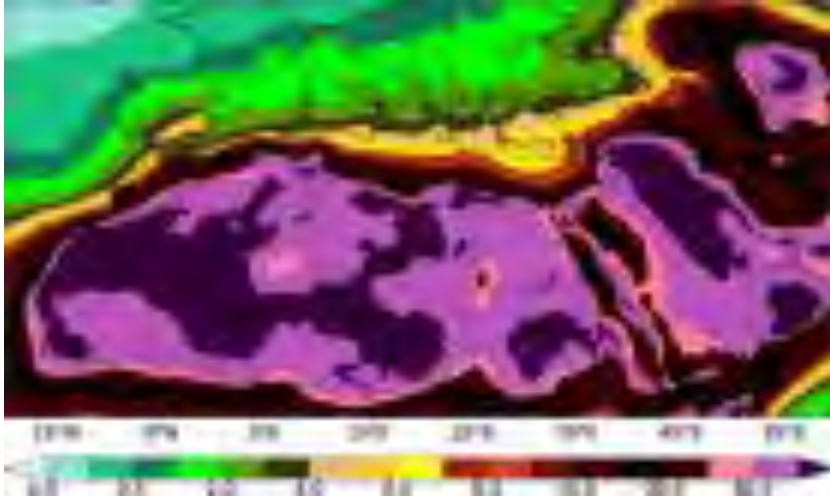


FIG. 4.1. Calculated mean dust concentrations in $\mu\text{g}/\text{m}^3$, obtained from the DREAMCLIMATE model. The model integration area covers region of North Africa, Southern Europe and Middle East, with 15 km horizontal resolution in 28 vertical levels for the year 2005.

TABLE 4.1
Total CPD and LC premature mortalities for the threshold concentrations between 0 and $10 \mu\text{g}/\text{m}^3$.

Baseline concentration (in $\mu\text{g}/\text{m}^3$)	0	5.0	7.5	10
CPD premature mortality (in thousands)	765	615	567	524
LC premature mortality (in thousands)	14.8	10.2	9.1	8.4

are taken from the Columbia University Center for International Earth Science Information Network (CIESIN) database. We used the population cohort of 30 years and older in the health impact function.

Applying the health impact function to the considered population, the DREAM model output suggests a significant contribution of desert dust to premature human mortality. For the global background of dust concentration of $7.5 \mu\text{g}/\text{m}^3$ i.e., threshold below which no premature mortality occurs, the estimated premature mortality (per grid cell) by cardiopulmonary disease (CPD) and lung cancer (LC) is illustrated in Fig. 4.2. In total, around 570,000 premature deaths in the model domain are predicted to occur during a one-year period, as a negative consequence of dust. According to our results, top five countries with the highest induced CPD-mortality in the year 2005 are: Egypt with 74,000; Iraq with 67,000; Iran with 50,000; Nigeria with 46,000; Sudan with 45,000. On the other hand, top five countries with the highest induced LC-mortality in the same year are: Iraq with 1,200; Iran with 900; Sudan with 800; Egypt with 800; Uzbekistan and Turkey with 500 premature deaths each.

We also investigated the sensitivity of our results on the value of the threshold concentrations, which is above assumed to be $7.5 \mu\text{g}/\text{m}^3$. Table 4.1 gives the obtained total CPD and LC premature mortalities for the threshold concentrations between 0 and $10 \mu\text{g}/\text{m}^3$. This analysis is presented to showcase capabilities of the model and the developed DREAMCLIMATE service, and can be efficiently used to study desired regions and time periods if the required input data are provided.

5. Conclusions. Using the VI-SEEM project infrastructure and services, we have successfully re-factored the DREAM atmospheric model. We have developed and implemented the DREAMCLIMATE service, which is tuned for usage on high-performance computing infrastructures available today. In order to demonstrate a typical use-case, we have produced a dataset with the aerosol optical thickness and surface dust concentration for the one-year period for the wide region of North Africa, Southern Europe and Middle East. We have used

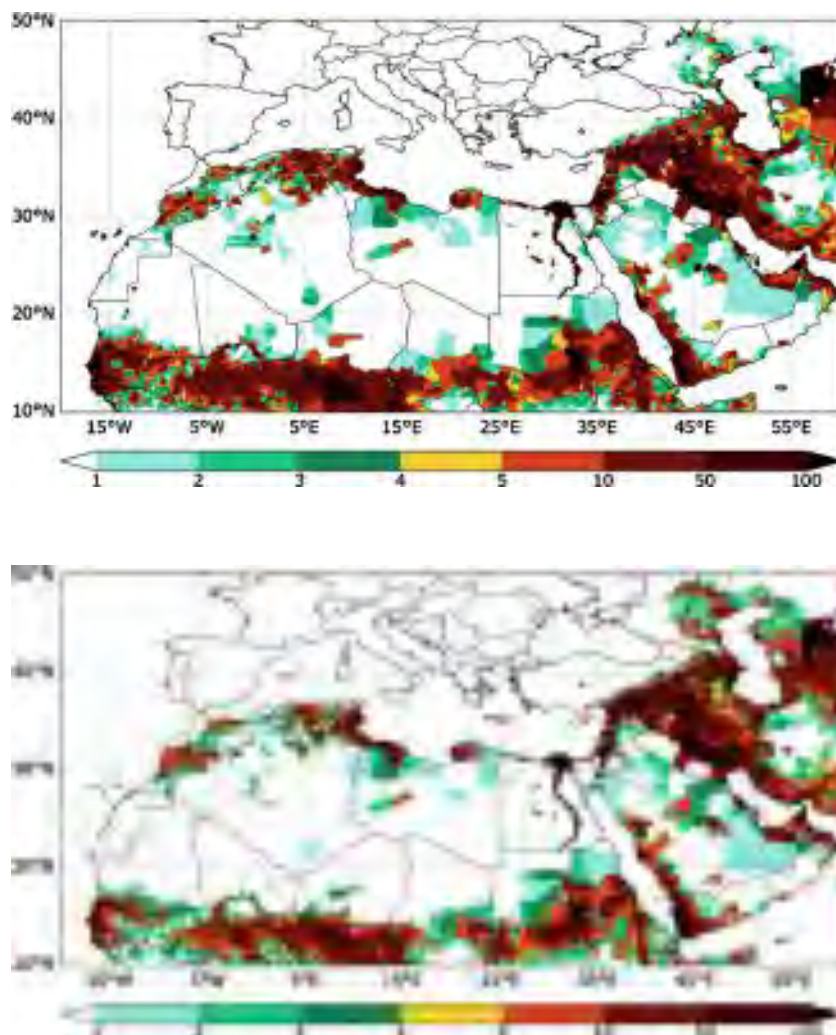


FIG. 4.2. Estimated global premature mortality per grid cell by cardiopulmonary disease (top) and lung cancer (down) due to the long-term exposure to desert dust with an aerodynamic diameter smaller than $2.5 \mu\text{m}$, calculated by the VI-SEEM DREAMCLIMATE service.

both the 30 km and the 15 km horizontal resolution, with 28 vertical levels. To showcase how results of the DREAMCLIMATE service can be applied, using the human health impact function and calculated global fine particulate matter concentrations, we have estimated the premature mortality caused by the long-term exposure to airborne desert dust with an aerodynamic diameter smaller than $2.5 \mu\text{m}$ for the year 2005 in the considered region. The results show that the large total number of premature deaths (around 570,000) in the model domain is mainly due to cardiopulmonary disease, but a significant number of deaths is also caused by lung cancer. The model also shows high sensitivity of the results on the threshold concentration, which is a significant parameter of relevance to public health.

Acknowledgments. This work was supported by the Ministry of Education, Science, and Technological Development of the Republic of Serbia under projects ON171017 and III43007, and by the European Commission under H2020 project VI-SEEM, Grant No. 675121. Numerical simulations were run on the PARADOX supercomputing facility at the Scientific Computing Laboratory of the Institute of Physics Belgrade.

REFERENCES

- [1] S. NIČKOVIĆ, G. KALLOS, A. PAPADOPOULOS AND O. KAKALIAGOU, *A model for prediction of desert dust cycle in the atmosphere*, J. Geophys. Res., 106 (2001), pp. 18113-18129.
- [2] D. YIN AND W. A. SPRIGG, *Modeling Airborne Mineral Dust: A Mexico - United States Trans-boundary Perspective*, in Southwestern Desert Resources, W. Halvorson, C. Schwalbe and C. van Riper, eds., University of Arizona Press, Tucson, AZ, (2010), pp. 303-317.
- [3] D. YIN, S. NICKOVIC AND W. A. SPRIGG, *The impact of using different land cover data on wind-blown desert dust modeling results in the southwestern*, Atmos. Environ., 41 (2007), pp. 2214-2224.
- [4] W. A. SPRIGG, S. NIČKOVIĆ, J. N. GALGANI, G. PEJANOVIĆ, S. PETKOVIĆ, M. VUJADINOVIĆ, A. VUKOVIĆ, M. DACIĆ, S. DI BIASE, A. PRASAD AND H. EL-ASKARY, *Regional dust storm modeling for health services: The case of valley fever*, Aeolian Res., 14 (2014), pp. 53-73.
- [5] A. VUKOVIĆ, M. VUJADINOVIĆ, G. PEJANOVIĆ, J. ANDRIĆ, M. R. KUMJIAN, V. DJURDJEVIĆ, M. DACIĆ, A. K. PRASAD, H. M. EL-ASKARY, B. C. PARIS, S. PETKOVIĆ, S. NIČKOVIĆ AND W. A. SPRIGG, *Numerical simulation of "an American haboob"*, Atmos. Chem. Phys., 14 (2014), pp. 3211-3230.
- [6] D. VUDRAGOVIĆ, P. JOVANOVIĆ AND A. BALAŽ, *VI-SEEM Virtual Research Environment*, 10th RO-LCG Conference, Sinaia, Romania, 26-28 October 2017.
- [7] D. GIANNADAKI, A. POZZER AND J. LELIEVELD, *Modeled global effects of airborne desert dust on air quality and premature mortality*, Atmos. Chem. Phys., 14 (2014), pp. 957-968.
- [8] Z. I. JANJIĆ, *The Step-Mountain Coordinate: Physical Package*, Mon. Wea. Rev., 118 (1990), pp. 1429-1443.
- [9] Z. I. JANJIĆ, *The Step-mountain Eta Coordinate Model: Further developments of the convection, viscous sublayer and turbulence closure schemes*, Mon. Wea. Rev., 122 (1994), pp. 927-945.
- [10] S. NIČKOVIĆ AND S. DOBRICIC, *A model for long-range transport of desert dust*, Mon. Wea. Rev., 124 (1996), pp. 2537-2544.
- [11] Grid Analysis and Display System (GrADS),
<http://cola.gmu.edu/grads/>
- [12] V. SLAVNIĆ, *Overview of Grid and High Performance Computing activities in Serbia*, 7th RO-LCG Conference, Bucharest, Romania, 3-5 November 2014.
- [13] DREAMCLIMATE code at the VI-SEEM Code Repository,
<https://code.vi-seem.eu/petarj/dreamclimate>
- [14] DREAMCLIMATE datasets at the VI-SEEM Data Repository,
<https://repo.vi-seem.eu/handle/21.15102/VISEEM-86>
- [15] S. C. ANENBERG, L. W. HOROWITZ, D. Q. TONGAND AND J. J. WEST, *An estimate of the global burden of anthropogenic ozone and fine particulate matter on premature human mortality using atmospheric modeling*, Environ. Health Perspect., 118 (2010), pp. 1189-1195.
- [16] J. LELIEVELD, C. BARLAS, D. GIANNADAKI AND A. POZZER, *Model calculated global, regional and megacity premature mortality due to air pollution*, Atmos. Chem. Phys., 13 (2013), pp. 7023-7037.

Edited by: Aneta Karaivanova

Received: Jan 5, 2018

Accepted: Apr 12, 2018

Chapter 15

Science Gateway for the Serbian Condensed Matter Physics Community

Dušan Vudragović and Antun Balaž

Abstract The Academic and Educational Grid Initiative of Serbia hosts and maintains the scientific gateway of the Serbian condensed matter physics community. The gateway is built around a code set addressing problems from the physics of ultracold quantum gases, solving the nonlinear Schroedinger equation, the Gross–Pitaevskii equation in real and imaginary time, and a path integral algorithm for estimation of quantum-mechanical transition amplitudes, which are relevant for various applications. Here we present the realization of the gateway and technologies used for its implementation.

15.1 Introduction

Condensed matter physics and materials science address problems that highly relevant for fundamental research, as well as for practical applications and society. The development of high-impact materials with enhanced and engineered properties, or research in quantum information, for example, depend on the results from these areas of physical sciences, and contribute to the IT and smartphone industry, semiconductor technology, the energy sector, and others.

Numerical simulations are now indispensable tools in science and technology, and are used to speed up the research and development while decreasing the costs. In condensed matter physics, scientists deploy a broad range of algorithms, such as solving nonlinear partial differential equations, classical and quantum Monte Carlo techniques, including solving of the Bose–Hubbard and Fermi–Hubbard models, exact diagonalization techniques for strongly correlated systems, etc. Whichever

D. Vudragović (✉) · A. Balaž

Scientific Computing Laboratory, Institute of Physics Belgrade, University of Belgrade,
Belgrade, Serbia

e-mail: dusan@ipb.ac.rs

A. Balaž

e-mail: antun@ipb.ac.rs

algorithm is used, typically it requires large-scale computing resources for simulations of relevant physical systems.

In the Serbian condensed matter physics community (CMPC), the most prominent use of computing resources is related to the three applications developed at the national level: SPEEDUP, QSPEEDUP, and GP-SCL.

SPEEDUP code (Balaz 2012-1) uses Monte Carlo-based path integral algorithms for the calculation of quantum mechanical transition amplitudes for 1D models. It is based on the use of higher-order short-time effective actions in the time of propagation (Monte Carlo time step), which substantially improves the convergence of discretized amplitudes to their exact continuum values.

QSPEEDUP code (Vudrag 2010) presents a quasi-Monte Carlo extension of the SPEEDUP code. The extended algorithm uses Sobol's set of quasi-random numbers for generation of trajectories relevant for calculation of transition amplitudes in the path integral formalism. Both applications use identical algorithm, supplied with different random number generators, which allows their unification into a single application designated as (Q)SPEEDUP.

GP-SCL (Vudrag 2012) is a set of codes parallelized using the OpenMP approach for calculating the dynamics and ground states of quantum fluids (such as Bose–Einstein condensates and superfluids). Quantum fluids represent macroscopic quantum phenomena where large numbers of atoms or molecules behave coherently, allowing special properties to emerge. In the mean-field regime, such systems can be described by a nonlinear Schrödinger equation, usually called the Gross–Pitaevskii equation (Pethick 2008). GP-SCL codes solve the time-(in) dependent Gross–Pitaevskii nonlinear partial differential equation in one, two, and three space dimensions in an arbitrary trapping potential using imaginary-time and real-time propagation. The equation is solved using the semi-implicit split-step Crank–Nicolson method by discretizing space and time, as described in Murug (2009). The discretized equation is then propagated in imaginary or real time over small time steps.

Applications have been developed by scientists from the Scientific Computing Laboratory (SCL 2014) of the Institute of Physics Belgrade (IPB 2014) and are used by an increasing number of collaborators within Serbia and also from other countries in Europe, as well as from Brazil, India, and China. The applications are deployed on the computing infrastructure provided by the Academic and Educational Grid Initiative of Serbia (AEGIS 2014), which is part of the European Grid Infrastructure (EGI 2014).

To increase the potential user base of the applications, we have decided to create the AEGIS CMPC science gateway (SG) in the framework of the SCI-BUS project (SCI-BUS 2014), to provide seamless access to the software and the data generated by the applications. This science gateway also hides the complexity of use of the Grid and applications, which was a barrier for many scientists.

15.2 Building the Science Gateway

Before the AEGIS CMPC science gateway was built and put into production, the default interface to DCI within the AEGIS CMPC was based on gLite technology provided by the European Middleware Initiative (EMI 2014). This is a command line interface, and it requires a personal certificate issued by one of recognized certificate authorities, membership in a virtual organization (VO) that supports the applications, and access to a user interface (UI) machine. A personal certificate is obtainable from the national AEGIS CA, while the Serbian AEGIS National Grid Initiative provides the VO membership service. A central UI machine is available at the IPB, but within the community personal UI virtual machines are used as well.

In this approach, the use of AEGIS CMPC applications requires preparation of a parameter input file that describes the physical system of interest. In addition, the DCI description of computational task has to be prepared as well. In a gLite-based UI machine this is typically done using the Job Description Language (JDL). Depending on machine architecture and the software stack provided by DCI in terms of available compilers, a CMPC application could be compiled locally at a UI machine or remotely at a DCI, on a target worker node. In the first case, a statically linked executable is submitted to the predefined architectures, while in the latter case the source code is transferred to the computation node, where one of the various predeployed compilers performs the compilation. A CMPC application with a physical system description from the parameter input file and with a DCI description of the computational task from the JDL file is submitted from the UI machine to the DCI by the gLite command line interface. Further job management (job cancelation, monitoring, and output retrieval) is done by the gLite command line interface as well.

This approach demands several skills: knowledge of CMPC application source codes and their parallelization techniques, knowledge of different compiler technologies, knowledge of Linux operating system and its common tools, and knowledge of gLite command line interface and DCI technology. This variety of skills, which is required for solving even trivial problems, creates a strong barrier that prevents ready use of CMPC applications within the community, and adversely affects attracting new people who are interested in numerical simulations based on the available set of codes. Since the knowledge of the underlying physics (quantum theory and Bose–Einstein condensation) and understanding of CMPC applications should be the only real requirements, the development of a scientific gateway effectively solves the identified problems and enables new users to perform numerical simulations in this field without much technical knowledge of the operating system, compiler technology, low-level DCI interface, and DCI itself. Furthermore, AEGIS CMPC SG promotes sharing of the results of simulations within the community, and in this way increases understanding of the behavior of particular physical systems of interest.

The desired level of automation of CMPC applications is achieved through the use of WS-PGRADE/gUSE (gUSE 2014) workflows. For example, typical usage of

the GP-SCL application first requires calculation of the ground state of the system, achieved by the imaginary-time propagation until convergence is reached, and then, starting from this result, one can study the dynamics of the system through the real time-propagation. A workflow concept unifies these two kinds of time-propagation algorithms into a single task, hiding the complexity from the end user. Furthermore, besides the results in the form of raw data that describe the propagation of the system in time, AEGIS CMPC scientific gateway provides visualization of the propagation in the form of graphs and movies.

In the case of the (Q)SPEEDUP codes, numerical convergence of quantum-mechanical transition amplitudes to their continuum values is achieved only when the number of Monte Carlo samples goes to infinity. The central limit theorem states that the statistical distribution of numerical results obtained using a large number of independent Monte Carlo samples is always a Gaussian. This allows automation of a process workflow for a desired maximal error of calculated transition amplitude, which is introduced as a new, more generic input parameter. In other words, for a described physical system of interest and predefined acceptable error of the result, AEGIS CMPC SG workflow provides sufficient statistics in execution of the code to achieve the desired accuracy of the amplitude.

15.3 Architecture of the Science Gateway

AEGIS CMPC science gateway has been developed to support SPEEDUP, QSPEEDUP, and GP-SCL applications. These programs are fully written in the C programming language, and do not depend on any external library. Codes could be compiled with different popular compilers: GNU's gcc compiler, Intel's icc compiler, IBM's xlc compiler, PGI's pgcc compiler, and Oracle's suncc (former Sun) compiler. Besides serial versions of the codes, parallel versions are produced as well. In the case of SPEEDUP and QSPEEDUP applications, parallelization is achieved through the message passing interface (MPI), while the GP-SCL code is parallelized using OpenMP API. All codes are accompanied by appropriate makefiles, which allow specification of the compiler, type of parallelization, and customization of compiler optimization flags. These makefiles play a significant role in the porting process, and simplify utilization of various hardware resources.

Although applications use different algorithms, from a purely technical point of view they have the common use scenario: for a particular description of physical system of interest, given in the form of a single input file, after considerable number-crunching each application produces corresponding output with numerical results. The generated numerical results are analyzed, classified, and visualized by the scientific gateway. This allows for the creation of a generic architecture for all AEGIS CMPC applications.

The generic architecture behind the AEGIS CMPC scientific gateway is illustrated in Fig. 15.1. It consists of four main blocks: the AEGIS CMPC portal, the

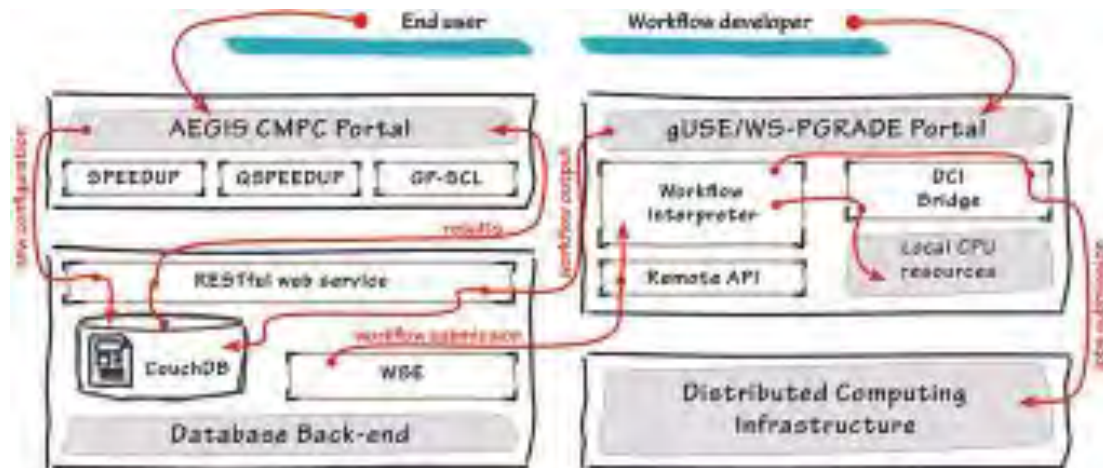


Fig. 15.1 Generic architecture behind AEGIS CMPC workflows

WS-PGRADE/gUSE portal, the database back-end, and the DCI used for calculations.

The AEGIS CMPC portal (CMPC 2014) (Fig. 15.2) is a user-oriented interface that visually unifies outputs of SPEEDUP, QSPEEDUP and GP-SCL applications. It provides a summary of collected numerical results, which is organized per application and per configuration of a physical system. In addition, the AEGIS CMPC portal allows querying of the available configurations, as well as submission of new configurations. While the submission requires authentication, browsing of the results is publicly available. Applications' configurations and results are stored in the database back-end. Communication between the portal and the database is established through a dedicated RESTful web service. On the database side, the

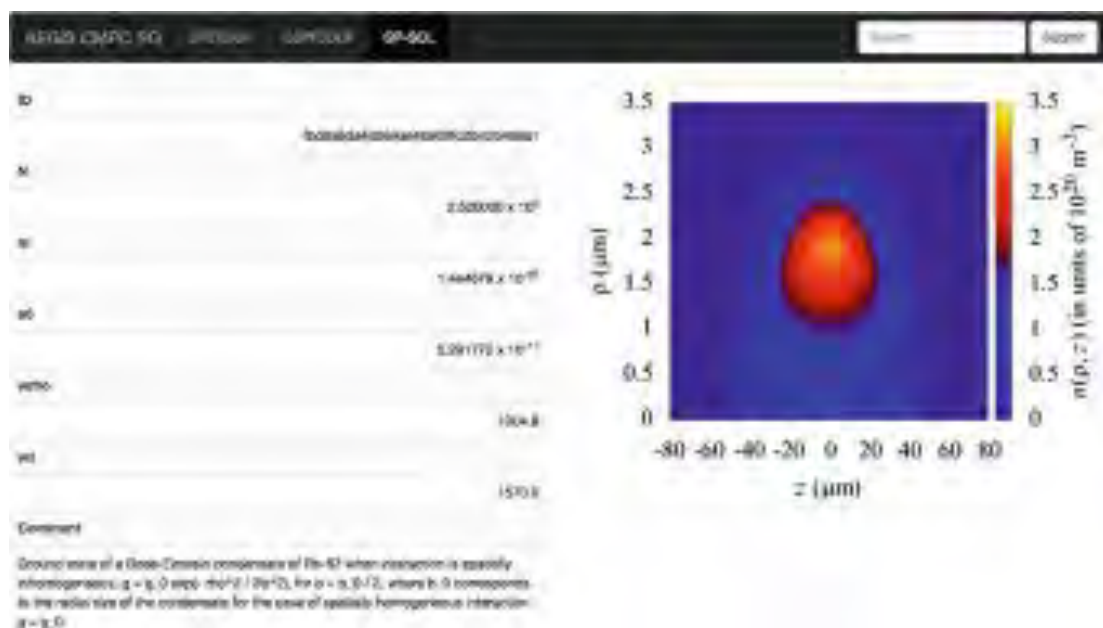


Fig. 15.2 GP-SCL view of the AEGIS CMPC Portal

workflow submission engine (WSE) daemon process looks for configurations waiting for the executions, and performs application-specific workflow submission through the WS-PGRADE/gUSE Remote API interface. The portal was developed within the Google Web Toolkit (Tacy 2013) environment using Bootstrap (Cochran 2012) front-end framework, and it was deployed through the Apache Tomcat (Brittain 2007) server (available at: <http://sci-bus.ipb.ac.rs/>).

The WS-PGRADE/gUSE Portal is a workflow developer-oriented interface based on the WS-PGRADE/gUSE technology. It allows creation of new workflows, modification of existing ones, and manual testing. Use of the portal requires a Liferay-based (Liferay 2014) account, a valid digital certificate and membership in cmpc.aegis.rs VO. Potential users are able to request Liferay-based account by filling out the generic Liferay Create Account form available at home page of AEGIS CMPC SG. The National Grid Initiative (NGI) AEGIS VOMS-admin portal provides management of cmpc.aegis.rs VO membership. The membership request form of the VOMS-admin portal requires a digital certificate, and therefore, in order to fill it out, a workflow developer has to import a personal certificate into the web browser. The AEGIS WS-PGRADE/gUSE Portal extends the default WS-PGRADE/gUSE installation with the Remote API plugin that enables usage of the core gUSE services without the WS-PGRADE user interface component. The Remote API allows one to run and manage workflows from a custom user interface, such as the AEGIS CMPC Portal.

Workflows of AEGIS CMPC applications are created within the WS-PGRADE/gUSE Portal, and are exposed for the external usage through the Remote API component. Since SPEEDUP and QSPEEDUP applications use identical algorithms, just supplied with different random number generators, both applications use a single workflow—a (Q)SPEEDUP workflow. In order to minimize the network overhead, all application binaries are preinstalled on each of DCI resource centers supporting the cmpc.aegis.rs VO. The VO software area is used for this purpose, while the installation and upgrade of particular applications is performed by VO managers.

The workflow behind the (Q)SPEEDUP application is illustrated in Fig 15.3. It has three main components:

- (Q)SPEEDUP-PREPARATION retrieves user-defined physical system configurations from the database. Retrieved JSON output is then converted to the application-specific configuration file, which is forwarded to the next process in the workflow. Together with the configuration file, technical metadata (consumed CPU time, application version, random number generator stream, etc.) produced in this part of the workflow are forwarded to the next process. This is not a CPU-intensive task, and it is executed at the server that hosts the WS-PGRADE/gUSE portal (localhost).
- (Q)SPEEDUP-EXECUTION is responsible for the application execution at the DCI, and then it retrieves the results. It equips the application with the wrapper that is able to determine the location of the preinstalled application at the DCI, supply input parameters, initiate execution, and collect results. This CPU-intensive

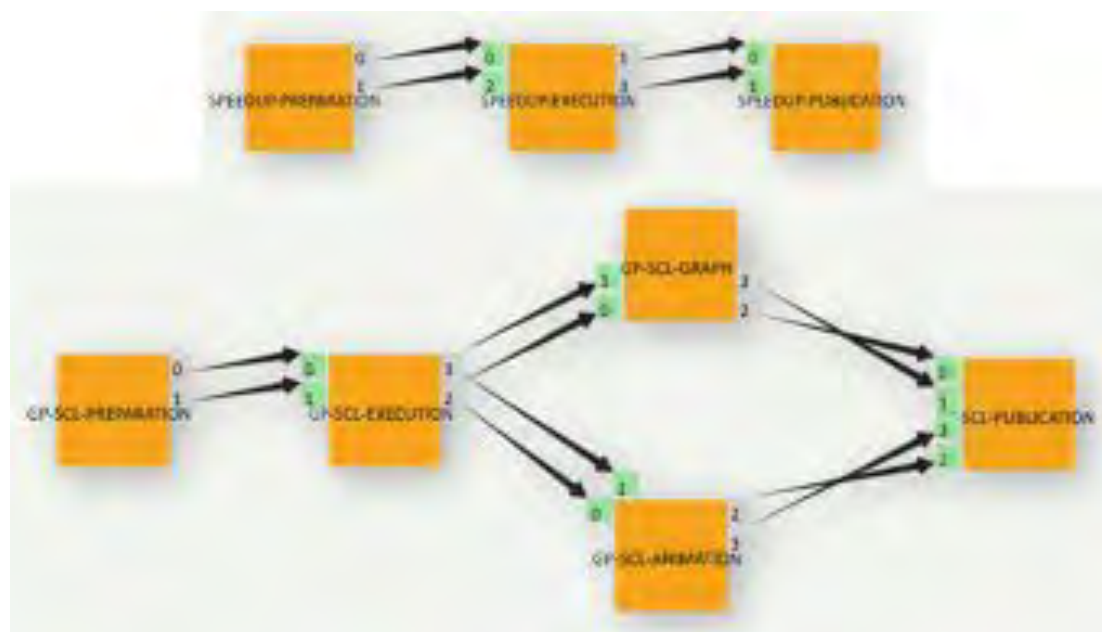


Fig. 15.3 AEGIS CMPC (Q)SPEEDUP (*top*) and GP-SCL (*bottom*) workflows

task is executed on the DCI. Outputs of the application are permanently stored on the storage elements provided by the DCI, while the workflow engine is informed of their locations.

- (Q)SPEEDUP-PUBLICATION transforms the collected results from the previous two tasks to a corresponding JSON structure, and stores the result in the database through the RESTful web service.

The AEGIS CMPC GP-SCL portlet relies on the workflow illustrated in Fig. 15.3. The workflow has the following components:

- GP-SCL-PREPARATION retrieves the physical system configuration from the database, and produces an application-specific parameter input file. The task is executed on the server hosting the WS-PGRADE/gUSE portal. Technical metadata collected in this part of the workflow are forwarded to the next process. Each node in the workflow will expand this initial metadata structure, while the last node will upload collected metadata together with the application results to the database.
- GP-SCL-EXECUTION performs submission of the simulation to the DCI and output retrieval. After the execution, the produced results are divided between two tasks running in parallel: GP-SCL-GRAPH and GP-SCL-ANIMATION. Results are permanently stored on the DCI, and only their locations are transferred back to the science gateway.
- GP-SCL-GRAPH produces graphs requested in the configuration. Graphs are produced using gnuplot-based APIs. This task is not CPU-intensive, and therefore it is performed on the local machine. Only part of the total output

produced within the GP-SCL-EXECUTION task is transferred from the DCI to the machine running the science gateway for this purpose.

- GP-SCL-ANIMATION produces animation (movie) of a dilute, trapped Bose–Einstein condensate evolution in time. This part of the workflow is CPU intensive and is executed on the DCI.
- GP-SCL-PUBLICATION accumulates results, technical metadata, graphs, and locations of the movies, and stores them in the document-oriented database.

AEGIS CMPC DB is a document-oriented database that stores configurations and numerical results from all applications supported by the science gateway. Initially, it was deployed using a relational database, but with the increase of the number of physical properties to be monitored, it has become very difficult to break-out the design of the SG into relational schemas. Instead of perpetual reorganization of schemas, the database back-end has been migrated to the document-oriented data model. Due to several additional features, such as offline replication, multiversion concurrency control, incremental replication, and fault-tolerance, MySQL technology (Harrison 2008) has been replaced by CouchDB technology (Anderson 2009).

Querying of and structuring the information available in the science gateway is realized by CouchDB views. Different views are constructed by functions that act as a mapping part of the map/reduce operation. These functions take the documents and transform them into single values that they return. CouchDB indexes the view and keep the indexes updated as new documents are added, removed, or updated.

Authentication and authorization of the requests coming to the AEGIS CMPC SG, together with the tracking and merging mechanisms, are implemented as an additional layer placed in front of the CouchDB. In order to change or add new information (POST and PUT methods), a workflow developer has to be authenticated and authorized; however, reading of information is publicly available (GET method). Authentication and authorization could be done by username/password, an X.509 certificate, or an X.509 RFC 3,820-compliant proxy certificate; this is followed by an update of the document with the JSON tracking structure. This section contains workflow developer information, the IP address of the client from which the request was triggered, and the timestamp of the action. For this reason, each document stored in AEGIS CMPC CouchDB has additional JSON structure related to the tracking mechanism.

All documents stored in CouchDB are versioned, and CouchDB determines which of the changes will be stored as the latest revision. When doing this, it does not attempt to merge the conflicting revision. A developer always decides how the merging should be done, and it is up to a developer to specify the latest revision. This task is simplified with the AEGIS CMPC CouchDB merging mechanism, and a workflow developer no longer needs to deal with the CouchDB revisions. The system automatically discovers the latest version of a particular document, and performs merging of the existing information with additional information. Existing CouchDB documents could be updated with different or new information only, which is not the case in the standard CouchDB model. In addition, the AEGIS

CMPC CouchDB instance sanctions DELETE requests in order to prevent loss of any information.

DCI used by the AEGIS CMPC SG is organized around the `cmpc.aegis.rs` VO. Establishment of a separate VO has allowed lobbying at the resource providers for additional or new resources. Also, it guarantees execution of jobs submitted from the scientific gateways in reasonable time, and provides an exact mechanism for tracking the of number of users, CPU usage, and other DCI-related statistics. The `cmpc.aegis.rs` VO is currently supported by three NGI_AEGIS Grid sites, part of EGI infrastructure (AEGIS01-IPB-SCL, AEGIS04-KG, and AEGIS11-MISANU), and by the largest HPC installation in Serbia, the PARADOX cluster, totaling to more than 2,700 CPUs and 140 TBs of storage space. Recently, AEGIS CMPC scientific gateway has been also supported by the largest HPC installation in Serbia. PARADOX cluster is equipped with 1,696 Sandy Bridge CPUs at a frequency of 2.6 GHz, 106 NVIDIA Tesla M2090 GPU cards, and 100 TBs of storage space. It is interconnected via the QDR Infiniband technology, and achieves peak computing performance of 105 TFlops.

Management of VO membership is centralized and provided by the NGI_AEGIS VOMS-admin portal. Core Grid services necessary for users to be able to access all computing and data storage resources are provided by the NGI_AEGIS as well, in particular: the BDII information system (`bdii.ipb.ac.rs`), workload management system (`wms.ipb.ac.rs`, `wms-aegis.ipb.ac.rs`), logging and bookkeeping service (`lb.ipb.ac.rs`, `lb-aegis.ipb.ac.rs`), myproxy service (`myproxy.ipb.ac.rs`), and logical file catalogue (`lfc.ipb.ac.rs`). All services are running the latest version of the middle-ware EMI 3 (Monte Bianco) release.

15.4 Usage of the Scientific Gateway

AEGIS CMPC SG achieved production mode in September 2013. Currently, there are 20 registered users, and according to the EGI accounting portal, 19,000 `cmpc.aegis.rs` VO jobs have been so far submitted from the portal. Jobs are uniformly distributed over the CMPC applications, while the average execution time per job is around 24 h.

With the introduction of the science gateway, the CPMC job success rate has dramatically increased. One of the indicators is the ratio between totally consumed CPU time and the number of jobs. Currently this ratio is approximately 23 h, which corresponds to the average execution time per job. In the case of failures, this time would be smaller. Users are allowed to tune application's configuration only, so there is not much space for changes that will lead to application crashes or an unpredictable behavior. Also, only CPU-intensive parts of the workflow are executed on the DCI, and other tasks are executed locally, on the machine running the science gateway. The success rate of the local jobs is practically 100 %, while the jobs submitted to the DCI may fail due to various infrastructure problems. For this reason, each job submitted to the DCI is configured to allow automatic resubmission.

There are two kinds of resubmissions supported by the NGL_AEGIS DCI: deep resubmission and shallow resubmission. The resubmission is deep when the job fails after it has started running on the computation node, and shallow otherwise. Both deep and shallow resubmissions are limited by default to five attempts for AEGIS CMPC SG jobs. Furthermore, even if after these five attempts (Q)SPEEDUP job fails, it will not affect the results, since they are obtained using a large number of independent jobs. For GP-SCL jobs this is not the case, and results will not be produced if the workflow node fails. This could be overseen by an additional module that monitors relations between configurations and corresponding results, and performs complete workflow resubmissions when necessary.

In this period, AEGIS CMPC SG was mainly used for:

- Study of Faraday waves in binary nonmiscible Bose–Einstein condensates (Balaz 2012-2);
- Study of Faraday waves in single-component Bose–Einstein condensates with spatially inhomogeneous atomic interactions (Balaz 2014), as well as condensates with dipolar interactions (Nikolic 2013);
- Study of fragmentation of a Bose–Einstein condensate through periodic modulation of the scattering length (Vidan 2011);
- Study of geometric resonances in Bose–Einstein condensates with two- and three-body interactions (Jibbouri 2013).

Using the numerical results obtained via the AEGIS CMPC SG and analytical variational calculations, it was shown that elongated binary nonmiscible Bose–Einstein condensates subject to periodic modulation of the radial confinement exhibit a Faraday instability, similar to that seen in one-component condensates. Modulation of the radial confinement leads to the emergence of density waves in the longitudinal direction. Considering two hyperfine states of rubidium condensates, AEGIS CMPC GP-SCL application was able to calculate two experimentally relevant stationary-state configurations: one in which the components form a dark-bright symbiotic pair (the ground state of the system), and one in which the components are segregated (first excited state). For each of these two configurations, it was shown numerically that far from resonances, the Faraday waves excited in the two components are of similar periods, emerge simultaneously, and do not impact the dynamics of the bulk of the condensate. This numerical result was confirmed analytically, and it was shown that the period of the Faraday waves can be estimated using a variational treatment of the coupled Gross–Pitaevskii equations combined with a Mathieu-type analysis for the selection mechanism of the excited waves.

Numerical study of Faraday waves in systems with spatially inhomogeneous atomic interactions has revealed that in the regime of weak inhomogeneity, the system practically behaves as in the homogeneous case. However, for the case of strong inhomogeneity, the properties of density waves substantially depend on the typical inhomogeneity scale. For systems with dipolar interaction, the stability of the ground state was found to be the major issue. Only for smaller numbers of atoms (up to several tens of thousands) is the system stable enough to support the

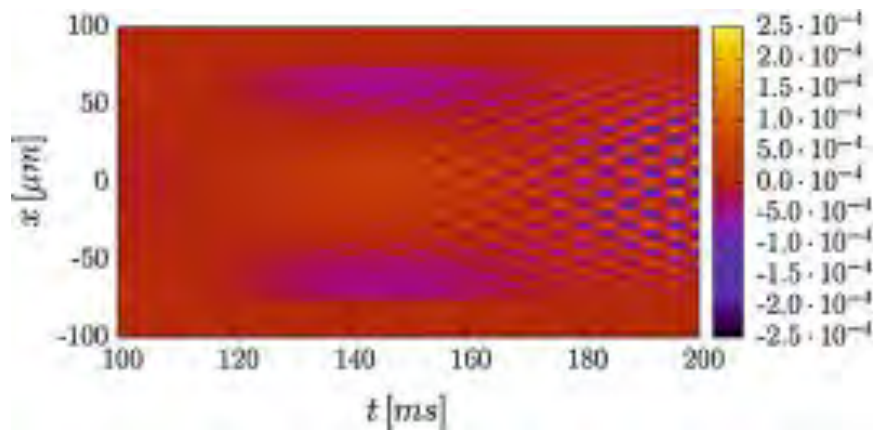


Fig. 15.4 Emergence of Faraday waves in the density profile of dipolar Bose–Einstein condensate of chromium

ground state. Harmonic modulation of the radial part of the confining potential is found again to generate Faraday density waves. For strong dipolar interaction, periods of emergent density waves (see Fig. 15.4) are found to be multiples of the corresponding periods when only contact interaction is present—a feature that has yet to be understood.

Investigation of fragmentation of Bose–Einstein condensates through periodic modulation of the scattering length is motivated by recent experimental results on the dynamics of a cigar-shaped Bose–Einstein condensate of atomic lithium. Dynamics of such system is investigated numerically, using the AEGIS CMPC SG, and analytically. It was shown that for resonant drives of large amplitude the condensate reaches a fragmented state. The fragmented state is a hybrid state of the condensate that includes a quadrupole mode on which a longitudinal resonant density wave is grafted.

Geometric resonances in Bose–Einstein condensates were investigated by solving the underlying time-dependent Gross–Pitaevskii equation for systems with two- and three-body interactions in an axially symmetric harmonic trap. For this, a recently developed analytical method (Vidan 2011) was used, as well as a detailed numerical study of a set of ordinary differential equations for variational parameters. By changing the anisotropy of the confining potential, strong nonlinear effects can be observed numerically and analytically—these are shifts in the frequencies of collective oscillation modes of the system. Additionally, coupling of collective modes can be seen, with the coupling strength strongly depending on the geometry of the system. Such results are highly relevant for experimental studies and help plan the parameters of experimental setups.

15.5 Conclusions

A new AEGIS CMPC science gateway (CMPC 2014) was developed and deployed for the Serbian condensed matter physics community in the framework of the SCI-BUS (2014) project. It was based on the WS-PGRADE/gUSE technology, and was implemented using the workflows approach. Three modules within the science gateway are responsible for managing user interaction with the supported applications (SPEEDUP, QSPEEDUP, and GP-SCL). Since September 2013, when this science gateway achieved the production status, its usage is steadily increasing, and the job success rate is high and stable.

Further developments will include support for more applications used within this user community, as well as adding more workflows for specific use cases requested by the scientists. We also plan to extend support to the Serbian computational chemistry community, which is of considerable size and already uses a number of applications on computing resources of the Academic and Educational Grid Initiative of Serbia (AEGIS 2014) and European Grid Initiative (EGI 2014).

SEE-GRID eInfrastructure for Regional eScience

Ognjen Prnjat¹, Antun Balaz², Dusan Vudragovic², Ioannis Liabotis¹,
Cevat Sener³, Branko Marovic⁴, Miklos Kozlovszky⁵ and Gabriel Neagu⁶

1. GRNET, Greece

2. SCL, Institute of Physics Belgrade, Serbia

3. Middle East Technical University, Ankara, Turkey

4. University of Belgrade Computer Centre, Serbia

5. MTA SZTAKI, Budapest, Hungary

6. ICI, Bucharest, Romania

Abstract In the past 6 years, a number of targeted initiatives, funded by the European Commission via its information society and RTD programmes and Greek infrastructure development actions, have articulated a successful regional development actions in South East Europe that can be used as a role model for other international developments. The SEEREN (South-East European Research and Education Networking initiative) project, through its two phases, established the SEE segment of the pan-European G²EANT network and successfully connected the research and scientific communities in the region. Currently, the SEE-LIGHT project is working towards establishing a dark-fiber backbone that will interconnect most national Research and Education networks in the region. On the distributed computing and storage provisioning i.e. Grid plane, the SEE-GRID (South-East European GRID e-Infrastructure Development) project, similarly through its two phases, has established a strong human network in the area of scientific computing and has set up a powerful regional Grid infrastructure, and attracted a number of applications from different fields from countries throughout the South-East Europe. The current SEEGRID-SCI project, ending in April 2010, empowers the regional user communities from fields of meteorology, seismology and environmental protection in common use and sharing of the regional e-Infrastructure. Current technical initiatives in formulation are focusing on a set of coordinated actions in the area of HPC and application fields making use of HPC initiatives. Finally, the current SEERA-EI project brings together policy makers – programme managers from 10 countries in the region. The project aims to establish a communication platform between programme managers, pave the way towards common e-Infrastructure strategy and vision, and implement concrete actions for common funding of electronic infrastructures on the regional level. The regional vision on establishing an e-Infrastructure compatible with European developments, and empowering the scientists in the region in equal participation in the use of pan-European infrastructures, is materializing through the above initiatives. This model has a number of concrete operational and organizational guidelines which can be adapted to help e-Infrastructure developments in other world regions. In this

paper we review the most important developments and contributions by the SEE-GRID-SCI project.

1 INTRODUCTION

Science is becoming largely digital -it needs to deal with ever increasing amounts of data and computational needs. Numerical simulations become more detailed, experimental science uses more sophisticated sensors to make precise measurements, and shift from the tradition of individuals-based science work towards more collaborative models now starts to dominate.

Computing resources and services able to support needs of such a new model of scientific work are available at different layers: local computing centers, national and regional computing centers, and European supercomputing centers. The gap between needs of various user communities and computing resources able to satisfy their requirements is addressed by introduction of Grid technology on the top of pan-European academic network.

Computing Grids are conceptually not unlike electrical grids. In an electrical grid, the wall outlets allow us to link to and use an infrastructure of resources, which generate, distribute, and bill for electrical power. When we connect to the electrical grid, we do not need to know details on the power plant currently generating the electricity we use. In the same way Grid technology uses middleware layer to coordinate and organize into one logical resource a set of available distributed computing and storage resources across a network, allowing users to access them in a unified fashion. The computing Grids, like electrical grids, aim to provide users with easy access to all the resources they need, whenever they need them, regardless of the underlying physical topology and management model of individual clusters.

Grids address two distinct but related goals: providing remote access to information technology (IT) assets, and aggregating processing and storage power. The most obvious resources included in Grids are processors (CPUs), but Grids also can encompass various sensors, data-storage systems, applications, and other types of resources. One of the first commonly known Grid initiatives was the SETI@HOME project, which solicited several millions of volunteers to download a screensaver, which was able to use idle processor time to analyze the astronomical data in the search for extraterrestrial life.

In the past 6 years the European Commission has funded through a number of targeted initiatives activating of new user communities and enabling collaborative research across a number of fields in order to close existing technological and scientific gaps, and thus bridging the digital divide, stimulating research and consequently alleviating the brain drain in the less-developed regions of Europe. This was especially successful in the South-East Europe (SEE), where a number of such initiatives show excellent results. In the Grid arena, the South-East European GRid eInfrastructure Development (SEE-GRID) project [1], through its two 2-

year phases, has established a strong human network in the area of scientific computing and has set up a powerful regional Grid infrastructure, attracting large number of applications from diverse fields from countries throughout the South-East Europe. The third phase of the SEE-GRID program (SEE-GRID-SCI) aims to have a catalytic and structuring effect on a number of SEE user groups, with a strong focus on the key seismological, meteorological, and environmental communities.

SEE-GRID-SCI (SEE-GRID eInfrastructure for regional eScience) involves three strategic international scientific communities (Virtual Organisations): seismology, meteorology, environmental protection. It aims to further stimulate the use and expansion of the existing regional eInfrastructure and its services, and capitalize on the existing human network to further strengthen scientific collaboration and cooperation among participating SEE communities in the area of eInfrastructures. The inclusion of the new scientific communities and the expansion of the infrastructure in terms of both size and geographical spread, together with a set of coordinated actions aimed at strengthening the National Grid Infrastructures (NGIs) in the region, ensures that at the end of the project each country in the region will be ready to join the long-term, sustainable European Initiatives as a full-fledged peer.

Overall, the project is composed of four Networking Activities (NA), one Service Activity (SA), and one Joint Research Activity (JRA). NA1 activity deals with the project administrative and technical management, while NA2 activity provides support to NGIs and coordinates international collaboration. It focuses on supporting non-EGEE countries of the Western Balkans, Moldova, Georgia and Armenia. Guidelines for NGI best-practices are developed and refined, and a set of coherent actions are carried out to ensure that NGIs reach the adequate maturity levels and organizational models for joining EGI. The other line of action is the dissemination of the NGI know-how to other peripheral regions, and establishing strong collaboration channels with other regional Grid initiatives as well as with pan-European initiatives. The collaboration goes beyond NGI issues and will also involve other project activities such as applications development and application-level services, operations, training and dissemination. NA3 activity deals with the dissemination and training, while NA4 activity provides round-the-clock support to user communities. Grid infrastructure operations and management of regional resources is done by the SA1 activity, which ensures that user community needs in terms of size and availability of computing, storage, networking and application-specific resources are catered for. In research activities, JRA1 deals with the development of application-level services and application-related operational extensions, customized to the needs of the specific user communities.

2 GRID INFRASTRUCTURE OPERATIONS

The regional Grid infrastructure [2] operated by SEE-GRID-SCI project is built on top of the pilot infrastructure established by the first SEE-GRID project (2004-2006), which was since then substantially extended and enlarged in terms of resources and number of Grid sites, and upgraded in terms of the deployed middleware and core services provided to existing and new user communities during the SEE-GRID-2 project (2006-2008).

The operations activity [3] adopted the pragmatic model of the 2-layered infrastructures in which mature sites move to EGEE production infrastructure while the start-up sites from new institutes and user communities incubate within the SEE-GRID infrastructure. In this way, both SEE-wide and national-level applications are able to benefit from the computing resources of both infrastructures, by mainly using the pilot infrastructure in the incubation phase and production infrastructure in the production phase. Moreover, this approach ensured that smaller sites, typical for the region, have a chance to be a part of the regional SEE-GRID infrastructure acting as an incubator for their maturing into EGEE production. As applications mature, new VOs spun off with the relevant core services supported by SEE-GRID-SCI. Discipline-specific services are deployed over the infrastructure and supported by SA1. Sophisticated operational tools some of them developed within JRA1 -are used to enhance infrastructure performance.

SEE-GRID-SCI project continues to operate and further extend, develop and improve this infrastructure, with the aim to cater for the need of all activated user communities in the region, with special emphasis on the three identified target areas: meteorology, seismology, and environmental sciences. Apart from computing and storage resources made available to these user communities, SA1 activity provides and maintains a set of existing and new operational and monitoring tools so as to ensure proper operation of the infrastructure, and a set of primary and secondary core services for all deployed VOs in order to ensure optimal geographical distribution according to the underlying network structure, load sharing, and quality of the service to end users.

Currently SEE-GRID-SCI infrastructure encompasses approximately 54 Grid sites, more than 6600 CPUs, and around 750 TBs of available data storage capacity, which is illustrated in Tab. 1 and in Fig. 1.

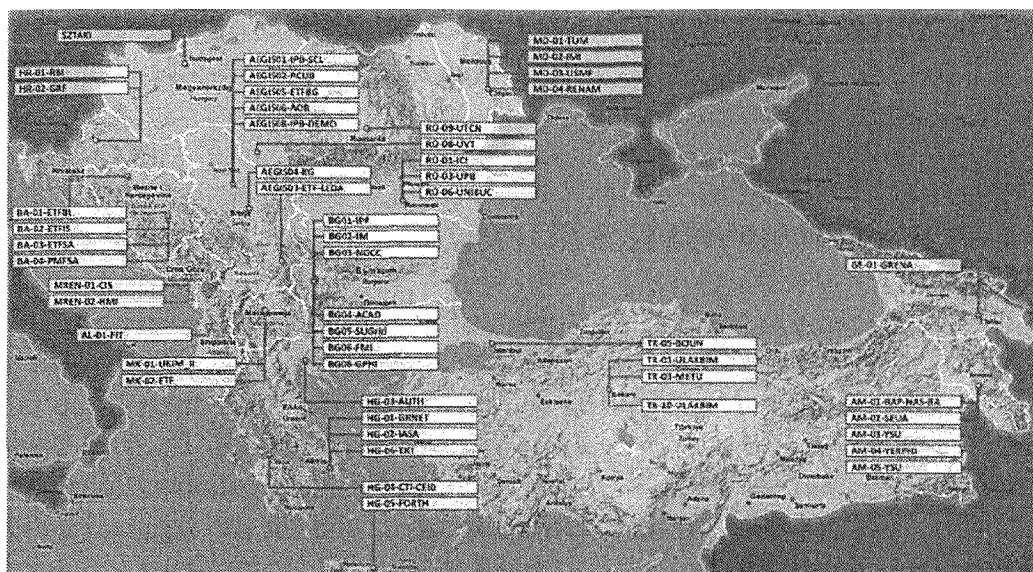


Fig. 1: Overview of the SEE-GRID-SCI infrastructure.

Table 1: SEE-GRID-SCI computing and storage resources.

Country	Total number of CPUs	Total storage [TB]
Greece	1200	66.8
Bulgaria	1210	42.3
Romania	120	4.0
Turkey	2380	528.0
Hungary	8	2.0
Albania	20	1.3
Bosnia-Herzegovina	80	1.1
FYR of Macedonia	80	4.1
Serbia	974	97.0
Montenegro	40	0.6
Moldova	24	6.5
Croatia	44	0.2
Armenia	424	0.2
Georgia	16	0.1
Total	6620	754.2

Overall number of CPUs has grown from 2400 at the beginning of the project in May 2008 to currently more than 6600, while the number of dedicated CPUs for SEE-GRID-SCI VOs is currently around 1500. Grid operations activity successfully maintains such a large, geographically disperse and ever growing infrastructure, harmonizing its operation with the pan-European EGEE infrastructure. In addition to this, one of the most important achievements of SAI activity is

transfer of knowledge and Grid know-how to all participating countries, and support to their NGI operation teams to reach the level of expertise needed for sustainable EGI-based operational model.

3 USER COMMUNITIES SUPPORT

SEE-GRID-SCI aims to accelerate e-Infrastructure uptake by new user groups extending over the region. Hence, the NA4 user communities support activities provide round-the-clock user support for a range of applications from three target fields: seismology, meteorology and environmental protection. Each of them is structured in the form of a virtual organization to facilitate collaborations among researchers from the field [4]. Dedicated support teams for the regional applications provide both gridification support and run-time production-level user support including training of interested researchers.

3.1 Meteorology VO

Weather forecasting is based on the use of numerical weather prediction (NWP) models that are able to perform the necessary calculations that describe/predict the major atmospheric processes. NWP applications require considerable processing power and data storage resources, and thus can benefit from the offerings of grid technologies.

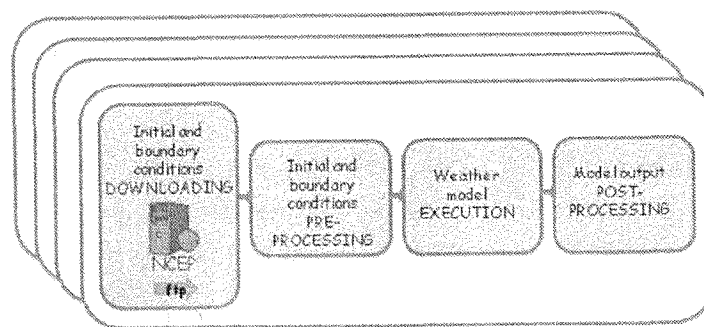


Fig. 2: REFS workflow.

- In the frame of Meteorology VO two NWP applications are ported to the grid:
- First, a regional scale multi-model, multi-analysis ensemble forecasting system (REFS) was built and ported on the grid infrastructure and it is currently in production phase. REFS is based on the use of four limited area models (namely BOLAM, MM5, ETA, and NMM) that are run using a multitude of initial and boundary conditions over the Mediterranean [5]. This activity involves the need of large infrastructure that is

not easily available at medium-scale research centers and institutions. Its workflow is summarized in Fig. 2.

- Moreover, the Weather Research and Forecasting Advanced Research WRF (WRF-ARW) prognostic model has been ported to the grid as the second application of this VO. The SEE region is a big challenge for the meteorologists because of the complexity of the reproduction/forecasting of the airflow over complex terrain. High resolution model grids are thus needed to study complex

- terrain airflow, and this is a quite demanding application in CPU, memory and data storage. To address these needs, WRF-ARW is used for weather research purposes as well as for operational weather forecasting.

3.2 *Seismology VO*

Scientists in the seismology field need computational resources for mathematical modeling of seismic phenomena, as well as storage resources for massive collections of seismic data from geographically distributed sensors. Seismology VO [6] aims to bring seismology data from the SEE region to the grid platform and also to gridify seismology applications that are of interest to not only the seismologists but also to the industry such as the insurance companies. To realize these goals, the Seismic Data Server Application Service (SDSAS) was developed to provide distributed storage and serving of seismic data from different partner countries, logical organization and indexing of distributed seismic data, and programming tools, developed for automatically downloading waveform data from the NERIES/ORFEUS datacenter in addition to the client interface for downloading earthquake event quakeml files from European-Mediterranean Seismological Centre.

The applications gridified within this VO include Seismic Risk Assessment, Numerical Modeling of Mantle Convection, Fault Plane Solution, Earthquake Location Finding, Massive Digital Seismological Signal Processing with Wavelet Analysis and Web Interface to SDSAS.

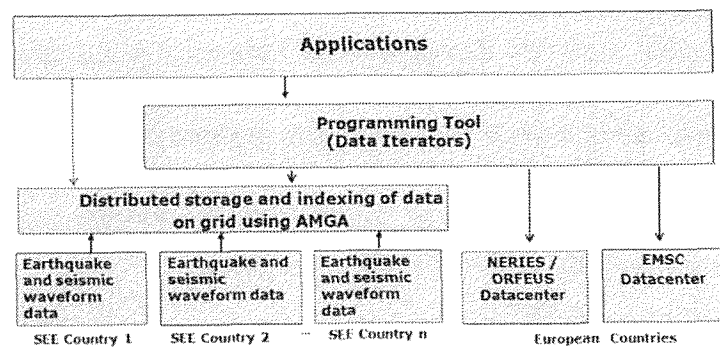


Fig. 3: Seismology VO platform.

3.3 Environmental VO

The applications from this VO, developed and deployed within the project, include Multi-Scale Atmospheric Composition Modeling [7], Monte Carlo Sensitivity Analysis for Environmental Systems [8], Refinement of surface and vegetation parameters in SEE region based on satellite images, Modeling System for Emergency Response to the Release of Harmful Substances in the Atmosphere, Groundwater Flow Simulation System, Changes of Environment with Remote Sensing, Modeling the assessment of climate change impact on air quality, based on an established methodology, Regional Ocean Modeling System. The use of Grid resources enabled the researchers to achieve results which they could not obtain using their local clusters or workstations. For example, the validation of the model for simulation of climate change impact on air quality for the period 1991-2000 takes tens of compute nodes with 8 CPU cores each for several days and produces terabytes of intermediate data (Fig. 4).

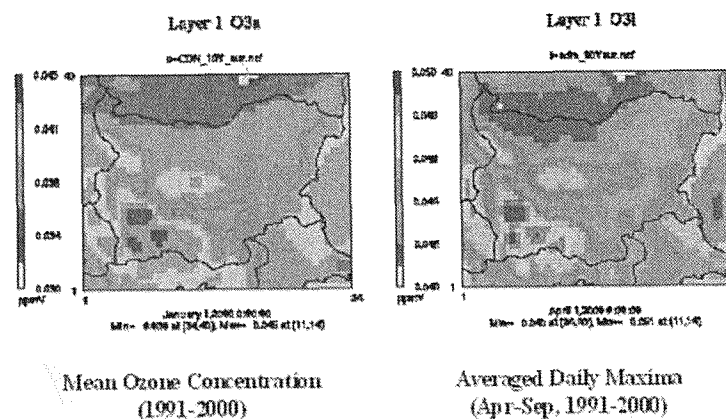


Fig. 4: Pollution levels for the period 1991-2000.

4 DEVELOPMENT OF APPLICATION-LEVEL SERVICES AND OPERATIONAL TOOLS

In course of the SEE-GRID-SCI project, a growing number of applications have been gridified within the regional user communities working in the three earth science disciplines. All three disciplines require inter-application teamwork in addressing common issues and emphasize the importance of data sharing and support for distributed collaboration.

The SEE-GRID-SCI JRA1 (Joint Research Activity) facilitates development and gridification of applications and usage of the underlying grid infrastructure by employing the expertise that goes beyond local communities. It aims to improve the usability of the infrastructure and Grid services for the end-users from target communities and manageability of the infrastructure by focusing in:

- Addressing some issues common to several user communities and their applications that are not addressed by the existing middleware and infrastructure, thus contributing to enhancement of services provided to end-users.
- Researching in the application-focused features of operational tools and development of new or extending of existing operational tools.

All SEE-GRID-SCI software developers were asked to provide their recommendations for development, deployment, internal and user documentation, maintenance, licensing, support practices and tools, and interaction of developed software with gLite grid environment. The resulting guidelines intend to address the quality of the software produced and facilitate support and extendibility of the tools and services.

Details of these services and operational tools are available at JRA1 commonalities wiki [9], which provides information on their purpose, status, architecture, requirements, deployment, code and documentation, usage, relation with other developments, dissemination, partnerships, practical and scientific impact, and expected long-term developments.

A number of application services was identified and developed, including: FMJ-API (SEE-GRID File Management Java API), DM-Web (Data Management Web Portal), SDSAS (SDS (Seismic Data Server Application Service, see Fig. 3), AWT (Advanced-Workflow Development Tool and Orchestration Service), ULMON (User Level Monitoring Tool), Work Binder, RAS (Rendering Application Service), ESIP Platform (Environment Oriented Satellite Data Processing Platform), CWRE (Common Workflow Repository Extension of P-GRADE Portal), Event Logger, and MEWS (Mathematical Expressions Web Service).

A set of applications services is already deployed and used by the grid applications demonstrating their usage and their benefits for the user communities of the project.

The JRA1 operational and monitoring tools developments include: JTS (Job Track Service), BBmSAM Extensions illustrated in Fig. 5, GSSVA (Grid Site Software Vulnerability Analyzer), NMTT (No Mercy Ticketing System), USGIME (User/Application Specific Grid Infrastructure Monitoring Extension), Logwatch-G, and Alert Messaging Service. GSSVA and Logwatch-G are related to site-level monitoring, while the others are related to grid-level monitoring and control. All 7 operational tools are in production usage.

Some of the developed applications services are already essential building blocks of specific applications, while other services and tools are used to facilitate user level monitoring and/or operational support for more effective and easy usage of the underlying grid resources.

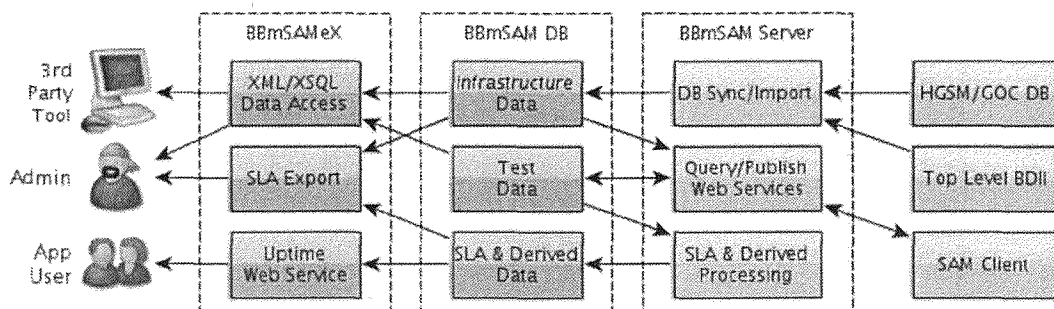


Fig. 5: BBmSAM overview.

A further effort was made to develop the application services using software engineering standards that would allow them to become more accessible and able to be adopted by any interested user community. Some application services are specifically promoted outside the scope of SEE-GRID-SCI. For example, Work Binder and ESIP Platform application services were submitted to EGEE for inclusion in its RESPECT program [10], while FM-J-API was a subject of a recent EUAsiaGrid lecture [11]. About 30 journal and conference papers were produced.

The expected overall impact of JRA1 activity will be to ease the involvement of new users, applications and resource providers, automating and simplifying common and burdensome tasks. In a wider context, it will make its results available to other regional and global initiatives, providing its most successful tools and components to other projects and contributing to optimal development and use of eInfrastructures and establishing a feature rich grid environment.

5 TRAINING AND DISSEMINATION

The SEE-GRID-SCI project established a central knowledge database on Grid-technology [12] including ready-made training materials, and a large set of grid technology educated trainers, who are able to train different Grid user groups (trainthe trainer concept). The SEE-GRID-SCI and its predecessor projects build up an effective training model with a training infrastructure and carry out lot of training events in order to raise the national-level and regional-level expertise and end-user adoption.

All SEE-GRID-SCI project partners are heavily involved in training activities, in total almost 40 trainers are qualified to deliver trainings in the SEE region (Fig. 6). Setting up a stable trainer community was an important milestone in the life of the project, enabling easy access to trainers and specialized knowledge.

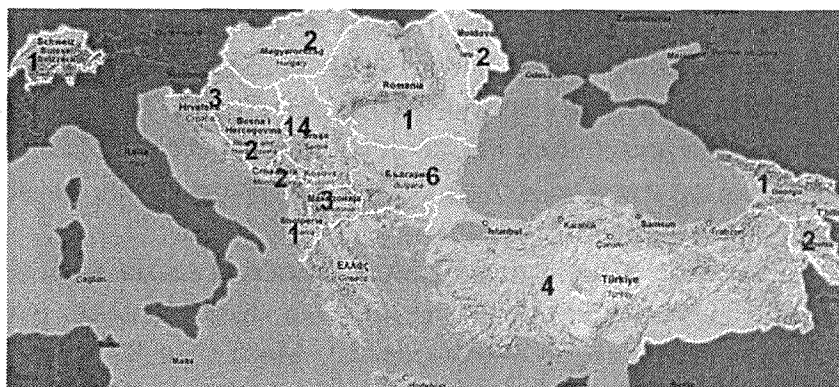


Fig. 6: Trainer community distribution within the SEE region.

Training infrastructure has been set up early in the project, and has proven to be a crucial tool for enabling flexible on-demand trainings. The training VO (SGDEMO VO) is supported on a set of smaller SEE-GRID sites. In addition to this, all core services are provided to this VO, so that during the training events the usage of Grid infrastructure can be fully demonstrated to users. The created training infrastructure offers a homogenous, reliable, grid-focused training environment, with standardized access control. To avoid delays and organizational overhead, special SEE-GRID Demo Certification Authority is used, which allows trainers to generate necessary number of temporary Grid certificates before any training event. These certificates are automatically added to the SGDEMO VO, so that users can access the Grid from the start of each training event. The training environment offers as additional service: annotated training material repository, a training agenda system, on-line surveys to evaluate the trainings and assure quality control. Older materials created from previous training events plays also an important knowledge resource, therefore it is accessible to everyone and can be reused for future trainings: these materials are freely available also by the wider public.

SEE-GRID-SCI project consortium performed focused dissemination events at regional and at national level during the project years, with the aim to bring together members of the targeted scientific communities and demonstrate to them examples of the Grid paradigm, strength scientific collaboration and cooperation among participating SEE communities in the area of eInfrastructures.

SEE-GRID-SCI is maintaining close ties with other key eInfrastructure projects, most notably the SEEREN initiative, the GEANT project, with EDGeS, EELA, BSI, GENESI-DR, BELIEF, as well as EGEE-III. The project participated both on numerous international conferences (EGEE Conference 2008 and 2009), User Forums (EGEE User Forum 2009 and 2010) and attracted a large audience, with a large number of dedicated project speeches during these conferences. The EELA2 project collaboration continues strongly on the basis of previous collaborations, mainly in the field of operations and SEE-GRID-SCI support for the Latin American National Grid Initiatives. The EGI DS project was provided with a number of concrete inputs from SEE-GRID-SCI, including operations, applications, and, most importantly, NGIs. GENESI-DR collaboration is reflected in exchange of scientific data and applications. BELIEF link is mainly exploited through disseminations and mutual PR support. The project established 5 Memoranda of Understanding during the first year of the project with the above mentioned key international projects.

The project has developed content-rich websites, generic and VO-specific posters, released 5 internal newsletters, carried out disseminations public media (TV, press releases, newspapers, e-newspapers). More than 80 scientific papers have been published as a result of the project's research work.

Main target of the developed training model is to provide discipline-specific trainings for the new SEE-GRID-SCI communities with a self-sustaining training environment. The project has created a trainer community, defined a "Grid evolution path". It categorized training community targets and materials, established a training material repository and supports trainers with information how to use or reuse these training materials.

6 CONCLUSIONS

The SEE-GRID series of projects have successfully led the Grid-related developments in the South-East Europe in the past 6 years. This included establishing, development, maintenance and operation of the largest computing resource in the region, training of users and site administrators and coordination of operations in all countries of the region, reaching the level of sustainable NGI-based operations and expertise needed in transition to the EGI operations model. In addition to the infrastructure-related achievements, the project has actively worked on the development of policy and international collaboration, and spearheaded the establishment of NGIs in all partner countries. The dissemination events carried out by the project have substantially boosted public awareness of Grid technology and attracted interest of policy makers to the development of distributed research infrastructures in SEE countries, and their inclusion to the pan-European eScience infrastructures.

7 ACKNOWLEDGEMENTS

This work was supported by the European Commission under FP7 project SEE-GRID-SCI (INFRA-2007-1.2.2 grant no. 211338), and by the Ministry of Science and Technological Development of the Republic of Serbia (project no. OI141035).

REFERENCES

- [1] SEE-GRID-SCI Project, <http://www.see-grid-sci.eu/>
- [2] SEE-GRID-SCI Grid Infrastructure, <http://goc.grid.sinica.edu.tw/gstat/seegrid/>
- [3] SEE-GRID-SCI Grid Operations Wiki, http://wiki.egee-see.org/index.php/SEE-GRID_Wiki
- [4] SEE-GRID-SCI VO Applications, http://wiki.egee-see.org/index.php/SEE-GRID_Wiki#SEE-GRID-SCI_VO_Applications
- [5] K. Lagouvardos, E. Floros, V. Kotroni: A Grid-enabled Regional-scale Ensemble Forecasting System in the Mediterranean. *Int. J. of Grid Computing*, doi: 10.1007/s1072301091503 (2010).
- [6] C. Ozturan, B. Bektas, M. Yilmazer, C. Sener, Challenges Faced in Building A Seismology VO for Southeastern Europe, e-Challenges Conference, Istanbul, Oct. 21-23 2009.
- [7] D. Syrakov, M. Prodanova, K. Ganev, N. Miloshev, E. Atanassov, T. Gurov, A. Karaivanova: Grid Computing for Multi-Scale Atmospheric Composition Modeling for the Balkan Region, *Journal of International Scientific Publication: Ecology&Safety*, Vol. 3, Part 1, 2009, pp. 4-21.
- [8] E. Atanassov, A. Karaivanova, T. Gurov, S. Ivanovska, M. Durchova, Using Sobol Sequence in Grid Environment, *Proceeding of 32nd International Convention MIPRO/GVS 2009*, pp. 290-294.
- [9] SEE-GRID-SCI JRA1 commonalities wiki, http://wiki.egee-see.org/index.php/JRA1_Commonalities
- [10] RESPECT program, <http://technical.eu-egee.org/index.php?id=290>
- [11] EUAsiaGrid lecture, http://www.euasiagrid.org/wiki/index.php/Data_Management_Java_API
- [12] SEE-GRID-SCI Training Center, <http://www.lpds.sztaki.hu/stc/>

Implementation and Benchmarking of New FFT Libraries in Quantum ESPRESSO

Dušan Stanković, Petar Jovanović, Aleksandar Jović, Vladimir Slavnić,
Dušan Vudragović, and Antun Balaž

Scientific Computer Laboratory, Institute of Physics Belgrade,
University of Belgrade, Pregrevica 118, 11080 Belgrade, Serbia
{`dusan.stankovic,petar.jovanovic,aleksandar.jovic,vladimir.slavnic,`
`dusan.vudragovic,antun.balaz`}@ipb.ac.rs

Abstract. Quantum ESPRESSO (QE) software package allows electronic-structure calculations and materials modeling at the nanoscale, based on density-functional theory, plane waves, and pseudopotentials. It extensively uses Fast Fourier Transform (FFT) during all computations. In addition to the built-in FFT libraries, QE enables integration of newly developed FFT algorithms. Since Fastest Fourier Transform of the East (FFTE) library has shown performance comparable with the widely used and vendor-supplied libraries, the same behavior is foreseen in QE. In this paper we present FFTE-enabled and thread-enabled FFTW3 extensions of QE, together with benchmarking and performance results.

Keywords: FFT, Quantum ESPRESSO, multithreading, hybrid parallelism, OpenMP, MPI.

1 Introduction

Quantum Espresso is an integrated suite of open-source codes for electronic structure calculations and materials modeling at the nanoscale. It is based on density-functional theory, plane waves and pseudopotentials [1].

Fourier transformation is used in a large part in calculations performed in QE, so any gains in FFT performance would be positively reflected in the performance of the entire QE suite. Most major hardware platforms, along with their corresponding numerical libraries, are already supported in QE (such as IBM ESSL, Intel MKL, SGI SCSL and so on), which include routines for FFT calculations. Also, the open-source FFTW (version 2) and FFTW3 libraries [2] are supported.

Parallelization in Quantum ESPRESSO is achieved using MPI and OpenMP, and hybrid parallelism using both MPI and OpenMP together is currently supported only with the internally supplied FFTW library. The work on implementing the support for the open-source FFTE library was motivated by its performance results [3], so it was expected to show better performance than the open-source libraries already supported in QE. The work on implementing the support for hybrid FFTW3 library was considered because hybrid parallelism

is becoming more important, as computing nodes on modern HPC systems often comprise many CPU cores. Since the open-source FFTW3 library is widely used, and has both multi-threaded routines, and serial thread-safe routines, it was selected for implementation.

2 Quantum ESPRESSO Code Structure and Applied Modifications

Quantum ESPRESSO is written mostly in FORTRAN 90. It has a modular structure, with different modules for higher level domain specific calculations (for example, CP or PW modules), and also some general purpose parts which are then used in many other modules (for example FFT calculations or time logging).

The development of this project used QE 5.0 as a baseline, and was localized to the parts of the code responsible for FFT calculations. Analysis of the QE source code revealed that all the routines for performing FFT are located in a file named *fft_scalar.f90*. Routines for 1D, 2D and 3D FFT are defined in this file. They serve as wrappers and invoke corresponding routines of the aforementioned numerical libraries, where the actual computation is performed. Selecting which particular numerical library will be used is performed by conditional compilation, using pre-processor directives (such as `#ifdef`, `#elif`, `#endif` and so on). Whenever a numerical library supporting FFT is found during the configuration phase of the QE software package, a corresponding macro parameter is defined in the Makefile, and is used to select an appropriate compilation path. For example, when the FFTW3 library is used, a macro parameter named `__FFTW3` will be defined, and only the code where FFTW3 routines are called will be compiled.

2.1 Enabling FFTE Library in Quantum ESPRESSO

We have extended QE to utilize the FFTE numerical library for performing FFT in 1D, 2D or 3D. The version of FFTE used is 5.0, accessible on the website [3]. FFTE is written in Fortran, supports parallelism with MPI, OpenMP, or both when hybrid variant is used. Also, FFT transformations for up to 3 dimensions are supported. Code development was done according to Quantum ESPRESSO development manual [4], which defines guidelines regarding the programming style.

A new macro parameter named `__FFTE` was created, and used in parts of the source code whenever a FFTE routine is called, or some initialization is performed. The configure script was also modified so that the configuration process can recognize if the FFTE library is present on the system, whether on the system path, or in the path specified during configuration. If the library is found, the `__FFTE` macro parameter is added to the Makefile. Variables needed to initialize FFTE, or store data between execution of FFTE routines were introduced as to be easily distinguishable by their prefix (`ffte_`).

In Quantum ESPRESSO, an internal decomposition of the data is used to perform 3D FFT transforms as a combination of multiple calls to serial 1D and 2D FFT routines, which are divided among processes. MPI is used for communication and data exchange in-between these phases. The reason for this approach is to avoid performing unnecessary transforms of subsections of the large 3D grid which already have zero values, as this pattern is common in data sets used by QE. A more detailed explanation of this decomposition can be found in Ref. [5].

It should be mentioned that the FFTE library does not support computation on many Fourier Transforms (on different arrays), in a single routine call. This can have some impact on the performance, because in QE there are many calls to 1D and 2D routines needed to complete transform on the entire data set. Also, when using FFTE, an initialization routine needs to be called before each transform, which includes even more overhead during execution. Significant drops in performance were not observed during our testing, but these factors should be considered when using the FFTE library in other projects.

2.2 Enabling FFTW3 Threading in Quantum ESPRESSO

Second extension of QE is related to support of threading of the FFTW3 library, which would enable hybrid parallelism (when used combined with the MPI), since it is already supported in Quantum ESPRESSO. The FFTW3 library supports threading in two modes:

- implicit, where an additional library `libfftw3_omp` has to be installed; in this case, FFTW3 routines support multi-threaded execution internally, so they are called like the serial ones, and
- explicit, where serial routines are used, but are called from within multiple threads running in parallel; this is possible because routines for FFT execution are thread-safe.

The following pseudocode representation roughly shows how the two threading modes were implemented in Quantum ESPRESSO (for the implicit mode, a single internally threaded routine call performs `ns1` transforms on arrays with length of `dim_z`, and for the explicit mode each routine call is serial):

- implicit

```
fftw_execute_many_dft(fw_plan, c, cout, ns1, dim_z)
```

- explicit

```
#pragma omp for
for i=1 to ns1
  offset=(i-1)*dim_z
  fftw_execute_dft(fw_plan, c[offset], cout[offset])
end for
```

The FFTW3 library supports reusing of plans, and also supports calculation of many transforms within a single routine call. This allows greater flexibility when using multiple transforms, and is optimal in terms of performance. More details on this can be found in Ref. [6].

In order to use implicit threading, FFTW3 thread initialization routines had to be called before calling any FFTW3 routines for FFT planning and execution. After the thread initialization has been successfully performed, the code for serial version can be reused, and threading is done automatically in the library routines.

With explicit threading, some modifications had to be made with the code. Because in the serial version many 1D or 2D transforms are aggregated in a single call for efficiency, execution had to be split into separate routine calls for each transform. This way, we actually had many routine calls, which can then be called from parallel threads. An OpenMP `parallel for` region was inserted, where in each iteration of the loop, FFT is performed on a separate sub-array. Since these routines are executed in parallel, and there are no data dependencies between loop iterations, this approach could be applied successfully.

3 Performance Tests

Here we will present performance tests done to compare newly supported FFTE library, and also performance of threaded FFTW3 library. Benchmarks were performed so that the performance was compared to most similar numerical libraries already supported in Quantum ESPRESSO.

3.1 FFTE Performance

We have tested Quantum ESPRESSO with enabled FFTE library, and compared it with the FFTW3 library that is already supported. These tests show only performances of serial libraries, since threaded FFTE was not implemented (because it wasn't always reliable when built with some compilers).

The cluster used for testing is made of nodes containing two AMD Magny-Cours Opteron 6174 processors, with 12 cores each. Nodes are connected via Infiniband network. The GCC compiler suite [7] was used in testing on this cluster. Our implementation was tested on benchmarks for PW module of Quantum ESPRESSO. FFTE Code was compiled with gfortran, version 4.1.2 with flags `-O3`, and the FFTW3 library was compiled with gcc, version 4.1.2 with flags

```
-O3 -fomit-frame-pointer -fstrict-aliasing -fno-schedule-insns
-ffast-math.
```

For the first test, up to 6 computing nodes were used (up to 72 processes). Execution times and scaling of the PW module are shown in Figure 1 for the case when the number of MPI processes is increased, and in Figure 2 when the problem size is increased, and the number of MPI processes stays constant (24 MPI processes were used in this test).

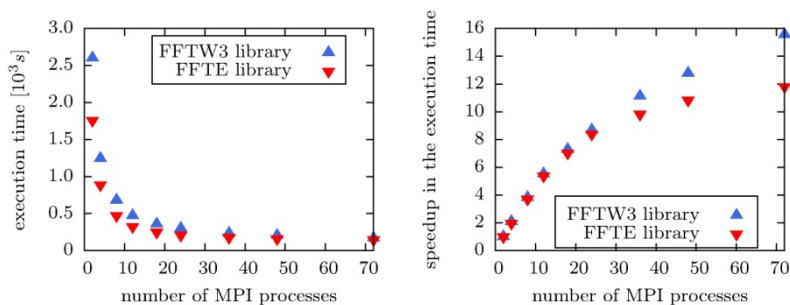


Fig. 1. Performance of the PW module of QE FFTE extension compared with the QE FFTW3 implementation: (left) Execution times of QE FFTW3/FFTE codes for different number of MPI processes; (right) Speedup in the execution time of QE FFTW3/FFTE codes as a function of a number of MPI processes (execution time on 1 MPI process used as a baseline)

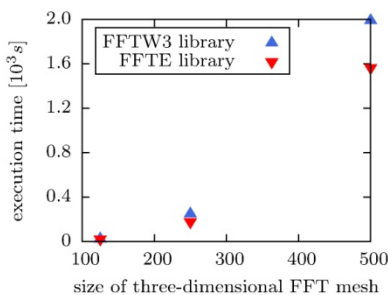


Fig. 2. Performance of the PW module of QE FFTE extension compared with the QE FFTW3 implementation: execution times as a function of 3D FFT mesh size

It can be seen that the FFTE library slightly outperforms FFTW3 in both cases (execution times are lower for the FFTE). The gap in performance grows as the size of the problem grows, so the FFTE seems suitable for large test cases. The difference in performance that is related to the problem size is also exhibited in the test case with the increasing number of MPI processes. As the number of MPI processes grows, each process gets less and less data to compute, and the difference in execution time diminishes. Because of this, the FFTE library shows worse speedup than the FFTW3.

3.2 FFTW3 Threaded Performance

For the performance testing of the threaded FFTW3 library, an FFTW (version 2) library internally supplied with Quantum ESPRESSO was selected for comparison. This was done because it was the only library supporting threading in

the hybrid mode (when used together with the MPI), and is also open-source and widely available.

Implementation of threaded FFTW3 was tested on a cluster with Intel Xeon processors, with two quad-core CPUs per node, and with Gigabit Ethernet interconnecting network. Library code was compiled with the Intel's `icc` compiler version 11.1 with the `-O3` flag, and Intel's `ifortran` was used for compilation of Quantum ESPRESSO.

Hybrid extension of the FFTW3 library was also tested with benchmarks for the PW module of QE. Tests were conducted again in the similar way, increasing the number of CPU cores in one case, and increasing input grid size in another. Configurations of 2 and 4 threads per MPI process were used, and also compared to the pure MPI case. Both threading variants (implicit and explicit) were tested with the FFTW3 library, and its performance is shown along with the internally supplied FFTW library (labeled as FFTW internal) in Figures 3 and 4. Total number of computing cores at some point is fixed, and is equal to a number of MPI processes times the number of threads per MPI process.

From this we see that both threading variants implemented for FFTW3 outperform the internal FFTW when executed with hybrid parallelism for most cases. Although, both threaded libraries are still slower than the pure MPI version. This is probably due to the fact that for the type of input data used with Quantum ESPRESSO, the overhead related to the thread management is probably greater than benefits of reduced MPI communication. Evidence for this are runs with four threads per MPI process, where performance gets significantly worse.

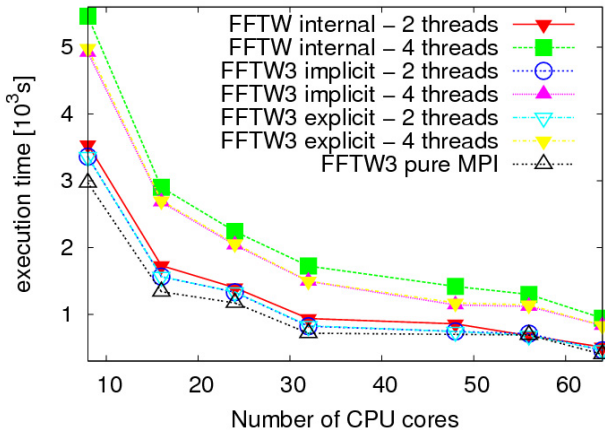


Fig. 3. Performance of the PW module of QE FFTW3 threaded extensions compared with the internal QE FFTW hybrid implementation and pure MPI FFTW3 implementation: Execution times of QE FFTW3 implicit and explicit/internal FFTW/pure MPI codes for different number of MPI processes

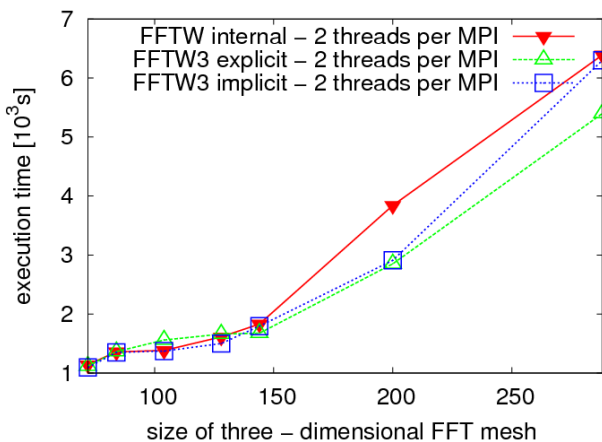


Fig. 4. Performance of the PW module of QE FFTW3 threaded extensions compared with the internal QE FFTW hybrid implementation and pure MPI FFTW3 implementation: QE FFTW3 implicit and explicit / internal FFTW execution times as functions of 3D FFT mesh size.

These results agree with what was presented in Ref. [5], where similar thing was investigated, and was shown that threading does not increase performance in all cases. Better performance was observed only in some cases where the number of MPI processes was significantly large. Also, Quantum ESPRESSO has other ways to control parallelism in software (for example, task groups, pools of processes, etc.) which is related to a particular input data set. Because these options were not primarily designed with hybrid parallelism in mind, it is not easy to fine tune Quantum ESPRESSO to achieve optimal performance when threading is used.

It is also worth mentioning that no significant difference in performance between implicit and explicit variants of FFTW3 threading was noticed. Looking at how threading is implemented in those two cases, an advantage of the explicit mode is that the OpenMP parallel region is created only once, and inside of it there are calls to many routines where FFT is computed. This should be optimal with regards to the overhead related to thread creation and synchronization. On the other hand, when using implicit threading, a new OpenMP parallel region has to be created with every routine call. However, because an advanced FFTW3 interface is used with implicit threading mode, it allows many transforms on different arrays to be aggregated in a single routine call from FORTRAN. It is possible that the native implementation of FFTW3 threaded library is aware of that, and that it successfully avoids unnecessary creation of parallel regions for each separate Fourier Transform.

4 Conclusions

In this project two extensions to Quantum ESPRESSO were implemented: the support for FFTE library for computing Fourier Transform in the serial mode, as well as the FFTW3 library in threaded mode. These extensions showed better performance compared to default QE libraries (open-source FFTW version 2 and 3 were selected for comparison). In the case of the FFTE library, performance increase could be significant when the large charge density mesh is requested for the simulation of a physical system. Both the explicit and implicit variants of FFTW3 threading showed better performance compared to internally supplied FFTW (version 2) when tested in hybrid configuration (two and four threads per MPI process), and while still not faster than the pure MPI version, should be considered when there is a need for hybrid parallelism. It is expected that a much larger problem size and more CPU cores are needed in order to get satisfactory performance of the hybrid FFTW3, which can match, or even surpass the performance of the pure MPI version.

Acknowledgements. Numerical results were obtained on the PARADOX cluster at the Scientific Computing Laboratory of the Institute of Physics Belgrade and on the NIIFI SC in Hungary. We acknowledge the support by the Serbian Ministry of Education, Science and Technological Development under projects No. ON171017 and III43007, and by the European Commission under FP7 projects HP-SEE, PRACE-2IP, PRACE-3IP and EGI-InSPIRE.

References

1. Quantum ESPRESSO official web site, <http://www.quantum-espresso.org>
2. Frigo, M., Johnson, S.G.: The Design and Implementation of FFTW3. Proceedings of the IEEE 93, 216 (2005)
3. FFTE: A Fast Fourier Transform package, <http://www.ffte.jp/>
4. Developer's Manual for Quantum ESPRESSO, http://www.quantum-espresso.org/?page_id=47
5. Spiga, F.: Implementing and Testing Mixed Parallel Programming Model into Quantum ESPRESSO. In: Science and Supercomputing in Europe - research highlights 2009, CINECA Consorzio Interuniversitario, Bologna (2010)
6. FFTW3 advanced interface, <http://www.fftw.org/doc/Advanced-Interface.html>
7. GCC compiler suite, <http://gcc.gnu.org/>

UNIVERSITY OF BELGRADE
FACULTY OF PHYSICS

Dušan Vudragović

FARADAY WAVES IN ULTRACOLD
DIPOLAR BOSE GASES

Doctoral dissertation

Belgrade, 2019

УНИВЕРЗИТЕТ У БЕОГРАДУ
ФИЗИЧКИ ФАКУЛТЕТ

Душан Вудраговић

Фарадејеви таласи у ултрахладним
диполним Бозе гасовима

Докторска дисертација

Београд, 2019. година

Thesis advisor, Committee member:

Dr. Antun Balaž

Research Professor

Institute of Physics Belgrade

University of Belgrade

Committee member:

Dr. Ivana Vasić

Associate Research Professor

Institute of Physics Belgrade

University of Belgrade

Committee member:

Prof. Dr. Milan Damnjanović

Professor

Faculty of Physics

University of Belgrade

Committee member:

Prof. Dr. Milan Knežević

Professor

Faculty of Physics

University of Belgrade

Acknowledgements

This thesis was completed at the Scientific Computing Laboratory, National Center of Excellence for the Study of Complex Systems, Institute of Physics Belgrade under the supervision of Dr. Antun Balaž. The presented research was supported by the Ministry of Education, Science, and Technological Development of the Republic of Serbia under projects ON171017 (led by Dr. Antun Balaž), and III43007 (work-package PP4, led by Dr. Aleksandar Bogojević). I thank Dr. Antun Balaž and Dr. Aleksandar Bogojević for giving me the opportunity to participate and contribute to these projects.

Trying to avoid any pathetic here, I would like to say that any discussion with Antun somehow makes you feel smart, and makes you feel that you together can solve any problem. I believe that this is crucial in the education process and in establishing a productive scientific environment such as the Scientific Computing Laboratory. However, this imposes many obligations on you as well, to do better, to work harder, to keep trying in order to achieve and exceed the excellence established by him.

Working on the thesis, I have been surrounded by very kind and helpful colleagues at the Institute of Physics Belgrade. Implementation of the algorithm has been done with the assistance of the PARADOX team, and I give thanks to them for their help in writing the codes, and usage of the PARADOX Supercomputing Facility. I would also like to express my gratitude to Dr. Axel Pelster from the Technical University of Kaiserslautern, Dr. Alexandru Nicolin from the University of Bucharest, and Dr. Sadhan Kumar Adhikari from the São Paulo State University for all the generous help and productive discussions.

Abstract

After pioneering experiments that realized Bose-Einstein condensates in systems of ultracold atoms with weak contact interactions, it took a decade for experimental techniques to advance and enable measurement of effects of the dipole-dipole interaction that exist between atoms or molecules with a permanent or induced electric or magnetic dipole moment. The first such experiment was realized in 2005 with chromium atoms, followed by the experiments with atoms with much larger magnetic moments, such as dysprosium and erbium. Furthermore, the dipolar condensates comprised of polar molecules with much stronger electrical or magnetic dipole moments were also realized. While the contact interaction is symmetric and has a short range, the dipole-dipole interaction between atoms or molecules is anisotropic and has a long range. These features are responsible for a whole series of new phenomena that appear in ultracold dipolar gases. If we take into account that the strength of the contact interactions can be varied over many orders of magnitude using the Feshbach resonance technique, and that the dipole-dipole interaction strength can also be tuned using a fast rotating magnetic or electric field, it is easy to see that such a versatility of dipolar quantum gases is unparalleled and makes them an obligatory element in a toolbox for engineering quantum devices and sensors.

The main contribution of this thesis is the study of Faraday and resonant density waves in ultracold bosonic systems with the contact and the dipole-dipole interaction. Such waves emerge in Bose-Einstein condensates as a result of the harmonic driving of the system. They represent nonlinear excitations and are generated due to the interaction-induced coupling of collective oscillation modes and the existence of parametric resonances. We introduce here a variational mean-field approach for the description of the dynamics of the Faraday and resonant waves in dipolar condensates. This approach is based on the Gaussian variational ansatz, which includes the condensate widths and the conjugated dynamical phases as parameters. The ansatz also includes the density modulations in order to capture the dynamics of density waves.

Using the developed variational approach, as well as a full numerical approach, we study in detail the properties of density waves in dipolar condensates at zero temperature, where breaking of the symmetry due to anisotropy of the dipole-dipole interaction plays an important role. We derive equations of motion for the dynamics of a driven dipolar system and identify the most unstable modes that correspond to the Faraday and resonant waves. Based on this, we derive the analytical expressions for spatial periods of both types of density waves as functions of the contact and the dipole-dipole interaction strength. We compare the obtained variational results with the results of extensive numerical simulations that solve the dipolar Gross-Pitaevskii equation in three dimensions, and find a very good agreement.

In this thesis, we also study the effects of the contact and the dipole-dipole interaction on the properties of the ground state and of the collective oscillation modes of dipolar condensates. While the increase of the contact interaction strength always leads to an increase of condensate widths, the situation is more complex when the dipole-dipole interaction is varied. In a cigar-shaped geometry, when the dipoles are oriented in the radial direction, the increase of the dipole-dipole interaction strength leads to the increase of condensate widths in the weak-confinement direction and in the direction of the dipoles, while the width in the third direction decreases. We also study the frequencies of the collective modes, where the interaction effects turn out to be less pronounced, in particular for the breathing and the quadrupole mode, whose values practically remain constant over the whole range of experimentally relevant values of both interaction strengths. The frequency of the radial-quadrupole mode is more sensitive to changes of interaction strengths, especially the contact interaction strength, and shows a nonmonotonous behavior as a function of the dipole-dipole interaction strength.

Keywords: Bose-Einstein condensate, pattern formation, dipole-dipole interaction, parametric resonance, interaction effects

Research field: Physics

Research subfield: Condensed matter physics

UDC number: 538.9

Резиме

Након пионирских експеримената са системима ултрахладних атома у којима је реализована Бозе-Ајнштајн кондензација са слабом контактном интеракцијом, била је потребна читава деценија да би се прецизност експеримената повећала и омогућила мерење ефеката дипол-дипол интеракције која постоји између атома или молекула са перманентним или индукованим електричним или магнетним диполним моментом. Први такав експеримент је изведен 2005. године са атомима хрома, а након тога су уследили експерименти са диспрозијумом и ербијумом, атомима са јаким магнетним диполним моментима, као и са поларним молекулима са далеко већим електричним и магнетним диполним моментима. Док је контактна интеракција симетрична и кратकोдометна, дипол-дипол интеракција између атома или молекула је анизотропна и дугодометна и узрок је читавог низа нових особина ултрахладних бозонских система. Ако узмемо у обзир да се у експериментима јачина контактне интеракције може мењати од јако одбојне до јако привлачне користећи технику Фешбах резонанци, као и то да се јачина дипол-дипол интеракције може контролисати помоћу брзо ротирајућег магнетног или електричног поља, лако је закључити да прилагодљивост и разноврсност особина диполних квантних гасова чини ове системе неупоредивим и обавезним алатом у инжењерингу квантних уређаја и сензора.

Главни допринос ове дисертације је проучавање феномена Фарадејевих и резонантних таласа густине у ултрахладним бозонским системима са контактном и дипол-дипол интеракцијом. Овакви таласи настају као резултат хармонијске модулације система и представљају нелинеарне ексцитације система услед присуства интеракција, спрезањем колективних осцилација и параметарских резонанци. У овој дисертацији смо у оквиру теорије средњег поља развили варијациони приступ за опис динамике Фарадејевих и резонантних таласа у диполним кондензатима. Овај приступ је заснован на Гаусовом варијационом анзацу који за параметре има ширине кондензата, конјуговане фазе, а укључује и модулације густине како би описао динамику таласа густине.

Користећи развијени варијациони приступ, као и пун нумерички приступ, детаљно смо проучавали особине таласа густине у диполним кондензатима на нултој температури, где дипол-дипол интеракција игра важну улогу због нарушења симетрије услед анизотропије система. Извели смо једначине кретања које описују динамику модулисаног диполног бозонског система и идентификовали најнестабилније моде које одговарају Фарадејевим и резонантним таласима. Даље, на основу тога, извели смо аналитичке изразе за просторне периоде оба типа таласа густине, као и њихову зависност од јачине контактне и дипол-дипол интеракције. Добијене варијационе резултате упоредили смо са резултатима детаљних нумеричких симулација које решавају диполну Грос-Питаевски једначину у три просторне димензије и добили смо веома добро слагање.

У овој дисертацији проучавали смо и утицај контактне и дипол-дипол интеракције на својства основног стања и колективних осцилација диполних кондензата. Док повећање јачине контактне интеракције увек доводи до ширења кондензата, ситуација је сложенија када се мења јачина дипол-дипол интеракције. За замку у облику цигаре у којој су диполи оријентисани у радијалном смеру, повећање јачине дипол-дипол интеракције доводи до ширења кондензата у лонгитудиналном правцу и у правцу поларизације, док се ширина у трећем правцу смањује. Поред тога, проучавали смо и фреквенције колективних мода, где су ефекти интеракција мање изражени. Ово се посебно односи на монополну (дишућу) и квадруполну моду, чије вредности практично остају константне у целом распону експериментално релевантних вредности јачина интеракција. Са друге стране, фреквенција радијалне квадруполне моде је осетљивија на промену јачине интеракције, посебно јачине контактне интеракције, док при промени јачине дипол-дипол интеракције показује немонотono понашање.

Кључне речи: Бозе-Ајнштајн кондензација, формирање патерна, дипол-дипол интеракција, параметарска резонанца, ефекти интеракције

Научна област: Физика

Ужа научна област: Физика кондензованог стања

УДК број: 538.9

Contents

Acknowledgements	iv
Abstract	v
Contents	ix
List of figures	xii
List of table	xv
1 Introduction	1
1.1 Role of interactions	3
1.2 Collective oscillation modes	5
1.3 This thesis	8
2 Bose-Einstein condensation and dipole-dipole interaction	10
2.1 Noninteracting Bose gas	13
2.2 Weakly-interacting Bose gas	15
2.3 Mean-field theory for dipolar Bose gas in a trap	19
2.4 Variational approach	22

3	Ground-state properties	26
3.1	Variational description of the ground state	27
3.2	Ground state of ^{52}Cr , ^{168}Er and ^{164}Dy BECs	29
3.3	Interaction effects on the ground state	34
4	Collective oscillation modes	38
4.1	Variational description of collective modes	39
4.2	Interaction effects and the collective modes	44
5	Faraday and resonant waves	48
5.1	Variational approach	50
5.2	Faraday waves in ^{52}Cr , ^{168}Er and ^{164}Dy BECs	56
5.3	Interaction effects and properties of Faraday waves	64
5.4	Resonant waves	68
6	Algorithm for solving the dipolar GPE	73
6.1	Split-step semi-implicit Crank-Nicolson method	76
6.2	Dipole-dipole interaction	79
6.3	Calculation of physical quantities	81
6.4	Numerical integration and derivation	82
6.5	Algorithm wrap-up	83
6.6	Parallelization and optimization	85

7	Conclusions	87
A	Fourier transform of the DDI potential	90
B	Lagrangian of the DDI term	92
C	Anisotropy function	94
D	Parameters of the system	98
E	Semi-implicit Crank–Nicolson scheme	101
F	Details on testing of the scaling of programs	104
	References	106
	Biography of the author	116

List of figures

1.1	The first experimental realization of a Bose-Einstein condensate. . . .	2
2.1	Condensate fraction as a function of temperature for noninteracting Bose gas.	15
2.2	Illustration of dipole-dipole interaction in a condensate of atoms whose dipole moments are polarized along z axis.	20
3.1	Integrated ground-state densities of a condensate obtained by taking into account the dipole-dipole interaction.	31
3.2	Integrated ground-state densities of a condensate obtained by neglecting the dipole-dipole interaction.	32
3.3	Convergence of the chemical potential of a condensate during imaginary-time propagation.	33
3.4	Condensate's ground-state widths as functions of the contact interaction strength.	35
3.5	Condensate's ground-state widths as functions of the dipole-dipole interaction strength.	37
4.1	Frequencies of the collective modes of a condensate obtained using the variational approach and neglecting the dipole-dipole interaction.	42
4.2	Effects of the contact interaction on the frequency of collective oscillation modes.	46
4.3	Effects of the dipole-dipole interaction on the frequency of collective oscillation modes.	47

5.1	Time evolution of the integrated density in condensate's longitudinal direction – emergence of Faraday waves in dipolar condensates.	57
5.2	Time evolution of the integrated densities in condensate's radial directions.	58
5.3	Time evolution of the integrated density profile variation in condensate's longitudinal direction – emergence of Faraday waves in dipolar condensates.	60
5.4	Time evolution of the integrated density profile variations in condensate's radial directions.	61
5.5	Fourier spectrum in the time-frequency domain of the integrated 1D density profile variations at the trap center – Faraday waves.	63
5.6	Fourier spectrum in the spatial-frequency domain of the integrated 1D density profile variations – Faraday waves.	64
5.7	Emergence time of Faraday waves and interaction strength.	66
5.8	Wave vector of Faraday waves as a function of the contact interaction strength.	67
5.9	Wave vector of Faraday waves as a function of the dipole-dipole interaction strength.	68
5.10	Time evolution of the integrated density profile variation in condensate's longitudinal direction – emergence of resonant waves in dipolar condensates.	69
5.11	Fourier spectrum in the time- and spatial-frequency domain of the integrated 1D density profile variations – resonant waves.	70
5.12	Wave vector of resonant waves as a function of the contact and dipole-dipole interaction strength.	71

5.13	Time evolution of the integrated density profile variation in condensate's longitudinal direction – emergence of resonant waves (second harmonic) in dipolar condensates.	72
6.1	Flowchart of the algorithm for solving the dipolar Gross-Pitaevskii equation.	84
6.2	Speedup and efficiency of the algorithm for solving the dipolar Gross-Pitaevskii equation.	85

List of tables

1	Relative differences of the ground-state condensate widths caused by neglecting dipolar interactions.	33
2	Relative differences of the ground-state condensate widths due to the contact interaction.	36
3	Relative differences of the ground-state condensate widths due to the dipole-dipole interaction.	36
4	Summary of atomic species parameters used in numerical simulations and variational calculations.	98

1 Introduction

According to the quantum statistical physics, there is a critical temperature below which the weakly-interacting bosons populate the lowest energy state of the system, which becomes macroscopically occupied. For temperatures well below the critical one, the thermal excitations can be usually neglected, and the same applies to the quantum fluctuations. The emergence of a macroscopically occupied ground state represents one of the few macroscopic quantum phenomena and is known as the Bose-Einstein condensation. It was experimentally realized for the first time in 1995 in dilute ultracold atomic gases of alkali metals, such as lithium ${}^7\text{Li}$ [1], rubidium ${}^{87}\text{Rb}$ [2] and sodium ${}^{23}\text{Na}$ [3]. Theoretically, the Bose-Einstein condensate (BEC) as a new phase of matter was predicted in 1924 by Indian physicist Satyendra Nath Bose [4] and German physicist Albert Einstein [5]. The theoretical study of BECs and a long quest for its experimental realization has significantly contributed to the development of quantum statistical physics, condensed matter physics, atomic and molecular physics, quantum optics, and laser physics, as well as to the other areas of physics, such as quantum information, quantum field theory, high-energy physics, and even the theory of general relativity. Such a wide applicability stems from the fact that BECs represent almost ideal Feynman's quantum simulators [6] for many physical systems.

In typical experiments with BECs, an ultracold dilute atomic cloud has a number density between $10^{19} - 10^{21} \text{ m}^{-3}$, i.e., three to six orders of magnitude lower than the density of air at room temperature and atmospheric pressure. The system is usually confined in a magneto-optical trap that can be described by a harmonic

potential, which is experimentally realized by a six-beam laser setup, where two counter-propagating beams in each spatial direction provide harmonic confinement. Atoms of selected species are cooled down to the nanokelvin temperatures using a combination of different techniques, such as the Zeeman slower, the laser cooling, and the evaporative cooling. In order to experimentally realize a BEC in a system with weak inter-atomic interactions, it is essential that the gas is rarefied. If this is the case, the system is close to the ideal gas of bosons, and the standard Bogoliubov theory can be applied. In practice, the diluteness requirement can be expressed by the condition [7, 8]:

$$na_s^3 \ll 1, \quad (1.1)$$

where n is the number density and a_s is the s -wave scattering length of atoms, which characterizes atomic interactions, seen as scattering processes in a dilute gas. Figure 1.1 illustrates the experimentally measured momentum distribution of a sodium

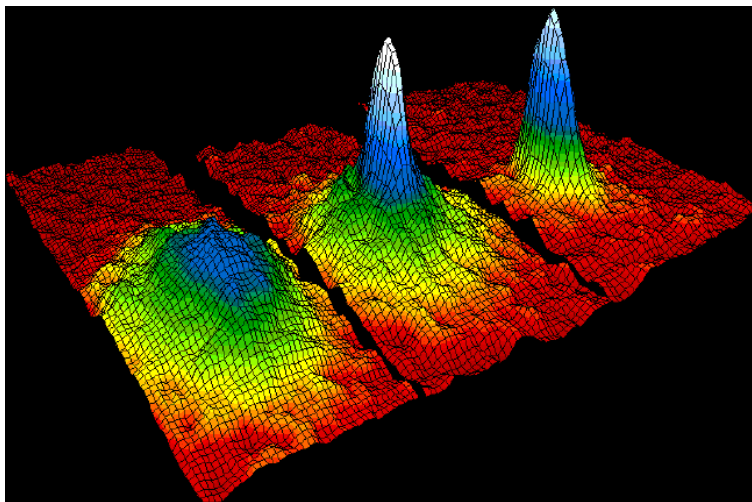


Figure 1.1: The first experimental realization of a BEC in 1995 in a dilute ultracold atomic gas of sodium ^{23}Na . The three momentum distributions at different temperatures illustrate how the condensation sets in: well above T_c we have the Maxwell-Boltzmann distribution (left); at T_c the peak corresponding to the macroscopic occupation of the ground state appears (middle); well below T_c the thermal cloud disappears and only the peak around $\mathbf{p} = 0$ remains (right). The figure is taken from Wikipedia and authored by NIST/JILA/CU-Boulder [NIST Image, public domain, https://commons.wikimedia.org/wiki/File:Bose_Einstein_condensate.png].

gas at three different temperatures. The distribution on the left-hand side corresponds to the thermal (Maxwell–Boltzmann) distribution at a temperature well above the critical one (T_c), while the distribution in the middle represents the results for the system at the critical temperature $T_c = 170$ nK. This distribution is bimodal, containing both the thermal component and a peak that corresponds to the emerging condensed fraction of atoms. The distribution on the right-hand side is obtained after an additional evaporative cooling brings the system down to the temperature $T = 20$ nK $\ll T_c$. Since the system is now significantly below the critical temperature, practically all atoms are in the condensate, and the experimental momentum distribution exhibits a single-peak distribution that corresponds just to the condensed fraction.

1.1 Role of interactions

Investigation of ultracold quantum gases is a very attractive research field that involves a large number of theoretical and experimental groups worldwide. Such a widespread interest comes from the fact that properties of the BEC systems can be broadly tuned in an unprecedented range. In particular, this applies to the strength of contact interactions that can be varied over many orders of magnitude using the Feshbach resonance [9] technique. The existence of Feshbach resonances is related to atomic bound states and can be practically manipulated by an external magnetic field, thus adjusting the electronic structure of atoms. In this way, close to a Feshbach resonance, the strength of the contact interaction can be dynamically tuned over a wide range of values. Furthermore, not only the amplitude, but also the sign of the interaction can be changed, i.e., the interaction can be tuned from very repulsive to very attractive.

After pioneering experiments that realized BEC in systems with weak contact interactions, it took a decade of work on accuracy improvement of experimental techniques to enable measurement of effects of the dipole-dipole interaction (DDI) that exists between atoms or molecules with a permanent or induced electrical or

magnetic dipole moment. The very first such experiment was realized in 2005 with chromium atoms ^{52}Cr [10], while the experiments with atoms with much larger magnetic moments, such as dysprosium ^{164}Dy [11] and erbium ^{168}Er [12] came after. Furthermore, the dipolar condensates comprised of ultracold polar molecules with much stronger electrical [13] and magnetic [14] dipole moment were realized some years ago. While the contact interaction is symmetric and has a short-range, the DDI between atoms or molecules is anisotropic and long-range. These features are responsible for a whole series of new phenomena that appear in ultracold dipolar gases [15]. For example, due to the attractive component of the DDI, an instability exists, and the system is stable only for a number of atoms below the critical one. This is closely related to the trap geometry, and if the system contains a number of particles larger than the critical one, it may still be quasi-stable or collapse. The stability of the system depends not only on the trap geometry, but also on its interplay with the orientation of the dipoles. Note that in experiments the dipoles are not randomly oriented, but usually follow a preferential direction, determined by an external magnetic or electric field. If the system becomes unstable due to changes in the geometry of the trap or due to a number of particles which is above the critical, it undergoes a dynamical collapse during which interesting structures appear [16–18].

Although quantum fluctuations can be usually neglected, close to stability border they may play a crucial role and lead to new states of matter, such as the quantum droplets that were recently observed in dipolar condensates of dysprosium [19, 20] and erbium [21]. In these recent experiments, it was observed that the Rosensweig instability [22] due to the DDI is compensated by the stabilizing effect of quantum fluctuations. Note that the quantum droplets, emerging from the partial condensate collapse, are arranged in a lattice that, under certain circumstances can behave as the elusive supersolid state of matter [23]. Another interesting feature of quantum droplets is that they can be considered to be made of an incompressible quantum liquid.

The strength of the DDI can be also tuned using a fast rotating magnetic or

electric field [24, 25]. Therefore, both the contact interaction and the DDI strength can be varied in experiments, and they represent the important parameters of the system. We also note that the dimensionality of the system can be tuned and considered as a free parameter. Namely, by manipulating the harmonic trap frequencies, the geometry of the system can be transformed from the three-dimensional to quasi-two-dimensional or quasi-one-dimensional. Furthermore, this can also be done dynamically, during the experiment, at the same time as possible changes of the contact interaction and the DDI. Due to all of these features, the versatility of dipolar quantum gases is unparalleled and makes them obligatory elements of a toolbox for engineering quantum devices and sensors.

1.2 Collective oscillation modes

The very first BEC experiments have focused on the measurement of frequencies of low-lying collective oscillations modes of the system [26, 27]. Until nowadays such experiments remain the most accurate, and the frequencies of the collective oscillations can be measured with the precision of few per mill. These experiments are also the most natural ones, since they measure the response of the system to small perturbations. In a typical experiment, the system is prepared such that it occupies the ground state for a given set of parameters and the trap geometry. Afterward, the system is excited by a small perturbation of one of the parameters, e.g., a small variation of one of the trap frequencies, or moving of the trap origin, or change of the interaction strength. Such a perturbation generates the dynamical response of the system, which can be measured by imaging of the density profile of the system. This is done by the time-of-flight imaging or using one of *in situ* techniques [7, 8], which allow to measure the time dependence of the BEC properties, such as a center of mass position, condensate widths, etc. The Fourier analysis of these time dependencies reveals frequencies of the low-lying collective modes, typically breathing, quadrupole, radial-quadrupole, and dipole mode.

However, this approach does not allow the specific collective modes to be iden-

tified with the corresponding frequencies. Only if we know how the system should be excited in order to induce only one of the modes, it is possible to measure its frequency. Even if this the case, BEC systems are nonlinear and different collective modes are coupled. Therefore, although initially only one mode could be excited, other collective modes will get excited over time through the transfer of energy. Only detailed theoretical modeling of the systems' dynamics allows us to identify the frequencies with the corresponding collective modes properly. One of the most conventional methods for this is the time-dependent variational approach. Usually, variational parameters include the condensate widths and their dynamics reveal not only the frequencies, but also the type of the collective modes. The variational approach leads to a set of nonlinear differential equations, which reflect the nonlinear nature of BECs. The analysis of these equations allows to calculate not only the collective oscillation modes, but also to study the dynamics of the system. This includes the response of the system to driving of one of the parameters and the emergence of parametric resonances.

From a theoretical point of view, a BEC is usually studied in the formalism of second quantization. The corresponding many-body Hamiltonian includes the two-body interactions between the particles, which are of two types: the short-range contact interaction and the long-range DDI. Since the interactions are usually weak, they can be treated perturbatively, and the mean-field theory gives a basic description of the system. At zero temperature, we can neglect thermal excitations, and the mean-field theory yields the Gross–Pitaevskii equation (GPE). For dipolar systems, the standard GPE has to be extended to include the corresponding dipolar interaction term. These equations, which are also called nonlinear Schrödinger equations, due to the presence of nonlinear interaction-induced terms, are capable of describing practically all phenomena that appear in BEC systems, with reasonable precision. In particular, the GPE can be used as a basis for the variational approach, as outlined above. However, if a more precise description of the system is necessary, a full numerical solution of the GPE may be required. Its analysis can also be used to calculate the frequencies of the collective modes. Since the frequencies of the collective modes are measured experimentally with high accuracy, they are used to

estimate the accuracy of all theoretical and numerical approaches for the modeling of BECs. While the variational and other theoretical approaches enable the derivation of functional dependencies of the collective mode frequencies on the system's parameters, it is clear that their accuracy is limited by the selection of the variational ansatz and by the approximation order in a perturbation expansion. On the other hand, a full numerical approach is much more accurate. It allows direct solving of the mean-field theory equations, or higher-order theories, but requires a numerical simulation for each given set of parameters. Only a combination of analytical and numerical approaches, and a comparison with experimental results, provide us with full description and understanding of the system in a comprehensive way.

In addition to well-known low-lying excitation modes mentioned previously, due to nonlinearity in ultracold quantum gases some other types of excitations can emerge as well. Density waves are an important example of nonlinear excitations and can be induced by a harmonic modulation of the trap frequencies or interaction strength. The motivation for this comes from the classical phenomenon of Faraday waves, which may appear on the surface of the shallow layer of liquid under certain conditions. Namely, if the container with the liquid is harmonically oscillated in a vertical direction, the wave patterns may emerge, depending on the ratio of the liquid depth and the container size, as well as depending on the modulation frequency. This phenomenon was first studied and described by Michael Faraday at the beginning of the XIX century [28]. The interest for such type of excitations arose again during the 1980s in the context of nonlinear liquids. In the context of ultracold gases, Faraday waves were first investigated theoretically in 2002 by Staliunas [29]. After his first theoretical and numerical results for the systems with contact interaction where he assumed that the interaction strength is harmonically modulated, the Faraday waves were first measured in the BEC experiments with rubidium atoms in 2007 by Engels [30]. In the experiment, the radial part of the harmonic trap was modulated instead of interaction strength. However, qualitatively this leads to the same type of density waves. Although in the case of nonlinear liquids the generated waves are surface waves, in the literature the same name, i.e., Faraday waves is also used for the density waves that emerge as a result of the harmonic modulation in

the realm of ultracold quantum gases.

Faraday waves in ultracold gases are a consequence of the existence of parametric resonances in the system. While the spatial period of these waves depends on the geometry of the system and other parameters, the frequency of their oscillations is constant and is two times smaller than the modulation frequency. This is characteristic of all parametric resonant phenomena, and in the variational approach leads to the Mathieu-like differential equation that gives the observed ratio of the frequency of Faraday waves and the modulation. The Faraday density waves with half of the modulation frequency, are not the only nonlinear excitation of the system. In a driven system, there are always excitations corresponding to waves that have the same frequency as the modulation. However, they become resonant when the modulation frequency corresponds to one of the collective mode frequencies, or their linear combination, or a multiple. The resonant waves develop in the system and grow exponentially, much faster than the Faraday waves. Therefore, these two phenomena can be easily distinguished, not only by comparing their frequencies, but also the corresponding onset times. So far, Faraday and resonant waves have been studied in a single [29] and binary BEC systems [31], both with spatially homogeneous and inhomogeneous contact interactions [32].

1.3 This thesis

The focus of this thesis is on the study of excitation modes of dipolar Bose-Einstein condensates, including the collective oscillation modes, and density waves that emerge as a result of the driving of the system. In particular, the thesis investigates the Faraday waves and effects of the contact and dipole-dipole interaction.

Chapter 1 gives an introduction into the field of ultracold atoms and important role that interactions play for the properties of Bose-Einstein condensates. It also introduces collective oscillation modes, Faraday and resonant waves, and discusses the theoretical approaches used for their description.

Chapter 2 describes in detail noninteracting Bose gases at zero temperature, and presents a mean-field theory for weakly interacting Bose systems with the short-range contact and the long-range dipole-dipole interaction. This chapter also presents a variational approach for the description of static and dynamic properties of dipolar BECs.

Ground-state properties of dipolar condensates are explored in Chapter 3. Using the variational approach introduced in Chapter 2, the corresponding equations for the ground state are derived, including the special cases of cylindrical symmetry, and pure contact interaction. The variational results are compared with full numerical results obtained by solving the three-dimensional dipolar GPE for three atomic species that possess the magnetic dipolar moments: chromium, erbium, and dysprosium.

Chapter 4 provides a variational description of the collective oscillation modes and derives the expressions for their frequencies as functions of the contact and dipole-dipole interaction strength, which are then verified by comparison with the full numerical results.

The Faraday and resonant waves are studied in Chapter 5. At first, a variational approach is developed, that is capable of capturing the emergence and dynamics of density waves in dipolar condensates. Using the properties of Mathieu's differential equation, the most unstable modes are identified and the expressions for the spatial periods of Faraday and resonant waves are derived. The phenomenon of density waves is then studied numerically in detail for the three atomic species and the obtained results are compared with the variational ones [33].

Chapter 6 presents details on the algorithm we use to solve the dipolar GPE and the split-step semi-implicit Crank-Nicolson method. Finally, Chapter 7 summarizes all results and gathers our conclusions. Appendices A – F present further analytical and numerical details that are relevant for certain chapters, but would overburden the main text.

2 Bose-Einstein condensation and dipole-dipole interaction

BEC is usually described in the formalism of second quantization [7,8]. First, using this formalism we will show that the macroscopic occupation of the ground state leads to the spatial coherence in the condensate, i.e., to the off-diagonal long-range order (ODLRO). The system is described in terms of the one-body density matrix, which can be defined in the coordinate space by

$$\rho(\mathbf{r}, \mathbf{r}') = \langle \hat{\Psi}^\dagger(\mathbf{r}) \hat{\Psi}(\mathbf{r}') \rangle, \quad (2.1)$$

where $\hat{\Psi}^\dagger(\mathbf{r})$ is a creation operator and $\hat{\Psi}(\mathbf{r})$ is the corresponding annihilation operator, and the averaging is performed over the ensemble. These operators describe a creation or annihilation of a particle at the position \mathbf{r} , and, in the case of bosons, satisfy the bosonic commutation relations

$$[\hat{\Psi}(\mathbf{r}), \hat{\Psi}^\dagger(\mathbf{r}')] = \delta(\mathbf{r} - \mathbf{r}'), \quad [\hat{\Psi}(\mathbf{r}), \hat{\Psi}(\mathbf{r}')] = 0, \quad [\hat{\Psi}^\dagger(\mathbf{r}), \hat{\Psi}^\dagger(\mathbf{r}')] = 0. \quad (2.2)$$

For the system consisting of N identical bosons in a pure state, which is described by the N -body wave function $\Psi_n(\mathbf{r}_1, \dots, \mathbf{r}_N)$, the one-body density matrix can be written as an integral

$$\rho_n(\mathbf{r}, \mathbf{r}') = N \int d\mathbf{r}_2 \cdots d\mathbf{r}_N \Psi_n^*(\mathbf{r}, \mathbf{r}_2, \dots, \mathbf{r}_N) \Psi_n(\mathbf{r}', \mathbf{r}_2, \dots, \mathbf{r}_N), \quad (2.3)$$

which motivates the name of the matrix ρ . In a more general case, for a system in a mixed state in thermodynamic equilibrium, the one-body density matrix is calculated as an ensemble average, where the weights are given by the Boltzmann

distribution

$$\rho(\mathbf{r}, \mathbf{r}') = \frac{1}{Z} \sum_n e^{-\beta E_n} \rho_n(\mathbf{r}, \mathbf{r}'), \quad (2.4)$$

where n enumerates system's eigenstates Ψ_n , $\beta = 1/(k_B T)$ is the inverse temperature, and $Z = \sum_n e^{-\beta E_n}$ is the partition function. The diagonal elements of the density matrix correspond to the particle density

$$\rho(\mathbf{r}, \mathbf{r}) = \langle \hat{\Psi}^\dagger(\mathbf{r}) \hat{\Psi}(\mathbf{r}) \rangle = n(\mathbf{r}), \quad (2.5)$$

and the total number of particles can be calculated as $N = \int d\mathbf{r} n(\mathbf{r}) \equiv \int d\mathbf{r} \rho(\mathbf{r}, \mathbf{r})$.

Similarly, the one-body density matrix can be represented in the momentum space

$$\rho(\mathbf{p}, \mathbf{p}') = \langle \hat{\Psi}^\dagger(\mathbf{p}) \hat{\Psi}(\mathbf{p}') \rangle, \quad (2.6)$$

where the field operator in momentum space can be obtained from the coordinate representation by a Fourier transform

$$\hat{\Psi}(\mathbf{p}) = \frac{1}{(2\pi\hbar)^{3/2}} \int d\mathbf{r} e^{-\frac{i}{\hbar}\mathbf{p}\cdot\mathbf{r}} \hat{\Psi}(\mathbf{r}). \quad (2.7)$$

Again, the diagonal elements give the density of the particles, this time in momentum space, $n(\mathbf{p}) = \rho(\mathbf{p}, \mathbf{p})$, and the total number of particles can be calculated in a similar manner, $N = \int d\mathbf{p} n(\mathbf{p})$. In a Bose-Einstein-condensed system, we have a macroscopic occupation of the ground state, which means that the particle density in momentum space has a form

$$n(\mathbf{p}) = N_0 \delta(\mathbf{p}) + \tilde{n}(\mathbf{p}), \quad (2.8)$$

where the occupation $N_0/N \lesssim 1$. Let us see what consequences this has for the density matrix. If we insert equation (2.7) into equation (2.6) for $\mathbf{p} = \mathbf{p}'$, we get

$$n(\mathbf{p}) = \frac{1}{(2\pi\hbar)^3} \int d\mathbf{R} ds \rho\left(\mathbf{R} + \frac{\mathbf{s}}{2}, \mathbf{R} - \frac{\mathbf{s}}{2}\right) e^{\frac{i}{\hbar}\mathbf{p}\cdot\mathbf{s}}. \quad (2.9)$$

where \mathbf{R} represents center-of-mass coordinate, and \mathbf{s} the distance between the two arguments in density matrix. For a uniform and isotropic system of volume V , where we assume that in the thermodynamic limit $N, V \rightarrow \infty$ the particle density is constant $n = N/V$, the one-body density matrix depends only on the distance

s , and not on the center-of-mass coordinate \mathbf{R} , i.e., $\rho(\mathbf{R} + \mathbf{s}/2, \mathbf{R} - \mathbf{s}/2) = \rho(s)$. Therefore, the above equation for the density yields

$$\rho(s) = \frac{1}{V} \int d\mathbf{p} n(\mathbf{p}) e^{-\frac{i}{\hbar} \mathbf{p} \cdot \mathbf{s}}. \quad (2.10)$$

For a normal system with a smooth momentum distribution $n(\mathbf{p})$ at small momenta, the one-body density vanishes in the limit $s \rightarrow \infty$, due to oscillatory nature of the phase factor $e^{-\frac{i}{\hbar} \mathbf{p} \cdot \mathbf{s}}$. However, the condensed system, which contains a delta function at $\mathbf{p} = 0$ gives a surprising result that $\rho(s) \rightarrow N_0/N$ when $s \rightarrow \infty$. The fact that off-diagonal elements of the one-body density matrix do not vanish even in the limit $s \rightarrow \infty$, shows that the existence of the condensate leads to coherence in the system, i.e., the long-range order.

To study excitations of the system, we use eigenstates of the density matrix $\varphi_i(\mathbf{r})$, where we assume, for simplicity, that the spectrum is discrete. In this basis, the density matrix is expressed as

$$\rho(\mathbf{r}, \mathbf{r}') = N_0 \varphi_0^*(\mathbf{r}) \varphi_0(\mathbf{r}') + \sum_{i>0} N_i \varphi_i^*(\mathbf{r}) \varphi_i(\mathbf{r}'). \quad (2.11)$$

Here φ_0 represents the single-particle state with the occupancy N_0 , while N_i are occupancies of excited states. Note that the above equation leads to expression (2.8) for the density $n(\mathbf{p})$ using equation (2.9) and orthonormality of the eigenstates $\varphi_i(\mathbf{r})$. For a uniform system of non-interacting bosons, the eigenstates are plane waves $\varphi_{\mathbf{p}}(\mathbf{r}) = e^{i\mathbf{p} \cdot \mathbf{r}/\hbar} / \sqrt{V}$, while in a general case the functions φ_i have to be determined by solving the corresponding eigenproblem. Using this basis, the field operator can be expressed as

$$\hat{\Psi}(\mathbf{r}) = \sum_i \varphi_i \hat{a}_i. \quad (2.12)$$

where new bosonic operators \hat{a}_i represent elementary excitations of the system and obey bosonic commutation relations

$$[\hat{a}_i, \hat{a}_j^\dagger] = \delta_{ij}, \quad [\hat{a}_i, \hat{a}_j] = 0, \quad [\hat{a}_i^\dagger, \hat{a}_j^\dagger] = 0. \quad (2.13)$$

If the system is well below the critical temperature for Bose-Einstein condensation, we can use a zero-temperature approximation and neglect thermal excitations. We

can also assume that practically all of the particles are in the ground state and that only a small fraction is excited, which corresponds to the following decomposition of the field operator

$$\hat{\Psi}(\mathbf{r}) = \Psi_0(\mathbf{r}) + \delta\hat{\Psi}(\mathbf{r}), \quad (2.14)$$

where $\Psi_0(\mathbf{r}) \equiv \varphi_0(\mathbf{r}) \hat{a}_0 \approx \sqrt{N_0} \varphi_0$ is the wave function of the condensate and $\delta\hat{\Psi}(\mathbf{r}) = \sum_{i \neq 0} \varphi_i(\mathbf{r}) \hat{a}_i$ represents excitations due to quantum fluctuation. Note that the ground-state operators \hat{a}_0 and \hat{a}_0^\dagger can be replaced by a c -number $\sqrt{N_0}$ due to macroscopic occupation of the ground state, and the fact that Bose-Einstein condensation corresponds to breaking of the $U(1)$ symmetry associated with the phase of the wave function [8]. In other words, below the critical temperature the order parameter does not vanish,

$$\langle \hat{a}_0 \rangle = \langle \hat{a}_0^\dagger \rangle = \sqrt{N_0} \neq 0. \quad (2.15)$$

The time evolution of the system is determined by $e^{-i\hat{H}t/\hbar}$, where \hat{H} is the Hamiltonian of the system, so the evolution of the ground-state wave function of the condensate is given by

$$\Psi_0(\mathbf{r}, t) = \Psi_0(\mathbf{r}) e^{-i\mu t/\hbar}, \quad (2.16)$$

where

$$\mu = E(N_0) - E(N_0 - 1) = \left. \frac{\partial E}{\partial N} \right|_{N=N_0} \quad (2.17)$$

is the system's chemical potential.

2.1 Noninteracting Bose gas

Previously we have neglected the thermal excitations and have used the zero-temperature approximation. However, depending on the temperature, we may have to take into account thermal excitations. For a uniform noninteracting Bose gas in a box of volume V , the eigenstates are plain waves that satisfy the periodic boundary conditions and have a dispersion relation $\epsilon(\mathbf{p}) = p^2/2m$. According to the Bose-Einstein distribution function, the number of atoms in thermal (excited) states is

given by

$$N_{\text{th}}(T) = \sum_{\mathbf{p} \neq 0} \frac{1}{e^{\beta(p^2/2m - \mu)} - 1}, \quad (2.18)$$

where m is the mass of an atom. Using a semi-classical approximation and replacing the above sum with the integral, $\sum_{\mathbf{p}} \rightarrow V/(2\pi\hbar)^3 \int d\mathbf{p}$, we obtain

$$N_{\text{th}}(T) = \frac{V}{\lambda_T^3} \frac{2}{\sqrt{\pi}} \int_0^\infty \frac{x^{1/2} dx}{e^{-\beta\mu} e^x - 1} = \frac{V}{\lambda_T^3} g_{3/2}(e^{\beta\mu}), \quad (2.19)$$

where $\lambda_T = \sqrt{2\pi\hbar^2\beta/m}$ is the thermal wavelength and $g_p(z) = \sum_{l=1}^\infty z^l/l^p$ is Bose function. From the above equation we obtain the critical temperature T_c at which all atoms are in the thermal population, i.e., $N_{\text{th}}(T_c) = N$. This leads to

$$k_B T_c = \frac{2\pi\hbar^2}{m} \left(\frac{n}{g_{3/2}(1)} \right)^{2/3}, \quad (2.20)$$

where $n = N/V$ is the density of the gas and $g_{3/2}(1) \approx 2.612$. Note that the chemical potential of a uniform system above the critical temperature can be taken to be zero due to the dispersion relation, such that $e^{\beta\mu} = 1$. Above the critical temperature all particles are in the thermal cloud, and we have $N = V g_{3/2}(1)/\lambda_{T_c}^3$, according to equation (2.19). On the other hand, below T_c the number of thermal atoms decreases, and we have $N_{\text{th}}(T) = (T/T_c)^{3/2} N$, which is obtained by combining equations (2.19) and (2.20). Therefore, the number of particles in the condensate is given by

$$N_0(T) = N \left[1 - \left(\frac{T}{T_c} \right)^{3/2} \right], \quad (2.21)$$

and becomes macroscopic for $T < T_c$.

The situation changes in the presence of an external trapping potential. The most frequently encountered and experimentally used potential is a harmonic trap, given by

$$U(x, y, z) = \frac{m}{2} (\omega_x^2 x^2 + \omega_y^2 y^2 + \omega_z^2 z^2), \quad (2.22)$$

where ω_i , $i \in \{x, y, z\}$, are the trapping frequencies. The temperature dependence of the number of atoms in the condensate is now different and reads

$$N_0(T) = N \left[1 - \left(\frac{T}{T_c} \right)^3 \right]. \quad (2.23)$$

This is illustrated in Figure 2.1, where the blue line represents the condensate fraction for a homogeneous system, and red line the condensate fraction in the presence of an external harmonic trap. Not only that temperature dependence is modified by the presence of the trap, but also the critical temperature changes, and is now defined as

$$k_B T_c = \hbar\omega \left(\frac{N}{\zeta(3)} \right)^{1/3}, \quad (2.24)$$

where $\omega = (\omega_x \omega_y \omega_z)^{1/3}$ is the geometric average of the trap frequencies, and $\zeta(3) = g_3(1) \approx 0.94$. Note that the energy scale for the critical temperature is now given by the trap energy $\hbar\omega$, and that T_c now depends on the number of particles as $N^{1/3}$, while for the uniform case it was $N^{2/3}$.

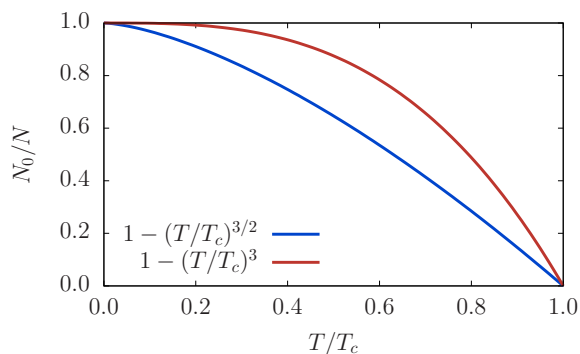


Figure 2.1: The condensate fraction N_0/N as a function of the temperature T/T_c for a noninteracting Bose gas: homogeneous case (blue line) and harmonically trapped case (red line).

2.2 Weakly-interacting Bose gas

The ground-state energy of an ideal Bose gas is equal to zero, this leads to zero pressure and infinite compressibility. However, the presence of interactions in the system, even the weak ones, dramatically changes this. Here we briefly outline the Bogoliubov theory to first order in the interaction strength, which is capable of describing a dilute Bose-Einstein-condensed gas. Precisely such systems were experimentally realized, and it was shown that only two-particle interactions significantly contribute to the energy of the systems, while interactions of three and more particles can be neglected. Also, due to large inter-particle distances, the details of the

two-body interactions can be neglected as well, i.e., they can be modeled just as s -wave scattering processes in a dilute Bose gas, described by the s -wave scattering length. The many-body Hamiltonian of such a system is given by

$$\hat{H} = \frac{\hbar^2}{2m} \int d\mathbf{r} \nabla \hat{\Psi}^\dagger(\mathbf{r}) \nabla \hat{\Psi}(\mathbf{r}) + \frac{1}{2} \int d\mathbf{r} d\mathbf{r}' \hat{\Psi}^\dagger(\mathbf{r}) \hat{\Psi}^\dagger(\mathbf{r}') U_c(\mathbf{r} - \mathbf{r}') \hat{\Psi}(\mathbf{r}') \hat{\Psi}(\mathbf{r}), \quad (2.25)$$

where $U_c(\mathbf{r})$ represents the model potential for the above-described contact interactions. The field operator in the case of a uniform gas and in the basis of plane waves reads $\hat{\Psi}(\mathbf{r}) = \sum_{\mathbf{p}} \hat{a}_{\mathbf{p}} e^{i\mathbf{p}\cdot\mathbf{r}/\hbar} / \sqrt{V}$, where $\hat{a}_{\mathbf{p}}$ is the operator annihilating a particle in the state with momentum \mathbf{p} . Inserting this into the above Hamiltonian, we obtain

$$\hat{H} = \sum_{\mathbf{p}} \frac{p^2}{2m} \hat{a}_{\mathbf{p}}^\dagger \hat{a}_{\mathbf{p}} + \frac{1}{2V} \sum_{\mathbf{q}, \mathbf{p}_1, \mathbf{p}_2} U_c(\mathbf{q}) \hat{a}_{\mathbf{p}_1+\mathbf{q}}^\dagger \hat{a}_{\mathbf{p}_2-\mathbf{q}}^\dagger \hat{a}_{\mathbf{p}_1} \hat{a}_{\mathbf{p}_2}, \quad (2.26)$$

where \mathbf{p}_1 and \mathbf{p}_2 denote momenta of the interacting particles before the collision, \mathbf{q} the exchanged momentum in the collision, while $U_c(\mathbf{q}) = \int U_c(\mathbf{r}) e^{-i\mathbf{q}\cdot\mathbf{r}/\hbar} d\mathbf{r}$ is a Fourier transform of the interaction potential. For the temperatures below the critical one, the main contribution of the interaction to the Hamiltonian is due to the particles with small momenta, $\mathbf{q} \approx 0$. If we denote the zero-momentum component by $g \equiv U_c(\mathbf{q} = 0)$, the Hamiltonian of the system can be rewritten as

$$\hat{H} = \sum_{\mathbf{p}} \frac{p^2}{2m} \hat{a}_{\mathbf{p}}^\dagger \hat{a}_{\mathbf{p}} + \frac{g}{2V} \sum_{\mathbf{p}_1, \mathbf{p}_2} \hat{a}_{\mathbf{p}_1}^\dagger \hat{a}_{\mathbf{p}_2}^\dagger \hat{a}_{\mathbf{p}_1} \hat{a}_{\mathbf{p}_2}. \quad (2.27)$$

Note that the above approximation is mathematically equivalent to replacing the real inter-particle interaction potential with the modeled contact potential $U_c(\mathbf{r} - \mathbf{r}') = g \delta(\mathbf{r} - \mathbf{r}')$.

As we have seen, below the critical temperature the order parameter does not vanish and we can replace the operators \hat{a}_0 and \hat{a}_0^\dagger by a c -number $\sqrt{N_0}$, where $N_0 = N$ at zero temperature, when all particles are condensed. If we restrict the sums in equation (2.27) to zero momentum contributions, which yield the ground state, we obtain for the ground-state energy

$$E_0 = \frac{gN^2}{2V} = \frac{1}{2} Nng. \quad (2.28)$$

The interaction coupling constant g can be expressed via s -wave scattering length a_s as $g = 4\pi\hbar^2 a_s / m$. Contrary to the noninteracting case, the pressure P of a condensed

weakly-interacting Bose gas does not vanish at zero temperature. Instead, it is given by $P = -\partial E_0/\partial V = gn^2/2$, and the compressibility is now finite, $\partial n/\partial P = 1/(gn)$. The compressibility is related to the speed of sound c by a relation $1/(mc^2) = \partial n/\partial P$. Using this, we can derive the sound velocity in the condensate and obtain $c = \sqrt{gn/m}$.

The above zeroth-order approximation is capable of providing us with the estimates for the ground-state energy, but not more than that. In order to describe the system in more detail, we have to go to the higher-order approximation such that we include the operators $\hat{a}_{\mathbf{p}}$ and $\hat{a}_{\mathbf{p}}^\dagger$ with $\mathbf{p} \neq 0$. The Hamiltonian does not contain the linear terms in $\hat{a}_{\mathbf{p}}$, and the first non-trivial approximation is quadratic,

$$\hat{H} = \frac{g}{2V} \hat{a}_0^\dagger \hat{a}_0^\dagger \hat{a}_0 \hat{a}_0 + \sum_{\mathbf{p}} \frac{p^2}{2m} \hat{a}_{\mathbf{p}}^\dagger \hat{a}_{\mathbf{p}} + \frac{g}{2V} \sum_{\mathbf{p} \neq 0} \left(\hat{a}_0^\dagger \hat{a}_{\mathbf{p}}^\dagger \hat{a}_0 \hat{a}_{\mathbf{p}} + \hat{a}_{\mathbf{p}}^\dagger \hat{a}_{-\mathbf{p}}^\dagger \hat{a}_0 \hat{a}_0 + \hat{a}_0^\dagger \hat{a}_0^\dagger \hat{a}_{\mathbf{p}} \hat{a}_{-\mathbf{p}} \right). \quad (2.29)$$

Luckily, quadratic Hamiltonians can be explicitly diagonalized, which we do here following Bogoliubov prescription. As it was done in the zeroth-order approximation, in the terms in brackets of Equation (2.29) we replace the operators \hat{a}_0 and \hat{a}_0^\dagger with \sqrt{N} , while for the first term we have to use a better approximation that is obtained from the normalization $\hat{a}_0^\dagger \hat{a}_0 + \sum_{\mathbf{p} \neq 0} \hat{a}_{\mathbf{p}}^\dagger \hat{a}_{\mathbf{p}} = N$, which leads to

$$\hat{a}_0^\dagger \hat{a}_0^\dagger \hat{a}_0 \hat{a}_0 = N^2 - 2N \sum_{\mathbf{p} \neq 0} \hat{a}_{\mathbf{p}}^\dagger \hat{a}_{\mathbf{p}}, \quad (2.30)$$

up to terms quadratic in $\hat{a}_{\mathbf{p}}$. Note that the scattering theory [34], to the same approximation order, requires the renormalization of the interaction strength g

$$g \rightarrow g \left(1 + \frac{g}{V} \sum_{\mathbf{p} \neq 0} \frac{m}{p^2} \right). \quad (2.31)$$

By substituting Equations (2.30) and (2.31) into the Hamiltonian (2.29), we obtain

$$\hat{H} = g \frac{N^2}{2V} + \sum_{\mathbf{p}} \frac{p^2}{2m} \hat{a}_{\mathbf{p}}^\dagger \hat{a}_{\mathbf{p}} + \frac{1}{2} gn \sum_{\mathbf{p} \neq 0} \left(2\hat{a}_{\mathbf{p}}^\dagger \hat{a}_{\mathbf{p}} + \hat{a}_{\mathbf{p}}^\dagger \hat{a}_{-\mathbf{p}}^\dagger + \hat{a}_{\mathbf{p}} \hat{a}_{-\mathbf{p}} + \frac{mgn}{p^2} \right), \quad (2.32)$$

which can be diagonalized using the Bogoliubov transformation

$$\hat{a}_{\mathbf{p}} = u_{\mathbf{p}} \hat{b}_{\mathbf{p}} + v_{-\mathbf{p}}^* \hat{b}_{-\mathbf{p}}^\dagger, \quad \hat{a}_{\mathbf{p}}^\dagger = u_{\mathbf{p}}^* \hat{b}_{\mathbf{p}}^\dagger + v_{-\mathbf{p}} \hat{b}_{-\mathbf{p}}. \quad (2.33)$$

We require that new operators $\hat{b}_{\mathbf{p}}$ and $\hat{b}_{\mathbf{p}}^\dagger$ obey the same bosonic commutation relations as the operators $\hat{a}_{\mathbf{p}}$ and $\hat{a}_{\mathbf{p}}^\dagger$, which leads to the condition $|u_{\mathbf{p}}|^2 - |v_{-\mathbf{p}}|^2 = 1$. From this, we see that the coefficients u and v can be parametrized as follows

$$u_{\mathbf{p}} = \cosh \alpha_{\mathbf{p}}, \quad v_{-\mathbf{p}} = \sinh \alpha_{\mathbf{p}}. \quad (2.34)$$

In the above equation, the parameter $\alpha_{\mathbf{p}}$ has to be chosen such that non-diagonal elements of the Hamiltonian (2.32) vanish. For such $\alpha_{\mathbf{p}}$, the Hamiltonian becomes

$$\hat{H} = \tilde{E}_0 + \sum_{\mathbf{p} \neq 0} \epsilon(\mathbf{p}) \hat{b}_{\mathbf{p}}^\dagger \hat{b}_{\mathbf{p}}, \quad (2.35)$$

where

$$\tilde{E}_0 = E_0 + \frac{1}{2} \sum_{\mathbf{p} \neq 0} \left[\epsilon(\mathbf{p}) - gn - \frac{p^2}{2m} + \frac{m(gn)^2}{p^2} \right], \quad (2.36)$$

with $\epsilon(\mathbf{p})$ given by

$$\epsilon(\mathbf{p}) = \sqrt{\left(\frac{p^2}{2m}\right)^2 + c^2 p^2}, \quad (2.37)$$

which is known as the Bogoliubov dispersion law. Here c stands for the speed of sound $c = \sqrt{gn/m}$. The diagonalization of the system using the Bogoliubov transformation allows us to connect the system of interacting bosons with a noninteracting system of particles with the energy $\epsilon(\mathbf{p})$, whose annihilation and creation operators are $\hat{b}_{\mathbf{p}}$ and $\hat{b}_{\mathbf{p}}^\dagger$, respectively. Although this system is noninteracting, the dispersion is modified and is not given by a free particle expression $p^2/2m$. In the limit of small momenta $p \ll mc$, the dispersion (2.37) becomes $\epsilon(p) = cp$. From this, we see that elementary excitations of the system in the long-wavelength regime correspond to sound waves. From a symmetry point of view, these elementary excitations can be thought of as the Goldstone modes that correspond to breaking of the $U(1)$ symmetry of quantum mechanics due to the Bose-Einstein phase transition.

Note that the ground-state energy \tilde{E}_0 is given by

$$\tilde{E}_0 = E_0 \left(1 + \frac{128}{15\sqrt{\pi}} \sqrt{na_s^3} \right), \quad (2.38)$$

which is expressed in terms of the perturbation parameter na_s^3 . Therefore, we see that the Bogoliubov theory is valid if the previously introduced criterion (1.1) is satisfied, such that the correction to the energy, given in brackets of Equation (2.38) is small.

2.3 Mean-field theory for dipolar Bose gas in a trap

Bose-Einstein condensation is experimentally realized with a dilute Bose gas trapped in the external potential. Such a setup produces a nonuniform system, which is experimentally necessary to provide confinement of the system. However, this changes the properties of the system and is responsible for new phenomena, such as collective oscillations. Here we briefly outline the mean-field theory for a nonuniform Bose gas in the external potential $U(\mathbf{r}, t)$, both for stationary and non-stationary systems. However, as outlined in Chapter 1, in this thesis, we consider not only the short-range contact interaction $U_c(\mathbf{r} - \mathbf{r}') = g\delta(\mathbf{r} - \mathbf{r}')$, but also the long-range dipole-dipole interaction

$$U_{\text{dd}}(\mathbf{r}) = \frac{\mu_0}{4\pi} \frac{\mathbf{d}^2 \mathbf{r}^2 - 3(\mathbf{r} \cdot \mathbf{d})^2}{r^5}, \quad (2.39)$$

where μ_0 is the vacuum permeability and \mathbf{d} is the magnetic dipole moment. We assume that all dipoles are oriented in the same direction, as in experiments where, due to the present magnetic fields, this is always the case. If the dipoles are oriented in the z direction of the Cartesian coordinate system, the potential has the form

$$U_{\text{dd}}(\mathbf{r}) = \frac{\mu_0 \mu_{\text{d}}^2}{4\pi} \frac{1 - 3\cos^2\theta}{r^3}, \quad (2.40)$$

where θ is the angle made by the vector \mathbf{r} and the polarization direction z . The angle θ determines if DDI is attractive or repulsive. For instance, for $\theta = 0$ we have an attractive DDI, while for $\theta = \pi/2$ the interaction is repulsive, as illustrated in Figure 2.2. Note that the strength of the DDI is usually defined by the dipolar length

$$a_{\text{dd}} = \frac{\mu_0 \mu_{\text{d}}^2 m}{12\pi \hbar^2}. \quad (2.41)$$

This is convenient since it allows us to express the DDI in a similar way as the contact interaction strength is expressed in terms of the s -wave scattering length.

With all these ingredients, the Hamiltonian of the system in the Heisenberg picture is given by

$$\begin{aligned} \hat{H} = & \frac{\hbar^2}{2m} \int d\mathbf{r} \nabla \hat{\Psi}^\dagger(\mathbf{r}, t) \nabla \hat{\Psi}(\mathbf{r}, t) + \int d\mathbf{r} \hat{\Psi}^\dagger(\mathbf{r}, t) U(\mathbf{r}, t) \hat{\Psi}(\mathbf{r}, t) \\ & + \frac{1}{2} \int d\mathbf{r} d\mathbf{r}' \hat{\Psi}^\dagger(\mathbf{r}, t) \hat{\Psi}^\dagger(\mathbf{r}', t) U_{\text{int}}(\mathbf{r} - \mathbf{r}') \hat{\Psi}(\mathbf{r}', t) \hat{\Psi}(\mathbf{r}, t), \end{aligned} \quad (2.42)$$

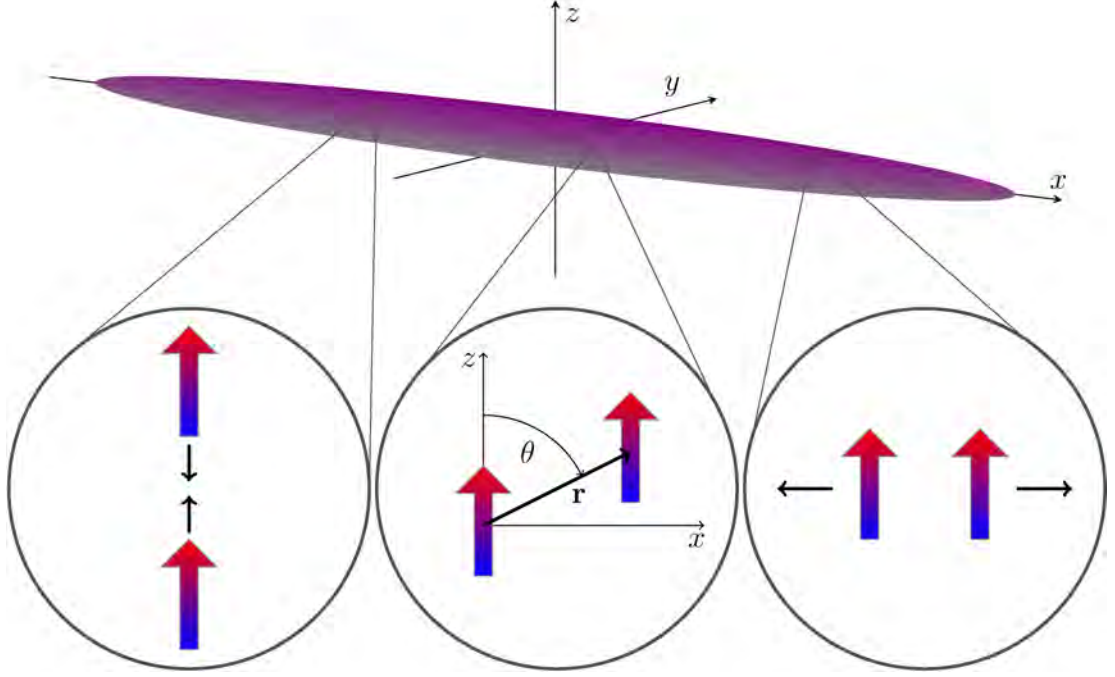


Figure 2.2: Illustration of dipole-dipole interactions of atoms whose dipole moments are polarized along the z axis. In the middle, we have a generic case determined by relative position between atoms \mathbf{r} and angle between the polarization axis z and vector \mathbf{r} . On the left-hand side is a special case $\theta = 0$, which is usually called head-to-tail configuration, when the dipoles attract each other. On the right-hand side is another special case, corresponding to $\theta = \pi/2$, when the dipoles repel. This configuration is usually called side-by-side.

where $U_{\text{int}}(\mathbf{r}) = U_c(\mathbf{r}) + U_{\text{dd}}(\mathbf{r})$. The dynamics of the system is governed by the Heisenberg equation

$$i\hbar \frac{\partial}{\partial t} \hat{\Psi}(\mathbf{r}, t) = [\hat{\Psi}(\mathbf{r}, t), \hat{H}] . \quad (2.43)$$

For the Hamiltonian (2.42), the above commutator can be readily calculated, and we obtain the equation of motion as follows

$$i\hbar \frac{\partial}{\partial t} \hat{\Psi}(\mathbf{r}, t) = \left[-\frac{\hbar^2}{2m} \nabla^2 + U(\mathbf{r}, t) + \int d\mathbf{r}' \hat{\Psi}^\dagger(\mathbf{r}', t) U_{\text{int}}(\mathbf{r} - \mathbf{r}') \hat{\Psi}(\mathbf{r}', t) \right] \hat{\Psi}(\mathbf{r}, t) . \quad (2.44)$$

The mean-field theory is obtained, according to (2.14), when we replace the field operator with the wave function of the condensate $\hat{\Psi}(\mathbf{r}, t) = \psi(\mathbf{r}, t)$ and neglect

quantum fluctuations, yielding the dipolar GPE in the form

$$i\hbar\frac{\partial}{\partial t}\psi(\mathbf{r},t) = \left[-\frac{\hbar^2}{2m}\nabla^2 + U(\mathbf{r},t) + g|\psi(\mathbf{r},t)|^2 + \int d\mathbf{r}'\psi^*(\mathbf{r}',t)U_{\text{dd}}(\mathbf{r}-\mathbf{r}',t)\psi(\mathbf{r}',t) \right] \psi(\mathbf{r},t). \quad (2.45)$$

The above equation is also called the nonlinear Schrödinger equation, where two types of nonlinearities are present due to the two types of interactions, namely the contact interaction and the DDI.

The dipolar GPE can be cast into a dimensionless form, which is useful for analytical and numerical considerations. This is done by choosing a reference frequency ω_r , and by expressing all other physical variables in units defined by it, i.e., lengths in units of harmonic oscillator length $l = \sqrt{\hbar/(m\omega_r)}$, time in units of $1/\omega_r$, and energy in units of $\hbar\omega_r$. This leads to dimensionless variables

$$x \rightarrow \frac{x}{l}, \quad y \rightarrow \frac{y}{l}, \quad z \rightarrow \frac{z}{l}, \quad a_s \rightarrow \frac{a_s}{l}, \quad a_{\text{dd}} \rightarrow \frac{a_{\text{dd}}}{l}, \quad t \rightarrow \omega_r t, \\ \psi(\mathbf{r},t) \rightarrow l^{3/2}\psi(\mathbf{r},t), \quad U(\mathbf{r},t) \rightarrow \frac{1}{\hbar\omega_r}U(\mathbf{r},t), \quad U_{\text{dd}}(\mathbf{r},t) \rightarrow \frac{1}{\hbar\omega_r}U_{\text{dd}}(\mathbf{r},t). \quad (2.46)$$

This rescales the harmonic trapping potential to the form

$$U(\mathbf{r},t) = \frac{1}{2}(\gamma^2x^2 + \nu^2y^2 + \lambda^2z^2), \quad (2.47)$$

where $\gamma = \omega_x/\omega_r$, $\nu = \omega_y/\omega_r$, and $\lambda = \omega_z/\omega_r$ are the trap aspect ratios, which may be time-dependent. Taking all this into account, the dimensionless dipolar GPE reads

$$i\frac{\partial\psi(\mathbf{r},t)}{\partial t} = \left[-\frac{1}{2}\nabla^2 + \frac{1}{2}(\gamma^2x^2 + \nu^2y^2 + \lambda^2z^2) + 4\pi Na_s|\psi(\mathbf{r},t)|^2 + 3Na_{\text{dd}}\int d\mathbf{r}'\frac{1-3\cos^2\theta}{|\mathbf{r}-\mathbf{r}'|^3}|\psi(\mathbf{r}',t)|^2 \right] \psi(\mathbf{r},t), \quad (2.48)$$

where θ is the angle between the vector $\mathbf{r}-\mathbf{r}'$ and z axis. The wave function here is normalized to unity $\int d\mathbf{r}|\psi(\mathbf{r},t)|^2 = 1$, and the density profile is given by $n(\mathbf{r},t) = N|\psi(\mathbf{r},t)|^2$. In the mean-field approximation, the many-body wave function can be written as

$$\Psi(\mathbf{r}_1, \dots, \mathbf{r}_N, t) \approx \prod_{i=1}^N \frac{1}{\sqrt{N}} \psi(\mathbf{r}_i, t). \quad (2.49)$$

The above time-dependent dipolar GPE describes the dynamics of the system. Since the ground state wave function has a common phase, it can be chosen to be zero, thus making the wave function real. The time-independent ground state wave function $\psi_0(\mathbf{r})$ satisfies the time-independent GPE, or the eigenequation

$$\begin{aligned} \mu \psi_0(\mathbf{r}) = & \left[-\frac{1}{2} \nabla^2 + \frac{1}{2} (\gamma^2 x^2 + \nu^2 y^2 + \lambda^2 z^2) + 4\pi N a_s |\psi(\mathbf{r})|^2 \right. \\ & \left. + 3N a_{\text{dd}} \int d\mathbf{r}' \frac{1 - 3 \cos^2 \theta}{|\mathbf{r} - \mathbf{r}'|^3} |\psi(\mathbf{r}')|^2 \right] \psi(\mathbf{r}), \end{aligned} \quad (2.50)$$

where the chemical potential μ is the corresponding eigenvalue. Both the time-dependent and time-independent dipolar GPE can be exactly solved only numerically. In this thesis, we do so using the Crank-Nicolson split-step semi-implicit method [35–37]. From the analytic point of view, we use the variational approach, which is presented in the next section.

2.4 Variational approach

The dipolar GPE equation can be written as the Euler-Lagrange equation for the following Lagrangian density

$$\begin{aligned} \mathcal{L}(\psi, \psi^*) = & \frac{i}{2} (\psi^* \dot{\psi} - \dot{\psi} \psi^*) + \frac{1}{2} \psi^* \nabla^2 \psi - U |\psi|^2 - 2\pi N a_s |\psi|^4 \\ & - \frac{3N a_{\text{dd}}}{2} |\psi|^2 \int d\mathbf{r}' \frac{1 - 3 \cos^2 \theta}{|\mathbf{r} - \mathbf{r}'|^3} |\psi(\mathbf{r}')|^2, \end{aligned} \quad (2.51)$$

where the wave function of the condensate is a function of space and time variables $\psi \equiv \psi(\mathbf{r}, t)$, and the trap potential $U \equiv U(\mathbf{r}, t)$ is given by Equation (2.47). The GPE (2.48) is obtained as the Euler-Lagrange equation with respect to ψ^* , or as the complex-conjugate of the Euler-Lagrange equation with respect to ψ . The above Lagrangian can be used as a starting point for a variational description of the ground state and the dynamics of a BEC. This is done by selecting a suitable ansatz for the wave function, calculating the Lagrangian of the system $L(t) = \int d\mathbf{r} \mathcal{L}$, and deriving the equations of motion for the variational parameters present in the wave function ansatz. The variational approach is a valuable method to study the behavior and properties of BECs and we use it to investigate the collective modes and density waves.

For the variational study, we use the Gaussian ansatz [38–41]

$$\psi(x, y, z, t) = \frac{1}{\pi^{3/4} \sqrt{u_x u_y u_z}} e^{-\frac{x^2}{2u_x^2} - \frac{y^2}{2u_y^2} - \frac{z^2}{2u_z^2} + ix^2 \phi_x + iy^2 \phi_y + iz^2 \phi_z}, \quad (2.52)$$

where the six variational parameters $\{u_i, \phi_i\}$ are functions of time and represent the condensate widths and conjugated phases, respectively. If only the ground state is studied, then the phases ϕ_i can be omitted, and the condensate widths can be assumed to be constant. However, if we want to study the system's dynamics, then the phases are necessary, and therefore we take them into account. The coefficient in front of the exponent function is chosen so as to keep the wave function normalized to unity.

Using the Lagrangian density (2.51) and ansatz function (2.52), by integration we calculate Lagrangian of the system, consisting of five terms

$$L(t) = L_1(t) + L_2(t) + L_3(t) + L_4(t) + L_5(t). \quad (2.53)$$

We calculate all term independently. The first one reads

$$L_1(t) = \frac{i}{2} \int d\mathbf{r} \left(\psi^* \dot{\psi} - \psi \dot{\psi}^* \right) = -\frac{1}{2} \left(u_x^2 \dot{\phi}_x + u_y^2 \dot{\phi}_y + u_z^2 \dot{\phi}_z \right), \quad (2.54)$$

while the kinetic energy term gives

$$L_2(t) = \frac{1}{2} \int d\mathbf{r} \psi^* \nabla^2 \psi = -\frac{1}{4} \left(\frac{1}{u_x^2} + \frac{1}{u_y^2} + \frac{1}{u_z^2} + 4u_x^2 \phi_x^2 + 4u_y^2 \phi_y^2 + 4u_z^2 \phi_z^2 \right). \quad (2.55)$$

The term corresponding to the potential energy yield

$$L_3(t) = - \int d\mathbf{r} U |\psi|^2 = -\frac{1}{4} \left(\gamma^2 u_x^2 + \nu^2 u_y^2 + \lambda^2 u_z^2 \right), \quad (2.56)$$

and the contact interaction term gives

$$L_4(t) = -2\pi N a_s \int d\mathbf{r} |\psi|^4 = -\frac{N a_s}{\sqrt{2\pi} u_x u_y u_z}. \quad (2.57)$$

The DDI term is more complex to calculate. It reads

$$L_5(t) = -\frac{3N a_{\text{dd}}}{2} \int d\mathbf{r} |\psi(\mathbf{r})|^2 \int d\mathbf{r}' U_{\text{dd}}(\mathbf{r} - \mathbf{r}') |\psi(\mathbf{r}')|^2, \quad (2.58)$$

where, in the rescaled units, the dipolar potential is given by

$$U_{\text{dd}}(\mathbf{r}) = \frac{1 - 3 \cos^2 \theta}{r^3}. \quad (2.59)$$

The \mathbf{r}' integral can be calculated using the convolution theorem,

$$L_5(t) = -\frac{3Na_{\text{dd}}}{2} \int d\mathbf{r} |\psi(\mathbf{r})|^2 \mathcal{F}^{-1} \left\{ \mathcal{F}[U_{\text{dd}}](\mathbf{k}) \mathcal{F}[|\psi|^2](\mathbf{k}) \right\}(\mathbf{r}). \quad (2.60)$$

where \mathcal{F} stands for the direct and \mathcal{F}^{-1} for the inverse Fourier transform. The above expression can be further simplified if we explicitly write the inverse Fourier transform,

$$L_5(t) = -\frac{3Na_{\text{dd}}}{2(2\pi)^3} \int d\mathbf{k} \mathcal{F}[U_{\text{dd}}](\mathbf{k}) \mathcal{F}[|\psi|^2](\mathbf{k}) \int d\mathbf{r} |\psi(\mathbf{r})|^2 e^{i\mathbf{k}\cdot\mathbf{r}}. \quad (2.61)$$

The last integral is equal to $\mathcal{F}[|\psi|^2]$, which can be readily calculated,

$$\mathcal{F}[|\psi|^2](\mathbf{k}) = e^{-\frac{1}{4}(k_x^2 u_x^2 + k_y^2 u_y^2 + k_z^2 u_z^2)}. \quad (2.62)$$

The Fourier transform of the dipolar potential $\mathcal{F}[U_{\text{dd}}](\mathbf{k})$ is calculated in Appendix A and reads

$$\mathcal{F}[U_{\text{dd}}](\mathbf{k}) = \frac{4\pi}{3} (3 \cos^2 \theta - 1) = \frac{4\pi}{3} \left(\frac{3k_z^2}{k^2} - 1 \right). \quad (2.63)$$

If we put all these elements together, the DDI term of the Lagrangian is given by

$$L_5(t) = -\frac{3Na_{\text{dd}}}{(2\pi)^2} \int d\mathbf{k} \left(3 \frac{k_z^2}{k_x^2 + k_y^2 + k_z^2} - 1 \right) e^{-\frac{1}{2}(k_x^2 u_x^2 + k_y^2 u_y^2 + k_z^2 u_z^2)}, \quad (2.64)$$

and, as shown in Appendix B, can be expressed in terms of the anisotropy function f ,

$$L_5(t) = \frac{Na_{\text{dd}}}{\sqrt{2\pi} u_x u_y u_z} f \left(\frac{u_x}{u_z}, \frac{u_y}{u_z} \right). \quad (2.65)$$

The anisotropy function [42] is defined as

$$f(x, y) = -\frac{1}{4\pi} \int_0^{2\pi} d\varphi \int_0^\pi d\theta \sin \theta \left(\frac{3x^2 y^2 \cos^2 \theta}{(x^2 \sin^2 \varphi + y^2 \cos^2 \varphi) \sin^2 \theta + x^2 y^2 \cos^2 \theta} - 1 \right), \quad (2.66)$$

and its solution can be expressed via elliptic integrals [43] of the first and the second kind. Details on the anisotropy function and how it can be expressed for different values of the arguments x and y are given in Appendix C. Now that we have calculated the Lagrangian of the system, we derive the Euler-Lagrange equations for the variational parameters,

$$\frac{d}{dt} \left(\frac{\partial L}{\partial \dot{q}_i} \right) - \frac{\partial L}{\partial q_i} = 0, \quad q_i \in \{u_x, u_y, u_z, \phi_x, \phi_y, \phi_z\}, \quad (2.67)$$

that describe the time evolution of the parameters. We first proceed with the equations for the phases ϕ_i , which turn out to be

$$\phi_i = \frac{\dot{u}_i}{2u_i}. \quad (2.68)$$

The Euler-Lagrange equations for the condensate widths u_i contain the phases ϕ_i and their derivatives, which can be eliminated using the above equations. This leads to the second-order differential equations for the parameters u_i in the form

$$\ddot{u}_x + \gamma^2 u_x - \frac{1}{u_x^3} - \sqrt{\frac{2}{\pi}} \frac{N}{u_x^2 u_y u_z} \left[a_s - a_{\text{dd}} f \left(\frac{u_x}{u_z}, \frac{u_y}{u_z} \right) + a_{\text{dd}} \frac{u_x}{u_z} f_1 \left(\frac{u_x}{u_z}, \frac{u_y}{u_z} \right) \right] = 0 \quad (2.69)$$

$$\ddot{u}_y + \nu^2 u_y - \frac{1}{u_y^3} - \sqrt{\frac{2}{\pi}} \frac{N}{u_x u_y^2 u_z} \left[a_s - a_{\text{dd}} f \left(\frac{u_x}{u_z}, \frac{u_y}{u_z} \right) + a_{\text{dd}} \frac{u_y}{u_z} f_2 \left(\frac{u_x}{u_z}, \frac{u_y}{u_z} \right) \right] = 0 \quad (2.70)$$

$$\ddot{u}_z + \lambda^2 u_z - \frac{1}{u_z^3} - \sqrt{\frac{2}{\pi}} \frac{N}{u_x u_y u_z^2} \left[a_s - a_{\text{dd}} f \left(\frac{u_x}{u_z}, \frac{u_y}{u_z} \right) - a_{\text{dd}} \frac{u_x}{u_z} f_1 \left(\frac{u_x}{u_z}, \frac{u_y}{u_z} \right) - a_{\text{dd}} \frac{u_y}{u_z} f_2 \left(\frac{u_x}{u_z}, \frac{u_y}{u_z} \right) \right] = 0 \quad (2.71)$$

where f_1 and f_2 are partial derivatives of the anisotropy function with respect to the first and the second argument. More details on these derivatives are given in Appendix C.

The above equations are used to variationally study the dipolar BEC dynamics, as well as the corresponding ground state. The algebraic equations determining the ground state are obtained by assuming that the condensate widths are constant, thus removing their second derivatives from the equations of motion.

3 Ground-state properties

In the previous section, we have seen that the condensation corresponds to the accumulation of a macroscopic number of particles in the ground state. In the mean-field theory at zero temperature, all atoms are condensed in the lowest single-particle quantum state, while the ground-state wave function $|\psi(\mathbf{r})|^2 = n(\mathbf{r})$ determines the density distribution of atoms. The wave function is a complex quantity, whose square of the modulus describes the contribution of the condensate to the diagonal elements of the density matrix ρ , and whose phase has a role in the coherence characterization. The wave function is defined up to a constant phase factor, reflecting the $U(1)$ symmetry of quantum mechanics. For a system with a time-independent Hamiltonian, the condensation leads to a symmetry breaking, such that the whole condensate is described by a constant phase, which can be set to zero. This can be also seen as a consequence of the off-diagonal long-range order discussed earlier. Since its phase can be set to zero, the wave function of the ground state can be always taken to be real-valued. In BEC experiments, the ground state usually represents the first step and is achieved by cooling an atomic or molecular sample using a variety of techniques. The ground state can be reliably described by the GPE [7, 8], as discussed previously. In typical experiments, the dynamics of the system is induced from the ground state by perturbing the system or changing some of the system parameters, such as the interaction strength or the trap geometry. The behavior of the system is then observed using the time-of-flight imaging technique or *in-situ* types of measurements.

For a noninteracting system, the GPE reduces to a Schrödinger equation with a

given trap potential. In case of a harmonic potential (2.22), the ground state of a noninteracting bosonic system is determined by the lowest single-particle quantum state, which is given by the Gaussian function

$$\psi(x, y, z) = \left(\frac{m}{\pi\hbar}\right)^{3/4} (\omega_x \omega_y \omega_z)^{1/4} e^{-\frac{m}{2\hbar}(\omega_x x^2 + \omega_y y^2 + \omega_z z^2)}. \quad (3.1)$$

Therefore, in the weak-interaction limit a Gaussian function represents a good choice for a perturbative or variational treatment of the system. In the other limiting case, when the interaction is strong such that the kinetic energy term can be neglected, one can use the inverted parabola of the Thomas-Fermi approximation as a starting point for various analytic approaches.

3.1 Variational description of the ground state

To describe the ground state variationally, we rely on the Gaussian ansatz (2.52). In the static case, the dynamical equations of motion (2.69) - (2.71) have the following form

$$\gamma^2 u_x - \frac{1}{u_x^3} - \sqrt{\frac{2}{\pi}} \frac{Na_s}{u_x^2 u_y u_z} + \sqrt{\frac{2}{\pi}} \frac{Na_{dd}}{u_x^2 u_y u_z} f\left(\frac{u_x}{u_z}, \frac{u_y}{u_z}\right) - \sqrt{\frac{2}{\pi}} \frac{Na_{dd}}{u_x u_y u_z^2} f_1\left(\frac{u_x}{u_z}, \frac{u_y}{u_z}\right) = 0, \quad (3.2)$$

$$\nu^2 u_y - \frac{1}{u_y^3} - \sqrt{\frac{2}{\pi}} \frac{Na_s}{u_x u_y^2 u_z} + \sqrt{\frac{2}{\pi}} \frac{Na_{dd}}{u_x u_y^2 u_z} f\left(\frac{u_x}{u_z}, \frac{u_y}{u_z}\right) - \sqrt{\frac{2}{\pi}} \frac{Na_{dd}}{u_x u_y u_z^2} f_2\left(\frac{u_x}{u_z}, \frac{u_y}{u_z}\right) = 0, \quad (3.3)$$

$$\begin{aligned} \lambda^2 u_z - \frac{1}{u_z^3} - \sqrt{\frac{2}{\pi}} \frac{Na_s}{u_x u_y u_z^2} + \sqrt{\frac{2}{\pi}} \frac{Na_{dd}}{u_x u_y u_z^2} f\left(\frac{u_x}{u_z}, \frac{u_y}{u_z}\right) + \sqrt{\frac{2}{\pi}} \frac{Na_{dd}}{u_y u_z^3} f_1\left(\frac{u_x}{u_z}, \frac{u_y}{u_z}\right) \\ + \sqrt{\frac{2}{\pi}} \frac{Na_{dd}}{u_x u_z^3} f_2\left(\frac{u_x}{u_z}, \frac{u_y}{u_z}\right) = 0. \end{aligned} \quad (3.4)$$

The ground state of the system is characterized by the constant condensate widths u_i , $i \in \{x, y, z\}$. Solving the above system of nonlinear algebraic equations we directly obtain the widths of the condensate. In some special cases, this can be done analytically. For example, if we neglect the dipole-dipole interaction by setting $a_{dd} = 0$, and if the system is cylindrically symmetric, such that $u_y = u_z = u_\rho$, the

variational equations reduce to

$$\gamma^2 u_x^4 = 1 + \sqrt{\frac{2}{\pi}} \frac{N a_s u_x}{u_\rho^2}, \quad (3.5)$$

$$u_\rho^4 = 1 + \sqrt{\frac{2}{\pi}} \frac{N a_s}{u_x}. \quad (3.6)$$

Because the number of atoms in the system is much larger than 1, the first term in the above equations can be neglected and the widths of the condensate can be expressed as

$$u_x \approx \left(\sqrt{\frac{2}{\pi}} \frac{N a_s}{\gamma^4} \right)^{1/5}, \quad u_\rho \approx \left(\sqrt{\frac{2}{\pi}} N a_s \gamma \right)^{1/5}. \quad (3.7)$$

As we can see, if we have only the contact interaction, the size of the condensate increases in all directions with the increase of the interaction strength as $a_s^{1/5}$. We also see that the condensate width u_x in the direction of weak confinement is always larger than u_ρ , since $u_x/u_\rho = 1/\gamma \gg 1$.

If we now take into account the dipole-dipole interaction, the system of equations (3.2) - (3.4) cannot be analytically solved anymore. However, it can be simplified when the direction of weak confinement matches the direction of the dipoles' polarization. Assuming cylindrical symmetry of the trap, the anisotropy function satisfies the following limit

$$\lim_{y \rightarrow x} x f_1(x, y) = \lim_{y \rightarrow x} y f_2(x, y) = \frac{(2 + x^2) f_s(x)}{2(1 - x^2)} - 1, \quad (3.8)$$

where $f_s(x) = f(x, x)$ is the cylindrically symmetric anisotropy function which is defined in Appendix C. Using this the variational equations (3.2) - (3.4) lead to the system

$$\gamma^2 u_x^4 = 1 + \sqrt{\frac{2}{\pi}} \frac{N u_x}{u_\rho^2} [a_s - a_{\text{dd}} A_x(\kappa)], \quad (3.9)$$

$$u_\rho^4 = 1 + \sqrt{\frac{2}{\pi}} \frac{N}{u_x} [a_s - a_{\text{dd}} A_\rho(\kappa)], \quad (3.10)$$

where $\kappa = u_\rho/u_x$, while functions $A_x(\kappa)$ and $A_\rho(\kappa)$ are defined by

$$A_x(\kappa) = \frac{2 - 7\kappa^2 - 4\kappa^4 + 9\kappa^4 d(\kappa)}{2(1 - \kappa^2)^2}, \quad (3.11)$$

$$A_\rho(\kappa) = \frac{1 + 10\kappa^2 - 9\kappa^2 d(\kappa) - 2\kappa^4}{(1 - \kappa^2)^2}, \quad (3.12)$$

with

$$d(\kappa) = \frac{\tanh^{-1} \sqrt{1 - \kappa^2}}{\sqrt{1 - \kappa^2}}. \quad (3.13)$$

In the limit of small κ , the above functions have limits $A_x(\kappa) \rightarrow 1$, $A_\rho(\kappa) \rightarrow 1$, with $\kappa^2 d(\kappa) \rightarrow 0$. If we again neglect the first term in Equations (3.9) and (3.10) due to $N \gg 1$, this system can be solved analytically in the zeroth-order in κ . The solutions are the same as (3.7), with a_s replaced by $\tilde{a}_s = a_s - a_{\text{dd}}$. However, depending on the value of κ , the corrections of the order κ and higher could be important, such that the system (3.9) and (3.10) has to be solved without applying $\kappa \rightarrow 0$ approximation. In this case, the above equations cannot be solved analytically and the numerical approach is necessary. As we are considering a case when the dipoles are oriented in the z direction and the cylindrical symmetry is not present anymore, we have to use the full set of variational equations (3.2) - (3.4) in order to determine the ground state widths.

Note that the above equations for the ground state widths, with or without cylindrical symmetry, can be used to assess the stability of the system as well. Namely, we know that even in the absence of the dipole-dipole interaction the system can become unstable if the contact interaction is attractive ($a_s < 0$). This happens if the number of atoms is sufficiently large, such that the right-hand sides of equations (3.2) - (3.4) become negative. The situation is more complex in the presence of the dipole-dipole interaction, which is anisotropic and can lead to instability due to the trap geometry, even for a large and positive contact interaction. The numerical appearance of negative condensate widths can be used to detect the onset of instability in the solutions of the above equations.

3.2 Ground state of ^{52}Cr , ^{168}Er and ^{164}Dy BECs

Now we will explore how the ground state looks like for condensates of atomic chromium ^{52}Cr , erbium ^{168}Er , and dysprosium ^{164}Dy , using a numeric and a varia-

tional approach for the system which parameters are given in detail in Appendix D. As outlined in Chapter 6, the numerical calculation of the ground state relies on the imaginary-time propagation. As a starting point we always use a Gaussian wave function that corresponds to the noninteracting case (3.1), i.e., the variational ansatz (2.52) with $u_i = 1/\sqrt{\omega_i/\omega_r}$ and $\phi_i = 0$, given by Equation D.3. Starting from such a state, depending on how far from the ground state it is, the imaginary-time propagation evolves it exponentially fast to the ground state. Figure 3.1 shows the ground-state condensate density for $N = 10^4$ atoms of the considered atomic species, together with the chosen Gaussian initial state. We plot the corresponding integrated densities

$$n(x) = \iint dy dz |\psi(x, y, z)|^2, \quad (3.14)$$

$$n(y) = \iint dz dx |\psi(x, y, z)|^2, \quad (3.15)$$

$$n(z) = \iint dx dy |\psi(x, y, z)|^2, \quad (3.16)$$

where blue line represents the corresponding initial, Gaussian state density n_i , and red line the numerically obtained ground state density n_f . The trap weakly confines the atoms in the x direction, and therefore the condensate density $n_f(x)$ is much more elongated than the other two densities. This can be seen in Figure 3.1 for all species, with the corresponding width for ^{52}Cr of around $35.706 \mu\text{m}$, while for ^{168}Er and ^{164}Dy the widths are around $23.201 \mu\text{m}$ and $23.339 \mu\text{m}$, respectively. Here the widths w_i , $i \in \{x, y, z\}$ are defined as two times the root-mean-square of the corresponding coordinate, i.e., $2\sqrt{\langle x^2 \rangle}$, $2\sqrt{\langle y^2 \rangle}$, $2\sqrt{\langle z^2 \rangle}$. Note that for the initial states we have $w_i = 2u_i = 2/\sqrt{\omega_i/\omega_r}$. The differences in the numerically obtained values of w_x are mainly the result of the contact interaction, i.e., a combination of the s -wave scattering lengths and masses of atoms. The values of a_s for all three species are quite similar, and therefore the main difference in the ground state widths comes from the mass difference, while the dipole-dipole effects are very small due to the small density $n(x)$. It is one order of magnitude smaller than the densities in other directions, as can be seen from Figure 3.1. However, the dipole-dipole interaction significantly changes the densities in the $y - z$ plane. Although the trap is cylindrically symmetric in that plane, the dipole-dipole interaction breaks

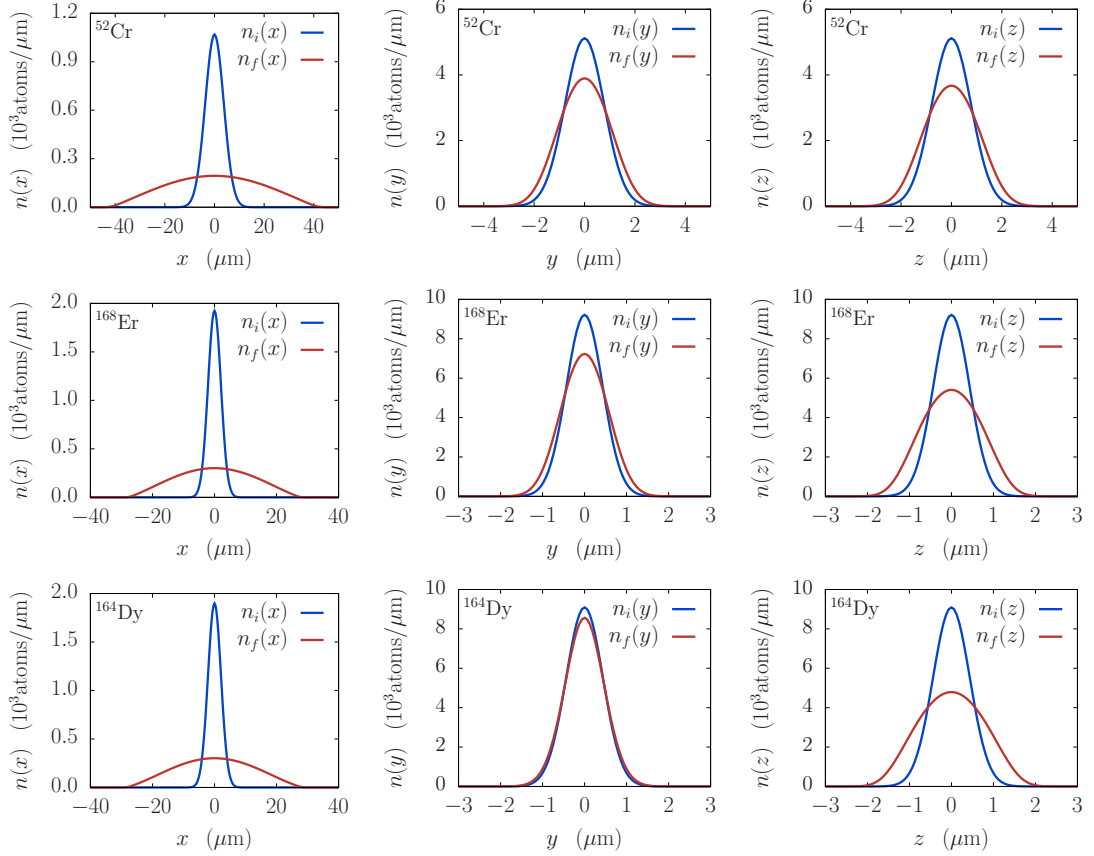


Figure 3.1: Integrated ground-state densities (red lines) of BEC of $N = 10^4$ atoms of chromium ^{52}Cr (first row), erbium ^{168}Er (second row), and dysprosium ^{164}Dy (third row). The initial Gaussian wave function that corresponds to the noninteracting case (blue) is propagated in the imaginary time for 100 ms to obtain the ground state (red line). The first, second, and third column give the corresponding integrated densities in x , y , and z direction, respectively. The observed significant elongation of the condensate in the x direction is due to the trap geometry defined in Appendix D.

this symmetry, which can be seen by comparing the middle and the right-hand side column in Figure 3.1.

In recent experiments it was demonstrated that the strength of the dipole-dipole interaction can be tuned by applying a fast-rotating magnetic field, or for electric dipoles, a fast-rotating electric field [24, 25]. In our description, this corresponds to changing the value of the parameter a_{dd} . If we set $a_{\text{dd}} = 0$, then the system is reduced to a BEC with only the contact interaction. Note that this can be effectively achieved if the external field that orders the dipoles is switched off. To compare how

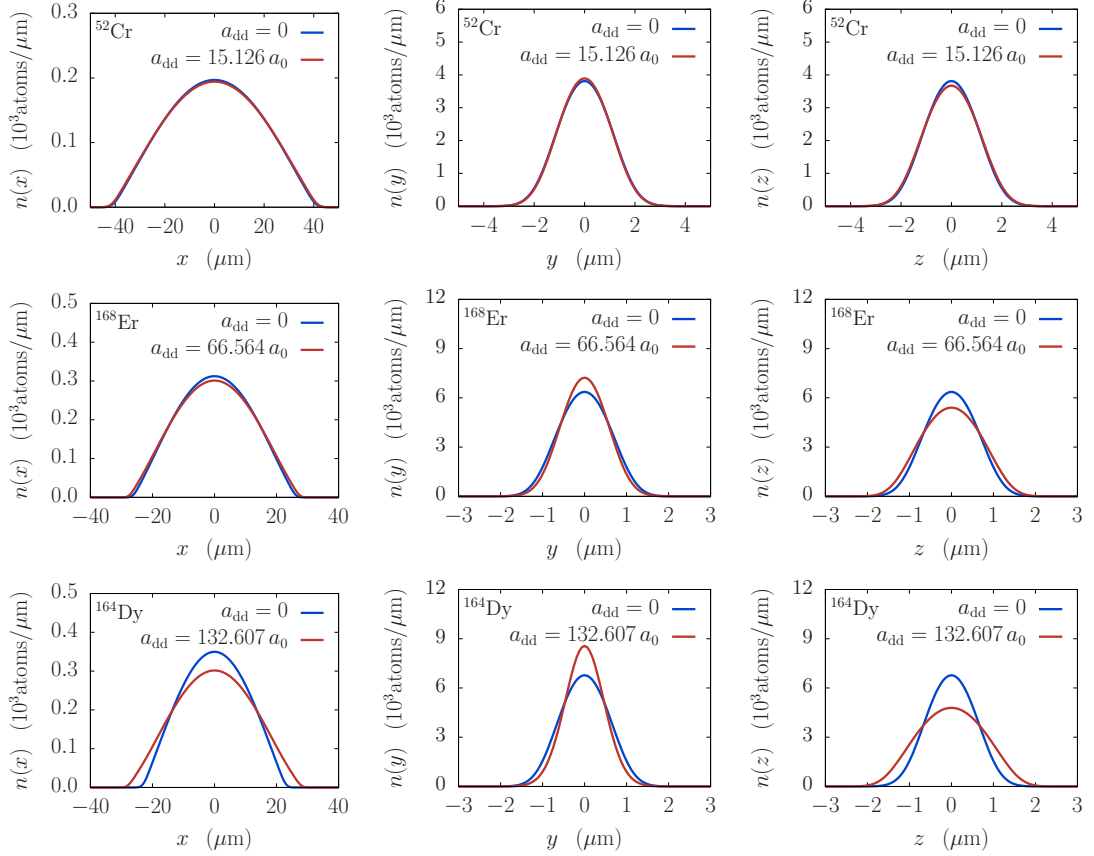


Figure 3.2: Integrated ground-state densities of BEC of $N = 10^4$ atoms of chromium ^{52}Cr (first row), erbium ^{168}Er (second row), and dysprosium ^{164}Dy (third row). Red lines correspond to the densities obtained by taking into account the dipole-dipole interaction, while blue lines are obtained for $a_{\text{dd}} = 0$. The first, second, and third column give the corresponding integrated densities in x , y , and z direction, respectively. Table 1 gives relative differences in the condensate widths due to dipolar effects.

the dipole-dipole interaction contributes to the ground state properties, Figure 3.2 gives the corresponding results for chromium ^{52}Cr (first row), erbium ^{168}Er (second row), and dysprosium ^{164}Dy (third row), with (red) and without (blue lines) the dipole-dipole interaction. As expected, the figure shows cylindrical symmetry in the $y - z$ plane when the dipolar effects are neglected, while the asymmetry grows when they are taken into account, from chromium to dysprosium, as the dipole moment increases. Table 1 gives relative differences of the condensate widths due to the dipole-dipole interaction, $\Delta w_i/w_i = 1 - w_i(0)/w_i(a_{\text{dd}})$. Positive values correspond

Table 1: Relative differences of the ground-state condensate widths due to the dipole-dipole interaction. The values correspond to the integrated densities from Figure 3.2 for a BEC of $N = 10^4$ atoms. The differences are calculated as $\Delta w_i/w_i = 1 - w_i(0)/w_i(a_{\text{dd}})$, $i \in \{x, y, z\}$. A positive value represents an increase of the width, and negative the opposite.

Species	$a_{\text{dd}} (a_0)$	$\Delta w_x/w_x (\%)$	$\Delta w_y/w_y (\%)$	$\Delta w_z/w_z (\%)$
^{52}Cr	15.126	0.959	-1.055	2.044
^{168}Er	66.564	4.009	-10.987	13.469
^{164}Dy	132.607	3.624	-25.457	20.748

to the increase of the width due to dipolar effects, and negative values the opposite. As expected, the condensate elongates in the direction of the dipoles, while due to the interplay of geometry and interaction effects, its width increases in the x and decreases in the y direction. As noted earlier, the relative change in the x direction is negligible, while in other directions it is quite significant for species with large dipole moments.

As mentioned earlier, propagation in imaginary-time is used to calculate the true ground state of the system starting from any initial state (provided that it is not orthogonal to the ground state). The convergence to the ground state can be detected by the convergence of all physical quantities that describe the system, in

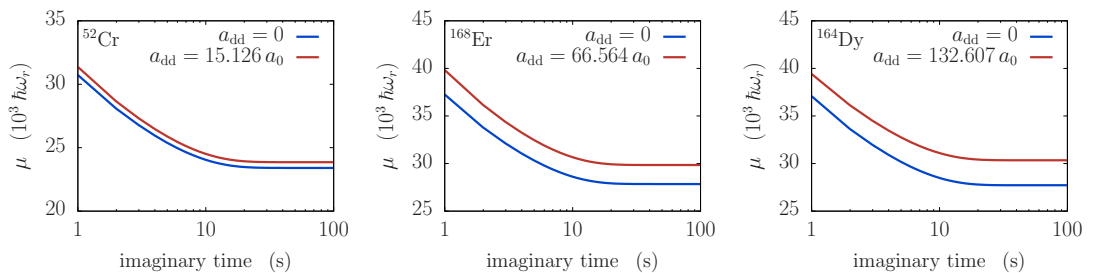


Figure 3.3: Convergence of the chemical potential of a BEC of $N = 10^4$ atoms of chromium ^{52}Cr (left), erbium ^{168}Er (middle), and dysprosium ^{164}Dy (right) during imaginary-time propagation, with (red) and without (blue line) the dipole-dipole interaction for the system parameters given in Appendix D.

particular, its chemical potential, energy, and the expectation value of the system's size. Therefore, the convergence of these quantities is used as a criterion in numerical simulations, which is illustrated in Figure 3.3. In the left panel we can see the decrease of the chemical potential for chromium ^{52}Cr , in the middle panel for erbium ^{168}Er , and in the right panel for dysprosium ^{164}Dy , both with and without dipole-dipole interaction. The chemical potential is expressed in units of $\hbar\omega_r$, where $\omega_r = 160.5 \times 2\pi$ Hz is rescaling frequency. From Figure 3.3, we observe that the dipole-dipole interaction increases the energy of the system. Furthermore, this energy difference increases with the strength of the interaction a_{dd} , and reads $306 \hbar\omega_r$, $1444 \hbar\omega_r$, and $2101 \hbar\omega_r$, respectively for the listed atoms.

3.3 Interaction effects on the ground state

In this section, we study the influence of the short-range contact interaction on the ground state properties of dipolar condensates. For the first experimental realization of BEC, it was possible to tune the strength of contact interactions over a wide range using the Feshbach resonance technique [9]. By adjusting the external magnetic field close to a Feshbach resonance, the contact interaction strength can be tuned from large positive to large negative values, i.e., it is even possible to switch between repulsive and attractive interactions. To model this, we keep fixed the dipole-dipole interaction strength to experimentally measured values listed in Appendix D for each species, and investigate the ground state properties when the contact interaction parameter is varied in the interval from $a_s = 10 a_0$ to $a_s = 200 a_0$ for the condensate of $N = 10^4$ atoms. It turns out that erbium ^{168}Er BEC is unstable for low values of a_s , so we use the region from $a_s = 40 a_0$ to $a_s = 200 a_0$ in this case. Similarly, for dysprosium ^{164}Dy we use the interval from $a_s = 90 a_0$ to $a_s = 200 a_0$. Figure 3.4 illustrates the contact interaction strength dependence of the condensate widths in x , y , and z direction obtained from the numerical simulations (red) and variational calculation (blue line). As expected, the increase of the repulsive contact interaction leads to the increase of condensate widths in all directions. Results of numerical simulations agree with the results of the variational analysis with the relative error

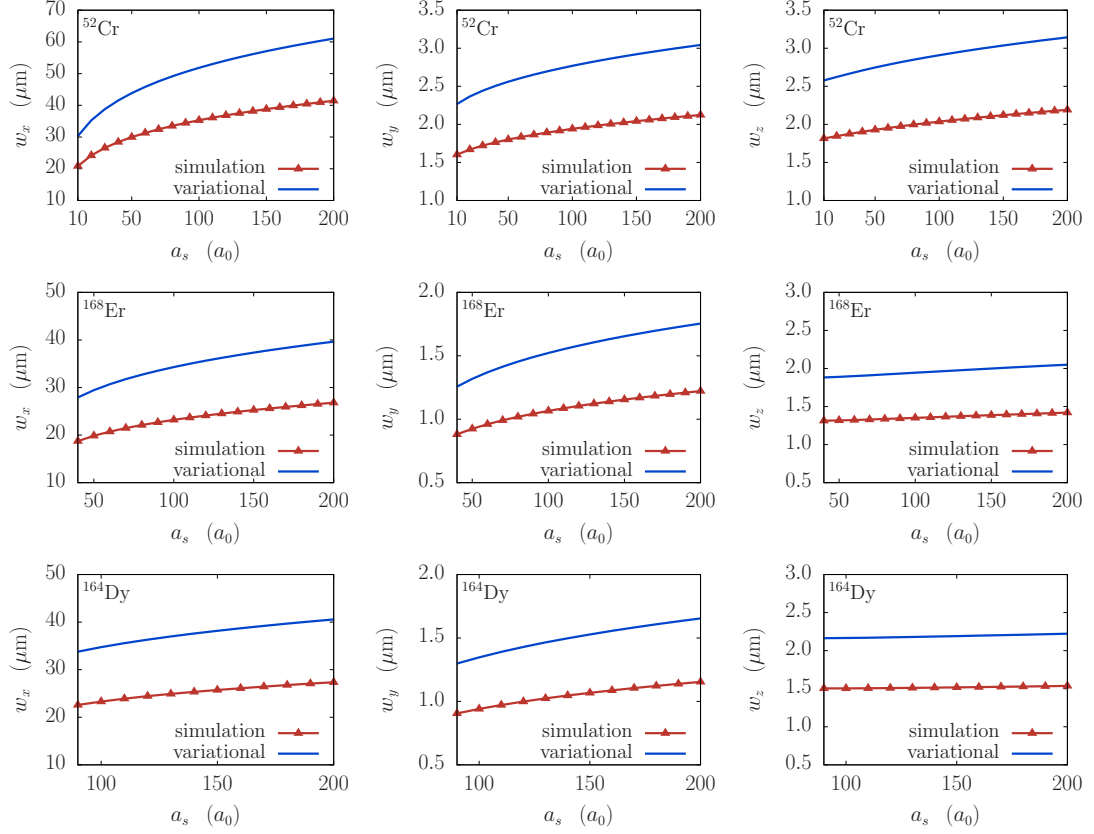


Figure 3.4: Condensate widths as functions of the contact interaction strength for a BEC of $N = 10^4$ atoms of chromium ^{52}Cr (first row), erbium ^{168}Er (second row), and dysprosium ^{164}Dy (third row). Results are obtained for fixed dipole-dipole interaction strengths given in Table 2. Red lines represent numerically obtained widths, and blue lines the variational ones.

of around 30%. As we can see from Table 2, which lists relative differences of the ground-state condensate widths for two values of the contact interaction strength, $a_s = 90 a_0$ and $a_s = 200 a_0$, the increase of the repulsive contact interaction increases the condensate width in all directions and for all species. We also observe that the dipole-dipole interaction suppresses elongation of the condensate in z direction, where it is attractive.

Although more difficult, it is also possible to tune-down the strength of the dipole-dipole interaction for magnetic atomic species using a fast-rotating magnetic field [24, 25]. The maximal possible values are defined by the permanent magnetic moment of the corresponding species. To investigate the effects of the dipole-dipole

Table 2: Relative differences of the ground-state condensate widths due to the contact interaction. The values correspond to the condensate widths from Figure 3.4 for a BEC of $N = 10^4$ atoms. The differences are calculated as $\Delta w_i/w_i = w_i(200 a_0)/w_i(90 a_0) - 1$, $i \in \{x, y, z\}$.

Species	$a_{\text{dd}} (a_0)$	$\Delta w_x/w_x$ (%)	$\Delta w_y/w_y$ (%)	$\Delta w_z/w_z$ (%)
^{52}Cr	15.126	16.917	9.748	7.957
^{168}Er	66.564	15.361	14.612	5.353
^{164}Dy	132.607	17.446	21.554	2.139

interaction on the ground-state properties, we numerically and variationally calculate the condensate widths of chromium ^{52}Cr , erbium ^{168}Er , and dysprosium ^{164}Dy in the interval from $a_{\text{dd}} = 0 a_0$ to $a_{\text{dd}} = 170 a_0$, keeping the contact interaction strength fixed. Due to the instability of erbium and dysprosium condensates for large values of a_{dd} , we have used the interval from $a_{\text{dd}} = 0 a_0$ to $a_{\text{dd}} = 140 a_0$ for those two species. Figure 3.5 illustrates the striking effect of the dipole-dipole interaction which has a non-monotonous behavior of the condensate width in x direction, causes a decrease in y direction and increase in z direction. The agreement between numerical and variational results as quite reasonable, with the error of around 30%. Table 3 gives relative differences of the ground-state condensate widths for $a_{\text{dd}} = 0$ and $a_{\text{dd}} = 100 a_0$. As we see, the change is most prominent in y and z direc-

Table 3: Relative differences of the ground-state condensate widths due to the dipole-dipole interaction. The values correspond to the condensate widths from Figure 3.5 for a BEC of $N = 10^4$ atoms. The differences are calculated as $\Delta w_i/w_i = 1 - w_i(100 a_0)/w_i(0)$, $i \in \{x, y, z\}$. A positive value represents an increase of the width, and negative the opposite.

Species	$a_s (a_0)$	$\Delta w_x/w_x$ (%)	$\Delta w_y/w_y$ (%)	$\Delta w_z/w_z$ (%)
^{52}Cr	105	5.004	-12.180	14.676
^{168}Er	100	4.290	-17.326	17.388
^{164}Dy	100	4.308	-17.205	17.336

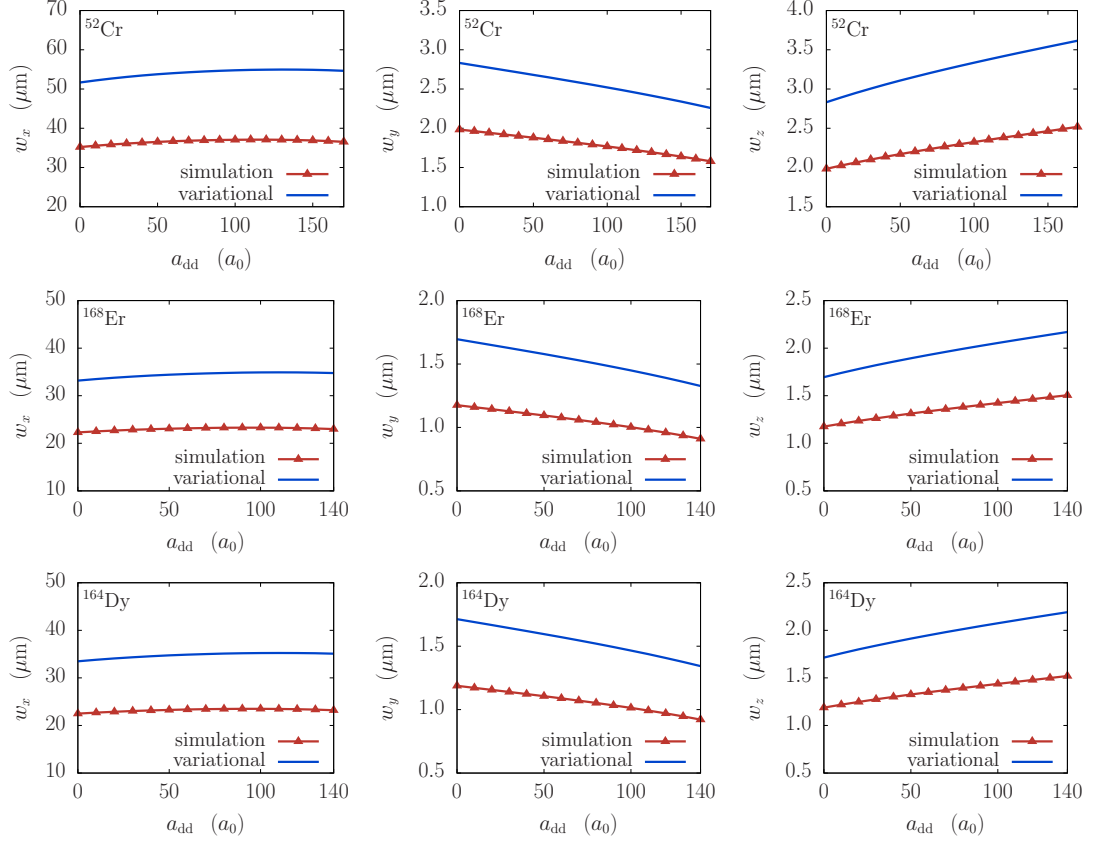


Figure 3.5: Condensate widths as functions of the dipole-dipole interaction strength for a BEC of $N = 10^4$ atoms of chromium ^{52}Cr (first row), erbium ^{168}Er (second row), and dysprosium ^{164}Dy (third row). Results are obtained for fixed contact interaction strengths given in Table 3. Red lines represent numerically obtained widths, and blue lines the variational ones.

tion. With an increase of the dipole-dipole interaction, the size of the condensate increases in z direction, and decreases in y direction. This is expected since it is well known that the condensate elongates along the direction of maximal attraction of the dipole-dipole interaction. On the other hand, the increase of the size in x direction is also observed but is much smaller.

4 Collective oscillation modes

Calculation of the system's ground state is usually the first step in analytical and numerical approaches. The same applies to the experimental studies, where obtaining and characterizing the ground state represents the first and necessary step before proceeding to further measurements. The characterization of the ground state includes measurement of its density profile and condensate widths, as we have seen in the previous section. In addition to these static properties, an important way to probe the system is to study its low-lying excitations or collective modes. Such excitations can be generated from the ground state by a small perturbation of the system's parameters. This results in small oscillations of the condensate density and its widths, which can be experimentally observed using the time-of-flight imaging or some of the *in-situ* techniques. The analysis of experimental results, as well as the results obtained in numerical simulations, includes the Fourier analysis of condensate widths, which yields the frequencies of the collective modes [44–46].

It is well known that the collective oscillation modes of a noninteracting Bose gas are disentangled, i.e., independent in each spatial direction, with the frequency equal to twice the corresponding trap frequency. The presence of interactions in the system couples different modes, which results in the appearance of the breathing mode, quadrupole mode, radial-quadrupole mode, dipole mode, etc. Their frequencies are shifted with respect to the noninteracting case, and the study of these interaction-induced frequency shifts represents one of the important characterization methods used to describe the ground-state properties. From the experimental point of view, probing of the collective excitations is one of the most accurate measurements that

can be performed in ultracold atom systems, with the precision of the order of one per mille. Therefore, a comparison of numerically or analytically obtained estimates for the frequencies of collective modes is an excellent method to check the validity and level of confidence of the models used. As in our case, there are two types of interaction in the system, and both of them independently affect the collective modes and their frequencies, which we study in this section.

In the case of externally driven systems, which is necessary to generate the density excitations, such as Faraday waves, one can expect the appearance of resonances in the system. This usually happens when the driving frequency is close to one of the frequencies of the collective modes, or their linear combination. In some cases, this leads to the emergence of the Faraday waves, while sometimes resonant waves appear, as we show in Chapter 5. Therefore, it is essential to understand well the collective modes of the system, to either avoid resonant behavior or to induce it when necessary.

4.1 Variational description of collective modes

For the variational study of the collective modes, we use the Gaussian variational ansatz (2.52), and equations of motion (2.69) - (2.71) derived in Section (2.4). The system is perturbed from the ground state by a small change of one of its parameters, such that the condensate widths become time-dependent,

$$u_i(t) = u_{i0} + \delta u_i(t), \quad i \in \{x, y, z\}, \quad (4.1)$$

where u_{i0} are the constant ground-state widths, and $\delta u_i(t)$ are small oscillation amplitudes, $|\delta u_i(t)| \ll u_{i0}$. If we insert the expression (4.1) for the condensate widths into the equations of motion (2.69) - (2.71), and linearize the system by expanding it in the small parameters $\delta u_i(t)$ and keeping only the terms of the first order, we obtain a coupled system of ordinary linear differential equations of the second order, which can be expressed in the matrix form as

$$\delta \ddot{\mathbf{u}}(t) + M \delta \mathbf{u}(t) = 0. \quad (4.2)$$

Here $\delta\mathbf{u}(t)$ is a vector $[\delta u_x(t) \ \delta u_y(t) \ \delta u_z(t)]^T$, and elements of the matrix M are calculated from the Lagrangian of the system (2.53),

$$M_{ij} = -2 \frac{\partial^2 L(\mathbf{u})}{\partial u_i \partial u_j} \Big|_{\mathbf{u}=\mathbf{u}_0}, \quad i, j \in \{x, y, z\}. \quad (4.3)$$

To calculate the frequencies of the oscillations induced in the system, we write the solution of equation (4.2) in the following form

$$\delta\mathbf{u}(t) = \delta\mathbf{u} e^{i\omega t}, \quad (4.4)$$

where $\delta\mathbf{u}$ is a constant vector, and ω denotes a collective mode frequency. If we insert this into the matrix equation (4.2), the collective mode frequencies are eigenvalues of the matrix M , i.e., solution of the following eigenproblem

$$\det(M - \omega^2 I) = 0. \quad (4.5)$$

The above eigenproblem can be analytically solved in a simple way in some special cases. For example, if the system is cylindrically symmetric, such that $u_y = u_z \equiv u_\rho$, the problem is essentially two dimensional leading to additional symmetry in the matrix M , which now has the form

$$M = \begin{bmatrix} m_1 & m_4 & m_4 \\ m_4 & m_2 & m_3 \\ m_4 & m_3 & m_2 \end{bmatrix}. \quad (4.6)$$

Due to this, the corresponding eigenproblem can be fully solved in a closed form.

The frequencies of the collective modes in this case are

$$\omega_B^2 = \frac{m_1 + m_2 + m_3 + \sqrt{(m_3 + m_2 - m_1)^2 + 8m_4^2}}{2}, \quad (4.7)$$

$$\omega_Q^2 = \frac{m_1 + m_2 + m_3 - \sqrt{(m_3 + m_2 - m_1)^2 + 8m_4^2}}{2}, \quad (4.8)$$

$$\omega_{RQ}^2 = m_2 - m_3, \quad (4.9)$$

with the corresponding eigenvectors

$$\mathbf{u}_B = \left[\frac{m_1 - m_2 - m_3 + \sqrt{(m_3 + m_2 - m_1)^2 + 8m_4^2}}{2m_4} \quad 1 \quad 1 \right]^T, \quad (4.10)$$

$$\mathbf{u}_Q = \left[\frac{m_1 - m_2 - m_3 - \sqrt{(m_3 + m_2 - m_1)^2 + 8m_4^2}}{2m_4} \quad 1 \quad 1 \right]^T, \quad (4.11)$$

$$\mathbf{u}_{RQ} = \frac{1}{\sqrt{2}} \begin{bmatrix} 0 & -1 & 1 \end{bmatrix}^T. \quad (4.12)$$

In the above expressions, index B denotes the breathing mode, Q the quadrupole mode and RQ the radial-quadrupole mode. The modes can be identified by analyzing the corresponding eigenvectors. In the first case, all three components of \mathbf{u}_B are positive, which means that it corresponds to the breathing mode. In the second case, the longitudinal component of \mathbf{u}_Q is of the opposite sign of the radial components, thus it represents the quadrupole mode, and in the third case, the longitudinal component of \mathbf{u}_{RQ} is zero, while the two radial components are of the opposite sign, which means that this mode can be identified with the radial-quadrupole mode.

Next, we consider the system with contact interaction only. If we set $a_{\text{dd}} = 0$, the derivatives (4.3) of Lagrangian (2.53) yield the following elements of matrix M

$$m_1 = \gamma^2 + \frac{3}{u_{x0}^4} + 2\sqrt{\frac{2}{\pi}} \frac{Na_s}{u_{x0}^3 u_{\rho0}^2}, \quad (4.13)$$

$$m_2 = 1 + \frac{3}{u_{\rho0}^4} + 2\sqrt{\frac{2}{\pi}} \frac{Na_s}{u_{x0} u_{\rho0}^4}, \quad (4.14)$$

$$m_3 = \sqrt{\frac{2}{\pi}} \frac{Na_s}{u_{x0} u_{\rho0}^4}, \quad (4.15)$$

$$m_4 = \sqrt{\frac{2}{\pi}} \frac{Na_s}{u_{x0}^2 u_{\rho0}^3}, \quad (4.16)$$

where u_{i0} , $i \in \{x, \rho\}$ are the ground-state condensate widths given by equations (3.5) and (3.6). Using the above expressions in (4.7) - (4.9), we can calculate the frequencies of the collective modes as functions of the contact interaction strength a_s , the number of particles N , and the trap aspect ratio γ . For the noninteracting system, in the limit $a_s \rightarrow 0$, we obtain for the collective mode frequencies $\omega_B = 2$, $\omega_Q = 2\gamma$, and $\omega_{RQ} = 2$. These frequencies are given in dimensionless units, while the physical values are obtained by multiplying them with the referent frequency $\omega_r = \omega_y = \omega_z$, such that $\omega_B = 2\omega_r$, $\omega_Q = 2\omega_x$, and $\omega_{RQ} = 2\omega_r$. As mentioned earlier, in this special case we obtain the collective mode frequencies equal to twice the trap frequencies.

If the contact interaction is present in the system, then the collective mode frequencies depend on its strength a_s . Figure 4.1 shows this dependence, obtained from the variational approach for a BEC of $N = 10^4$ atoms of chromium ^{52}Cr , where the

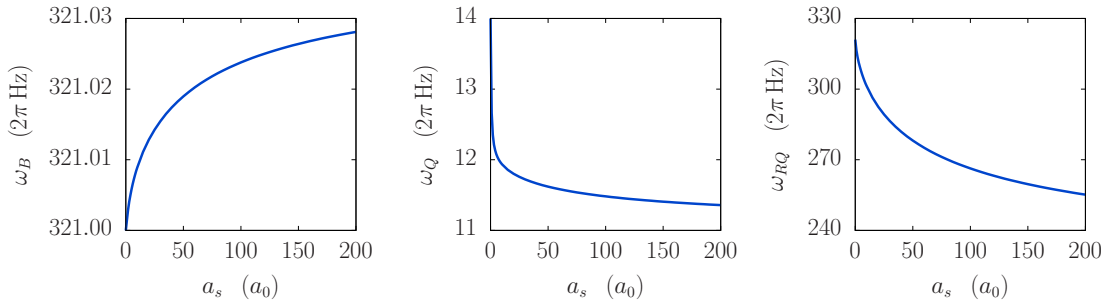


Figure 4.1: Frequencies of the breathing (left), quadrupole (middle), and radial-quadrupole (right) collective mode as functions of the contact interaction strength for a BEC of $N = 10^4$ atoms of chromium ^{52}Cr . Results are obtained using the variational approach, and neglecting the dipole-dipole interactions.

dipole-dipole interaction is neglected. As we can see, when the contact interaction parameter is varied in the interval from $a_s = 0$ to $a_s = 200 a_0$, the frequency of the breathing mode slowly increases, while the frequency of the quadrupole mode slowly decreases. The decrease in the frequency of the radial-quadrupole mode is more prominent than in the case of the quadrupole mode. On this figure we also observe that in the noninteracting limit ω_B and ω_{RQ} tend to $321 \times 2\pi$ Hz = $2 \times 160.5 \times 2\pi$ Hz, and that ω_Q tends to $14 \times 2\pi$ Hz = $2 \times 7 \times 2\pi$ Hz.

In order to compare the variational results with experiments, we use the values obtained in Reference [44] for a BEC of $N = 1.5 \times 10^7$ atoms of ^{23}Na . For a trap with the frequencies $16.93(2) \times 2\pi$ Hz and $\omega_\rho = 230(20) \times 2\pi$ Hz, the experimentally measured value of the quadrupole mode frequency was $\omega_Q = 1.569(4) \omega_x$, which is in excellent agreement with our variationally result $\omega_Q = 1.581 \omega_x$. For the same parameters, the results of numerical simulations yield the frequency $\omega_Q = 1.575 \omega_x$, which is in even better agreement with the experimental value. Therefore, we conclude that the above variational and numerical approach can be reliably applied to study ultracold atomic systems.

While it is still justified to neglect the dipole-dipole interaction for atomic species such as ^{52}Cr , for species with larger values of the dipole moment it is necessary to take it into account. We now present the variational calculation of the collective mode frequencies for the case of a cylindrically symmetric system with the dipoles

oriented in the direction of weak confinement. In this case, the elements of matrix M again have the form given by Equation (4.6). We have calculated the ground-state widths (3.9) and (3.10) for such a system in the previous section, which allows us to calculate the elements of matrix M as follows

$$m_1 = \gamma^2 + \frac{3}{u_{x0}^4} + 2\sqrt{\frac{2}{\pi}} \frac{N}{u_{x0}^3 u_{\rho0}^2} (a_s - a_{dd} A_{xx}(\kappa)) , \quad (4.17)$$

$$m_2 = 1 + \frac{3}{u_{\rho0}^4} + 2\sqrt{\frac{2}{\pi}} \frac{N}{u_{x0} u_{\rho0}^4} (a_s - a_{dd} A_{\rho\rho}(\kappa)) , \quad (4.18)$$

$$m_3 = \sqrt{\frac{2}{\pi}} \frac{N}{u_{x0} u_{\rho0}^4} (a_s - a_{dd} A_{x\rho}(\kappa)) , \quad (4.19)$$

$$m_4 = \sqrt{\frac{2}{\pi}} \frac{N}{u_{x0}^2 u_{\rho0}^3} (a_s - a_{dd} A_{\rho x}(\kappa)) , \quad (4.20)$$

where $\kappa = u_{\rho0}/u_{x0}$, and functions $A_{ij}(\kappa)$, $i, j \in \{x, \rho\}$ are defined by

$$A_{xx}(\kappa) = \frac{4\kappa^6 - 12\kappa^4 - 9\kappa^4 d(\kappa) + 51\kappa^2 - 36\kappa^2 d(\kappa) + 2}{2(1 - \kappa^2)^3} , \quad (4.21)$$

$$A_{\rho\rho}(\kappa) = \frac{32\kappa^6 - 99\kappa^6 d(\kappa) + 141\kappa^4 - 36\kappa^4 d(\kappa) - 54\kappa^2 + 16}{16(1 - \kappa^2)^3} , \quad (4.22)$$

$$A_{x\rho}(\kappa) = \frac{16\kappa^6 - 45\kappa^6 d(\kappa) + 51\kappa^4 - 30\kappa^2 + 8}{8(1 - \kappa^2)^3} , \quad (4.23)$$

$$A_{\rho x}(\kappa) = \frac{4\kappa^6 - 36\kappa^4 + 45\kappa^4 d(\kappa) - 15\kappa^2 + 2}{2(1 - \kappa^2)^3} , \quad (4.24)$$

with

$$d(\kappa) = \frac{\tanh^{-1} \sqrt{1 - \kappa^2}}{\sqrt{1 - \kappa^2}} . \quad (4.25)$$

During the calculation of the matrix elements (4.21) - (4.24), in addition to (3.8), we have used the following identities satisfied by the anisotropy function

$$\lim_{y \rightarrow x} f_{11}(x, y) = \lim_{y \rightarrow x} f_{22}(x, y) = \frac{9[(4 + x^2) f_s(x) - 2(1 - x^2)]}{8(1 - x^2)^2} , \quad (4.26)$$

$$\lim_{y \rightarrow x} f_{12}(x, y) = \lim_{y \rightarrow x} f_{21}(x, y) = \frac{(8 + 8x^2 - x^4) f_s(x) - 2(4 - 5x^2 + x^4)}{8x^2(1 - x^2)^2} , \quad (4.27)$$

where $f_s(x) \equiv f(x, x)$ is the cylindrically symmetric anisotropy function, and f_{ij} are second partial derivatives,

$$f_{ij}(x_1, x_2) = \frac{\partial^2}{\partial x_i \partial x_j} f(x_1, x_2) . \quad (4.28)$$

In the limit of small κ , which corresponds to the cigar-shaped trap geometry that we consider ($\gamma \ll 1$), the above functions can be approximated in the zeroth

order by $A_{xx}(\kappa) = A_{\rho\rho}(\kappa) = A_{x\rho}(\kappa) = A_{\rho x}(\kappa) \rightarrow 1$, with $\kappa^2 d(\kappa) \rightarrow 0$. In this approximation, the matrix elements can be cast in the same form as Equations (4.13) - (4.16), just with a_s replaced by $\tilde{a}_s = a_s - a_{\text{dd}}$. The corresponding collective mode frequencies are given again by Equations (4.7) - (4.9), which are evaluated using the above-approximated values of m_i .

We now consider the experimentally relevant system when the dipoles are oriented in the z direction, such that the cylindrical symmetry is not present anymore, although the trap remains cylindrically symmetric. In this case, the matrix M is just a symmetric matrix, without the additional symmetry we had before. After a lengthy, but straightforward calculation, we obtain

$$M_{11} = \gamma^2 + \frac{3}{u_{x0}^4} + 2\sqrt{\frac{2}{\pi}} \frac{N}{u_{x0}^3 u_{y0} u_{z0}} \left[a_s - a_{\text{dd}} \left(f - \kappa_{xz} f_1 + \frac{\kappa_{xz}^2}{2} f_{11} \right) \right], \quad (4.29)$$

$$M_{22} = 1 + \frac{3}{u_{y0}^4} + 2\sqrt{\frac{2}{\pi}} \frac{N}{u_{x0} u_{y0}^3 u_{z0}} \left[a_s - a_{\text{dd}} \left(f - \kappa_{yz} f_2 + \frac{\kappa_{yz}^2}{2} f_{22} \right) \right], \quad (4.30)$$

$$M_{33} = 1 + \frac{3}{u_{z0}^4} + 2\sqrt{\frac{2}{\pi}} \frac{N}{u_{x0} u_{y0} u_{z0}^3} \left[a_s - a_{\text{dd}} \left(f + 2\kappa_{xz} f_1 + 2\kappa_{yz} f_2 + \right. \quad (4.31)$$

$$\left. \kappa_{xz} \kappa_{yz} f_{12} + \frac{\kappa_{xz}^2}{2} f_{11} + \frac{\kappa_{yz}^2}{2} f_{22} \right), \quad (4.32)$$

$$M_{12} = \sqrt{\frac{2}{\pi}} \frac{N}{u_{x0}^2 u_{y0}^2 u_{z0}} \left[a_s - a_{\text{dd}} \left(f - \kappa_{xz} f_1 - \kappa_{yz} f_2 + \kappa_{xz} \kappa_{yz} f_{12} \right) \right], \quad (4.33)$$

$$M_{13} = \sqrt{\frac{2}{\pi}} \frac{N}{u_{x0}^2 u_{y0} u_{z0}^2} \left[a_s - a_{\text{dd}} \left(f - \kappa_{xz} f_1 + \kappa_{yz} f_2 - \kappa_{xz} \kappa_{yz} f_{12} - \kappa_{xz}^2 f_{11} \right) \right], \quad (4.34)$$

$$M_{23} = \sqrt{\frac{2}{\pi}} \frac{N}{u_{x0} u_{y0}^2 u_{z0}^2} \left[a_s - a_{\text{dd}} \left(f + \kappa_{xz} f_1 - \kappa_{yz} f_2 - \kappa_{xz} \kappa_{yz} f_{12} - \kappa_{yz}^2 f_{22} \right) \right], \quad (4.35)$$

where we have used abbreviations $\kappa_{ij} = u_{i0}/u_{j0}$, $f \equiv f(\kappa_{xz}, \kappa_{yz})$, and

$$f_i = \frac{\partial}{\partial \kappa_{iz}} f(\kappa_{xz}, \kappa_{yz}), \quad f_{ij} = \frac{\partial^2}{\partial \kappa_{iz} \partial \kappa_{jz}} f(\kappa_{xz}, \kappa_{yz}). \quad (4.36)$$

4.2 Interaction effects and the collective modes

The usual low-lying collective oscillation modes, such as the breathing, quadrupole, and radial-quadrupole mode, are direct consequences of the existence of interactions in the system. In the absence of interactions, the many-body physics is reduced to a

one-body problem, and for bosons this amounts to simple disentangled oscillations along the trap axes as the normal modes, with the frequencies equal to twice the corresponding trap frequencies. In this noninteracting case, although each atom would oscillate independently with the corresponding frequency even if no other atoms are present, the fact that the atoms are identical and that all of them would perform the same type of oscillations makes their dynamics practically a collective mode.

The presence of interactions, even if quite weak, changes the situation dramatically and allows the emergence of the well-known collective modes [44]. In the previous section, we have derived the variational expressions for the frequencies of those collective modes and we now study how they are affected by the strength of the contact and the dipole-dipole interaction. We have already seen in Figure 4.1, where the frequencies of the collective modes are calculated variationally as functions of the contact interaction strength by neglecting the DDI, that the breathing and the quadrupole mode frequencies depend very weakly on a_s , while the radial-quadrupole mode is more sensitive. Figure 4.2 presents numerical and variational results for all three atomic species, where we take into account the DDI, both numerically when solving the dipolar GPE and variationally, using the expressions derived in Section 4.1. Not surprisingly, the breathing and the quadrupole mode frequencies still exhibit the flat behavior, while the radial-quadrupole mode shows a significant dependence on a_s . Therefore, the contact interaction strength, which can be tuned in experiments in a very broad range, can be considered as a control parameter only for the radial-quadrupole mode, whose frequency can be adjusted this way, although in a limited range.

From Figure 4.2, we see that our variational approach properly captures the functional behavior of all the modes and gives frequency values, which are in very good agreement with the numerical ones. The absolute errors are of the order of few Hz, which makes them practically negligible for the breathing and the radial-quadrupole mode, while in the case of the quadrupole mode, due to its low value of around 12 Hz, the relative error amounts to 10%.

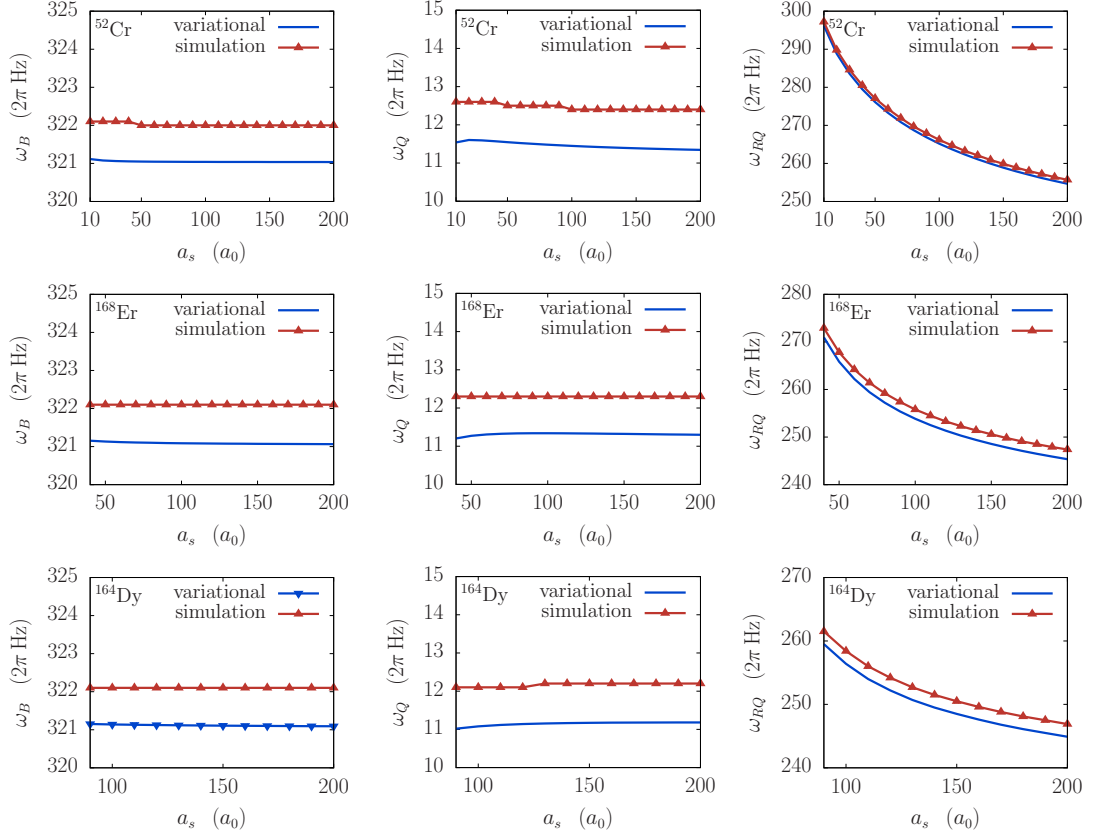


Figure 4.2: Effects of the contact interaction on frequencies of collective oscillation modes: the breathing mode (left column), the quadrupole mode (middle column), the radial-quadrupole mode (right column), for a BEC of $N = 10^4$ atoms of chromium ^{52}Cr (top row), ^{168}Er (middle row), and ^{164}Dy (bottom row), for a fixed dipole-dipole interaction strength given in Appendix D. Red upper triangles are numerically obtained values using the FFT analysis, and blue lines are variational results from Section 4.1.

Next, we focus on the effects of the dipole-dipole interaction strength, presented in Figure 4.3. The results for the breathing and the quadrupole mode are quite similar, although one can see a slight increase in the breathing mode frequency and a slight decrease in the quadrupole mode frequency as a_{dd} increases. However, the radial-quadrupole mode frequency shows a nonmonotonous behavior, albeit in an even more limited range. The variational approach works equally well here as in the case of the contact interaction, and, in particular, it properly describes the nonmonotonous behavior of the radial-quadrupole mode.

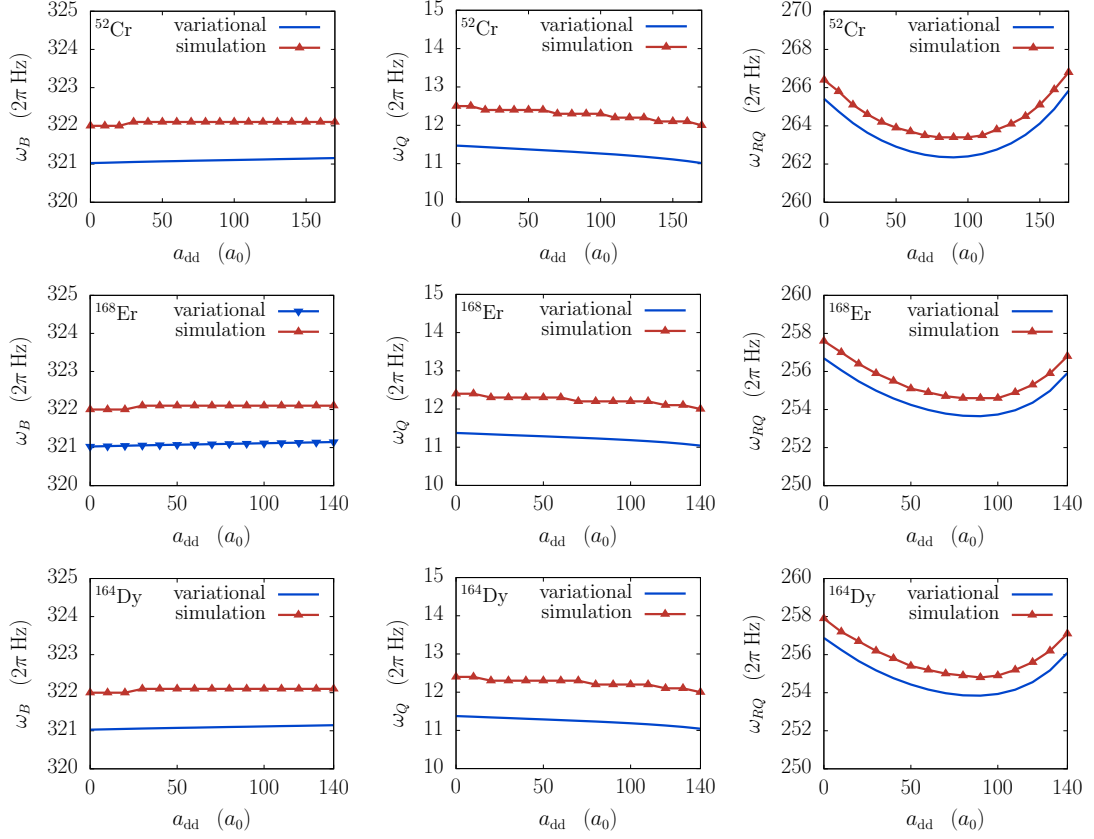


Figure 4.3: Effects of the dipole-dipole interaction on frequencies of collective oscillation modes: the breathing mode (left column), the quadrupole mode (middle column), the radial-quadrupole mode (right column), for a BEC of $N = 10^4$ atoms of chromium ^{52}Cr (top row), ^{168}Er (middle row), and ^{164}Dy (bottom row), for a fixed contact interaction strength given in Appendix D. Red upper triangles are numerically obtained values using the FFT analysis, and blue lines are variational results from Section 4.1.

The precise knowledge of the collective oscillation mode frequencies is essential not only for comparison with the experiments, where measurements of these frequencies are the most precise and can be used for testing of various theoretical and numerical approaches, but also for a deeper understanding of the dynamical response of the system in many experimental situations. This is of particular interest for driven systems, where resonances may appear close to frequencies of collective oscillation modes. This is also relevant for the study of Faraday waves, which can be generated only by modulating the system at non-resonant frequencies, as we will see in Chapter 5.

5 Faraday and resonant waves

In the previous section, we have seen that a small perturbation of one of the system parameters generates collective oscillation modes, which we have analyzed using the spectral analysis of the condensate widths. We demonstrated that frequencies of the collective modes depend on the geometry of the system, as well as on the strength of the contact and the dipole-dipole interactions, but we did not discuss the spatial period of the induced waves since it was much larger than the size of condensate. Therefore, one can assume that the condensate density is only slightly spatially modulated in the presence of collective modes. However, if the perturbation is performed periodically, i.e., if one of the system parameters is harmonically modulated in time, the spatial period can become small enough to produce observable density patterns in the condensate. The classical phenomenon of Faraday waves inspired this line of research [28], and although oscillations of a shallow layer of liquid generate surface waves, while periodic modulation of one of the system parameters of a quantum fluid produces density waves, both share the common name in the literature – Faraday waves.

Bose-Einstein condensates are usually termed quantum fluids, which encompasses a broader range of physical systems where quantum effects are either dominant or very much pronounced. Despite their name, some of quantum fluids do not share the trademark property of classical fluids, incompressibility. In fact, the BECs are made of rarefied gases, but their fluid-like behavior stems from the quantum coherence of such systems. Therefore, while in classical fluids density modulations can be excited only under extreme conditions, in quantum fluids the density waves

represent one of the natural collective excitations. Parametric driving of system parameters can lead to pattern formation not only in BECs, where Faraday waves are experimentally observed in cigar-shaped rubidium [30] and lithium [47] condensates, but also in helium cells [48]. The actual experimental observation of this phenomenon in 2007 was preceded by numerical studies starting in 2002 [29, 49–53], all focusing on systems with short-range, contact interactions. More recently, Faraday waves have been studied in dipolar [33, 54–56] and two-component condensates, including the systems with spatially-dependent contact interaction [31, 32]. Numerical studies of Faraday waves have also been extended to mixtures of Bose and Fermi gases [57], as well as Fermi gases exhibiting superfluid behavior [58, 59]. An interesting phenomenon of Bose fireworks [60] is related to Faraday waves, but appears during the free expansion of the system, when density patterns may also emerge [61–63].

The parametric modulation of a BEC system generically leads to the emergence of the Faraday waves. However, resonant behavior can also be observed if the system is modulated at one of its collective mode frequencies [64]. In that case, the Faraday waves are suppressed and resonant waves emerge on a much shorter time scale. Interestingly this can happen not only by modulation of the interaction strength, but also by the modulation of the trapping potential or even the spatial modulation of the trap [65–79].

In the context of dipolar BECs, the study of Faraday waves was limited mostly to their excitation spectrum in one-dimensional and two-dimensional systems [54], while the properties of resonant waves were not studied to the best of our knowledge. Here, we focus on an analytical description of Faraday and resonant waves in dipolar condensates [33]. In particular, we study how such waves develop in ultracold systems of three dipolar species: chromium [10], erbium [12], dysprosium [11]. We consider the system with the parameters specified in Appendix D, with the dipoles oriented along z direction and the cigar-shaped trap in the weakly confined x direction. The radial ($y - z$) component of the trap is harmonically modulated,

$$\omega_y(t) = \omega_z(t) = \Omega_0(1 + \epsilon \sin \omega_m t), \quad (5.1)$$

where $\epsilon = 0.1 - 0.2$ is the modulation amplitude and ω_m is modulation frequency. These are typical values taken from the experiment of Reference [30].

In this chapter, we develop a variational approach for the study of the dynamics of a driven dipolar BEC and identify the instability of the system leading to the emergence of Faraday and resonant waves. Using this approach, we calculate the dependence of wave properties on the strength of the contact and the dipole-dipole interaction. The analytically obtained expressions for the spatial period of Faraday and resonant waves are compared to results of the extensive numerical simulations, which solve the full three-dimensional mean-field equations for a dipolar BEC.

5.1 Variational approach

For a variational study of Faraday and resonant waves in dipolar condensates, we use a modification [31, 32, 49–53, 56, 64, 80, 81] of the Gaussian ansatz (2.52) to capture the induced density waves in the direction of weak confinement (x direction),

$$\psi(x, y, z, t) = A e^{-\frac{x^2}{2u_x^2} - \frac{y^2}{2u_y^2} - \frac{z^2}{2u_z^2} + ix^2\phi_x + iy^2\phi_y + iz^2\phi_z} [1 + (\alpha + i\beta) \cos kx], \quad (5.2)$$

where $A \equiv A(u_x, u_y, u_z, \alpha, \beta, k)$ ensures the normalization of the wave function to unity,

$$A = \frac{1}{\pi^{3/4} \sqrt{u_x u_y u_z}} \frac{\sqrt{2}}{\sqrt{2 + \alpha^2 + \beta^2 + 4\alpha e^{-k^2 u_x^2/4} + (\alpha^2 + \beta^2) e^{-k^2 u_x^2}}}. \quad (5.3)$$

The above variational ansatz involves eight variational parameters $\{u_i, \phi_i, \alpha, \beta\}$, which are functions of time. The parameters u_i represent the condensate widths, while ϕ_i are the conjugated phases, which are necessary to describe the system's dynamics properly. Note that these phases can be omitted when we are interested only in the ground state. The multiplicative factor $1 + (\alpha + i\beta) \cos kx$ describes the density modulation along x direction, and the variational parameters α and β represent the real and the imaginary part of the amplitude of the wave. The wave vector k , which is related to the spatial period ℓ of the density waves by $\ell = 2\pi/k$, is not treated here as a variational parameter. We determine its value from the condition for the instability emergence, which leads to Faraday or resonant waves.

If we insert the modified Gaussian ansatz (5.2) into the Lagrangian density (2.51), we obtain the expressions for the five terms (2.53) of the Lagrangian of the system. The first term reads

$$L_1(t) = \frac{i}{2} \int d\mathbf{r} \left(\psi^* \dot{\psi} - \psi \dot{\psi}^* \right) = -\frac{1}{2} \left(u_x^2 \dot{\phi}_x + u_y^2 \dot{\phi}_y + u_z^2 \dot{\phi}_z \right) - \frac{\alpha\dot{\beta} - \beta\dot{\alpha}}{2 + \alpha^2 + \beta^2}, \quad (5.4)$$

and the kinetic energy term is equal to

$$\begin{aligned} L_2(t) &= \frac{1}{2} \int d\mathbf{r} \psi^* \nabla^2 \psi \\ &= -\frac{1}{4} \left(\frac{1}{u_x^2} + \frac{1}{u_y^2} + \frac{1}{u_z^2} + 4u_x^2 \phi_x^2 + 4u_y^2 \phi_y^2 + 4u_z^2 \phi_z^2 \right) - \frac{(\alpha^2 + \beta^2) k^2}{2(2 + \alpha^2 + \beta^2)}. \end{aligned} \quad (5.5)$$

The potential energy term is calculated using the expression (2.47) for the potential, yielding

$$L_3(t) = - \int d\mathbf{r} U |\psi|^2 = -\frac{1}{4} (\gamma^2 u_x^2 + \nu^2 u_y^2 + \lambda^2 u_z^2), \quad (5.6)$$

while the contact interaction term reads

$$L_4(t) = -2\pi N a_s \int d\mathbf{r} |\psi|^4 = -\frac{N a_s}{\sqrt{2\pi} u_x u_y u_z} \left(1 + \frac{\alpha^4 + 16\alpha^2 + 2\alpha^2\beta^2 + \beta^4}{2(2 + \alpha^2 + \beta^2)^2} \right). \quad (5.7)$$

The Lagrangian term that corresponds to the DDI is calculated following a procedure similar to the one described in Section 2.4. However, due to the modulation term in the modified Gaussian ansatz, it is not possible to perform exact integration to obtain $L_5(t)$. Using the convolution theorem, the DDI term can be written as

$$L_5(t) = -\frac{3N a_{\text{dd}}}{2(2\pi)^3} \int d\mathbf{k} \mathcal{F}[U_{\text{dd}}](\mathbf{k}) \mathcal{F}[|\psi|^2](\mathbf{k}) \int d\mathbf{r} |\psi|^2 e^{i\mathbf{k}\cdot\mathbf{r}}, \quad (5.8)$$

where the last integral is equal to $\mathcal{F}[|\psi|^2](\mathbf{k})$, and can be calculated exactly,

$$\mathcal{F}[|\psi|^2](\mathbf{k}) = B e^{-\frac{1}{4}(k_x^2 u_x^2 + k_y^2 u_y^2 + k_z^2 u_z^2)}, \quad (5.9)$$

where $B \equiv B(k_x, u_x, \alpha, \beta, k)$ is given by

$$B = \frac{4 + 4(e^{-\frac{k}{4}(k-2k_x)u_x^2} + e^{-\frac{k}{4}(k+2k_x)u_x^2})\alpha + (2 + e^{-k(k-k_x)u_x^2} + e^{-k(k+k_x)u_x^2})(\alpha^2 + \beta^2)}{2 \left[2 + 4e^{-\frac{1}{4}k^2 u_x^2} \alpha + (1 + e^{-k^2 u_x^2})(\alpha^2 + \beta^2) \right]}. \quad (5.10)$$

Grouping all elements together, the DDI term of the Lagrangian becomes

$$L_5(t) = -\frac{3N a_{\text{dd}}}{(2\pi)^2} \int d\mathbf{k} \left(3 \frac{k_z^2}{k_x^2 + k_y^2 + k_z^2} - 1 \right) B^2 e^{-\frac{1}{2}(k_x^2 u_x^2 + k_y^2 u_y^2 + k_z^2 u_z^2)}, \quad (5.11)$$

and cannot be exactly calculated. To proceed further, we take into account that the condensate width in the weak confinement direction is large compared to the order widths, as well as compared to the spatial period of the density waves, such that $ku_x \gg 1$. We also take into account that the wave amplitude is small immediately after the waves emerge, such that $\alpha, \beta \ll 1$. Therefore, we approximate the expression for B^2 in the following manner

$$B^2 \approx 1 + \frac{\alpha}{2 + \alpha^2 + \beta^2} B_1^2 + \frac{\alpha^2}{(2 + \alpha^2 + \beta^2)^2} B_2^2, \quad (5.12)$$

where $B_1^2 \equiv B_1^2(k_x, u_x, k)$ and $B_2^2 \equiv B_2^2(k_x, u_x, k)$ are given by

$$B_1^2 = 4 e^{-\frac{1}{4}k(k+2k_x)u_x^2} \left(e^{\frac{1}{2}kk_x u_x^2} - 1 \right)^2, \quad (5.13)$$

$$B_2^2 = 4 e^{-\frac{1}{4}k(k+2k_x)u_x^2} \left(e^{\frac{1}{2}kk_x u_x^2} - 1 \right)^2 \left(e^{kk_x u_x^2} - 6e^{\frac{1}{2}kk_x u_x^2} + 1 \right), \quad (5.14)$$

and correspond to the coefficients in front of the terms linear and quadratic in the wave amplitude, respectively. Since the integral over \mathbf{k} cannot be performed exactly even for the approximate expression (5.12), we replace the coefficients B_1^2 and B_2^2 by their averages over k_x ,

$$\langle B_i^2 \rangle = \frac{\int dk_x \left(3 \frac{k_x^2}{k_x^2 + k_y^2 + k_z^2} - 1 \right) B_i^2 e^{-\frac{1}{2}k_x^2 u_x^2}}{\int dk_x \left(3 \frac{k_x^2}{k_x^2 + k_y^2 + k_z^2} - 1 \right) e^{-\frac{1}{2}k_x^2 u_x^2}} \approx \frac{\int dk_x \left(3 \frac{k_x^2}{k_x^2} - 1 \right) B_i^2 e^{-\frac{1}{2}k_x^2 u_x^2}}{\int dk_x \left(3 \frac{k_x^2}{k_x^2} - 1 \right) e^{-\frac{1}{2}k_x^2 u_x^2}} \quad (5.15)$$

After that, we obtain $\langle B_1^2 \rangle \approx 0$ and $\langle B_2^2 \rangle \approx -8$. Note that we have neglected all terms proportional to $e^{-k^2 u_x^2 / 8}$ and its powers, as already argued that ku_x is a large quantity. Therefore, B^2 turns out to depend only on α and β , and reads

$$B^2 \approx 1 - \frac{8\alpha^2}{(2 + \alpha^2 + \beta^2)^2}. \quad (5.16)$$

If we look at the expression (5.11), we see that now B^2 can be put in front of the integral sign, and integration over \mathbf{k} can now proceed as in Section 2.4, yielding, i.e., the DDI term of the Lagrangian in terms of the anisotropy function f becomes

$$L_5(t) = \frac{Na_{\text{dd}}}{\sqrt{2\pi} u_x u_y u_z} f \left(\frac{u_x}{u_z}, \frac{u_y}{u_z} \right) \left(1 - \frac{8\alpha^2}{(2 + \alpha^2 + \beta^2)^2} \right). \quad (5.17)$$

Let us compare the calculated Lagrangian terms (2.54)–(2.57) and (2.65) in Section 2.4 with expressions (5.4)–(5.7) and (5.17), respectively. Except for the potential energy term $L_3(t)$, which remains unchanged, we see that all other terms are

modified by an additional additive or multiplicative factor, arising due to additional variational parameters α and β . The Euler-Lagrange equations for the system are given by

$$\frac{d}{dt} \left(\frac{\partial L}{\partial \dot{q}_i} \right) - \frac{\partial L}{\partial q_i} = 0, \quad q_i \in \{u_x, u_y, u_z, \phi_x, \phi_y, \phi_z, \alpha, \beta\}, \quad (5.18)$$

where L is a sum of all five calculated terms. Assuming that the wave amplitudes α and β are small, such that their quadratic and higher-order terms can be neglected, the equations for the condensate widths, turn out to coincide with those obtained in Section 2.4. The three equations for the phases ϕ_i yield, as in Section 2.4,

$$\phi_i = \frac{\dot{u}_i}{2u_i}. \quad (5.19)$$

After elimination of the phases ϕ_i from the corresponding set of equations for the condensate widths u_i , we obtain the second-order differential equations (2.69)–(2.71) again. The Euler-Lagrange equation for the variational parameters β yields

$$\beta = \frac{2\dot{\alpha}}{k^2}, \quad (5.20)$$

which we use to eliminate β from the corresponding equation for the parameter α , as was done with the phases. With this, the equation for α turns out to be the second-order differential equation,

$$\ddot{\alpha} + \left\{ \frac{k^4}{4} + \sqrt{\frac{2}{\pi}} \frac{N}{u_x u_y u_z} \left[a_s + a_{\text{dd}} f \left(\frac{u_x}{u_z}, \frac{u_y}{u_z} \right) \right] k^2 \right\} \alpha = 0. \quad (5.21)$$

In the context of variational analysis of Faraday and resonant waves, the above equation of motion for the wave amplitude α is usually cast into the form of the Mathieu-like equation

$$\ddot{\alpha} + [a(k) + \epsilon b(k) \sin 2\tau] \alpha = 0. \quad (5.22)$$

This equation can be solved perturbatively in the small modulation amplitude ϵ . Assuming a solution in the form of a harmonic oscillator

$$\alpha(\tau, \epsilon) = P(\epsilon\tau) \cos \left(\tau \sqrt{a(k)} \right) + Q(\epsilon\tau) \sin \left(\tau \sqrt{a(k)} \right), \quad (5.23)$$

we obtain that functions P and Q are exponentials of the form $e^{\pm i\xi\tau}$, where ξ is a complex number. The existence of the imaginary part of ξ leads to the instability,

i.e., to the exponential growth of the wave amplitude, which yields Faraday or resonant waves. It was shown in Reference [82] that the nonvanishing imaginary part of ξ appears for $a(k) = n^2$, where $n \in \mathbb{N}$, and this represents the mathematical form of the instability condition.

In order to cast Equation (5.21) into the Mathieu-like form (5.22), we need to take into account that the radial trap frequencies are modulated, such that the corresponding trap aspect ratio is given by $\nu(t) = \lambda(t) = \lambda_0(1 + \epsilon \sin \eta_m t)$, where $\lambda_0 = \Omega_0/\omega_r$ and $\eta_m = \omega_m/\omega_r$. This generates the dynamics of the system and we need to obtain approximate expressions for the condensate widths in order to get an explicit form of the quantities $a(k)$ and $b(k)$. We assume that the condensate width u_x slowly varies, and can be taken to be constant at the onset of instability. We also assume that second derivatives of the radial widths u_y and u_z , with respect to time, can be neglected, since they are proportional to the small modulation amplitude ϵ . Furthermore, for simplicity, we assume $u_y \approx u_z \equiv u_\rho$, which now satisfies the modified equation (2.70) or (2.71),

$$\lambda^2(t)u_\rho^4 = 1 + \sqrt{\frac{2}{\pi}} \frac{N}{u_x} \left[a_s + \frac{a_{\text{dd}}}{2} f_s \left(\frac{u_\rho}{u_x} \right) - a_{\text{dd}} f'_s \left(\frac{u_\rho}{u_x} \right) \right]. \quad (5.24)$$

On the right-hand side of the above equation we assume that the ratio u_ρ/u_x is constant and equal to the corresponding ratio for the ground state, which can be calculated as in Section 3.1. To derive Equation (5.24), we also use the following limits of the anisotropy function

$$\begin{aligned} f'_s(x) &= \lim_{y \rightarrow x} x f_1(x, y) = \lim_{y \rightarrow x} y f_2(x, y) = \frac{(2 + x^2)f_s(x)}{2(1 - x^2)} - 1, \\ \lim_{y \rightarrow 1} f(x, y) &= -\frac{1}{2} f_s(1/x), \quad \lim_{y \rightarrow 1} x f_1(x, y) = f'_s(1/x), \end{aligned} \quad (5.25)$$

If we express u_ρ^2 from Equation (5.24), and use it to estimate the quantity $u_y u_z \approx u_\rho^2$ in Equation (5.21), as well as the above limits, that yield

$$f \left(\frac{u_x}{u_z}, \frac{u_y}{u_z} \right) = -\frac{1}{2} f_s \left(\frac{u_\rho}{u_x} \right), \quad (5.26)$$

the equation for the variational parameter α can be written as

$$\ddot{\alpha} + \left[\frac{k^4}{4} + \frac{\Lambda k^2}{4} \lambda(t) \right] \alpha = 0, \quad (5.27)$$

where Λ is given by

$$\Lambda = \frac{4\sqrt{\frac{2}{\pi}} N \left[a_s - \frac{a_{\text{dd}}}{2} f_s \left(\frac{u_\rho}{u_x} \right) \right]}{u_x \left\{ 1 + \sqrt{\frac{2}{\pi}} \frac{N}{u_x} \left[a_s + \frac{a_{\text{dd}}}{2} f_s \left(\frac{u_\rho}{u_x} \right) - a_{\text{dd}} f_s' \left(\frac{u_\rho}{u_x} \right) \right] \right\}^{1/2}}. \quad (5.28)$$

Inserting the explicit form for $\lambda(t)$, we obtain

$$\ddot{\alpha} + [a(k) + \epsilon b(k) \sin \eta_m t] \alpha = 0, \quad (5.29)$$

where

$$a(k) = \frac{k^4}{4} + \frac{\lambda_0 \Lambda k^2}{4}, \quad b(k) = \frac{\lambda_0 \Lambda k^2}{4}. \quad (5.30)$$

In order to transform the above equation into the Mathieu-like equation (5.22), we need to make a variable change $\eta_m t \rightarrow 2\tau$, which finally yields the expressions for the coefficients $a \equiv a(k)$ and $b \equiv b(k)$,

$$a(k) = \frac{k^4}{\eta_m^2} + \frac{\lambda_0 \Lambda k^2}{\eta_m^2}, \quad b(k) = \frac{\lambda_0 \Lambda k^2}{\eta_m^2}. \quad (5.31)$$

As previously discussed, the instability condition for the Faraday waves reads $a(k) = 1$, which can be used to calculate the wave vector of waves shortly after the emergence of the waves,

$$k_F = \sqrt{-\frac{\lambda_0 \Lambda}{2} + \sqrt{\frac{\lambda_0^2 \Lambda^2}{4} + \eta_m^2}}. \quad (5.32)$$

This represents the variational prediction for the wave vector k and the spatial period $\ell = 2\pi/k$ of the Faraday waves, which can be directly compared with numerical or experimental results. Let us also stress that the above analysis is consistent with the main characteristic of the Faraday waves, namely, that their oscillation frequency is half that of the driving frequency. Since $\tau = \eta_m t/2$, from Equation (5.22) we see that indeed, the solution of the derived Mathieu-like equation oscillates with the frequency $\eta_m/2$, i.e., with the frequency $\omega_m/2$.

If the modulation frequency is close to one of the collective oscillation modes, the system will exhibit resonant behavior, which is suppressed for an arbitrary value of the modulation frequency. While the system's dynamics will certainly include the Faraday mode at the frequency $\omega_m/2$ even close to a resonance, the resonant

mode with the frequency ω_m will have a larger amplitude and will develop much faster. Although it is clear that the analysis of this section would break down, the condition for the emergence of resonant waves still corresponds to $a(k) = 2^2$, i.e., the wave vector of the resonant wave is given by

$$k_R = \sqrt{-\frac{\lambda_0 \Lambda}{2} + \sqrt{\frac{\lambda_0^2 \Lambda^2}{4} + 4\eta_m^2}}. \quad (5.33)$$

In that case, according to $\tau = \eta_m t/2$ and Equation (5.23), the resonant density wave will oscillate with the frequency whose aspect ratio is $(\eta_m/2)\sqrt{2^2} = \eta_m$, i.e., with the frequency ω_m . Depending on the system's parameters, higher resonant modes can also appear corresponding to the conditions $a(k) = n^2$, where n is an integer, corresponding to the oscillation frequencies $n\omega_m/2$.

5.2 Faraday waves in ^{52}Cr , ^{168}Er and ^{164}Dy BECs

In order to study Faraday waves in dipolar condensates, we have performed extensive numerical simulations of the real-time dynamics and solved the dipolar GPE using the programs described in Chapter 6. The parameters for these simulations closely match the physical parameters of BECs of chromium ^{52}Cr , erbium ^{168}Er , and dysprosium ^{164}Dy , which are given in detail in Appendix D. It is well known [65–79] that Faraday waves can be expected as a main excitation mode of the system when the modulation frequency ω_m does not match any of the characteristic frequencies of the system, i.e., when it is sufficiently far from any of the collective oscillations modes or the trap frequencies. Therefore, we use the value $\omega_m = 200 \times 2\pi$ Hz, which we know satisfies these conditions from our study of collective modes from Chapter 4, and the values of the trap frequencies listed in Appendix D.

Figure 5.1 shows time dependence of the integrated density profile in the weak confinement direction $n(x, t)$, which is obtained by integrating the condensate density over the radial coordinates y and z according to Equation (3.14). The emergence of spatial patterns is clearly visible for all three atomic species after around 150 ms. This is consistent with earlier experimental observations [30, 47] and theoretical re-

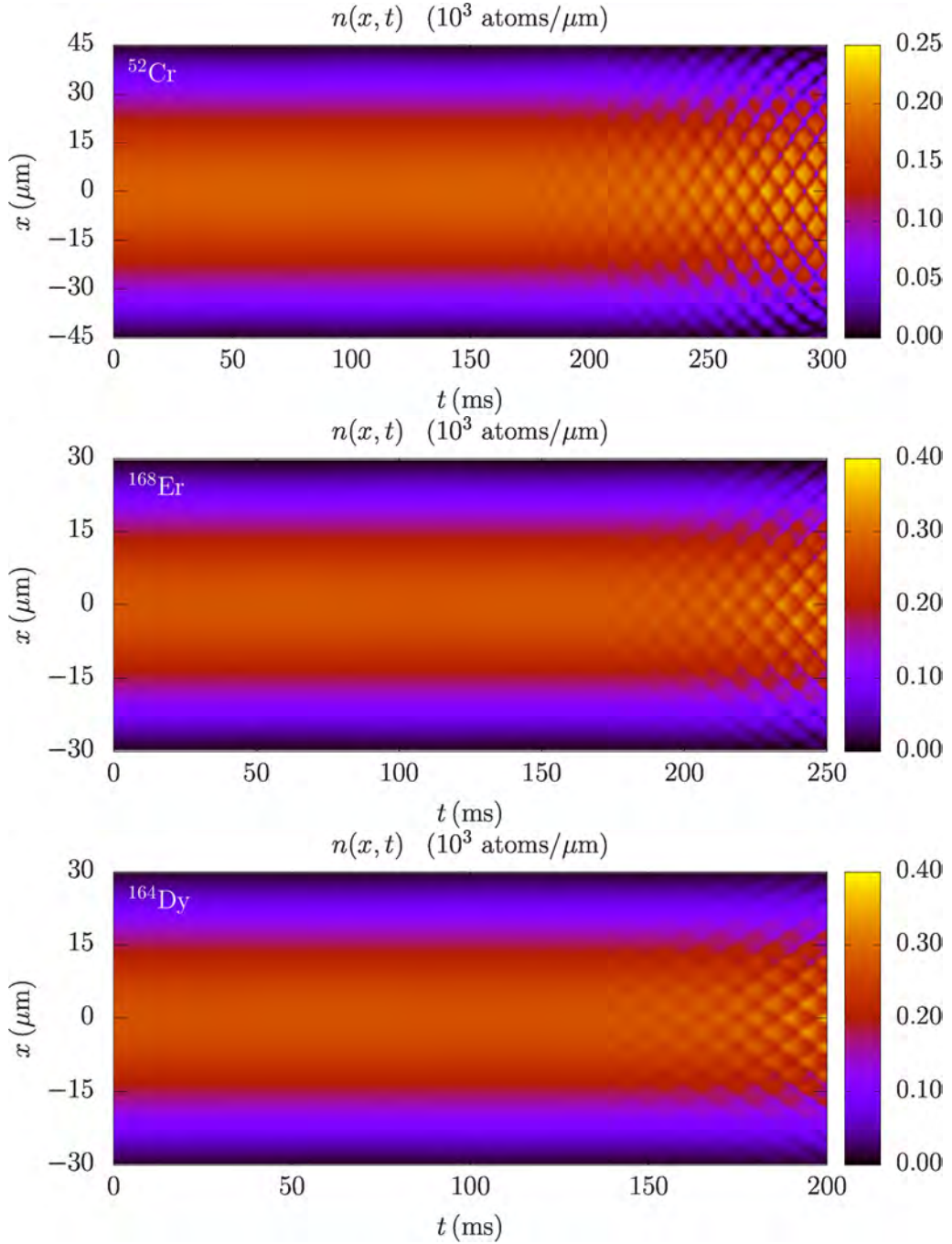


Figure 5.1: Time evolution of the integrated density in the weak confinement direction for a BEC of $N = 10^4$ atoms of chromium ^{52}Cr (top), erbium ^{168}Er (middle), and dysprosium ^{164}Dy (bottom). The results are obtained for a periodic modulation of the trap frequencies ω_y and ω_z according to Equation 5.1 with $\epsilon = 0.2$ and $\omega_m = 200 \times 2\pi$ Hz. The contact interaction strength is $a_s = 150 a_0$ and the DDI strength is given in Appendix D for each species. The Faraday waves can be visually observed after approximately 150 ms for all three species.

sults [65–79]. The density waves in x direction from Figure 5.1 take time to develop and are the result of the transfer of energy from the modes that are directly excited in the radial directions, where the trap is modulated. This can be seen in Figure 5.2, where we show the corresponding time dependence of integrated density profiles in y and z direction. The density waves in the radial directions emerge immediately after the modulation is switched on at $t = 0$, and their frequency is equal to the mod-

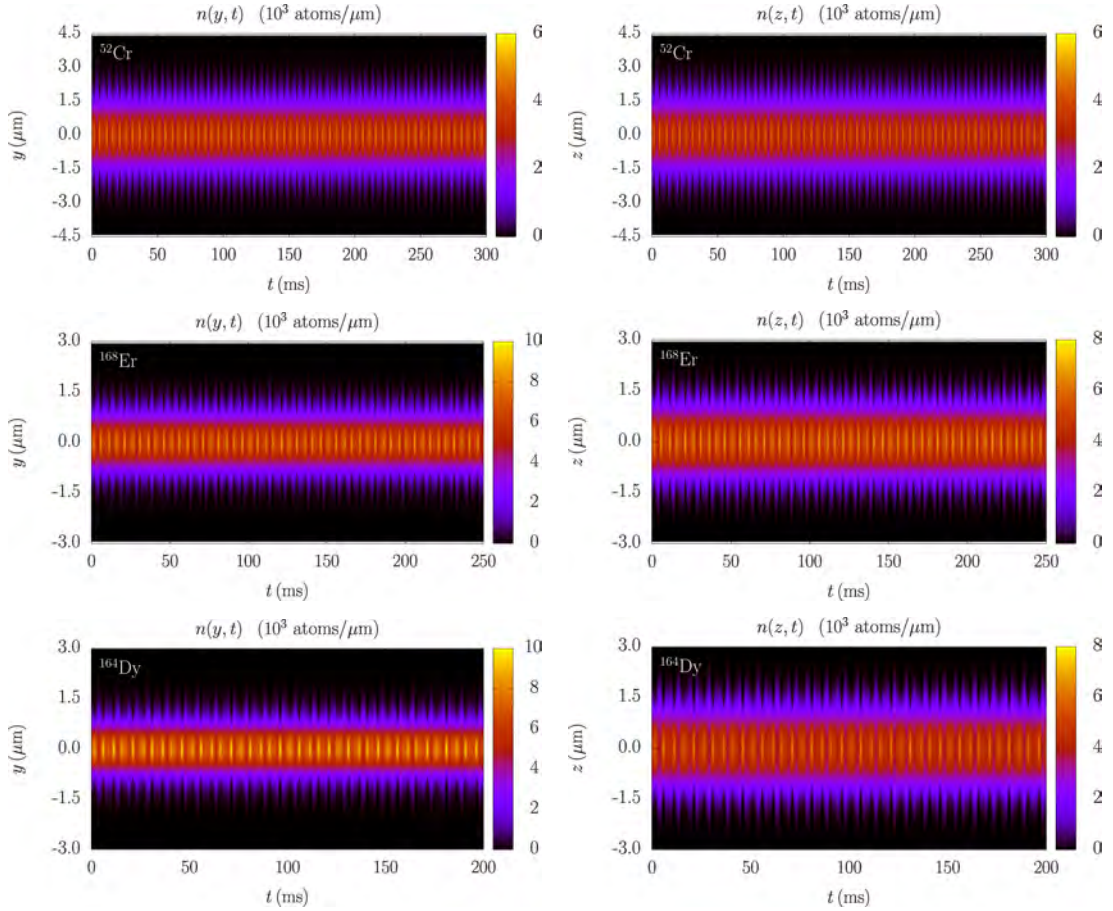


Figure 5.2: Time evolution of the integrated density in y direction (left column) and z direction (right column) for a BEC of $N = 10^4$ atoms of chromium ^{52}Cr (first row), erbium ^{168}Er (second row), and dysprosium ^{164}Dy (third row). The results are obtained for the same parameters as in Figure 5.1. The frequency of oscillations of the condensate densities in the radial direction is equal to $\omega_m = 200 \times 2\pi$ Hz. We see that, due to the dipole-dipole interaction, the width of the condensate is larger in the direction parallel to the dipoles (z direction) than in the orthogonal direction (y direction), in particular for ^{168}Er and ^{164}Dy , as already shown in Section 3.3.

ulation frequency. Comparing the left and right column in Figure 5.2, we can also directly observe the DDI effects. As we know, the dipole-dipole interaction causes the elongation of the condensate width in the polarization direction of the dipoles. Although the trap frequencies in y and z direction are equal, we see in Figure 5.2 that the condensate widths in z direction for all three species are larger than the corresponding y direction widths, and the difference increases as the strength of the DDI increases from chromium to dysprosium.

In order to characterize the density waves, we typically analyze their FFT spectra in the time-frequency and in the spatial-frequency domain. This enables us to determine the frequencies of the main excitation modes, as well as the spatial period of the observed density patterns. However, instead of directly analyzing the density profiles presented in Figures 5.1 and 5.2, for the FFT it is advantageous to have a clearer signal, which can be obtained by considering only the density variations compared to the initial state, i.e., the ground state of the system, before the modulation is switched on. The integrated density profile variation in the confined x direction is shown in Figure 5.3, and the corresponding density profile variations in y and z directions are presented in Figure 5.4.

As expected, the emergence of Faraday waves is now more easily discernible in Figure 5.3, and the same applies to the oscillations of the density shown in Figure 5.4. By looking at these two figures, we can even estimate the main oscillation frequency, e.g., counting the number of maxima or minima in a given time interval. For instance, in the last 50 ms in each of the panels in Figure 5.3 we count 5 periods, which corresponds to the frequency $100 \times 2\pi \text{ Hz} = \omega_m/2$. This is a distinguishing characteristic of Faraday waves, and therefore we directly determine that in this case the system develops this type of collective oscillations. On the other hand, in Figure 5.4 we can count 10 periods (maxima or minima) in a given 50 ms time interval, which corresponds to the modulation frequency ω_m . Thus, in the radial directions we observe as the main excitation mode the direct response of the system to the harmonic modulation of the trap.

However, this way we can determine only the main excitation modes. The dy-

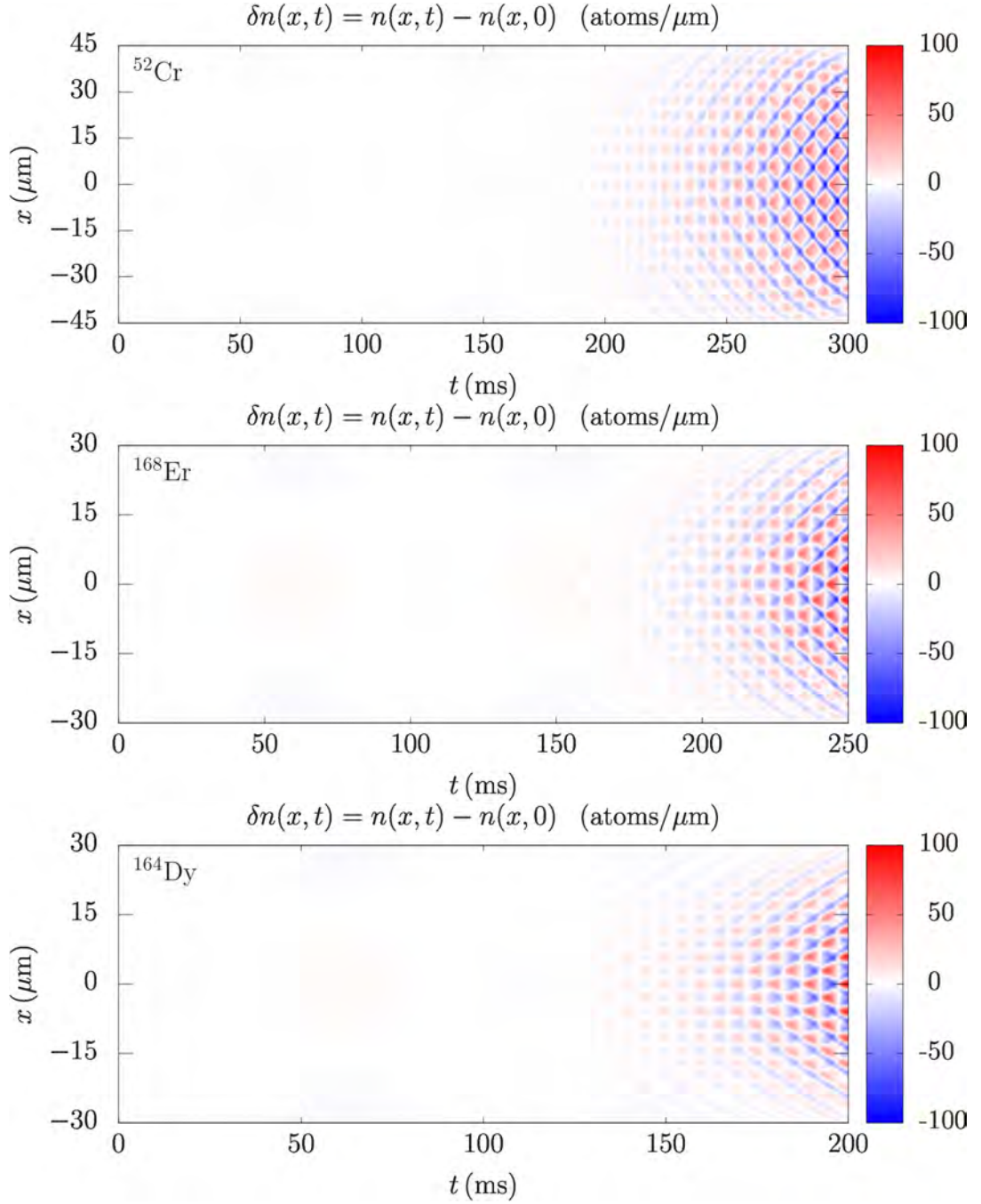


Figure 5.3: Time evolution of the integrated density profile variation in the weak confinement direction for a BEC of $N = 10^4$ atoms of chromium ^{52}Cr (top), erbium ^{168}Er (middle), and dysprosium ^{164}Dy (bottom), for the same parameters as in Figure 5.1. The variations $\delta n(x, t)$ are obtained by subtracting the density profile of the ground state $n(x, t = 0)$ from the time-dependent integrated density $n(x, t)$ presented in Figure 5.1.

namics of the system contains other modes as well, and, over time, they can develop and even start to dominate the behavior of the system. Therefore, it is important to analyze the spectra in more detail. This is done in Figure 5.5 for all integrated density profile variations from Figures 5.3 and 5.4. For simplicity, the FFT analysis is performed for the profiles at the trap center. As expected, in the weak confinement direction, the left column in Figure 5.5, the main excitation mode has a frequency $\omega_m/2$. In addition to this, we observe two other modes, at ω_m and $3\omega_m/2$. This

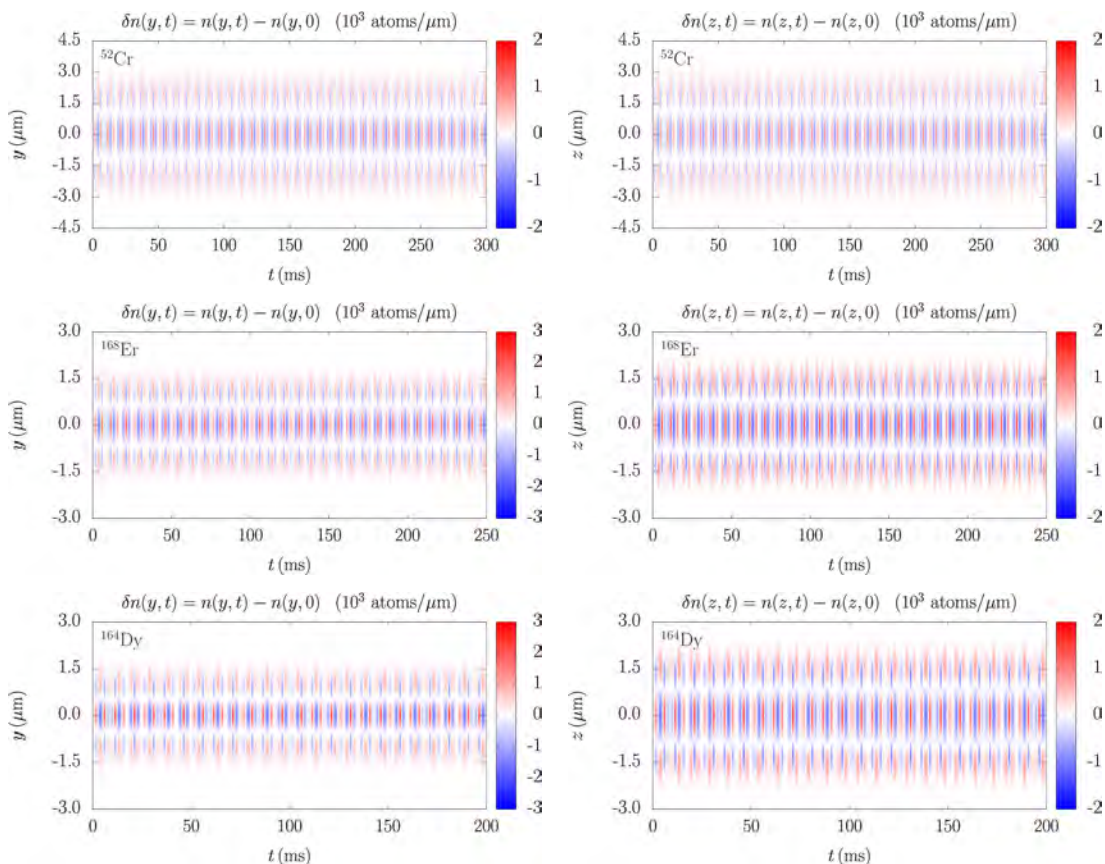


Figure 5.4: Time evolution of the integrated density profile variations in y direction (left column) and in z direction (right column) for a BEC of $N = 10^4$ atoms of chromium ^{52}Cr (first row), erbium ^{168}Er (second row), and dysprosium ^{164}Dy (third row), for the same parameters as in Figure 5.1. The variation in a given direction y or z is obtained by subtracting the density profile of the ground state from the corresponding time-dependent integrated density presented in Figure 5.2. The difference between the condensate widths in y and z direction, which was observed in Figure 5.2, is also clearly visible here.

is expected from the theoretical analysis in Section 5.1, but could not be discerned directly from the density profiles or their variations.

In the Fourier spectra of the integrated density profile variations in the radial directions, middle and right column in Figure 5.5, we see a somewhat richer set of excitation modes. In addition to the main mode corresponding to the trap modulation at ω_m , we see that also the breathing mode is excited at the frequency $\omega_B \approx 321 \times 2\pi$ Hz, which was determined in Section 4.1. The spectra prominently contain the second modulation harmonic at $2\omega_m$ as well. We see some other peaks in the spectra as well. For instance, the small peak at around $120 \times 2\pi$ Hz, which can be due to the linear combination of the modes $\omega_B - \omega_m$. However, such an identification would require further theoretical and numerical analysis, which is out of the scope of this thesis.

While the Fourier analysis in the time-frequency domain can be used to determine the character of the induced density waves (Faraday, collective, resonant), the analysis in the spatial-frequency domain enables us to characterize the density patterns and calculate their spatial period. This is illustrated in Figure 5.6 for Faraday waves for all three considered atomic species. The integrated density profile variations are analyzed at appropriate times, which are determined to correspond to the evolution stage when Faraday waves have fully emerged, but the system is still far from the violent dynamics that inevitably follows after the long driving period.

In all three panels of Figure 5.6 the main peak corresponds to the wave vector k_F of the Faraday waves, and we see significant differences: for ^{52}Cr we obtain $k_F = 0.57 \mu\text{m}^{-1}$, yielding the spatial period $\ell = 2\pi/k_F = 11.02\mu\text{m}$; for ^{168}Er we get $k_F = 0.98 \mu\text{m}^{-1}$ and $\ell = 6.41\mu\text{m}$; for ^{164}Dy we have $k_F = 1.10 \mu\text{m}^{-1}$ and $\ell = 5.71\mu\text{m}$. The variational analysis presented in Section 5.1 yields results which are in good agreement with the numerical ones, namely $k_F = 0.51 \mu\text{m}^{-1}$ for ^{52}Cr , $k_F = 0.91 \mu\text{m}^{-1}$ for ^{168}Er , and $k_F = 1.06 \mu\text{m}^{-1}$ for ^{164}Dy . These variational results are shown in Figure 5.6 by vertical blue lines, which illustrates their agreement with the Fourier analysis. The presented spectra also contain some additional peaks that correspond to other geometrical features of the analyzed density profile variations,

such as the condensate width and its higher harmonics, as well as the higher harmonics of the Faraday wave periods, and linear combinations of all of these. However, they are not of interest in our analysis and we will not study them further.

Note that the spatial period of Faraday waves can be also determined by directly looking at the density profile variations in Figure 5.3, and estimating the spacing between the consecutive minima or maxima at the appropriate evolution time. For

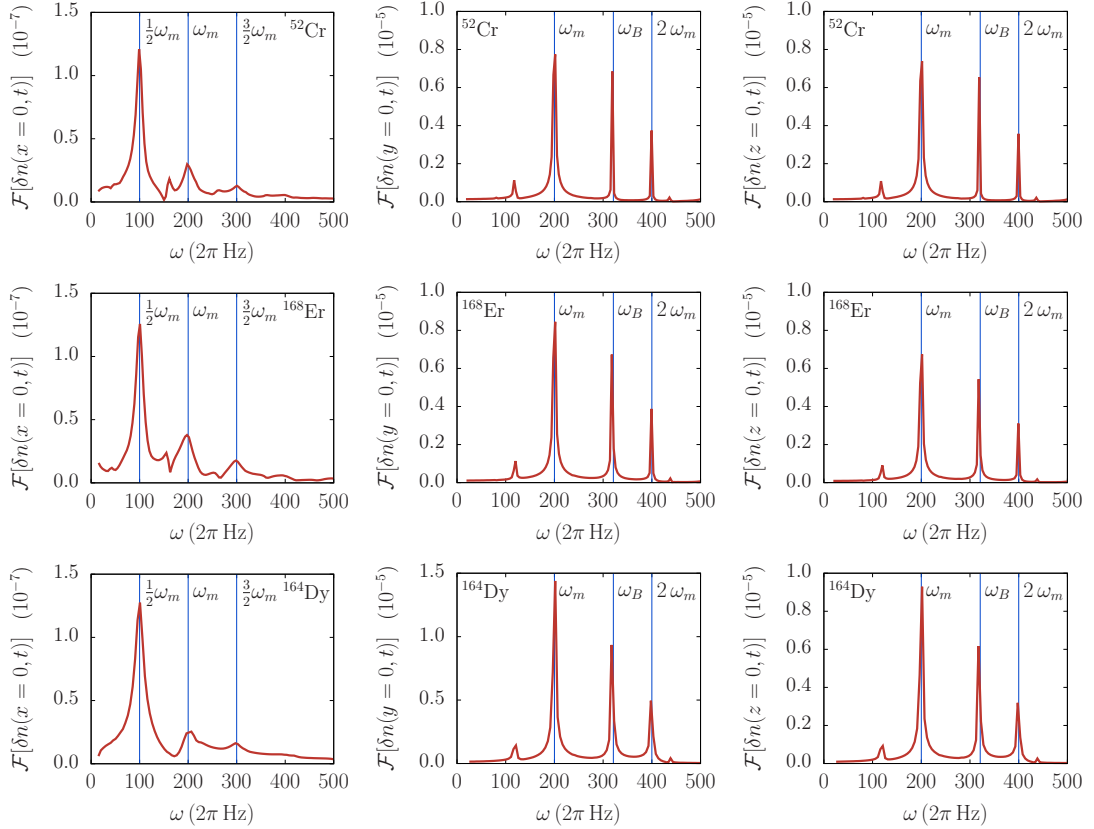


Figure 5.5: The Fourier spectrum in the time-frequency domain of the integrated 1D density profile variations of Faraday waves at the trap center $\delta n(x = 0, t)$ in x direction (first column), $\delta n(y = 0, t)$ in y direction (second column), and $\delta n(z = 0, t)$ in z direction (third column) for a BEC of $N = 10^4$ atoms of chromium ^{52}Cr (first row), erbium ^{168}Er (second row), and dysprosium ^{164}Dy (third row). The corresponding density profile variations are shown in Figures 5.3 and 5.4. Vertical blue lines represent theoretical predictions, where $\omega_m/2$ corresponds to Faraday waves, ω_m and $2\omega_m$ to resonant waves, and ω_B is the variational result for the breathing mode frequency obtained in Section 4.1.

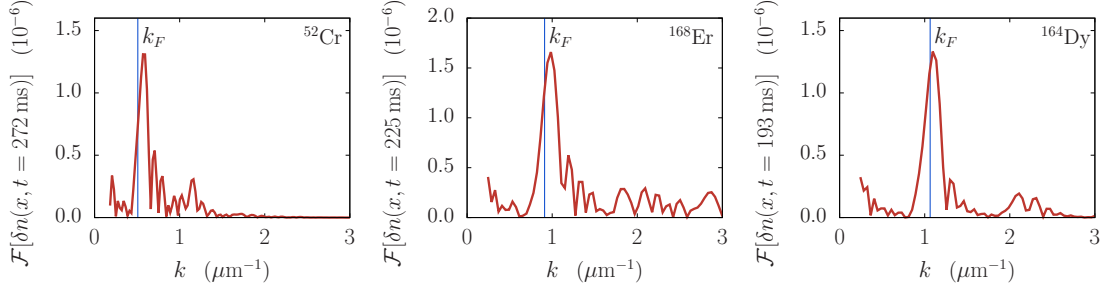


Figure 5.6: The Fourier spectrum in the spatial-frequency domain of the integrated 1D density profile variations of Faraday waves in x direction $\delta n(x, t = 272 \text{ ms})$ for ^{52}Cr (left), $\delta n(x, t = 225 \text{ ms})$ for ^{168}Er (middle), and $\delta n(x, t = 193 \text{ ms})$ for ^{164}Dy (right) BECs with $N = 10^4$ atoms. The corresponding density profile variations are shown in Figure 5.3. Vertical blue lines represent theoretical predictions for the wave vector k_F of the Faraday waves, i.e., the variational result obtained in Section 5.1, Equation (5.32).

instance, for chromium, we count three minima over the spatial extent of $30 \mu\text{m}$, yielding an estimate $\ell \approx 10\mu\text{m}$. Similarly, for erbium, we count 5 minima over the spatial extent of $30 \mu\text{m}$, yielding $\ell \approx 6\mu\text{m}$, and for dysprosium, the count and the estimate are the same. Obviously, these estimates are not as precise as the Fourier analysis results, and therefore we rely on FFT spectra to systematically determine the spatial periods of Faraday waves and their functional dependencies on the contact and dipole-dipole interaction strength.

5.3 Interaction effects and properties of Faraday waves

In the previous section, we have shown how Fourier analysis can be used to calculate the spatial period of Faraday waves. Now we systematically study the interaction effects, i.e., how the contact and the dipole-dipole interaction strength affect the properties of generated density waves. First, we explore the influence of the contact interaction on the emergence time and the spatial period of Faraday waves for a fixed value of the dipole-dipole interaction strength, by varying the s -wave scattering length in the experimentally relevant regime. In laboratory this can be achieved by employing the Feshbach resonance technique, which allows to tune a_s by changing

the external magnetic field, thus changing the electronic structure of atoms and their scattering properties.

The existence of Faraday waves is a consequence of nonlinearity of the system, i.e., the presence of the contact and the dipole-dipole interaction terms in the Hamiltonian. In a linear system, described by the pure Schrödinger equation, the harmonic modulation of the trap in the radial direction would not be transferred into the longitudinal direction. Therefore, the emergence time of Faraday waves (and other types of density waves in the longitudinal direction) critically depends on the strength of interatomic interactions. However, if interaction strengths become sufficiently large, the emergence time is less sensitive to their changes. Since we are considering three species where the dipole-dipole interaction is strong in erbium and dysprosium, we can expect that the emergence time of Faraday waves significantly depends on the contact interaction strength only in chromium, where a_{dd} is small.

This is illustrated in Figure 5.7, where we see the density profile variations for chromium for three different values of a_s . Let us first note that the amplitude of density variations is much smaller in the top panel for $a_s = 60 a_0$ than in the middle panel for $a_s = 80 a_0$, and significantly smaller than in the bottom panel for $a_s = 150 a_0$. This is also evident from the fact that in the top and middle panel we can clearly see the quadrupole collective oscillation mode, which has a frequency of around $\omega_Q = 12 \times 2\pi$ Hz. This can be estimated from the figure and compared to the value obtained in Section 4.2 for chromium, Figure 4.2. When the interaction is sufficiently large, the amplitude of Faraday waves is much larger than those of the collective modes, and they cannot be even discerned in the bottom panel in Figure 5.7. Only for weak interactions the amplitude of the Faraday waves is comparable to the amplitude of the collective modes, and this is the reason why we can see them all for small values of a_s .

Like all other excitations, Faraday waves start to develop immediately after the modulation is switched on. The question on their emergence time is related to their amplitude, which is time-dependent and grows exponentially, as can be seen from the solution (5.23) of the Mathieu-like equation that describes the dynamics of the

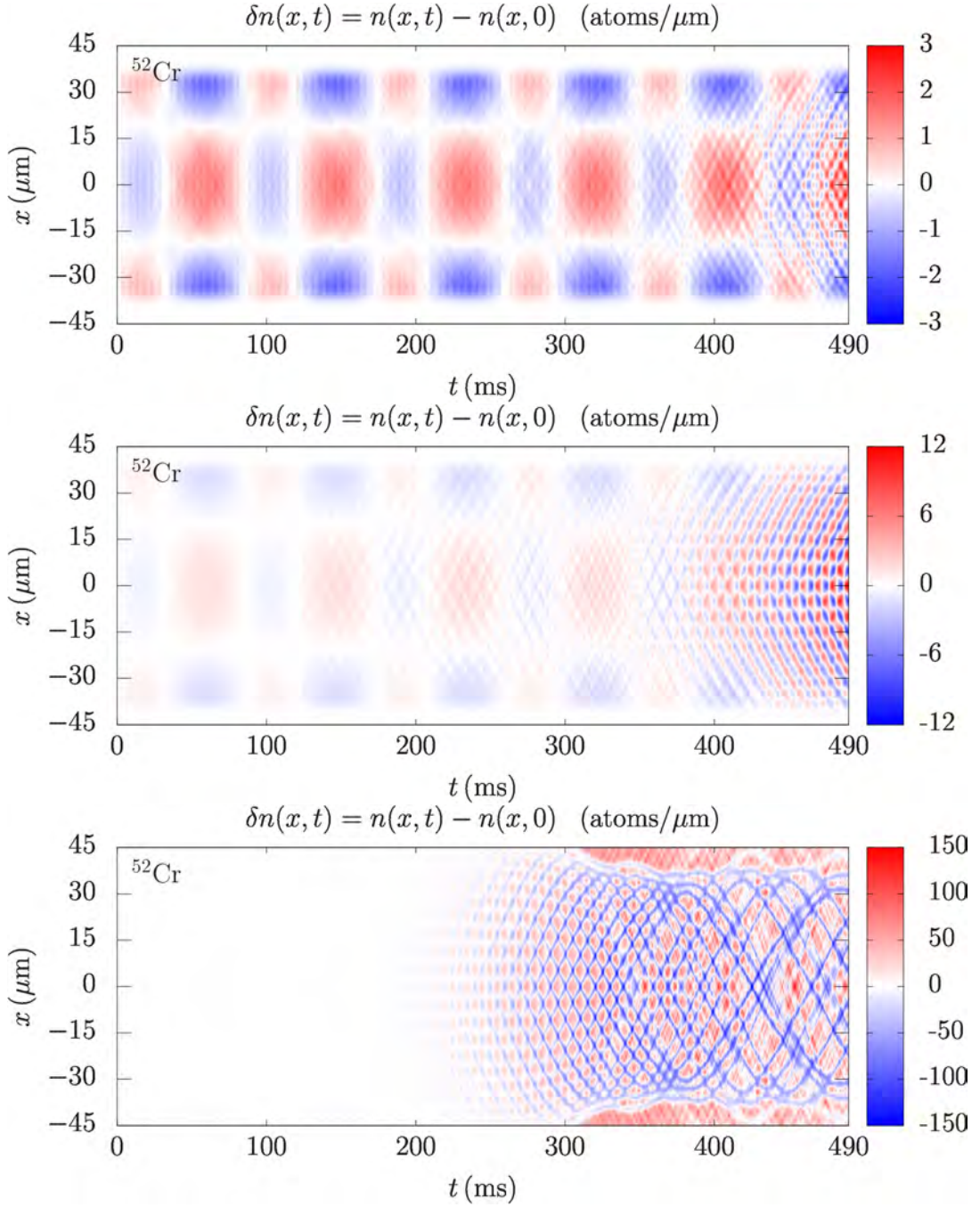


Figure 5.7: Emergence of Faraday waves for different strengths of the contact interaction: $a_s = 60 a_0$ (top), $a_s = 80 a_0$ (middle), and $a_s = 150 a_0$ (bottom) for a BEC of $N = 10^4$ atoms of ^{52}Cr . From these integrated 1D density profile variations $\delta n(x,t)$, obtained for a fixed value of the dipole-dipole interaction strength given in Appendix D, we observe that Faraday waves emerge faster as the contact interaction strength increases.

Faraday density oscillations. The imaginary part of the parameter ξ in Equation (5.23) is responsible for the exponential growth of the Faraday waves' amplitude, which is not the case for collective modes. Therefore, in practical terms, the definition of the emergence time of Faraday waves is always arbitrary and can be expressed as a time needed for the density variations to reach a certain absolute or relative (compared to the total density) value. One can even relate this to the experimental point of view, where there is a threshold for the density variations that can be observed, due to measurement errors. However, in numerical simulations there are no such limitations and one can easily use an arbitrary definition to estimate the emergence time of density waves. The more relevant quantity to study would be the exponent that governs the growth of the wave amplitude, which depends on the interaction strength.

Now we turn our attention to spatial features of the Faraday waves. Figure 5.8 presents the dependence of the wave vector k_F on the s -wave scattering length a_s for all three considered species. We also show the variational results for the dependence $k_F(a_s)$ derived in Section 5.1. The agreement is very good, with errors of the order of 10 - 15 %. We stress that the derived variational expression closely follows the numerical results not only by their values, but, even more importantly, it follows their functional dependence properly.

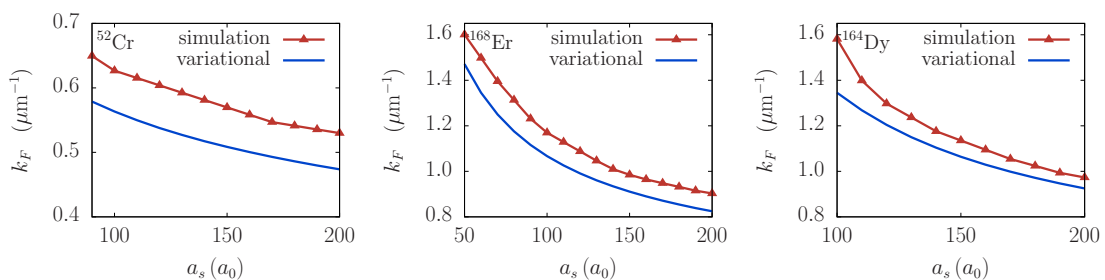


Figure 5.8: Wave vector of the Faraday waves k_F as a function of the contact interaction strength for a BEC of $N = 10^4$ atoms of ^{52}Cr (left), ^{168}Er (middle), and ^{164}Dy (right), for a fixed dipole-dipole interaction strength given in Appendix D. Red upper triangles are numerically obtained values using the FFT analysis as in Figure 5.6, and blue lines are the variational results according to Equation (5.32).

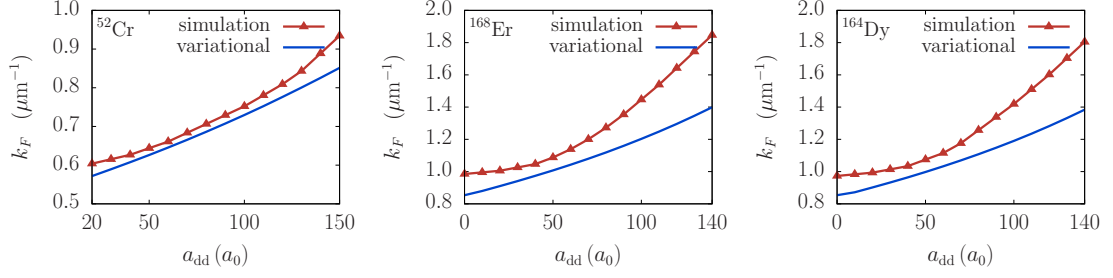


Figure 5.9: Wave vector of the Faraday waves k_F as a function of the dipole-dipole interaction strength for a BEC of $N = 10^4$ atoms of ^{52}Cr (left), ^{168}Er (middle), and ^{164}Dy (right), for a fixed contact interaction strength given in Appendix D. Red upper triangles represent numerically obtained values using the FFT analysis as in Figure 5.6, and blue lines are the variational results according to Equation (5.32).

Next, we study the effects of the dipole-dipole interaction strength for a fixed value of the contact interaction. Figure 5.9 shows the corresponding dependence of k_F on a_{dd} . In contrast to the contact interaction dependence, where k_F was a decreasing function of a_s , here we see that k_F increases as the dipole-dipole interaction strength is increased. Figure 5.9 also shows the variational results, where the level of agreement with the numerically obtained results is different, with errors as small as 7 % for chromium up to around 25 % for erbium and dysprosium for largest values of a_{dd} . Due to complex approximations made in the derivation of variational results, in particular those related to the dipole-dipole interaction term, the obtained functional dependence is not as good as in the case of contact interaction, but still provides reasonable estimates of the wave vector values for the Faraday waves.

5.4 Resonant waves

In the presence of interactions various excitation modes in dipolar BECs are coupled and the energy pumped into the system by periodic driving can be transferred from the driving direction to other, orthogonal directions. In the previous section, we have seen this for non-resonant driving, when the harmonic modulation in the radial direction was transferred to the longitudinal direction in the form of Faraday waves, which were the main excitation mode generated. The main distinguishing property

of these excitations is halving of the oscillation frequency, i.e., the induced density waves have the frequency $\omega_m/2$. Here we study the other important case, when the modulation frequency is resonant, such that the induced density waves have the same frequency. This happens when ω_m is close to one of the characteristic frequencies of the system, e.g., one of the frequencies of the collective oscillation modes or one of the trap frequencies. Although Faraday waves and all other collective oscillation modes are also excited in this case, the largest amplitude corresponds to resonant waves with the frequency ω_m . When generated, these resonant waves dominate the behavior of the system and make all other excitations negligible for the dynamics.

Figure 5.10 shows the integrated density profile variation of ^{168}Er for a resonant wave induced by a harmonic modulation of the radial part of the trapping potential at $\omega_m = \omega_y = \omega_z$, i.e., when the modulation frequency coincides with the radial trapping frequency. In this case, the density waves develop much faster than for non-resonant modulation and are clearly visible already after 55 ms. Due to a vi-

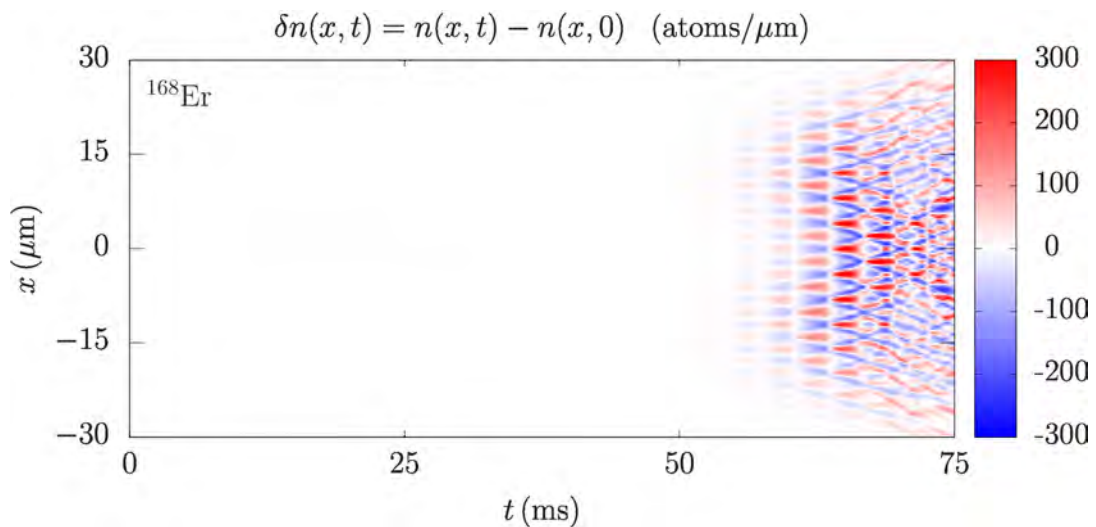


Figure 5.10: Time evolution of the integrated density profile variation in the weak confinement direction for a BEC of $N = 10^4$ atoms of erbium ^{168}Er . The parameters of the system are given in Appendix D, and the modulation frequency used is equal to the weak confinement frequency, $\omega_m = 160.5 \times 2\pi$ Hz = $\omega_y = \omega_z$. We observe resonant behavior corresponding to the first harmonic of the resonant frequency $\omega_y = \omega_z$, which sets in after around 55 ms.

olent dynamics that emerges in the system very fast, it is not easy to estimate the frequency of the waves directly from Figure 5.10, as was possible before. Therefore, we rely on the Fourier analysis in the time-frequency domain, presented in the left panel of Figure 5.11. The obtained FFT spectrum clearly shows that the main excitation mode has a frequency equal to ω_m . We also see that the spectrum is continuous, practically without distinct individual peaks, and only the second harmonic at $2\omega_m = 321 \times 2\pi$ Hz yields a small local maximum. This demonstrates that the system is far from the regime of small perturbations, where individual excitation modes can be observed.

In the right panel of Figure 5.11 we see the Fourier spectrum in the spatial-frequency domain, which yields the wave factor k_R of resonant waves. The FFT results give the value $k_R = 1.59 \mu\text{m}^{-1}$ and the corresponding spatial period $\ell = 2\pi/k_R = 3.95 \mu\text{m}$ for ^{168}Er . In the figure we also present the variational result $k_R = 1.40 \mu\text{m}^{-1}$, calculated using Equation (5.33). The agreement is again quite

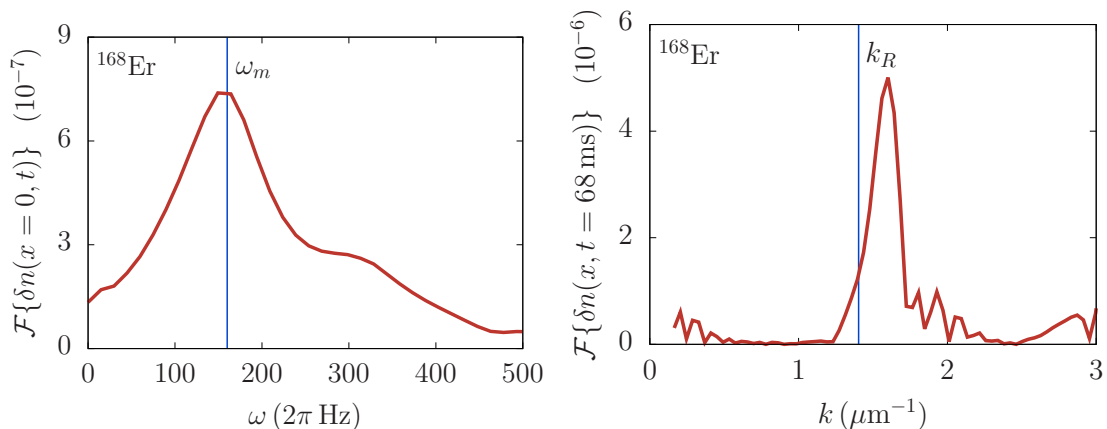


Figure 5.11: The Fourier spectrum of the integrated 1D density profile variations $\delta n(x, t)$ at the trap center in the time-frequency domain (left), and of the density profile variations in x direction $\delta n(x, t = 68 \text{ ms})$ in the spatial-frequency domain (right) of resonant waves for a BEC of $N = 10^4$ atoms of ^{168}Er for the same parameters as in Figure 5.10. The vertical blue line in the left panel represents the modulation frequency ω_m , while in the right panel it corresponds to the theoretical prediction for the wave vector k_R of the resonant waves derived in Section 5.1, Equation (5.33).

good, which indicates that the variational approach we developed in this thesis can be reliably used not only for the Faraday waves, but also for the resonant waves.

This can also be concluded from Figure 5.12, which presents the results for the dependence of the resonant wave vector k_R on the contact and dipole-dipole interaction strength. The agreement between the numerical and variational results is of the order of 10 % over the whole experimentally relevant domain. We see similar behavior for the resonant waves as for the Faraday ones, namely the wave vector decreases as the contact interaction strength increases, while the opposite is true for the dipole-dipole interaction. Again the functional dependence obtained from the variational approach properly describes the numerical results, thus confirming that Equation (5.33) can be used to calculate the spatial period of resonant waves.

It is interesting to note that resonant behavior appears not only under the conditions mentioned above, when ω_m is equal to one of the characteristic frequencies, but also when it matches their higher harmonics. Figure 5.13 illustrates this for ^{168}Er , which is harmonically modulated at twice the radial trapping frequency,

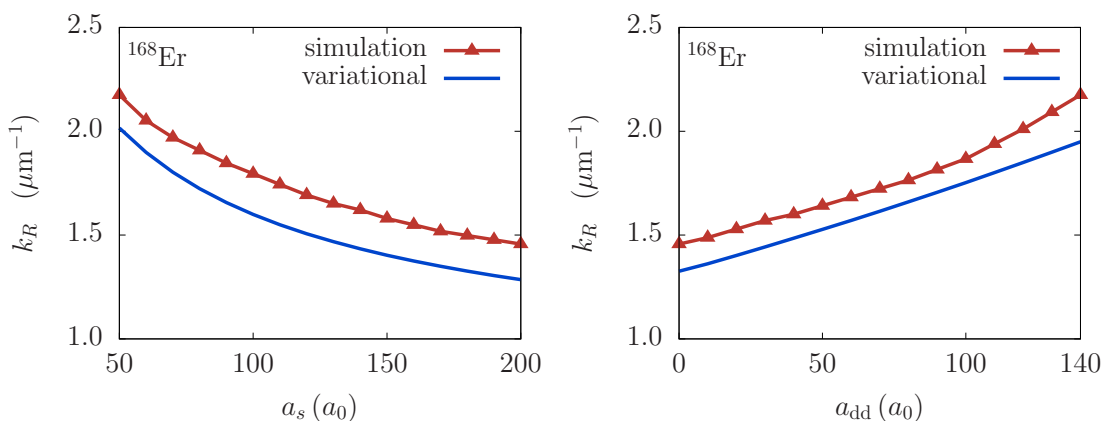


Figure 5.12: Wave vector of the resonant waves k_R as a function of the contact (left) and dipole-dipole (right) interaction strength for a BEC of $N = 10^4$ atoms of ^{168}Er . The results in the left panel are obtained for a fixed dipole-dipole interaction strength given in Appendix D, and similarly, in the right panel, a fixed contact interaction strength from Appendix D is used. In both panels, red upper triangles represent numerically obtained values using the FFT analysis as in the right panel of Figure 5.11, and blue lines are the variational results according to Equation (5.33).

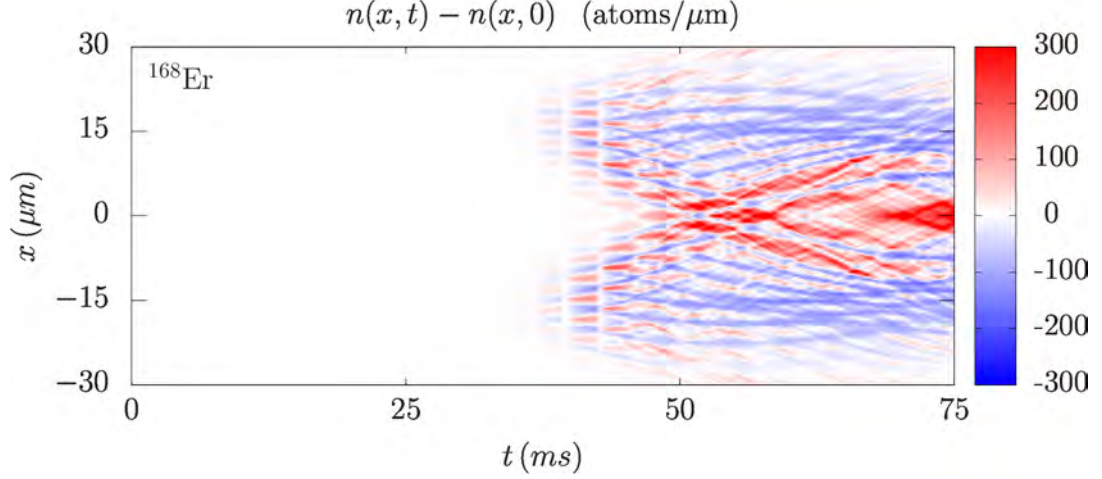


Figure 5.13: Time evolution of the integrated density profile variation in the weak confinement direction for a BEC of $N = 10^4$ atoms of erbium ^{168}Er . The parameters of the system are given in Appendix D, and the modulation frequency used is equal to twice the weak confinement frequency, $\omega_m = 321 \times 2\pi$ Hz = $2\omega_y$. We observe resonant behavior corresponding to the second harmonic of the resonant frequency $\omega_y = \omega_z$, which sets in faster than the first harmonic, already after around 30 ms.

$\omega_m = 321 \times 2\pi$ Hz. In this case, the amplitude of the resonant mode grows even faster and significant density variations can be observed already after 30 ms. Therefore, we see that the modulation at the second harmonic yields even more violent dynamics than the first harmonic. The Fourier analysis in the time-frequency domain reveals that the main excitation mode again has a frequency of $160.5 \times 2\pi$ Hz, but the mode at $\omega_m = 321 \times 2\pi$ Hz is also present. From the experimental point of view, resonant driving is very dangerous and leads to the destruction of the system in a matter of tens of milliseconds. While numerical simulations can be performed for longer time periods, the atoms leave the condensate due to a large, resonant transfer of energy to the system. As the condensate is depleted, the mean-field description of the system breaks down and it cannot be anymore simulated by the dipolar GPE.

6 Algorithm for solving the dipolar GPE

The existence of nonlinear terms in equations describing various physical systems is usually a source of novel phenomena. However, their understanding requires detailed and careful analysis, mainly because we can no longer rely on our intuition based on linear equations and instinctively predict the evolution of the system. From the experimental point of view, the analysis requires development and fine-tuning of new methods that focus on particular phenomena in the condensate. On the other hand, it is often necessary to establish or further develop an analytical or numerical method to solve the corresponding set of equations, usually a set of nonlinear partial differential equations. In the case of a BEC with dipole-dipole interaction, we mostly rely on the dipolar GPE.

A wide range of different numerical methods was developed in the literature. Some of them are focused on the calculation of the ground state properties [83–86], while others focus on the dynamics of the time-dependent GPE [87–95]. Also, there are several methods able to calculate a numerical solution both for the ground state and non-stationary dynamics of a BEC [87–95]. These methods can be divided into several categories: finite difference, split-step, and spectral methods.

A finite difference method approximates the spatial and time derivatives with finite differences, up to the desired order of accuracy, which is derived from the Taylor series expansion. This approach introduces discretization of space and time, with the time step denoted by Δt , and the space step denoted by Δh . Note that the space discretization step can be different in different directions, in which case

we denote the corresponding steps by Δh_j , where $j = 1, 2, 3$. When dealing with dipolar GPE, such discretization is usually implemented using a forward, backward, or central difference scheme in time and a second-order central difference scheme for space derivatives. An algorithm that implements a forward difference scheme in time is known as an explicit method, a backward difference approach yields an implicit method, and a central difference approach in time is a combination of the two, and is designated as a semi-implicit algorithm, or the Crank–Nicolson semi-implicit algorithm [35–37]. In its usual form, it introduces a quadratic error in the calculation in the discretization steps, $\mathcal{O}(\Delta t^2) + \mathcal{O}(\Delta h^2)$, both in the time and the space steps. The fact that we are using a semi-implicit algorithm, i.e., that the space derivatives are expressed as averages of their finite difference approximations in the present and future time step, makes the Crank-Nicolson scheme unconditionally stable [36, 37]. We have used this method in all our implementations.

The split-step method relies on the splitting of the time evolution in each time step into several sub-steps, which corresponds to splitting the Hamiltonian that governs the system’s dynamics into several parts, and then evolving the wave function independently with respect to each of them. This method is usually combined with the finite difference method, and practically realized by splitting the Hamiltonian $\hat{H} = \hat{T} + \hat{V}$ into the kinetic energy part \hat{T} and the potential energy part \hat{V} , which includes the trap potential and nonlinear terms corresponding to the contact and the dipole-dipole interaction. In order to implement the splitting of the Hamiltonian and calculate the time evolution of the system we use the Baker-Campbell-Hausdorff lemma [96]

$$e^{\Delta t(\hat{O}_1 + \hat{O}_2)} = e^{\Delta t \hat{O}_1} e^{\Delta t \hat{O}_2} e^{-\frac{\Delta t^2}{2} [\hat{O}_1, \hat{O}_2]} e^{\frac{\Delta t^3}{6} (2[\hat{O}_2, [\hat{O}_1, \hat{O}_2]] + [\hat{O}_1, [\hat{O}_1, \hat{O}_2]])} \dots \quad (6.1)$$

The above form of the lemma, known as the Zassenhaus formula [97], expresses the exponential of the sum of two operators \hat{O}_1 and \hat{O}_2 , that do not commute in general, by a product of their individual exponentials and higher-order terms that contain quadratic and higher orders of the parameter Δt . If the parameter Δt is small we can neglect these higher-order terms and use the splitting formula which, for the

case of the time evolution of the Hamiltonian $\hat{H} = \hat{T} + \hat{V}$ reads

$$e^{-\frac{i}{\hbar}\hat{H}\Delta t} = e^{-\frac{i}{\hbar}(\hat{T}+\hat{V})\Delta t} = e^{-\frac{i}{\hbar}\hat{T}\Delta t} e^{-\frac{i}{\hbar}\hat{V}\Delta t} + \mathcal{O}(\Delta t^2). \quad (6.2)$$

In this way, we make the error of the same order as the one due to the finite difference scheme used to approximate time derivatives. In principle, we can go to higher orders in the Zassenhaus formula, but this would be numerically very time-consuming. It would also have to be accompanied by a higher order of approximation for the time derivative. The numerical complexity of such a method would be even higher due to this and therefore is rarely used. One can achieve the desired accuracy of the calculation by using smaller values of the discretization steps. In addition to split-step methods there are also other, direct methods for solving the GPE (or, in general, partial differential equations) such as Euler or Runge-Kutta [98], where time evolution is done in one step, avoiding the Hamiltonian division altogether.

Spectral methods rely on expressing the solution of the GPE in an appropriately chosen basis as a linear combination of orthonormal special functions. In this case, the original equation is rewritten as a set of equations for the corresponding coefficients of the wave function expansion in the selected basis. For instance, if we use the plane-wave basis we get the most common spectral decomposition of the wave function. The kinetic energy part and the potential energy part of the Hamiltonian are diagonal in the k -space and in the real space, respectively, and forward and backward Fourier transformation enables us to compute the evolution with respect to the corresponding part of the Hamiltonian. Note that the spectral methods also belong to the category of split-step approaches and use the Zassenhaus approximation (6.2).

Our numerical algorithm to solve the GPE combines the split-step approach with the semi-implicit Crank-Nicolson method [35–37]. The ground state of the system is calculated using propagation in the imaginary-time [84–86] starting from an arbitrary initial state, while the system’s dynamics is obtained using the real-time propagation from a given initial wave function. Our programs that practically

implement the algorithm solve the dimensionally reduced form of the GPE

$$i \frac{\partial \psi(\mathbf{r}, t)}{\partial t} = \left[-\frac{1}{2} \nabla^2 + U(\mathbf{r}, t) + 4\pi N a_s |\psi(\mathbf{r}, t)|^2 + 3N a_{\text{dd}} \int d\mathbf{r}' U_{\text{dd}}(\mathbf{r} - \mathbf{r}') |\psi(\mathbf{r}', t)|^2 \right] \psi(\mathbf{r}, t). \quad (6.3)$$

Equation (6.3) is derived from the dimensional GPE (2.45) by choosing a reference frequency ω_r , and by expressing all other physical variables in units defined using this frequency

$$x \rightarrow \frac{x}{l}, \quad y \rightarrow \frac{y}{l}, \quad z \rightarrow \frac{z}{l}, \quad a_s \rightarrow \frac{a_s}{l}, \quad a_{\text{dd}} \rightarrow \frac{a_{\text{dd}}}{l}, \quad t \rightarrow \omega_r t, \quad (6.4)$$

$$\psi(\mathbf{r}, t) \rightarrow l^{3/2} \psi(\mathbf{r}, t), \quad U(\mathbf{r}, t) \rightarrow \frac{1}{\hbar \omega_r} U(\mathbf{r}, t), \quad U_{\text{dd}}(\mathbf{r}, t) \rightarrow \frac{1}{\hbar \omega_r} U_{\text{dd}}(\mathbf{r}, t).$$

Here the unit of length l is harmonic oscillator length $l = \sqrt{\hbar/(m\omega_r)}$ for the frequency ω_r and the mass m of the atoms in the condensate. In order to transform the numerical results obtained in simulations to the physical units, one has to perform the inverse rescaling.

As a result of this, the trapping potential $U(\mathbf{r}, t)$ is transformed into a dimensionless form

$$U(\mathbf{r}, t) = \frac{1}{2} (\gamma^2 x^2 + \nu^2 y^2 + \lambda^2 z^2), \quad (6.5)$$

where $\gamma = \omega_x/\omega_r$, $\nu = \omega_y/\omega_r$, and $\lambda = \omega_z/\omega_r$ are the trap aspect ratios. For practical reasons, we usually set one of the trap frequencies as the referent ω_r . Another convenient choice is the geometric mean of the trap frequencies, $\omega_r = (\omega_x \omega_y \omega_z)^{1/3}$. Our programs allow to use all three trap aspect ratios independently, but in our simulations, with the cigar-shaped condensates along the x -axis, we choose $\omega_r = \omega_y = \omega_z$, so that the trap aspect ratios ν and λ are equal to 1.

6.1 Split-step semi-implicit Crank-Nicolson method

The split-step semi-implicit Crank-Nicolson method introduces the discretization of time and spatial coordinates. The total time of simulation T is discretized into N equal sub-steps $\Delta t = T/N$. The simulation is performed in three spatial dimensions, and we introduce a spatial mesh with N_x , N_y , and N_z equidistant points in x , y , and z

direction, respectively. The corresponding spatial extents of the system (simulation box sizes) are $L_x = N_x \Delta x$, $L_y = N_y \Delta y$, and $L_z = N_z \Delta z$, where Δx , Δy , and Δz are the discretization steps. It is customary to place the coordinate system in the center of the simulation box, such that the coordinates x , y , and z take values from the intervals $[-L_x/2, L_x/2]$, $[-L_y/2, L_y/2]$, and $[-L_z/2, L_z/2]$, respectively.

During the small evolution time Δt , the split-step approach of the algorithm divides the Hamiltonian into the non-derivative (\hat{H}_0) and derivative (\hat{H}_1 , \hat{H}_2 , \hat{H}_3) parts, as follows

$$\hat{H}_0 = U(\mathbf{r}; t) + 4\pi N a_s |\psi(\mathbf{r}; t)|^2 + 3N a_{\text{dd}} \int d\mathbf{r}' U_{\text{dd}}(\mathbf{r} - \mathbf{r}'; t) |\psi(\mathbf{r}'; t)|^2, \quad (6.6)$$

$$\hat{H}_1 = \frac{\partial^2}{\partial x^2}, \quad \hat{H}_2 = \frac{\partial^2}{\partial y^2}, \quad \hat{H}_3 = \frac{\partial^2}{\partial z^2}, \quad (6.7)$$

where the Laplacian is split into three parts. Therefore, the initial dipolar GPE given by equation (6.3) transforms into four sequential partial differential equations,

$$i \frac{\partial \psi(\mathbf{r}; t)}{\partial t} = \hat{H}_j \psi(\mathbf{r}; t), \quad j = 0, 1, 2, 3, \quad (6.8)$$

which are solved one after the other in the algorithm.

Starting from a preceding solution $\psi^n(\mathbf{r})$, obtained in the previous complete time step, the time evolution with respect to \hat{H}_0 in the current time step yields an intermediate solution $\psi^{n+1/4}(\mathbf{r})$ of equation (6.8) for $j = 0$. The superscript 1/4 denotes that this is a first of four sub-steps in the current time iteration. Since \hat{H}_0 has no derivatives, it is diagonal in real space and the solution can be written exactly as

$$\psi^{n+1/4}(\mathbf{r}) = e^{-i\hat{H}_0\Delta t} \psi^n(\mathbf{r}) \equiv \hat{\mathcal{P}}(\hat{H}_0) \psi^n(\mathbf{r}). \quad (6.9)$$

From this intermediate solution, using the semi-implicit Crank-Nicolson scheme, the time propagation of the wave function continues and is calculated by solving the

series of partial differential equations,

$$i \frac{\psi^{n+2/4}(\mathbf{r}) - \psi^{n+1/4}(\mathbf{r})}{\Delta t} = \frac{1}{2} \hat{H}_1 [\psi^{n+2/4}(\mathbf{r}) + \psi^{n+1/4}(\mathbf{r})] , \quad (6.10)$$

$$i \frac{\psi^{n+3/4}(\mathbf{r}) - \psi^{n+2/4}(\mathbf{r})}{\Delta t} = \frac{1}{2} \hat{H}_2 [\psi^{n+3/4}(\mathbf{r}) + \psi^{n+2/4}(\mathbf{r})] , \quad (6.11)$$

$$i \frac{\psi^{n+1}(\mathbf{r}) - \psi^{n+3/4}(\mathbf{r})}{\Delta t} = \frac{1}{2} \hat{H}_3 [\psi^{n+1}(\mathbf{r}) + \psi^{n+3/4}(\mathbf{r})] . \quad (6.12)$$

On the left-hand side, partial derivatives in time are estimated by a two-point formula, and on the right-side, the wave function is averaged over the current and the future time sub-step, which is a characteristic for the finite-difference semi-implicit Crank–Nicolson method. Equations (6.10) - (6.12) have a formal solution that propagates the wave function to the next intermediate solution,

$$\psi^{n+2/4}(\mathbf{r}) = \frac{1 - i\hat{H}_1\Delta t/2}{1 + i\hat{H}_1\Delta t/2} \psi^{n+1/4}(\mathbf{r}) \equiv \hat{\mathcal{P}}(\hat{H}_1) \psi^{n+1/4}(\mathbf{r}) , \quad (6.13)$$

$$\psi^{n+3/4}(\mathbf{r}) = \frac{1 - i\hat{H}_2\Delta t/2}{1 + i\hat{H}_2\Delta t/2} \psi^{n+2/4}(\mathbf{r}) \equiv \hat{\mathcal{P}}(\hat{H}_2) \psi^{n+2/4}(\mathbf{r}) , \quad (6.14)$$

$$\psi^{n+1}(\mathbf{r}) = \frac{1 - i\hat{H}_3\Delta t/2}{1 + i\hat{H}_3\Delta t/2} \psi^{n+3/4}(\mathbf{r}) \equiv \hat{\mathcal{P}}(\hat{H}_3) \psi^{n+3/4}(\mathbf{r}) . \quad (6.15)$$

The numerical algorithm for solving the above equations is worked out in Appendix E. Let us denote by $\psi_i^{n+j/4}$ the wave function value in the current time iteration after sub-step j and at the position i in the mesh in the corresponding spatial direction. The algorithm determines the wave function by a recursive relation

$$\psi_{i+1}^{n+(j+1)/4} = \alpha_i^j \psi_i^{n+(j+1)/4} + \beta_i^{n+j/4} , \quad (6.16)$$

for $j = 1, 2, 3$, where j corresponds to spatial direction x , y , and z direction, respectively. The coefficients α_i^j and $\beta_i^{n+j/4}$ are defined via backward recursion relations

$$\alpha_{i-1}^j = \gamma_i^j A_j^- , \quad (6.17)$$

$$\beta_{i-1}^{n+j/4} = \gamma_i^j \left(A_j^+ \beta_i^{n+j/4} - B_i^{n+j/4} \right) , \quad (6.18)$$

where coefficients γ_i^j , A_j^- , A_j^+ , A_j^0 , and $B_i^{n+j/4}$ are defined by relations

$$A_j^- = A_j^+ = -\frac{\Delta t}{4\Delta h_j^2} , \quad A_j^0 = 1 + i \frac{\Delta t}{2\Delta h_j^2} , \quad (6.19)$$

$$B_i^{n+j/4} = i \frac{\Delta t}{4\Delta h_j^2} \left(\psi_{i+1}^{n+j/4} - 2\psi_i^{n+j/4} + \psi_{i-1}^{n+j/4} \right) + \psi_i^{n+j/4} , \quad (6.20)$$

where Δh_j denote spatial mesh step in Δx , Δy , and Δz direction for $j = 1, 2, 3$, respectively. The above backward recursion expresses the coefficients $B_i^{n+j/4}$ explicitly in terms of the wave function in the previous sub-step, thus disentangling the semi-implicit form of equations (6.10) - (6.12). From the technical point of view, we see that the coefficients A_j^\pm , A_j^0 , α_i^j , and γ_i^j do not depend on the wave function (i.e., on the time step n), and therefore can be calculated before the time loop in a particular simulation. In other words, these coefficients depend only on the discretization parameters. Within the main time loop, only coefficients $\beta_i^{n+j/4}$ have to be recalculated in each sub-step.

6.2 Dipole-dipole interaction

While the calculation of the potential and nonlinear contact interaction term within the non-derivative part of the Hamiltonian (\hat{H}_0) of equation (6.8) for $j = 0$ is straightforward, the calculation of the nonlinear term corresponding to the dipole-dipole interaction at each mesh point introduces additional convolution integral. The integral can be easily solved by moving to the Fourier space, i.e., by treating the dipole-dipole interaction term in momentum space as

$$\int d\mathbf{r}' U_{\text{dd}}(\mathbf{r} - \mathbf{r}') |\psi(\mathbf{r}')|^2 = \mathcal{F}^{-1} \{ \mathcal{F}[U_{\text{dd}}](\mathbf{k}) \mathcal{F}[|\psi|^2](\mathbf{k}) \}(\mathbf{r}), \quad (6.21)$$

where \mathcal{F} represents Fourier transform and \mathcal{F}^{-1} inverse Fourier transform, defined respectively by

$$\mathcal{F}[f](\mathbf{k}) = \tilde{f}(\mathbf{k}) = \int d\mathbf{r} f(\mathbf{r}) e^{-i\mathbf{k}\cdot\mathbf{r}}, \quad (6.22)$$

$$\mathcal{F}^{-1}[\tilde{f}](\mathbf{r}) = f(\mathbf{r}) = \frac{1}{(2\pi)^3} \int d\mathbf{k} \tilde{f}(\mathbf{k}) e^{i\mathbf{k}\cdot\mathbf{r}}. \quad (6.23)$$

Implementation of the algorithm uses Fast Fourier transform (FFT) for calculation of Fourier transform of the density of wave function, while the Fourier transform of the dipole potential is calculated analytically in Appendix A, yielding

$$\mathcal{F}[U_{\text{dd}}](\mathbf{k}) = \frac{4\pi}{3} (3 \cos^2 \theta - 1) = \frac{4\pi}{3} \left(\frac{3 k_z^2}{k^2} - 1 \right), \quad (6.24)$$

where θ is the angle between the orientation of dipoles and vector \mathbf{k} , i.e., in our setup, angle between z direction and vector \mathbf{k} . Within the same time step, orientations are constant, so the transformation is performed once per time step Δt . The Fourier transform of density $|\psi(\mathbf{r})|^2$ and inverse Fourier transform is evaluated numerically by using a standard FFT algorithm. The FFT algorithm is carried out in Cartesian coordinates, and the GPE is solved in 3D irrespective of the symmetry of the trapping potential.

Successful implementation of the split-step Crank-Nicolson method using Fourier transformation has to ensure that the wave function and the interaction term disappear at the boundary of the discretization mesh. For the Fourier transform of the long-range dipolar potential, this is not true, and equation (6.24) is undefined at the origin in k -space, i.e., at boundaries in coordinate space. Since the same domain is used for Fourier and inverse Fourier transform in treating the dipolar potential, cutting off the k -space origin will affect the space domain. Thus, boundary effects can play a role when finding the Fourier transform, and a sufficiently large space domain has to be used to have accurate values of the Fourier transform involving the long-range dipolar potential. Inspired by equation (A.10), it was suggested [99] that this could be avoided by truncating the dipolar interaction conveniently at large distances $r = R$ so that it does not affect the boundary, provided R is taken to be larger than the size of the condensate. Then the truncated dipolar potential will cover the whole condensate wave function and will have a continuous Fourier transform at the origin. This improves the accuracy of a calculation using a small space domain. The Fourier transform of the dipolar potential truncated at $r = R$ is used in our implementation of the algorithm for solving dipolar GPE as

$$\tilde{U}_{\text{dd}}(\mathbf{k}) = \frac{4\pi}{3} \left(\frac{3k_z^2}{\mathbf{k}^2} - 1 \right) \left[1 + 3 \frac{\cos(kR)}{k^2 R^2} - 3 \frac{\sin(kR)}{k^3 R^3} \right]. \quad (6.25)$$

The difficulty in using a large space domain is the most severe in 3D algorithms for solving dipolar GPE by the split-step Crank-Nicolson method. The cut-off parameter R of equation (6.25) improves the accuracy of the calculation.

6.3 Calculation of physical quantities

During the evolution of the system, the relevant physical quantities can be calculated using the obtained time-dependent wave function. Since the wave function is obtained with the time resolution of Δt , we can calculate all physical quantities with the same time resolution or choose to calculate them less frequently, to decrease the computation time. Here we list the expectation values calculated by our programs by default.

The size of the system in x , y , and z direction is expressed by the root-mean-square of the corresponding coordinate,

$$x_{\text{rms}} = \sqrt{\langle x^2 \rangle}, \quad \langle x^2 \rangle = \int d\mathbf{r} x^2 |\psi(\mathbf{r})|^2, \quad (6.26)$$

$$y_{\text{rms}} = \sqrt{\langle y^2 \rangle}, \quad \langle y^2 \rangle = \int d\mathbf{r} y^2 |\psi(\mathbf{r})|^2, \quad (6.27)$$

$$z_{\text{rms}} = \sqrt{\langle z^2 \rangle}, \quad \langle z^2 \rangle = \int d\mathbf{r} z^2 |\psi(\mathbf{r})|^2, \quad (6.28)$$

while the size of the whole system is estimated by the quadratic mean,

$$r_{\text{rms}} = \sqrt{\langle x^2 \rangle + \langle y^2 \rangle + \langle z^2 \rangle}. \quad (6.29)$$

For stationary states, the wave function has a trivial time dependence $\psi(\mathbf{r}, t) = \psi(\mathbf{r}) e^{-i\mu t}$, where μ is the chemical potential. If we substitute this into Equation (6.3), and multiply it by $\psi^*(\mathbf{r})$, taking into account that the wave function is normalized to 1, we obtain the following formula for the chemical potential

$$\begin{aligned} \mu = \int d\mathbf{r} \left[\frac{1}{2} |\nabla \psi(\mathbf{r})|^2 + U(\mathbf{r}) |\psi(\mathbf{r})|^2 + 4\pi N a_s |\psi(\mathbf{r})|^4 \right. \\ \left. + 3N a_{\text{dd}} \int d\mathbf{r}' U_{\text{dd}}(\mathbf{r} - \mathbf{r}') |\psi(\mathbf{r}')|^2 |\psi(\mathbf{r})|^2 \right]. \end{aligned} \quad (6.30)$$

The above expression can be also used for non-stationary states, to obtain the expectation values of the Hamiltonian.

The following expression for the energy E is obtained by multiplying the inter-

action terms by 1/2 in equation (6.30)

$$E = \int d\mathbf{r} \left[\frac{1}{2} |\nabla\psi(\mathbf{r})|^2 + U(\mathbf{r}) |\psi(\mathbf{r})|^2 + 2\pi N a_s |\psi(\mathbf{r})|^4 + \frac{3}{2} N a_{\text{dd}} \int d\mathbf{r}' U_{\text{dd}}(\mathbf{r} - \mathbf{r}') |\psi(\mathbf{r}')|^2 |\psi(\mathbf{r})|^2 \right]. \quad (6.31)$$

In a variational approach, the GPE can be obtained by minimizing the above functional with respect to the wave function.

The norm of the wave function is calculated by definition

$$\int d\mathbf{r} |\psi(\mathbf{r})|^2, \quad (6.32)$$

and in the real-time propagation, it should be always equal to 1. The Crank-Nicolson scheme conserves the normalization of the wave function, but its monitoring can be used as an early check of the validity of the simulation. However, this is not the case in imaginary-time propagation, since then the evolution operator is not unitary. Therefore, it is necessary to normalize the wave function again after each time step Δt .

6.4 Numerical integration and derivation

Numerical integration within the algorithm is implemented using Simpson's rule

$$\int dx f(x) \approx \frac{\Delta x}{3} \sum_{i=1}^{N/2} (f_{2i-2} + 4f_{2i-1} + f_{2i}) \quad (6.33)$$

where N is a number of equidistant points and Δx the size of a spatial step.

In order to calculate the energy and the chemical potential we also need spatial derivatives of the wave function. For this we use the Richardson extrapolation formula of the fourth order. For instance, the spatial derivative of the wave function in direction j is approximated with

$$\frac{\partial\psi_i^n}{\partial h_j} \approx \frac{1}{12\Delta h_j} (\psi_{i-2}^n - 8\psi_{i-1}^n + 8\psi_{i+1}^n - \psi_{i+2}^n). \quad (6.34)$$

6.5 Algorithm wrap-up

Practical usage of the programs that implement the algorithm for solving the dipolar GPE requires the preparation of an input file that provides the parameter values of the system of interest. This includes a number of atoms in the condensate, which is typically between 10^4 and 10^6 . One also has to specify a unit of length l in units of Bohr radius ($a_0 = 5.2917721092 \times 10^{-11}$ m). For a chosen reference frequency ω_r it is calculated as $l = \sqrt{\hbar/(m\omega_r)}$ for atoms with mass m , and is typically of the order of μm . Physical parameters of the system also include the s -wave scattering length a_s , which measures the contact interaction strength, and the dipolar length a_{dd} , which measures dipole-dipole interaction strength. Both are expressed in units of Bohr radius within the input file.

In addition of physical parameters, we also have to supply discretization details such as the time step Δt (in units of $1/\omega_r$) and the number of iterations N . Typical values of the time step Δt we used for our simulations was between 10^{-2} and 10^{-3} , which corresponds to $10^{-2} - 10^{-3}$ ms after re-scaling with the frequency $\omega_r = 2\pi \times 160.5$ Hz. Therefore, for the simulation of the evolution for 250 ms, the number of iterations N has to be between 2.5×10^4 and 2.5×10^5 .

The spatial discretization is defined by the size of steps and the number of mesh points in x , y , and z direction. In the simulations, we have used equal numbers of mesh points in all directions, $N_x = N_y = N_z = 500$, with different step sizes, typically $\Delta x = 0.5$ and $\Delta y = \Delta z = 0.1$, due to the cigar shape of the condensate. Such mesh creates a simulation box of the volume of approximately $250 \times 50 \times 50 \mu\text{m}^3$.

Flowchart of the algorithm for solving the dipolar GPE is illustrated in Figure 6.1. Using the parameters specified in the configuration input file, the algorithm in the very first step generates an initial wave function or reads its values from the external file. This is represented by the operator $\hat{\mathcal{I}}$, which will initialize the wave function matrix to be propagated within the main loop of the algorithm. In the case of imaginary-time propagation, most frequently, the initial wave function will

be generated in the form of a predefined Gaussian, or if it is explicitly defined in the input file, it will be populated by the values from the external file. For real-time propagation, the initial wave function is always read from the external file. Usually, it is a wave function obtained from the previous calculation, either in imaginary- or real-time propagation.

Using the initial wave function, the algorithm in N equal time steps Δt propagates the wave function. Each time step consists of four sub-steps, which are implemented using the operators $\hat{\mathcal{P}}(\hat{H}_0)$, $\hat{\mathcal{P}}(\hat{H}_1)$, $\hat{\mathcal{P}}(\hat{H}_2)$, $\hat{\mathcal{P}}(\hat{H}_3)$. After each step, the operator $\hat{\mathcal{M}}$ calculates the relevant physical quantities. In the case of imaginary-time propagation, there is an additional operation in which we normalize the wave function to 1 using the operator $\hat{\mathcal{N}}$. After the main loop is finished, the simulation saves the wave function for further use (operator $\hat{\mathcal{E}}$).

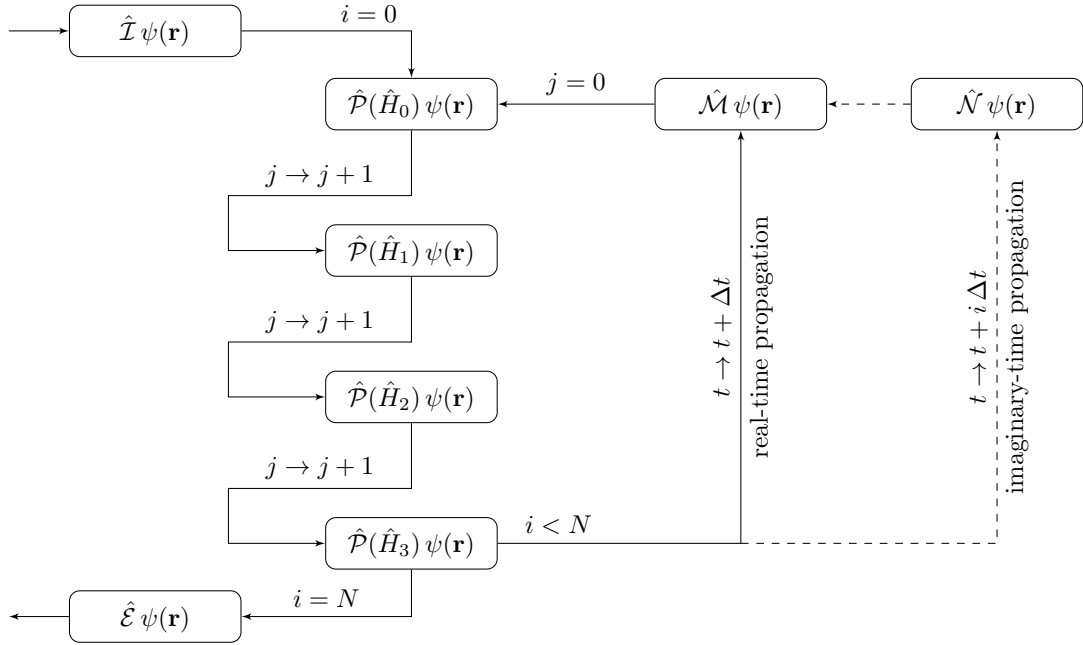


Figure 6.1: Flowchart of the algorithm for solving the dipolar GPE. The operator $\hat{\mathcal{I}}$ is responsible for the initialization of the wave function matrix. Propagation of the wave function is done in four sub-steps using operators $\hat{\mathcal{P}}(\hat{H}_0)$, $\hat{\mathcal{P}}(\hat{H}_1)$, $\hat{\mathcal{P}}(\hat{H}_2)$, $\hat{\mathcal{P}}(\hat{H}_3)$. The operator $\hat{\mathcal{M}}$ calculates physical quantities of the system, and the operator $\hat{\mathcal{E}}$ saves the wave function for further use. In the case of imaginary-time propagation, the operator $\hat{\mathcal{N}}$ normalizes the wave function.

6.6 Parallelization and optimization

The algorithm for solving fully-anisotropic three-dimensional dipolar GPE is developed based on our previous programs [88, 89]. The original program for the contact interaction GPE was written in Fortran [87] by Adhikari and Muruganandam. Later on, we have rewritten this program in the C programming language, and parallelized it using the Open Multi-Processing (OpenMP) library [90–92, 95]. Afterward, we have developed the programs that include both the contact and the dipole-dipole interaction in C and in Fortran [93, 94]. We have demonstrated excellent agreement of recent experimental observation of dipolar BECs of ^{52}Cr , ^{164}Dy , and ^{168}Er atoms with the numerical results. The programs had to be parallelized, which allows the utilization of all available processors/cores on a shared memory computer, leading to the speedup of 70 – 90% of the ideal one.

Figure 6.2 illustrates the speedup (blue down triangles) and the efficiency (red up triangles) in the execution time of the imaginary-time (left panel) and real-time (right panel) propagation as a function of a number of utilized CPU cores. The speedup $S(N_c)$ is calculated as a ratio of the execution time of a simulation on a single CPU core and a simulation using N_c cores. The efficiency $E(N_c) = S(N_c)/N_c$

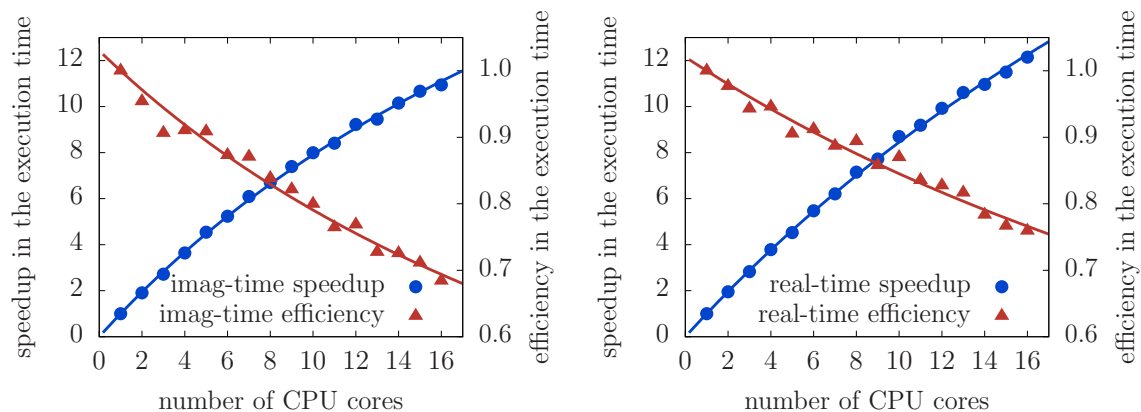


Figure 6.2: Speedup (blue down triangles) and efficiency (red up triangles) of the algorithm for solving the dipolar GPE during imaginary-time (left) and real-time (right) propagation as a function of the number of utilized CPU cores. Solid lines represent fits to measured data according to Amdahl’s law.

is defined as a ratio of the speedup, measured in numerical experiments, and the ideal one which is equal to N_c . In all simulations, we have used a consistent spatial mesh of the size of $500 \times 500 \times 500$. Starting from a single CPU core, we gradually increase the number of utilized cores up to 16 on an Intel Xeon CPU E5-2670 machine with a clock frequency of 2.60 GHz. The programs are compiled and optimized using the Intel compiler.

Based on Amdahl's law [100], the expected execution times of a sequential (which remains constant) and a parallelized region of the code (which scales with a number of cores N_c). If p is parallelized fraction of the code, the expected speedup is given by

$$S(N_c) = \frac{1}{(1-p) + p/N_c}, \quad (6.35)$$

and similarly for $E(N_c)$. Solid lines in Figure 6.2 represent the fits to measured data according to relation (6.35), which allows us to verify the consistency of the performance of our programs and to estimate the parallel fraction p .

Details on the testing of parallelization scaling are given in Appendix F.

7 Conclusions

This thesis explores the Faraday and resonant density waves in ultracold dipolar Bose-Einstein condensates. It also studies the collective oscillation modes of dipolar condensates and their ground-state properties for experimentally relevant atomic species with the permanent magnetic dipole moment: chromium ^{52}Cr , erbium ^{168}Er , and dysprosium ^{164}Dy . The interplay of the contact and the dipole-dipole interaction in such systems is a hot research topic today, but a detailed understanding of their dynamics and even the stability is still lacking. This thesis contributes to variational and numerical description of driven dipolar systems and their properties, which are important for ongoing experiments, and will be of particular interest as the strongly dipolar regime becomes experimentally available.

We have introduced here a variational approach and used it to describe the ground state, the collective oscillation modes, and the Faraday and resonant waves in dipolar BECs. This approach is based on the Gaussian variational ansatz, which includes the condensate widths and the conjugated dynamical phases as parameters. The ansatz is extended to include density modulations in order to capture the dynamics of density waves. Using our approach, we have derived analytical expressions for the ground-state widths of the condensate, and the frequencies of the collective oscillation modes: the breathing, the quadrupole, and the radial-quadrupole mode. These results are verified by comparison with the numerical results obtained by solving the dipolar GPE for each of the three atomic species. We have found very good agreement between the analytical and numerical results, and confirmed that the derived expressions for the ground-state widths and collective oscillation frequencies

can be reliably used in the relevant parameter ranges.

We have studied the effects of the contact and the dipole-dipole interaction on the properties of the ground state and of the collective oscillation modes. While the increase of the contact interaction strength always leads to an increase of condensate widths, the situation is more complex when the dipole-dipole interaction is varied. In a cigar-shaped geometry when the dipoles are oriented in the radial direction, the increase of the DDI strength leads to the increase of condensate widths in the weak-confinement direction and in the direction of the dipoles, while the width in the third direction decreases. We have also studied the frequencies of the collective modes, where the interaction effects turn out to be less pronounced, in particular for the breathing and the quadrupole mode, whose values practically remain constant over the whole range of experimentally relevant values of a_s and a_{dd} . The frequency of the radial-quadrupole mode is more sensitive to changes of interaction strengths, especially the contact interaction strength a_s , and shows a nonmonotonous behavior as a function of the dipole-dipole interaction strength a_{dd} .

The main contribution of the thesis is the study of driven dipolar BECs, where the emergence of density waves is expected. This phenomenon is investigated in an experimentally-inspired setup, where the dipolar condensate is confined into a cigar-shaped harmonic trap. The dipole moments of the atoms are assumed to be orthogonal to the weak confinement axis, since this maximizes the stability of the system. The driving of the system is achieved by harmonic modulation of the radial part of the trap, and the density waves were observed in the longitudinal, weak-confinement direction.

Using our variational approach, the obtained equations for the dynamical evolution of the system are cast into the form of the Mathieu-like differential equation. This allowed us to identify the most unstable solutions of the Mathieu's equation with the Faraday and the resonant waves, which we have observed numerically. Based on this idea, we have derived analytical expressions for the periods of these two types of density waves. Performing the FFT analysis of the results of extensive numerical simulations, we were able to calculate the corresponding periods numer-

ically, as functions of the contact and the dipole-dipole interaction strength. The comparison of variational and numerical results shows very good agreement and demonstrates that the derived analytical expressions provide a full understanding of the properties of density waves in dipolar condensates.

The thesis presents the split-step semi-implicit Crank-Nicolson method used to solve the dipolar GPE, as well as the details about the corresponding programs, including the calculation of the dipole-dipole interaction term and relevant physical quantities. We have also presented the scalability testing results of our parallel programs, which demonstrate their efficiency on parallel computer clusters.

A Fourier transform of the DDI potential

In contrast to the contact interaction, which is symmetric and has a short range, the dipolar interaction between atoms or molecules is anisotropic and has a long range. The dipolar effects are brought in into the GPE through an additional nonlinear interaction term that reads in the dimensionless form

$$3Na_{\text{dd}} \int d\mathbf{r}' U_{\text{dd}}(\mathbf{r} - \mathbf{r}') |\psi(\mathbf{r}')|^2, \quad (\text{A.1})$$

where N is the number of atoms in the condensate, a_{dd} the length that quantifies the strength of the DDI, $|\psi(\mathbf{r}')|^2$ the density of the condensate, and $U_{\text{dd}}(\mathbf{r} - \mathbf{r}')$ the DDI potential. For an arbitrary orientation of the dipoles defined by a unit vector \mathbf{m} , the dipolar potential is given by

$$U_{\text{dd}}(\mathbf{r}) = \frac{\mathbf{r}^2 - 3(\mathbf{r} \cdot \mathbf{m})^2}{r^5}. \quad (\text{A.2})$$

If the dipoles are oriented in z direction, the above expression transforms into

$$U_{\text{dd}}(\mathbf{r}) = \frac{1 - 3\cos^2\theta}{r^3}. \quad (\text{A.3})$$

where θ is the angle between the vector \mathbf{r} and the polarization axis (z direction).

In coordinate space, due to issues with the numerical divergence at short distances, calculation of the dipolar term in the GPE is not straightforward. This is usually resolved by switching to the \mathbf{k} -space, where the calculation does not suffer from a singular behavior. Additionally, this allows the use of the FFT, which speeds up numerical calculations. By means of the convolution theorem, the integral (A.1) transforms into

$$\int d\mathbf{r}' U_{\text{dd}}(\mathbf{r} - \mathbf{r}') |\psi(\mathbf{r}')|^2 = \mathcal{F}^{-1} \{ \mathcal{F}[U_{\text{dd}}](\mathbf{k}) \mathcal{F}[|\psi|^2](\mathbf{k}) \}(\mathbf{r}), \quad (\text{A.4})$$

where \mathcal{F} represents the Fourier transform and \mathcal{F}^{-1} the inverse Fourier transform, defined respectively by

$$\mathcal{F}[f](\mathbf{k}) = \tilde{f}(\mathbf{k}) = \int d\mathbf{r} f(\mathbf{r}) e^{-i\mathbf{k}\cdot\mathbf{r}}, \quad (\text{A.5})$$

$$\mathcal{F}^{-1}[\tilde{f}](\mathbf{r}) = f(\mathbf{r}) = \frac{1}{(2\pi)^3} \int d\mathbf{k} \tilde{f}(\mathbf{k}) e^{i\mathbf{k}\cdot\mathbf{r}}. \quad (\text{A.6})$$

The Fourier transform of the dipolar potential $\tilde{U}_{\text{dd}}(\mathbf{k})$ can be calculated analytically using the spherical coordinates,

$$\begin{aligned} \tilde{U}_{\text{dd}}(\mathbf{k}) &= \int d\mathbf{r} U_{\text{dd}}(\mathbf{r}) e^{-i\mathbf{k}\cdot\mathbf{r}} = \int_0^\infty dr \int_0^{2\pi} d\varphi \int_0^\pi \sin\theta d\theta \\ &\times \frac{1 - 3\cos^2\theta}{r} e^{-ikr(\sin\theta \sin\theta_k \cos(\varphi-\varphi_k) + \cos\theta \cos\theta_k)}, \end{aligned} \quad (\text{A.7})$$

where, in spherical coordinates, $\mathbf{k} = (k, \theta_k, \varphi_k)$. Although the coordinate system is chosen such that the vector \mathbf{m} is oriented along z axis, we still have the freedom to rotate it around this axis, which makes it possible to eliminate the angle φ_k . If we denote the θ_k in the selected coordinate system by α , the integral (A.7) becomes

$$\tilde{U}_{\text{dd}}(\mathbf{k}) = \int_0^\infty dr \int_0^{2\pi} d\varphi \int_0^\pi d\theta \sin\theta \frac{1 - 3(\sin\alpha \sin\theta \sin\varphi + \cos\alpha \cos\theta)^2}{r} e^{-ikr \cos\theta}. \quad (\text{A.8})$$

After integration over the variable φ , we obtain

$$\tilde{U}_{\text{dd}}(\mathbf{k}) = \pi (3\cos^2\alpha - 1) \int_0^\infty dr \int_0^\pi d\theta \sin\theta \frac{1 - 3\cos^2\theta}{r} e^{-ikr \cos\theta}. \quad (\text{A.9})$$

The θ -integral above is solved by a variable change $u = \cos\theta$, yielding

$$\tilde{U}_{\text{dd}}(\mathbf{k}) = 4\pi (1 - 3\cos^2\alpha) \int_0^\infty dr \left[\frac{\sin(kr)}{kr^2} + \frac{3\cos(kr)}{k^2r^3} - \frac{3\sin(kr)}{k^3r^4} \right]. \quad (\text{A.10})$$

This integral is calculated using another variable change $v = kr$,

$$\begin{aligned} \tilde{U}_{\text{dd}}(\mathbf{k}) &= 4\pi (1 - 3\cos^2\alpha) \lim_{b \rightarrow 0} \int_{kb}^\infty dv \left[\frac{\sin v}{v^2} + \frac{3\cos v}{v^3} - \frac{3\sin v}{v^4} \right] \\ &= 4\pi (1 - 3\cos^2\alpha) \lim_{b \rightarrow 0} \frac{kb \cos(kb) - \sin(kb)}{(kb)^3} \\ &= \frac{4\pi}{3} (3\cos^2\alpha - 1) = \frac{4\pi}{3} \left(\frac{3k_z^2}{k^2} - 1 \right). \end{aligned} \quad (\text{A.11})$$

According to this, we can immediately write the general expression for an arbitrary orientation of the dipoles \mathbf{m} in the form

$$\tilde{U}_{\text{dd}}(\mathbf{k}) = \frac{4\pi}{3} \left[\frac{3(\mathbf{m} \cdot \mathbf{k})^2}{k^2} - 1 \right]. \quad (\text{A.12})$$

B Lagrangian of the DDI term

Using the Lagrangian density (2.51), we calculate the Lagrangian term (2.64) that corresponds to the DDI energy for the Gaussian ansatz (2.52), used in the variational study of the collective oscillation modes, as well as the term (5.11) for the modified ansatz (5.2), used to describe the Faraday and resonant waves. Note that both expressions can be written in the form

$$L_5(t) = -\frac{3Na_{\text{dd}}}{(2\pi)^2} B^2 \int d\mathbf{k} \left(3 \frac{k_z^2}{k_x^2 + k_y^2 + k_z^2} - 1 \right) e^{-\frac{1}{2}(k_x^2 u_x^2 + k_y^2 u_y^2 + k_z^2 u_z^2)}, \quad (\text{B.1})$$

where expression (2.64) is obtained for $B = 1$, while we get expression (5.11) for

$$B^2 = 1 - \frac{8\alpha^2}{(2 + \alpha^2 + \beta^2)^2}. \quad (\text{B.2})$$

The above integral describes the anisotropic character of the dipole-dipole interaction in ultracold quantum gases. After switching to the spherical coordinate system via the following change of variables

$$k_x u_x = k \sin \theta \cos \varphi, \quad k_y u_y = k \sin \theta \sin \varphi, \quad k_z u_z = k \cos \theta, \quad (\text{B.3})$$

the above integral transforms into

$$L_5(t) = -\frac{Na_{\text{dd}}}{(2\pi)^2 u_x u_y u_z} B^2 \int_0^\infty dk k^2 e^{-k^2/2} \int_0^{2\pi} d\varphi \int_0^\pi d\theta \sin \theta \times \left(\frac{3 \frac{1}{u_z^2} \cos^2 \theta}{\frac{1}{u_x^2} \sin^2 \theta \cos^2 \varphi + \frac{1}{u_y^2} \sin^2 \theta \sin^2 \varphi + \frac{1}{u_z^2} \cos^2 \theta} - 1 \right). \quad (\text{B.4})$$

The integral over k is of the Gaussian type that can be solved analytically, leading to

$$L_5(t) = -\frac{Na_{\text{dd}}}{(2\pi)^2 u_x u_y u_z} B^2 \sqrt{\frac{\pi}{2}} \int_0^{2\pi} d\varphi \int_0^\pi d\theta \sin \theta \times \left(\frac{3 \frac{u_x^2 u_y^2}{u_z^4} \cos^2 \theta}{\frac{u_y^2}{u_z^2} \sin^2 \theta \cos^2 \varphi + \frac{u_x^2}{u_z^2} \sin^2 \theta \sin^2 \varphi + \frac{u_x^2 u_y^2}{u_z^4} \cos^2 \theta} - 1 \right). \quad (\text{B.5})$$

If we introduce the dipolar anisotropy function [42], see Appendix C for details,

$$f(x, y) = -\frac{1}{4\pi} \int_0^{2\pi} d\varphi \int_0^\pi d\theta \sin \theta \left(\frac{3x^2 y^2 \cos^2 \theta}{x^2 \sin^2 \varphi \sin^2 \theta + y^2 \cos^2 \varphi \sin^2 \theta + x^2 y^2 \cos^2 \theta} - 1 \right), \quad (\text{B.6})$$

we can write $L_5(t)$ as

$$L_5(t) = \frac{Na_{\text{dd}}}{\sqrt{2\pi} u_x u_y u_z} B^2 f\left(\frac{u_x}{u_z}, \frac{u_y}{u_z}\right), \quad (\text{B.7})$$

where exact expressions for the anisotropy function in terms of the elliptic integrals of the first (F) and the second (E) kind for different values of its arguments are listed in Appendix C. For our analysis, due to geometry of the system described in Appendix D, the most relevant region of parameters is $0 < u_y/u_z < 1 < u_x/u_z$, in which the anisotropy function can be written as

$$f(x, y) = \frac{1 + 2y^2}{1 - y^2} - \frac{3xy\sqrt{x^2 - y^2} E(\theta, k)}{(x^2 - 1)(1 - y^2)} + \frac{3xy F(\theta, k)}{(x^2 - 1)\sqrt{x^2 - y^2}}, \quad (\text{B.8})$$

where $k = \sqrt{(x^2 - 1)/(x^2 - y^2)}$, and $\sin \theta = \sqrt{x^2 - y^2}/x$.

C Anisotropy function

In theoretical studies of dipolar ultracold atomic or molecular systems, the anisotropy function emerges as a consequence of the anisotropic character of the dipole-dipole interaction [42]. It is defined as

$$\begin{aligned} f(x, y) &= -\frac{1}{4\pi} \int_0^{2\pi} d\varphi \int_0^\pi d\theta \sin \theta \left(\frac{3x^2y^2 \cos^2 \theta}{x^2 \sin^2 \varphi \sin^2 \theta + y^2 \cos^2 \varphi \sin^2 \theta + x^2y^2 \cos^2 \theta} - 1 \right) \\ &= 1 - \frac{3x^2y^2}{4\pi} \int_0^\pi d\theta \sin \theta \cos^2 \theta \int_0^\pi d\varphi \frac{1}{(x^2 \sin^2 \varphi + y^2 \cos^2 \varphi) \sin^2 \theta + x^2y^2 \cos^2 \theta}. \end{aligned} \quad (\text{C.1})$$

According to the above definition, we can assume $x, y \geq 0$ without loss of generality. The φ integral can be solved using relation (3.642.1) from Reference [43], yielding

$$f(x, y) = 1 - \frac{3xy}{2} \int_0^\pi d\theta \sin \theta \frac{\cos^2 \theta}{\sqrt{1 - (1 - x^2) \cos^2 \theta} \sqrt{1 - (1 - y^2) \cos^2 \theta}}. \quad (\text{C.2})$$

Note that function f is symmetric in its arguments $f(x, y) = f(y, x)$ [42]. Depending on the values of the arguments x and y , we can consider the following cases:

1. $x < y < 1$

Using the substitution $u = \sqrt{1 - x^2} \cos \theta$, the integral (C.2) becomes

$$f(x, y) = 1 + \frac{3xy}{(1 - x^2)^{3/2}} \int_0^{\sqrt{1-x^2}} du \frac{u^2}{\sqrt{1 - k^2 u^2} \sqrt{1 - u^2}}, \quad (\text{C.3})$$

where $k^2 = (1 - y^2)/(1 - x^2) < 1$. The solution of the above u -integral can be expressed via elliptic integrals [43] of the first and the second kind, respectively,

$$F(\theta, k) = \int_0^{\sin \theta} du \frac{1}{\sqrt{(1 - u^2)(1 - k^2 u^2)}} = \int_0^\theta d\theta \frac{1}{\sqrt{1 - k^2 \sin^2 \theta}}, \quad (\text{C.4})$$

$$E(\theta, k) = \int_0^{\sin \theta} du \frac{\sqrt{1 - k^2 u^2}}{\sqrt{1 - u^2}} = \int_0^\theta d\theta \sqrt{1 - k^2 \sin^2 \theta}, \quad (\text{C.5})$$

yielding

$$f(x, y) = 1 + 3xy \frac{E(\theta, k) - F(\theta, k)}{(1 - y^2)\sqrt{1 - x^2}}, \quad (\text{C.6})$$

where $\sin \theta = \sqrt{1 - x^2}$.

2. $y < x < 1$

Due to the symmetry of the anisotropy function, its value $f(x, y)$ can be calculated as $f(y, x)$ according to case 1.

3. $x < 1 < y$

In this region it is necessary to analytically continue the function (C.6) using the table (8.127) from Reference [43]. With the transformations

$$k_1 = \frac{ik}{k'}, \quad \sin \theta_1 = \frac{k' \sin \theta}{\Delta \theta}, \quad \cos \theta_1 = \frac{\cos \theta}{\Delta \theta}, \quad (\text{C.7})$$

we obtain

$$f(x, y) = \frac{1 + 2x^2}{1 - x^2} + \frac{3xy\sqrt{y^2 - x^2} E(\theta_1, k_1)}{(y^2 - 1)(x^2 - 1)} + \frac{3xy F(\theta_1, k_1)}{(y^2 - 1)\sqrt{y^2 - x^2}}, \quad (\text{C.8})$$

where $k_1 = \sqrt{\frac{y^2 - 1}{y^2 - x^2}}$ and $\sin \theta_1 = \sqrt{y^2 - x^2}/y$.

4. $y < 1 < x$

Due to the symmetry of the anisotropy function, its value $f(x, y)$ can be calculated as $f(y, x)$ according to case 3.

5. $1 < x < y$

In this region we proceed similarly as in the case 3, using the transformations

$$k_1 = \frac{k'}{ik}, \quad \sin \theta_1 = -\frac{ik \sin \theta}{\Delta \theta}, \quad \cos \theta_1 = \frac{1}{\Delta \theta}, \quad (\text{C.9})$$

where $k' = \sqrt{1 - k^2}$ and $\Delta \theta = \sqrt{1 - k^2 \sin^2 \theta}$, and obtain

$$f(x, y) = \frac{1 + 2x^2}{1 - x^2} + \frac{3xy E(\theta_1, k_1)}{(x^2 - 1)\sqrt{y^2 - 1}}, \quad (\text{C.10})$$

where $k_1 = \sqrt{\frac{y^2 - x^2}{y^2 - 1}}$ and $\sin \theta_1 = \sqrt{y^2 - 1}/y$.

6. $1 < y < x$

Due to the symmetry of the anisotropy function, its value $f(x, y)$ can be calculated as $f(y, x)$ according to case 5.

7. $x = y$

In the special case of equal arguments, $x \rightarrow y$, which corresponds to cylindrical symmetry of the system, the anisotropy function depends only on a single argument, and is given as

$$f_s(x) = \lim_{x \rightarrow y} f(x, y) = \frac{1 + 2x^2 - 3x^2 d(x)}{1 - x^2}, \quad (\text{C.11})$$

where $d(x)$ is given by

$$d(x) = \begin{cases} \frac{1}{\sqrt{1-x^2}} \tanh^{-1} \sqrt{1-x^2}, & x < 1, \\ 0, & x = 1, \\ \frac{1}{\sqrt{x^2-1}} \tan^{-1} \sqrt{x^2-1}, & 1 < x. \end{cases} \quad (\text{C.12})$$

8. $x \neq y = 1$

$$f(x, 1) = \lim_{y \rightarrow 1} f(x, y) = -\frac{1}{2} f_s(1/x) \quad (\text{C.13})$$

9. $x = 1 \neq y$

$$f(1, y) = f(y, 1) = -\frac{1}{2} f_s(1/y) \quad (\text{C.14})$$

In this thesis, the parameters of the anisotropy function are ratios of the condensate widths u_x/u_z and u_y/u_z . As we have seen in Chapter 3, due to geometry of the system, the condensate in the ground state is much more elongated in x direction than in the other two directions. Also, we have observed that the dipole-dipole interaction increases the condensate width in z direction, and decreases it in y direction. The same relationships between the condensate widths are valid during the non-stationary dynamics of the condensate, as we have seen in Chapters 4 and 5. Therefore, in our analysis $0 < u_y < u_z < u_x$, i.e., $0 < u_y/u_z < 1 < u_x/u_z$, which corresponds to the case 4 above.

In the thesis we use $f_i(x, y)$ to denote the first partial derivative of the anisotropy function with respect to its argument $i = 1, 2$, and f_{ij} to denote the second partial derivative

$$f_{ij}(x_1, x_2) = \frac{\partial^2}{\partial x_i \partial x_j} f(x_1, x_2). \quad (\text{C.15})$$

In our analysis of the cylindrically symmetric ultracold quantum gases, which exists if the polarization direction matches the weak confinement direction of the trap, we have used the following useful limits:

$$\lim_{y \rightarrow x} x f_1(x, y) = \lim_{y \rightarrow x} y f_2(x, y) = f'_s(x) = \frac{(2 + x^2)f_s(x)}{2(1 - x^2)} - 1, \quad (\text{C.16})$$

$$\lim_{y \rightarrow x} f_{11}(x, y) = \lim_{y \rightarrow x} f_{22}(x, y) = \frac{9[(4 + x^2)f_s(x) - 2(1 - x^2)]}{8(1 - x^2)^2}, \quad (\text{C.17})$$

$$\lim_{y \rightarrow x} f_{12}(x, y) = \lim_{y \rightarrow x} f_{21}(x, y) = \frac{(8 + 8x^2 - x^4)f_s(x) - 2(4 - 5x^2 + x^4)}{8x^2(1 - x^2)^2}, \quad (\text{C.18})$$

$$\lim_{y \rightarrow 1} x f_1(x, y) = f'_s(1/x). \quad (\text{C.19})$$

D Parameters of the system

In all numerical simulations and variational calculations we have used the system and discretization parameters specified here, unless otherwise stated. We have considered three atomic species and Table 4 lists the corresponding values of the mass m in atomic mass units u , the s -wave scattering length a_s in units of Bohr radius a_0 , the dipole moment μ_d in units of Bohr magneton μ_B , the dipole-dipole interaction strength a_{dd} in units of Bohr radius (a_0), and the harmonic oscillator length l with respect to the chosen referent frequency $\omega_r = 160.5 \times 2\pi$ Hz.

Table 4: Summary of atomic species parameters used in numerical simulations and variational calculations.

Species	m (u)	a_s (a_0)	μ_d (μ_B)	a_{dd} (a_0)	l (μm)
^{52}Cr	51.94050	105	6	15.126	1.10112
^{168}Er	167.93237	100	7	66.564	0.61238
^{164}Dy	163.92918	100	10	132.607	0.61981

All simulations and calculations are performed with the same number of atoms, $N = 10^4$.

We have considered the harmonically trapped system, with the frequencies taken from Reference [30], i.e., $\omega_x = 7 \times 2\pi$ Hz, $\omega_y = 160.5 \times 2\pi$ Hz, and $\omega_z = 160.5 \times 2\pi$ Hz. The trapping potential is defined by Equation (2.22), and for the chosen frequencies the atoms are weakly confined in x direction, i.e., we have used a cigar-shaped trap. Therefore, we refer to x direction as the longitudinal one, while y and z direction represent the radial ones. In order to cast the underlying equations into a dimensionless form, we have chosen the referent frequency $\omega_r = \omega_y = \omega_z = 160.5 \times 2\pi$ Hz, which defines the length scale through the harmonic oscillator length $l = \sqrt{\hbar/(m\omega_r)}$, the time scale as $1/\omega_r$, the energy scale as $\hbar\omega_r$. The trapping frequencies are also expressed in units of ω_r through the trap aspect ratios $\gamma = \omega_x/\omega_r = 0.04361$, $\nu = \omega_y/\omega_r = 1$, and $\lambda = \omega_z/\omega_r = 1$.

We assume that the dipoles are oriented along z direction, i.e., orthogonal to the weakly confined x direction. The Fourier transform of the dipolar interaction potential is thus

$$\mathcal{F}[U_{\text{dd}}(\mathbf{r})](\mathbf{k}) = \frac{4\pi}{3} \left(\frac{3k_z^2}{\mathbf{k}^2} - 1 \right). \quad (\text{D.1})$$

The system is driven by a harmonic modulation of the frequencies in the tightly confined y and z direction,

$$\omega_y(t) = \omega_z(t) = \Omega_0(1 + \epsilon \sin \omega_m t), \quad (\text{D.2})$$

where $\Omega_0 = \omega_y = \omega_z$ has a value given above, $\epsilon = 0.1 - 0.2$ is the modulation amplitude, and ω_m is the modulation frequency. The modulation frequency is expressed in units of ω_r through the aspect ratio $\eta_m = \omega_m/\omega_r$.

We have studied the properties of the ground state, collective oscillation modes, Faraday and resonant waves as functions of the contact and the dipole-dipole interaction strength. This models BEC experiments, where the strength of the contact interaction can be varied over a broad range of values using the Feshbach resonance technique [9]. This is also possible for the strength of the DDI, which can be tuned using a fast rotating magnetic field [24, 25]. Therefore, the values of a_s and a_{dd} listed in Table 4 are used whenever we refer to their fixed values, while in some calculations we have considered experimentally relevant ranges of these interaction strengths.

In numerical simulations, we have discretized space and time by defining the corresponding spacings and the time step, as well as the size of the space mesh and the number of the time steps. In our simulations we have used equal numbers of mesh points in all directions, $N_x = N_y = N_z = 500$, with different spacings, $\Delta x = 0.5$ and $\Delta y = \Delta z = 0.1$. This choice was made due to the cigar shape of the condensate. Such a mesh corresponds to the simulation box of the volume of approximately $250 \times 50 \times 50 \mu\text{m}^3$, which is appropriate for the above trapping potential and the considered atomic species.

Time was discretized using the time step Δt with the typical values between

10^{-2} and 10^{-3} in units of $1/\omega_r$. For the Faraday and resonant waves, the number of time steps (iterations) N was in the range $1 - 2 \times 10^5$, which corresponds to the simulation of the evolution in the range 250-500 ms. For the calculation of the collective oscillation modes, we had to use much larger iteration numbers, for at least one order of magnitude, in order to achieve the accuracy of 0.1 Hz.

The value of the cutoff parameter R from Equation (6.25) in all simulations was $R = 10$.

The ground state of the condensate was calculated using the imaginary-time propagation starting from the Gaussian initial wave function, defined by

$$\psi(x, y, z) = \frac{(\gamma \nu \lambda)^{1/4}}{\pi^{3/4}} e^{-\frac{1}{2}(\gamma x^2 + \nu y^2 + \lambda z^2)}. \quad (\text{D.3})$$

It corresponds to the solution of the Schrödinger equation, i.e., the GPE for $a_s = a_{\text{dd}} = 0$, and represents the dimensionless form of Equation (3.1).

The values of the physical constants used are as follows:

$$u = 1.6605390 \times 10^{-27} \text{ kg (atomic mass unit),}$$

$$a_0 = 5.29177210 \times 10^{-11} \text{ m (Bohr radius),}$$

$$\mu_B = 9.2740099 \times 10^{-24} \text{ JT}^{-1} \text{ (Bohr magneton).}$$

E Semi-implicit Crank–Nicolson scheme

Here we describe the practical implementation of the semi-implicit Crank–Nicolson algorithm [35–37]. In Chapter 6 we have introduced the time and the spatial discretization used to solve the dipolar GPE. The total evolution time T that will be simulated is discretized by dividing it into N_t equal sub-steps of the duration $\Delta t = T/N_t$. The spatial coordinates are discretized by introducing a spatial mesh of N_x , N_y , and N_z equidistant points in x , y , and z direction, respectively. The spatial extents of the system considered are given by $L_x = N_x \Delta x$, $L_y = N_y \Delta y$, and $L_z = N_z \Delta z$, where Δx , Δy , and Δz are discretization steps in the corresponding directions. For practical reasons, the center of the coordinate system coincides with the simulation box center, such that the coordinates take the values $x \in [-L_x/2, L_x/2]$, $y \in [-L_y/2, L_y/2]$, and $z \in [-L_z/2, L_z/2]$.

In addition to this, within each time step Δt , the split-step nature of the algorithm divides our Hamiltonian into four parts: the non-derivative part \hat{H}_0 , and the three parts that contain spatial derivatives, \hat{H}_1 , \hat{H}_2 , \hat{H}_3 , which read

$$\hat{H}_0 = U(\mathbf{r}, t) + 4\pi N a_s |\psi(\mathbf{r}, t)|^2 + 3N a_{\text{dd}} \int d\mathbf{r}' U_{\text{dd}}(\mathbf{r} - \mathbf{r}') |\psi(\mathbf{r}', t)|^2, \quad (\text{E.1})$$

$$\hat{H}_1 = \frac{\partial^2}{\partial x^2}, \quad \hat{H}_2 = \frac{\partial^2}{\partial y^2}, \quad \hat{H}_3 = \frac{\partial^2}{\partial z^2}. \quad (\text{E.2})$$

By doing this, we have approximated our single dipolar GPE with the four sequential partial differential equations,

$$i \frac{\partial \psi(\mathbf{r}, t)}{\partial t} = \hat{H}_0 \psi(\mathbf{r}, t), \quad (\text{E.3})$$

$$i \frac{\partial \psi(\mathbf{r}, t)}{\partial t} = \hat{H}_1 \psi(\mathbf{r}, t), \quad i \frac{\partial \psi(\mathbf{r}, t)}{\partial t} = \hat{H}_2 \psi(\mathbf{r}, t), \quad i \frac{\partial \psi(\mathbf{r}, t)}{\partial t} = \hat{H}_3 \psi(\mathbf{r}, t), \quad (\text{E.4})$$

which are solved one after the other in the algorithm.

In a given time step n , we start with the wave function $\psi^n(\mathbf{r})$, obtained in the previous time step. We point out that the time dependence of the wave function is now denoted by the superscript n , which corresponds to the time $t = n \Delta t$. The time propagation proceeds by solving Equation (E.3), which can be done explicitly

according to (6.9). This produces the intermediate solution $\psi^{n+1/4}(\mathbf{r})$, ready to be propagated in time by solving Equations (E.4). This is done by expressing the corresponding derivative operators in a semi-implicit form,

$$i \frac{\psi^{n+2/4}(\mathbf{r}) - \psi^{n+1/4}(\mathbf{r})}{\Delta t} = \frac{1}{2} \hat{H}_1 [\psi^{n+2/4}(\mathbf{r}) + \psi^{n+1/4}(\mathbf{r})] , \quad (\text{E.5})$$

$$i \frac{\psi^{n+3/4}(\mathbf{r}) - \psi^{n+2/4}(\mathbf{r})}{\Delta t} = \frac{1}{2} \hat{H}_2 [\psi^{n+3/4}(\mathbf{r}) + \psi^{n+2/4}(\mathbf{r})] , \quad (\text{E.6})$$

$$i \frac{\psi^{n+1}(\mathbf{r}) - \psi^{n+3/4}(\mathbf{r})}{\Delta t} = \frac{1}{2} \hat{H}_3 [\psi^{n+1}(\mathbf{r}) + \psi^{n+3/4}(\mathbf{r})] . \quad (\text{E.7})$$

The complete propagation procedure outlined above yields the wave function $\psi^{n+1}(\mathbf{r})$ at the moment $t = (n+1)\Delta t$. On the left-hand sides of Equations (E.5) - (E.7) the partial derivative with respect to time is expressed by a two-point formula, while on the right-hand sides instead of the wave function at the current time, we use a linear combination of the current and the future wave function values to improve the stability of the algorithm. This makes the algorithm semi-implicit.

For convenience, let us denote the spatial mesh step in the x , y , and z direction by Δh_i , respectively, and use the lower index of the wave function to define a position in the mesh in the given direction. For instance, when we are considering Equation (E.5) along x direction, $\psi_i^{n+j/4}$ denotes the wave function value at $x = -L_x/2 + i \Delta h_1$, while the values of the other two coordinates are implicitly assumed. In this notation, with the three-point formula for the Laplacian on the right-hand side of Equations (E.5) - (E.7), the equation in the given direction j reads

$$i \frac{\psi_i^{n+(j+1)/4} - \psi_i^{n+j/4}}{\Delta t} = \frac{1}{4 \Delta h_j^2} \left(\psi_{i+1}^{n+(j+1)/4} - 2 \psi_i^{n+(j+1)/4} + \psi_{i-1}^{n+(j+1)/4} + \psi_{i+1}^{n+j/4} - 2 \psi_i^{n+j/4} + \psi_{i-1}^{n+j/4} \right) , \quad (\text{E.8})$$

where $j = 1, 2, 3$ defines the spatial direction of propagation. In the above equation, the known quantities have the upper index $n + j/4$, while the unknown quantities have the superscript $n + (j + 1)/4$. Taking this into account, Equation (E.8) can be written in the form of a series of tridiagonal equations,

$$A_j^- \psi_{i-1}^{n+(j+1)/4} + A_j^0 \psi_i^{n+(j+1)/4} + A_j^+ \psi_{i+1}^{n+(j+1)/4} = B_i^{n+j/4} , \quad (\text{E.9})$$

where the following coefficients are defined by the known quantities,

$$A_j^- = A_j^+ = -\frac{\Delta t}{4\Delta h_j^2}, \quad A_j^0 = 1 + i\frac{\Delta t}{2\Delta h_j^2}, \quad (\text{E.10})$$

$$B_i^{n+j/4} = i\frac{\Delta t}{4\Delta h_j^2} \left(\psi_{i+1}^{n+j/4} - 2\psi_i^{n+j/4} + \psi_{i-1}^{n+j/4} \right) + \psi_i^{n+j/4}. \quad (\text{E.11})$$

Equation (E.9) is solved by using the forward recursion method, i.e., by expressing the mesh values of the propagated wave function in each spatial direction in the form

$$\psi_{i+1}^{n+(j+1)/4} = \alpha_i^j \psi_i^{n+(j+1)/4} + \beta_i^{n+j/4}. \quad (\text{E.12})$$

Inserting the above rule into Equation (E.9), the propagated mesh values of the wave function are given by

$$\psi_i^{n+(j+1)/4} = \gamma_i^j \left(A_j^- \psi_{i-1}^{n+(j+1)/4} + A_j^+ \beta_i^{n+j/4} - B_i^{n+j/4} \right), \quad (\text{E.13})$$

with

$$\gamma_i^j = -\frac{1}{A_j^0 + A_j^+ \alpha_i^j}. \quad (\text{E.14})$$

We now obtain the backward recursion relations for the coefficients α_i^j and $\beta_i^{n+j/4}$ from Equations (E.12) and (E.13),

$$\alpha_{i-1}^j = \gamma_i^j A_j^-, \quad (\text{E.15})$$

$$\beta_{i-1}^{n+j/4} = \gamma_i^j \left(A_j^+ \beta_i^{n+j/4} - B_i^{n+j/4} \right). \quad (\text{E.16})$$

In the algorithm, the coefficients $\alpha_i^{j/4}$ and $\beta_i^{n+j/4}$ are calculated starting from $i = N_j - 2$ to $i = 0$. Since the value of the wave function must vanish at the mesh boundary, we chose the initial border values of $\alpha_{N_j-1}^{j/4}$ and $\beta_{N_j-1}^{n+j/4}$ to be equal to 0. The coefficients A_j^- , A_j^+ , A_j^0 , α_i^j , and γ_i^j do not depend on the time step n , and are therefore constant for a particular mesh setup. Only the coefficients $\beta_i^{n+j/4}$, and consequentially $B_i^{n+j/4}$, have to be recalculated after each time step, for each spatial direction $j = 1, 2, 3$.

F Details on testing of the scaling of programs

Here we give the details related to the testing setup used in Chapter 6. The code that implements the algorithm for solving the dipolar GPE is optimized for use with the commercially-licensed Intel and the free, open-source GNU compiler suite. We have also tested and verified the compilation with IBM's xlc compiler, PGI's pgcc compiler, and Oracle's suncc (former Sun's) compiler. Beside of the most generic, fully-anisotropic three-dimensional trap, we have written additional independent codes for 1D and 2D systems, for 3D system with cylindrical (effectively 2D) and spherical (effectively 1D) symmetry, and 2D systems with cylindrical symmetry (effectively 1D). All outputs from the simulations are stored using the Hierarchical Data Format (HDF) library [101], which is designed to store and organize large amounts of data. Using HDF, the average size of the results of a typical simulation is around 2 GB of storage space. This includes the wave function calculated in the imaginary-time simulation and all results of the real-time propagation. Compared to the same amount of information stored in a plain text format, HDF provides compression by an average factor of ten. Also, since HDF is a widely used format, various externally developed visualization tools can be used for the analysis of the obtained results.

In addition to the OpenMP-parallelized version of the code [90–92], our group has parallelized the algorithm using the Message Passing Interface (MPI) library [92] that enables utilization of distributed memory computing systems (computer clusters). Furthermore, using the CUDA toolkit, the group has developed algorithms optimized for the graphics processing units (GPU) able to utilize hardware accelerators [93]. Finally, combining all parallelization techniques (OpenMP, MPI, and CUDA), hybrid programs for solving the dipolar GPE were also developed and made publicly available [94]. These programs are able to utilize state-of-the-art computing clusters available today.

The PARADOX computing cluster at the Scientific Computing Laboratory, Cen-

ter for the Study of Complex Systems of the Institute of Physics Belgrade has been used for development and testing of the programs. This resource has more than 2,500 Intel Xeon E5-2670 Sandy Bridge processing cores at a frequency of 2.6 GHz and 32 GB of RAM (2 GB per CPU core). Additional 106 NVIDIA Tesla M2090 graphic cards with 6 GB of RAM are distributed over available computing nodes. The cluster nodes are interconnected via a QDR Infiniband technology, through a non-blocking 144-port Mellanox QDR Infiniband switch. The communication speed of all nodes is 40 Gbps in both directions, while the peak computing power of PARADOX is 105 TFlops. The cluster provides around 100 TB of storage space, which is distributed via a Lustre high-performance parallel file system that uses Infiniband technology.

References

- [1] C. C. Bradley, C. A. Sackett, J. J. Tollett, and R. G. Hulet, *Evidence of Bose-Einstein Condensation in an Atomic Gas with Attractive Interactions*, [Phys. Rev. Lett. **75**, 1687 \(1995\)](#).
- [2] M. H. Anderson, J. R. Ensher, M. R. Matthews, C. E. Wieman, and E. A. Cornell, *Observation of Bose-Einstein condensation in a dilute atomic vapor*, [Science **269**, 198 \(1995\)](#).
- [3] K. B. Davis, M. O. Mewes, M. R. Andrews, N. J. van Druten, D. S. Durfee, D. M. Kurn, and W. Ketterle, *Bose-Einstein condensation in a gas of sodium atoms*, [Phys. Rev. Lett. **75**, 3969 \(1995\)](#).
- [4] S. N. Bose, *Plancks gesetz und lichtquantenhypothese*, [Z. Phys. **26**, 178 \(1924\)](#).
- [5] A. Einstein, *Quantentheorie des einatomigen idealen Gases*, [Sitzungsber. Preuss. Akad. Wiss., Phys. Math. Kl. **22**, 261 \(1924\)](#).
- [6] R. P. Feynman, *Simulating physics with computers*, [Int. J. Theor. Phys. **21**, 467 \(1982\)](#).
- [7] C. J. Pethick and H. Smith, *Bose-Einstein condensation in dilute gases*, [Cambridge University Press \(2008\)](#).
- [8] L. P. Pitaevskii and S. Stringari, *Bose-Einstein condensation*, Oxford University Press (2003).
- [9] S. Inouye, M. R. Andrews, J. Stenger, H. J. Miesner, D. M. Stamper-Kurn, and W. Ketterle, *Observation of Feshbach resonances in a Bose-Einstein condensate*, [Nature **392**, 32354 \(1998\)](#).
- [10] T. Lahaye, T. Koch, B. Fröhlich, M. Fattori, J. Metz, A. Griesmaier, S. Giovanazzi, and T. Pfau, *Strong dipolar effects in a quantum ferrofluid*, [Nature **448**, 672 \(2007\)](#).

- [11] M. Lu, N. Q. Burdick, S. H. Youn, and B. L. Lev, *Strongly dipolar Bose-Einstein condensate of dysprosium*, [Phys. Rev. Lett. **107**, 190401 \(2011\)](#).
- [12] K. Aikawa, A. Frisch, M. Mark, S. Baier, A. Rietzler, R. Grimm, and F. Ferlaino, *Bose-Einstein condensation of erbium*, [Phys. Rev. Lett. **108**, 210401 \(2012\)](#).
- [13] M. H. G. de Miranda, A. Chotia, B. Neyenhuis, D. Wang, G. Quemener, S. Ospelkaus, J. L. Bohn, J. Ye, and D. S. Jin, *Controlling the quantum stereodynamics of ultracold bimolecular reactions*, [Nat. Phys. **7**, 502 \(2011\)](#).
- [14] A. Frisch, M. Mark, K. Aikawa, S. Baier, R. Grimm, A. Petrov, S. Kotochigova, G. Quemener, M. Lepers, O. Dulieu, and F. Ferlaino, *Ultracold dipolar molecules composed of strongly magnetic atoms*, [Phys. Rev. Lett. **115**, 203201 \(2015\)](#).
- [15] M. A. Baranov, *Theoretical progress in many-body physics with ultracold dipolar gases*, [Phys. Rep. **464**, 71 \(2008\)](#).
- [16] N. G. Parker, C. Ticknor, A. M. Martin, and D. H. J. O'Dell, *Structure formation during the collapse of a dipolar atomic Bose-Einstein condensate*, [Phys. Rev. A **79**, 013617 \(2009\)](#).
- [17] R. M. Wilson, S. Ronen, and J. L. Bohn, *Angular collapse of dipolar Bose-Einstein condensates*, [Phys. Rev. A **80**, 023614 \(2009\)](#).
- [18] A. Junginger, J. Main, G. Wunner, and T. Bartsch, *Symmetry-breaking thermally induced collapse of dipolar Bose-Einstein condensates*, [Phys. Rev. A **86**, 023632 \(2012\)](#).
- [19] H. Kadau, M. Schmitt, M. Wenzel, C. Wink, T. Maier, I. Ferrier-Barbut, and T. Pfau, *Observing the Rosensweig instability of a quantum ferrofluid*, [Nature **530**, 194 \(2016\)](#).
- [20] I. Ferrier-Barbut, H. Kadau, M. Schmitt, M. Wenzel, and T. Pfau, *Observation of quantum droplets in a strongly dipolar Bose gas*, [Phys. Rev. Lett. **116**, 215301 \(2016\)](#).

- [21] L. Chomaz, S. Baier, D. Petter, M. J. Mark, F. Wachtler, L. Santos, and F. Ferlaino, *Quantum-fluctuation-driven crossover from a dilute Bose-Einstein condensate to a macrodroplet in a dipolar quantum fluid*, [Phys. Rev. X **6**, 041039 \(2016\)](#).
- [22] R. E. Rosensweig, *Ferrohydrodynamics*, [Cambridge University Press \(1985\)](#).
- [23] F. Böttcher, J-N. Schmidt, M. Wenzel, J. Hertkorn, M. Guo, T. Langen, and T. Pfau, *Transient Supersolid Properties in an Array of Dipolar Quantum Droplets*, [Phys. Rev. X **9**, 011051 \(2019\)](#).
- [24] S. Giovanazzi, A. Görlitz, and T. Pfau, *Tuning the Dipolar Interaction in Quantum Gases*, [Phys. Rev. Lett. **89**, 130401 \(2002\)](#).
- [25] Y. Tang, W. Kao, K-Y. Li, and B. L. Lev, *Tuning the Dipole-Dipole Interaction in a Quantum Gas with a Rotating Magnetic Field*, [Phys. Rev. Lett. **120**, 230401 \(2018\)](#).
- [26] D. S. Jin, J. R. Ensher, M. R. Matthews, C. E. Wieman, and E. A. Cornell, *Collective excitations of a Bose-Einstein condensate in a dilute gas*, [Phys. Rev. Lett. **77**, 420 \(1996\)](#).
- [27] M. O. Mewes, M. R. Andrews, N. J. van Druten, D. M. Kurn, D. S. Durfee, C. G. Townsend, and W. Ketterle, *Collective excitations of a Bose-Einstein condensate in a magnetic trap*, [Phys. Rev. Lett. **77**, 988 \(1996\)](#).
- [28] M. Faraday, *On a peculiar class of acoustical figures; and on certain forms assumed by groups of particles upon vibrating elastic surfaces*, [Phil. Trans. R. Soc. Lond. **121**, 299 \(1831\)](#).
- [29] K. Staliunas, S. Longhi, and G. J. de Valcárcel, *Faraday patterns in Bose-Einstein condensates*, [Phys. Rev. Lett. **89**, 210406 \(2002\)](#).
- [30] P. Engels, C. Atherton, and M. A. Hofer, *Observation of Faraday waves in a Bose-Einstein condensate*, [Phys. Rev. Lett. **98**, 095301 \(2007\)](#).

- [31] A. Balaž and I. Nicolin, *Faraday waves in binary nonmiscible Bose-Einstein condensates*, [Phys. Rev. A **85**, 023613 \(2012\)](#).
- [32] A. Balaž, R. Paun, A. I. Nicolin, S. Balasubramanian, and R. Ramaswamy, *Faraday waves in collisionally inhomogeneous Bose-Einstein condensates*, [Phys. Rev. A **89**, 023609 \(2014\)](#).
- [33] D. Vudragović and A. Balaž, *Faraday and Resonant Waves in Dipolar Cigar-Shaped Bose-Einstein Condensates*, [Symmetry **11**, 1090 \(2019\)](#).
- [34] L. D. Landau and E. M. Lifshitz, *Quantum Mechanics 3rd Edition*, Pergamon (1977).
- [35] J. Crank and P. Nicolson, *A practical method for numerical evaluation of solutions of partial differential equations of the heat-conduction type*, [P. Adv Comput Math **6**, 207 \(1996\)](#).
- [36] W. Ames, *Numerical Methods for Partial Differential Equations 3rd Edition*, Academic Press (1992).
- [37] R. Dautray and J.-L. Lions, *Mathematical Analysis and Numerical Methods for Science and Technology*, [Springer-Verlag Berlin Heidelberg \(2000\)](#).
- [38] S. Yi and L. You, *Trapped atomic condensates with anisotropic interactions*, [Phys. Rev. A **61**, 041604 \(2000\)](#).
- [39] L. Santos, G. V. Shlyapnikov, P. Zoller, and M. Lewenstein, *Bose-Einstein Condensation in Trapped Dipolar Gases*, [Phys. Rev. Lett. **85**, 1791 \(2000\)](#).
- [40] S. Yi and L. You, *Probing dipolar effects with condensate shape oscillation*, [Phys. Rev. A **66**, 013607 \(2002\)](#).
- [41] S. Yi and L. You, *Calibrating Dipolar Interaction in an Atomic Condensate*, [Phys. Rev. Lett. **92**, 193201 \(2004\)](#).
- [42] S. Giovanazzi, P. Pedri, L. Santos, A. Griesmaier, M. Fattori, T. Koch, J. Stuhler, and T. Pfau, *Expansion dynamics of a dipolar Bose-Einstein condensate*, [Phys. Rev. A **74**, 013621 \(2006\)](#).

- [43] I. S. Gradshteyn and I. M. Ryzhik, *Table of Integrals, Series, and Products 7th Edition*, Academic Press is an imprint of Elsevier (1985).
- [44] D. M. Stamper-Kurn, H.-J. Miesner, S. Inouye, M. R. Andrews, and W. Ketterle, *Collisionless and Hydrodynamic Excitations of a Bose-Einstein Condensate*, *Phys. Rev. Lett.* **81**, 500 (1998).
- [45] S. Stringari, *Collective Excitations of a Trapped Bose-Condensed Gas*, *Phys. Rev. Lett.* **77**, 2360 (1996).
- [46] S. Giovanazzi, L. Santos, and T. Pfau, *Collective oscillations of dipolar Bose-Einstein condensates and accurate comparison between contact and dipolar interactions*, *Phys. Rev. A* **75**, 015604 (2007).
- [47] S. E. Pollack, D. Dries, R. G. Hulet, K. M. F. Magalhães, E. A. L. Henn, E. R. F. Ramos, M. A. Caracanhas, and V. S. Bagnato, *Collective excitation of a Bose-Einstein condensate by modulation of the atomic scattering length*, *Phys. Rev. A* **81**, 053627 (2010).
- [48] H. Abe, T. Ueda, M. Morikawa, Y. Saitoh, R. Nomura, and Y. Okuda, *Faraday instability of superfluid surface*, *Phys. Rev. E* **76**, 046305 (2007).
- [49] A. I. Nicolin, R. Carretero-González, and P. G. Kevrekidis, *Faraday waves in Bose-Einstein condensates*, *Phys. Rev. A* **76**, 063609 (2007).
- [50] A. I. Nicolin and M. C. Raportaru, *Faraday waves in high-density cigar-shaped Bose-Einstein condensates*, *Physica A* **389**, 4663 (2010).
- [51] A. I. Nicolin and M. C. Raportaru, *Faraday waves in one-dimensional Bose-Einstein condensates*, *Proc. Rom. Acad.* **12**, 209 (2011).
- [52] A. I. Nicolin, *Faraday waves in Bose-Einstein condensates subject to anisotropic transverse confinement*, *Rom. Rep. Phys.* **63**, 1329 (2011).
- [53] S. Balasubramanian, R. Ramaswamy, and A. I. Nicolin, *Faraday waves in cigar-shaped Bose-Einstein condensates with radially inhomogeneous scattering lengths*, *Rom. Rep. Phys.* **65**, 820 (2013).

- [54] R. Nath and L. Santos, *Faraday patterns in two-dimensional dipolar Bose-Einstein condensates*, [Phys. Rev. A **81**, 033626 \(2010\)](#).
- [55] K. Łakomy, R. Nath, and L. Santos, *Faraday patterns in coupled one-dimensional dipolar condensates*, [Phys. Rev. A **86**, 023620 \(2012\)](#).
- [56] A. I. Nicolin, *Density waves in dipolar Bose-Einstein condensates*, *Proc. Rom. Acad.* **14**, 35 (2013).
- [57] F. Kh. Abdullaev, M. Ögren, and M. P. Sørensen, *Faraday waves in quasi-one-dimensional superfluid Fermi-Bose mixtures*, [Phys. Rev. A **87**, 023616 \(2013\)](#).
- [58] P. Capuzzi and P. Vignolo, *Faraday waves in elongated superfluid fermionic clouds*, [Phys. Rev. A **78**, 043613 \(2008\)](#).
- [59] R. A. Tang, H. C. Li, and J. K. Xue, *Faraday instability and Faraday patterns in a superfluid Fermi gas*, [J. Phys. B **44**, 115303 \(2011\)](#).
- [60] H. Fu, L. Feng, B. M. Anderson, L. W. Clark, J. Hu, J. W. Andrade, C. Chin, and K. Levin, *Density Waves and Jet Emission Asymmetry in Bose Fireworks*, [Phys. Rev. Lett. **121**, 243001 \(2018\)](#).
- [61] L. Salasnich, N. Manini, F. Bonelli, M. Korbman, and A. Parola, *Self-induced density modulations in the free expansion of Bose-Einstein condensates*, [Phys. Rev. A **75**, 043616 \(2007\)](#).
- [62] A. Imambekov, I. E. Mazets, D. S. Petrov, V. Gritsev, S. Manz, S. Hofferberth, T. Schumm, E. Demler, and J. Schmiedmayer, *Density ripples in expanding low-dimensional gases as a probe of correlations*, [Phys. Rev. A **80**, 033604 \(2009\)](#).
- [63] S. Manz, R. Bücker, T. Betz, Ch. Koller, S. Hofferberth, I. E. Mazets, A. Imambekov, E. Demler, A. Perrin, J. Schmiedmayer, and T. Schumm, *Two-point density correlations of quasicondensates in free expansion*, [Phys. Rev. A **81**, 031610 \(2010\)](#).
- [64] A. I. Nicolin, *Resonant wave formation in Bose-Einstein condensates*, [Phys. Rev. E **84**, 056202 \(2011\)](#).

- [65] P. Capuzzi, M. Gattobigio, and P. Vignolo, *Suppression of Faraday waves in a Bose-Einstein condensate in the presence of an optical lattice*, [Phys. Rev. A **83**, 013603 \(2011\)](#).
- [66] K. Staliunas, *Removal of excitations of Bose-Einstein condensates by space- and time-modulated potentials*, [Phys. Rev. A **84**, 013626 \(2011\)](#).
- [67] C. Gaul, E. Díaz, R. P. A. Lima, F. Domínguez-Adame, and C. A. Müller, *Stability and decay of Bloch oscillations in the presence of time-dependent non-linearity*, [Phys. Rev. A **84**, 053627 \(2011\)](#).
- [68] E. Díaz, A. G. Mena, K. Asakura, and C. Gaul, *Super-Bloch oscillations with modulated interaction*, [Phys. Rev. A **87**, 015601 \(2013\)](#).
- [69] I. Brouzos and P. Schmelcher, *Controlled excitation and resonant acceleration of ultracold few-boson systems by driven interactions in a harmonic trap*, [Phys. Rev. A **85**, 033635 \(2012\)](#).
- [70] F. K. Diakonov, P. A. Kalozoumis, A. I. Karanikas, N. Manifavas, and P. Schmelcher, *Geometric-phase-propagator approach to time-dependent quantum systems*, [Phys. Rev. A **85**, 062110 \(2012\)](#).
- [71] I. Vidanović, A. Balaž, H. Al-Jibbouri, and A. Pelster, *Nonlinear Bose-Einstein-condensate dynamics induced by a harmonic modulation of the s-wave scattering length*, [Phys. Rev. A **84**, 013618 \(2011\)](#).
- [72] H. Al-Jibbouri and A. Pelster, *Breakdown of the Kohn theorem near a Feshbach resonance in a magnetic trap*, [Phys. Rev. A **88**, 033621 \(2013\)](#).
- [73] D. Kobayakov, A. Bezett, E. Lundh, M. Marklund, and V. Bychkov, *Quantum swapping of immiscible Bose-Einstein condensates as an alternative to the Rayleigh-Taylor instability*, [Phys. Rev. A **85**, 013630 \(2012\)](#).
- [74] W. H. Hu, L. Jin, and Z. Song, *Dynamics of one-dimensional tight-binding models with arbitrary time-dependent external homogeneous fields*, [Quantum Inf. Process. **12**, 3569 \(2013\)](#).

- [75] R. R. Sakhel, A. R. Sakhel, and H. B. Ghassib, *Nonequilibrium Dynamics of a Bose-Einstein Condensate Excited by a Red Laser Inside a Power-Law Trap with Hard Walls*, *J. Low Temp. Phys.* **173**, 177 (2013).
- [76] A. Balaž, I. Vidanović, A. Bogojević, A. Belić, and A. Pelster, *Fast converging path integrals for time-dependent potentials: I. Recursive calculation of short-time expansion of the propagator*, *J. Stat. Mech.: Theory Exp.* **2011**, P03004 (2011).
- [77] I. Vidanović, A. Bogojević, A. Balaž, and A. Belić, *Properties of quantum systems via diagonalization of transition amplitudes. II. Systematic improvements of short-time propagation*, *Phys. Rev. E* **80**, 066706 (2009).
- [78] A. Bogojević, I. Vidanović, A. Balaž, and A. Belić, *Fast convergence of path integrals for many-body systems*, *Phys. Lett. A* **372**, 3341 (2008).
- [79] A. Bogojević, A. Balaž, and A. Belić, *Asymptotic properties of path integral ideals*, *Phys. Rev. E* **72**, 036128 (2005).
- [80] J. B. Sudharsan, R. Radha, M. C. Raportaru, A. I. Nicolin, and A. Balaz, *Faraday and resonant waves in binary collisionally-inhomogeneous Bose-Einstein condensates*, *J. Phys. B: At. Mol. Opt.* **49**, 165303 (2016).
- [81] A. I. Nicolin, *Variational treatment of Faraday waves in inhomogeneous Bose-Einstein condensates*, *Physica A* **391**, 1062 (2012).
- [82] N. W. McLachlan, *Theory and Application of Mathieu Functions*, Oxford University Press: New York (1951).
- [83] W. Bao and W. Tang, *Ground-state solution of Bose-Einstein condensate by directly minimizing the energy functional*, *J. Comput. Phys.* **187**, 230 (2003).
- [84] M. L. Chiofalo, S. Succi, and M. P. Tosi, *Ground state of trapped interacting Bose-Einstein condensates by an explicit imaginary-time algorithm*, *Phys. Rev. E* **62**, 7438 (2000).

- [85] L. Lehtovaara, J. Toivanen, and J. Eloranta, *Solution of time-independent Schrödinger equation by the imaginary time propagation method*, [J. Comput. Phys.](#) **221**, 148 (2007).
- [86] M. M. Cerimele, M. L. Chiofalo, and F. Pistella, *Numerical solution of the stationary Gross–Pitaevskii equation: tests of a combined imaginary-time-marching technique with splitting*, [Nonlinear Anal. Theory Methods Appl.](#) **47**, 3345 (2001).
- [87] P. Muruganandam and S. K. Adhikari, *Fortran programs for the time-dependent Gross-Pitaevskii equation in a fully anisotropic trap*, [Comput. Phys. Commun.](#) **180**, 1888 (2009).
- [88] D. Vudragović, I. Vidanović, A. Balaž, P. Muruganandam, and S. K. Adhikari, *C Programs for solving the time-dependent Gross-Pitaevskii equation in a fully anisotropic trap*, [Comput. Phys. Commun.](#) **183**, 2021 (2012).
- [89] R. K. Kumar, Luis E. Young-S., D. Vudragović, A. Balaž, P. Muruganandam, and S. K. Adhikari, *Fortran and C programs for the time-dependent dipolar Gross-Pitaevskii equation in an anisotropic trap*, [Comput. Phys. Commun.](#) **195**, 117 (2015).
- [90] Luis E. Young-S., D. Vudragović, P. Muruganandam, S. K. Adhikari, and A. Balaž, *OpenMP Fortran and C programs for solving the time-dependent Gross-Pitaevskii equation in an anisotropic trap*, [Comput. Phys. Commun.](#) **204**, 209 (2016).
- [91] Luis E. Young-S., P. Muruganandam, S. K. Adhikari, V. Lončar, D. Vudragović, and A. Balaž, *OpenMP GNU and Intel Fortran programs for solving the time-dependent Gross-Pitaevskii equation*, [Comput. Phys. Commun.](#) **220**, 503 (2017).
- [92] B. Satarić, V. Slavnić, A. Belić, A. Balaž, P. Muruganandam, and S. K. Adhikari, *Hybrid OpenMP/MPI programs for solving the time-dependent Gross–Pitaevskii equation in a fully anisotropic trap*, [Comput. Phys. Commun.](#) **200**, 411 (2016).

- [93] V. Lončar, A. Balaž, A. Bogojević, S. Škrbić, P. Muruganandam, and S. K. Adhikari, *CUDA programs for solving the time-dependent dipolar Gross–Pitaevskii equation in an anisotropic trap*, *Comput. Phys. Commun.* **200**, 406 (2016).
- [94] V. Lončar, Luis E. Young-S., S. Škrbić, P. Muruganandam, S. K. Adhikari, and A. Balaž, *OpenMP, OpenMP/MPI, and CUDA/MPI C programs for solving the time-dependent dipolar Gross–Pitaevskii equation*, *Comput. Phys. Commun.* **209**, 190 (2016).
- [95] R. K. Kumar, V. Lončar, P. Muruganandam, S. K. Adhikari, and A. Balaž, *C and Fortran OpenMP programs for rotating Bose–Einstein condensates*, *Comput. Phys. Commun.* **240**, 74 (2019).
- [96] R. Achilles and A. Bonfiglioli, *The early proofs of the theorem of Campbell, Baker, Hausdorff, and Dynkin*, *A. Arch. Hist. Exact Sci.* **66**, 295 (2012).
- [97] F. Casas, A. Murua, and M. Nadinic, *Efficient computation of the Zassenhaus formula*, *Comput. Phys. Commun.* **183**, 2386 (2012).
- [98] M. Edwards and K. Burnett, *Numerical solution of the nonlinear Schrödinger equation for small samples of trapped neutral atoms*, *Phys. Rev. A* **51**, 1382 (1995).
- [99] S. Ronen, D. C. E. Bortolotti, and J. L. Bohn, *Bogoliubov modes of a dipolar condensate in a cylindrical trap*, *Phys. Rev. A* **74**, 013623 (2006).
- [100] G. M. Amdahl, *Validity of the Single Processor Approach to Achieving Large Scale Computing Capabilities*, *Spring Joint Computer Conference*, Atlantic City, New Jersey, 18-20 April 1967.
- [101] The HDF Group, *Hierarchical Data Format, version 5*, (1997-2019).

Biography of the author

Dušan Vudragović was born on 3 May 1980 in Sremska Mitrovica, Republic of Serbia. He completed his primary school education at the Elementary school “Dositej Obradović” in Putinci, and continued his education at the “Stevan Puzić” high school in Ruma. He started undergraduate studies in the field of applied physics and informatics at the Faculty of Physics, University of Belgrade in 1999. During the studies, he received scholarships from the Ministry of Science of the Republic of Serbia, and the Government of the Republic of Serbia, as well as the award for the best 1000 students in Serbia from the Norwegian Embassy in Belgrade. He graduated in 2005 with GPA 9.62/10. Dušan’s diploma thesis entitled “Measurement of the Effective Transverse Ion Beam Emission” was done under the supervision of Prof. Dr. Ivan Aničin.

From 2006 to 2008 he worked at CERN, Geneva within the framework of the FP6 projects SEE-GRID-2 (SEE-GRID eInfrastructure for regional eScience) and EGEE-II (Enabling Grids for E-science). He started PhD studies in the field of particle physics at the Faculty of Physics, University of Belgrade in 2012, and switched to the condensed matter physics in 2016 under the supervision of Dr. Antun Balaž.

Dušan Vudragović is employed at the Institute of Physics Belgrade as a research assistant at the Scientific Computing Laboratory of the National Center of Excellence for the Study of Complex Systems. He is a member of two national research projects: ON171017, led by Dr. Antun Balaž, and III43007, as part of the workpackage PP4 led by Dr. Aleksandar Bogojević. As a part of international cooperation, he was involved in several FP6, FP7, and Horizon 2020 projects. Currently, he is involved in two Horizon 2020 projects, SMARTCHAIN and NI4OS-Europe.

Dušan Vudragović has published 23 papers in peer-reviewed international journals and presented his results at various international conferences. The results of this thesis are published in 5 papers in leading international journals.

Изјава о ауторству

Име и презиме аутора - Душан Вудраговић

Број индекса – 2016/8020

Изјављујем

да је докторска дисертација под насловом

Faraday waves in ultracold dipolar Bose gases

(Фарадејеви таласи у ултрахладним диполним Бозе гасовима)

- резултат сопственог истраживачког рада;
- да дисертација у целини ни у деловима није била предложена за стицање друге дипломе према студијским програмима других високошколских установа;
- да су резултати коректно наведени и
- да нисам кршио/ла ауторска права и користио/ла интелектуалну својину других лица.

Потпис аутора

У Београду, 31. 08. 2019. год.

Душан Вудраговић

Изјава о истоветности штампане и електронске верзије докторског рада

Име и презиме аутора – **Душан Вудраговић**

Број индекса – **2016/8020**

Студијски програм - **Физика кондензованог стања**

Наслов рада - **Faraday waves in ultracold dipolar Bose gases (Фарадејеви таласи у ултрахладним диполним Бозе гасовима)**

Ментор - **др Антун Балаж**

Изјављујем да је штампана верзија мог докторског рада истоветна електронској верзији коју сам предао ради похрањења у **Дигиталном репозиторијуму Универзитета у Београду**.

Дозвољавам да се објаве моји лични подаци везани за добијање академског назива доктора наука, као што су име и презиме, година и место рођења и датум одбране рада.

Ови лични подаци могу се објавити на мрежним страницама дигиталне библиотеке, у електронском каталогу и у публикацијама Универзитета у Београду.

Потпис аутора

У Београду, 31. 08. 2019. год.



Изјава о коришћењу

Овлашћујем Универзитетску библиотеку „Светозар Марковић“ да у Дигитални репозиторијум Универзитета у Београду унесе моју докторску дисертацију под насловом:

Faraday waves in ultracold dipolar Bose gases (Фарадејеви таласи у ултрахладним диполним Бозе гасовима)

која је моје ауторско дело.

Дисертацију са свим прилозима предао/ла сам у електронском формату погодном за трајно архивирање.

Моју докторску дисертацију похрањену у Дигиталном репозиторијуму Универзитета у Београду и доступну у отвореном приступу могу да користе сви који поштују одредбе садржане у одабраном типу лиценце Креативне заједнице (Creative Commons) за коју сам се одлучио/ла.

1. Ауторство (CC BY)
2. Ауторство – некомерцијално (CC BY-NC)
3. Ауторство – некомерцијално – без прерада (CC BY-NC-ND)
4. Ауторство – некомерцијално – делити под истим условима (CC BY-NC-SA)
5. Ауторство – без прерада (CC BY-ND)
6. Ауторство – делити под истим условима (CC BY-SA)

(Молимо да заокружите само једну од шест понуђених лиценци.
Кратак опис лиценци је саставни део ове изјаве).

Потпис аутора

У Београду, 31. 08. 2019. год.

Зоран Вујковић

1. **Ауторство.** Дозвољаваате умножавање, дистрибуцију и јавно саопштавање дела, и прераде, ако се наведе име аутора на начин одређен од стране аутора или даваоца лиценце, чак и у комерцијалне сврхе. Ово је најслободнија од свих лиценци.

2. **Ауторство – некомерцијално.** Дозвољаваате умножавање, дистрибуцију и јавно саопштавање дела, и прераде, ако се наведе име аутора на начин одређен од стране аутора или даваоца лиценце. Ова лиценца не дозвољава комерцијалну употребу дела.

3. **Ауторство – некомерцијално – без прерада.** Дозвољаваате умножавање, дистрибуцију и јавно саопштавање дела, без промена, преобликовања или употребе дела у свом делу, ако се наведе име аутора на начин одређен од стране аутора или даваоца лиценце. Ова лиценца не дозвољава комерцијалну употребу дела. У односу на све остале лиценце, овом лиценцом се ограничава највећи обим права коришћења дела.

4. **Ауторство – некомерцијално – делити под истим условима.** Дозвољаваате умножавање, дистрибуцију и јавно саопштавање дела, и прераде, ако се наведе име аутора на начин одређен од стране аутора или даваоца лиценце и ако се прерада дистрибуира под истом или сличном лиценцом. Ова лиценца не дозвољава комерцијалну употребу дела и прерада.

5. **Ауторство – без прерада.** Дозвољаваате умножавање, дистрибуцију и јавно саопштавање дела, без промена, преобликовања или употребе дела у свом делу, ако се наведе име аутора на начин одређен од стране аутора или даваоца лиценце. Ова лиценца дозвољава комерцијалну употребу дела.

6. **Ауторство – делити под истим условима.** Дозвољаваате умножавање, дистрибуцију и јавно саопштавање дела, и прераде, ако се наведе име аутора на начин одређен од стране аутора или даваоца лиценце и ако се прерада дистрибуира под истом или сличном лиценцом. Ова лиценца дозвољава комерцијалну употребу дела и прерада. Слична је софтверским лиценцама, односно лиценцама отвореног кода.



На основу члана 29 Закона о општем управном поступку («Службени гласник РС» број 18/2016 и 95/2018), и члана 149 Статута Универзитета у Београду - Физичког факултета, по захтеву ДУШАНА ВУДРАГОВИЋА, мастер физичара, издаје се следеће

У В Е Р Е Њ Е

ДУШАН ВУДРАГОВИЋ, мастер физичар, дана 24. децембра 2019. године, одбранио је докторску дисертацију под називом

"FARADAY WAVES IN ULTRACOLD DIPOLAR BOSE GASES"
(Фарадејеви таласи у ултрахладним диполним Бозе гасовима)

пред Комисијом Универзитета у Београду - Физичког факултета и тиме испунио све услове за промоцију у ДОКТОРА НАУКА – ФИЗИЧКЕ НАУКЕ.

Уверење се издаје на лични захтев, а служи ради регулisaња права из радног односа и важи до промоције, односно добијања докторске дипломе.

Уверење је ослобођено плаћања таксе.



ДЕКАН ФИЗИЧКОГ ФАКУЛТЕТА

Проф. др Иван Белча